On the Dynamics of Magnetic Swimmers in Stokes Flow

Thèse N° 9551

Présentée le 30 août 2019

à la Faculté des sciences de base
Chaire d'analyse appliquée
Programme doctoral en mathématiques

pour l'obtention du grade de Docteur ès Sciences

par

Pauline Marie RÜEGG-REYMOND

Acceptée sur proposition du jury

Prof. F. Nobile, président du jury
Prof. J. Maddocks, Dr T. O. D. Lessinnes, directeurs de thèse
Prof. T. Powers, rapporteur
Prof. A. DeSimone, rapporteur
Prof. S. Sakar, rapporteur

2019

ÉCOLE POLYTECHNIQUE
FÉDÉRALE DE LAUSANNE

Acknowledgements

It is still uncommon, and it is a challenge, to raise a child while successfully conducting a PhD without needing extra time. Before anything else, I want to acknowledge that I was not alone on the child care and household chores front, and thank all the people who have been part of the team. Sharing housework equally would remain wishful thinking without a partner who actually commits to it: merci Jo d’avoir fait plus que ta part quand j’en avais besoin. I was never worried that my son would lack affection when I was less available emotionally: merci Maman et Béa d’avoir décidé de prendre autant de temps pour votre petit-fils alors que vous êtes toutes les deux actives professionnellement et que vous avez plein d’autres projet. Merci aux équipes de la Croq’cinelle et de la Chenille d’avoir fourni à Solal un environnement où il s’épanouit. Merci Lucinda d’être une vraie fée du logis. Merci à Guy et à toutes celles et tous ceux qui se sont occupés de Solal occasionnellement au pied levé.

I think I should acknowledge that every other person in my extended family holds a PhD. It has probably made it easier for me to go down the same road, if only because no one questioned this choice. Merci Papa pour tous tes conseils qui m’ont aidé à me frayer un chemin dans le monde académique.

Thanks to Prof. John Maddocks for trusting me. Merci Thomas de m’avoir écoutée, soutenue et conseillée tout au long de ce processus; c’est un plaisir de travailler avec toi. Merci Alex pour tout le temps que tu as passé au tableau noir à répondre à mes questions. Many thanks to Prof. A. DeSimone, Prof. F. Nobile, Prof. T. Powers and Prof. M. S. Sakar for having accepted to be members of the jury, and for your discerning remarks. This work also benefitted of interactions with Prof. A. Petruska and Prof. O. Gonzalez.

Merci Carine pour ton soutien moral et administratif, sans toi rien ne fonctionnerait. Thanks Suliana and Victor for your wise advice. Thanks to all my colleagues, et en particulier merci Alessandro d’avoir traversé les mêmes étapes que moi au même moment que moi.

Je n’arriverais pas à travailler efficacement sans moments de détente. Merci Jul’ et Zach, merci à tous mes amis et en particulier aux amateurs de pauses café. Finalement, merci Solal de m’avoir obligé à apprendre à gérer mon stress et d’être une source d’émerveillement constant.

Ce travail a été soutenu par le Fonds National Suisse (FNS) pour la recherche scientifique, projet 200021-156403.

Abstract

In the past decade, the engineering community has conceived, manufactured and tested micro-swimmers, i.e. microscopic devices which can be steered in their intended environment. Foreseen applications range from microsurgery and targeted drug delivery to environmental decontamination. This thesis presents a mathematical analysis of the dynamics of rigid magnetic swimmers in a Stokes flow driven by a steadily rotating external uniform magnetic field. The swimmer is assumed to be made of a permanent magnetic material and to be placed in a fluid that fills an infinite enveloping space. A specific swimmer is prescribed by its magnetic moment and mobility matrix. For a given swimmer, its dynamics depend on two parameters that can be changed during an experiment: the Mason number, related to the magnitude and angular speed of the magnetic field, and the conical angle between the magnetic field and its axis of rotation. As these two parameter vary, strikingly different regimes of response occur.

The swimmer's trajectory is entirely governed by its rotational dynamics: once its orientation dynamics are known, its position trajectory can be recovered. For neutrally buoyant swimmers, this work provides a complete classification of the steady states of the rotational dynamics, along with a study of non-steady solutions in the asymptotic limits of small and large Mason number, and small conical angle. Predicted out-of-equilibrium solutions are in good agreement with numerical simulations. Full swimmer trajectories corresponding to steady states and periodic solutions of the rotational dynamics are then recovered. Finally, the effect of buoyancy is taken into account, and the relative equilibria of swimmers with a different density than that of the fluid are determined when the axis of rotation of the magnetic field is aligned with gravity.

Résumé

Pendant ces dix dernières années, la communauté scientifique a conçu, fabriqué et produit des micro-nageurs, c'est-à-dire des dispositifs microscopiques qui peuvent être dirigés dans un environnement spécifique. Les applications prévues vont de la microchirurgie à la décontamination environnementale en passant par la médication ciblée . Cette thèse présente une analyse mathématique de la dynamique de nageurs rigides et magnétique dans un fluide de Stokes propulsés par un champ magnétique externe, uniforme dans l'espace et qui tourne à vitesse constante autour d'un axe de rotation. On suppose que le nageur est fait d'un aimant permanent et qu'il est placé dans un fluide qui remplit un espace infini l'entourant. Un nageur spécifique est prescrit par son moment magnétique et sa matrice de mobilité. La dynamique d'un nageur donné dépend de deux paramètres qui peuvent être modifiés pendant une expérience : le nombre de Mason, lié à l'amplitude et à la vitesse angulaire du champ magnétique, et l'angle conique entre le champ magnétique et son axe de rotation. Lorsque ces deux paramètres changent, des régimes de réponse remarquablement divers apparaissent.

La trajectoire d'un nageur est entièrement gouvernée par sa dynamique rotationnelle : une fois que la dynamique de son orientation est connue, la trajectoire de sa position peut être retrouvée. Pour des nageurs ayant une densité similaire à celle du fluide, ce travail fournit une classification complète des états d'équilibre de la dynamique rotationnelle, ainsi qu'une étude des solutions non stationnaires dans les limites asymptotiques d'un petit et d'un grand nombre de Mason et d'un petit angle conique. Les solutions non stationnaires prédites sont en accord remarquable avec des simulations numériques. Les trajectoires du nageur sont ensuite recouvrées pour les états d'équilibres et les solutions périodiques de la dynamique rotationnelle. Enfin, l'effet de la flottabilité est pris en compte et les équilibres relatifs des nageurs ayant une densité différente de celle du fluide sont déterminés dans le cas où l'axe de rotation du champ magnétique est aligné à la gravité.

Contents

List of Figures

1 Introduction

Analysing the motion of microorganisms in fluids at very low Reynolds number has long been an active research area [1, 2, 3, 4, 5]. More recently, engineers have set about building artificial swimmers imitating microorganisms in size and locomotion strategies. The foreseen applications range from microsurgery [6] to environmental decontamination [7, 8].

Some microorganisms (e.g. E. Coli) swim by rotating their flagella [9]. While the molecular rotary motor at the origin of this movement has not been imitated, several other ways to drive artificial micro-swimmers have been suggested. In particular, external magnetic fields have been proposed as a power source. The micro-swimmers that have inspired the present work are magnetised and are driven by a spatially uniform rotating magnetic field [10].

This thesis provides a mathematical analysis of the motion of a rigid body in Stokes flow under the action of a steadily rotating external magnetic field. It aims at a better understanding of the dynamics of a particular swimmer according to loading parameters that can be changed from one experiment to the next: specifically the Mason number a, and the conical angle ψ between the magnetic field and its axis of rotation (cf. fig. 1.1). The Mason number is a non-dimensional scale that is proportional to the angular velocity of the magnetic field α, and inversely proportional to the field magnitude.

The swimmer itself is characterised by its magnetic moment $\boldsymbol{m}$, which determines the response of the swimmer to the external magnetic field, and by its mobility matrix $\mathbb{M}$, that describes the loads exerted on the swimmer by the surrounding fluid. This work focuses on swimmers that consist of i) a rigid body made of a permanent magnetic material ii) immersed in an infinite space-filling fluid; accordingly, both $\boldsymbol{m}$ and $\mathbb{M}$ are constant in the body frame.

After a transient initial layer in time, the rotational dynamics of such swimmers decouples from the translational dynamics: knowing the orientation of the swimmer as it changes over time is sufficient to recover its entire trajectory. Accordingly, this work first examines the rotational dynamics, and then transfers the results to the overall swimmer motion. The analysis is also split between neutrally buoyant swimmers, which take up the most part of the presentation,

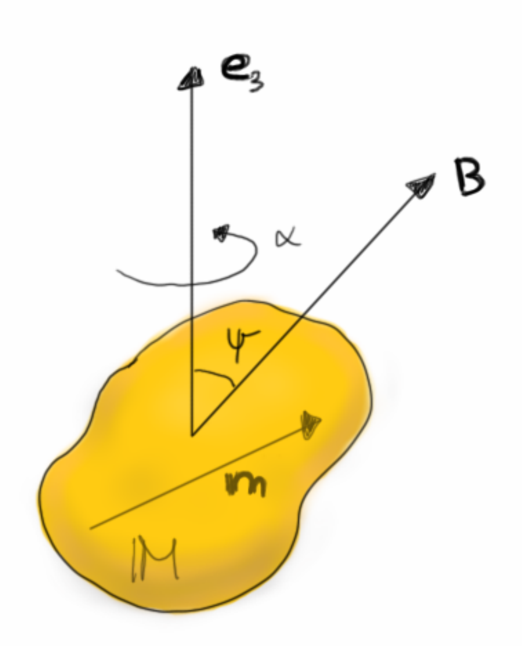

Figure 1.1 – **Sketch of the experimental setup**. A swimmer is characterised by its magnetic moment $\boldsymbol{m}$ and its mobility matrix $\mathbb{M}$, which we assume are prescribed constants in the body frame. This work explores the dependence of its dynamics on two experimental external loading parameters: the Mason number proportional to the angular velocity α of the rotating magnetic field $\boldsymbol{B}$ around an axis $\boldsymbol{e}_3$, and the (constant) conical angle ψ between the magnetic field and its axis of rotation.

and swimmers with a density higher than the fluid, which are considered in chapter 8.

The necessary background material is presented in chapter 2. First, the equations governing the motion of a rigid body in Stokes flow under the action of generic external loads are developed in a non-dimensional form. Prescribing the hydrodynamic loads requires computing the mobility matrix $\mathbb{M}$, that depends on the swimmer's shape. The theoretical part of this work assumes $\mathbb{M}$ as a given. The code used to compute it in various numerical examples was developed by Prof. O. Gonzalez and collaborators [11, 12, 13] and is discussed in chapter 2. The averaging method, which is used in chapter 5, is also introduced, and a review of the relevant literature regarding experimental and theoretical work on swimmers in Stokes flow is provided.

Chapter 3 introduces the specific system of equations studied in chapters 4-7, i.e. the equations governing the motion of a rigid permanent magnet in an unbounded fluid satisfying Stokes equation when the external loads are due to a spatially uniform steadily rotating magnetic field. The rotational dynamics is shown to decouple from the translational dynamics. Several equivalent formulations of the equations governing the rotational dynamics are presented, and the symmetries of the system are discussed.

Chapter 4 focuses on the steady states of the equations governing the rotational dynamics. It closely parallels the analysis done by Gonzalez et al. [14] for the case where the external loadings are due to buoyancy only. A complete classification of all steady states as a function of the Mason number a and conical angle ψ is presented. In particular, the set of all steady states is a locally two-dimensional surface in one-to-one correspondence with the cylinder $\mathbb{S}^1 \times [0, \pi]$ (where $\mathbb{S}^1$ is the unit circle). This parametrisation leads to the following result: at fixed a and ψ, the system generically admits either 0, 4 or 8 steady states. Furthermore, the extent of the set of steady states in the (a, ψ)-parameter plane is limited. A visualisation of the set of steady states is proposed, and their stability is computed. This allows the parameter plane to be partitioned into different regions according to the numbers of steady states and their stability and corresponding to different dynamical regimes. Phase portraits depicting the rotational dynamics in different parameter regimes are also presented.

Chapter 5 explores the unsteady rotational dynamics using asymptotic expansions [15] in three distinct limits: small Mason number, large Mason number, and small conical angle. The limit of asymptotically small Mason number corresponds either to a strong magnetic field, or a magnetic field rotating very slowly. It is shown that the rotational dynamics are then either in steady state, when the conical angle ψ is within some interval, or periodic when ψ is outside this interval. More precisely, in the periodic regime, the magnetic moment $\boldsymbol{m}$ tends to align with the magnetic field $\boldsymbol{B}$ at the zeroth order of the expansion. The first-order correction reveals that the body experiences a slow residual periodic rotation about its magnetic moment. The period is characterised as a function of the swimmer's material parameters and the conical angle ψ.

In the limit of asymptotically large Mason number, which is obtained for magnetic fields rotating very fast or magnetic fields of low magnitude, an averaging method [16] is used to obtain an effective equation called the guiding system. Its analysis shows that the magnetic moment $\boldsymbol{m}$ tends to align with the average magnetic field, which corresponds either to its axis of rotation $\boldsymbol{e}_3$ or to its opposite $-\boldsymbol{e}_3$. Higher order terms reveal a slow residual rotation of the body about the average field.

In the limit of asymptotically small conical angle, which corresponds to the magnetic fields being almost parallel or anti-parallel to its axis of rotation, the analysis reveals a continuous change between the two regimes of small and large Mason number: the magnetic moment $\boldsymbol{m}$ remains close to the magnetic field $\boldsymbol{B}$ at small Mason numbers, and close to its average at large Mason numbers. The analysis also allows a characterisation of the average position of the magnetic moment $\boldsymbol{m}$ with respect to the magnetic field, and the amplitude of the excursions of $\boldsymbol{m}$ away from its average position.

The theoretical results of chapters 4 and 5 are valid for swimmers of any shape and magnetic moment, but the example visualisations presented in chapter 4 are for two particular rigid swimmers that have the shape of a helical rod. Helical swimmers have been the focus of many experimental works, both in imitation of microorganisms with a helical flagellum, and because their good swimming abilities have been recognised [17, 18, 19]. Chapter 6 displays a gallery of examples, mostly of helical swimmers. In particular, the set of steady states corresponding to each swimmer is visualised as in chapter 4, and phase portraits of the rotational dynamics in several parameter regimes are shown. Then, the analytical predictions of chapter 5 are compared with numerical simulations. The agreement is very good in all three limits, and the predictions stay qualitatively representative of the dynamics even for parameter values beyond the expected scope of the asymptotic analyses.

Recovering the swimmer's trajectories from the rotational dynamics is carried out in chapter 7. Steady states of the rotational dynamics yield helical trajectories. Formulas for the pitch and radius of the resulting helical steady states are provided. When the radius vanishes, the trajectory becomes a straight line, and when the pitch vanishes, the trajectory becomes a circle. The conditions for these degenerate cases to occur are discussed. The axial velocity is also examined, and a method to optimally choose the magnetic moment direction for a swimmer of a given shape is proposed. Then, the trajectories of swimmers corresponding to periodic solutions of the rotational dynamics are studied using Fourier analysis, and an averaging procedure to obtain the effective displacement is introduced. It is shown that if the period p and the Mason number a satisfy $a\,p/2\pi \in \mathbb{Z}$, then the effective displacement is a linear function of time, and its direction depends on the initial orientation of the swimmer.

In chapters 3-7, the swimmer is assumed to be neutrally buoyant, so that the effect of buoyancy can be neglected. The subject of chapter 8 is the dynamics of swimmers that have a different density from the fluid – it is still assumed that the centres of buoyancy and mass coincide. We explicitly treat the case where the swimmer is heavier than the fluid. Again the rotational dynamics decouple. The steady states of the rotational dynamics are studied in the specific case where the axis of rotation of the magnetic field is aligned with gravity. Similarly to the neutrally buoyant case, the number of steady states is shown to be generically 0, 4 or 8 depending on the values of experimental parameters. The corresponding swimmer's trajectories are described, and optimisation of axial velocity is considered. Finally, the first order perturbation when the axis of rotation of the magnetic field is not exactly aligned with gravity is studied in order to quantify the deviation from a trajectory that corresponds to a steady state.

Chapter 9 contains a discussion of the results and outlook. In particular, various cases that have not been considered in this work are reviewed. For example swimmers evolving close to the tank wall or bottom rather than in infinite space, soft magnets rather than permanent magnets, and flexible swimmers rather than rigid bodies. Each of these alternative hypotheses, although leading to a system more difficult to study mathematically, is relevant from the point of view of experiment.

2 Background Material

When a rigid body, characterised by its mass M and inertia tensor I_{cm}, moves under the effect of external resultant force $\boldsymbol{f}$ and torque $\boldsymbol{\tau}$, its motion is described by curves $\boldsymbol{x} \in \mathbb{R}^3$ and $R \in \mathrm{SO}(3)$ that represent its position and orientation as functions of time. The tangents to these curves are the body linear velocity $\boldsymbol{v}$ and angular velocity $\boldsymbol{\omega}$. Furthermore, we note by $\boldsymbol{p}$ and $\boldsymbol{L}$ respectively the linear and angular momentum of the body. These quantities obey the equations:

$$\dot{\boldsymbol{x}} = \boldsymbol{v}\,, \tag{2.1a}$$

$$\boldsymbol{p} = M\,\boldsymbol{v}\,, \tag{2.1b}$$

$$\dot{\boldsymbol{p}} = \boldsymbol{f}\,, \tag{2.1c}$$

$$\dot{R} = [\boldsymbol{\omega}\times]\,R\,, \tag{2.1d}$$

$$\boldsymbol{L} = I_{\text{cm}}\,\boldsymbol{\omega}\,, \tag{2.1e}$$

$$\dot{\boldsymbol{L}} = \boldsymbol{\tau}\,, \tag{2.1f}$$

where for any $\boldsymbol{z} \in \mathbb{R}^3$, the notation $[\boldsymbol{z}\times]$ refers to the matrix

$$\boldsymbol{z} = \begin{bmatrix} 0 & -z_3 & z_2 \\ z_3 & 0 & -z_1 \\ -z_2 & z_1 & 0 \end{bmatrix}.$$

In this work, the resultant loads $\boldsymbol{f}$ and $\boldsymbol{\tau}$ arise from hydrodynamic drag, magnetism, and gravity, so that the balance of linear and angular momentum (2.1c, 2.1f) are respectively rewritten as

$$\dot{\boldsymbol{p}} = \boldsymbol{f}^{(d)} + \boldsymbol{f}^{(m)} + \boldsymbol{f}^{(g)}\,, \tag{2.2a}$$

$$\dot{\boldsymbol{L}} = \boldsymbol{\tau}^{(d)} + \boldsymbol{\tau}^{(m)} + \boldsymbol{\tau}^{(g)}\,, \tag{2.2b}$$

where the superscript (d) refers to drag, (m) to magnetism, and (g) to gravity. In the Stokes limit, the loads due to hydrodynamic drag satisfy

$$\begin{bmatrix} \boldsymbol{f}^{(d)} \\ \boldsymbol{\tau}^{(d)} \end{bmatrix} = -\mathbb{D} \begin{bmatrix} \boldsymbol{v} \\ \boldsymbol{\omega} \end{bmatrix}, \tag{2.3}$$

where $\mathbb{D}$ is a 6-by-6 symmetric positive-definite matrix, which will be referred to as the *drag matrix* [20]. The loads arising from magnetism are given by

$$\boldsymbol{f}^{(m)} = \nabla\left(\boldsymbol{m}\cdot\boldsymbol{B}\right), \quad (2.4a) \qquad \boldsymbol{\tau}^{(m)} = \boldsymbol{m}\times\boldsymbol{B}, \quad (2.4b)$$

where $\boldsymbol{m}$ is the magnetic moment of the body, and $\boldsymbol{B}$ is the magnetic induction field, which will be referred to as the magnetic field [21]. Writing the gravitational acceleration as the vector $-\boldsymbol{g}$, the loads due to gravity and buoyancy are

$$\boldsymbol{f}^{(g)} = \left(\rho_f - \rho_s\right) V \boldsymbol{g}, \quad (2.5a) \qquad \boldsymbol{\tau}^{(g)} = \rho_f V \boldsymbol{\Delta}\times\boldsymbol{g}, \quad (2.5b)$$

where ρ_s and ρ_f are the densities of the swimmer and fluid respectively, V is the volume of the body, and $\boldsymbol{\Delta}$ is the vector from the centre of mass of the rigid body to its centre of buoyancy, which is constant in the body frame [20].

The hydrodynamics load in Stokes flow leading to equations (2.3), and methods for computing the drag matrix $\mathbb{D}$, are discussed in section 2.1. In section 2.2, a detailed derivation of the scaling and non-dimensionalisation of equations (2.1) is carried out for a rigid body in a Stokes fluid filling an infinite space and under the action of generic external loads. In section 2.3, standard singular perturbation methods are used to obtain a zeroth-order approximation of the non-dimensional equations of motion valid on a "long" timescale. In section 2.4, specific external loads are considered (action of a rotating magnetic field (2.4) and effect of gravity and buoyancy (2.5)), and their relative importance is discussed. The equations obtained will be the starting point of the analysis carried out in subsequent chapters. This analysis will use in particular the averaging method that is summarised in section 2.5 [16]. A review of the relevant literature is provided in section 2.6.

2.1 Loads due to Hydrodynamic Drag in the Stokes Flow Limit

2.1.1 Swimming in Stokes Flow

The incompressible fluid will be assumed to follow Stokes equations

$$\begin{aligned} &\eta\, \Delta \boldsymbol{u} = \nabla p, \\ &\nabla\cdot\boldsymbol{u} = 0, \end{aligned} \tag{2.6}$$

where p is the pressure field and $\boldsymbol{u}$ the velocity field of the fluid, defined at all positions $\boldsymbol{x}$ within the fluid volume. This corresponds to the limit of Navier-Stokes equations for an incompressible fluid when the Reynolds number is asymptotically small. The Reynolds number Re is defined by

$$\mathrm{Re} = \frac{\rho_f\, v\, \ell}{\eta}, \tag{2.7}$$

where ρ_f is the fluid density, η its viscosity, v is a characteristic velocity for the particular problem considered, and ℓ a characteristic length. An asymptotically small Reynolds number is obtained either if the body is very small, or if it moves very slowly, or if the fluid is very viscous.

The mathematical study of swimming at the micro-scale was founded by G. I. Taylor and Edward Mills Purcell. Taylor came up with this idea as he was invited to look at bull spermatozoa through a microscope. He looked at the swimming micro-organisms through his mathematician's eyes, and his first paper investigating motion at low Reynolds number was published in 1951 [22]. In it, he investigates how sinusoidal travelling waves of a sheet can lead to displacement [1].

Purcell's understanding of motion in Stokes flow was expounded in a talk he gave in 1976 that became one of the most cited papers in the domain of motion at low Reynolds number [3]. In this paper, he translates into his own worldview the discovery made by Howard Berg that bacteria swim by rotating their flagellum [9]. His approach enabled him to state what he called the "Scallop theorem": at low Reynolds number, "time doesn't matter. The pattern of motion is the same, whether slow or fast, whether forward or backward in time" [3, p.5]. A scallop swims by opening its shell slowly, and closing it very fast, ejecting water. This wouldn't allow the scallop to have an overall motion at low Reynolds number: closing would make it reverse the path it followed when opening.

Understanding how a body moves in a fluid amounts to the same thing as understanding how the fluid moves around the body. If a body is completely immersed in fluid, and if the boundaries of the fluid domain are immobile (w.r.t an inertial lab frame) and far enough compared to its size, the fluid boundaries are assumed to be at infinity [20]. Suppose the body occupies a volume $\Omega \in \mathbb{R}^3$. Then the fluid is assumed to fill $\mathbb{R}^3 \backslash \Omega$. The fluid is assumed to satisfy Stokes equations (2.6), which, together with no-slip boundary conditions, give the system

$$\begin{aligned} \eta \Delta \boldsymbol{u} &= \nabla p && \text{in } \mathbb{R}^3 \backslash \Omega \\ \nabla \cdot \boldsymbol{u} &= 0 && \text{in } \mathbb{R}^3 \backslash \Omega \\ \boldsymbol{u} &= \boldsymbol{v} && \text{on } \partial\Omega \\ \boldsymbol{u}(\boldsymbol{x}, t) &\to 0 && \text{as } |\boldsymbol{x}| \to \infty, \end{aligned} \tag{2.8}$$

where $\boldsymbol{v}$ is the Eulerian velocity of the material point of the body situated at $\boldsymbol{x}$. The last line is here to account for the boundaries of the infinite immobile tank [20]. It can be shown that the solution to (2.8) is unique [23].

The fluid surrounding the body Ω exerts on it a hydrodynamic force given by

$$\boldsymbol{f}^{(d)} = \int_{\partial\Omega} \boldsymbol{\sigma}\, d\boldsymbol{S}, \tag{2.9}$$

and a hydrodynamic torque about a point $\boldsymbol{x}_0 \in \Omega$ given by

$$\boldsymbol{\tau}^{(d)} = \int_{\partial\Omega} [(\boldsymbol{x} - \boldsymbol{x}_0)\times]\, \boldsymbol{\sigma}\, d\boldsymbol{S}, \tag{2.10}$$

where $d\boldsymbol{S}$ is directed outwards from the body, and $\boldsymbol{\sigma}$ is the stress tensor, given for an incompressible Newtonian fluid by

$$\boldsymbol{\sigma} = -p\mathbf{I} + \eta\left(\nabla\boldsymbol{u} + \nabla\boldsymbol{u}^T\right). \tag{2.11}$$

For a rigid body Ω, the velocity $\boldsymbol{v}$ of any point in the body $\boldsymbol{x} \in \Omega$ is the velocity $\boldsymbol{v}_0$ of a particular point $\boldsymbol{x}_0 \in \Omega$ plus the velocity of $\boldsymbol{x}$ relative to $\boldsymbol{x}_0$ due to the change of orientation of the body, i.e.

$$\boldsymbol{v} = \boldsymbol{v}_0 + \boldsymbol{\omega}_0 \times (\boldsymbol{x} - \boldsymbol{x}_0), \tag{2.12}$$

where $\boldsymbol{\omega}_0$ is the angular velocity of the body relative to the point $\boldsymbol{x}_0$. Thus, the boundary condition on $\partial\Omega$ in (2.8) can be rewritten in terms of the linear and angular velocities $\boldsymbol{v}_0$ and $\boldsymbol{\omega}_0$, so that the system (2.8) becomes

$$\begin{aligned} \eta\,\Delta\boldsymbol{u} &= \nabla p && \text{in } \mathbb{R}^3\backslash\Omega \\ \nabla\cdot\boldsymbol{u} &= 0 && \text{in } \mathbb{R}^3\backslash\Omega \\ \boldsymbol{u} &= \boldsymbol{v}_0 + \boldsymbol{\omega}_0 \times (\boldsymbol{x} - \boldsymbol{x}_0) && \text{on } \partial\Omega \\ \boldsymbol{u}(\boldsymbol{x}, t) &\to 0 && \text{as } |\boldsymbol{x}| \to \infty. \end{aligned} \tag{2.13}$$

The linearity of this system implies that the hydrodynamic loads (2.9, 2.10) are linear in $\boldsymbol{v}_0$ and $\boldsymbol{\omega}_0$. In particular, there are matrices D_{11}, D_{12}, D_{21}, and D_{22}, obtained by integration over $\partial\Omega$ of tensors depending on Ω only through the choice of $\boldsymbol{x}_0$, such that

$$\boldsymbol{f}^{(d)} = -D_{11}\,\boldsymbol{v}_0 - D_{12}\,\boldsymbol{\omega}_0, \qquad \boldsymbol{\tau}^{(d)} = -D_{21}\,\boldsymbol{v}_0 - D_{22}\,\boldsymbol{\omega}_0.$$

The drag matrix is the 6-by-6 matrix

$$\mathbb{D} = \begin{bmatrix} D_{11} & D_{12} \\ D_{21} & D_{22} \end{bmatrix}. \tag{2.14}$$

The matrix $\mathbb{D}$ is constant in the body frame. It is symmetric and positive definite, which implies $D_{21} = D_{12}^T$, and D_{11} and D_{22} are also symmetric and positive definite (cf. [20] for a detailed derivation). The mobility matrix $\mathbb{M}$ is the inverse of the drag matrix $\mathbb{M} = \mathbb{D}^{-1}$.

In case the fluid domain is not assumed to be infinite, i.e. the fluid domain is $\Omega_f \subset \mathbb{R}^3$, where the inclusion is strict, the system (2.13) becomes

$$\begin{aligned} \eta\,\Delta \boldsymbol{u} &= \nabla p && \text{in } \Omega_f \backslash \Omega \\ \nabla \cdot \boldsymbol{u} &= 0 && \text{in } \Omega_f \backslash \Omega \\ \boldsymbol{u} &= \boldsymbol{v}_0 + \boldsymbol{\omega}_0 \times (\boldsymbol{x} - \boldsymbol{x}_0) && \text{on } \partial\Omega \\ \boldsymbol{u} &= 0 && \text{on } \partial\Omega_f\,. \end{aligned}$$

A difficulty arises because as the swimmer moves, the position of Ω with respect to Ω_f varies. The linearity of the system still enables the computation of a drag matrix $\mathbb{D}$ that determines the force and torque due to hydrodynamic drag in terms of the linear and angular velocities of the swimmer, but $\mathbb{D}$ is not constant in the body frame anymore. In many experiments in the Stokes regime, the body is close to one of the tank's walls. The fluid domain is then often modelled as the half-space $\{\boldsymbol{x} \in \mathbb{R}^3 : x_3 > 0\}$ [24].

A time-dependent domain also needs to be considered in case a flexible body is considered. By decomposing the body motion into shape change and overall motion, the linearity of Stokes equations can still be exploited to find a time-dependent drag matrix [25].

2.1.2 Computing The Stokes Flow Drag Matrix

Although analytical expressions for the matrices D_{ij} in (2.14) as integrals over $\partial\Omega$ can be obtained [20], computing them for complex geometries is not straightforward. Obtaining good numerical approximations is of itself a research area [2, 26, 27, 28, 29, 30, 24].

One of these methods was developed by Prof. O. Gonzalez and collaborators [11, 12, 13] and he was kind enough to share his numerical code with us. The code is designed to solve the dynamics for helical rods of circular cross-section although the method can be applied for body of generic shapes. Gonzalez' approach and the advantages of his method are outlined in the following.

It will later become apparent that the off-diagonal block D_{12} plays a key role in achieving high linear velocity in the setting considered in this work. In particular, body geometries for which this block is zero will not be able to convert the magnetic torque into linear motion. Chiral bodies[31] have the desired feature of a non-zero coupling block D_{12}, and experimental evidence has highlighted that helical rods are good swimmers. Accordingly, these are the examples this work mainly focuses on. Other methods that can be used to compute the drag matrix of a helical swimmer are presented to conclude this section.

Boundary Integral Formulation of Exterior Stokes Flow

The main results of [11, 12, 13] are summarised here.

Solutions of the non-dimensionalised Stokes equation

$$\begin{aligned} \mathit{\Delta}\boldsymbol{u} &= \nabla p && \text{in } \mathbb{R}^3\backslash\{\boldsymbol{x}_0\} \\ \nabla\cdot\boldsymbol{u} &= 0 && \text{in } \mathbb{R}^3\backslash\{\boldsymbol{x}_0\} \\ \boldsymbol{u}(\boldsymbol{x}) &\to 0 && \text{as } |\boldsymbol{x}|\to\infty \end{aligned} \tag{2.15}$$

defined everywhere except at a singularity $\boldsymbol{x}_0$ are called singular solutions. Several singular solutions are known analytically: the point-source

$$\boldsymbol{u}_{\text{ps}}(\boldsymbol{x},\boldsymbol{x}_0) = \frac{\boldsymbol{x}-\boldsymbol{x}_0}{|\boldsymbol{x}-\boldsymbol{x}_0|^3}, \qquad p_{\text{ps}} \equiv 0;$$

the point-source dipole defined with an arbitrary vector $\boldsymbol{z}$ as

$$\boldsymbol{u}_{\text{psd}}^{(\boldsymbol{z})}(\boldsymbol{x},\boldsymbol{x}_0) = \left(-\frac{1}{|\boldsymbol{x}-\boldsymbol{x}_0|^3}\mathbf{I} + \frac{3}{|\boldsymbol{x}-\boldsymbol{x}_0|^5}(\boldsymbol{x}-\boldsymbol{x}_0)\otimes(\boldsymbol{x}-\boldsymbol{x}_0)\right)\boldsymbol{z}, \qquad p_{\text{psd}} \equiv 0;$$

the stokeslet (or point-force) defined with an arbitrary vector $\boldsymbol{z}$ as

$$\begin{aligned} \boldsymbol{u}_{\text{sto}}^{(\boldsymbol{z})}(\boldsymbol{x},\boldsymbol{x}_0) &= \left(\frac{1}{|\boldsymbol{x}-\boldsymbol{x}_0|}\mathbf{I} + \frac{1}{|\boldsymbol{x}-\boldsymbol{x}_0|^3}(\boldsymbol{x}-\boldsymbol{x}_0)\otimes(\boldsymbol{x}-\boldsymbol{x}_0)\right)\boldsymbol{z}, \\ p_{\text{sto}}^{(\boldsymbol{z})}(\boldsymbol{x},\boldsymbol{x}_0) &= \frac{2}{|\boldsymbol{x}-\boldsymbol{x}_0|^3}(\boldsymbol{x}-\boldsymbol{x}_0)\cdot\boldsymbol{z}; \end{aligned}$$

the stresslet defined for an arbitrary tensor $\boldsymbol{Z}$ of dimension 2 as

$$\begin{aligned} \boldsymbol{u}_{\text{str}}^{(\boldsymbol{Z})}(\boldsymbol{x},\boldsymbol{x}_0) &= \left(\left(\frac{3}{|\boldsymbol{x}-\boldsymbol{x}_0|^5}(\boldsymbol{x}-\boldsymbol{x}_0)\otimes(\boldsymbol{x}-\boldsymbol{x}_0)\right):\boldsymbol{Z}\right)(\boldsymbol{x}-\boldsymbol{x}_0) \\ p_{\text{str}}^{(\boldsymbol{Z})}(\boldsymbol{x},\boldsymbol{x}_0) &= \left(-\frac{2}{|\boldsymbol{x}-\boldsymbol{x}_0|^3}\mathbf{I} + \frac{6}{|\boldsymbol{x}-\boldsymbol{x}_0|^5}(\boldsymbol{x}-\boldsymbol{x}_0)\otimes(\boldsymbol{x}-\boldsymbol{x}_0)\right):\boldsymbol{Z}, \end{aligned}$$

where the colon denotes the inner product for tensors; the rotlet (or couplet) defined for an arbitrary vector $\boldsymbol{z}$ as

$$\boldsymbol{u}_{\text{r}}^{(\boldsymbol{z})}(\boldsymbol{x},\boldsymbol{x}_0) = \frac{1}{|\boldsymbol{x}-\boldsymbol{x}_0|^3}\boldsymbol{z}\times(\boldsymbol{x}-\boldsymbol{x}_0) \qquad p_{\text{r}} \equiv 0;$$

and the point-force dipole defined for an arbitrary vector $\boldsymbol{z}$ and an arbitrary symmetric tensor $\boldsymbol{Z}$ of dimension 2 as

$$\boldsymbol{u}_{\text{pfd}}^{(\boldsymbol{z},\boldsymbol{Z})}(\boldsymbol{x},\boldsymbol{x}_0) = -\boldsymbol{u}_{\text{ps}}(\boldsymbol{x},\boldsymbol{x}_0)\,\text{Tr}\boldsymbol{Z} + \boldsymbol{u}_{\text{str}}^{(\boldsymbol{Z})}(\boldsymbol{x},\boldsymbol{x}_0) + \boldsymbol{u}_{\text{rot}}^{(\boldsymbol{z})}(\boldsymbol{x},\boldsymbol{x}_0), \quad p_{\text{pfd}}^{(\boldsymbol{z},\boldsymbol{Z})}(\boldsymbol{x},\boldsymbol{x}_0) = p_{\text{str}}^{(\boldsymbol{Z})}(\boldsymbol{x},\boldsymbol{x}_0).$$

A standard approach is to compute a solution valid around body $\mathit{\Omega}$, i.e. in $\mathbb{R}^3\backslash\mathit{\Omega}$, as a linear combination of singular solutions with singularities placed on the body's boundary $\partial\mathit{\Omega}$. This method yields a solution defined as

$$
\begin{aligned}
\boldsymbol{u}(\boldsymbol{x}) &= \int_{\partial\Omega} \boldsymbol{u}_s(\boldsymbol{x},\boldsymbol{x}_0)\,\mu(\boldsymbol{x}_0)\,dS_0 \\
p(\boldsymbol{x}) &= \int_{\partial\Omega} p_s(\boldsymbol{x},\boldsymbol{x}_0)\,\mu(\boldsymbol{x}_0)\,dS_0\,,
\end{aligned}
\tag{2.16}
$$

where $(\boldsymbol{u}_s(\boldsymbol{x},\boldsymbol{x}_0), p(\boldsymbol{x},\boldsymbol{x}_0))$ is a singular solution satisfying (2.15) with a singularity at $\boldsymbol{x}_0$, μ is a density defined on the surface $\partial\Omega$, and dS_0 represents surface integration with respect to the singularities $\boldsymbol{x}_0$. The type of singular solutions $(\boldsymbol{u}_s, p_s)$ is set in advance, and the problem is then to find a density μ such that the solution (2.16) satisfies the boundary condition (cf. eq. (2.8))

$$
\boldsymbol{u} = \boldsymbol{v} \quad \text{on } \partial\Omega\,.
$$

Two solutions of the form (2.16) are commonly used: the single-layer potential, based on stokeslets, and the double-layer potential, based on stresslets. Each of them has its advantages, but neither is well-suited for numerical integration on its own: discretisation of the integral equations for numerical integration yields a system with an unbounded condition number (numerical instability) in the case of the single-layer potential, and a rank-deficient system (incompleteness) in the case of the double-layer potential. In addition, both solutions have discontinuities at the boundary $\partial\Omega$ of the body.

A way to overcome these restrictions is to use linear combinations of both potentials, sometimes along with other classical singular solutions. Gonzalez [11] proposed such a combination that has all the desired properties for numerical integration: it is stable, complete, and has no singularities on the boundary $\partial\Omega$. Crucially, the single-layer potential is computed using singularities inside the body instead of singularities on the body's boundary. The single-layer potential is obtained by integration on a surface parallel to $\partial\Omega$ and offset towards the body's interior by a small distance ϕ, and is combined with a double-layer potential obtained by integration on $\partial\Omega$ as usual. Even though two surfaces are used, the relation between the two allows to use only one density μ. The equation that μ should satisfy can be written in the form

$$
\int_{\partial\Omega} K(\boldsymbol{x},\boldsymbol{x}_0)\,\mu(\boldsymbol{x}_0)\,dS_0 + c\,\mu(\boldsymbol{x}_0) = \boldsymbol{v}(\boldsymbol{x}) \quad \text{for } \boldsymbol{x} \in \partial\Omega\,. \tag{2.17}
$$

A remark here: $\mu(\boldsymbol{x}) \in \mathbb{R}^3$, which was not highlighted until now to avoid confusion. This is in agreement with the fact that $\boldsymbol{v}$ is three-dimensional. To be compatible with this, the singular solutions $\boldsymbol{u}_s$ and p_s in equation (2.16) need to be a 3-by-3 and a 3-by-1 matrix respectively. In fact, the products $\boldsymbol{u}_s\,\mu$ and $p_s\,\mu$ can be thought of as linear combinations of three singular solutions to (2.15) for a given singularity. Gonzalez proves the existence and uniqueness of a continuous density μ satisfying this equation for a continuous boundary condition $\boldsymbol{v}$ on a sufficiently smooth surface $\partial\Omega$ [11].

Equations of the form (2.17) are known as Fredholm inhomogeneous equations of the second type. They can be solved numerically by using Nyström approximations [12, 13].

As singularities are chosen on a surface offset from the body's boundary by a distance ϕ towards the inside of the body, the maximal curvature $\kappa_{\max} = 1/r$ on the surface gives a maximal offset distance $\phi_{\max} = r$. For bodies with a slender rod-like shape of circular cross-section, this maximal offset distance is given by the rod radius, making the proposed formulation a natural one. Another parameter $0 \leq \theta \leq 1$ describes the relative weights of single-layer and double-layer potential in the combination used to obtain (2.17). The results are shown to be independent of the choice of parameters ϕ and θ, which can therefore by chosen for numerical convenience. Numerical experiments by Li and Gonzalez [12] on ellipsoids, tori, straight and helical rods of circular cross-sections show that their numerical scheme is extremely well-conditioned for a wide range of parameters, i.e. $1/8 \leq \phi/\phi_{\max} \leq 1/2$ and $1/3 \leq \theta \leq 2/3$ with low sensitivity to the mesh size chosen to discretise the surface, and that very good convergence rates are obtained for $\phi = \phi_{\max}/2$ and $\theta = 1/2$.

The code Gonzalez supplied was set up to compute hydrodynamic force and torque on a helical rod of circular cross-section with surrounding fluid assumed to fill the entire space, for boundary conditions corresponding to unit linear or angular velocities in one of the three body-frame directions, with respect to a chosen point in the body frame. To compute the corresponding drag matrices, we modified the code in order to compute in parallel the forces and torque for all six unit boundary conditions and then assembled them into a 6-by-6 matrix. The drag matrices were computed with respect to the centre of mass, obtained geometrically assuming that the body is homogeneous.

Drag matrix of a helical swimmer

Other methods have been used to compute the drag matrix of a helix. Liu et al [30] developed a method based on boundary integrals. Their driving idea is that for long helices translating in the direction of the helical axis, or rotating with respect to it, the loads exerted on all cross-sections of the helical rod can be obtained straightforwardly from the loads on one particular cross-section.

A method commonly used for rod-like bodies is resistive force theory [32, 2]. The assumption underlying it is that the linearity between loads and velocities (2.3) is also verified locally. The loads acting on a cross-section of the rod are decomposed in components tangential and normal to the rod centreline, and drag coefficients are given linking these loads components to analogue components of the velocities. This allows to obtain a closed-form expression of the total drag, which makes it very useful in many practical cases, in particular when deformation of the rod is considered [33]. However, its accuracy is limited by the fact that drag induced by self-interactions of the body are not taken into account [34]. Resistive force theory coefficients for helical rods can be found in [35, 36].

Slender-body theory [37, 2, 26] is yet another method for computing hydrodynamic drag of a rod-like body, closer in spirit to the boundary integral methods discussed before. In this method, the singularities are distributed along the centreline of the rod. The solution obtained is exact in the limit of a very small cross-sectional radius compared to the total arc-length of the rod.

Rodenborn et al. [38] have carried out comparisons between experiments at low Reynolds number with macro-scale helical swimmers in a viscous fluid and numerical results obtained using resistive force theories by Gray and Handcock [32] and Lighthill [2], slender-body theories by Lighthill [2] and Johnson [26], regularised stokeslet – which is also a boundary-integral method [28, 29] – and the method of Gonzalez [11, 12]. They show good agreement between the experiment, slender-body theories, regularised stokeslet, and Gonzalez' method for a wide range of helix pitches and arc-length, whereas resistive force theories are comparatively inaccurate for long helices and small pitches – which is to be expected since resistive force theories don't take into account interactions between different parts of the rod.

Another comparison between experiment with helical swimmers, the same two versions of resistive force theories and slender-body theories, and the authors' own boundary-element method was realised by Liu et al. [30] with similar conclusions. Predictions from resistive force theories were taken in the limit of asymptotically large ratio of rod radius to rod length, and they also exhibit only qualitative agreement with experiment and other numerical methods; the error is especially large for small pitches. Slender-body theories and the original method presented in [30] are in good agreement with experiments, which were done with macroscopic rigid helical rods in viscous fluids: the helical rod was immersed vertically in the fluid, and the upper end was attached to a motor rotating it at constant angular speed [39].

2.2 Scaling and Non-Dimensionalisation of the Equations of Motion for a Rigid Body in Stokes Flow with Generic External Loads

2.2.1 Body Frame Expressions of the Equations Governing Rigid Body Motion in Stokes Flow

The motion of a rigid body in Stokes flow is described in the lab frame by (2.1), where we can split

$$\boldsymbol{f} = \boldsymbol{f}^{(d)} + \boldsymbol{f}^{(\text{ext})}, \qquad (2.18a) \qquad\qquad \boldsymbol{\tau} = \boldsymbol{\tau}^{(d)} + \boldsymbol{\tau}^{(\text{ext})}, \qquad (2.18b)$$

with

$$\begin{bmatrix} \boldsymbol{f}^{(d)} \\ \boldsymbol{\tau}^{(d)} \end{bmatrix} = -\mathbb{D} \begin{bmatrix} \boldsymbol{v} \\ \boldsymbol{\omega} \end{bmatrix}. \qquad (2.3)$$

The lab frame is given by fixed axes $\boldsymbol{e}_j$, $j = 1, 2, 3$. The body frame is given by axes $\boldsymbol{d}_j$ defined by the columns of the orientation matrix R as

$$\boldsymbol{d}_1 = R\begin{bmatrix}1\\0\\0\end{bmatrix}, \qquad \boldsymbol{d}_2 = R\begin{bmatrix}0\\1\\0\end{bmatrix}, \qquad \boldsymbol{d}_3 = R\begin{bmatrix}0\\0\\1\end{bmatrix}.$$

For a vector $\boldsymbol{z} \in \mathbb{R}^3$, the sans-serif notation $\boldsymbol{\mathsf{z}}$ represents the triple of body frame components, i.e.

$$\boldsymbol{\mathsf{z}} = \begin{bmatrix}\mathsf{z}_1\\ \mathsf{z}_2\\ \mathsf{z}_3\end{bmatrix},$$

where $\mathsf{z}_j = \boldsymbol{z} \cdot \boldsymbol{d}_j$, while the notation $\boldsymbol{z}$ used until now represents the lab frame components. For vectors denoted by greek letters, upright font is used to denote body frame components in contrast to italic font used for lab frame components. Note that

$$\boldsymbol{\mathsf{e}}_1 = R^T\begin{bmatrix}1\\0\\0\end{bmatrix}, \qquad \boldsymbol{\mathsf{e}}_2 = R^T\begin{bmatrix}0\\1\\0\end{bmatrix}, \qquad \boldsymbol{\mathsf{e}}_3 = R^T\begin{bmatrix}0\\0\\1\end{bmatrix}. \tag{2.19}$$

The equations of rigid body motion are rewritten in the body frame as

$$\dot{\boldsymbol{x}} = R^T\,\boldsymbol{\mathsf{v}} \tag{2.20a}$$

$$\boldsymbol{\mathsf{p}} = M\boldsymbol{\mathsf{v}} \tag{2.20b}$$

$$\dot{\boldsymbol{\mathsf{p}}} + \boldsymbol{\upomega} \times \boldsymbol{\mathsf{p}} = \boldsymbol{\mathsf{f}} \tag{2.20c}$$

$$\dot{R} = R\,[\boldsymbol{\upomega}\times] \tag{2.20d}$$

$$\boldsymbol{\mathsf{L}} = \boldsymbol{\mathsf{I}}_{\mathrm{cm}}\,\boldsymbol{\upomega} \tag{2.20e}$$

$$\dot{\boldsymbol{\mathsf{L}}} + \boldsymbol{\upomega} \times \boldsymbol{\mathsf{L}} = \boldsymbol{\uptau}, \tag{2.20f}$$

where $\boldsymbol{\mathsf{I}}_{\mathrm{cm}}$ is a constant matrix.

The drag matrix $\mathbb{D}$ depends only on the fluid viscosity and the shape of the swimmer and fluid domain. For rigid swimmers in an infinite space, $\mathbb{D}$ is constant in the body frame. Substituting their body frame expression in (2.20c, 2.20f) yields

$$\begin{aligned}\dot{\boldsymbol{\mathsf{p}}} + \boldsymbol{\upomega} \times \boldsymbol{\mathsf{p}} &= -\,\mathsf{D}_{11}\boldsymbol{\mathsf{v}} - \mathsf{D}_{12}\boldsymbol{\upomega} + \boldsymbol{\mathsf{f}}^{(\mathrm{ext})}\\ \dot{\boldsymbol{\mathsf{L}}} + \boldsymbol{\upomega} \times \boldsymbol{\mathsf{L}} &= -\,\mathsf{D}_{12}^T\boldsymbol{\mathsf{v}} - \mathsf{D}_{22}\boldsymbol{\upomega} + \boldsymbol{\uptau}^{(\mathrm{ext})},\end{aligned} \tag{2.21}$$

where the 3-by-3 blocks D_{ij} of $\mathbb{D}$ are constant, and $\boldsymbol{\mathsf{f}}^{(\mathrm{ext})}$ and $\boldsymbol{\uptau}^{(\mathrm{ext})}$ are the body frame components of the resultant force and torque exerted on the micro-swimmer besides hydrodynamics drag.

2.2.2 Non-Dimensionalisation and Scaling

This section is focused on the scaling and non-dimensionalisation of (2.21), without assuming any specific external load. It follows the treatment carried out in [14] in the specific case where the external loads are due to gravity and buoyancy.

The swimmer, i.e. the rigid body whose dynamics are studied, provides two relevant scales: a characteristic length ℓ and its mass M. Another two scales come from the liquid in which the body moves: the dynamic viscosity of the fluid η, and its mass density ρ_f. One last scale pertains to the external loads: the magnitude N of the applied force – note that if the external loads arise from several sources, one may choose the largest one for a typical magnitude; in particular, if the largest external load arises from applied torque, N is chosen such that $N\ell$ is the magnitude of that torque.

The external loads can be scaled as

$$\mathbf{f}^{(\mathrm{ext})} = N\overline{\mathbf{f}}^{(\mathrm{ext})}, \qquad\qquad \boldsymbol{\tau}^{(\mathrm{ext})} = \ell N \overline{\boldsymbol{\tau}}^{(\mathrm{ext})},$$

and at least one of $\overline{\mathbf{f}}^{(\mathrm{ext})}$, $\overline{\boldsymbol{\tau}}^{(\mathrm{ext})}$ is of order 1. The drag matrix $\mathbb{D}$ can be scaled as [20, 14]

$$\mathsf{D}_{11} = \ell\eta\overline{\mathsf{D}}_{11}, \qquad \mathsf{D}_{12} = \ell^2\eta\overline{\mathsf{D}}_{12}, \qquad \mathsf{D}_{22} = \ell^3\eta\overline{\mathsf{D}}_{22}. \tag{2.22}$$

Where $\overline{\mathsf{D}}_{11}$ and $\overline{\mathsf{D}}_{22}$ are expected to be approximately of order 1, but the magnitude of $\overline{\mathsf{D}}_{12}$ is highly dependent on the body geometry as discussed in section 2.1.

A timescale – or equivalently a velocity scale – now needs to be chosen. The scaling

$$\mathbf{v} = \frac{N}{\ell\eta}\overline{\mathbf{v}}, \qquad\qquad \boldsymbol{\omega} = \frac{N}{\ell^2\eta}\overline{\boldsymbol{\omega}}$$

ensures that if the non-dimensional loads $\overline{\mathbf{f}}$, $\overline{\boldsymbol{\tau}}$, drag components $\overline{\mathsf{D}}_{ij}$, and velocities $\overline{\mathbf{v}}$, $\overline{\boldsymbol{\omega}}$ are all of order one, the hydrodynamic drag and external loads may balance one another. Then, to ensure that the velocity scale $N/(\ell\eta)$ corresponds to ℓ/t_c, where t_c is the characteristic timescale for the problem, we set

$$t_c = \frac{\ell^2\eta}{N},$$

and scale time as $t = t_c\overline{t}$. Finally, the linear and angular momenta are scaled as

$$\mathbf{p} = \frac{M\ell}{t_c}\overline{\mathbf{p}} = \frac{MN}{\ell\eta}\overline{\mathbf{p}}, \qquad\qquad \mathbf{L} = \frac{M\ell^2}{t_c}\overline{\mathbf{L}} = \frac{MN}{\eta}\overline{\mathbf{L}}.$$

In particular, relations (2.20b, 2.20e) between momenta and velocities imply

$$\overline{\mathbf{p}} = \overline{\mathbf{v}}, \qquad\qquad \overline{\mathbf{L}} = \frac{1}{\ell^2 M}\mathsf{I}_{\mathrm{cm}}\overline{\boldsymbol{\omega}} =: \overline{\mathsf{I}_{\mathrm{cm}}}\,\overline{\boldsymbol{\omega}}. \tag{2.23}$$

Gathering all scaled quantities, equation (2.21) becomes

$$\begin{aligned}
\frac{M\ell}{t_c^2}\left(\dot{\overline{\mathbf{v}}} + \overline{\boldsymbol{\omega}}\times\overline{\mathbf{v}}\right) &= N\left(-\overline{\mathsf{D}}_{11}\overline{\mathbf{v}} - \overline{\mathsf{D}}_{12}\overline{\boldsymbol{\omega}} + \overline{\mathbf{f}}^{(\mathrm{ext})}\right)\\
\frac{M\ell^2}{t_c^2}\left(\dot{\overline{\mathbf{L}}} + \overline{\boldsymbol{\omega}}\times\overline{\mathbf{L}}\right) &= \ell N\left(-\overline{\mathsf{D}}_{12}^T\overline{\mathbf{v}} - \overline{\mathsf{D}}_{22}\overline{\boldsymbol{\omega}} + \overline{\boldsymbol{\tau}}^{(\mathrm{ext})}\right),
\end{aligned}$$

or equivalently

$$\begin{aligned}\frac{M}{t_c\,\ell\,\eta}\left(\dot{\bar{\mathbf{v}}}+\bar{\boldsymbol{\omega}}\times\bar{\mathbf{v}}\right)&=-\bar{\mathsf{D}}_{11}\,\bar{\mathbf{v}}-\bar{\mathsf{D}}_{12}\,\bar{\boldsymbol{\omega}}+\bar{\mathbf{f}}^{(\text{ext})}\\ \frac{M}{t_c\,\ell\,\eta}\left(\dot{\bar{\mathbf{L}}}+\bar{\boldsymbol{\omega}}\times\bar{\mathbf{L}}\right)&=-\bar{\mathsf{D}}_{12}^{T}\,\bar{\mathbf{v}}-\bar{\mathsf{D}}_{22}\,\bar{\boldsymbol{\omega}}+\bar{\boldsymbol{\tau}}^{(\text{ext})}\,.\end{aligned}\tag{2.24}$$

The only assumption so far is that the Reynolds number Re $\ll 1$. Recall that

$$\text{Re}=\frac{\rho_f\,v\,\ell}{\eta}\,,\tag{2.7}$$

where v is a characteristic speed: here $v=\ell/t_c$. Setting V to be the volume of the swimmer, and ρ_s to be its mass density, the coefficient $M/(t_c\,\ell\,\eta)$ appearing in equation (2.24) can be rewritten as

$$\frac{M}{t_c\,\ell\,\eta}=\frac{\rho_s V}{t_c\,\ell\,\eta}=\frac{\rho_s}{\rho_f}\,\frac{V}{\ell^3}\,\frac{\rho_f\,\ell^2}{t_c\,\eta}=\frac{\rho_s}{\rho_f}\,\frac{V}{\ell^3}\text{Re}\,.$$

Defining

$$\varepsilon=\frac{V}{\ell^3}\text{Re}\,,\qquad\qquad \varepsilon_g=\frac{\rho_f}{\rho_s}-1\,,$$

equation (2.24) is rewritten as

$$\begin{aligned}\frac{\varepsilon}{1+\varepsilon_g}\left(\dot{\bar{\mathbf{v}}}+\bar{\boldsymbol{\omega}}\times\bar{\mathbf{v}}\right)&=-\left(\bar{\mathsf{D}}_{11}\bar{\mathbf{v}}+\bar{\mathsf{D}}_{12}\bar{\boldsymbol{\omega}}\right)+\bar{\mathbf{f}}^{(\text{ext})}\\ \frac{\varepsilon}{1+\varepsilon_g}\left(\dot{\bar{\mathbf{L}}}+\bar{\boldsymbol{\omega}}\times\bar{\mathbf{L}}\right)&=-\left(\bar{\mathsf{D}}_{12}^{T}\bar{\mathbf{v}}+\bar{\mathsf{D}}_{22}\bar{\boldsymbol{\omega}}\right)+\bar{\boldsymbol{\tau}}^{(\text{ext})}\,.\end{aligned}\tag{2.25}$$

2.3 Outer Expansion

The Stokes flow limit implies $\varepsilon\to 0$. In this section, we make use of this fact to approximate (2.25) by a simpler equation valid for $t\gg\varepsilon$.

A standard result used by several authors (cf. section 2.6.2) is that the linear and angular velocities can be approximated for large times as the solutions to the system

$$\begin{aligned}\mathbf{0}&=-\left(\bar{\mathsf{D}}_{11}\bar{\mathbf{v}}+\bar{\mathsf{D}}_{12}\bar{\boldsymbol{\omega}}\right)+\bar{\mathbf{f}}^{(\text{ext})}\\ \mathbf{0}&=-\left(\bar{\mathsf{D}}_{12}^{T}\bar{\mathbf{v}}+\bar{\mathsf{D}}_{22}\bar{\boldsymbol{\omega}}\right)+\bar{\boldsymbol{\tau}}^{(\text{ext})}\,,\end{aligned}\tag{2.26}$$

which corresponds to the limit $\varepsilon=0$ of equation (2.25). A derivation of this result is proposed in this section. Standard singular perturbation techniques [15] are used to find a uniform leading order solution to (2.25), with ε_g bounded away from -1 and in the limit $\varepsilon\to 0$. This is a slight generalisation of the treatment in [14]. We are unaware of it being already described elsewhere.

Note that the limit $\varepsilon \to 0$ could also be satisfied without $\mathrm{Re} \to 0$, in a thin rod for example. However, hydrodynamic loads defined by equation (2.3) require $\mathrm{Re} \ll 1$ to be valid, and therefore so do equations (2.25).

Note that ε_g is defined such that if the external loads arise solely from gravity and buoyancy, the body sinks if $\varepsilon_g < 0$, floats if $\varepsilon_g > 0$ and is neutrally buoyant if $\varepsilon_g = 0$. In principle, the limit $\varepsilon_g \to -1$ could be studied, and the inertial effects would then need to be taken into account. In practice however, even for swimmers made of a metallic alloy, i.e. swimmers that have a high density compared to the density of the fluid, the order of magnitude of the swimmer's density ρ_s will not exceed about $10\rho_f$, so that $1+\varepsilon_g$ is of order 10^{-1}. Then, one must require $\varepsilon \ll 10^{-1}$ to ensure that $\varepsilon/(1+\varepsilon_g) \ll 1$ so that inertial effects can be neglected.

Expanding all unknowns in (2.25) in ε as $\mathbf{z} = \mathbf{z}^{[0]} + \varepsilon\,\mathbf{z}^{[1]} + \mathcal{O}(\varepsilon^2)$ yields

$$\begin{aligned}
\frac{\varepsilon}{1+\varepsilon_g}\left(\dot{\mathbf{v}}^{[0]} + \boldsymbol{\omega}^{[0]} \times \mathbf{v}^{[0]}\right) + \mathcal{O}(\varepsilon^2) &= -\left(\mathsf{D}_{11}\mathbf{v}^{[0]} + \mathsf{D}_{12}\boldsymbol{\omega}^{[0]}\right) + \mathbf{f}^{(\mathrm{ext})} \\
&\quad - \varepsilon\left(\mathsf{D}_{11}\mathbf{v}^{[1]} + \mathsf{D}_{12}\boldsymbol{\omega}^{[1]}\right) + \mathcal{O}(\varepsilon^2) \\
\frac{\varepsilon}{1+\varepsilon_g}\left(\dot{\mathbf{L}}^{[0]} + \boldsymbol{\omega}^{[0]} \times \mathbf{L}^{[0]}\right) + \mathcal{O}(\varepsilon^2) &= -\left(\mathsf{D}_{12}^T\mathbf{v}^{[0]} + \mathsf{D}_{22}\boldsymbol{\omega}^{[0]}\right) + \boldsymbol{\tau}^{(\mathrm{ext})} \\
&\quad - \varepsilon\left(\mathsf{D}_{12}^T\mathbf{v}^{[1]} + \mathsf{D}_{22}\boldsymbol{\omega}^{[1]}\right) + \mathcal{O}(\varepsilon^2)\,.
\end{aligned}$$

The overbars have been dropped for readability. Matching orders, the zeroth order solution is

$$\begin{bmatrix} \mathbf{v}^{[0]} \\ \boldsymbol{\omega}^{[0]} \end{bmatrix} = \mathbb{D}^{-1} \begin{bmatrix} \mathbf{f}^{(\mathrm{ext})} \\ \boldsymbol{\tau}^{(\mathrm{ext})} \end{bmatrix} = \mathbb{M} \begin{bmatrix} \mathbf{f}^{(\mathrm{ext})} \\ \boldsymbol{\tau}^{(\mathrm{ext})} \end{bmatrix}. \tag{2.27}$$

In the inner layer, time is rescaled as $T = t/\varepsilon$. The unknowns are expanded in orders of ε but as functions of T as $\mathbf{z} = \mathbf{z}_0 + \varepsilon\,\mathbf{z}_1 + \mathcal{O}(\varepsilon^2)$ (note the indices instead of superscripts used for the expansion in t) and (2.25) becomes

$$\begin{aligned}
\frac{1}{1+\varepsilon_g}\frac{d\mathbf{v}_0}{dT} + \frac{\varepsilon}{1+\varepsilon_g}\left(\frac{d\mathbf{v}_1}{dT} + \boldsymbol{\omega}_0 \times \mathbf{v}_0\right) + \mathcal{O}(\varepsilon^2) &= -\left(\mathsf{D}_{11}\mathbf{v}_0 + \mathsf{D}_{12}\boldsymbol{\omega}_0\right) + \mathbf{f}^{(\mathrm{ext})} \\
&\quad - \varepsilon\left(\mathsf{D}_{11}\mathbf{v}_1 + \mathsf{D}_{12}\boldsymbol{\omega}_1\right) + \mathcal{O}(\varepsilon^2) \\
\frac{1}{1+\varepsilon_g}\frac{d\mathbf{L}_0}{dT} + \frac{\varepsilon}{1+\varepsilon_g}\left(\frac{d\mathbf{L}_1}{dT} + \boldsymbol{\omega}_0 \times \mathbf{L}_0\right) + \mathcal{O}(\varepsilon^2) &= -\left(\mathsf{D}_{12}^T\mathbf{v}_0 + \mathsf{D}_{22}\boldsymbol{\omega}_0\right) + \boldsymbol{\tau}^{(\mathrm{ext})} \\
&\quad - \varepsilon\left(\mathsf{D}_{12}^T\mathbf{v}_1 + \mathsf{D}_{22}\boldsymbol{\omega}_1\right) + \mathcal{O}(\varepsilon^2)\,,
\end{aligned}$$

so that matching orders yields the zeroth order equation

$$\frac{1}{1+\varepsilon_g}\frac{d}{dT}\begin{bmatrix} \mathbf{v}_0 \\ \mathbf{L}_0 \end{bmatrix} = -\mathbb{D}\begin{bmatrix} \mathbf{I} & 0 \\ 0 & \mathsf{I}_{\mathrm{cm}}^{-1} \end{bmatrix}\begin{bmatrix} \mathbf{v}_0 \\ \mathbf{L}_0 \end{bmatrix} + \begin{bmatrix} \mathbf{f}^{(\mathrm{ext})} \\ \boldsymbol{\tau}^{(\mathrm{ext})} \end{bmatrix}.$$

Assuming that the external loads $\mathbf{f}^{(\mathrm{ext})}$ and $\boldsymbol{\tau}^{(\mathrm{ext})}$ vary little over the timescale ε of the initial layer, i.e. $\|d\mathbf{f}^{(\mathrm{ext})}/dT\| \ll 1$ and $\|d\boldsymbol{\tau}^{(\mathrm{ext})}/dT\| \ll 1$, this equation has solution

$$\begin{bmatrix} \mathbf{v}_0(T) \\ \mathbf{L}_0(T) \end{bmatrix} = G^{-1} \begin{bmatrix} \mathbf{f}^{(\mathrm{ext})}(0) \\ \boldsymbol{\tau}^{(\mathrm{ext})}(0) \end{bmatrix} + \exp\{-T\,(1+\varepsilon_g)\,G\} \left(\begin{bmatrix} \mathbf{v}_0(0) \\ \mathbf{L}_0(0) \end{bmatrix} - G^{-1} \begin{bmatrix} \mathbf{f}^{(\mathrm{ext})}(0) \\ \boldsymbol{\tau}^{(\mathrm{ext})}(0) \end{bmatrix} \right)$$

for T of order 1, where

$$G = \mathbb{D} \begin{bmatrix} \mathbf{I} & 0 \\ 0 & \mathsf{I}_{\mathrm{cm}}^{-1} \end{bmatrix},$$

and $\mathbf{v}_0(0)$, $\mathbf{L}_0(0)$ satisfy initial conditions. Using $\mathbf{L} = \mathsf{I}_{\mathrm{cm}}\,\boldsymbol{\omega}$, this is equivalent to

$$\begin{bmatrix} \mathbf{v}_0(T) \\ \boldsymbol{\omega}_0(T) \end{bmatrix} = \mathbb{M} \begin{bmatrix} \mathbf{f}^{(\mathrm{ext})}(0) \\ \boldsymbol{\tau}^{(\mathrm{ext})}(0) \end{bmatrix} + \exp\{-T\,(1+\varepsilon_g)\,G\} \left(\begin{bmatrix} \mathbf{v}_0(0) \\ \boldsymbol{\omega}_0(0) \end{bmatrix} - \mathbb{M} \begin{bmatrix} \mathbf{f}^{(\mathrm{ext})}(0) \\ \boldsymbol{\tau}^{(\mathrm{ext})}(0) \end{bmatrix} \right), \tag{2.28}$$

which is compatible with the limit $t \to 0$ of (2.27) as $T \to \infty$. Combining (2.27) and the initial layer (2.28), the leading order solution [15]

$$\begin{bmatrix} \mathbf{v}(t) \\ \boldsymbol{\omega}(t) \end{bmatrix} = \mathbb{M} \begin{bmatrix} \mathbf{f}^{(\mathrm{ext})}(t) \\ \boldsymbol{\tau}^{(\mathrm{ext})}(t) \end{bmatrix} + \exp\left\{-t\,\frac{1+\varepsilon_g}{\varepsilon}\,G\right\} \left(\begin{bmatrix} \mathbf{v}(0) \\ \boldsymbol{\omega}(0) \end{bmatrix} - \mathbb{M} \begin{bmatrix} \mathbf{f}^{(\mathrm{ext})}(0) \\ \boldsymbol{\tau}^{(\mathrm{ext})}(0) \end{bmatrix} \right) \tag{2.29}$$

is obtained. This solution is valid as long as the loadings $\mathbf{f}^{(\mathrm{ext})}$ and $\boldsymbol{\tau}^{(\mathrm{ext})}$ vary slowly compared to the timescale ε of the initial layer. Namely, $||\dot{\mathbf{f}}^{(\mathrm{ext})}|| \ll \frac{1}{\varepsilon}$ and $||\dot{\boldsymbol{\tau}}^{(\mathrm{ext})}|| \ll \frac{1}{\varepsilon}$ are assumed.

Note that this provides a mathematically meaningful solution to (2.25). However, the Stokes flow limit does not apply to the inner layer, because effects of comparable magnitude to viscous drag typically occur as a body leaves a state of rest [40]. The solution (2.29) is therefore expected to be inaccurate in the inner layer. Accordingly, we focus on the outer layer.

After a transient, i.e. for $t \gg \varepsilon$, the leading order solution is entirely prescribed by (2.27) and is independent of initial conditions. The motion of the rigid body is consequently entirely prescribed by

$$\dot{\boldsymbol{x}} = R^T\,\mathbf{v}, \tag{2.20a}$$

$$\dot{R} = R\,[\boldsymbol{\omega}\times], \tag{2.20d}$$

where the linear and angular velocities are approximated as

$$\mathbf{v} = \mathsf{M}_{11}\,\mathbf{f}^{(\mathrm{ext})} + \mathsf{M}_{12}\,\boldsymbol{\tau}^{(\mathrm{ext})}, \tag{2.30a}$$

$$\boldsymbol{\omega} = \mathsf{M}_{12}^T\,\mathbf{f}^{(\mathrm{ext})} + \mathsf{M}_{22}\,\boldsymbol{\tau}^{(\mathrm{ext})}, \tag{2.30b}$$

and M_{ij} are 3-by-3 matrices representing the corresponding blocks of the 6-by-6 matrix $\mathbb{M}$.

2.4 The case of a rigid hard-magnet in Stokes flow subjected to a rotating magnetic field

The focus of this work is the case of external loads that arise from a spatially uniform magnetic field $\boldsymbol{B}$ rotating about a fixed axis in the lab frame.

The magnetic loads experienced by a magnetic body with magnetic moment $\boldsymbol{m}$ in a magnetic induction field $\boldsymbol{B}$ are given by [21]

$$\boldsymbol{f}^{(m)} = \nabla\left(\boldsymbol{m}\cdot\boldsymbol{B}\right), \tag{2.4a}$$

$$\boldsymbol{\tau}^{(m)} = \boldsymbol{m}\times\boldsymbol{B}. \tag{2.4b}$$

The magnetic moment $\boldsymbol{m}$ is determined by the electric currents due to orbiting electrons within the body material. In a permanent (or hard) magnet, the electron orbits are aligned even in the absence of external field – this phenomenon is called ferromagnetism. This magnetic property might be due to previous exposure to strong magnetic fields: ferromagnetic materials typically show hysteresis in their response to external fields. When exposed to fields weak enough to leave their magnetic properties unchanged, the magnetic moment $\boldsymbol{m}$ of a hard magnet is assumed constant [21]. This work focuses on this type of magnets.[1]

Provided the magnetic moment $\boldsymbol{m}$ of a body is specified either as a constant vector in the body frame, or as a function of $\boldsymbol{B}$, the magnetic force and torque (2.4) define the effect of applied field $\boldsymbol{B}$ on it. In practice, for the cases considered in this work, the magnetic field $\boldsymbol{B}$ can be assumed to be spatially uniform over the length scale of the body [41, 10, 42]. As a result, the magnetic force reduces to

$$\boldsymbol{f}^{(m)} = \boldsymbol{0}. \tag{2.31}$$

Note that it is not trivial to design a set-up that is able to generate a magnetic field that can be assumed uniform. The region in which the field is be assumed to be uniform is small (about 10 mm^3 [43]), and the field still has a small variation in this region (<1% [44]). This work nevertheless assumes that the magnetic force takes the form (2.31).

Furthermore, in the setting studied here, the magnetic field $\boldsymbol{B}$ is of constant magnitude B and rotates steadily around a fixed axis in the lab frame. Without loss of generality, the lab frame can be chosen so that the basis vector $\boldsymbol{e}_3$ aligns with the axis of rotation of the magnetic field and that $\boldsymbol{B}$ lies in the $(\boldsymbol{e}_1, \boldsymbol{e}_3)$-plane at time $t = 0$. That is, $\boldsymbol{B}$ can be explicitly written in the lab frame as

$$\boldsymbol{B} = B\,R_3\left(\alpha\, t\right)\begin{bmatrix}\sin\psi\\ 0\\ \cos\psi\end{bmatrix}, \tag{2.32}$$

---

[1] In the other extreme, soft magnets are made of materials that do not retain alignment of electron orbits in the absence of external field – such phenomena are called paramagnetism or diamagnetism according to whether the material are attracted or repulsed by external fields. Their magnetic moment is approximated as $\boldsymbol{m} = \mathscr{X}\,\boldsymbol{B}^{(\mathrm{ext})}$, where $\mathscr{X}$ is called the permeability tensor [21].

where α is the constant angular speed of the magnetic field (assumed constant), ψ is the constant conical angle between $\boldsymbol{B}$ and its axis of rotation $\boldsymbol{e}_3$, and R_3 is the matrix of rotation around $\mathbf{e}_3$ defined by

$$R_3\left(s\right) = \begin{bmatrix} \cos s & -\sin s & 0 \\ \sin s & \cos s & 0 \\ 0 & 0 & 1 \end{bmatrix}.$$

In this work, we consider only hard magnetic swimmers. Accordingly, the magnetic moment $\mathbf{m}$ is assumed to be constant in the body frame from now on.

The body frame expressions of the dimensional magnetic loads (2.31, 2.4b) are

$$\mathbf{f}^{(m)} = \mathbf{0}, \qquad \boldsymbol{\tau}^{(m)} = \mathbf{m} \times \mathbf{B},$$

where

$$\mathbf{B}(t) = B\, R^T(t)\, R_3(\alpha\, t) \begin{bmatrix} \sin\psi \\ 0 \\ \cos\psi \end{bmatrix}.$$

The magnetic field $\mathbf{B}$ and magnetic moment $\mathbf{m}$ defining magnetic torque $\boldsymbol{\tau}^{(m)} = \mathbf{m} \times \mathbf{B}$ are then non-dimensionalised so that their dimensionless counterparts $\overline{\mathbf{B}}$ and $\overline{\mathbf{m}}$ are unit vectors:

$$\overline{\mathbf{B}}\left(\overline{t}\right) = R^T\left(\overline{t}\right) R_3\left(a\,\overline{t}\right) \begin{bmatrix} \sin\psi \\ 0 \\ \cos\psi \end{bmatrix}, \quad (2.33) \qquad \mathbf{m} = m\overline{\mathbf{m}}, \quad (2.34)$$

where $m = |\mathbf{m}|$, and

$$a = \alpha\, t_c = \alpha \frac{\ell^2 \eta}{N}. \tag{2.35}$$

Because experiments occur in a gravitational field, the influence of buoyancy is also considered: this allows to quantify if and when these loads can be neglected with little loss of accuracy. The dimensional loads arising from gravity and buoyancy are given in (2.5). In the body frame, their non-dimensionalised versions are

$$\overline{\mathbf{f}}^{(g)} = \gamma \frac{\varepsilon_g}{1+\varepsilon_g} \overline{\mathbf{g}}, \qquad \overline{\boldsymbol{\tau}}^{(g)} = \gamma \overline{\boldsymbol{\Delta}} \times \overline{\mathbf{g}}$$

where $\boldsymbol{\Delta} = \ell\,\overline{\boldsymbol{\Delta}}$, $\mathbf{g} = |\boldsymbol{g}|\,\overline{\mathbf{g}}$, and

$$\gamma = \frac{\rho_f\, V\, |\mathbf{g}|}{N}.$$

Here $|\boldsymbol{g}|$ is the (known) gravitational acceleration (on earth).

Because we intend to study cases where the magnetic loads dominate, the force scale used for non-dimensionalising is $N = m B/\ell$, where m is the magnitude of the magnetic moment.

The non-dimensional parameter a defined by relation (2.35) is called the *Mason number*[2] (cf. refs [35, 45]):

$$a = \alpha \frac{\ell^3 \eta}{m B}. \tag{2.36}$$

The Mason number is proportional to the angular speed of the rotating magnetic field, and inversely proportional to its magnitude.

With loads arising from magnetism, gravity, and buoyancy, the system (2.25) becomes

$$\begin{aligned} \frac{\varepsilon}{1+\varepsilon_g}\left(\dot{\overline{\mathbf{v}}} + \overline{\boldsymbol{\omega}} \times \overline{\mathbf{v}}\right) &= -\left(\overline{\mathsf{D}}_{11}\overline{\mathbf{v}} + \overline{\mathsf{D}}_{12}\overline{\boldsymbol{\omega}}\right) & &+ \gamma \frac{\varepsilon_g}{1+\varepsilon_g}\overline{\mathbf{g}} \\ \frac{\varepsilon}{1+\varepsilon_g}\left(\dot{\overline{\mathbf{L}}} + \overline{\boldsymbol{\omega}} \times \overline{\mathbf{L}}\right) &= -\left(\overline{\mathsf{D}}_{12}^T\overline{\mathbf{v}} + \overline{\mathsf{D}}_{22}\overline{\boldsymbol{\omega}}\right) + \overline{\mathbf{m}} \times \overline{\mathbf{B}} & &+ \gamma \overline{\boldsymbol{\Delta}} \times \overline{\mathbf{g}}, \end{aligned} \tag{2.37}$$

where $\overline{\mathbf{m}}$, $\overline{\mathbf{B}}$, and $\overline{\mathbf{g}}$ are unit vectors, and γ is the non-dimensional ratio between magnetic and buoyancy loads, i.e.

$$\gamma = \frac{\rho_f V |\mathbf{g}| \ell}{m B}.$$

System (2.37) is written in the body frame, where the $\overline{\mathsf{D}}_{ij}$ are constant, as well as $\overline{\mathbf{m}}$ and $\overline{\boldsymbol{\Delta}}$. The vector $\overline{\mathbf{g}}$ is constant in the lab frame, while the magnetic field $\overline{\mathbf{B}}$ is steadily rotating in the lab frame.

Dropping again the overbars for readability, the leading order solution (2.29) becomes

$$\begin{aligned} \begin{bmatrix} \mathbf{v}(t) \\ \boldsymbol{\omega}(t) \end{bmatrix} =& \mathbb{M}\left(\begin{bmatrix} \mathbf{0} \\ \mathbf{m} \times \mathbf{B}(t) \end{bmatrix} + \gamma \begin{bmatrix} \frac{\varepsilon_g}{1+\varepsilon_g}\mathbf{g}(t) \\ \boldsymbol{\Delta} \times \mathbf{g}(t) \end{bmatrix}\right) \\ &+ \exp\left\{-t\,\frac{1+\varepsilon_g}{\varepsilon}G\right\}\left(\begin{bmatrix} \mathbf{v}(0) \\ \boldsymbol{\omega}(0) \end{bmatrix} - \mathbb{M}\left(\begin{bmatrix} \mathbf{0} \\ \mathbf{m} \times \mathbf{B}(0) \end{bmatrix} + \gamma \begin{bmatrix} \frac{\varepsilon_g}{1+\varepsilon_g}\mathbf{g}(0) \\ \boldsymbol{\Delta} \times \mathbf{g}(0) \end{bmatrix}\right)\right) \end{aligned} \tag{2.38}$$

and the long-term dynamics is entirely prescribed by the analogue of (2.27)

$$\mathbf{v} = \mathsf{M}_{12}\left(\mathbf{m} \times \mathbf{B} + \gamma \boldsymbol{\Delta} \times \mathbf{g}\right) + \gamma \frac{\varepsilon_g}{1+\varepsilon_g}\mathsf{M}_{11}\mathbf{g} \tag{2.39}$$

$$\boldsymbol{\omega} = \mathsf{M}_{22}\left(\mathbf{m} \times \mathbf{B} + \gamma \boldsymbol{\Delta} \times \mathbf{g}\right) + \gamma \frac{\varepsilon_g}{1+\varepsilon_g}\mathsf{M}_{12}^T\mathbf{g} \tag{2.40}$$

together with

$$\dot{\boldsymbol{x}} = R^T\mathbf{v}, \tag{2.20a}$$

$$\dot{R} = R\,[\boldsymbol{\omega}\times]. \tag{2.20d}$$

---

[2] The Mason number is usually denoted Ma. Since we will use the Mason number in various expansions, we prefer using the single letter notation a in order to improve readability of later computations and expansions in orders of a and orders of $1/a$.

A neutrally buoyant, uniform body would have $\varepsilon_g = 0$ and $\boldsymbol{\Delta} = \mathbf{0}$. In practice, these equalities are never exactly achieved. However, neglecting the loads arising from gravity and buoyancy should yield a good approximation when $|\varepsilon_g|, |\overline{\boldsymbol{\Delta}}| \ll 1/\gamma$. The long-term dynamics are then prescribed by

$$\mathbf{v} = \mathsf{M}_{12} \left(\mathbf{m} \times \mathbf{B}\right), \qquad (2.41a) \qquad\qquad \boldsymbol{\omega} = \mathsf{M}_{22} \left(\mathbf{m} \times \mathbf{B}\right). \qquad (2.41b)$$

The system (2.20a, 2.20d, 2.41) is the starting point for the analysis of a neutrally buoyant magnetic micro-swimmer that will be carried out in this work.

2.5 The Averaging Method

To analyse the outer layer approximation (cf. chapter 5), we will use the spirit of the averaging method outlined here based on [16].

Consider the system

$$\dot{\boldsymbol{z}} = \varepsilon F^{[1]}(\boldsymbol{z}, t) + \varepsilon^2 \Phi(\boldsymbol{z}, t, \varepsilon), \qquad \boldsymbol{z}(0) = C, \tag{2.42}$$

where functions $F^{[1]}$ and Φ are T-periodic in t, sufficiently smooth, and of order ε^0. Periodic averaging of this system allows to find an approximation to the solution that describes its effective behaviour and leaves aside small periodic effects.

For any function $G(\boldsymbol{z}, t)$ T-periodic in t, the average function $\overline{G}(\boldsymbol{z})$ is defined as

$$\overline{G}(\boldsymbol{z}) = \frac{1}{T} \int_0^T G(\boldsymbol{z}, s)\, ds, \tag{2.43}$$

where integration is performed while holding $\boldsymbol{z}$ fixed.

Using this definition, the averaged equation is obtained from system (2.42) as

$$\dot{\boldsymbol{z}} = \varepsilon \overline{F^{[1]}}(\boldsymbol{z}), \qquad \boldsymbol{z}(0) = C. \tag{2.44}$$

Then, under some technical assumptions[3], the solutions $\boldsymbol{z}$ to (2.42) and $\boldsymbol{z}_{\text{av}}$ to (2.44) satisfy

$$|\boldsymbol{z}(t,\varepsilon) - \boldsymbol{z}_{\text{av}}(t,\varepsilon)| \leq a\varepsilon \quad \text{for } 0 \leq t \leq L/\varepsilon, \tag{2.45}$$

for some positive constants a and L.

---

[3] The technical hypotheses required for result (2.45) on the accuracy of averaged solution are that Φ is continuous, there exist constants ε_0, $L > 0$ and a connected bounded open set $D \subset \mathbb{R}^n$ such that the initial condition $C \in D$, and the solutions $\boldsymbol{z}(t,\varepsilon)$ to (2.42) and $\boldsymbol{z}_{\text{av}}(t,\varepsilon)$ to (2.44) for $0 \leq \varepsilon \leq \varepsilon_0$ remain in D for $0 \leq t \leq L/\varepsilon$, and such that the function $F^{[1]}$ is Lipschitz-continuous on D.

In practice, equation (2.44) is usually not solved directly. Instead, time is rescaled as $\tau = \varepsilon\, t$ in order to obtain the *guiding system*

$$\frac{d\boldsymbol{y}}{d\tau} = \overline{F^{[1]}}(\boldsymbol{y}), \qquad \boldsymbol{y}(0) = C, \tag{2.46}$$

which is independent of ε. The solution $\boldsymbol{z}_{\text{av}}$ to averaged equation (2.44) can be obtained from the solution $\boldsymbol{y}$ to (2.46) as

$$\boldsymbol{z}_{\text{av}}(t, \varepsilon) = \boldsymbol{y}(t\,\varepsilon).$$

The procedure of periodic averaging can be generalised to build higher-order approximations of the solutions to T-periodic systems

$$\dot{\boldsymbol{z}} = \sum_{n=1}^{N-1} \varepsilon^n F^{[n]}(\boldsymbol{z}, t) + \varepsilon^N \Phi(\boldsymbol{x}, t, \varepsilon), \qquad \boldsymbol{z}(0) = C.$$

The solution $\boldsymbol{z}$ to this system can be approximated as

$$\boldsymbol{z} = \boldsymbol{z}_{\text{av}} + \sum_{n=1}^{N-1} \varepsilon^n Z^{[n]}(\boldsymbol{z}_{\text{av}}, t) + \mathcal{O}(\varepsilon^N),$$

where the $Z^{[n]}$ are T-periodic in t, and $\boldsymbol{z}_{\text{av}}$ is the solution to

$$\dot{\boldsymbol{z}} = \varepsilon\, \overline{F^{[1]}}(\boldsymbol{z}) + \sum_{n=2}^{N-1} \varepsilon^n\, \overline{G^{[n]}}(\boldsymbol{z}),$$

for some functions $G^{[n]}$ defined in an appropriate way. The solution $\boldsymbol{z}_{\text{av}}$ is usually found by rescaling time as $\tau = t/\varepsilon$ and using asymptotic expansions. This approximation is valid for t of order up to $1/\varepsilon$.

The first coefficients $Z^{[1]}$, $G^{[2]}$ and $Z^{[2]}$ are given by

$$\begin{aligned}
&\frac{\partial}{\partial t} Z^{[1]}(\boldsymbol{z}, t) = F^{[1]}(\boldsymbol{z}, t) - \overline{F^{[1]}}(\boldsymbol{z}) \\
&G^{[2]}(\boldsymbol{z}, t) = F^{[2]}(\boldsymbol{z}, t) + \left(\nabla_{\boldsymbol{z}} F^{[1]}(\boldsymbol{z}, t)\right) Z^{[1]}(\boldsymbol{z}, t) - \left(\nabla_{\boldsymbol{z}} Z^{[1]}(\boldsymbol{z}, t)\right) \overline{F^{[1]}}(\boldsymbol{z}) \\
&\frac{\partial}{\partial t} Z^{[2]}(\boldsymbol{z}, t) = G^{[2]}(\boldsymbol{z}, t) - \overline{G^{[2]}}(\boldsymbol{z}).
\end{aligned} \tag{2.47}$$

The averaging method is used in chapter 5 to approximate periodic solutions of the system of interest.

2.6 Review of literature on swimmers in Stokes flow

2.6.1 Bio-inspired design, engineering, and experiment

Many microorganisms swim using flagella. A well-known example is the sperm cell, the movement of which was analysed in detail at the beginning of the 1950s by Gray: it propels by undulations travelling from the base to the tip of its tail [46, 47]. It is noteworthy that Gray's investigations went hand in hand with mathematical modelling from the very beginning [1, 32]. Another kind of flagellar motion is displayed by Escheria coli bacteria. Each bacterium has several flagella which assemble in a bundle that takes a helical shape. This was known in the early 20th century [17], but it took until 1973 before Berg and Anderson understood how it generates movement: there is a molecular motor at the flagella's foundations driving them to rotate [9].

The idea of artificial micro-swimmers is seeded in Purcell's 1977 article, where he imagines "animals" that have no biological basis but whose shape configurations would allow them to move in Stokes flow [3]. The first artificial swimmer of a size comparable to a micro-organism was built in 2005 by Dreyfus et al. [48]. It consists of a 24 µm long chain of magnetic beads linked together by DNA strands and attached to a red blood cell. This artificial flagellum beats as a result of an external magnetic field of varying direction with which it aligns.

External magnetic fields were also used to imitate the rotary movement of E. coli flagella without building a molecular rotary motor. In 1996, Honda et al. proposed macro-scale prototypes of swimmers made of a helical copper wire attached to a magnetic head that were put into motion by a rotating magnetic field [49]. The idea was taken up by the group of Nelson, who presented the first micro-swimmer on this model in 2007 [10]. Since then, they have perfected many different techniques to build magnetic micro- and nano-swimmers [17, 50, 51, 52].

Proposed applications of micro-swimmers include microsurgery, targeted drug delivery, cell manipulation, environmental monitoring, and pollutant removal [53, 7]. While research is investigating cargo transport [54, 18], environmental and bio-compatibility, motion in organic fluids, and how to control navigation inside the body [55, 56], the first experiments with magnetic micro-swimmers controlled by an external magnetic field in vivo or in physiological conditions have been conducted. Servant et al. guided a swarm of helical micro-swimmers inside the peritoneal cavity of a mouse [57]; Medina-Sánchez et al. used them to assist live sperm cells with deficient motility towards an oocyte for in vitro fecundation [58]; Yan et al. used micro-swimmers made from micro-algae for remote diagnostic sensing in rodents' stomachs [59].

Extensive lab testing was necessary to make these applications possible, in particular to investigate the control of trajectories [60, 61, 8] and characterise swimming characteristics of the micro-robots [62, 63]. Experimentalists consistently observe that the speed of swimmers increases as the magnetic field rotates faster up to a certain point, called step-out, at which the speed decreases suddenly [50, 64]. To understand this behaviour, and answer other questions such as how the swimmer's shape impacts its motion, theoretical approaches have been proposed. These will be discussed in the next section. Techniques to track the trajectories of micro-swimmers are developed to enable comparison between experiments and theoretical predictions [65].

2.6.2 Modelling swimmers in Stokes flow

Mathematical models of swimmers in Stokes flow emerged at the same time as biological investigations into the locomotion strategies of micro-organisms. Some of the early theoretical work was mentioned in section 2.1.1, and specific contributions to the computation of the drag matrix were presented in section 2.1.2. Other works include the investigations of Keller and Rubinov into the trajectories of microorganisms propelled by means of either a planar or a helical flagellum [66]. They compute the linear and angular velocities $\mathbf{v}$ and $\boldsymbol{\omega}$ from the force and torque $\mathbf{f}^{(s)}$ and $\boldsymbol{\tau}^{(s)}$ due to shape change by assuming that hydrodynamic drag and deformation are the only loads impacting the system, and that the total force and torque vanish. This yields

$$0 = \begin{bmatrix} \mathbf{f}^{(s)} \\ \boldsymbol{\tau}^{(s)} \end{bmatrix} - \mathbb{D} \begin{bmatrix} \mathbf{v} \\ \boldsymbol{\omega} \end{bmatrix} ,$$

which is equivalent to equation (2.26) replacing external loads by the force and torque due to shape changes [25]. Prescribing the flagella's geometry over time, they solve this system using Cox' slender-body method [37] for obtaining the drag matrix $\mathbb{D}$, which in this case is not constant since it depends on shape. A review of the contributions to a mathematical understanding of how microorganisms swim, including flagellar motion, is provided by Lauga and Powers [4], and more recent works exploring the relation between shape change and trajectories can be found in [67, 68, 5].

A lot of effort has also been put into understanding the trajectories of rigid artificial swimmers. The particular case of hard-magnetic swimmers in Stokes flow actuated by a rotating magnetic field has been considered by several authors. A few contributions that are closely related to this work are presented here: Ghosh et al. [69], Morozov et al. [31, 70], Man and Lauga [35], and Meshkati and Fu [45]. Within each of these contributions, the underlying assumption is that the dynamics of the swimmer were given by a balance of hydrodynamic drag (2.3) and magnetic loads (2.31, 2.4b) with a spatially uniform magnetic field. This corresponds to assuming (cf. section 2.4)

$$\mathbf{v} = \mathsf{M}_{12} (\mathbf{m} \times \mathbf{B}) , \qquad (2.41a) \qquad\qquad \boldsymbol{\omega} = \mathsf{M}_{22} (\mathbf{m} \times \mathbf{B}) . \qquad (2.41b)$$

In particular, this relation gives an expression for the angular velocity $\boldsymbol{\omega}$ appearing in equation (2.20d) governing the orientation of the body frame with respect to the lab frame, and relates the linear velocity $\mathbf{v}$ to $\boldsymbol{\omega}$ through

$$\mathbf{v} = \mathsf{M}_{12}\,\mathsf{M}_{22}^{-1}\,\boldsymbol{\omega}\,,$$

so that the dynamics are completely defined by (2.20d) with $\boldsymbol{\omega}$ satisfying (2.41b). The order in which these contributions are discussed reflects the increasing degree of similarity with the present work.

Ghosh et al. [69] studied a cylindrical swimmer subjected to a magnetic field steadily rotating and perpendicular to its axis of rotation. Casting (2.41) in the body frame, so that the mobility matrix $\mathbb{M}$ and the magnetic moment $\mathbf{m}$ are constant, they wrote the magnetic field $\mathbf{B}$ with explicit dependence on the rotation matrix R^T. Writing R^T in Euler angles, the authors derived a system of ordinary differential equations equivalent to (2.1d) for these angles. They defined steady states configurations as configurations for which two of the three Euler angles are constant, allowing the body to rotate about the same axis of rotation as the magnetic field. Solving analytically the ode for the third angle, they classified solutions into precession and tumbling regimes, according to the angle formed between the long axis of the cylindrical body and the plane in which the magnetic field $\mathbf{B}$ rotates. They also computed numerically the stability of these regimes, and found values of the angular speed α of the magnetic field for which steady states exist both for tumbling and for precession regimes. It should be noted that the tumbling regime doesn't fit into the definition of steady states used in the present work or in any of the contributions discussed hereafter. Actually, the tumbling regime pertains only to swimmers with a rotational symmetry about their long axis, like a cylinder.

Morozov et al. [31, 70] studied an arbitrary shaped swimmer subjected to a magnetic field rotating perpendicularly to its axis of rotation. They derived the Euler angle formulation of (2.1d), which reduces to the formulation in Ghosh et al. [69] in the case of a swimmer with rotational symmetry about its long axis, and looked for solutions where two of the Euler angles are constant, and the third angle, which is about the rotation axis of the magnetic field, is equal to $\alpha\, t$, where α is the angular speed of the magnetic field. Such solutions have the body frame locked to the magnetic field and its axis of rotation, so that the angular velocity $\boldsymbol{\omega}$ is aligned with the axis of rotation $\mathbf{e}_3$. The authors studied these solutions in several particular cases where the geometry of the swimmer and the orientation of the magnetic moment $\mathbf{m}$ have specific properties: when $\mathbf{m}$ is an eigenvector of M_{22}, and when the two smallest eigenvalues of M_{22} are equal (transverse rotational isotropy), which is the case for cylinders and prolate spheroids. They also discussed the value of the angle ϕ between the magnetic field $\mathbf{B}$ and magnetic moment $\mathbf{m}$, and the component of linear velocity $\mathbf{v}$ along the axis of rotation $\mathbf{e}_3$ and its dependence on the mobility matrix $\mathbb{M}$ of the swimmer.

Man and Lauga [35] studied a helical swimmer subjected to a uniform magnetic field steadily rotating perpendicularly to its axis of rotation. Non-dimensionalisation of (2.41) yielded a unique parameter, the Mason number a, on which the equations depend (cf. section 2.2).

Numerical simulation of

$$\dot{\boldsymbol{d}}_j = \boldsymbol{\omega} \times \boldsymbol{d}_j \quad \text{for } j = 1, 2, 3, \tag{2.48}$$

which is equivalent to (2.1d), with the computed value of angular velocity $\boldsymbol{\omega}$ was used to investigate solutions for different Mason numbers. The authors studied in particular the wobbling angle, defined as the angle between the helix axis of the swimmer with the axis of rotation of the magnetic field, which was observed to be inversely proportional to the Mason number. They also derived an expression for the mobility matrix of a helical swimmer with an integer number of turns using resistive force theory. They performed an asymptotic analysis for small helicity angles, i.e. helical swimmers of asymptotically infinite pitch, that confirmed analytically the observation that the wobbling angle is inversely proportional to the Mason number.

Meshkati and Fu [45] studied swimmers of arbitrary geometries subjected to a steadily rotating uniform magnetic field that is not necessarily perpendicular to its axis of rotation. Looking for solutions to (2.1d,2.41) in which the body frame is locked to the rotating magnetic field, they studied equilibrium condition

$$\alpha \mathbf{e}_3 = \mathsf{M}_{22} (\mathbf{m} \times \mathbf{B}) \tag{2.49}$$

for magnetic field $\mathbf{B}$ and unit axis of rotation $\mathbf{e}_3$ constant in the body frame, where α is the angular speed of the rotating magnetic field. Writing the magnetic field $\mathbf{B}$ in spherical coordinates, the authors found that the equilibrium condition yielded geometric constraints relating the two spherical angles with the angular speed α and the angle ψ between the magnetic field $\mathbf{B}$ and its axis of rotation $\mathbf{e}_3$. The authors also discussed the axial velocity

$$\mathbf{e}_3 \cdot \mathsf{M}_{12} (\mathbf{m} \times \mathbf{B})$$

for magnetic field $\mathbf{B}$ and axis of rotation $\mathbf{e}_3$ satisfying equilibrium condition. Finally, they performed numerical simulations for a specific swimmer consisting of three rigidly linked beads, computing its mobility matrix using the method of regularised stokeslet. In another publication [19], Fu et al. went on to study the dependence of axial velocity on the direction of magnetic moment $\mathbf{m}$ and the geometry of helical swimmers, using resistive force theory to obtain an explicit expression of the mobility matrix $\mathbb{M}$ as a function of helical parameters.

Abbott et al. [71] obtained estimates of the axial velocity of a helical micro-swimmer by assuming that the axis of rotation of the magnetic field is aligned with the helical axis, which restricts the six-dimensional equation (2.41) to a two-dimensional equation. This yields results in good agreement with experiments.

Other works have studied how to design a micro-swimmer to optimise its swimming abilities. Gadêlha showed that a swimmer made of a magnetic head and an elastic tail moves faster if its head is an prolate spheroid rather than a sphere [72]. Walker and Keaveny studied numerical optimisation of shape by solving Stokes equation (2.13) for rod-like magnetic swimmers using boundary integral methods [73]. Fu et al. maximised swimmer's velocity along the magnetic field's rotation axis in motions corresponding to relative equilibria (2.49). They considered hard-magnetic rigid swimmers with a helical shape and let the direction of magnetic moment and geometrical parameters of the helix vary. The drag matrix was computed using resistive force theory so that its dependence on shape parameters was explicit [19]. Walker et al. showed experimentally with theoretical support that a helical propeller with a given radius and pitch attached to a cargo has an optimal length allowing it to swim faster [74].

The works just cited all stay in the realm of helical or rod-like swimmers, but others are not constrained to them. Cheang et al. investigated how simple the shape of a swimmer can be and still achieve forward propulsion. They proposed a rigid swimmer formed of three unaligned spheres and showed that its ability to propel depends on the direction of the magnetic moment $\mathbf{m}$ [75]. Vach et al. studied experimentally the velocities of rigid magnetic swimmers of arbitrary shapes [76]. Finally, numerical optimisation was used by Mirzae et al. to explore the optimal shape of swimmers made of randomly aggregated beads [77].

In this work, we provide a complete characterisation of solutions to equilibrium condition (2.49) in a non-dimensionalised version, depending on two parameters: the Mason number a (which appears also in [35, 45]), and the conical angle ψ between the magnetic field $\mathbf{B}$ and its axis of rotation $\mathbf{e}_3$ (cf. chapter 4). This extends the geometric description of relative equilibria introduced by Meshkati and Fu [45]. Many of the contributions discussed above focus on helical swimmers, and the examples presented in this work remain in this territory (cf. chapter 6). Our theoretical results, however, are independent of the swimmer shape.

2.6.3 The case of a rigid body in Stokes flow under gravitation

We approached the problem of magnetic micro-swimmers taking inspiration from the work of Gonzalez et al. [14], which is summarised here.

The motion of a rigid body in Stokes flow subjected only to gravity is given by (2.21), where the external force is gravitational force $\mathbf{g}$, and external torque is zero provided the centres of mass and buoyancy coincide.[4] This is written as (cf. eq. (2.21))

$$\begin{aligned} \dot{\mathbf{p}} + \boldsymbol{\omega} \times \mathbf{p} &= -\mathsf{D}_{11}\mathbf{v} - \mathsf{D}_{12}\boldsymbol{\omega} + \mathbf{g} \\ \dot{\mathbf{L}} + \boldsymbol{\omega} \times \mathbf{L} &= -\mathsf{D}_{12}^{T}\mathbf{v} - \mathsf{D}_{22}\boldsymbol{\omega}, \end{aligned} \tag{2.50}$$

where all vectors are expressed in the body frame. Since the gravitational force $\mathbf{g}$ is constant in the lab frame, its body frame expression satisfies

$$\dot{\mathbf{g}} + \boldsymbol{\omega} \times \mathbf{g} = 0. \tag{2.51}$$

---

[4] Although most of the analysis in [14] is done in the case where the centres of mass and buoyancy coincide, which is the case presented here, the authors also study the case where the centres of mass and buoyancy do not coincide.

In Stokes flow, the long term dynamics of the rigid body is entirely prescribed by (2.51) and (cf. section 2.3)

$$\begin{aligned}0 &= -\mathsf{D}_{11}\mathbf{v} - \mathsf{D}_{12}\boldsymbol{\omega} + \mathbf{g}\\ 0 &= -\mathsf{D}_{12}^T\mathbf{v} - \mathsf{D}_{22}\boldsymbol{\omega}\,,\end{aligned}$$

which can be inverted as

$$\begin{aligned}\mathbf{v} &= \mathsf{M}_{11}\,\mathbf{g}\\ \boldsymbol{\omega} &= \mathsf{M}_{12}^T\mathbf{g}\,.\end{aligned}$$

Substituting $\boldsymbol{\omega}$ in (2.51) yields

$$\dot{\mathbf{g}} + (\mathsf{M}_{12}^T\mathbf{g}) \times \mathbf{g} = 0\,. \tag{2.52}$$

Solving this equation for $\mathbf{g}$ is then sufficient to reconstruct the entire motion, and steady states of (2.52) give steady states for the whole problem with the same stability. The gravitational force $\mathbf{g}$ gives a steady states of (2.52) if and only if it is an eigenvector of M_{12}^T. Scaling is done in such a way that $\mathbf{g}$ is a unit vector. Thus the question is to understand and characterise the motions given by unit eigenvectors of M_{12}^T.

Steady state motions can be: vertical translations if $\mathbf{g}$ is an eigenvector of both M_{12}^T and M_{11}, and the eigenvalue associated with M_{12}^T is $\lambda = 0$; non-vertical translation if $\mathbf{g}$ is an eigenvector of M_{12}^T with associated eigenvalue $\lambda = 0$, and is not an eigenvector of M_{11}; vertical spin if $\mathbf{g}$ is an eigenvector of both M_{12}^T and M_{11}, and the eigenvalue associated with M_{12}^T is $\lambda \neq 0$; or helical spin in the generic case, i.e. $\mathbf{g}$ is an eigenvector of M_{12}^T for $\lambda \neq 0$, and is not an eigenvector of M_{11}. The radius r and pitch p of the helical trajectory are given by

$$\begin{aligned}r &= \frac{|\mathbf{g} \times \mathsf{M}_{11}\,\mathbf{g}|}{|\lambda|}\\ p &= 2\pi\,\frac{\mathbf{g}\cdot\mathsf{M}_{11}\mathbf{g}}{|\lambda|}\,.\end{aligned}$$

Stability of steady states is studied in the only two generic cases: either M_{12}^T has one real eigenvalue and a pair of complex conjugate eigenvalue; or M_{12}^T has three distinct real eigenvalues, and the corresponding eigenvectors satisfy a genericity condition excluding for example that M_{12}^T is a symmetric matrix. In the first case, there is a pair of unit eigenvectors ±$\mathbf{g}$ corresponding to the real eigenvalue. One of them defines a steady state that is globally asymptotically stable, and the other one an unstable steady state. In the second case, the two pairs of steady states corresponding to unit eigenvectors of the maximal and minimal eigenvalues each contain a stable and an unstable solution, while the pair of unit eigenvectors corresponding to the middle eigenvalue are both unstable. These theoretical results were validated by numerical simulations of bodies with ideal knot shapes, whose mobility matrices satisfy genericity conditions.

3 Different Formulations of the Governing Equations

3.1 Governing Equations

3.1.1 Decoupling Rotational and Translational Motions

The setup we are studying is a magnetic micro-swimmer: an object of prescribed shape and prescribed magnetic moment immersed in Stokes flow. This swimmer is subjected to a uniform magnetic field $\boldsymbol{B}$ rotating around a fixed axis $\boldsymbol{e}_3$ with a constant angular speed α. In this work, we are investigating how the motion of the swimmer depends on the angle ψ between $\boldsymbol{B}$ and $\boldsymbol{e}_3$, and the Mason number a (proportional to the angular speed α, and inversely proportional to the field's strength $|\boldsymbol{B}|$ cf. section 2.4). We call ψ and a the experimental parameters: they can be changed from one experiment to the next without altering the swimmer. Other parameters are dependent on the specific swimmer considered, in particular its shape and magnetic moment. We are restricting our inquiry to hard-magnetic swimmers: for these, the magnetic moment $\boldsymbol{m}$ is fixed in the body frame, i.e. $\mathbf{m}$ is constant (cf. section 2.4). The shape of the swimmer enters into play in its interaction with the fluid, which is prescribed by its drag matrix $\mathbb{D}$ (cf. section 2.1.1). The inverse of $\mathbb{D}$, the mobility matrix $\mathbb{M}$ will appear in computations. Both $\mathbb{D}$ and $\mathbb{M}$ are constant in the body frame.

As discussed in section (2.4), outside an initial layer the dynamics of a neutrally buoyant magnetic Stokes swimmer subjected to a spatially uniform rotating magnetic field are prescribed by

$$\dot{\boldsymbol{x}} = R^T \mathbf{v}\,, \tag{3.1a}$$

$$\mathbf{v} = \mathsf{M}_{12}\,[\mathbf{m}\times]\,\mathbf{B}\,, \tag{3.1b}$$

$$\dot{R} = R\,[\boldsymbol{\omega}\times]\,, \tag{3.1c}$$

$$\boldsymbol{\omega} = \mathsf{M}_{22}\,[\mathbf{m}\times]\,\mathbf{B}\,, \tag{3.1d}$$

$$\mathbf{B} = R^T R_3(a\,t)\begin{bmatrix}\sin\psi\\ 0\\ \cos\psi\end{bmatrix}, \tag{3.1e}$$

where M_{12}, M_{22}, $\mathbf{m}$ are material parameters, and a, and ψ are experimental parameters. The left column gathers all equations where the translational velocity and the position of the swimmer appears. The right column contains equations pertaining to the rotational motion.

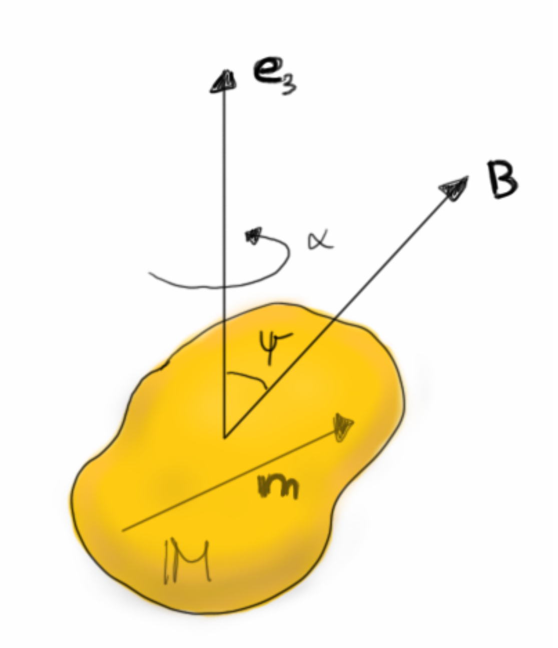

Figure 3.1 – The system studied here defines the motion of a swimmer with given mobility matrix $\mathbb{M}$ and magnetic moment $\mathbf{m}$ (material parameters), and under the influence of a magnetic field $\mathbf{B}$, rotating at angular speed α around axis $\mathbf{e}_3$, with which it forms a conical angle ψ. The angular speed α is proportional to the Mason number a. The parameters a and ψ can be changed from one experiment to the next without altering the swimmer (experimental parameters).

In this system, the translational motion decouples and is entirely determined by the rotational motion. Indeed the three equations (3.1c, 3.1d, 3.1e) form a closed system: substituting (3.1e) in (3.1d) and the result in (3.1c) yields

$$\dot{R} = R\left[\left(\mathsf{M}_{22}\,[\mathbf{m}\times]\,R^T R_3(a\,t)\begin{bmatrix}\sin\psi\\ 0\\ \cos\psi\end{bmatrix}\right)\times\right], \tag{3.2}$$

which is a single ode on SO(3). Once (3.2) is solved, $\mathbf{v}$ can be recovered through

$$\mathbf{v} = \mathsf{M}_{12}\,\mathsf{M}_{22}^{-1}\,\boldsymbol{\omega} = \mathsf{M}_{12}\,[\mathbf{m}\times]\,R^T R_3(a\,t)\begin{bmatrix}\sin\psi\\ 0\\ \cos\psi\end{bmatrix}, \tag{3.3}$$

and $\boldsymbol{x}$ is found by direct integration since the right-hand side of (3.1a) has no dependence on position. Accordingly, the focus is placed on the system (3.1c, 3.1d, 3.1e) describing rotational motion.

3.1.2 Magnetic Frame

After non-dimensionalisation, $\mathbf{m}$ is a constant unit vector (cf. section 2.4), and $\mathsf{M}_{22} \in R^{3\times3}$ is also constant. Consequently, all time-dependence of the rotational motion prescribed by (3.1c, 3.1d, 3.1e) comes from the rotating magnetic field B. We introduce a frame $\tilde{E}$ that rotates with the magnetic field $\boldsymbol{B}$ so that both the magnetic field $\boldsymbol{B}$ and its axis of rotation $\boldsymbol{e}_3$ are constant when expressed in frame $\tilde{E}$. Namely, the magnetic frame $\tilde{E}$ is defined as

$$\tilde{E} = E\,R_3(a\,t)\,,$$

where E is the body frame given by the axes $\boldsymbol{e}_j$ for $j = 1,2,3$. In the magnetic frame, the magnetic field $\boldsymbol{B}$ is expressed as $\begin{bmatrix} \sin\psi \\ 0 \\ \cos\psi \end{bmatrix}$, and its axis of rotation $\boldsymbol{e}_3$ as $\left[\begin{smallmatrix} 0 \\ 0 \\ 1 \end{smallmatrix}\right]$. The matrix $Q \in \mathrm{SO}(3)$ is the relative rotation between the magnetic frame and the body frame D, i.e.

$$\tilde{E} = D\,Q\,,$$

and satisfies

$$Q = R^T\,R_3(a\,t)\,, \tag{3.4}$$

so that (3.1e) rewrites as

$$\mathsf{B} = Q \begin{bmatrix} \sin\psi \\ 0 \\ \cos\psi \end{bmatrix}. \tag{3.5}$$

Using the matrix Q instead of R leads to an autonomous dynamical system. Indeed, substituting (3.4) in (3.1c) and (3.5) in (3.1e) transforms the system (3.1c, 3.1d, 3.1e) into

$$\dot{Q} = [(a\mathbf{e}_3 - \boldsymbol{\omega})\times]\,Q\,, \tag{3.6a}$$

$$\boldsymbol{\omega} = \mathsf{M}_{22}\,[\mathbf{m}\times]\,\mathsf{B}\,, \tag{3.6b}$$

$$\mathsf{B} = Q \begin{bmatrix} \sin\psi \\ 0 \\ \cos\psi \end{bmatrix}, \tag{3.6c}$$

$$\mathbf{e}_3 = Q \left[\begin{smallmatrix} 0 \\ 0 \\ 1 \end{smallmatrix}\right], \tag{3.6d}$$

which can be written in closed form as

$$\dot{Q} = \left[\left(aQ\left[\begin{smallmatrix} 0 \\ 0 \\ 1 \end{smallmatrix}\right] - \mathsf{P}\,Q\begin{bmatrix} \sin\psi \\ 0 \\ \cos\psi \end{bmatrix}\right)\times\right] Q\,, \tag{3.7}$$

where P is the matrix defined as

$$\mathsf{P} = \mathsf{M}_{22}\,[\mathbf{m}\times]\,. \tag{3.8}$$

Much of this work is dedicated to studying the solutions of (3.7) and their dependence on the parameters a and ψ. The Mason number a and conical angle ψ are the parameters that can be varied from one experiment to the other using the same swimmer. The swimmer itself impacts the the system through its mobility matrix $\mathbb{M}$, and its magnetic moment $\mathbf{m}$. These material parameters appear in (3.7) exclusively through the matrix P. The key properties of P

are examined in section 3.2.

We will also use variants of (3.7). Provided $\sin\psi \neq 0$, knowing Q is equivalent to knowing $\mathbf{e}_3$ and $\mathbf{B}$. Indeed, equations (3.6c) and (3.6d) give $\mathbf{B}$ and $\mathbf{e}_3$ in terms of Q and Q can be recovered from $\mathbf{B}$ and $\mathbf{e}_3$ column by column according to

$$Q = \left[\frac{1}{\sin\psi}(\mathbf{B} - \cos\psi\,\mathbf{e}_3) \,\middle|\, \frac{1}{\sin\psi}\mathbf{e}_3 \times \mathbf{B} \,\middle|\, \mathbf{e}_3 \right].$$

The vectors $\mathbf{e}_3$ and $\mathbf{B}$ satisfy

$$\dot{\mathbf{e}}_3 = -(\mathsf{P}\,\mathbf{B}) \times \mathbf{e}_3\,, \qquad \dot{\mathbf{B}} = (a\,\mathbf{e}_3 - \mathsf{P}\,\mathbf{B}) \times \mathbf{B}\,, \tag{3.9}$$

with constraints

$$\mathbf{e}_3 \cdot \mathbf{e}_3 = 1\,, \qquad \mathbf{B} \cdot \mathbf{B} = 1\,, \qquad \mathbf{e}_3 \cdot \mathbf{B} = \cos\psi\,. \tag{3.10}$$

3.1.3 Quaternion Formulation

For numerical integration, we use a variant of (3.7) where rotations are parametrised by unit quaternions (or equivalently Euler-Rodrigues parameters) [78], identified with vectors of dimension four on the hypersphere $\mathbb{S}^3$. Specifically, a unit quaternion q is identified with

$$q = \begin{bmatrix} q_0 \\ \mathsf{q} \end{bmatrix} \in \mathbb{S}^3$$

such that $q_0 \in \mathbb{R}$ is the scalar part of the quaternion, and $\mathsf{q} \in \mathbb{R}^3$ its vector part. It parametrises the rotation of angle $\phi = \arccos(2q_0)$ around axis q (cf. [78]).

The two quaternions q and $-q$ both parametrise the same rotation, while the inverse of a rotation parametrised by a unit quaternion q is parametrised by its conjugate $\bar{q}$, defined by (cf. [78])

$$\bar{q} = \begin{bmatrix} q_0 \\ -\mathsf{q} \end{bmatrix} \in \mathbb{S}^3\,.$$

The matrix $Q \in \mathrm{SO}(3)$ parametrising the same rotation as $q \in \mathbb{S}^3$ can be obtained through

$$Q = \left(q_0\,\mathbf{I} + [\mathsf{q}\times]\right)^2 + \mathsf{q} \otimes \mathsf{q}\,, \tag{3.11}$$

whereas $q \in \mathbb{S}^3$ can be obtained from $Q \in \mathrm{SO}(3)$ using (cf. [78])

$$\mathrm{Tr}Q = 4q_0^2 - 1\,, \qquad \frac{1}{2}\left(Q - Q^T\right) = 2q_0\,[\mathsf{q}\times]\,. \tag{3.12}$$

For $q \in \mathbb{R}^4$, the matrices

$$M_L(q) = \begin{bmatrix} q_0 & -\mathsf{q}^T \\ \mathsf{q} & q_0 \mathbf{I} + [\mathsf{q}\times] \end{bmatrix}, \qquad M_R(q) = \begin{bmatrix} q_0 & -\mathsf{q}^T \\ \mathsf{q} & q_0 \mathbf{I} - [\mathsf{q}\times] \end{bmatrix}$$

represent the quaternion multiplication on the left and on the right. In particular, for $p, q \in \mathbb{R}^4$, $M_L(p)\, q = M_R(q)\, p$. For a unit quaternion $q \in \mathbb{S}^3$, the matrices $M_L(q)$ and $M_R(q)$ are such that

$$M_L(q)\, M_R(\bar{q}) = \begin{bmatrix} 1 & 0 \\ 0 & Q \end{bmatrix},$$

where $Q \in \mathrm{SO}(3)$ is the matrix parametrising the same rotation as q.

Equation (3.7) can be written in quaternion form as (cf. [79])

$$\dot{q} = \frac{1}{2} M_R(q) \left(a\, M_L(q)\, M_R(\bar{q}) \begin{bmatrix} 0 \\ 0 \\ 0 \\ 1 \end{bmatrix} - \begin{bmatrix} 1 & 0 \\ 0 & \mathsf{P} \end{bmatrix} M_L(q)\, M_R(\bar{q}) \begin{bmatrix} 0 \\ \sin\psi \\ 0 \\ \cos\psi \end{bmatrix} \right). \tag{3.13}$$

All solution $q \in \mathbb{R}^4$ to this equation verifies $q \cdot \dot{q} = 0$, i.e. the equation is norm preserving.

However, the Jacobian of the right-hand side of (3.13) is singular at steady states. As this is problematic for some numerical treatment, issues are prevented by using the penalised form

$$\dot{q} = \frac{1}{2} M_R(q) \left(a\, M_L(q)\, M_R(\bar{q}) \begin{bmatrix} 0 \\ 0 \\ 0 \\ 1 \end{bmatrix} - \begin{bmatrix} 1 & 0 \\ 0 & \mathsf{P} \end{bmatrix} M_L(q)\, M_R(\bar{q}) \begin{bmatrix} 0 \\ \sin\psi \\ 0 \\ \cos\psi \end{bmatrix} \right) - \frac{1}{2}(|q|^2 - 1)\, q \tag{3.14}$$

instead. The extra term is orthogonal to the right-hand side in (3.13), and vanishes if q is of norm one. Accordingly, unit solutions to (3.13) also satisfy (3.14) and vice-versa.

The corrected form (3.14) will in particular be used for numerical continuation of branches of periodic orbits [80] as the parameters a and ψ are varied (cf. chapters 4 and 6). The linear stability of steady states and periodic orbits is undetermined for system (3.13) due to an ever present zero eigenvalue, and the correction (3.14) prevents this.

The linear stability of a unit steady state q of both systems (3.13, 3.14) is computed from the eigenvalues of the respective stability matrices: q is linearly stable if all eigenvalues have a negative real part [80]. Both stability matrices, which are computed as the Jacobians of the right-hand sides of systems (3.13, 3.14) evaluated at steady state q, admit q as an eigenvector; the associated eigenvalue vanishes for system (3.13) and is -1 for system (3.14). Accordingly, the linear stability of q is undetermined for the non-corrected system (3.13); for the corrected system (3.14), it is determined by the signs of the real parts of the three remaining eigenvalues.

This result follows the fact that the Jacobian $J(q)$ of the right-hand side of the non-corrected system (3.13) satisfies

$$J(q)\, q = 3\dot{q} \tag{3.15}$$

for all solutions q to (3.13). The Jacobian $J_{\mathrm{corr}}(q)$ of the right-hand side of the corrected system (3.14) is related to $J(q)$ by

$$J_{\mathrm{corr}}(q) = J(q) - \frac{1}{2}\big(|q|^2 - 1\big)\mathbf{I} - q \otimes q\,, \tag{3.16}$$

implying that for all unit solutions q to (3.14),

$$J_{\mathrm{corr}}(q)\, q = 3\dot{q} - q\,. \tag{3.17}$$

The stability of a periodic orbit is determined by its Floquet multipliers. These are eigenvalues of the monodromy matrix, which is defined from the Jacobian of the right-hand side of the differential equation, and plays the role of the linearised stability matrix for periodic solutions. One of the eigenvalues of the monodromy matrix is necessarily equal to 1. The Floquet multipliers are the other eigenvalues and define the stability of the periodic orbit: it is stable if all of them are inside the complex unit circle and unstable if they are outside the complex unit circle [80].

Let $q(t)$ be a unit T-periodic solution to both systems (3.13, 3.14). Then one of its Floquet multipliers associated with the non-corrected system (3.13) is 1, implying that the linear stability is undetermined; the corresponding Floquet multiplier associated with the corrected system (3.14) is $e^{-T} < 1$, so that the linear stability is determined by the two remaining Floquet multipliers.

The monodromy matrices of $q(t)$ for system (3.13) and (3.14) are defined as $M(T)$ and $M_{\mathrm{corr}}(T)$, where $M(t)$ and $M_{\mathrm{corr}}(t)$ are respectively the solutions to

$$\begin{aligned} &\dot{M} = J\big(q(t)\big)\, M\,, && M(0) = \mathbf{I}\,,\\ &\dot{M}_{\mathrm{corr}} = J_{\mathrm{corr}}\big(q(t)\big)\, M_{\mathrm{corr}}\,, && M_{\mathrm{corr}}(0) = \mathbf{I}\,. \end{aligned}$$

Both monodromy matrices admit $\dot{q}(0)$ as an eigenvector and the associated eigenvalue is 1. The Floquet multipliers are the other eigenvalues [80]. Here, both monodromy matrices also admit $q(0)$ as an eigenvector, with $M(T)\, q(0) = q(0)$, and $M_{\mathrm{corr}}(T)\, q(0) = e^{-T}\, q(0)$.

Indeed, q satisfies

$$\frac{d}{dt} q(3t) = 3\dot{q}(3t) \overset{(3.15)}{=} J\big(q(3t)\big)\, q(3t)\,,$$

and accordingly $q(3t) = M(t)\, q(0)$ for all t. Since q is T-periodic, we have

$$q(0) = q(3T) = M(T)\, q(0)\,,$$

so that $q(0)$ is an eigenvector of the monodromy matrix $M(T)$ for the eigenvalue 1.

On the other hand, q also satisfies

$$\frac{d}{dt}\left(e^{-t}\,q(3t)\right) = e^{-t}\,\left(3\,\dot{q}(3t) - q(3t)\right) \overset{(3.17)}{=} e^{-t} J_{\mathrm{corr}}\left(q(3t)\right) q(3t)\,,$$

which implies that $e^{-t}\,q(3t) = M_{\mathrm{corr}}(t)\,q(0)$, and in particular, since q is T-periodic, we have $e^{-T}\,q(0) = e^{-T}\,q(T) = M_{\mathrm{corr}}(T)\,q(0)$. Thus $q(0)$ is an eigenvector of the corrected monodromy matrix $M_{\mathrm{corr}}(T)$ for the eigenvalue e^{-T}.

So $q(0)$ is an eigenvector to both $M(T)$ and $M_{\mathrm{corr}}(T)$; the associated eigenvalue is 1 for $M(T)$ and e^{-T} for $M_{\mathrm{corr}}(T)$. Accordingly, $q(t)$ admits 1 as a Floquet multiplier for system (3.13) and e^{-T} as a Floquet multiplier for system (3.14). Its linear stability can therefore be computed from the Floquet multipliers corresponding to the corrected system (3.14), while it is undetermined for system (3.13).

3.2 Relevant Material Parameters

In the system studied here, picking a specific swimmer amounts to specifying its mobility matrix $\mathbb{M}$ and the direction $\mathbf{m}$ of its magnetic moment. These material properties of the swimmer enter the differential equation (3.7) through the single matrix P defined as

$$\mathsf{P} = \mathsf{M}_{22}\,[\mathbf{m}\times]\,. \tag{3.8}$$

When examining special solutions of (3.7) in chapters 4 and 5, we will use the singular value decomposition of P (see [81] for an introduction). The singular values σ_i, which are real and non-negative, left-singular vectors $\boldsymbol{\eta}_i$ and right-singular vectors $\boldsymbol{\beta}_i$ ($i = 0, 1, 2$) of P satisfy by definition

$$\mathsf{P}\,\boldsymbol{\beta}_i = \sigma_i\,\boldsymbol{\eta}_i, \qquad\qquad \mathsf{P}^T\,\boldsymbol{\eta}_i = \sigma_i\,\boldsymbol{\beta}_i. \tag{3.18}$$

Since P is constant in the body frame, its left- and right-singular vectors $\{\boldsymbol{\eta}_i\}_{i=0,1,2}$ and $\{\boldsymbol{\beta}_i\}_{i=0,1,2}$ form two orthogonal bases that are fixed in the body frame; they can be picked so that the two bases are orthonormal and right-handed, and this will be assumed from now on.

The particular form of P implies that it admits $\sigma_0 = 0$ as a singular value for the right-singular vector $\boldsymbol{\beta}_0 = \mathbf{m}$. The associated left-singular vector $\boldsymbol{\eta}_0$ is in the span of $\mathsf{M}_{22}^{-1}\,\mathbf{m}$. We pick

$$\boldsymbol{\eta}_0 = \frac{\mathsf{M}_{22}^{-1}\,\mathbf{m}}{|\mathsf{M}_{22}^{-1}\,\mathbf{m}|}$$

and since M_{22} is positive definite, this choice implies that $\boldsymbol{\beta}_0 \cdot \boldsymbol{\eta}_0 > 0$. The angle $\iota \in [0, \pi/2)$ between $\boldsymbol{\beta}_0$ and $\boldsymbol{\eta}_0$ will prove to be a crucial material parameter. There also exists an angle

$\zeta \in [0, 2\pi)$ such that the vector $\boldsymbol{\eta}_0$ written in the $\{\boldsymbol{\beta}_i\}$ basis is of the form

$$\boldsymbol{\eta}_0 = \cos\iota\,\boldsymbol{\beta}_0 + \sin\iota\,(\sin\zeta\,\boldsymbol{\beta}_1 - \cos\zeta\,\boldsymbol{\beta}_2)\,. \tag{3.19}$$

Since the $\boldsymbol{\beta}_i$ and $\boldsymbol{\eta}_i$ form right-handed orthonormal bases, they satisfy

$$\boldsymbol{\eta}_1 = \frac{1}{\sigma_1}\mathsf{P}\,\boldsymbol{\beta}_1 = \frac{1}{\sigma_1}\mathsf{M}_{22}\,[\mathbf{m}\times]\,\boldsymbol{\beta}_1 = \frac{1}{\sigma_1}\mathsf{M}_{22}\,\left[\boldsymbol{\beta}_0\times\right]\,\boldsymbol{\beta}_1 = \frac{1}{\sigma_1}\mathsf{M}_{22}\,\boldsymbol{\beta}_2\,,$$

and similarly

$$\boldsymbol{\eta}_2 = -\frac{1}{\sigma_2}\mathsf{M}_{22}\,\boldsymbol{\beta}_1\,,$$

which imply

$$\begin{aligned}
&\sigma_1 = |\mathsf{M}_{22}\,\boldsymbol{\beta}_2|\,, && \sigma_2 = |\mathsf{M}_{22}\,\boldsymbol{\beta}_1|\,,\\
&\mathsf{M}_{22}\,\boldsymbol{\beta}_1\cdot\mathsf{M}_{22}\,\boldsymbol{\beta}_2 = 0\,, && \sigma_1\,\boldsymbol{\eta}_1\cdot\boldsymbol{\beta}_1 = -\sigma_2\,\boldsymbol{\eta}_2\cdot\boldsymbol{\beta}_2\,,\\
&\boldsymbol{\eta}_0 = \frac{\mathsf{M}_{22}^{-1}\,\mathbf{m}}{|\mathsf{M}_{22}^{-1}\,\mathbf{m}|} = \frac{(\mathsf{M}_{22}\,\boldsymbol{\beta}_1)\times(\mathsf{M}_{22}\,\boldsymbol{\beta}_2)}{\sigma_1\,\sigma_2}\,.
\end{aligned}$$

These material parameters will also appear through

$$\begin{aligned}
c_{01} &= \boldsymbol{\beta}_0\cdot\mathsf{P}\,\boldsymbol{\beta}_1\\
c_{02} &= \boldsymbol{\beta}_0\cdot\mathsf{P}\,\boldsymbol{\beta}_2\\
c_{11} &= \boldsymbol{\beta}_1\cdot\mathsf{P}\,\boldsymbol{\beta}_1 = -\boldsymbol{\beta}_2\cdot\mathsf{P}\,\boldsymbol{\beta}_2\\
c_{12} &= \boldsymbol{\beta}_1\cdot(\mathsf{P}+\mathsf{P}^T)\,\boldsymbol{\beta}_2\,.
\end{aligned} \tag{3.20}$$

3.3 Symmetric Solutions

In a static spatially uniform magnetic field, a magnetic dipole is in stable equilibrium when its magnetic moment is aligned with the magnetic field, and in unstable equilibrium when it is anti-parallel to it [21]. A related phenomenon occurs in the setting described above: solutions to system (3.7) go by pairs linked by a flip of the magnetic moment with respect to the magnetic field – since the magnetic field varies with time, the symmetry is less straightforward however. These symmetric pairs of solutions have symmetric asymptotic behaviours as $t \to \infty$ for one of them and $t \to -\infty$ for the other, so that asymptotically stable solutions of the system as $t \to \infty$, are the symmetric twins of asymptotically unstable solutions as $t \to \infty$.

A flip of the magnetic moment with respect to the magnetic field amounts in the body frame – where the magnetic moment is constant – to an antisymmetry of the magnetic field, i.e. an operation on Q that brings

$$\mathbf{B} = Q \begin{bmatrix} \sin\psi \\ 0 \\ \cos\psi \end{bmatrix}$$

onto $-\mathbf{B}$. Composing Q with any rotation by π around an axis perpendicular to $\begin{bmatrix} \sin\psi \\ 0 \\ \cos\psi \end{bmatrix}$ accomplishes this. On the other hand, $\mathbf{B}$ varies in time by rotating around the axis $\mathbf{e}_3$, which also appears in the angular velocity of matrix Q (cf. eq. (3.6a)). The axis $\mathbf{e}_3$ changes sign if Q is composed with any rotation by π around an axis perpendicular to $\begin{bmatrix} 0 \\ 0 \\ 1 \end{bmatrix}$. The intersection of these two sets of operations is the composition of Q with a rotation by π around $\begin{bmatrix} 0 \\ 1 \\ 0 \end{bmatrix}$, denoted $R_2(\pi)$.

Let $Q(t)$ be a solution of (3.7) for the parameters a and ψ. Then there exists a symmetric solution for the same parameters given by

$$\breve{Q}(t) := Q(-t) \begin{bmatrix} -1 & 0 & 0 \\ 0 & 1 & 0 \\ 0 & 0 & -1 \end{bmatrix} =: Q(-t)\, R_2(\pi)\,. \tag{3.21}$$

Indeed $\breve{Q}$ thus defined satisfies

$$\begin{aligned}
\dot{\breve{Q}}(t) &= \frac{d}{dt}\big(Q(-t)\,R_2(\pi)\big) = -\dot{Q}(-t)\,R_2(\pi) \\
&= -\left[\left(a\,Q(-t)\begin{bmatrix} 0 \\ 0 \\ 1 \end{bmatrix} - \mathsf{P}\,Q(-t)\begin{bmatrix} \sin\psi \\ 0 \\ \cos\psi \end{bmatrix}\right)\times\right] Q(-t)\,R_2(\pi) \\
&= \left[\left(a\,Q(-t)\,R_2(\pi)\begin{bmatrix} 0 \\ 0 \\ 1 \end{bmatrix} - \mathsf{P}\,Q(-t)\,R_2(\pi)\begin{bmatrix} \sin\psi \\ 0 \\ \cos\psi \end{bmatrix}\right)\times\right] Q(-t)\,R_2(\pi) \\
&= \left[\left(a\,\breve{Q}(t)\begin{bmatrix} 0 \\ 0 \\ 1 \end{bmatrix} - \mathsf{P}\,\breve{Q}(t)\begin{bmatrix} \sin\psi \\ 0 \\ \cos\psi \end{bmatrix}\right)\times\right] \breve{Q}(t)\,.
\end{aligned}$$

It follows from (3.21) that the corresponding expressions for the magnetic field and its axis of rotation in the symmetric body frame are

$$\breve{\mathbf{B}}(t) = -\mathbf{B}(-t)\,, \qquad \breve{\mathbf{e}}_3(t) = -\mathbf{e}_3(-t)\,.$$

It is straightforward to see that $\breve{\mathbf{B}}$ and $\breve{\mathbf{e}}_3$ satisfy (3.9) and (3.10) for the same values of parameters a and ψ as $\mathbf{B}$ and $\mathbf{e}_3$.

We define the angle ϕ as the angle between the magnetic moment $\mathbf{m}$ and the magnetic field $\mathbf{B}$, i.e.

$$\cos\phi = \mathbf{m}\cdot\mathbf{B}\,. \tag{3.22}$$

The angle $\breve{\phi}$ between the magnetic moment $\mathbf{m}$ and the symmetric magnetic field $\breve{\mathbf{B}}$ satisfies $\cos\breve{\phi}(t) = \mathbf{m}\cdot\breve{\mathbf{B}}(t) = -\mathbf{m}\cdot\mathbf{B}(-t) = -\cos\phi(-t)$ or equivalently $\breve{\phi}(t) = \pi - \phi(-t)$.

Substituting $\breve{\mathbf{B}}$ into (3.1b) and (3.1d) implies that the symmetric velocities $\breve{\mathbf{v}}$ and $\breve{\boldsymbol{\omega}}$ satisfy

$\breve{\mathbf{v}}(t) = -\mathbf{v}(-t)$ and $\breve{\boldsymbol{\omega}}(t) = -\boldsymbol{\omega}(-t)$.

The corresponding symmetric trajectories in the lab frame are given respectively by position $\boldsymbol{x}(t)$ and $\breve{\boldsymbol{x}}(t) = \boldsymbol{x}_0 + R_2(\pi)(\boldsymbol{x}(t) - \boldsymbol{x}_0)$ and orientation $R(t)$ and $\breve{R}(t) = R_2(\pi)R(-t)$. Indeed

$$\breve{R}(t) := R_3(a\,t)\,\breve{Q}^T(t) = R_3(a\,t)\,R_2(\pi)\,Q^T(-t) = R_2(\pi)\,R_3(-a\,t)\,Q^T(-t) = R_2(\pi)\,R(-t)\,,$$

and

$$\begin{aligned}\breve{\boldsymbol{x}}(t) - \boldsymbol{x}_0 &= \int_0^t \breve{\boldsymbol{v}}(s)\,ds = \int_0^t \breve{R}(s)\,\breve{\mathbf{v}}(s)\,ds\\ &= \int_0^t R_2(\pi)\,R(-s)\,(-\mathbf{v}(-s))\,ds\\ &= R_2(\pi)\int_0^{-t} \boldsymbol{v}(s)\,ds = R_2(\pi)\,(\boldsymbol{x}(-t) - \boldsymbol{x}_0)\,.\end{aligned}$$

Finally, the time reversal appearing in the symmetry (3.21) implies that if Q is an asymptotically stable solution to (3.7) then $\breve{Q}$ is necessarily unstable. This will be exemplified for steady states in chapter 4 and periodic orbits in chapter 5.

4 Relative equilibria

4.1 The solution set

The motion of magnetic micro-swimmers is prescribed by

$$\dot{Q} = \left[\left(a Q \begin{bmatrix} 0 \\ 0 \\ 1 \end{bmatrix} - \mathsf{P} Q \begin{bmatrix} \sin\psi \\ 0 \\ \cos\psi \end{bmatrix} \right) \times \right] Q, \tag{3.7}$$

where the matrix Q represents the rotation between the magnetic frame and the body frame. The steady states of (3.7) therefore correspond to the magnetic frame being locked to the body frame. We work here in the body frame, but the steady states of (3.7) also correspond solutions for which the orientation of the swimmer is constant in the magnetic frame.

Relative equilibria are equilibria in a moving frame – here, the term relative equilibria will refer to equilibria in the body frame. Accordingly, the linear and angular velocities are constant in the body frame. The linear and angular velocities resulting from (3.7) are given by

$$\mathbf{v} = \mathsf{M}_{12}\,[\mathbf{m}\times]\,\mathbf{B}, \tag{3.1b}$$

$$\boldsymbol{\omega} = \mathsf{M}_{22}\,[\mathbf{m}\times]\,\mathbf{B}, \tag{3.1d}$$

where

$$\mathbf{B} = Q \begin{bmatrix} \sin\psi \\ 0 \\ \cos\psi \end{bmatrix}, \tag{3.6c}$$

so that relative equilibria are given by the steady states of (3.7).

Accordingly, relative equilibria occur if and only if

$$a Q \begin{bmatrix} 0 \\ 0 \\ 1 \end{bmatrix} = \mathsf{P} Q \begin{bmatrix} \sin\psi \\ 0 \\ \cos\psi \end{bmatrix}. \tag{4.1}$$

Using the body frame components $\mathbf{B}$ and $\mathbf{e}_3$ of the magnetic field and its axis of rotation, which satisfy (3.9), this condition is

$$a\mathbf{e}_3 = \mathsf{P}\mathbf{B}\,, \tag{4.2}$$

where $\mathbf{e}_3$ and $\mathbf{B}$ satisfy the constraints

$$\mathbf{e}_3 \cdot \mathbf{e}_3 = 1\,, \qquad \mathbf{B} \cdot \mathbf{B} = 1\,, \qquad \mathbf{e}_3 \cdot \mathbf{B} = \cos\psi\,. \tag{3.10}$$

Finding relative equilibria therefore amounts to finding pairs $(\mathbf{e}_3, \mathbf{B})$ satisfying (4.2, 3.10) for given parameters a and ψ.

The equilibrium conditions depend on two parameters a and ψ. Consequently, the set of all relative equilibria forms a two-dimensional set in the eight-dimensional space $(\mathbf{e}_3, \mathbf{B}, a, \psi)$. System (4.2, 3.10) indeed provides 6 equations for the eight degrees of freedom of $(\mathbf{e}_3, \mathbf{B}, a, \psi)$. We have identified a one-to-one parameterisation of the set of all relative equilibria, which we provide below. Visualising this set has helped us gaining insight on relative equilibria. As its elements are eight-dimensional, they need to be projected in 3D space to be understood. The projection we found the most useful is projection onto the space having for axes a, $\cos\psi$, and the angle ϕ between the magnetic field and magnetic moment given in (3.22). The set of relative equilibria is a two-dimensional surface in this space. By studying this surface, we obtained results on how many equilibria there are for given parameters and how this number can change as the parameters vary. In particular, folds of the system (3.7) in the sense of bifurcation theory [80] correspond to points of the surface admitting a vertical plane of tangency.

4.1.1 Parametrisation of the Set of Relative Equilibria

In order to build the parametrisation of the set of relative equilibria, notice that the equilibrium condition (4.2) constrains $\mathbf{e}_3$ to lie in the $(\boldsymbol{\eta}_1, \boldsymbol{\eta}_2)$-plane, where $\boldsymbol{\eta}_1$ and $\boldsymbol{\eta}_2$ are the left-singular vectors of P defined in (3.18). Indeed, P is a singular matrix: $\mathsf{P}\boldsymbol{\beta}_0 = 0$. So if the pair $(\mathbf{e}_3, \mathbf{B})$ satisfies (3.10, 4.2), then there exists an angle $\theta \in (-\pi, \pi]$ such that

$$\mathbf{e}_3 = \cos\theta\,\boldsymbol{\eta}_1 + \sin\theta\,\boldsymbol{\eta}_2\,. \tag{4.3}$$

The components $\mathbf{B}$ of the magnetic field in the body frame can be expanded in the $\{\boldsymbol{\beta}_i\}$-basis as

$$\mathbf{B} = \cos\phi\,\boldsymbol{\beta}_0 + \sin\phi\left(\cos\xi\,\boldsymbol{\beta}_1 + \sin\xi\,\boldsymbol{\beta}_2\right)$$

for some angles $\phi \in [0, \pi]$ and $\xi \in (-\pi, \pi]$. Note that ϕ is the angle between magnetic field and magnetic moment defined in (3.22) since $\boldsymbol{\beta}_0 = \mathbf{m}$. Substituting in (4.2) and using (3.18) yields a one-to-one correspondence between the angle ξ used to express $\mathbf{B}$, and the angle θ appearing in (4.3). The magnetic field $\mathbf{B}$ therefore can be expressed as

$$\mathbf{B} = \cos\phi\,\boldsymbol{\beta}_0 + \sin\phi\left(\frac{\cos^2\theta}{\sigma_1^2} + \frac{\sin^2\theta}{\sigma_2^2}\right)^{-1/2}\left(\frac{\cos\theta}{\sigma_1}\boldsymbol{\beta}_1 + \frac{\sin\theta}{\sigma_2}\boldsymbol{\beta}_2\right). \tag{4.4}$$

The angles ϕ and θ depend on the parameters a and ψ and must satisfy

$$\begin{aligned} a &= \sin\phi\left(\frac{\cos^2\theta}{\sigma_1^2} + \frac{\sin^2\theta}{\sigma_2^2}\right)^{-1/2} \\ \cos\psi &= \cos\phi\left(c_{01}\frac{\cos\theta}{\sigma_1} + c_{02}\frac{\sin\theta}{\sigma_2}\right) \\ &\quad + \sin\phi\left(\frac{\cos^2\theta}{\sigma_1^2} + \frac{\sin^2\theta}{\sigma_2^2}\right)^{-1/2}\left(c_{11}\left(\frac{\cos^2\theta}{\sigma_1^2} - \frac{\sin^2\theta}{\sigma_2^2}\right) + c_{12}\frac{\cos\theta\,\sin\theta}{\sigma_1\sigma_2}\right), \end{aligned} \tag{4.5}$$

where the c_{ij} are given in (3.20) (cf. p. 38), and depend only on the singular decomposition of P, which implies that they are body parameters.

As a result, the angles θ and ϕ are smooth coordinates on the set of relative equilibria. This means that a value (θ,ϕ) is in one-to-one correspondence with a unique relative equilibrium given as the point $(\mathbf{e}_3, \mathbf{B}, a, \psi) \in \mathbb{R}^8$ satisfying (4.3, 4.4, 4.5).

The area covered by pairs of parameters (a,ψ) for which there exist any steady state of (3.7) is delineated by parametrisation (4.5). In particular, for each conical angle ψ, there is a maximal value of the Mason number a for which relative equilibria exist, and it can be found using equations (4.5). The absolute maximum of a for which relative equilibria exist is $a_{\max} = \sigma_1$, where $\sigma_1 = \max\{\sigma_1, \sigma_2\}$, and it is obtained for the conical angle ψ given by $\cos\psi = c_{11}/\sigma_1$.

Recall that the Mason number is proportional to the angular speed α of the rotating magnetic field. Experimenters observe a behaviour they call step-out as α is increased: the axial velocity of swimmers suddenly drops [64]. It is believed that step-out corresponds to the transition between a parameter regime with steady states to a parameter regime without steady states [45]. If this is true, then equations (4.5) allows to determine the step-out angular speed α at all values of conical angle ψ.

4.1.2 Visualisation of the Set of Relative Equilibria

To visualise the set of relative equilibria embedded in 8D space, we project it onto the 3D space $(a, \cos\psi, \phi)$ as the surface

$$\mathscr{S} := \left\{\Sigma(\theta,\phi) := \left(a(\theta,\phi), \cos\psi(\theta,\phi), \phi\right) \middle| (\theta,\phi) \in (-\pi,\pi] \times [0,\pi]\right\}, \tag{4.6}$$

where $a(\theta,\phi)$ and $\cos\psi(\theta,\phi)$ are given by (4.5). An example corresponding to a particular swimmer, that we call swimmer A, is represented in figure 4.1. The shape and magnetic moment of swimmer A – its body parameters – are discussed in chapter 6, where other examples are also presented.

Note that this choice of projection involves ϕ because it is both physically and mathematically meaningful: it encodes the misalignment between the external magnetic field and the magnetisation of the body, and it allows (with θ) for a one-to-one parameterisation of the set of steady states. Naturally, other choices could also be interesting – the dissipation rate is a

a) Whole surface as mesh (viewpoint 1)   b) Whole surface as mesh (viewpoint 2)

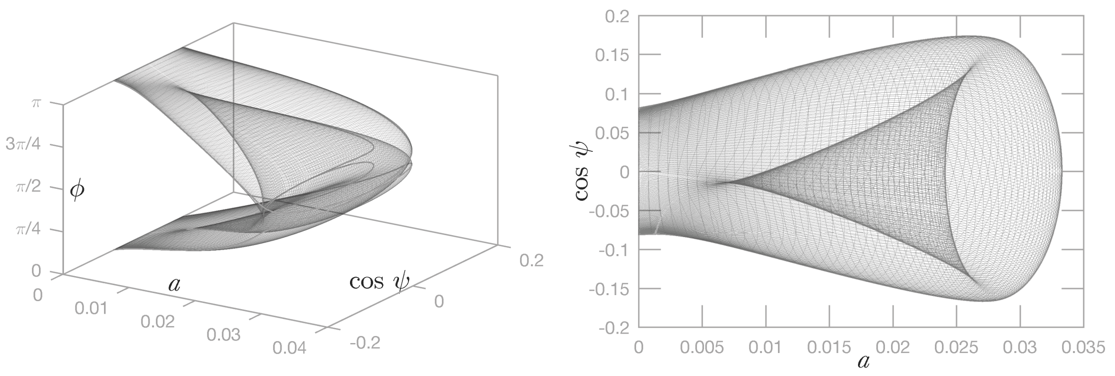

c) Whole surface (viewpoint 1)   d) Whole surface (viewpoint 2)

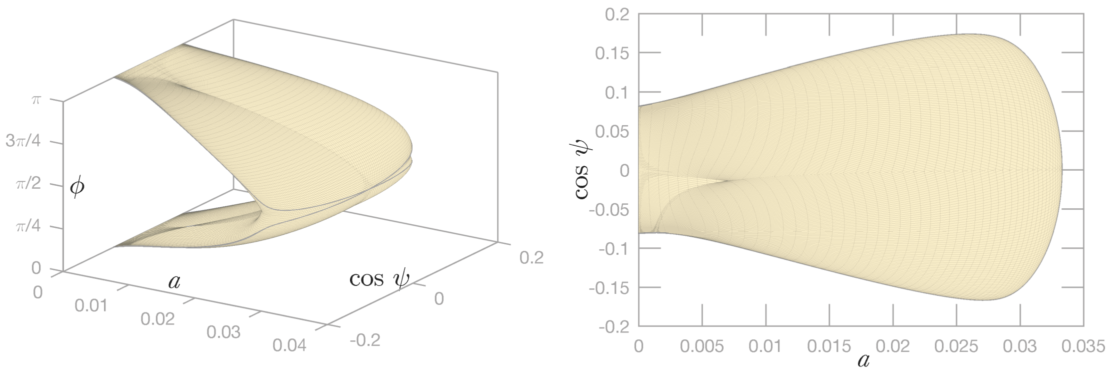

Figure 4.1 – The surface $\mathscr{S}$ representing steady state solutions to dynamical system (3.7) for a particular swimmer (called swimmer A in chapter 6).
For a given swimmer the set of steady states of (3.7) is a locally two-dimensional set in an eight-dimensional space: two-dimensional because it depends on the two parameters a and ψ related to the applied magnetic field. It is visualised here as a surface in a three-dimensional space by projecting it in the space of coordinates $\left(a, \cos\psi, \phi\right)$, where a is the Mason number, ψ the conical angle between the magnetic field and its axis of rotation and ϕ the angle between the magnetic field and the magnetic moment of the swimmer. This surface is parametrised by equation (4.6).
All panels show the same surface, as a transparent mesh in panels a and b, and as a plain surface in panels c and d. The folds of the surface are especially noticeable in panel b. Note that the surface is not symmetric about the plane $\cos\psi = 0$.
To view this surface from more points of view, click here (password: thesisPR) or scan the barcode.

classical candidate.

The intrinsic symmetry of equation (3.7), described in section 3.3, translates to a geometric symmetry of the surface $\mathscr{S}$: indeed the symmetric twin to an equilibrium parametrised by (θ,ϕ) is parametrised by $(\pi+\theta\,(\mathrm{mod}\,2\pi),\pi-\phi)$. This relation between θ and $\pi+\theta$ is due to the symmetry between $\mathbf{e}_3$ and $-\mathbf{e}_3$ (cf. section 3.3). The surface $\mathscr{S}$ therefore has a mirror symmetry about the plane $\phi=\frac{\pi}{2}$ (cf. fig. 4.2).

The geometry of surface $\mathscr{S}$ is difficult to understand due to its self-intersections. To overcome this – at least partially – we are splitting $\mathscr{S}$ as follows. For $\theta_0=\arctan\left(-c_{01}\,\sigma_2/(c_{02}\,\sigma_1)\right)$, the surface point $\Sigma\left(\theta_0,\phi\right)=\Sigma\left(\theta_0+\pi,\phi\right)$ for all ϕ, so the surface self-intersects at those points. The two equilibria parametrised respectively by $\left(\theta_0,\phi\right)$ and $\left(\theta_0+\pi,\phi\right)$ for a given ϕ are nevertheless truly distinct as they correspond to different pairs of $\mathbf{e}_3$ and $\mathbf{B}$ as given by (4.3) and (4.4).

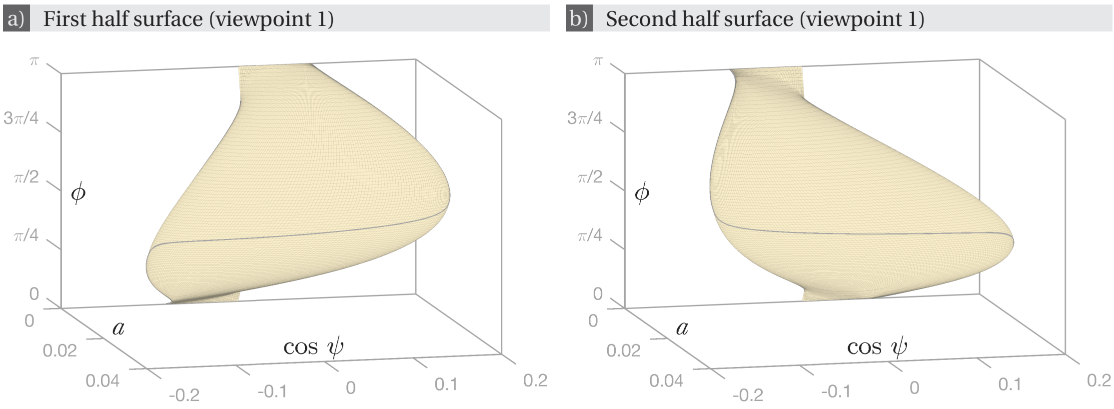
a) First half surface (viewpoint 1)

b) Second half surface (viewpoint 1)

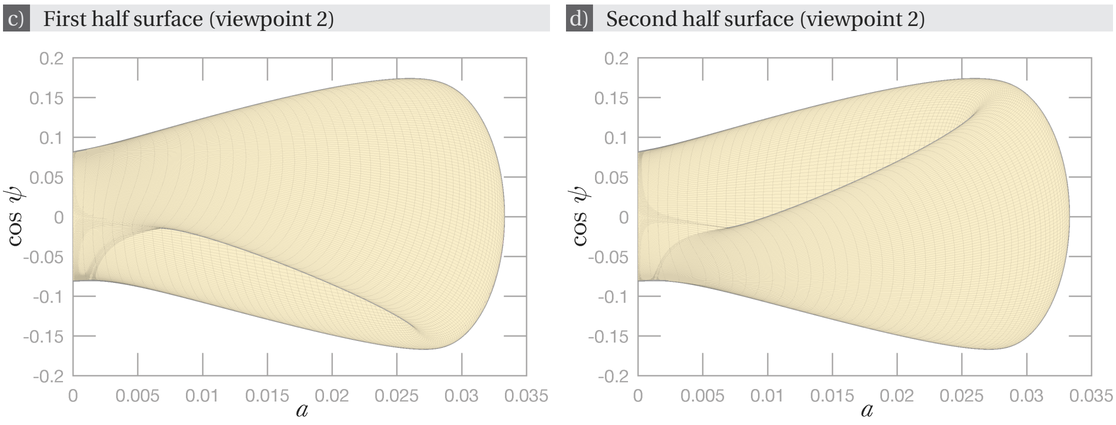
c) First half surface (viewpoint 2)

d) Second half surface (viewpoint 2)

Figure 4.2 – The two symmetric halves $\mathscr{S}_1$ and $\mathscr{S}_2$ of surface $\mathscr{S}$ represented in figure 4.1. The splitting along a self-intersection of $\mathscr{S}$ is done as described in equation (4.7).
Each steady state represented on the first half surface $\mathscr{S}_1$ is connected to a steady state on the second half surface $\mathscr{S}_2$ by the symmetry discussed in section 3.3. The two half-surfaces are mirror images of one another through reflection in the plane $\phi=\pi/2$. To view these surfaces from more points of view, click here (password: thesisPR) or scan the barcode.

To improve visualisation, we split the surface $\mathscr{S}$ along the self-intersection at $\theta = \theta_0$ and define the half surfaces

$$\begin{aligned} \mathscr{S}_1 &:= \left\{\Sigma\left(\theta,\phi\right) : \theta \in [\theta_0 - \pi, \theta_0), \phi \in [0,\pi]\right\}, \quad \text{and} \\ \mathscr{S}_2 &:= \left\{\Sigma\left(\theta,\phi\right) : \theta \in [\theta_0, \theta_0 + \pi), \phi \in [0,\pi]\right\}. \end{aligned} \tag{4.7}$$

Beyond helping visualisation, this splitting of the surface also has the advantageous feature of partitioning the surface into two sets related by the symmetry discussed in section 3.3: the symmetric twin to an equilibrium represented in $\mathscr{S}_1$ is in $\mathscr{S}_2$ and vice-versa.

4.1.3 Number of Relative Equilibria

Parametrising the set of all relative equilibria allows to make observations about the number of equilibria for a given pair of parameters (a, ψ).

Proposition Let $a^* > 0$ and $\psi^* \in [0, 2\pi)$. Then the number of steady states of equation (3.7) for $a = a^*$ and $\psi = \psi^*$ either is 0, 4, or 8, or the pair (a^*, ψ^*) belongs to a set of measure zero of parameter pairs for which the number of relative equilibria is either 2 or 6.

Proof Assume that (3.7) has at least one steady state for $a = a^*$ and $\psi = \psi^*$. This steady state can be represented by a point on either $\mathscr{S}_1$ or $\mathscr{S}_2$. Without loss of generality, assume that it is represented by a point on surface $\mathscr{S}_1$. Then its symmetric twin is represented on $\mathscr{S}_2$ and is a distinct steady state. Therefore **the number of steady states of (3.7) is even**.

Each steady state of (3.7) is parametrised by a pair (θ, ϕ) through (4.3, 4.4, 4.5), so that finding the number of steady states for parameter values (a^*, ψ^*) amounts to finding the number of

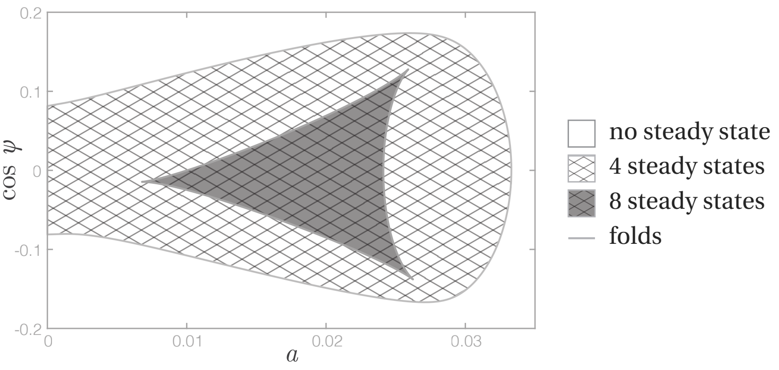

Figure 4.3 – Regions of parameter space according to the number of steady states of (3.7) for swimmer A. The steady states of swimmer A are also represented on figures 4.1 and 4.2. The boundaries between areas with different numbers of steady states correspond to fold bifurcations of the system. No steady state exists outside the area shown here.

(θ,ϕ) satisfying equation (4.5) for $a = a^*$ and $\psi = \psi^*$, i.e.

$$a^* = \sin\phi \left(\frac{\cos^2\theta}{\sigma_1^2} + \frac{\sin^2\theta}{\sigma_2^2} \right)^{-1/2}, \tag{4.8a}$$

$$\begin{aligned} \cos\psi^* = {} & \cos\phi \left(c_{01} \frac{\cos\theta}{\sigma_1} + c_{02} \frac{\sin\theta}{\sigma_2} \right) \\ & + \sin\phi \left(\frac{\cos^2\theta}{\sigma_1^2} + \frac{\sin^2\theta}{\sigma_2^2} \right)^{-1/2} \left(c_{11} \left(\frac{\cos^2\theta}{\sigma_1^2} - \frac{\sin^2\theta}{\sigma_2^2} \right) + c_{12} \frac{\cos\theta \sin\theta}{\sigma_1 \sigma_2} \right). \end{aligned} \tag{4.8b}$$

Equation (4.8a) allows the expression of ϕ in terms of a^* and θ as

$$\sin\phi = a^* \left(\frac{\cos^2\theta}{\sigma_1^2} + \frac{\sin^2\theta}{\sigma_2^2} \right)^{1/2}.$$

Substituting in (4.8b) yields

$$\begin{aligned} & \left(\frac{a^*}{\sigma_1\sigma_2} \left(c_{11} \left(\frac{\cos^2\theta}{\sigma_1^2} - \frac{\sin^2\theta}{\sigma_2^2} \right) + c_{12} \frac{\cos\theta \sin\theta}{\sigma_1 \sigma_2} \right) - \cos\psi^* \right)^2 \\ & + \left(a^{*2} \left(\frac{\cos^2\theta}{\sigma_1^2} + \frac{\sin^2\theta}{\sigma_2^2} \right) - 1 \right) \left(c_{01} \frac{\cos\theta}{\sigma_1} + c_{02} \frac{\sin\theta}{\sigma_2} \right)^2 = 0. \end{aligned}$$

This is a trigonometric polynomial of degree 4 in θ; **it has therefore at most 8 roots** in $[0,2\pi)$ [82].

Steady states for $a = a^*$ and $\psi = \psi^*$ represented on $\mathscr{S}_1$ are at the intersection of $\mathscr{S}_1$ and the straight line $a = a^*$ and $\psi = \psi^*$. The surface $\mathscr{S}$ is a closed surface: its parametrisation (4.6) is periodic in θ, and $a(\theta,\phi) = 0$ for all θ at both bounds $\phi = 0$ and $\phi = \pi$ of the parametrisation interval in ϕ. The splitting of $\mathscr{S}$ into $\mathscr{S}_1$ and $\mathscr{S}_2$ along a self-intersection of $\mathscr{S}$ then implies that $\mathscr{S}_1$ and $\mathscr{S}_2$ are both closed surfaces. This implies that slicing $\mathscr{S}_1$ in the plane $a = a^*$ results in a finite number of closed curves (cf. sketch below), so that the line $a = a^*$ and $\psi = \psi^*$ is either tangent to it or must enter it and leave it.

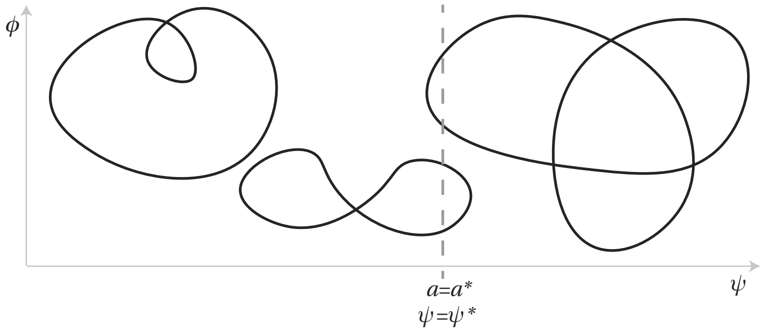

There is a finite number of values ψ^* such that the straight line is tangent to the $a = a^*$ section of $\mathscr{S}_1$, so generically it enters and leaves it. A section of $\mathscr{S}_1$ is not necessarily a simple curve, but a self-intersection represents two distinct steady states as each steady state is uniquely parametrised by (θ,ϕ) in the chosen intervals. Therefore $\mathscr{S}_1$ generically contains an even number of steady states for $a = a^*$ and $\psi = \psi^*$. Counting their symmetric twins in $\mathscr{S}_2$, **the number of steady states for $a = a^*$ and $\psi = \psi^*$ is a multiple of 4.**

In conclusion, the number of steady states of (3.7) for $a = a^*$ and $\psi = \psi^*$ is either 0, 4, or 8 – and 2 or 6 on the boundaries between each region, which constitute a set of measure zero. ■

In figure 4.3, parameter space is split into regions according to number of relative equilibria in the case of swimmer A. More examples can be found in chapter 6.

4.1.4 The Geometry of Surface $\mathscr{S}$

In order to better understand the surface $\mathscr{S}$ as a geometrical object, we give here a detailed account of all its self-intersections. Section 4.1.3 already revealed that it can be parametrised by a single chart (θ,ϕ). Furthermore, there is a self-intersection at $\theta = \theta_0$ and for all values of ϕ. The particular value θ_0 depends only on the swimmer. This self-intersection was used to split the surface into the two mirror image halves $\mathscr{S}_1$ and $\mathscr{S}_2$ (cf. fig. 4.2). The self-intersections of $\mathscr{S}$ are given by

$$\phi = \operatorname{arccot}\left(-\frac{c_{12}}{c_{02}}\left(\frac{\cos^2\theta}{\sigma_1^2}+\frac{\sin^2\theta}{\sigma_2^2}\right)^{-1/2}\frac{\cos\theta}{\sigma_1}\right) \qquad \text{where } \Sigma\left(\theta,\phi\right) = \Sigma\left(-\theta,\phi\right) \tag{4.9a}$$

$$\phi = \operatorname{arccot}\left(-\frac{c_{12}}{c_{01}}\left(\frac{\cos^2\theta}{\sigma_1^2}+\frac{\sin^2\theta}{\sigma_2^2}\right)^{-1/2}\frac{\sin\theta}{\sigma_2}\right) \qquad \text{where } \Sigma\left(\theta,\phi\right) = \Sigma\left(\pi-\theta,\phi\right) \tag{4.9b}$$

$$\theta = \theta_0, \theta_0 \pm \pi \qquad \text{where } \Sigma\left(\theta,\phi\right) = \Sigma\left(\theta+\pi,\phi\right) \tag{4.9c}$$

$$\phi = \frac{\pi}{2} \qquad \text{where } \Sigma\left(\theta,\phi\right) = \Sigma\left(\theta+\pi,\phi\right). \tag{4.9d}$$

Indeed, there is a self-intersection at $(a, \cos\psi, \phi) \in \mathscr{S}$ if there are $\theta_1 \neq \theta_2$ such that the parametrisation (4.5) coincides, i.e.

$$a = \sin\phi\left(\frac{\cos^2\theta_j}{\sigma_1^2}+\frac{\sin^2\theta_j}{\sigma_2^2}\right)^{-1/2} \tag{4.10}$$

$$\begin{aligned}\cos\psi = \cos\phi&\left(c_{01}\frac{\cos\theta_j}{\sigma_1}+c_{02}\frac{\sin\theta_j}{\sigma_2}\right)\\ &+\sin\phi\left(\frac{\cos^2\theta_j}{\sigma_1^2}+\frac{\sin^2\theta_j}{\sigma_2^2}\right)^{-1/2}\left(c_{11}\left(\frac{\cos^2\theta_j}{\sigma_1^2}-\frac{\sin^2\theta}{\sigma_2^2}\right)+c_{12}\frac{\cos\theta_j\sin\theta_j}{\sigma_1\sigma_2}\right)\end{aligned} \tag{4.11}$$

for $j = 1,2$. Equation (4.10) yields

$$\frac{\cos^2\theta_1}{\sigma_1^2}+\frac{1-\cos^2\theta_1}{\sigma_2^2}=\frac{\cos^2\theta_2}{\sigma_1^2}+\frac{1-\cos^2\theta_2}{\sigma_2^2},$$

which implies $\cos\theta_1 = \pm\cos\theta_2$ and $\sin\theta_1 = \pm\sin\theta_2$. Substituting in (4.11) with $\cos\theta_1 = \cos\theta_2$ and $\sin\theta_1 = -\sin\theta_2$ yields

$$c_{02}\cos\phi\,\frac{\sin\theta_1}{\sigma_2} + c_{12}\sin\phi\left(\frac{\cos^2\theta_1}{\sigma_1^2} + \frac{\sin^2\theta_1}{\sigma_2^2}\right)^{-1/2}\frac{\cos\theta_1\,\sin\theta_1}{\sigma_1\sigma_2} = 0,$$

which results in (4.9a). Substituting in (4.11) with $\cos\theta_1 = -\cos\theta_2$ and $\sin\theta_1 = \sin\theta_2$ gives

$$c_{01}\cos\phi\,\frac{\cos\theta_1}{\sigma_1} + c_{12}\sin\phi\left(\frac{\cos^2\theta_1}{\sigma_1^2} + \frac{\sin^2\theta_1}{\sigma_2^2}\right)^{-1/2}\frac{\cos\theta_1\,\sin\theta_1}{\sigma_1\sigma_2} = 0,$$

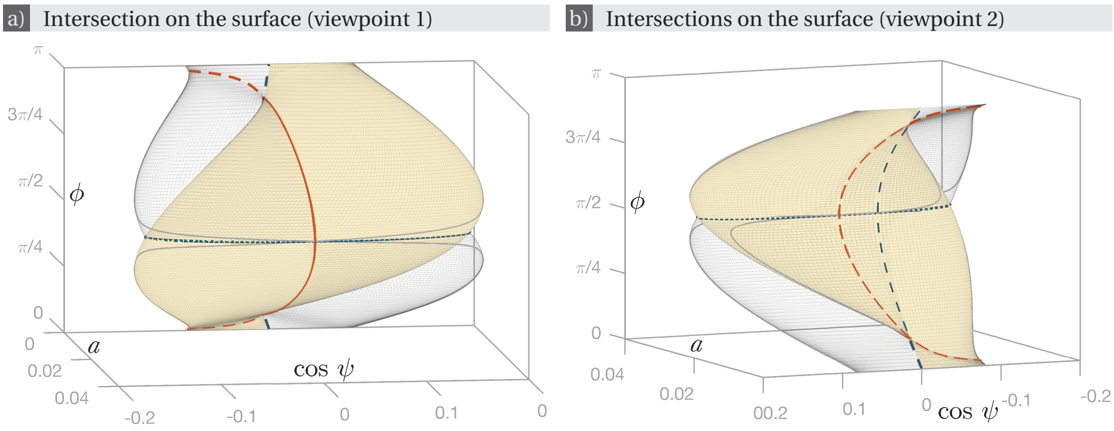
a) Intersection on the surface (viewpoint 1)

b) Intersections on the surface (viewpoint 2)

c) Intersections on the preimage of the surface chart

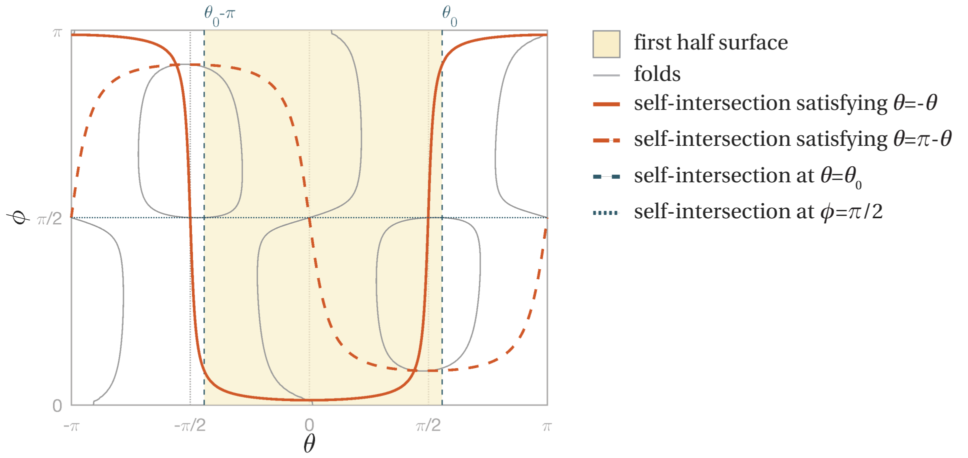

Figure 4.4 – Self-intersections of the surface $\mathscr{S}$ represented in figures 4.1 and 4.2. The first half-surface $\mathscr{S}_1$ is shown as a plain surface, while the second half-surface $\mathscr{S}_2$ is shown as a transparent mesh.
Panel c shows the self-intersections in the pre-image $(-\pi,\pi]\times[0,\pi]$ of the surface chart $(\theta,\phi)\mapsto\Sigma(\theta,\phi)$.
To view the 3D surface from more points of view, click here (password: thesisPR) or scan the barcode.

which can be rewritten as (4.9b). Substituting in (4.11) with $\cos\theta_1 = -\cos\theta_2$ and $\sin\theta_1 = -\sin\theta_2$, we obtain

$$\cos\phi\left(c_{01}\,\frac{\cos\theta_1}{\sigma_1} + c_{02}\,\frac{\sin\theta_1}{\sigma_2}\right) = 0\,,$$

which is satisfied for all values of ϕ if $\theta_1 = \theta_0 + k\pi$ for any integer k (intersection (4.9c)) and for all values of θ_1 if $\phi = \pi/2$ (intersection (4.9d).

Inspecting figures 4.1 and 4.2, it is apparent that the two halves $\mathscr{S}_1$ and $\mathscr{S}_2$ intersect each other at multiple locations. Visualisation has already been eased by splitting $\mathscr{S}$ into $\mathscr{S}_1$ and $\mathscr{S}_2$. To further specify what is seen, we want to determine self-intersections within the same half. Intersection (4.9c) defines the splitting between $\mathscr{S}_1$ and $\mathscr{S}_2$ while (4.9d) is necessarily an intersection between the two halves by definition of $\mathscr{S}_1$ and $\mathscr{S}_2$: the parametrisation $\big(a(\theta,\phi),\phi(\theta,\phi)\big)$ given by (4.5) is almost injective for $\phi = \pi/2$ and θ in an interval of length π, with at most two exceptions which satisfy either (4.9a) or (4.9b). Therefore self-intersections within the same half surface are either in the family (4.9a) or (4.9b).

Self-intersections of type (4.9a) of a half-surface $\mathscr{S}_i$ occur when θ is such that $|\tan\theta| < |\tan\theta_0|$: the closer θ_0 is to 0 or $\pm\pi$, the smaller the set of such θ. Type (4.9b) self-intersections of $\mathscr{S}_i$ arise for θ such that $|\tan\theta| > |\tan\theta_0|$: the closer θ_0 is to $\pm\frac{\pi}{2}$, the smaller the set of such θ. For swimmer A, θ_0 is quite close to $\frac{\pi}{2}$;therefore type (4.9b) self-intersections within the same half $\mathscr{S}_i$ are indiscernible. A larger set of θ satisfy the condition for type (4.9a) self-intersections to occur within the same half $\mathscr{S}_i$.

Note that the surface $\mathscr{S}$ presented in figures 4.1-4.4 is almost but not quite symmetric about the plane $\cos\psi = 0$. The surface $\mathscr{S}$ would feature an extra symmetry about $\cos\psi = 0$ if $c_{11} = 0$. Indeed, then for all $\theta \in [0, 2\pi)$, the relative equilibria parametrised by the pairs (θ,ϕ) and $(\theta+\pi,\phi)$ using equations (4.5) satisfy $a(\theta,\phi) = a(\theta+\pi,\phi)$ and $\cos\psi(\theta,\phi) = -\cos\psi(\theta+\pi,\phi)$. Here we have $c_{11} = 1.6878\cdot 10^{-5}$.

4.2 Stability of Relative Equilibria

The linear stability of steady states of

$$\dot{Q} = \left[\left(a\,Q\left[\begin{smallmatrix}0\\0\\1\end{smallmatrix}\right] - \mathrm{P}\,Q\left[\begin{smallmatrix}\sin\psi\\0\\\cos\psi\end{smallmatrix}\right]\right)\times\right]\,Q\,, \tag{3.7}$$

is given by the sign of the real part of the eigenvalues of the linearised dynamics matrix at a steady state. Linearisation around a steady state Q^* can either be obtained using the fact that a small perturbation of $Q^* \in \mathrm{SO}(3)$ can be written as $Q = Q^* + \varepsilon\,[\mathbf{u}\times]\,Q^* + \mathscr{O}(\varepsilon^2)$ (cf. appendix A), or using the quaternion formulation of (3.7) and linearising the dynamics as usual by treating quaternions like vectors of size 4 (cf. section 3.1.3). Using the expansion of $Q \in \mathrm{SO}(3)$ results in

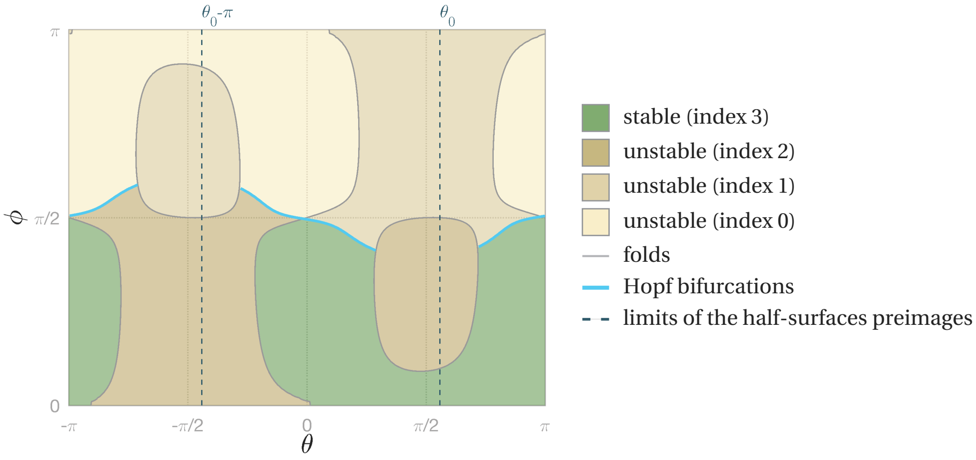

Figure 4.5 – Pre-image $(-\pi,\pi] \times [0,\pi]$ of the surface chart $(\theta,\phi) \mapsto \Sigma(\theta,\phi)$ coloured by stability index. The corresponding image $\mathscr{S}$ is shown in figure 4.6. Stability index changes at folds and at Hopf bifurcations. Stable steady states are all confined to $\phi < \pi/2$.

the linear stability matrix

$$A = \mathsf{P}\,[\mathbf{B}\times] - a\,[\mathbf{e}_3\times]\,;$$

with the vector-quaternion form, the stability matrix is similar to

$$\begin{bmatrix} A & 0 \\ 0 & 0 \end{bmatrix}$$

if the non-corrected form (3.13) is used, and to

$$\begin{bmatrix} A & 0 \\ 0 & -1 \end{bmatrix}$$

if the corrected form (3.14) is used instead (cf. section 3.1.3). A steady state is linearly stable if all three eigenvalues of A have a negative real part and unstable if its *index*, i.e. the number of eigenvalues of A with negative real part, is 0, 1, or 2 – that is, anything but 3. The form of A implies that symmetric pairs of equilibria given by $(\mathbf{e}_3, \mathbf{B})$ and $(-\mathbf{e}_3, -\mathbf{B})$ for the same parameters a and ψ have opposite eigenvalues. So either one equilibrium of the pair has index 1 and the other one has index 2 or one equilibrium has index 0 and the other one has index 3 - and is therefore stable.

Each point of $\mathscr{S}$ can be assigned a colour corresponding to the stability index of the steady state it represents (cf. fig. 4.5 and 4.6). As eigenvalues of A vary continuously on $\mathscr{S}$, the stability index changes only at bifurcation points of the dynamical system (3.7).

The generic bifurcations occurring in this system are folds and Hopf bifurcations. Folds are steady states at which the stability matrix A admits a zero eigenvalue and satisfy $\det A = 0$, while Hopf bifurcations are steady states at which the stability matrix A admits a pair of purely imaginary conjugate eigenvalues and satisfy $\det C = 0$, where C is defined from the components a_{ij} of A as

$$C = \begin{bmatrix} a_{22}+a_{11} & a_{23} & -a_{13} \\ a_{32} & a_{33}+a_{11} & a_{12} \\ -a_{31} & a_{21} & a_{33}+a_{22} \end{bmatrix}.$$

Accordingly, the stability index varies by ±1 at folds, and by ±2 at Hopf bifurcations [80].

Folds in the sense of bifurcation theory correspond to points of $\mathscr{S}$ where the tangent plane to $\mathscr{S}$ is vertical – recall that $\mathscr{S}$ lies in a space where the horizontal plane corresponds to the plane of parameters (a,ψ). Indeed folds are bifurcations where two steady states co-existing for values of the parameters (a,ψ) merge and disappear as the parameters are varied. In the system studied here, the other generic type of bifurcation is the Hopf bifurcation, and it does not involve a change in the number of steady states. Since the surface $\mathscr{S}$ lies in a 3D space defined in such a way that the horizontal plane is the parameter plane, folds correspond to the points where $\mathscr{S}$ is horizontally limited. These points are the points where $\mathscr{S}$ admits a vertical tangent plane. Indeed, the chart $(-\pi,\pi]\times(0,\pi)\to\mathscr{S}:(\theta,\phi)\mapsto\Sigma(\theta,\phi)=\big(a(\theta,\phi),\cos\psi(\theta,\phi),\phi\big)$, that parametrises $\mathscr{S}$ except at its boundary $a=0$, is smooth almost everywhere; that is the normal to the surface

$$\partial_\theta\Sigma\times\partial_\phi\Sigma = \begin{bmatrix} \partial_\theta a\,\partial_\phi\cos\psi - \partial_\phi a\,\partial_\theta\cos\psi \\ -\partial_\theta a \\ \partial_\theta\cos\psi \end{bmatrix} \neq \mathbf{0}$$

except for a finite number of (θ,ϕ) satisfying $\partial_\theta a = 0 = \partial_\theta\cos\psi$, which are given by $(\theta,\phi)\in\big\{(\pi/2,0)\pm\big(\pi/2,\arctan(c_{02}/c_{12})\big),\pm\big(\pi/2,-\arctan(c_{01}/c_{12})\big)\big\}$ (cf. eq (4.5)). The tangent plane to $\mathscr{S}$ is well defined at all other points. The points admitting a vertical tangent plane, which correspond to folds, are parametrised by θ and ϕ satisfying

$$0 = \begin{bmatrix} 0 \\ 0 \\ 1 \end{bmatrix}\cdot(\partial_\theta\Sigma\times\partial_\phi\Sigma) = \partial_\theta\cos\psi\,.$$

This equation defines a continuous one-dimensional set that includes the singular points of the surface mapping. By continuity, the singular points also correspond to folds.

In all the examples we studied, the curves of Hopf bifurcations are bounded on both sides by Bogdanov-Takens (BT) bifurcations [80]. Moreover, recall that Hopf bifurcations are characterised by a pair of purely imaginary eigenvalues of the stability matrix; BT bifurcations arise when the imaginary part of this pair vanishes, and mark the junction of a curve of Hopf bifurcations with a curve of folds.

The antisymmetry in stability of symmetric pairs implies that knowing the stability indices on the half-surface $\mathscr{S}_1$ is sufficient to deduce the stability indices on $\mathscr{S}_2$ and vice-versa. The stability index changes only at bifurcations. This is obvious in figure 4.5 which shows the

a) Whole surface (viewpoint 1) b) Whole surface (viewpoint 2)

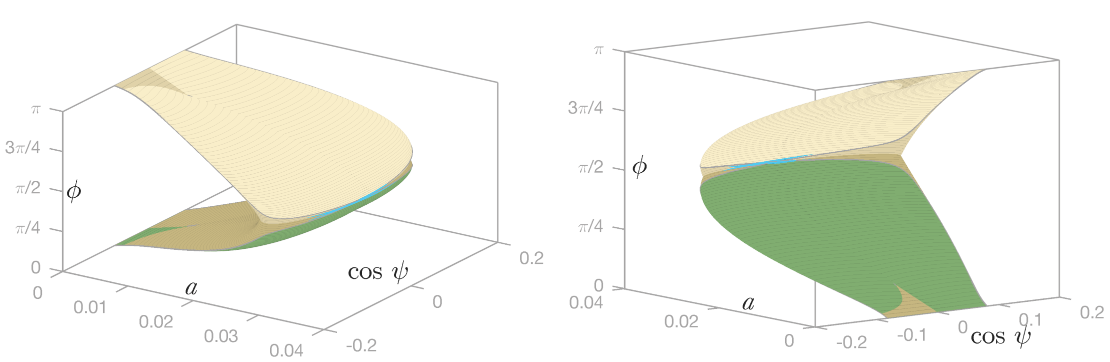

c) First half surface (viewpoint 1) d) First half surface (viewpoint 2)

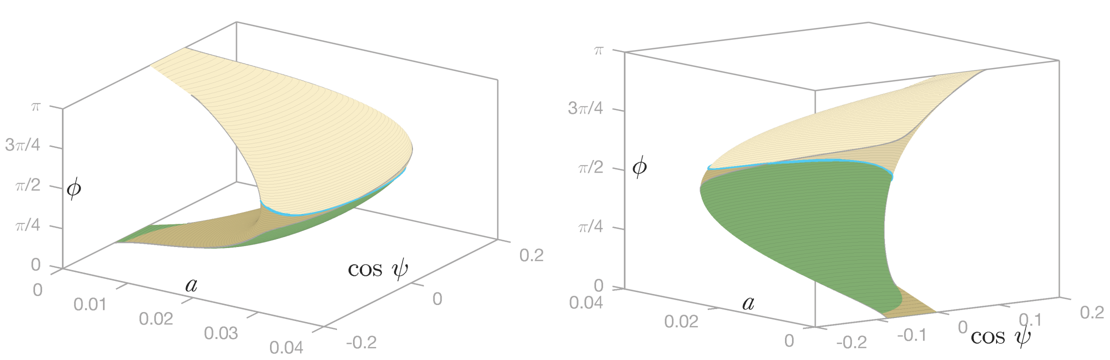

e) Second half surface (viewpoint 1) f) Second half surface (viewpoint 2)

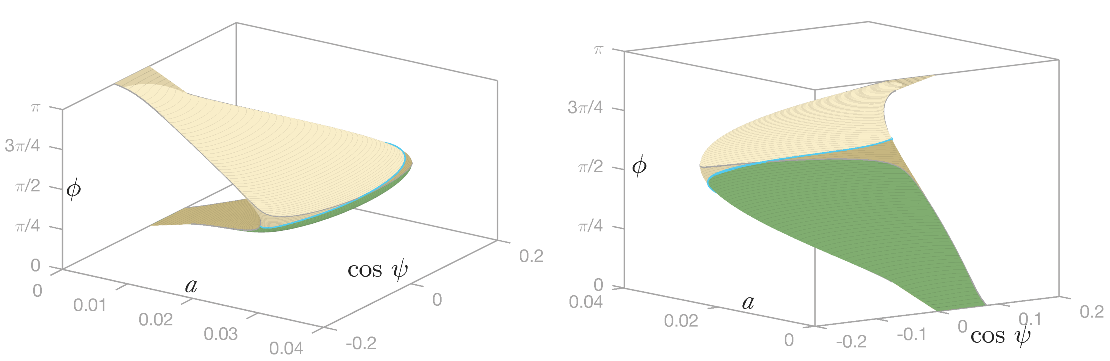

🟩 stable (index 3) 🟫 unstable (index 2) ▨ unstable (index 1) 🟨 unstable (index 0)
— folds — Hopf bifurcations

Figure 4.6 – Surface $\mathscr{S}$ and its halves $\mathscr{S}_1$ and $\mathscr{S}_2$ shown in figures 4.1 and 4.2 coloured by stability index. Stability index changes at Hopf bifurcations and at folds. Stable steady states are all confined to the lower half of $\mathscr{S}$ for which $\phi < \pi/2$.
The mirror symmetry through the plane $\phi = \pi/2$ relating $\mathscr{S}_1$ in panels c and d, and $\mathscr{S}_2$ in panels e and f reverses stability indices: the symmetric twin of a stable steady state on $\mathscr{S}_1$ is an unstable steady state on $\mathscr{S}_2$ of index 0, and vice-versa, while steady states of index 1 are symmetric to steady states of index 2.
To view these surfaces from more points of view, click here (password: thesisPR) or scan the barcode.

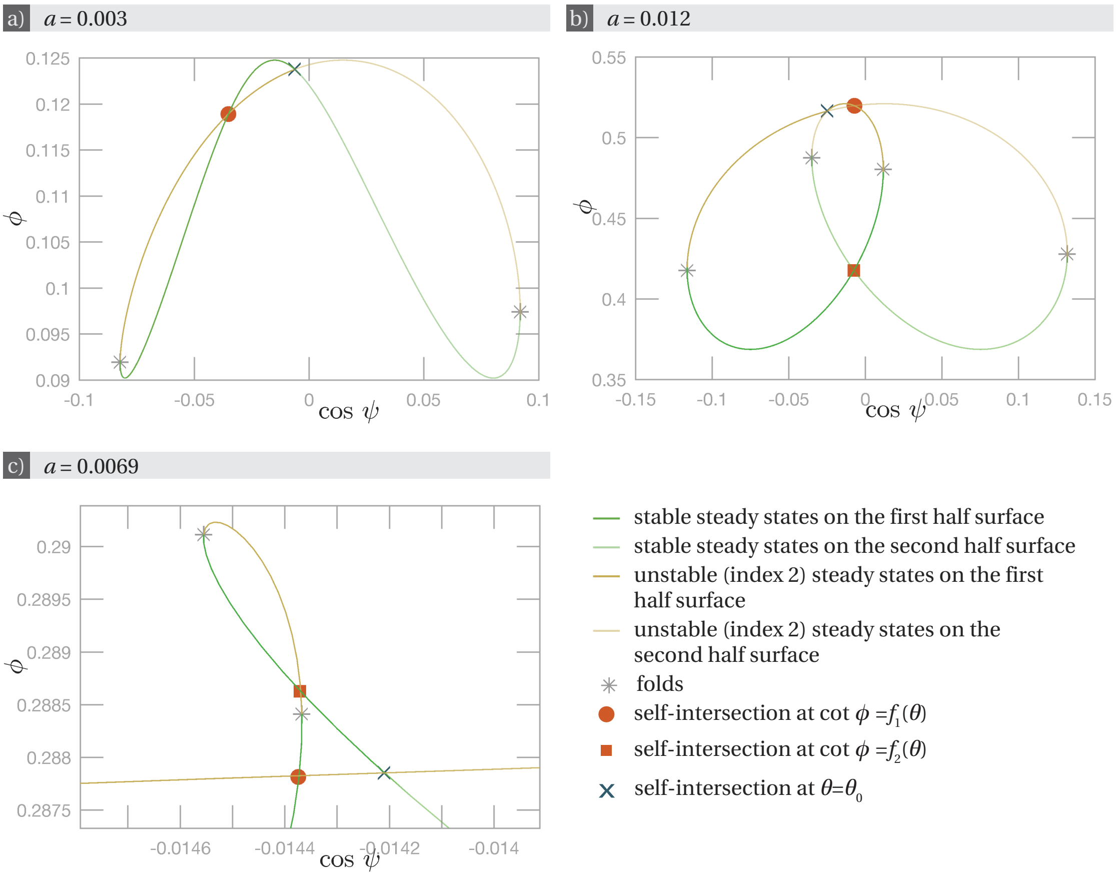

Figure 4.7 – Cross-sections of the surface $\mathscr{S}$ at constant a for different values of a with highlighted self-intersections (cf. fig. 4.4). Panels (a) and (b) show only section of the lower part of the surface ($\phi < \pi/2$); the upper part is symmetric to it. Panel c shows a detail of the lower part section, aimed at clarifying how section in panel (a) transforms into section in panel (b) as a grows.
The curve colours match the stability regions on surface $\mathscr{S}$ (cf. fig. 4.6). It changes at fold points marked by asterisks.

stability index in the pre-image of the surface mapping. Visualising the stability index on the surface $\mathscr{S}$ allows to put it into relation with the parameters a and ψ (cf. fig. 4.6). However, due to the self-intersections of $\mathscr{S}$, it is not obvious that the stability index changes only at bifurcations. To clarify this, sections of $\mathscr{S}$ at constant values of Mason number a are shown in figure 4.7. The knowledge of the self-intersections of the surface gained in section 4.1.4 is helpful.

In all the examples that we studied, stable steady states are located in the lower half of surface $\mathscr{S}$, which means that they are parametrised by $\phi < \pi/2$. This is in accordance with the intuition that the magnetic moment $\mathbf{m}$ tries to be aligned with magnetic field $\mathbf{B}$: recall that ϕ is the angle between the two. As of now, there is no analytical proof of this feature: that stable steady states all satisfy $\phi < \pi/2$ remains a conjecture.

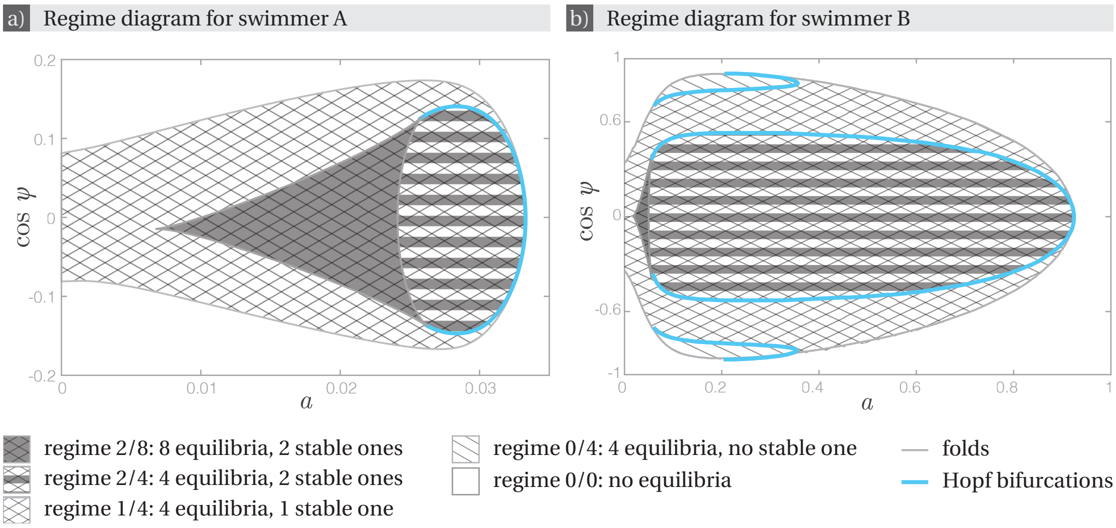

Figure 4.8 – Regime diagrams of the dynamical system (3.7) for two different swimmers: swimmer A in panel a and swimmer B in panel b (cf. chapter 6 for the specification of both swimmers). The steady states of swimmer A are also represented on figures 4.1, 4.2, and 4.6; analogue figures for swimmer B can be found in chapter 6. Note that the regime 0/4 exists for swimmer B but not for swimmer A. The boundaries between distinct regime areas correspond to folds and Hopf bifurcations of the system (cf. fig. 4.6, and fig. 6.3 in chapter 6).

4.3 Classification of Steady States for Given External Parameters

4.3.1 Parameter Regimes

Computing the stability indices on the surface $\mathscr{S}$, we could observe different regimes according to the choice of parameters a and ψ (cf. fig. 4.8). These regimes are labelled n_s/n, where n is the total number of steady states, and n_s is the number of stable steady states. The regimes that were observed in the examples we studied are 0/0, 0/4, 1/4, 2/4, and 2/8.

For most parameter values for which the system admits any steady state, at least one of them is stable. A notable exception is the parameter regime 0/4. This regime does not appear for all swimmers: for instance swimmer A does not exhibit it – in figure 4.8, we also show the regime diagram of another swimmer (swimmer[1] B) that displays regime 0/4. Regime 0/4 occurs only close to the regime 0/0 (no steady state at all): no pocket of regime without any stable steady state inside the region of parameter space for which there are steady states was observed.

Some regimes that could occur in principle were not observed among tens of examples, namely 0/8, 1/8, 3/8, and 4/8. Note that the number of stable steady state n_s can not exceed $n/2$, where n is the total number of steady states: each stable steady state has an unstable symmetric twin.

---

[1] Swimmer B is presented in more detail in chapter 6, and in particular figures representing its surface $\mathscr{S}$ analogous to figures 4.1, 4.2, and 4.6 can be found there.

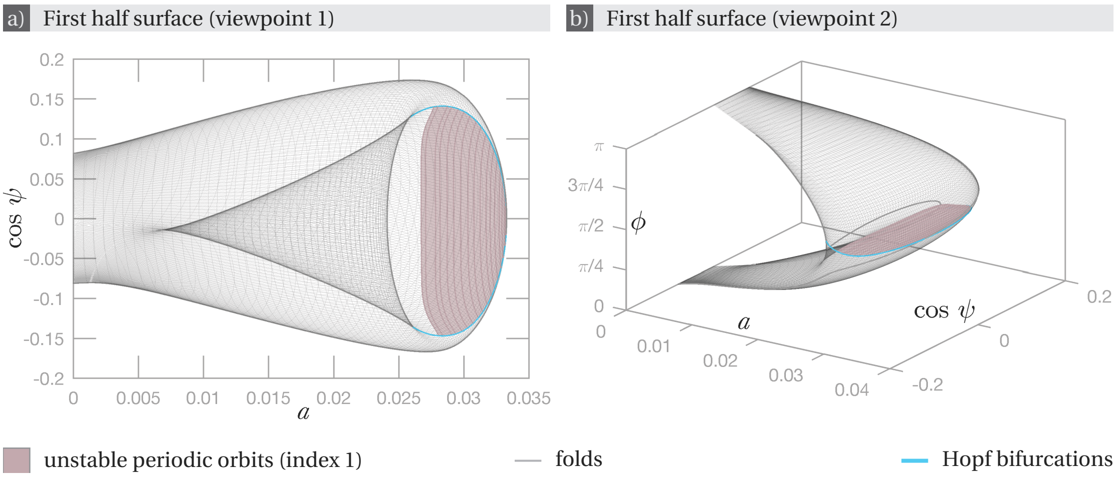

Figure 4.9 – Foil of periodic orbits branching from Hopf bifurcations on the half surface $\mathscr{S}_1$ shown in figure 4.6. In panel b, the vertical coordinate is the average of the angle ϕ over one period.
The foil is obtained by interpolation of the darker lines, which represent branches obtained by numerical continuation of system (3.14) with period kept constant. In panel a, it is visible that branches of periodic orbits could not be computed from bifurcations at both ends of the Hopf bifurcation curve: the period becomes asymptotically large at the tips. The foil remains within the region corresponding to parameter regime 2/4 (cf. fig. 4.8a). Here, all periodic orbits are unstable. Only the half $\mathscr{S}_1$ is shown; a similar foil is obtained from the symmetric curve of Hopf bifurcations on $\mathscr{S}_2$.
To view this surface from more points of view, click here (password: thesisPR) or scan the barcode.

The unobserved regimes 0/8, 1/8, 3/8 or 4/8 could arise for instance if there were Hopf bifurcations within the region of parameter plane for which the system admits eight steady states. In all examples observed, no such bifurcations occur, and this region is entirely occupied by regime 2/8. Regions with eight steady states are limited by folds; in the absence of Hopf bifurcation, bistability also remains until the fold: this seems to explain the prevalence of regime 2/8 and absence of regime 1/8.

In regimes exhibiting two stable steady states, namely regimes 2/4 and 2/8, each half surface $\mathscr{S}_1$ and $\mathscr{S}_2$ admits one of the stable steady states. Each half-surface contains at most four steady states for the same pair (a, ψ), so that in parameter regions with eight steady state, each half-surface contains exactly four of them. Regimes with three or more stable steady states (regimes 3/8 and 4/8) would require more than one stable steady state on each half-surface $\mathscr{S}_i$ for the same pair of parameters (a, ψ); this was never observed.

Each Hopf bifurcation gives rise to a branch of periodic orbits that can be found by numerical continuation [80]. Since we have two parameters a and ψ, there is a continuum of Hopf bifurcation: the branches of periodic orbits form a two-dimensional set, that we propose to call a foil. Each foil that was observed is associated to a unique curve of Hopf bifurcations:

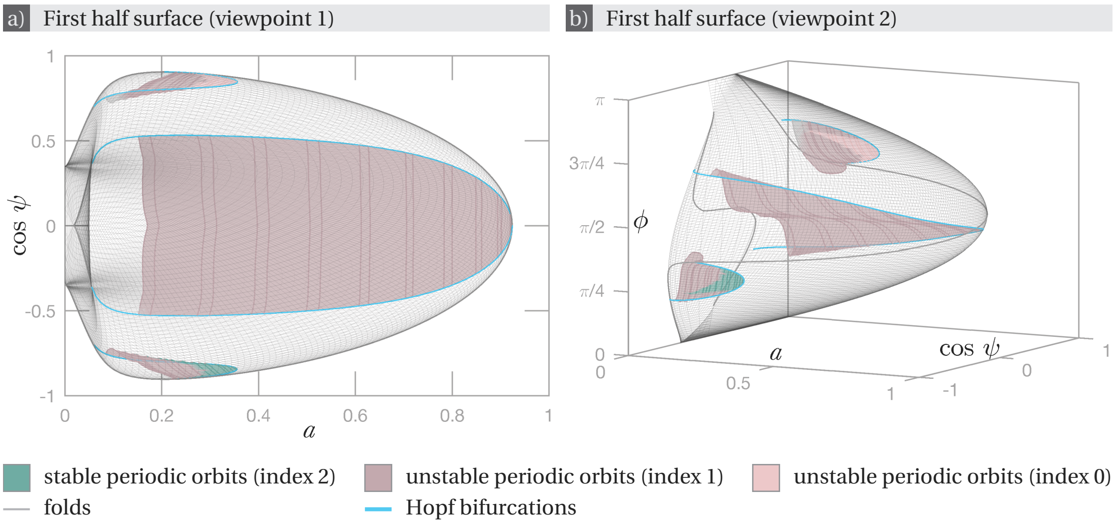

Figure 4.10 – Foils of periodic orbits branching from Hopf bifurcations on the half-surface $\mathscr{S}_1$ corresponding to swimmer B (cf. fig. 6.3 in chapter 6).
The foils are obtained by interpolation of the darker lines, which represent branches obtained by numerical continuation of system (3.14) with period kept constant. In panel a, it is visible that branches of periodic orbits could not be computed from bifurcations at both ends of the Hopf bifurcation curve: the period becomes asymptotically large at the tips. The central foil remains within the region corresponding to parameter regime 2/4, whereas the wing foils, which are mainly contained in the region corresponding to regime 0/4 stick out into regime 1/4 (cf. fig. 4.8b). In panel b, the vertical coordinate is the average of angle ϕ over one period. Here, periodic orbits of all possible stability indices occur. Only half $\mathscr{S}_1$ is shown; similar foils are obtained from the symmetric curves of Hopf bifurcations on $\mathscr{S}_2$ with reversed stability.
To view this surface from more points of view, click here (password: thesisPR) or scan the barcode.

foils do not connect distinct curves of Hopf bifurcations (cf. fig. 4.9 and 4.10).

In all the examples we studied, there are curves of Hopf bifurcations separating regime 2/4 from regime 1/4 (cf. fig. 4.8). The corresponding foils of periodic orbits were observed to be bounded to the region of regime 2/4. Furthermore, all periodic orbits in these foils are unstable, with stability index 1. These Hopf bifurcations are therefore subcritical [80]: they correspond to points where a stable steady state merges with an unstable periodic orbit to become an unstable steady state (cf. fig. 4.9 and 4.10).

Examples that feature regime 0/4 also exhibit curves of Hopf bifurcations separating regime 0/4 from regime 1/4. The corresponding foils are mainly covering the parameter region corresponding to regime 0/4, but they are not confined to it: they stick out into the region corresponding to regime 1/4. Tangent bifurcations occur within these foils, and they contain periodic orbits of different stability indices: in particular some are stable (cf. fig: 4.10).

In figures 4.9 and 4.10, the foils of periodic orbits are formed by interpolation of branches obtained by numerical continuation performed with the period kept constant. Such branches link two Hopf bifurcation on the same curve. Close to the ends of the Hopf bifurcation curves, which correspond to BT bifurcations, the period of branching periodic orbits becomes asymptotically large.

Numerical computation of branches of periodic orbits arising from Hopf bifurcations was done using the MATLAB package MatCont [83]. The maximal step size was set to 10^{-1}, the minimal step size to $\max\{\text{eigenvalue of } \mathsf{M}_{22}\} \cdot 10^{-6}$, the initial step size to 10^{-2}, and the initial amplitude to 10^{-4}. Starting at a Hopf bifurcation, the numerical procedure would reach another Hopf bifurcation on the same curve before going back along the same branch until it reaches again its starting point. To ensure that the procedure does not go on, the code is set to start checking whether the starting point is reached again after 20 steps. The other MatCont options were kept to their default values [84]. Floquet multipliers are obtained as an output of the numerical continuation and stability index computed accordingly. Theory predicts that one of the multipliers should be 1 and the other e^{-p} (see section 3.1.3) and we check a posteriori that this is the case.

To summarise: a pair of parameter (a, ψ) is said to correspond to regime n_s/n if for these parameters equation (3.7) admits n steady states including n_s stable ones. In the examples we studied, the parameter space is split in regions corresponding to regimes 0/0, 0/4, 1/4, 2/4, and 2/8 (cf. fig. 4.8). These regions are bordered by curves of bifurcations, namely folds or Hopf bifurcations. The curves of Hopf bifurcations are associated with foils of periodic orbits (cf. fig. 4.9 and 4.10).

4.3.2 Phase Portraits

Now that different parameter regimes have been examined, it is natural to ask: what is a typical phase portrait corresponding to a given regime? Phase portraits are typically sketched for dynamical systems with a state space of dimension two. In system (3.7), the state space is described by rotation matrices, which renders the task more difficult. Rotations can also be represented by unit quaternions (cf. equation (3.13)). Unit quaternions, which can be identified with elements of the hypersphere $\mathbb{S}^3$, which can be embedded in $\mathbb{R}^4$. So the challenge is to visualise a phase portrait in the four-dimensional object $\mathbb{S}^3$ on a two-dimensional sheet of paper.

First, recall that unit quaternions q and $-q$ represent the same rotation: we actually need to represent only half of $\mathbb{S}^3$ – we choose the half with positive scalar part, i.e. $q_0 \geq 0$. This makes things slightly simpler: just as the upper half of $\mathbb{S}^2$ can be flattened onto the unit disk in $\mathbb{R}^2$, half $\mathbb{S}^3$ can be projected orthogonally onto the unit ball in $\mathbb{R}^3$, and we are able to picture three-dimensional objects. It is important however to remember that on the boundary $q_0 = 0$, antipodal quaternions are identified. Pictured in the three-dimensional unit ball, this means that on the ball's boundary $\mathbb{S}^2$, antipodal points are identified: trajectories of the dynamical system (3.7) can continuously jump to the other side of the sphere.

A few such phase portraits are shown in figures 4.11, 4.12, and 4.13, and other examples can be found in chapter 6. Of course the difficulty of visualising three-dimensional space on a sheet of paper remains. Each three-dimensional object is shown under several angles. To supplement these views, the linked videos show them in rotation.

To obtain these phase portraits, we integrated dynamical system (3.14) numerically with many different initial conditions for a fixed pair of parameter (a,ψ) (see section 6.2 for details about the numerical procedure). Regime 1/4 is depicted in figure 4.11, regime 2/8 in figure 4.12, and regime 2/4 in figure 4.13. Similar figures corresponding to regimes 0/4 and 0/0 can be found in chapter 6.

Regime 1/4 (cf. fig. 4.11) is the only observed regime for which there is a unique stable steady state. In the phase portrait shown here, there is no other stable special solution, and all trajectories obtained by numerical integration of (3.14) reach the stable steady state after some time, suggesting that it is globally attracting. This is one of the two behaviours we observed for regime 1/4. For some swimmers, a stable periodic orbit coexists with a stable steady state for parameter regime 1/4. Each stable solution then has its own attraction basin. This second behaviour will be discussed in more detail in chapter 6.

Regime 2/8 (cf. fig. 4.12) exhibits a pair of steady states corresponding to each stability index: two stable steady states (index 3), two repulsive steady states (index 0), and four saddles (two with index 1 and two with index 2). The six unstable steady states lie on the boundary between the two basins of attraction. We conjecture the presence of two heteroclinic orbits, the first one including the two stable ones and two saddles of index 2, and the second one including the four remaining unstable steady states of indices 0 and 1. This conjecture is supported by the visible accumulation of solution curves along lines linking the involved steady states. The second conjectured heteroclinic orbit is also part of the boundary between the basins and seems to be the only sharp edge of this boundary, which looks otherwise quite smooth: we picture it as the core of an apple with basins of attraction arranged like apple quarters around it. Opposite quarters are actually connected due to equivalence of antipodal points on the boundary, and they belong to the same basin of attraction.

Regime 2/4 (cf. fig. 4.13) features two attractive (index 3) and two repulsive (index 0) steady states, as well as two unstable periodic orbits found by continuation from Hopf bifurcation with Floquet multipliers both inside and outside the complex unit circle. The special solutions are visually split in two groups, each containing one stable and one unstable steady state together with a periodic orbit. To schematise: each group resembles a small sphere with steady states at its poles and the periodic orbit circling its equator. Solution lines starting close to the unstable steady state of the group and passing inside the ring of the periodic orbit end up at the stable steady state of the group: the periodic orbit circles a confined region that belongs entirely to the basin of attraction of the stable steady state of the group. Solutions line starting around the same unstable steady state but passing outside the periodic orbit can end up at either stable steady states and the basins of attraction therefore look a bit entangled.

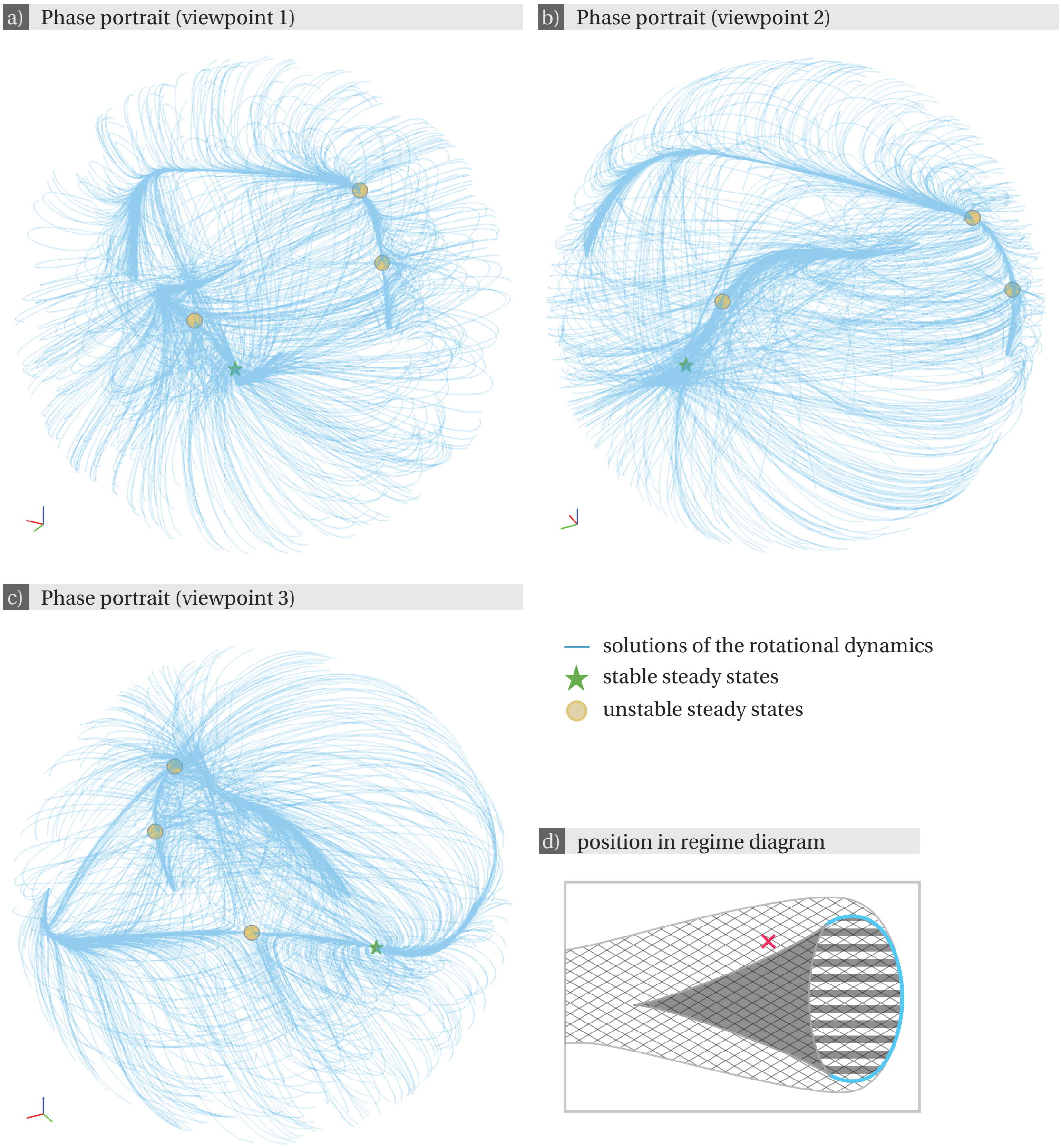

Figure 4.11 – Phase portrait of the dynamical system (3.14), which describes the rotational dynamics by means of quaternions, in regime 1/4. The data shown here corresponds to swimmer A (cf. fig. 4.1-4.8a and specification in chapter 6) with parameter values $a = 0.02$ and $\cos\psi = 0.1$ (cf. the cross in panel d).
Rotations are represented by quaternions with the convention $q_0 \geq 0$. The quaternions are represented here in 3D by their three vector components q_1, q_2, and q_3 (cf. section 4.3.2 for more details). The curves are solutions to (3.14) obtained by numerical integration for a variety of initial conditions. They all get asymptotically close to the stable steady state.
The steady states lie on two different accumulations of lines prefiguring the existence of two heteroclinic orbits, each linking together two steady states.
Panels a, b and c show the same object under different angles. To view it from different points of view, click here (password: thesisPR) or scan the barcode.

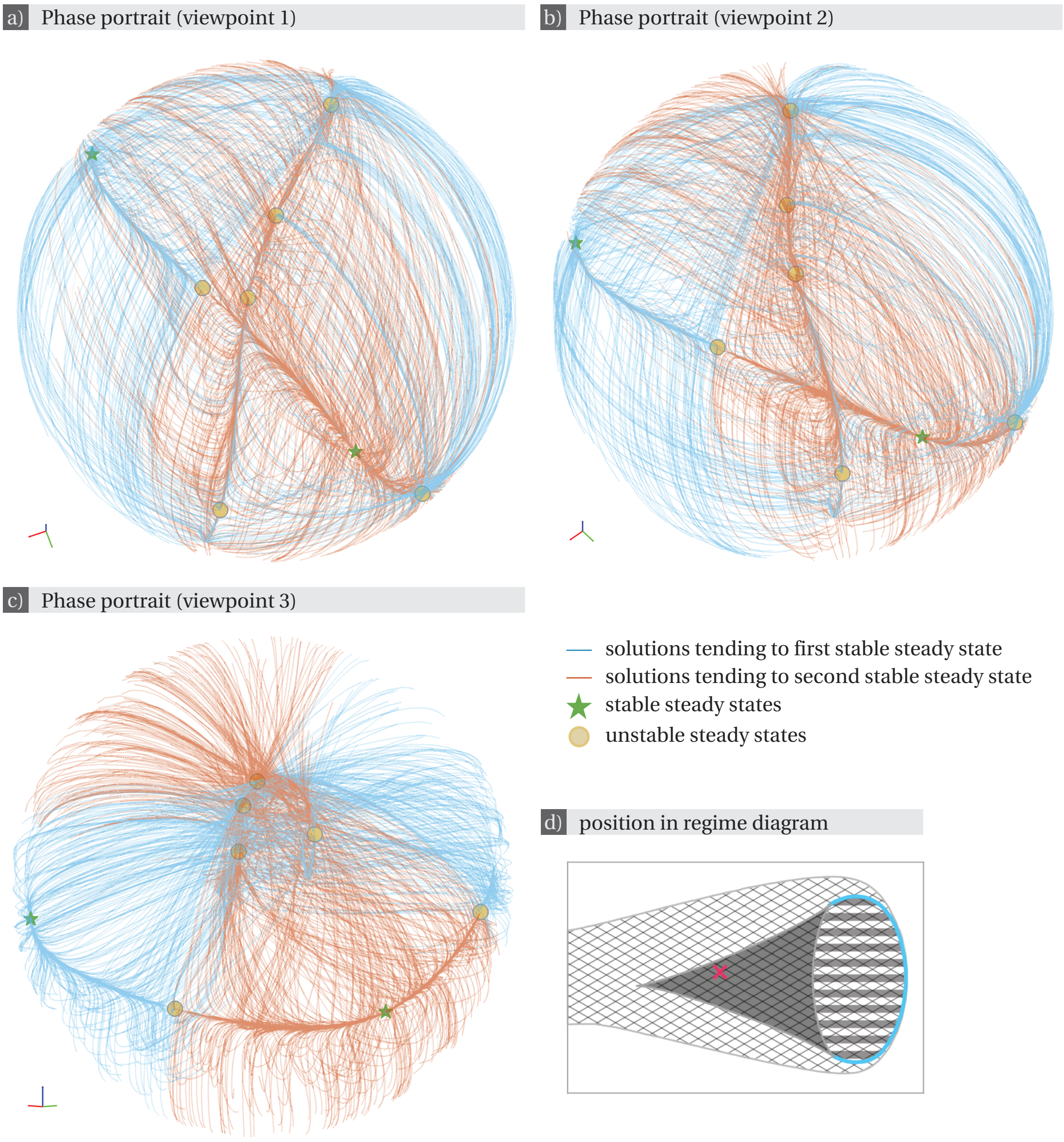

a) Phase portrait (viewpoint 1)

b) Phase portrait (viewpoint 2)

c) Phase portrait (viewpoint 3)

— solutions tending to first stable steady state
— solutions tending to second stable steady state
★ stable steady states
● unstable steady states

d) position in regime diagram

Figure 4.12 – Phase portrait of the dynamical system (3.14), which describes the rotational dynamics by means of quaternions, in regime 2/8. The data shown here corresponds to swimmer A (cf. fig. 4.1-4.8a and specification in chapter 6) with parameter values $a = 0.015$ and $\cos\psi = 0.01$ (cf. the cross in panel d).

Rotations are represented by means of unit quaternions (cf. section 4.3.2). The curves are solutions to (3.14) obtained by numerical integration for a variety of initial conditions and coloured according to their asymptotic behaviour.

The steady states lie on two different accumulations of lines prefiguring the existence of two heteroclinic orbits, each linking together four steady states.

Panels a, b and c show the same object under different angles. To view it from different points of view, click here (password: thesisPR) or scan the barcode.

4.3.3 Recap

To summarise: we provided a complete characterisation of the steady states of (3.7), which determine the relative equilibria of magnetic micro-swimmers. In particular, we built a parametrisation of the whole set of steady states, and a representation of it as a surface in 3D (cf. fig. 4.1-4.2). This visualisation is such that points were the surface admits a vertical tangent plane correspond to fold bifurcations of the dynamical system (cf. fig. 4.6). Linear stability was computed at steady states, and Hopf bifurcations on the set of steady states were deduced (cf. fig. 4.6). This procedure allowed us to split parameter space into regions corresponding to different behaviours of the dynamical system (3.7) (cf. fig. 4.8), and we showed phase portraits for different regimes (cf. fig. 4.11-4.13).

Further characterisation of the rotational dynamics, and especially of parameter regimes with no steady states of (3.7), requires other approaches: this is the topic of the next chapter.

The full swimmer motions corresponding to the steady states of the rotational dynamics explored in this chapter are discussed in chapter 7.

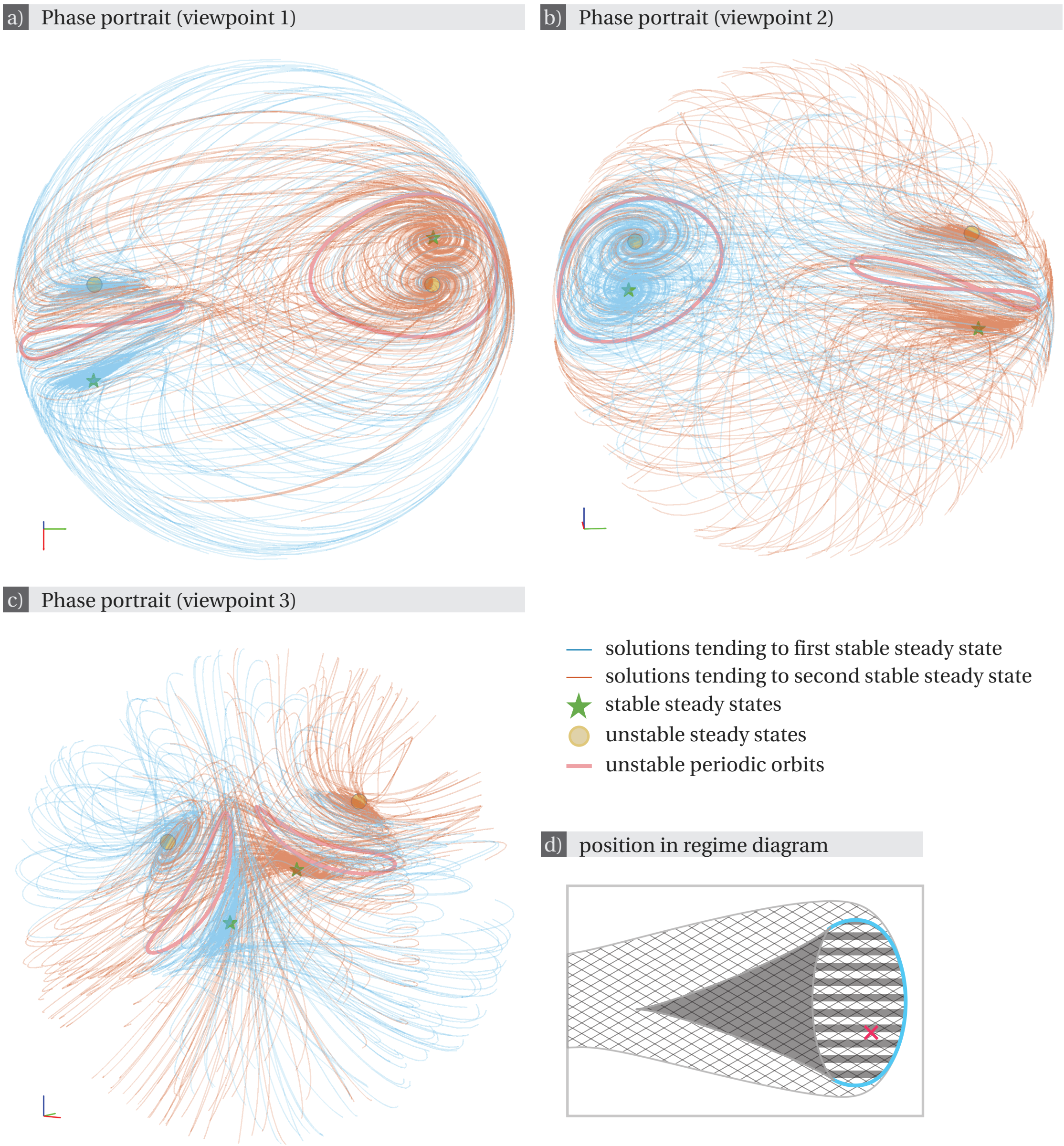

Figure 4.13 – Phase portrait of the dynamical system (3.14), which describes the rotational dynamics by means of quaternions, in regime 2/4. The data shown here corresponds to swimmer A (cf. fig. 4.1-4.8a and specification in chapter 6) with parameter values $a = 0.03$ and $\cos\psi = -0.06$ (cf. the cross in panel d).
Rotations are represented by means of unit quaternions (cf. section 4.3.2). The periodic orbits are obtained by interpolation of periodic orbits obtained by numerical continuation from Hopf bifurcations (cf. fig. 4.9). The curves are solutions to (3.14) obtained by numerical integration for a variety of initial conditions and coloured according to their asymptotic behaviour.
Panels a, b and c show the same object under different angles. To view it from different points of view, click here (password: thesisPR) or scan the barcode.

5 Asymptotic Dynamics

In the previous chapter, a complete characterisation of the steady states of

$$\dot{Q} = \left[\left(a\,Q\begin{bmatrix}0\\0\\1\end{bmatrix} - \mathsf{P}\,Q\begin{bmatrix}\sin\psi\\0\\\cos\psi\end{bmatrix}\right)\times\right] Q, \tag{3.7}$$

was introduced. In particular, the region of parameter space where any steady state exists was delineated. To further understand dynamics outside that region, we study analytically the asymptotic dynamics in three limits: when the Mason number a is asymptotically small, when it is asymptotically large, and when the magnetic field is almost aligned with its axis of rotation, i.e. $\sin\psi$ is asymptotically small.

Asymptotic expansions, singular perturbations and averaging methods are used to characterise the dynamics in these three cases. In the next chapter, we will use numerical experiments in some particular cases to suggest that the asymptotic regimes obtained here and the steady states obtained in the previous chapter give a good approximation of the dynamics of helical swimmers for a wide range of experimental input parameters.

5.1 Asymptotic Dynamics at Low Mason number

Recall that the Mason number is defined as

$$a = \alpha\,\frac{\eta\,\ell^3}{m\,B}, \tag{2.36}$$

where α is the angular speed of the rotating magnetic field, η is the dynamic velocity of the fluid, ℓ is a characteristic dimension of the body, m is the magnitude of the magnetic moment of the swimmer, and B is the magnitude of the magnetic field. Low values of a can be achieved experimentally either by considering strong magnetic effects, slowly rotating external fields, or particularly small bodies.

In this section, we will show that for small values of a, the magnetic field and the magnetic moment of the swimmer align on the time scale t_c. Once they are aligned, the leading order dynamics is completely specified by a one-dimensional first-order differential equation (equation (5.14)). As a result, after transients, only two different regimes occur depending on the values of the conical angle ψ, and the angle $\iota \in [0, \pi/2)$ defined in section 3.2 along with $\zeta \in [0, 2\pi)$ as the angles such that the right-singular vector $\boldsymbol{\eta}_0$ to P can be written in terms of the left-singular vectors $\boldsymbol{\beta}_j$ as

$$\boldsymbol{\eta}_0 = \cos\iota\,\boldsymbol{\beta}_0 + \sin\iota\,(\sin\zeta\,\boldsymbol{\beta}_1 - \cos\zeta\,\boldsymbol{\beta}_2)\,. \tag{3.19}$$

These two regimes are:

- if $\psi \in (\pi/2 - \iota, \pi/2 + \iota)$, then there exists a unique stable relative equilibrium;
- if $\psi \notin [\pi/2 - \iota, \pi/2 + \iota]$, then the leading order dynamics exhibits a single periodic orbit of period

$$\frac{2\pi\,\cos\iota}{a\sqrt{\cos(\iota+\psi)\,\cos(\iota-\psi)}}\,. \tag{5.1}$$

Let $a \ll 1$, which will be assumed throughout the section. First note that it takes a time of order $1/a$ for the magnetic field to make a full rotation around its axis. Accordingly, time is rescaled to a longer timescale $T = a\,t$. The dynamical system (3.7) consequently becomes

$$a\frac{d}{dT}Q = a\,[\mathbf{e}_3\times]\,Q - [\mathsf{P}\,\mathbf{B}\times]\,Q\,, \tag{5.2}$$

where

$$\mathbf{e}_3 = Q\begin{bmatrix}0\\0\\1\end{bmatrix} \qquad \text{and} \qquad \mathbf{B} = Q\begin{bmatrix}\sin\psi\\0\\\cos\psi\end{bmatrix}.$$

This equation will be analysed below using singular perturbation methods [15].

In the inner layer, that is when $T = \mathcal{O}(1/a)$ or equivalently when $t = \mathcal{O}(1)$, the governing equation are

$$\dot{Q} = a\,[\mathbf{e}_3\times]\,Q - [\mathsf{P}\,\mathbf{B}\times]\,Q\,, \tag{5.3}$$

where the dot denotes $\frac{d}{dt}$.

The matrix Q is expanded as (cf. appendix A)

$$Q = Q_0 + \mathcal{O}(a)\,. \tag{5.4}$$

substituting (5.4) in (5.3) and matching at the zeroth order in a yields

$$\dot{Q}_0 = -\,[\mathsf{P}\,\mathbf{B}_0\times]\,Q_0\,,$$

where

$$\mathbf{B}_0 = Q_0 \begin{bmatrix} \sin\psi \\ 0 \\ \cos\psi \end{bmatrix}.$$

In particular

$$\dot{\mathbf{B}}_0 = -(\mathsf{P}\,\mathbf{B}_0) \times \mathbf{B}_0. \tag{5.5}$$

This equation has two steady states $\mathbf{B}_0 = \pm\boldsymbol{\beta}_0$. The steady state $\mathbf{B}_0 = \boldsymbol{\beta}_0 = \mathbf{m}$ is stable and globally attracting while $\mathbf{B}_0 = -\boldsymbol{\beta}_0$ is unstable. Indeed, recall that

$$\mathsf{P} = \mathsf{M}_{22}\,[\mathbf{m}\times]\,, \tag{3.8}$$

and define the angle $z \in (0, \pi)$ between $\boldsymbol{\beta}_0$ and $\mathbf{B}_0 \neq \pm\boldsymbol{\beta}_0$ satisfying (5.5). The angle z satisfies $\cos z = \mathbf{B}_0 \times \boldsymbol{\beta}_0$ and

$$-\dot{z}\sin z = \dot{\mathbf{B}}_0 \cdot \boldsymbol{\beta}_0 = -(\mathsf{P}\,\mathbf{B}_0 \times \mathbf{B}_0)\cdot\boldsymbol{\beta}_0 \overset{(3.8)}{=} (\boldsymbol{\beta}_0 \times \mathbf{B}_0)\cdot \mathsf{M}_{22}\,(\boldsymbol{\beta}_0 \times \mathbf{B}_0) > 0\,.$$

Since $\sin z > 0$, z is strictly decreasing, and the solution $\mathbf{B}_0 = \boldsymbol{\beta}_0$ is globally attracting.

In the outer layer, that is when $T > 1$, Q is expanded as

$$Q = Q^{[0]} + a\left[\mathbf{u}^{[1]}\times\right] + \mathcal{O}(a^2)\,. \tag{5.6}$$

Substituting in (5.2) and matching at zeroth and first orders in a yields

$$0 = -\left[\mathsf{P}\,\mathbf{B}^{[0]}\times\right] Q^{[0]} \qquad \text{and} \tag{5.7}$$

$$\frac{d}{dT}Q^{[0]} = \left[\left(\mathbf{e}_3^{[0]} - \mathsf{P}(\mathbf{u}^{[1]} \times \mathbf{B}^{[0]})\right)\times\right] Q^{[0]} - \left[\mathsf{P}\mathbf{B}^{[0]}\times\right]\left[\mathbf{u}^{[1]}\times\right] Q^{[0]}\,, \tag{5.8}$$

where

$$\mathbf{B}^{[0]} = Q^{[0]} \begin{bmatrix} \sin\psi \\ 0 \\ \cos\psi \end{bmatrix} \qquad \text{and} \qquad \mathbf{e}_3^{[0]} = Q^{[0]} \begin{bmatrix} 0 \\ 0 \\ 1 \end{bmatrix}.$$

Equation (5.7) implies $\mathsf{P}\,\mathbf{B}^{[0]} = \mathbf{0}$ and hence $\mathbf{B}^{[0]} = \pm\boldsymbol{\beta}_0$. This yields the existence of a pair of one-dimensional families of zeroth order solutions

$$Q^{[0]} = \left[\boldsymbol{\beta}_1 | \boldsymbol{\beta}_2 | \boldsymbol{\beta}_0\right] \begin{bmatrix} 1 & 0 & 0 \\ 0 & \pm 1 & 0 \\ 0 & 0 & \pm 1 \end{bmatrix} R_3(\lambda)\,R_2(\psi)\,, \tag{5.9}$$

where λ is a parameter and

$$R_2(\psi) = \begin{bmatrix} \cos\psi & 0 & -\sin\psi \\ 0 & 1 & 0 \\ \sin\psi & 0 & \cos\psi \end{bmatrix}.$$

The solutions with the plus sign correspond to the attracting steady state in the inner layer, while the solutions with the minus sign are unstable. Accordingly, we study the solutions with the plus sign.

Since $\mathsf{P}\,\mathbf{B}^{[0]} = \mathbf{0}$, equation (5.8) reduces to

$$\frac{d}{dT} Q^{[0]} = \left[\left(\mathbf{e}_3^{[0]} - \mathsf{P}(\mathbf{u}^{[1]} \times \boldsymbol{\beta}_0)\right) \times\right] Q^{[0]} . \tag{5.10}$$

Furthermore, because of (5.9), there exists a function $\lambda(T)$ such that

$$Q^{[0]}(T) = [\boldsymbol{\beta}_1 | \boldsymbol{\beta}_2 | \boldsymbol{\beta}_0]\, R_3\big(\lambda(T)\big)\, R_2(\psi) , \tag{5.11}$$

implying

$$\frac{d}{dT} Q^{[0]}(T) = \frac{d\lambda}{dT}\, [\boldsymbol{\beta}_0 \times]\, Q^{[0]} . \tag{5.12}$$

Equations (5.10, 5.12) require that $\mathbf{u}^{[1]}$ and λ are related by

$$\frac{d\lambda}{dT} \boldsymbol{\beta}_0 = \mathbf{e}_3^{[0]} - \mathsf{P}(\mathbf{u}^{[1]} \times \boldsymbol{\beta}_0) . \tag{5.13}$$

Taking the dot product with the right-singular vector $\boldsymbol{\eta}_0$ of P with singular value 0 yields

$$\cos\iota \frac{d\lambda}{dT} = \boldsymbol{\eta}_0 \cdot \mathbf{e}_3^{[0]} \overset{(5.11)}{=} \boldsymbol{\eta}_0 \cdot \big(\cos\psi\, \boldsymbol{\beta}_0 - \sin\psi\, (\cos\lambda\, \boldsymbol{\beta}_1 + \sin\lambda\, \boldsymbol{\beta}_2)\big) .$$

This yields the equation for λ

$$\frac{d\lambda}{dT} = \cos\psi + \sin\psi\, \tan\iota\, \sin(\lambda - \zeta) . \tag{5.14}$$

To complete the specification of the first-order solution, $\mathbf{u}^{[1]}$ satisfying (5.13) needs to be found. Note that $\mathbf{u}_1$ can be chosen so that its component along $\boldsymbol{\beta}_0$ vanishes, since this component is not specified by (5.13). Accordingly, $\mathbf{u}^{[1]} = u_1\, \boldsymbol{\beta}_1 + u_2\, \boldsymbol{\beta}_2$, and u_1 and u_2 are found by projecting (5.13) on $\boldsymbol{\beta}_1$ and $\boldsymbol{\beta}_2$:

$$-\sin\psi \begin{bmatrix} \cos\lambda \\ \sin\lambda \end{bmatrix} = \begin{bmatrix} \boldsymbol{\beta}_1 \cdot \mathsf{M}_{22}\, \boldsymbol{\beta}_1 & \boldsymbol{\beta}_1 \cdot \mathsf{M}_{22}\, \boldsymbol{\beta}_2 \\ \boldsymbol{\beta}_2 \cdot \mathsf{M}_{22}\, \boldsymbol{\beta}_1 & \boldsymbol{\beta}_2 \cdot \mathsf{M}_{22}\, \boldsymbol{\beta}_2 \end{bmatrix} \begin{bmatrix} u_1 \\ u_2 \end{bmatrix} ,$$

which can be inverted as

$$\begin{bmatrix} u_1 \\ u_2 \end{bmatrix} = -\frac{\sin\psi}{\sigma_1 \sigma_2 \cos\iota} \begin{bmatrix} \boldsymbol{\beta}_2 \cdot \mathsf{M}_{22}\, \boldsymbol{\beta}_2 & -\boldsymbol{\beta}_1 \cdot \mathsf{M}_{22}\, \boldsymbol{\beta}_2 \\ -\boldsymbol{\beta}_2 \cdot \mathsf{M}_{22}\, \boldsymbol{\beta}_1 & \boldsymbol{\beta}_1 \cdot \mathsf{M}_{22}\, \boldsymbol{\beta}_1 \end{bmatrix} \begin{bmatrix} \cos\lambda \\ \sin\lambda \end{bmatrix} ,$$

so that

$$\begin{aligned}\mathbf{u}^{[1]} &= -\frac{\sin\psi}{\sigma_1\sigma_2\cos\iota}\left(\cos\lambda\,\boldsymbol{\beta}_1\otimes\boldsymbol{\beta}_2 - \sin\lambda\,\boldsymbol{\beta}_2\otimes\boldsymbol{\beta}_1\right)\left(\mathsf{M}_{22}\boldsymbol{\beta}_2 - \mathsf{M}_{22}\boldsymbol{\beta}_1\right)\\ &= -\frac{\sin\psi}{\sigma_1\sigma_2\cos\iota}\left(\cos\lambda\,\boldsymbol{\beta}_1\otimes\boldsymbol{\beta}_2 - \sin\lambda\,\boldsymbol{\beta}_2\otimes\boldsymbol{\beta}_1\right)\left(\sigma_1\boldsymbol{\eta}_1 - \sigma_2\boldsymbol{\eta}_2\right).\end{aligned}$$

This provides an approximation of the solution Q to (3.7) for $a \ll 1$ as

$$Q = Q^{[0]} + a\left[\mathbf{u}^{[1]}\times\right] + \mathscr{O}(a^2), \tag{5.6}$$

where all time-dependences of $Q^{[0]}$ and $\mathbf{u}^{[1]}$ appear in the function λ.

When $\pi/2-\iota<\psi<\pi/2+\iota$, the relation $|\cos\psi|<\sin\psi\tan\iota$ is satisfied, and (5.14) has two steady states given by

$$\lambda_\pm = \zeta - \frac{\pi}{2} \pm \arccos\left(\frac{\cos\psi\cos\iota}{\sin\psi\sin\iota}\right).$$

The steady state λ_+ is stable and λ_- is unstable. This is because the eigenvalue of the linearised system is

$$\sin\psi\tan\iota\cos(\lambda-\zeta),$$

where $\sin\psi\tan\iota>0$. Substituting $\lambda_\pm$ in this eigenvalue gives

$$\cos(\lambda_\pm-\zeta) = \pm\sqrt{1-\frac{\cos^2\psi\cos^2\iota}{\sin^2\psi\sin^2\iota}},$$

which is negative for the steady state λ_-, so that it is stable.

If $|\psi-\pi/2|>\iota$, then $|\cos\psi|>\sin\psi\tan\iota$ and $d\lambda/dT$ never changes sign. In consequence, the leading order dynamic exhibits a periodic solution of the form (5.6) that has period

$$\int_{\zeta-\pi}^{\zeta+\pi}\frac{d\lambda}{\cos\psi+\sin\psi\tan\iota\sin(\lambda-\zeta)} = \frac{2\pi\cos\iota}{\sqrt{\cos(\iota+\psi)\cos(\iota-\psi)}}. \tag{5.15}$$

In the body frame, this periodic dynamics corresponds to the axis of rotation $\mathbf{e}_3$ of the magnetic field itself rotating about $\boldsymbol{\beta}_0$; clockwise when $\psi\in(0,\pi/2-\iota)$ and anti-clockwise when $\psi\in(\pi/2+\iota,\pi)$. This bifurcation between stable equilibria for $\psi\in[\iota,\pi-\iota]$ and periodic orbits when $\psi\notin[\iota,\pi-\iota]$ occurs through a periodic solution of infinite period.

5.2 Asymptotic Solutions at Large Mason Number

Large values of the Mason number a occur for magnetic fields that are either weak or rapidly rotating. We show that in the limit $a\to\infty$, the magnetic moment $\mathbf{m}$ tends to align with the averaged magnetic field, which corresponds either to its axis of rotation $+\mathbf{e}_3$ or to the opposite of its axis of rotation $-\mathbf{e}_3$ depending on the conical angle ψ. The mismatch between the magnetic moment and $\pm\mathbf{e}_3$ is of order $1/a$. We also obtain a slow residual rotation of the swimmer about the averaged field, with period of order a.

To analyse the case of $a \gg 1$, we work with the dynamical system

$$\dot{R}^\top = \left[\left(-\mathsf{P}\, R^\top R_3(a\,t) \begin{bmatrix} \sin\psi \\ 0 \\ \cos\psi \end{bmatrix}\right) \times\right] R^\top , \tag{5.16}$$

which describes the evolution of lab axes in the body frame, since the columns of $R^\top$ are the vectors $\mathbf{e}_j$ (cf. section 2.2.1, equation (2.19)). Note that the solutions to (5.16) and the solutions to (3.7) are linked by $Q = R^\top R_3(a\,t)$. In particular

$$\mathbf{e}_3 = R^\top \begin{bmatrix} 0 \\ 0 \\ 1 \end{bmatrix}, \qquad \mathbf{B} = R^\top R_3(a\,t) \begin{bmatrix} \sin\psi \\ 0 \\ \cos\psi \end{bmatrix}.$$

We will analyse (5.16) by applying the averaging method as described in section 2.5. The main idea is that because $\mathbf{B}$ changes much faster than $\mathbf{e}_3$, we can approximate the effect of $\mathbf{B}$ on the dynamics of the system by averaging $\mathbf{B}$ over one of its period of revolution $\frac{2\pi}{a}$. The method transforms the non-autonomous system (5.16) into an autonomous averaged differential equation called the guiding system. The averaging procedure is carried out in Section 5.2.1 and the resulting guiding system is studied in Section 5.2.2.

5.2.1 Averaged dynamics

We first rescale time to $T = a\,t$ and define $\varepsilon = 1/a \ll 1$ so that (5.16) becomes

$$\frac{d}{dT} R^\top = -\varepsilon\, [(\mathsf{P}\,\mathbf{B})\times]\, R^\top . \tag{5.17}$$

The averaging operator, noted by an overline, is defined as follows (cf. section 2.5 and appendix A.3): to any function $X(R^\top, T)$ 2π-periodic in T, it associates the averaged function

$$\overline{X}(R^\top) = \frac{1}{2\pi} \int_0^{2\pi} X(R^\top, T)\, dT ,$$

where the integration is performed while keeping $R^\top$ constant. We also define the function $\mathbf{B}^\star$ which depends on a matrix S and a scalar T

$$\mathbf{B}^\star(S, T) = S\, R_3(T) \begin{bmatrix} \sin\psi \\ 0 \\ \cos\psi \end{bmatrix}, \tag{5.18}$$

such that $\mathbf{B}(T) = \mathbf{B}^\star\big(R^\top(T), T\big)$. Note that $\mathbf{B}^*(S)$ is linear in S, and $\overline{\mathbf{B}^\star}(S) = \cos\psi\, S \begin{bmatrix} 0 \\ 0 \\ 1 \end{bmatrix}$.

Given two functions $\mathbf{u}^{[1]}$ and $\mathbf{u}^{[2]}$, the near identity transformation (see appendix A)

$$R^{\top} = F + \varepsilon\,\left[\mathbf{u}^{[1]}\times\right]F + \varepsilon^2\left(\left[\mathbf{u}^{[2]}\times\right] + \frac{1}{2}\left[\mathbf{u}^{[1]}\times\right]^2\right)F + \mathcal{O}(\varepsilon^3) \tag{5.19}$$

transforms the differential equation (5.17) into a differential equation for $F \in \mathrm{SO}(3)$ of the form

$$\frac{d}{dT}F = \varepsilon\,\left[\mathbf{g}^{[1]}\times\right]F + \varepsilon^2\,\left[\mathbf{g}^{[2]}\times\right]F + \mathcal{O}(\varepsilon^3)\,. \tag{5.20}$$

The $\mathbf{g}^{[i]}$ are computed in the following, where the notation $\mathbf{f}_i$ will be used in reference to the i^{th}column of F as a shortcut for some computations.

The functions $\mathbf{u}^{[i]}$ $(i = 1, 2)$ appearing in (5.19) are to be understood as explicit functions of the matrix F and of time T. We further require that they are 2π-periodic in T. Then they can be chosen such that the functions $\mathbf{g}^{[i]}$ $(i = 1, 2)$ appearing in (5.20) depend on F but not on time. In that case, solutions of the truncated equation

$$\frac{d}{dT}F = \varepsilon\,\left[\mathbf{g}^{[1]}\times\right]F + \varepsilon^2\,\left[\mathbf{g}^{[2]}\times\right]F \tag{5.21}$$

are guaranteed to remain close to the solutions of (5.17) up to an order $\mathcal{O}(\varepsilon^2)$ on a timescale of order $T = \mathcal{O}(1/\varepsilon)$. There also exists a trade-off result [16]: solutions of the truncated equation (5.21) are guaranteed to remain close to the solutions of (5.17) up to an order $\mathcal{O}(\varepsilon)$ on a timescale of order $T = \mathcal{O}(1/\varepsilon^2)$.

In all of the above, *close* is used in the sense that there are some positive constants c and L such that (cf. section 2.5)

$$\left|R^{\top}(T,\varepsilon) - F(T,\varepsilon)\right| \le c\varepsilon^2\,, \qquad \text{for } 0 \le T \le L/\varepsilon\,,$$

and respectively

$$\left|R^{\top}(T,\varepsilon) - F(T,\varepsilon)\right| \le c\varepsilon\,, \qquad \text{for } 0 \le T \le L/\varepsilon^2\,,$$

where $|\cdot|$ denotes a sub-multiplicative norm[1] on $\mathbb{R}^{3\times 3}$. This means that in the original time scale, an approximation of order $\mathcal{O}(1/a)$ is guaranteed on a time scale of order $t = \mathcal{O}(a)$ (recalling that $a \gg 1$).

Substituting (5.19) and (5.21) in equation (5.17), expanding in ε and matching at each order gives (cf. appendix A.3)

$$\mathbf{g}^{[1]} + \partial_T\mathbf{u}^{[1]} = -\mathsf{P}\,\mathbf{B}^{\star}(F,T)\,, \tag{5.22}$$

$$\mathbf{g}^{[2]} + \partial_T\mathbf{u}^{[2]} + \partial_F\mathbf{u}^{[1]}\cdot\left(\left[\mathbf{g}^{[1]}\times\right]F\right) + \mathbf{u}^{[1]}\times\left(\mathbf{g}^{[1]} + \frac{1}{2}\partial_T\mathbf{u}^{[1]}\right) = -\mathsf{P}\,\mathbf{B}^{*}\left(\left[\mathbf{u}^{[1]}\times\right]F,T\right), \tag{5.23}$$

---

[1] A sub-multiplicative norm is a norm $|\cdot|$ on a group of matrices that satisfies $|AB| \le |A|\,|B|$ for all matrices A and B.

where $\partial_F \mathbf{u}^{[1]} \cdot \left([\mathbf{g}^{[1]}\times]\ F\right)$ denotes the vector $\left(\partial_{F_{ij}} \mathbf{u}^{[1]}\right) \left([\mathbf{g}^{[1]}\times]\ F\right)_{ij}$, with implied summation on repeated indices, and where the functions $\mathbf{u}^{[1]}$, $\mathbf{u}^{[2]}$ are evaluated at (F, T) and the functions $\mathbf{g}^{[1]}$ and $\mathbf{g}^{[2]}$ are evaluated at F.

Requiring the function $\mathbf{u}^{[1]}$ to be periodic implies that upon averaging, equation (5.22) becomes

$$\mathbf{g}^{[1]}(F) = -\overline{\mathsf{P}\,\mathbf{B}^\star}(F) = -\cos\psi\,\mathsf{P}\,F \begin{bmatrix} 0 \\ 0 \\ 1 \end{bmatrix} = -\cos\psi\,\mathsf{P}\,\mathbf{f}_3\,. \tag{5.24}$$

Substituting (5.24) in (5.22) gives

$$\partial_T \mathbf{u}^{[1]}\big|_{(F,T)} = -\mathsf{P}\,F\,R_3(T) \begin{bmatrix} \sin\psi \\ 0 \\ 0 \end{bmatrix} = -\mathsf{P}\,F \begin{bmatrix} \cos T\,\sin\psi \\ \sin T\,\sin\psi \\ 0 \end{bmatrix} = -\sin\psi(\cos T\,\mathsf{P}\,\mathbf{f}_1 + \sin T\,\mathsf{P}\,\mathbf{f}_2)\,,$$

and integration yields

$$\mathbf{u}^{[1]}(F,T) = -\mathsf{P}\,F \begin{bmatrix} -\sin T\,\sin\psi \\ \cos T\,\sin\psi \\ 0 \end{bmatrix} + \mathbf{A}(F) = -\sin\psi\left(-\sin T\,\mathsf{P}\,\mathbf{f}_1 + \cos T\,\mathsf{P}\,\mathbf{f}_2\right) + \mathbf{A}(F)\,, \tag{5.25}$$

where $\mathbf{A}$ is an arbitrary function. Here, we choose $\mathbf{A} = 0$ so that $\overline{\mathbf{u}^{[1]}} = 0$.

Averaging of equation (5.23) yields

$$\mathbf{g}^{[2]} + \frac{1}{2}\,\overline{\mathbf{u}^{[1]} \times \partial_T \mathbf{u}^{[1]}} = -\mathsf{P}\,\overline{\mathbf{u}^{[1]} \times \mathbf{B}^*}\,,$$

where functions $\mathbf{u}^{[1]}$ and $\mathbf{B}^*$ are evaluated at (F, T). Substituting expressions (5.25, 5.18) for $\mathbf{u}^{[1]}$ and $\mathbf{B}^*$ yields

$$\mathbf{g}^{[2]} + \frac{1}{2}\sin^2\psi\,(\mathsf{P}\,\mathbf{f}_1) \times (\mathsf{P}\,\mathbf{f}_2) = \frac{1}{2}\sin^2\psi\left(\mathsf{P}\,(\mathbf{f}_1 \times \mathsf{P}\,\mathbf{f}_2) - \mathsf{P}\,(\mathbf{f}_2 \times \mathsf{P}\,\mathbf{f}_1)\right),$$

so that

$$\mathbf{g}^{[2]}(F) = \frac{\sin^2\psi}{2}\left(\mathsf{P}\,(\mathbf{f}_1 \times \mathsf{P}\,\mathbf{f}_2) - \mathsf{P}\,(\mathbf{f}_2 \times \mathsf{P}\,\mathbf{f}_1) - (\mathsf{P}\,\mathbf{f}_1) \times (\mathsf{P}\,\mathbf{f}_2)\right). \tag{5.26}$$

Coming back to the time scale $t = T/a$, and substituting (5.24, 5.26) in (5.21), the guiding system becomes

$$\begin{aligned} \dot F &= -\cos\psi\ [(\mathsf{P}\,\mathbf{f}_3)\times]\ F \\ &\quad + \varepsilon\,\frac{\sin^2\psi}{2}\ \left[\left(\mathsf{P}\,(\mathbf{f}_1 \times \mathsf{P}\,\mathbf{f}_2) + \mathsf{P}\,(\mathsf{P}\,\mathbf{f}_1 \times \mathbf{f}_2) - (\mathsf{P}\,\mathbf{f}_1) \times (\mathsf{P}\,\mathbf{f}_2)\right)\times\right] F\,. \end{aligned} \tag{5.27}$$

5.2.2 Analysis of the Guiding System

The argument of the previous section transformed the non-autonomous system (5.16) into the approximate autonomous system (5.27). In this section we show that the first-order solution of (5.27) always exhibits stable periodic motion.

Zeroth order

The zeroth order dynamics of (5.27) is given by the equation

$$\dot{F} = -\cos\psi \; [(\mathsf{P}\,\mathbf{f}_3)\times] \; F. \tag{5.28}$$

This system is in steady state if and only if $\mathsf{P}\,\mathbf{f}_3 = 0$, which implies $\mathbf{f}_3 = \pm\boldsymbol{\beta}_0$. This gives two one-dimensional families of steady states of the form

$$F = \left[\boldsymbol{\beta}_1 | \boldsymbol{\beta}_2 | \boldsymbol{\beta}_0\right] R_3(\tau) \begin{bmatrix} 1 & 0 & 0 \\ 0 & \pm 1 & 0 \\ 0 & 0 & \pm 1 \end{bmatrix}, \tag{5.29}$$

where τ is a parameter.

All steady states in the family (5.29) with the sign in ± corresponding to $\varsigma = \operatorname{sign}(\cos\psi)$ are meta-stable in the sense that all eigenvalues of the associated stability matrix are strictly negative but for one that vanishes and corresponds to motion within the continuous family. Indeed the stability matrix is

$$|\cos\psi|\,\mathsf{P}\left[\boldsymbol{\beta}_0\times\right] \overset{(3.8)}{=} |\cos\psi|\mathsf{M}_{22}\left[\boldsymbol{\beta}_0\times\right]^2 = |\cos\psi|\mathsf{M}_{22}\left(\boldsymbol{\beta}_0 \otimes \boldsymbol{\beta}_0 - \mathbf{I}\right),$$

which admits $\boldsymbol{\beta}_0$ as an eigenvector for eigenvalue 0, and its two other eigenvalue must be negative because M_{22} is positive definite. We will refer to the family of steady states of the form

$$F = \left[\boldsymbol{\beta}_1 | \boldsymbol{\beta}_2 | \boldsymbol{\beta}_0\right] R_3(\tau)\,\Sigma \qquad \text{with } \Sigma = \begin{bmatrix} 1 & 0 & 0 \\ 0 & \varsigma & 0 \\ 0 & 0 & \varsigma \end{bmatrix} \tag{5.30}$$

as the stable manifold, and the family (5.29) with opposite sign in ± as the unstable manifold.

The stable manifold is almost globally attracting – that is it is attracting for all initial values that do not lie strictly on the manifold of unstable steady states. Indeed, for a solution F to (5.28), the angle $z \in [0,\pi]$ between $\varsigma\boldsymbol{\beta}_0$, which corresponds to the third column of a matrix in the stable manifold (5.30), and the third column $\mathbf{f}_3$ of a solution F to (5.28) is decreasing. Indeed, it satisfies

$$-\dot{z}\sin z = \frac{d}{dt}(\cos z) = \frac{d}{dt}(\varsigma\,\boldsymbol{\beta}_0 \cdot \mathbf{f}_3) = \varsigma\,\boldsymbol{\beta}_0 \cdot \dot{\mathbf{f}}_3\,.$$

Using (5.28) and the fact that $\sin z \geq 0$, and that $\mathbf{f}_3$ is the third column of F satisfying (5.28), this yields

$$\begin{aligned}-\dot{z}\,|\sin z| &= -|\cos\psi|\,\boldsymbol{\beta}_0\cdot(\mathsf{P}\mathbf{f}_3\times\mathbf{f}_3) = |\cos\psi|\,\mathsf{P}\,\mathbf{f}_3\cdot(\boldsymbol{\beta}_0\times\mathbf{f}_3)\\ &\overset{(3.8)}{=} |\cos\psi|\,\big(\mathsf{M}_{22}\,(\boldsymbol{\beta}_0\times\mathbf{f}_3)\big)\cdot(\boldsymbol{\beta}_0\times\mathbf{f}_3)\geq 0\end{aligned}$$

since M_{22} is positive definite. The inequality is strict for $\mathbf{f}_3\neq\pm\boldsymbol{\beta}_0$, i.e. when F is not a steady state of (5.28). As a result, the angle z between $\mathbf{f}_3$ and $\varsigma\boldsymbol{\beta}_0$ is decreasing everywhere but on the steady state manifolds, which means that the third column $\mathbf{f}_3$ of F tends to align with $\varsigma\boldsymbol{\beta}_0$, so that F approaches the stable manifold asymptotically.

However as the system gets near this zeroth-order stable manifold, the magnitude of the zeroth order term in (5.27) decreases, and the first order term can no longer be neglected. For the long term behaviour of the system, the system is therefore expected to be close to but not quite on a stable steady state of the form (5.30). To explore the behaviour as the solution gets closer to the stable manifold and take into account higher order terms, we define a function

$$\tau(t) = \tau^{[0]}(t) + \varepsilon\,\tau^{[1]}(t) + \mathcal{O}(\varepsilon^2)$$

that specifies the solution on the stable manifold as

$$F^{[0]}(t) = \big[\boldsymbol{\beta}_1|\boldsymbol{\beta}_2|\boldsymbol{\beta}_0\big]\,R_3\big(\tau(t)\big)\,\Sigma\,. \tag{5.31}$$

An expansion of F around $F^{[0]}$ in ε has the form

$$F = F^{[0]} + \varepsilon\,[\mathbf{x}\times]\,F^{[0]} + \mathcal{O}(\varepsilon^2)\,, \tag{5.32}$$

for some function $\mathbf{x}=\mathbf{x}(t)$. Substituting (5.32) in the dynamical equation (5.27) for F and keeping only zeroth order terms gives

$$\varsigma\,\dot{\tau}^{[0]}\,\big[\boldsymbol{\beta}_0\times\big]\,F^{[0]} = 0\,,$$

so that $\tau^{[0]}\equiv\tau^*$ is constant. Substituting in (5.31) yields

$$F^{[0]} = \big[\boldsymbol{\beta}_1|\boldsymbol{\beta}_2|\boldsymbol{\beta}_0\big]\,R_3(\tau^*)\,\Sigma + \varepsilon\,\tau^{[1]}\,\big[\boldsymbol{\beta}_0\times\big]\,\big[\boldsymbol{\beta}_1|\boldsymbol{\beta}_2|\boldsymbol{\beta}_0\big]\,R_3(\tau^*)\,\Sigma + \mathcal{O}(\varepsilon^2)\,. \tag{5.33}$$

First order

Substituting (5.33) in (5.27), the equation at first order simplifies to (cf. appendix A, equation (A.16))

$$\dot{\tau}^{[1]}\,\boldsymbol{\beta}_0 + \dot{\mathbf{x}} = -\cos\psi\,\mathsf{P}\,[\mathbf{x}\times]\,\mathbf{f}_3^{[0]} + \mathbf{g}^{[2]}(F^{[0]})\,. \tag{5.34}$$

where $\mathbf{g}^{[2]}(F^{[0]})$ is given by (5.26). We assume that $\mathbf{x}(t) = x_1(t)\,\boldsymbol{\beta}_1 + x_2(t)\,\boldsymbol{\beta}_2$. Projecting (5.34) on $\boldsymbol{\beta}_0$, $\boldsymbol{\beta}_1$, and $\boldsymbol{\beta}_2$ yields

$$\begin{aligned}
\dot{\tau}^{[1]} &= \left(-\cos\psi\,\mathsf{P}\,[\mathbf{x}\times]\,\mathbf{f}_3^{[0]} + \mathbf{g}^{[2]}(F^{[0]})\right)\cdot\boldsymbol{\beta}_0\\
\dot{x}_1 &= \left(-\cos\psi\,\mathsf{P}\,[\mathbf{x}\times]\,\mathbf{f}_3^{[0]} + \mathbf{g}^{[2]}(F^{[0]})\right)\cdot\boldsymbol{\beta}_1\\
\dot{x}_2 &= \left(-\cos\psi\,\mathsf{P}\,[\mathbf{x}\times]\,\mathbf{f}_3^{[0]} + \mathbf{g}^{[2]}(F^{[0]})\right)\cdot\boldsymbol{\beta}_2\,.
\end{aligned}$$

Since $\tau^{[0]}$ is constant, the function $F^{[0]}(t)$ evolves on a slow time scale $\mathcal{O}(1/\varepsilon)$. This allows to look for steady states of the equations for x_1 and x_2 while keeping $F^{[0]}$ constant. Equations for x_1 and x_2 become

$$\begin{bmatrix}\dot{x}_1\\ \dot{x}_2\end{bmatrix} = -|\cos\psi|\,C\begin{bmatrix}x_1\\ x_2\end{bmatrix} + \begin{bmatrix}\mathbf{g}^{[2]}(F^{[0]})\cdot\boldsymbol{\beta}_1\\ \mathbf{g}^{[2]}(F^{[0]})\cdot\boldsymbol{\beta}_2\end{bmatrix},$$

where C is the matrix

$$C = \begin{bmatrix}-\boldsymbol{\beta}_1\cdot\mathsf{P}\boldsymbol{\beta}_2 & \boldsymbol{\beta}_1\cdot\mathsf{P}\boldsymbol{\beta}_1\\ -\boldsymbol{\beta}_2\cdot\mathsf{P}\boldsymbol{\beta}_2 & \boldsymbol{\beta}_2\cdot\mathsf{P}\boldsymbol{\beta}_1\end{bmatrix}.$$

It admits a single steady state of the form

$$\begin{bmatrix}x_1\\ x_2\end{bmatrix} = \frac{1}{|\cos\psi|}\,C^{-1}\begin{bmatrix}\mathbf{g}^{[2]}(F^{[0]})\cdot\boldsymbol{\beta}_1\\ \mathbf{g}^{[2]}(F^{[0]})\cdot\boldsymbol{\beta}_2\end{bmatrix},$$

which, after computing explicitly C^{-1} and using standard cross-product identities, can be simplified to

$$\begin{bmatrix}x_1\\ x_2\end{bmatrix} = \frac{1}{\sigma_1\sigma_2\cos\iota\,|\cos\psi|}\begin{bmatrix}\mathsf{P}\,\boldsymbol{\beta}_1\cdot\left(\boldsymbol{\beta}_0\times\mathbf{g}^{[2]}(F^{[0]})\right)\\ \mathsf{P}\,\boldsymbol{\beta}_2\cdot\left(\boldsymbol{\beta}_0\times\mathbf{g}^{[2]}(F^{[0]})\right)\end{bmatrix},$$

where σ_1, σ_2, and ι are the parameters defined from the matrix P in section 3.2. This leads to

$$\mathbf{x} = \frac{1}{\sigma_1\sigma_2\cos\iota\,|\cos\psi|}\left(\mathbf{I}-\boldsymbol{\beta}_0\otimes\boldsymbol{\beta}_0\right)\mathsf{P}^T\left(\boldsymbol{\beta}_0\times\mathbf{g}^{[2]}(F^{[0]})\right), \tag{5.35}$$

which is independent of τ: indeed, using (5.26, 5.31), $\mathbf{g}^{[2]}(F^{[0]})$ can be shown to satisfy the τ-independent equation

$$\mathbf{g}^{[2]}(F^{[0]}) = \varsigma\,\frac{\sin^2\psi}{2}\left(\mathsf{P}\,(\boldsymbol{\beta}_1\times\mathsf{P}\,\boldsymbol{\beta}_2 - \boldsymbol{\beta}_2\times\mathsf{P}\,\boldsymbol{\beta}_1) - \sigma_1\sigma_2\,\boldsymbol{\eta}_0\right),$$

where σ_1, σ_2, ζ, and $\boldsymbol{\eta}_0$ are the parameters defined from matrix P in section 3.2.

Substituting $\mathbf{x}$ accordingly, the equation (5.34) for $\tau^{[1]}$ becomes

$$\dot{\tau}^{[1]} = -\varsigma\,\sigma_1\,\sigma_2\,\frac{\sin^2\psi}{2\cos\iota}\,,$$

so that

$$\tau(t) = \tau^* - \varepsilon\,\varsigma\,\sigma_1\,\sigma_2\,\frac{\sin^2\psi}{2\cos\iota}\,t + \mathcal{O}(\varepsilon^2)\,. \tag{5.36}$$

In conclusion, we have shown that in the limit of large Mason number a, the magnetic moment $\mathbf{m}$ tends to align with the average magnetic field, which is $\pm\mathbf{e}_3$ depending on the sign of $\cos\psi$. The mismatch between $\mathbf{m}$ and $\pm\mathbf{e}_3$ is of order ε. Indeed gathering the results above yields

$$R^\top = F + \mathcal{O}(\varepsilon) = F^{[0]} + \mathcal{O}(\varepsilon)\,, \tag{5.37}$$

where

$$F^{[0]} = \left[\boldsymbol{\beta}_1|\boldsymbol{\beta}_2|\boldsymbol{\beta}_0\right] R_3\big(\tau(t)\big)\,\Sigma\,.$$

Using that $\boldsymbol{\beta}_0 = \mathbf{m}$ by definition (cf. section 3.2), this gives

$$\mathbf{e}_3 = \varsigma\,\mathbf{m} + \mathcal{O}(\varepsilon)\,,$$

where $\varsigma = \operatorname{sign}(\cos\psi)$. Furthermore,

$$\begin{aligned}
\mathbf{e}_1 &= \cos\tau(t)\,\boldsymbol{\beta}_1 + \sin\tau(t)\,\boldsymbol{\beta}_2 + \mathcal{O}(\varepsilon)\\
\mathbf{e}_2 &= -\varsigma\,\sin\tau(t)\,\boldsymbol{\beta}_1 + \varsigma\,\cos\tau(t)\,\boldsymbol{\beta}_2 + \mathcal{O}(\varepsilon)\,,
\end{aligned}$$

where $\tau(t)$ is given by (5.36), so that viewed from the lab frame, there is a slow residual rotation of the body frame about the average field.

To supplement this conclusion, remark that the first order approximation

$$R^\top = F + \varepsilon\,\left[\mathbf{u}^{[1]}(F)\times\right] F + \mathcal{O}(\varepsilon^2) = F^{[0]} + \varepsilon\,\left[\left(\mathbf{u}^{[1]}(F^{[0]}) + \mathbf{x}\right)\times\right] F^{[0]} + \mathcal{O}(\varepsilon^2)\,, \tag{5.38}$$

where $F^{[0]}$ is given by (5.31), $\mathbf{u}^{[1]}$ is by (5.25), and $\mathbf{x}$ by (5.35), is compatible with periodic orbits of the dynamics (3.7) for matrix $Q = R^\top R_3(a\,t)$. Indeed, substituting Q in (5.38) gives

$$Q = Q^{[0]} + \varepsilon\,\left[\left(\mathbf{u}^{[1]}(F^{[0]}) + \mathbf{x}\right)\times\right] Q^{[0]} + \mathcal{O}(\varepsilon^2)\,, \tag{5.39}$$

where

$$Q^{[0]} = F^{[0]} R_3(a\,t) = \left[\boldsymbol{\beta}_1|\boldsymbol{\beta}_2|\boldsymbol{\beta}_0\right] R_3\big(\tau(t)\big) \begin{bmatrix} 1 & 0 & 0\\ 0 & \varsigma & 0\\ 0 & 0 & \varsigma \end{bmatrix} R_3(a\,t)\,.$$

It is possible to choose the body frame so that it coincides with the frame given by the $\boldsymbol{\beta}_i$s, i.e.

$\left[\mathbf{d}_1|\mathbf{d}_2|\mathbf{d}_3\right] = \left[\boldsymbol{\beta}_1|\boldsymbol{\beta}_2|\boldsymbol{\beta}_0\right]$, and with this choice $Q^{[0]}$ becomes

$$Q^{[0]} = R_3\big(\varsigma\, a\, t + \tau(t)\big)\begin{bmatrix}1&0&0\\0&\varsigma&0\\0&0&\varsigma\end{bmatrix} == R_3\big(\tau^* + t\,(\varsigma\, a - \varepsilon\,\varsigma\, h) + \mathcal{O}(\varepsilon^2)\big)\begin{bmatrix}1&0&0\\0&\varsigma&0\\0&0&\varsigma\end{bmatrix},$$

where (cf. equation (5.36))

$$h = \sigma_1\,\sigma_2\,\frac{\sin^2\psi}{2\cos\iota}\,.$$

Therefore $Q^{[0]}$ is periodic, and has period

$$\frac{2\pi}{a - \varepsilon\, h + \mathcal{O}(\varepsilon^2)} = \frac{2\pi}{\frac{1}{\varepsilon} - \varepsilon\, h + \mathcal{O}(\varepsilon^2)} = \frac{2\pi\,\varepsilon}{1 - \varepsilon^2\, h + \mathcal{O}(\varepsilon^3)} = 2\pi\,\varepsilon + \mathcal{O}(\varepsilon^2)\,.$$

Furthermore, according to (5.25)

$$\mathbf{u}^{[1]}(F^{[0]}) = -\sin\psi\,\mathsf{P}\,F^{[0]}\,R_3(a\,t)\begin{bmatrix}0\\1\\0\end{bmatrix} \overset{(5.33)}{=} -\sin\psi\,\mathsf{P}\left[\boldsymbol{\beta}_1|\boldsymbol{\beta}_2|\boldsymbol{\beta}_0\right] R_3(\tau^*)\,\Sigma\, R_3(a\,t)\begin{bmatrix}0\\1\\0\end{bmatrix} + \mathcal{O}(\varepsilon)$$

and $\mathbf{x}$ is constant, so that the perturbation by $\big(\mathbf{u}^{[1]}(Q^{[0]}) + \mathbf{x}\big)$ appearing in the expansion (5.39) is also $2\pi\varepsilon$-periodic up to order ε. So the first-order approximation Q given by (5.39) in the limit of asymptotically large Mason number a is compatible with periodic solutions to the system (3.7) in Q. Numerical experiments discussed in chapter 6 exhibit corresponding periodic orbits at large a. The agreement of the solutions is discussed in section 6.3

5.3 Asymptotic solutions at low conical angle

In this section, we analyse the case of a magnetic field $\mathbf{B}$ almost parallel to its axis of rotation $\mathbf{e}_3$; this corresponds to $\sin\psi \ll 1$. We show that in the small $\sin\psi$ regime, the magnetic moment describes a circle in the magnetic frame, whose centre shifts from the time-dependent magnetic field $\mathbf{B}$ to the average magnetic field $\pm\mathbf{e}_3$ as the Mason number a goes from asymptotically small to asymptotically large, and whose radius goes to zero in both limits $a \to 0$ and $a \to \infty$. This regime thus bridges the small a regime studied in section 5.1 and the large a regime studied in 5.2.

Analysis of the case $\sin\psi \ll 1$ is performed by setting $\varepsilon = \sin\psi$ and performing an asymptotic expansion in ε. Note that the condition $\sin\psi \ll 1$ is satisfied both for $\psi \ll 1$ and for $\pi - \psi \ll 1$, that is for $\mathbf{B}$ close to either of $\pm\mathbf{e}_3$. The equation for the dynamics of the lab frame

$$\dot{R}^\top = \left[\left(-\mathsf{P}\,R^\top R_3(a\,t)\begin{bmatrix}\sin\psi\\0\\\cos\psi\end{bmatrix}\right)\times\right] R^\top\,, \tag{5.16}$$

becomes

$$\dot{R}^\top = -\varsigma\,\left[(\mathsf{P}\,\mathbf{e}_3)\times\right] R^\top - \varepsilon\,\left[\big(\mathsf{P}\,R_3(a\,t)\,\mathbf{e}_1\big)\times\right] R^\top - \varsigma\,\frac{\varepsilon^2}{2}\,\left[(\mathsf{P}\,\mathbf{e}_3)\times\right] R^\top + \mathcal{O}(\varepsilon^3)\,, \tag{5.40}$$

where $\varsigma = \operatorname{sign}(\cos\psi)$, $\mathbf{e}_i$ stands for the i^{th}column of $R^\top$, and we used

$$\cos\psi = \varsigma\sqrt{1-\varepsilon^2} = \varsigma + \varsigma\,\varepsilon^2 + \mathcal{O}(\varepsilon^3)\,.$$

5.3.1 Asymptotic expansion

Zeroth order

The zeroth order dynamics is given by the equation

$$\dot{R}^\top = -\varsigma\,[(\mathsf{P}\,\mathbf{e}_3)\times]\,R^\top$$

which is in equilibrium for $\mathsf{P}\,\mathbf{e}_3 = 0$, i.e. $\mathbf{e}_3 = \pm\boldsymbol{\beta}_0$. This implies that there are two families of steady states given by

$$R^\top = \left[\boldsymbol{\beta}_1|\boldsymbol{\beta}_2|\boldsymbol{\beta}_0\right] R_3(\tau)\begin{bmatrix}1&0&0\\0&\pm1&0\\0&0&\pm1\end{bmatrix}, \tag{5.41}$$

where τ is a parameter. Furthermore, the steady states for which the ± sign is ς are stable. As in section 5.2.2, the magnitude of the zeroth order term in (5.40) decreases as the system approaches this zeroth-order stable manifold. To study the long-term behaviour of the system, higher order terms must therefore also be taken into account, as the solutions to (5.40) are expected to be close to but not quite on steady state (5.41) with the sign matching ς. To this end we define a function

$$\tau(t) = \tau^{[0]}(t) + \varepsilon\,\tau^{[1]}(t) + \varepsilon^2\,\tau^{[2]}(t) + \mathcal{O}(\varepsilon^3)\,,$$

that specifies elements of the stable manifolds as

$$E^{[0]}(t) = \left[\boldsymbol{\beta}_1|\boldsymbol{\beta}_2|\boldsymbol{\beta}_0\right]\Sigma\,R_3\big(\tau(t)\big) \qquad \text{with } \Sigma = \begin{bmatrix}1&0&0\\0&\varsigma&0\\0&0&\varsigma\end{bmatrix}.$$

We then expand $R^\top$as

$$R^\top = E^{[0]} + \varepsilon\,E^{[1]} + \varepsilon^2\,E^{[2]} + \mathcal{O}(\varepsilon^3)\,, \tag{5.42}$$

where

$$E^{[1]} = \left[\mathbf{u}^{[1]}\times\right]E^{[0]}\,, \qquad E^{[2]} = \left[\mathbf{u}^{[2]}\times\right]E^{[0]} + \frac{1}{2}\left[\mathbf{u}^{[1]}\times\right]^2 E^{[0]}\,,$$

for some $\mathbf{u}^{[1]} = \mathbf{u}^{[1]}(t)$, $\mathbf{u}^{[2]} = \mathbf{u}^{[2]}(t) \in \mathbb{R}^3$ (see appendix A). Furthermore assume that $\mathbf{u}^{[1]}$ and $\mathbf{u}^{[2]}$ have no component along $\boldsymbol{\beta}_0$.

Substituting the expansion (5.42) in (5.40), and keeping only zeroth order terms, the equation becomes

$$\varsigma\,\dot{\tau}^{[0]}\left[\boldsymbol{\beta}_0\times\right]E^{[0]} = 0\,,$$

implying that $\tau^{[0]} \equiv \tau^*$ is constant, and that

$$E^{[0]} = \left[\boldsymbol{\beta}_1 | \boldsymbol{\beta}_2 | \boldsymbol{\beta}_0\right] \Sigma R_3(\tau^*) + \varepsilon \tau^{[1]} \left[\boldsymbol{\beta}_0 \times\right] \left[\boldsymbol{\beta}_1 | \boldsymbol{\beta}_2 | \boldsymbol{\beta}_0\right] \Sigma R_3(\tau^*) + \mathscr{O}(\varepsilon^2) . \tag{5.43}$$

First order

Substituting (5.42) in (5.40), and keeping only terms only up to order ε, the first order equation is (cf. appendix A, equation (A.16))

$$\varsigma \dot{\tau}^{[1]} \boldsymbol{\beta}_0 + \dot{\mathbf{u}}^{[1]} = -\mathsf{P}\,(\mathbf{u}^{[1]} \times \boldsymbol{\beta}_0) - \mathsf{P}\, R_3(a\,t) \left[\boldsymbol{\beta}_1 | \boldsymbol{\beta}_2 | \boldsymbol{\beta}_0\right] \Sigma R_3(\tau^*) \left[\begin{smallmatrix} 1 \\ 0 \\ 0 \end{smallmatrix}\right] . \tag{5.44}$$

This equation is solved for $\mathbf{u}^{[1]}(t) = u_1(t)\, \boldsymbol{\beta}_1 + u_2(t)\, \boldsymbol{\beta}_2$.

No assumption has been made on the body frame; it is always possible to choose it so that it coincides with $\left[\boldsymbol{\beta}_1 | \boldsymbol{\beta}_2 | \boldsymbol{\beta}_0\right]$, so that the expression (5.44) simplifies to

$$\varsigma \dot{\tau}^{[1]} \boldsymbol{\beta}_0 + \dot{\mathbf{u}}^{[1]} = -\mathsf{P}\,(\mathbf{u}^{[1]} \times \boldsymbol{\beta}_0) - \mathsf{P}\left(\cos(a\,t + \tau^*)\, \boldsymbol{\beta}_1 + \varsigma \sin(a\,t + \tau^*)\, \boldsymbol{\beta}_2\right) .$$

A projection of (5.44) on $\boldsymbol{\beta}_1$ and $\boldsymbol{\beta}_2$ – which now coincide with $\left[\begin{smallmatrix} 1 \\ 0 \\ 0 \end{smallmatrix}\right]$ and $\left[\begin{smallmatrix} 0 \\ 1 \\ 0 \end{smallmatrix}\right]$ – yields

$$\begin{bmatrix} \dot{u}_1 \\ \dot{u}_2 \end{bmatrix} = -C \begin{bmatrix} u_1 \\ u_2 \end{bmatrix} + C \begin{bmatrix} \varsigma \sin(a\,t + \tau^*) \\ -\cos(a\,t + \tau^*) \end{bmatrix} ,$$

where

$$C = \begin{bmatrix} -\boldsymbol{\beta}_1 \cdot \mathsf{P}\boldsymbol{\beta}_2 & \boldsymbol{\beta}_1 \cdot \mathsf{P}\boldsymbol{\beta}_1 \\ -\boldsymbol{\beta}_2 \cdot \mathsf{P}\boldsymbol{\beta}_2 & \boldsymbol{\beta}_2 \cdot \mathsf{P}\boldsymbol{\beta}_1 \end{bmatrix} .$$

This equation can be solved explicitly as

$$\begin{bmatrix} u_1 \\ u_2 \end{bmatrix} = -a\,(a^2 \mathbf{I} + C^2)^{-1} C \begin{bmatrix} \varsigma \cos(a\,t + \tau^*) \\ \sin(a\,t + \tau^*) \end{bmatrix} - (a^2 \mathbf{I} + C^2)^{-1} C^2 \begin{bmatrix} -\varsigma \sin(a\,t + \tau^*) \\ \cos(a\,t + \tau^*) \end{bmatrix} . \tag{5.45}$$

Projecting (5.44) on $\boldsymbol{\beta}_0$ and substituting (5.45) therein yields

$$\tau^{[1]} = \varsigma\, \tilde{\tau}_1 \cos(a\,t + \tau^*) + \varsigma\, \tilde{\tau}_2 \sin(a\,t + \tau^*) ,$$

where

$$\begin{aligned} \tilde{\tau}_1 &= \frac{1}{a} \begin{bmatrix} \mathsf{P}\boldsymbol{\beta}_2 \cdot \boldsymbol{\beta}_0 \\ -\mathsf{P}\boldsymbol{\beta}_1 \cdot \boldsymbol{\beta}_0 \end{bmatrix} \cdot \left(-a\,(a^2 \mathbf{I} + C^2)^{-1} C \left[\begin{smallmatrix} 0 \\ 1 \end{smallmatrix}\right] + \varsigma\,(a^2 \mathbf{I} + C^2)^{-1} C^2 \left[\begin{smallmatrix} 1 \\ 0 \end{smallmatrix}\right] \right) - \frac{1}{a} \mathsf{P}\boldsymbol{\beta}_2 \cdot \boldsymbol{\beta}_0 \\ \tilde{\tau}_2 &= \frac{1}{a} \begin{bmatrix} \mathsf{P}\boldsymbol{\beta}_2 \cdot \boldsymbol{\beta}_0 \\ -\mathsf{P}\boldsymbol{\beta}_1 \cdot \boldsymbol{\beta}_0 \end{bmatrix} \cdot \left(\varsigma\, a\,(a^2 \mathbf{I} + C^2)^{-1} C \left[\begin{smallmatrix} 1 \\ 0 \end{smallmatrix}\right] + (a^2 \mathbf{I} + C^2)^{-1} C^2 \left[\begin{smallmatrix} 0 \\ 1 \end{smallmatrix}\right] \right) + \frac{1}{a} \mathsf{P}\boldsymbol{\beta}_1 \cdot \boldsymbol{\beta}_0 . \end{aligned}$$

Note in particular that

$$\|\mathbf{u}^{[1]}\| \underset{a\to\infty}{\sim} \frac{1}{a}, \quad \text{and} \tag{5.46}$$

$$\|\mathbf{u}^{[1]}\| \underset{a\to 0}{\sim} 1, \tag{5.47}$$

which is consistent both with result (5.37) as $a \to \infty$

$$R^\top = \left[\boldsymbol{\beta}_1 | \boldsymbol{\beta}_2 | \boldsymbol{\beta}_0\right] R_3\big(\tau^*\big)\, \Sigma + \mathcal{O}(\varepsilon^2)\mathcal{O}(1/a),$$

and with result (5.11) as $a \to 0$, i.e.

$$\begin{aligned} Q(t) = R^\top R_3(a\,t) &= \left[\boldsymbol{\beta}_1 | \boldsymbol{\beta}_2 | \boldsymbol{\beta}_0\right] R_3\big(\lambda(t)\big)\, R_2(\psi) + \mathcal{O}(a) \\ &= \left[\boldsymbol{\beta}_1 | \boldsymbol{\beta}_2 | \boldsymbol{\beta}_0\right] R_3\big(\lambda(t)\big) \left[\begin{smallmatrix} \varsigma & 0 & 0 \\ 0 & 1 & 0 \\ 0 & 0 & \varsigma \end{smallmatrix}\right] + \varepsilon \left[\boldsymbol{\beta}_1 | \boldsymbol{\beta}_2 | \boldsymbol{\beta}_0\right] R_3\big(\lambda(t)\big) \left[\begin{smallmatrix} 0 & 0 & -1 \\ 0 & 0 & 0 \\ 1 & 0 & 0 \end{smallmatrix}\right] + \mathcal{O}(\varepsilon^2) + \mathcal{O}(a). \end{aligned}$$

Second order

At second order, the dynamics is given by (cf. appendix A, equation (A.17))

$$\begin{aligned} &\varsigma\, \dot{\tau}^{[2]}\, \boldsymbol{\beta}_0 + \dot{\mathbf{u}}^{[2]} + \varsigma\, \tau^{[1]}\, \mathbf{u}^{[1]} \times \boldsymbol{\beta}_0 + \frac{1}{2}\mathbf{u}^{[1]} \times \dot{\mathbf{u}}^{[1]} \\ &= -\,\mathsf{P}\left(\mathbf{u}^{[2]} \times \boldsymbol{\beta}_0 + \frac{1}{2}\mathbf{u}^{[1]} \times (\mathbf{u}^{[1]} \times \boldsymbol{\beta}_0)\right) \\ &\quad -\mathsf{P}\big(\cos(a\,t+\tau^*)\,\mathbf{u}^{[1]} \times \boldsymbol{\beta}_1 + \varsigma\, \sin(a\,t+\tau^*)\,\mathbf{u}^{[1]} \times \boldsymbol{\beta}_2\big). \end{aligned}$$

Again it is assumed that $\mathbf{u}^{[2]} \perp \boldsymbol{\beta}_0$ and this allows to find that $\mathbf{u}^{[2]}$ is an affine combination of $\cos(2\,a\,t + 2\,\tau^*)$ and $\sin(2\,a\,t + 2\,\tau^*)$ with coefficients depending on a.

We use this second order solution only to compare with the numerics in chapter 6.

5.3.2 Dynamics of the Magnetic Moment

The position of the magnetic moment in the magnetic frame is given by

$$Q^T\, \mathbf{m} = R_3^T(a\,t)\, R\, \boldsymbol{\beta}_0\,.$$

Substituting for R by its asymptotic expansion (5.42) for $\sin\psi = \varepsilon \ll 1$ yields

$$Q^T\, \mathbf{m} = R_3^T(a\,t+\tau^*)\left(\begin{bmatrix} 0 \\ 0 \\ \varsigma \end{bmatrix} + \varepsilon \begin{bmatrix} -u_2 \\ \varsigma\, u_1 \\ 0 \end{bmatrix} + \varepsilon^2 \begin{bmatrix} -\mathbf{u}^{[2]} \cdot \boldsymbol{\beta}_2 \\ \varsigma\, \mathbf{u}^{[2]} \cdot \boldsymbol{\beta}_1 \\ -\varsigma\, \frac{u_1^2 + u_2^2}{2} \end{bmatrix}\right) + \mathcal{O}(\varepsilon^3)\,. \tag{5.48}$$

When $1/a \leq \varepsilon$, using (5.46) in (5.48) yields

$$Q^T \mathbf{m} = \begin{bmatrix} 0 \\ 0 \\ \varsigma \end{bmatrix} + \mathcal{O}(\varepsilon^2)$$

in agreement with the results for $a \gg 1$ in section 5.2. When $a \leq \varepsilon$, using (5.47) allows to obtain

$$Q^T \mathbf{m} = \begin{bmatrix} 0 \\ 0 \\ \varsigma \end{bmatrix} + \begin{bmatrix} \varepsilon \\ 0 \\ 0 \end{bmatrix} + \mathcal{O}(\varepsilon^2)$$

in agreement with the prediction for $a \ll 1$ in section 5.1 since in the magnetic frame, the magnetic field is

$$\begin{bmatrix} \varepsilon \\ 0 \\ \varsigma\,(1+\varepsilon^2/2) + \mathcal{O}(\varepsilon^3) \end{bmatrix}.$$

Moreover, the trajectory of $Q^T \mathbf{m}$ at first order is a circle with radius r and centre $\boldsymbol{m}_0$ satisfying

$$\begin{aligned} r &= \frac{\varepsilon\, a}{2\det(a^2\mathbf{I}+A^2)} \sqrt{c_0 + c_1\, a + c_2\, a^2 + c_3\, a^3 + c_4\, a^4}\,, \\ \boldsymbol{m}_0 &= \begin{bmatrix} 0 \\ 0 \\ \varsigma \end{bmatrix} + \frac{\varepsilon}{2\det(a^2\mathbf{I}+A^2)} \begin{bmatrix} 2\,(\sigma_1\sigma_2\cos\iota)^2 - a^2\,(\boldsymbol{\beta}_1\cdot \mathsf{P}\,\mathsf{P}^T\boldsymbol{\beta}_1 + \boldsymbol{\beta}_2\cdot \mathsf{P}\,\mathsf{P}^T\boldsymbol{\beta}_2) \\ a\,(a^2+\sigma_1\sigma_2\cos\iota)\,(\boldsymbol{\beta}_2\cdot\mathsf{P}\,\boldsymbol{\beta}_1 - \boldsymbol{\beta}_1\cdot\mathsf{P}\,\boldsymbol{\beta}_2) \\ 0 \end{bmatrix}, \end{aligned}$$

where

$$\begin{aligned} c_0 =& \sigma_1^2\sigma_2^2\cos^2\iota\,\left((\mathsf{P}\boldsymbol{\beta}_1\cdot\boldsymbol{\beta}_1 - \mathsf{P}\,\boldsymbol{\beta}_2\cdot\boldsymbol{\beta}_2)^2 + (\mathsf{P}\,\boldsymbol{\beta}_1\cdot\boldsymbol{\beta}_2 + \mathsf{P}\,\boldsymbol{\beta}_2\cdot\boldsymbol{\beta}_1)^2\right), \\ c_1 =& 2\,\sigma_1\sigma_2\cos\iota\big(-\varsigma\,(\mathsf{P}\,\boldsymbol{\beta}_1\cdot\boldsymbol{\beta}_1 - \mathsf{P}\,\boldsymbol{\beta}_2\cdot\boldsymbol{\beta}_2)\,(-\mathsf{P}\,\boldsymbol{\beta}_1\cdot\boldsymbol{\beta}_0^2 - \mathsf{P}\,\boldsymbol{\beta}_2\cdot\boldsymbol{\beta}_0^2 + \sigma_1^2 + \sigma_2^2) \\ & -4\,(\mathsf{P}\,\boldsymbol{\beta}_1\cdot\boldsymbol{\beta}_2 + \mathsf{P}\,\boldsymbol{\beta}_2\cdot\boldsymbol{\beta}_1)\,(\mathsf{P}\,\boldsymbol{\beta}_1\cdot\boldsymbol{\beta}_0)\,(\mathsf{P}\,\boldsymbol{\beta}_2\cdot\boldsymbol{\beta}_0)\big), \\ c_2 =& -2\,\sigma_1\sigma_2\cos\iota\big((\mathsf{P}\,\boldsymbol{\beta}_1\cdot\boldsymbol{\beta}_1 - \mathsf{P}\,\boldsymbol{\beta}_2\cdot\boldsymbol{\beta}_2)^2 + (\mathsf{P}\,\boldsymbol{\beta}_1\cdot\boldsymbol{\beta}_2 + \mathsf{P}\,\boldsymbol{\beta}_2\cdot\boldsymbol{\beta}_1)^2\big) \\ & + (-\mathsf{P}\,\boldsymbol{\beta}_1\cdot\boldsymbol{\beta}_0^2 - \mathsf{P}\,\boldsymbol{\beta}_2\cdot\boldsymbol{\beta}_0^2 + \sigma_1^2 + \sigma_2^2)^2 + 4\,(\mathsf{P}\,\boldsymbol{\beta}_1\cdot\boldsymbol{\beta}_0)^2\,(\mathsf{P}\,\boldsymbol{\beta}_2\cdot\boldsymbol{\beta}_0)^2, \\ c_3 =& 2\,\varsigma\,(-\mathsf{P}\,\boldsymbol{\beta}_1\cdot\boldsymbol{\beta}_0^2 - \mathsf{P}\,\boldsymbol{\beta}_2\cdot\boldsymbol{\beta}_0^2 + \sigma_1^2 + \sigma_2^2)\,(\mathsf{P}\,\boldsymbol{\beta}_1\cdot\boldsymbol{\beta}_1 - \mathsf{P}\,\boldsymbol{\beta}_2\cdot\boldsymbol{\beta}_2) \\ & + 4\,(\mathsf{P}\,\boldsymbol{\beta}_1\cdot\boldsymbol{\beta}_0)\,(\mathsf{P}\,\boldsymbol{\beta}_2\cdot\boldsymbol{\beta}_0)\,(\mathsf{P}\,\boldsymbol{\beta}_1\cdot\boldsymbol{\beta}_2 + \mathsf{P}\,\boldsymbol{\beta}_2\cdot\boldsymbol{\beta}_1), \\ c_4 =& (\mathsf{P}\,\boldsymbol{\beta}_1\cdot\boldsymbol{\beta}_1 - \mathsf{P}\,\boldsymbol{\beta}_2\cdot\boldsymbol{\beta}_2)^2 + (\mathsf{P}\,\boldsymbol{\beta}_1\cdot\boldsymbol{\beta}_2 + \mathsf{P}\,\boldsymbol{\beta}_2\cdot\boldsymbol{\beta}_1)^2, \end{aligned}$$

and $\det(a^2\mathbf{I}+A^2) = (\sigma_1\sigma_2\cos\iota)^2 + a^2\,\mathrm{tr}(A^2) + a^4$.

This behaviour at small $\sin\psi$ matches the limits found at low and large Mason numbers a in sections 5.1 and 5.2. These findings are supported by numerical experiments that will be discussed in the next chapter.

6 Example Swimmers

The theoretical results presented in chapters 4 and 5 are valid for rigid bodies of any shape with a generic constant magnetic moment **m**. Helical swimmers have been observed to have good swimming properties [17], and accordingly, examples of helical swimmers were used to illustrate the theoretical results in chapter 4. In this chapter, we show how the theory applies to a few more specific examples. Section 6.1 presents these swimmer's geometry. Most of them are helical and their mobility matrix $\mathbb{M}$ is computed using the code provided by Prof. O. Gonzalez as introduced in chapter 2. The set of relative equilibria, as introduced in chapter 4, is displayed for each swimmer. In section 6.2, the rotational dynamics are explored for different parameter values, and different regimes are illustrated by phase portraits, as in chapter 4. Section 6.3 displays the excellent agreement between numerical results and the analytical predictions obtained in chapter 5 in the limits of small and large Mason number a, and in the limit of small conical angle ψ.

6.1 Swimmers Geometries, Material Parameters, and Surface of Equilibria

The figures presented in chapter 4 were obtained using material parameters (mobility matrix $\mathbb{M}$ and magnetic moment **m**) obtained from swimmers A and B, whose geometry is presented respectively in figures 6.1 and 6.2. In this section, the geometries and material parameters of a few more swimmers are presented, and the corresponding surfaces of equilibria (as defined in chapter 4) are shown.

The geometric parameters and mobility matrices are given in the non-dimensional units defined in chapter 2. Recall that the length scale ℓ is picked as the gyration radius of the swimmer. Therefore all lengths are given in terms of the gyration radius ℓ. The dimensional blocks of the mobility matrix $\mathbb{M}$ are non-dimensionalised as

$$\mathsf{M}_{11} = \frac{1}{\ell\eta}\overline{\mathsf{M}}_{11}, \qquad \mathsf{M}_{12} = \frac{1}{\ell^2\eta}\overline{\mathsf{M}}_{12}, \qquad \mathsf{M}_{22} = \frac{1}{\ell^3\eta}\overline{\mathsf{M}}_{22},$$

where the overbars denote non-dimensional quantities. The fluid viscosity η is scaled out before computing the drag matrices of helical swimmers.

The shape of swimmers A and B is based on helical micro-swimmers built by the group of Prof. Nelson [85], although the arc-length of swimmer A's centreline was divided by two in comparison to the manufactured device: the centreline of swimmer A is a helix of 1.5 turns, whereas the different swimmers created by Prof. Nelson's group were helices of 3 turns, like swimmer B. Swimmer A was picked because its regime diagram (cf. fig. 4.8a) is more obviously asymmetric about the axis $\cos\psi = 0$ than that of the other examples of helical swimmers. Both swimmers A and B are right-handed helices. Swimmer B' has exactly the same dimensions as swimmer B, but it is a left-handed helix. Swimmer C is a thin helical rod with a centreline making 8 turns. Swimmer D is a left-handed helical rod making 2.2749 turns. Swimmer E is a right-handed helical rod with a large pitch making approximately one full turn. Swimmer F is an assembly of three spherical beads and its specifications were taken from [45, 86].

The mobility matrices $\mathbb{M}$ and magnetic moments $\mathbf{m}$ given below for swimmers A-E are expressed in the body frame basis in which the helical rod's centreline can be parametrised as

$$\begin{bmatrix} r\cos(s) \\ r\sin(s) \\ \frac{ps}{2\pi} \end{bmatrix} \qquad \text{for } s \in [0, s_{\max}],$$

where r is the helix' radius and p the pitch. The convention used is that $r > 0$. The sign of p determines the handedness of the helix: helices with $p > 0$ are right-handed, and helices with $p < 0$ are left-handed. To obtain a smooth surface, the helical rod is capped at each ends by a hemisphere. The number of turns of helical centrelines indicated below do not take into account these hemispheres.

All the matrices $\mathbb{M}$ were obtained using Prof. Gonzalez' code discussed in section 2.1.2. The mesh size used for computations is displayed in the figures presenting the swimmers (cf. fig. 6.1, 6.2, 6.5, 6.8, 6.11 and 6.14). The code output is the matrix of hydrodynamic drag $\mathbb{D}$ about the centre of mass of the rod. Due to numerical error, the matrix $\mathbb{D}$ obtained was not strictly symmetric, although the theory predicts that it should be. In each case, we show

$$\frac{\|\mathbb{D} - \mathbb{D}^T\|}{\|\mathbb{D}\|}$$

to measure this numerical error, with $\|\cdot\|$ being the operator norm induced by the vector Euclidean norm, i.e.

$$\|D\| = \sup_{z \neq 0} \frac{|Dz|}{|z|}.$$

To obtain a symmetric mobility matrix, $\mathbb{M}$ was computed as $\mathbb{M} = \frac{1}{2}\left(\mathbb{D}^{-1} + \mathbb{D}^{-T}\right)$, where $\mathbb{D}$ is the

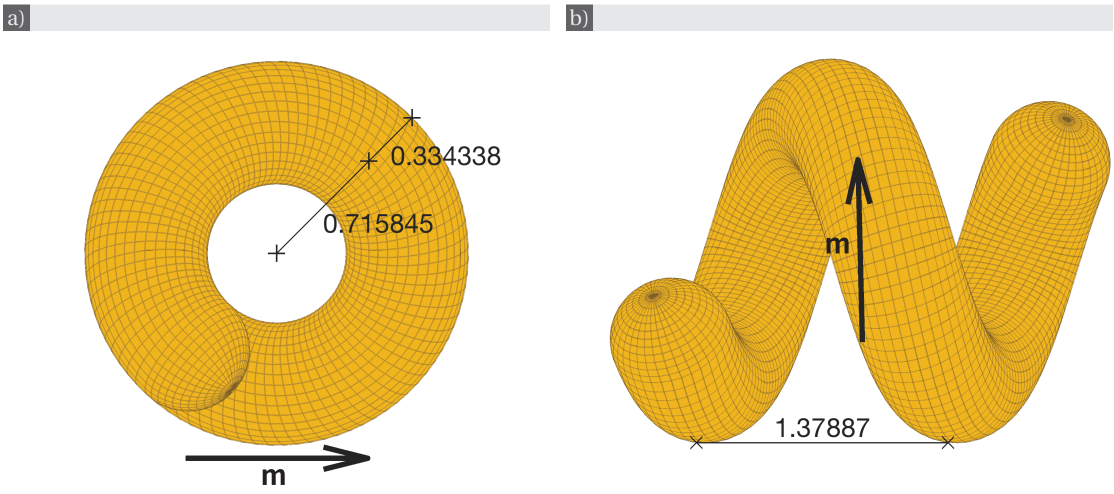

Figure 6.1 – **Swimmer A**. The mesh shows the discretisation used for numerical computation of the drag matrix $\mathbb{D}$. In panel (b) the magnetic moment $\mathbf{m}$ is in the plane of the paper.

code output.

The mobility matrix of swimmer A (cf. fig. 6.1) is

$$\mathbb{M}_A = \begin{bmatrix} 0.0481 & 0 & -0.00133799 & -0.000641566 & 0 & -0.000758049 \\ 0 & 0.047428 & 0 & 0 & 0.0000820823 & 0 \\ -0.00133799 & 0 & 0.0480591 & -0.0000553815 & 0 & 0.000843475 \\ -0.000641566 & 0 & -0.0000553815 & 0.0263123 & 0 & -0.00382609 \\ 0 & 0.0000820823 & 0 & 0 & 0.0236896 & 0 \\ -0.000758049 & 0 & 0.000843475 & -0.00382609 & 0 & 0.0320669 \end{bmatrix},$$

where all components smaller than 10^{-16} in absolute value have been rounded to 0. It is computed as $\mathbb{M}_A = \frac{1}{2}\left(\mathbb{D}_A^{-1} + \mathbb{D}_A^{-T}\right)$ with $\mathbb{D}_A$ such that

$$\frac{\|\mathbb{D}_A - \mathbb{D}_A^T\|}{\|\mathbb{D}_A\|} = 3.3195 \cdot 10^{-5}.$$

The magnetic moment of swimmer A is

$$\mathbf{m}_A = \begin{bmatrix} 0.675529 \\ -0.736927 \\ 0.0244727 \end{bmatrix}.$$

The pitch, radius, rod length and rod radius of swimmer B (cf. fig. 6.2) were chosen according to the specifications of a swimmer manufactured by the group of Prof. Nelson [85]. The manufactured swimmer has an elliptical cross-section, whereas the swimmer used in this analysis has a circular cross-section, the radius of which is between the two elliptical radii. The manufactured swimmer's surface presents asperities, whereas the rod was assumed to have a smooth boundary when computing the drag matrix. The rod has constant cross-section over

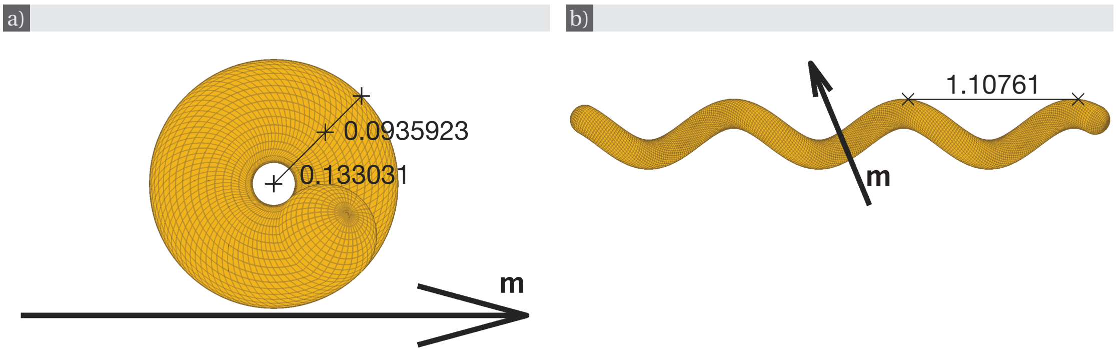

Figure 6.2 – **Swimmer B**. The mesh shows the discretisation used for numerical computation of the drag matrix $\mathbb{D}$. In panel (b) the magnetic moment $\mathbf{m}$ is in the plane of the paper.

three full turns and is capped by hemispheres. The mobility matrix of swimmer B is

$$\mathbb{M}_B = \begin{bmatrix} 0.0802287 & 0 & 0 & -0.000570578 & 0 & 0 \\ 0 & 0.0802111 & -0.000713529 & 0 & 0.000122079 & -0.00946932 \\ 0 & -0.000713529 & 0.108421 & 0 & 0.00257503 & 0.0220111 \\ -0.000570578 & 0 & 0 & 0.0497381 & 0 & 0 \\ 0 & 0.000122079 & 0.00257503 & 0 & 0.0500286 & -0.0192512 \\ 0 & -0.00946932 & 0.0220111 & 0 & -0.0192512 & 0.994177 \end{bmatrix},$$

where all components smaller than 10^{-15} in absolute value have been cut off to 0. It is computed as $\mathbb{M}_B = \frac{1}{2}\left(\mathbb{D}_B^{-1} + \mathbb{D}_B^{-T}\right)$ with $\mathbb{D}_B$ such that

$$\frac{\|\mathbb{D}_B - \mathbb{D}_B^T\|}{\|\mathbb{D}_B\|} = 8.9731 \cdot 10^{-7},$$

and its magnetic moment is

$$\mathbf{m}_B = \begin{bmatrix} 0.653281 \\ 0.653281 \\ 0.382683 \end{bmatrix}.$$

Figures 6.3-6.4 show the surface of relative equilibria of swimmer B. Its comparison with figure 4.6 immediately yields interesting observations. The two surfaces have similarities: the overall shapes look alike with fold lines following similar patterns. The lines of Hopf bifurcations present on fig. 4.6 have counterparts on fig. 6.3. However, the surface on fig. 6.3 exhibits extra lines of Hopf bifurcations close to extremal values of ψ. In particular, this feature allows the existence of parameter regime 0/4 (cf. also fig. 4.8b).

Note that there exist relative equilibria for a much wider range of parameters for swimmer B than for swimmer A, with $\cos\psi$ ranging from -0.9049 to 0.9048 and a up to 0.9244 compared to $\cos\psi \in [-0.1669, 0.1736]$ and $a \leq 0.0333$ for swimmer A. Moreover the projection on the parameter plane in fig. 6.3a looks more symmetric about the $\cos\psi = 0$ axis than projection in fig. 4.1b for swimmer A. Recall that the condition for a symmetric set of relative equilibria is

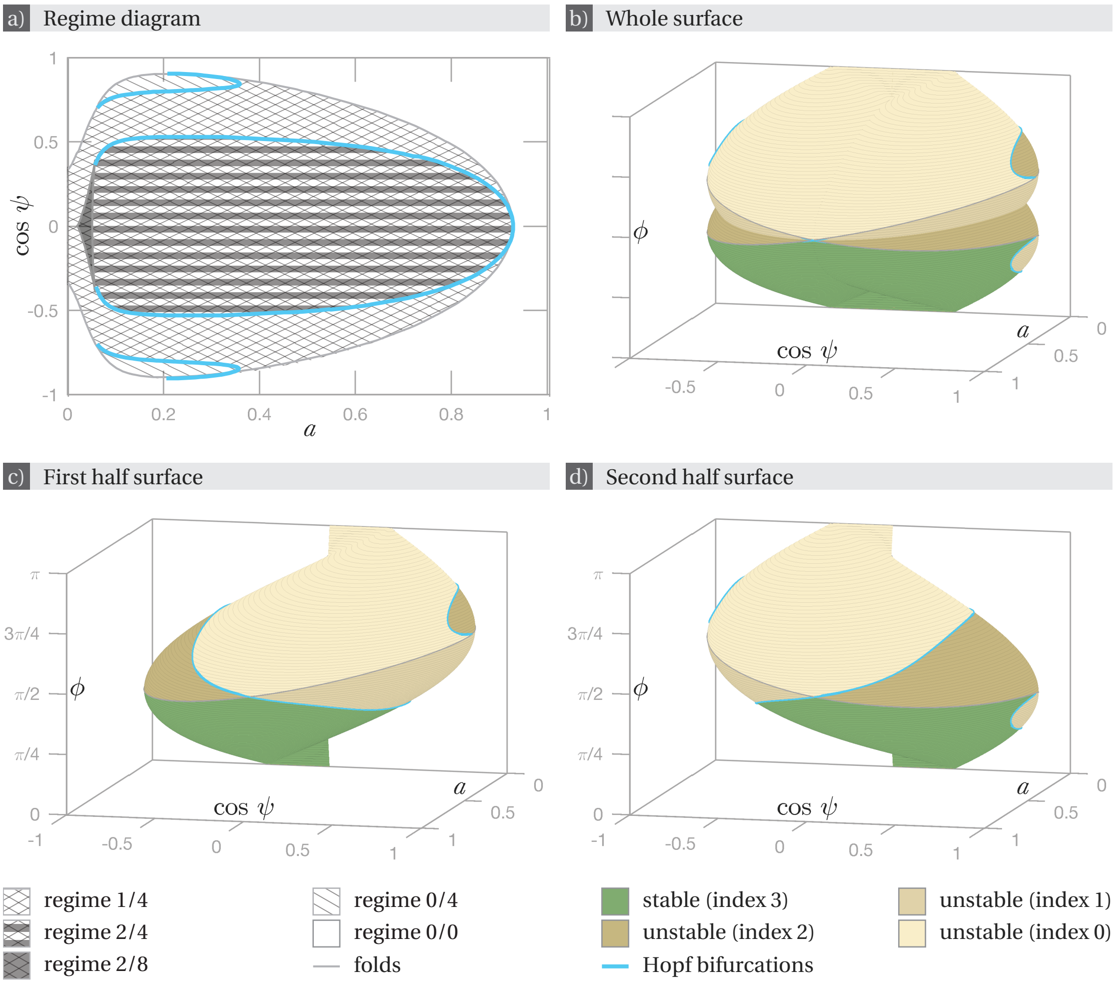

Figure 6.3 – **Swimmer B: surface of relative equilibria**. (a) Regime diagram. The different parameter regimes are separated by curves of bifurcations. There are no stable relative equilibria outside the cross-hatched region, which features one or two (in dark) stable relative equilibria. (b) Whole surface $\mathscr{S}$, (c) first half surface $\mathscr{S}_1$, and (d) second half surface $\mathscr{S}_2$ coloured by stability index. The mirror symmetry through the plane $\phi = \pi/2$ relating $\mathscr{S}_1$ on panel (c) and $\mathscr{S}_2$ on panel (d) reverses stability indices (cf. chapter 4).
To view these surfaces in rotation, click here (password: thesisPR) or scan the barcode.

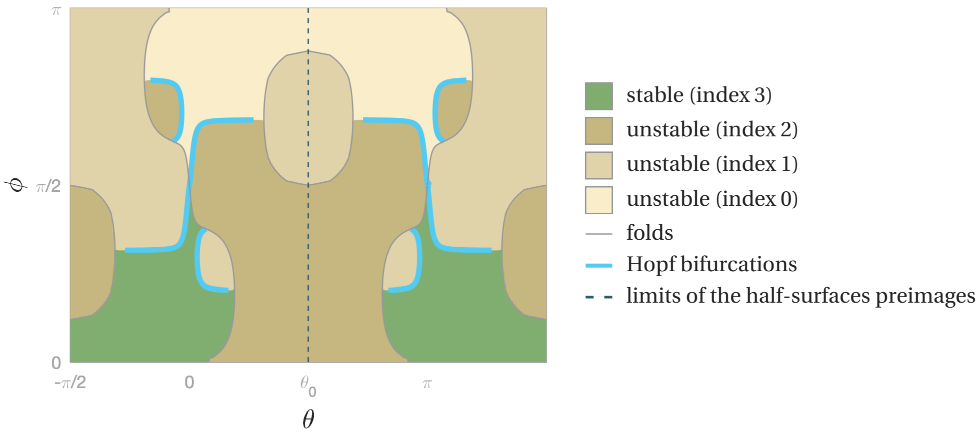

Figure 6.4 – **Swimmer B: pre-image of the relative equilibria mapping**. Each pair $(\theta, \phi) \in [\theta_0 - \pi, \theta_0 + \pi) \times [0, \pi]$ uniquely parametrises a relative equilibrium. The plane is coloured by stability index, and regions with different stability indices are separated by curves of bifurcations.

that $c_{11} = 0$, where c_{11} is given by (3.20) (cf section 4.1.4). For swimmer A, $c_{11} = 1.6878 \cdot 10^{-5}$ and for swimmer B, $c_{11} = -1.7003 \cdot 10^{-5}$. Both values of c_{11} have similar magnitudes, but for swimmer A we have $c_{11}/c_{12} = 0.0019$, while for swimmer B we obtain $c_{11}/c_{12} = -2.0837 \cdot 10^{-5}$, implying that the relative weight of c_{11} in (4.5) is larger for swimmer A than for swimmer B. We expect the difference in symmetric appearances to be due to the relative lengths of the swimmers: swimmer A is a helical rod of 1.5 turns while swimmer B has 3 turns. We conjecture that for long helices the diagram will be very close to symmetric regardless of the direction of the magnetic moment **m**.

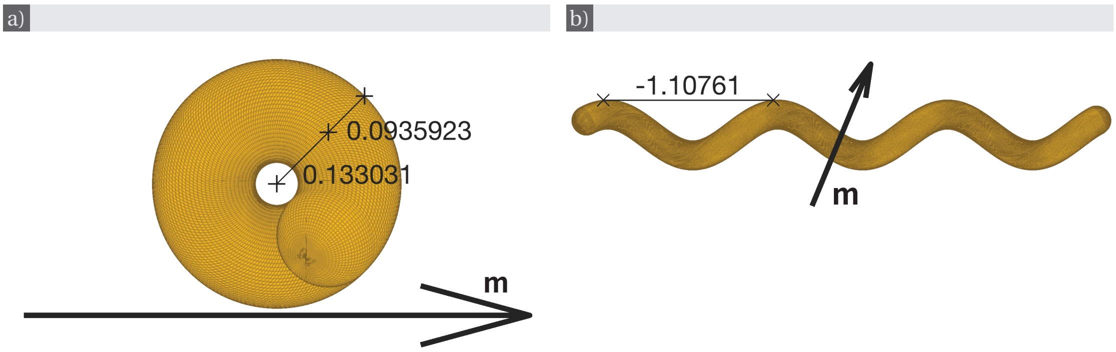

Figure 6.5 – **Swimmer B'**. The mesh shows the discretisation used for numerical computation of the drag matrix $\mathbb{D}$. In panel (b) the magnetic moment **m** is in the plane of the paper.

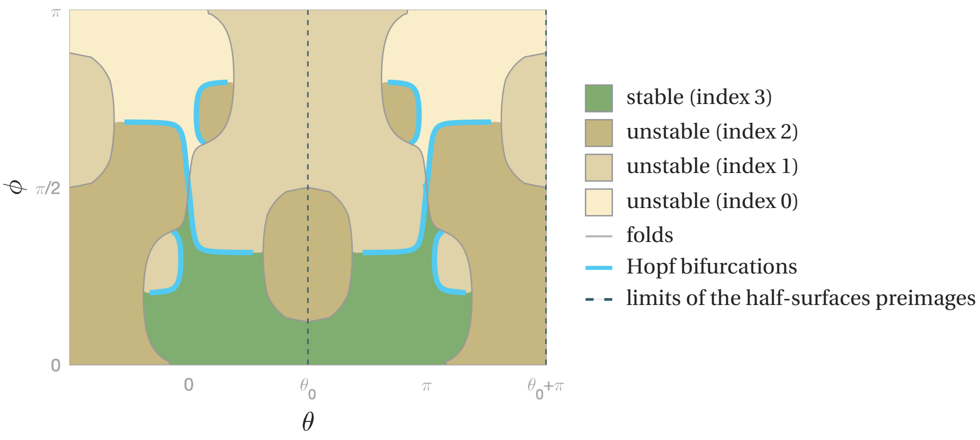

Figure 6.6 – **Swimmer B': pre-image of the relative equilibria mapping**. Each pair $(\theta,\phi) \in [\theta_0-\pi,\theta_0+\pi) \times [0,\pi]$ uniquely parametrises a relative equilibrium. The plane is coloured by stability index, and regions with different stability indices are separated by curves of bifurcations.

Swimmer B' (cf. fig. 6.5) is symmetric to swimmer B via a planar symmetry through the horizontal plane. Accordingly, swimmer B' is left-handed. The mobility matrix of swimmer B' is

$$\mathbb{M}_{B'} = \begin{bmatrix} 0.0802304 & 0 & 0 & 0.000570871 & 0 & 0 \\ 0 & 0.0802116 & 0.000715398 & 0 & -0.000122547 & -0.00946871 \\ 0 & 0.000715398 & 0.108427 & 0 & 0.00257702 & -0.0220142 \\ 0.000570871 & 0 & 0 & 0.0497398 & 0 & 0 \\ 0 & -0.000122547 & 0.00257702 & 0 & 0.0500327 & 0.0192559 \\ 0 & -0.00946871 & -0.0220142 & 0 & 0.0192559 & 0.994198 \end{bmatrix},$$

where all components smaller than 10^{-7} in absolute value have been cut off to 0. It is computed as $\mathbb{M}_{B'} = \frac{1}{2}\left(\mathbb{D}_{B'}^{-1} + \mathbb{D}_{B'}^{-T}\right)$ with $\mathbb{D}_{B'}$ such that

$$\frac{\|\mathbb{D}_{B'} - \mathbb{D}_{B'}^{T}\|}{\|\mathbb{D}_{B'}\|} = 8.9836 \cdot 10^{-7},$$

and its magnetic moment is

$$\mathbf{m}_{B'} = \begin{bmatrix} 0.653281 \\ 0.653281 \\ -0.382683 \end{bmatrix}.$$

The surface of equilibria for swimmer B' (cf. fig. 6.7-6.6) looks exactly the same as the surface of equilibria for swimmer B. The relative equilibria for a pair of parameters (a,ψ) for swimmer B are actually related to the relative equilibria for parameters $(a,\pi-\psi)$, as expected due to the change of handedness (cf. also fig. 7.11-7.14 in the next chapter). Thus there is a mirror symmetry about the plane $\cos\psi = 0$ between fig. 6.3 and fig. 6.7.

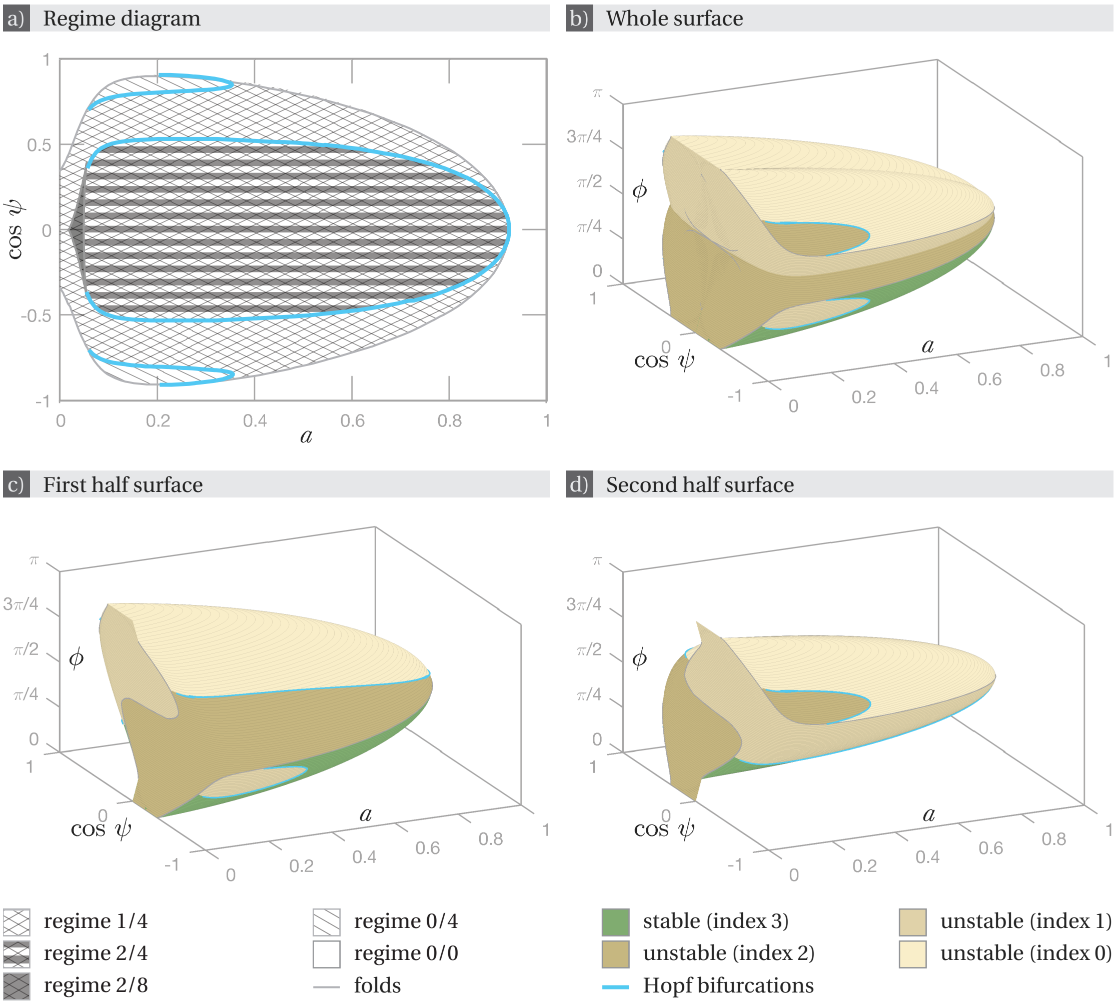

Figure 6.7 – **Swimmer B': surface of relative equilibria**. (a) Regime diagram. The different parameter regimes are separated by curves of bifurcations. There are no stable relative equilibria outside the cross-hatched region, which features one or two (in dark) stable relative equilibria. (b) Whole surface $\mathscr{S}$, (c) first half surface $\mathscr{S}_1$, and (d) second half surface $\mathscr{S}_2$ coloured by stability index. The mirror symmetry through the plane $\phi = \pi/2$ relating $\mathscr{S}_1$ on panel (c) and $\mathscr{S}_2$ on panel (d) reverses stability indices (cf. chapter 4).
To view these surfaces in rotation, click here (password: thesisPR) or scan the barcode.

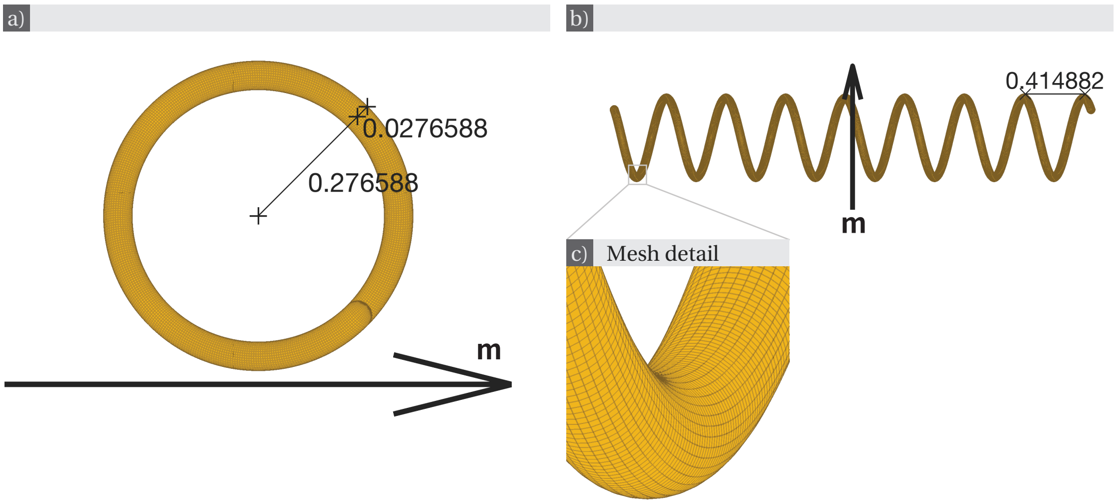

Figure 6.8 – **Swimmer C**. The mesh shows the discretisation used for numerical computation of the drag matrix $\mathbb{D}$. The magnetic moment $\mathbf{m}$ is in the plane of the paper.

Swimmer C (cf. fig. 6.8) is a a helical rod with a small rod radius compared to the helix radius and a larger number of turns than any other helical swimmers shown here: its centreline is a helix of 8 turns. The mobility matrix of swimmer C is

$$\mathbb{M}_C = \begin{bmatrix} 0.0715216 & 0 & 0 & -0.000522606 & 0 & 0 \\ 0 & 0.0714216 & -0.000937787 & 0 & 0.0000895093 & -0.00211724 \\ 0 & -0.000937787 & 0.0862869 & 0 & 0.000619434 & 0.00595169 \\ -0.000522606 & 0 & 0 & 0.0433569 & 0 & 0 \\ 0 & 0.0000895093 & 0.000619434 & 0 & 0.0434389 & -0.00636119 \\ 0 & -0.00211724 & 0.00595169 & 0 & -0.00636119 & 0.39126 \end{bmatrix},$$

where all components smaller than 10^{-15} in absolute value have been cut off to 0. It is computed as $\mathbb{M}_C = \frac{1}{2}\left(\mathbb{D}_C^{-1} + \mathbb{D}_C^{-T}\right)$ with $\mathbb{D}_C$ such that

$$\frac{\|\mathbb{D}_C - \mathbb{D}_C^T\|}{\|\mathbb{D}_C\|} = 3.7401 \cdot 10^{-5},$$

and its magnetic moment is

$$\mathbf{m}_C = \begin{bmatrix} 0.707107 \\ 0.707107 \\ 0 \end{bmatrix}.$$

The surface of relative equilibria for swimmer C (cf. fig. 6.9-6.10) looks very symmetric about the plane $\cos\psi = 0$, in accordance with the conjecture that this is the case for long helices. Accordingly, the parameter $c_{11} = 1.7737 \cdot 10^{-7}$, and $c_{11}/c_{12} = 5.0968 \cdot 10^{-7}$, so that the symmetry condition $c_{11} = 0$ is almost satisfied. Projection on the parameter plane in fig. 6.9a shows that the range of ψ for which there are equilibria when a is small is much more narrow than for swimmer A, B and B'. The surface comprises relative equilibria with parameters ranges $a \in (0, 0.3913]$ and $\cos\psi \in [-0.8006, 0.8005]$. These ranges are slightly narrower than those for swimmer B and B', but much wider than those of swimmer A.

Note that like swimmers B and B', the surface of relative equilibria for swimmer C shows curves of Hopf bifurcations close to extremal values of ψ. In the parameter plane on figure 6.9a, these curves seem to overlap with the other curves of Hopf bifurcations. The inner folds also appear to overlap with the outer folds. As a result, parameter regime 1/4 is almost but not quite nonexistent for swimmer C.

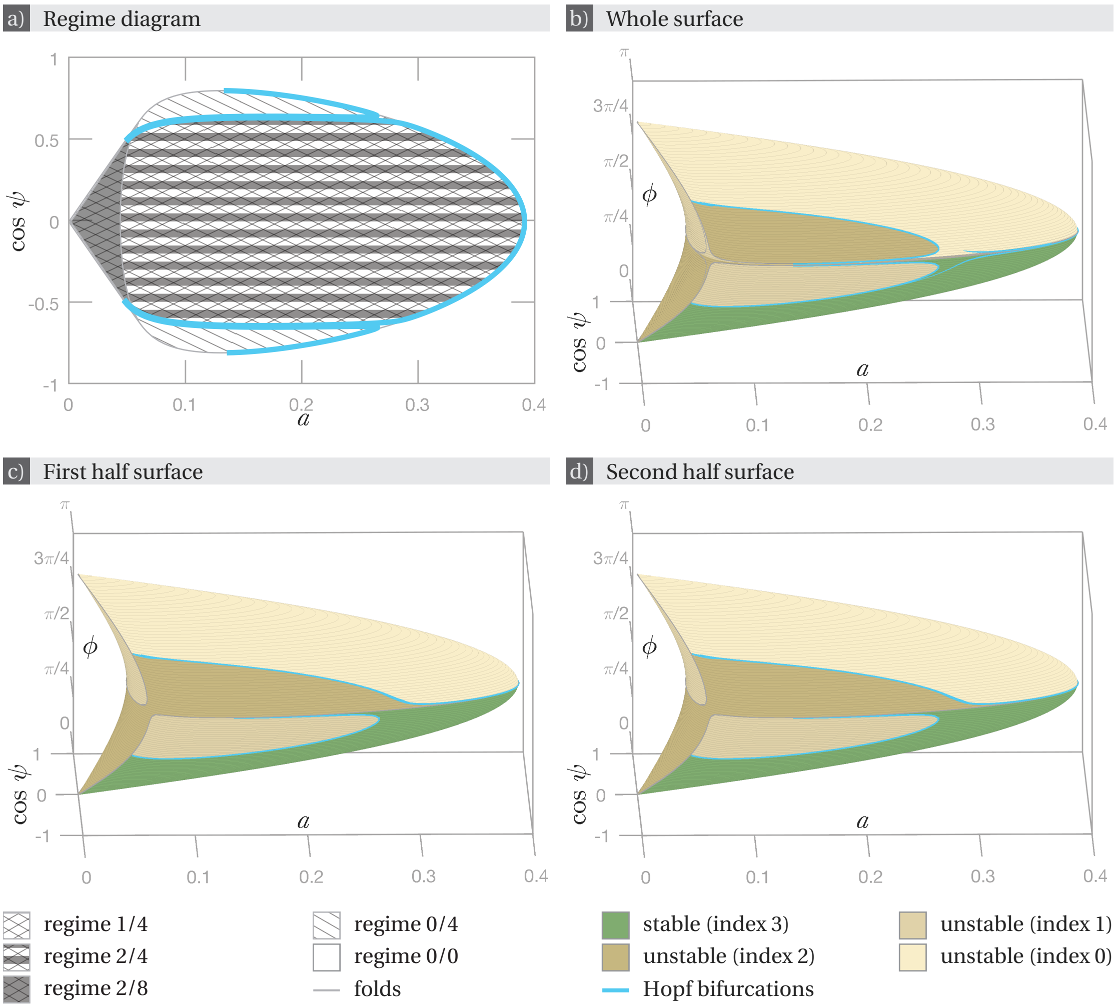

Figure 6.9 – **Swimmer C: surface of relative equilibria**: (a) Regime diagram. The different parameter regimes are separated by curves of bifurcations. There are no stable relative equilibria outside the cross-hatched region, which features one or two (in dark) stable relative equilibria. (b) Whole surface $\mathscr{S}$, (c) first half surface $\mathscr{S}_1$, and (d) second half surface $\mathscr{S}_2$ coloured by stability index. The mirror symmetry through the plane $\phi = \pi/2$ relating $\mathscr{S}_1$ on panel (c) and $\mathscr{S}_2$ on panel (d) reverses stability indices (cf. chapter 4).
To view these surfaces in rotation, click here (password: thesisPR) or scan the barcode.

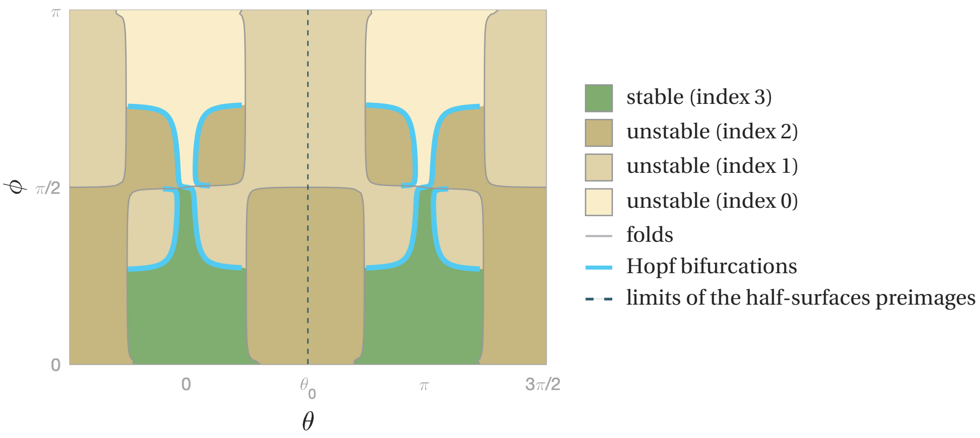

Figure 6.10 – **Swimmer C: pre-image of the relative equilibria mapping**. Each pair $(\theta,\phi) \in [\theta_0-\pi,\theta_0+\pi) \times [0,\pi]$ uniquely parametrises a relative equilibrium. The plane is coloured by stability index, and regions with different stability indices are separated by curves of bifurcations.

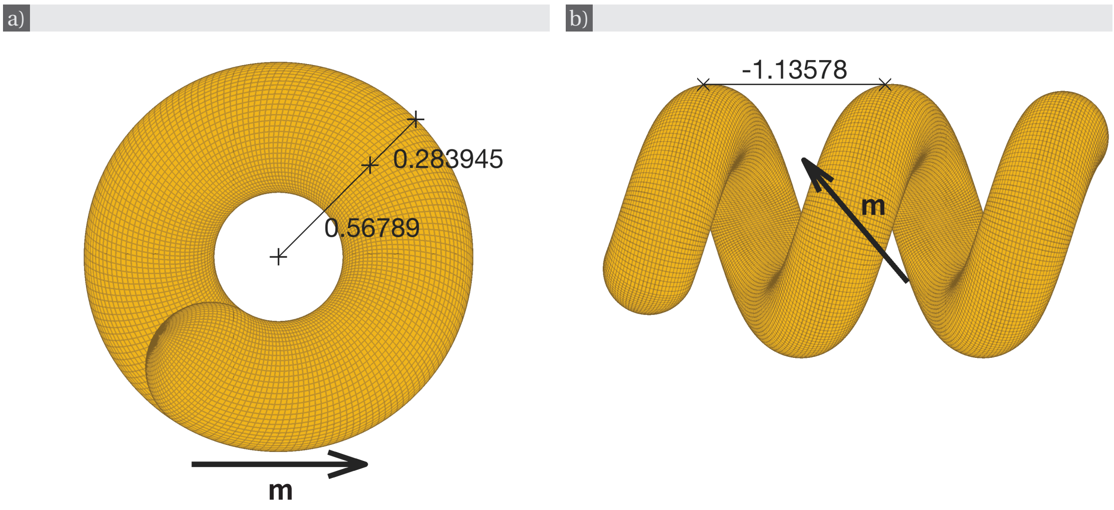

Figure 6.11 – **Swimmer D**. The mesh shows the discretisation used for numerical computation of the drag matrix $\mathbb{D}$. In panel (b) the magnetic moment **m** is in the plane of the paper.

Swimmer D (cf. fig. 6.11) has a large rod radius compared to the helix radius, and its helical centreline makes 2.2749 turns. The mobility matrix of swimmer D is

$$\mathbb{M}_D = \begin{bmatrix} 0.0477098 & -0.00023164 & -0.0000450358 & 0.000237019 & -0.0000624756 & 0.000649632 \\ -0.00023164 & 0.0476369 & 0.0000384992 & -0.0000624758 & 0.000217343 & -0.000555338 \\ -0.0000450358 & 0.0000384992 & 0.0514971 & -0.00114416 & 0.000978086 & -0.000997003 \\ 0.000237019 & -0.0000624758 & -0.00114416 & 0.0231344 & 0.000320644 & 0.000411059 \\ -0.0000624756 & 0.000217343 & 0.000978086 & 0.000320644 & 0.0232354 & -0.000351394 \\ 0.000649632 & -0.000555338 & -0.000997003 & 0.000411059 & -0.000351394 & 0.0422486 \end{bmatrix},$$

computed as $\mathbb{M}_D = \frac{1}{2}\left(\mathbb{D}_D^{-1} + \mathbb{D}_D^{-T}\right)$ with $\mathbb{D}_D$ such that

$$\frac{\|\mathbb{D}_D - \mathbb{D}_D^T\|}{\|\mathbb{D}_D\|} = 5.3478 \cdot 10^{-6}.$$

Its magnetic moment is

$$\mathbf{m}_D = \begin{bmatrix} -0.399589 \\ 0.648452 \\ 0.647949 \end{bmatrix}.$$

The surface of equilibria for swimmer D is shown in fig. 6.13. We can observe that as the Mason number a varies, the range of conical angles ψ for which there are relative equilibria stays approximately the same. Overall, relative equilibria have $\cos\psi \in [-0.2939, 0.2867]$ and $a \in (0, 0.0359]$.These are similar to the parameter ranges for swimmer A (cf. fig. 4.6). Like the surface of relative equilibria for swimmer A, figure 6.13 shows only one curve of Hopf bifurcations per half surface: curves close to extremal values of ψ displayed in figures 6.3, 6.7 and 6.9 for swimmers B, B' and C do not appear. As a result, regime 0/4 does not exist for swimmer D. The asymmetry of the surface about the plane $\cos\psi = 0$ is perceptible as for swimmer A, and indeed $c_{11}/c_{12} = -0.0032$ with $c_{11} = -3.5562 \cdot 10^{-5}$, so that even if c_{11} is very small, its relative weight in the parameterisation (4.5) is as important as for swimmer A.

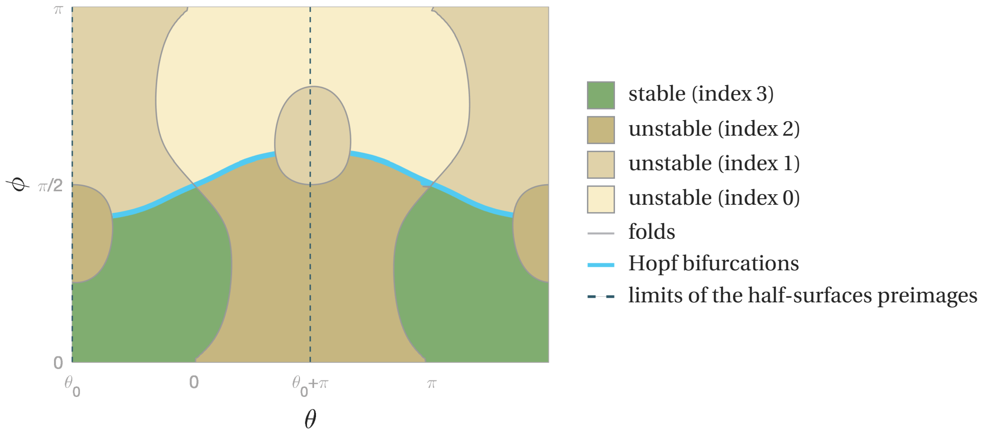

Figure 6.12 – **Swimmer D: pre-image of the relative equilibria mapping**. Each pair $(\theta, \phi) \in [\theta_0, \theta_0 + 2\pi) \times [0, \pi]$ uniquely parametrises a relative equilibrium. The plane is coloured by stability index, and regions with different stability indices are separated by curves of bifurcations.

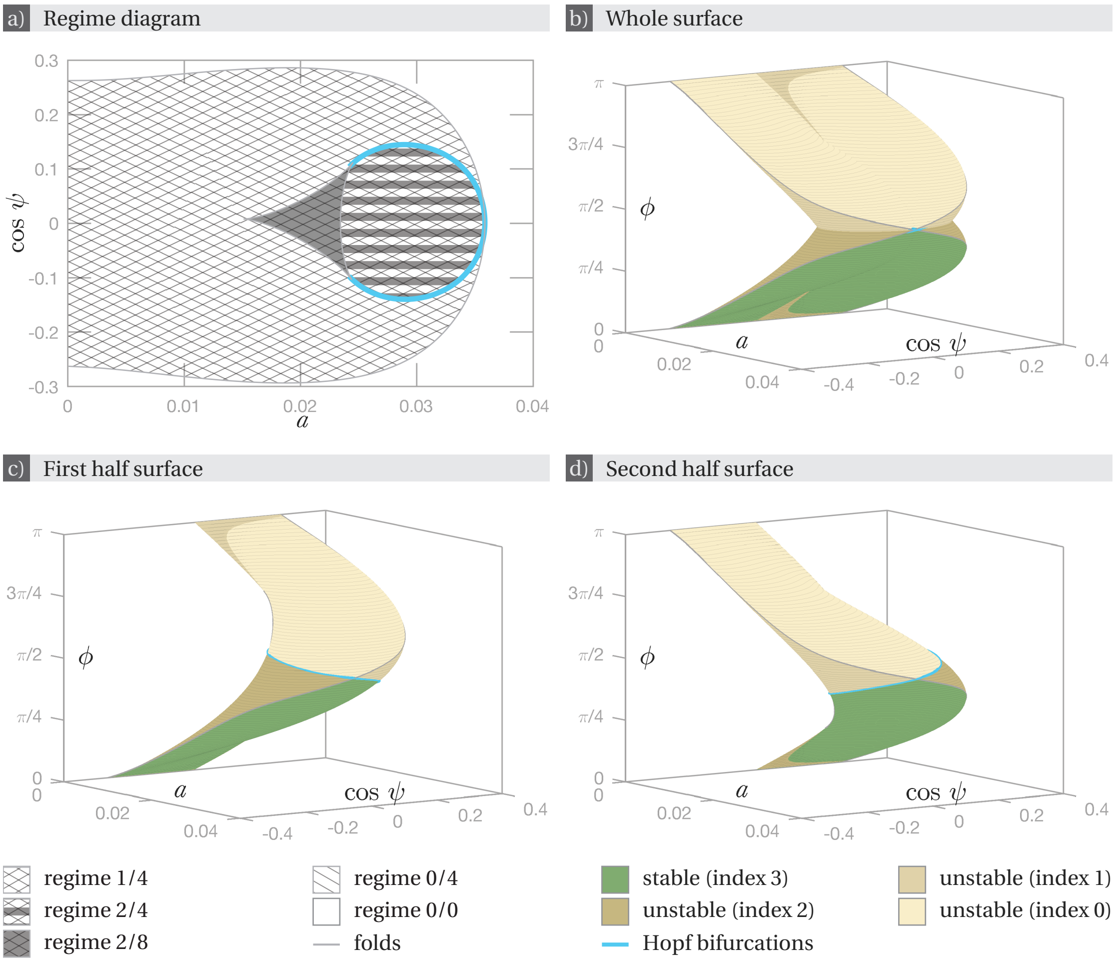

Figure 6.13 – **Swimmer D: surface of relative equilibria**. (a) Regime diagram. The different parameter regimes are separated by curves of bifurcations. There are no stable relative equilibria outside the cross-hatched region, which features one or two (in dark) stable relative equilibria. (b) Whole surface $\mathscr{S}$, (c) first half surface $\mathscr{S}_1$, and (d) second half surface $\mathscr{S}_2$ coloured by stability index. The mirror symmetry through the plane $\phi = \pi/2$ relating $\mathscr{S}_1$ on panel (c) and $\mathscr{S}_2$ on panel (d) reverses stability indices (cf. chapter 4).
To view these surfaces in rotation, click here (password: thesisPR) or scan the barcode.

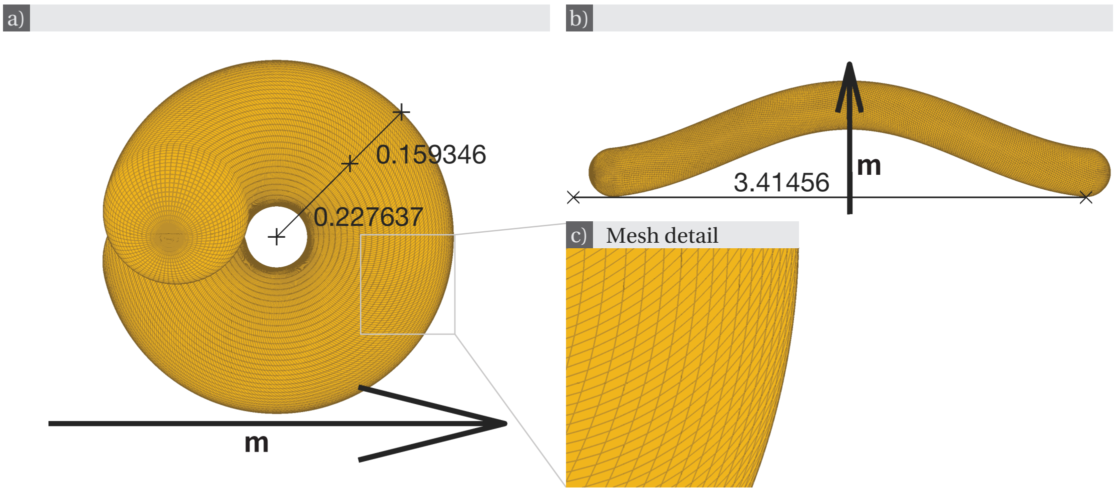

Figure 6.14 – **Swimmer E**. The mesh shows the discretisation used for numerical computation of the drag matrix $\mathbb{D}$. In panel (b) the magnetic moment $\mathbf{m}$ is in the plane of the paper.

The helical rod giving the shape of swimmer E (cf. fig. 6.14) makes approximately one full turn in total: its helical centreline makes exactly 0.9224 turns. It has a large rod radius compared to the helix radius and pitch. The mobility matrix of swimmer E is

$$\mathbb{M}_E = \begin{bmatrix} 0.0727139 & 0.0000379167 & -0.000390353 & -0.000658782 & 0.000450697 & -0.0034412 \\ 0.0000379167 & 0.0728568 & -0.00156832 & 0.000450696 & 0.0010398 & -0.0138257 \\ -0.000390353 & -0.00156832 & 0.0973941 & 0.00119352 & 0.0047952 & 0.0094237 \\ -0.000658782 & 0.000450696 & 0.00119352 & 0.0435315 & 0.00101378 & -0.0109227 \\ 0.000450697 & 0.0010398 & 0.0047952 & 0.00101378 & 0.0473522 & -0.0438842 \\ -0.0034412 & -0.0138257 & 0.0094237 & -0.0109227 & -0.0438842 & 0.461468 \end{bmatrix},$$

computed as $\mathbb{M}_E = \frac{1}{2}\left(\mathbb{D}_E^{-1} + \mathbb{D}_E^{-T}\right)$ with $\mathbb{D}_E$ such that

$$\frac{\|\mathbb{D}_E - \mathbb{D}_E^T\|}{\|\mathbb{D}_E\|} = 2.2614 \cdot 10^{-6},$$

and its magnetic moment is

$$\mathbf{m}_E = \begin{bmatrix} -0.97181 \\ 0.235758 \\ 0.00203479 \end{bmatrix}.$$

The surface of relative equilibria for swimmer E (cf. fig. 6.15-6.16) is qualitatively very similar to the one for swimmer C (cf. fig. 6.9). In particular, parameter regime 1/4 is almost nonexistent, as for swimmer C. Its parameter extents are $a \in (0, 0.4663]$ and $\cos\psi \in [-0.8321, 0.8320]$, which is slightly larger than the parameter extents for which swimmer C admits relative equilibria. The surface for swimmer E also looks symmetric about the plane $\cos\psi = 0$, and we have indeed $c_{11} = -7.0218 \cdot 10^{-9}$ and $c_{11}/c_{12} = -1.6576 \cdot 10^{-8}$ so that the symmetry condition $c_{11} = 0$ is almost satisfied.

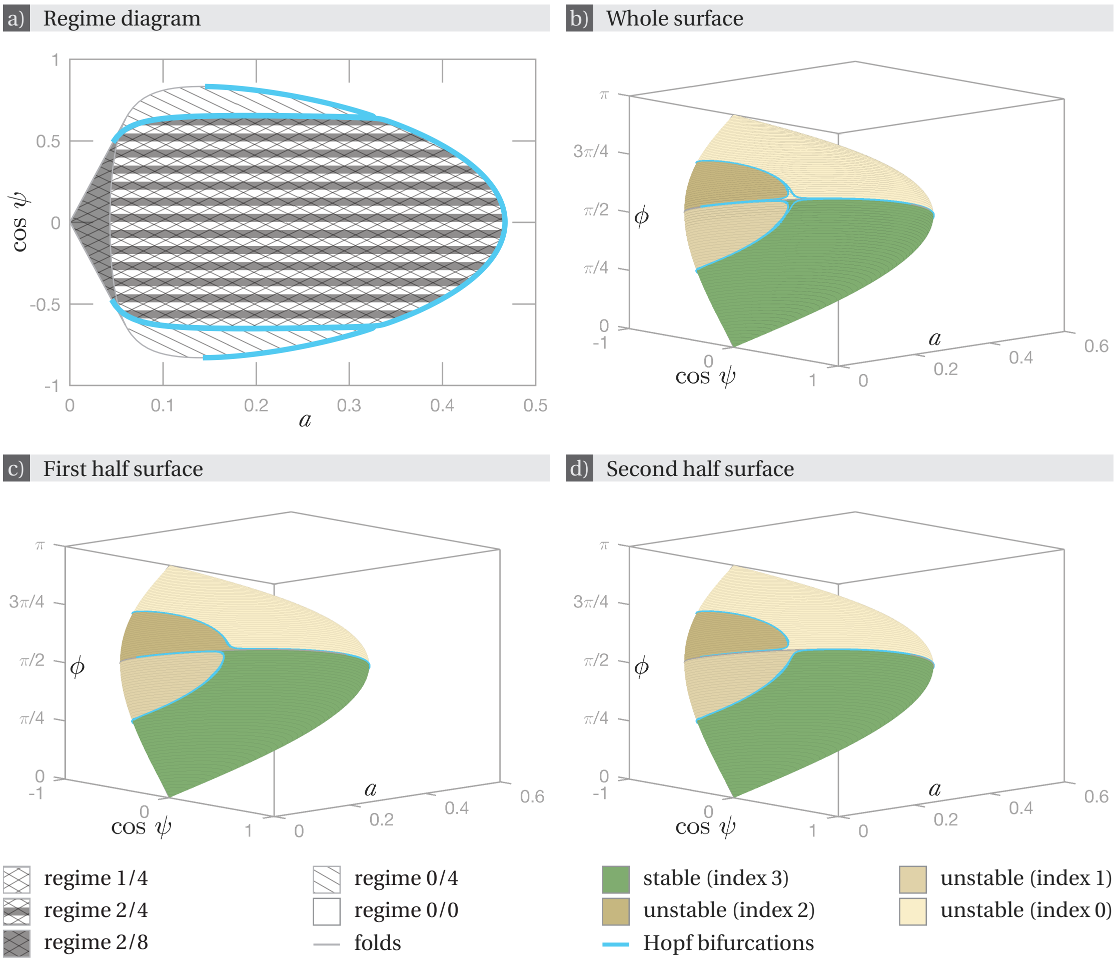

Figure 6.15 – **Swimmer E: surface of relative equilibria**. (a) Regime diagram. The different parameter regimes are separated by curves of bifurcations. There are no stable relative equilibria outside the cross-hatched region, which features one or two (in dark) stable relative equilibria. (b) Whole surface $\mathscr{S}$, (c) first half surface $\mathscr{S}_1$, and (d) second half surface $\mathscr{S}_2$ coloured by stability index. The mirror symmetry through the plane $\phi = \pi/2$ relating $\mathscr{S}_1$ on panel (c) and $\mathscr{S}_2$ on panel (d) reverses stability indices (cf. chapter 4).
To view these surfaces in rotation, click here (password: thesisPR) or scan the barcode.

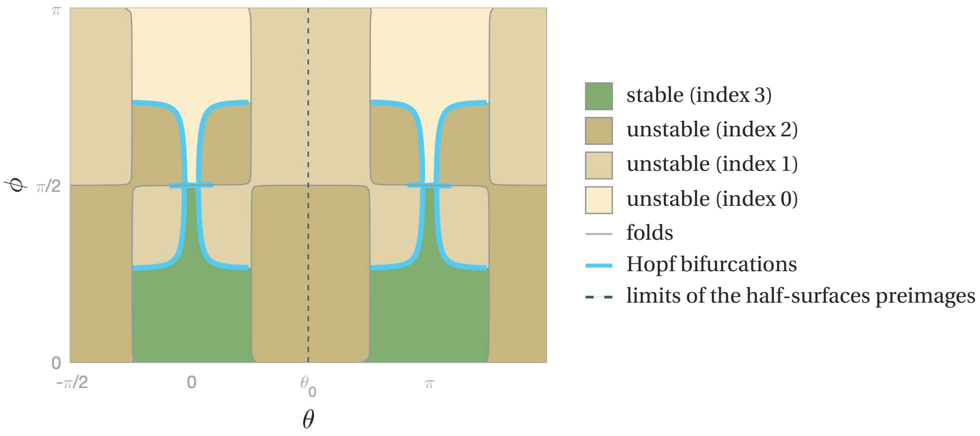

Figure 6.16 – **Swimmer E: pre-image of the relative equilibria mapping**. Each pair $(\theta, \phi) \in [\theta_0 - \pi, \theta_0 + \pi) \times [0, \pi]$ uniquely parametrises a relative equilibrium. The plane is coloured by stability index, and regions with different stability indices are separated by curves of bifurcations.

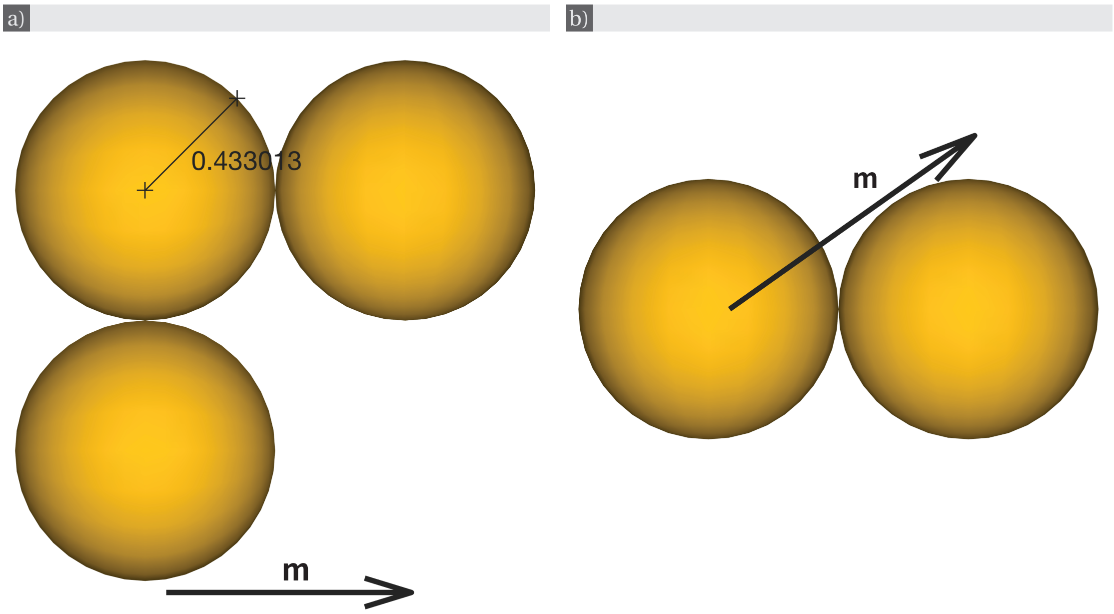

Figure 6.17 – **Swimmer F**, taken from [45, 86]. In panel (b) the magnetic moment **m** is in the plane of the paper.

Swimmer F (cf. fig. 6.17) is not a helical rod. It was taken from [45, 86]. The dimensional mobility matrix appearing in [45, 86] is given by

$$\mathbb{M}_{11} = \begin{bmatrix} 1.38 & 0 & 0 \\ 0 & 1.73 & 0 \\ 0 & 0 & 1.72 \end{bmatrix} \cdot 10^7 \, \frac{\mathrm{m}}{\mathrm{N \cdot s}}, \qquad \mathbb{M}_{12} = \begin{bmatrix} 0 & 0 & 0 \\ 0 & 0 & -1.16 \\ 0 & 1.94 & 0 \end{bmatrix} \cdot 10^{12} \, \frac{1}{\mathrm{N \cdot s}},$$

$$\mathbb{M}_{22} = \begin{bmatrix} 5.84 & 0 & 0 \\ 0 & 8.96 & 0 \\ 0 & 0 & 5.11 \end{bmatrix} \cdot 10^{17} \, \frac{1}{\mathrm{N \cdot s \cdot m}}.$$

Before using it here, it was scaled and non-dimensionalised according to (2.22) (cf. section 2.2), assuming that the fluid viscosity is $\eta = 10^{-3}$ Pa·s and that the characteristic length ℓ is the gyration radius, computed to be 10.05 µm. The mobility matrix was also recentred on the centre of mass $\boldsymbol{c}_m$ using [20]

$$\mathbb{M} = \begin{bmatrix} \mathbf{I} & \mathbf{0} \\ [\boldsymbol{c}_m \times]^T & \mathbf{I} \end{bmatrix} \mathbb{M}_0 \begin{bmatrix} \mathbf{I} & [\boldsymbol{c}_m \times] \\ \mathbf{0} & \mathbf{I} \end{bmatrix},$$

where $\mathbb{M}_0$ is the original mobility matrix about the origin in the lab frame. The non-dimensional mobility matrix of swimmer F is then

$$\mathbb{M}_F = \begin{bmatrix} 0.138633 & 0 & 0 & 0 & 0 & 0 \\ 0 & 0.164554 & 0 & 0 & 0 & 0.0944332 \\ 0 & 0 & 0.164331 & 0 & -0.175065 & 0 \\ 0 & 0 & 0 & 0.592078 & 0 & 0 \\ 0 & 0 & -0.175065 & 0 & 0.908393 & 0 \\ 0 & 0.0944332 & 0 & 0 & 0 & 0.518068 \end{bmatrix}$$

and its magnetic moment is

$$\mathbf{m}_F = \begin{bmatrix} 0.57735 \\ 0.57735 \\ 0.57735 \end{bmatrix} .$$

The asymmetry of the surface of relative equilibria about the plane $\cos\psi = 0$ is more obvious for swimmer F on fig. 6.18 than for any of the helical swimmers (cf. also fig. 6.19). We

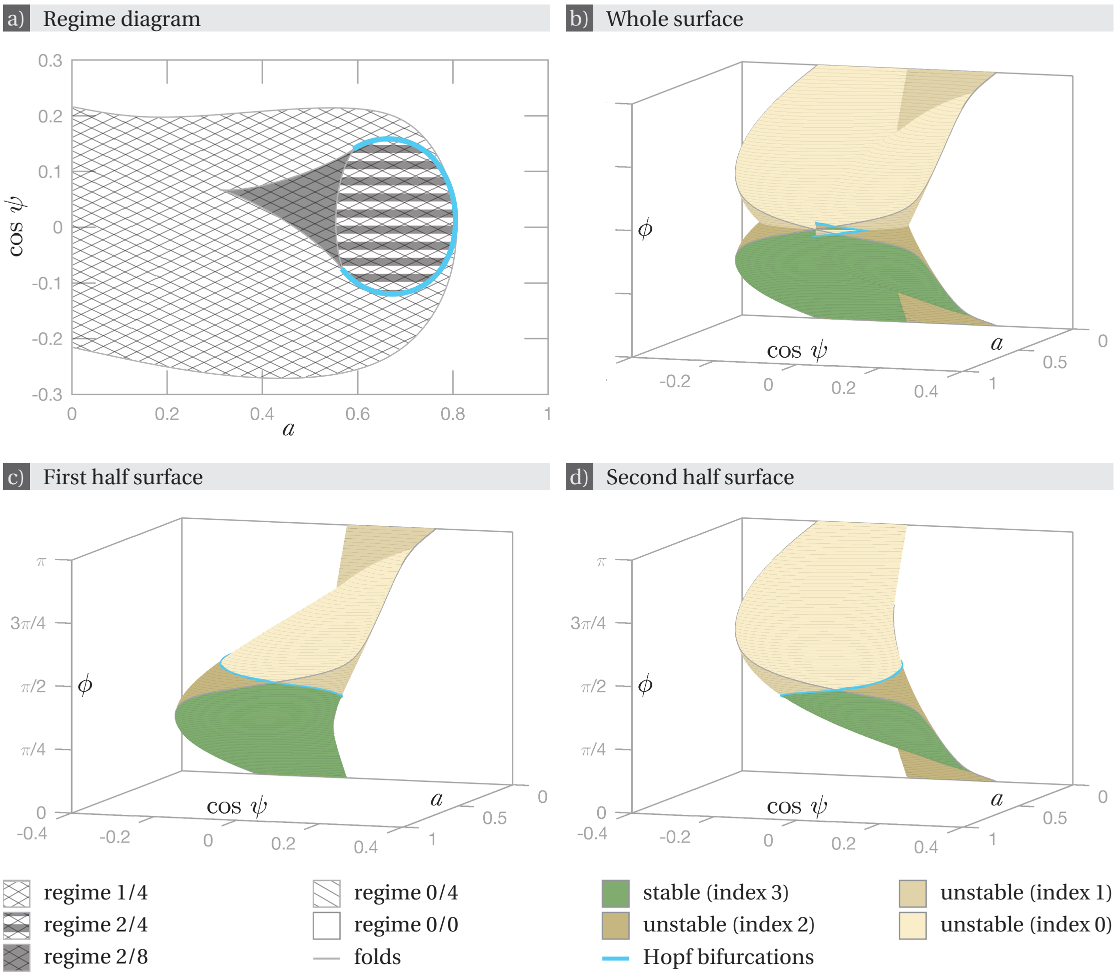
a) Regime diagram

b) Whole surface

c) First half surface

d) Second half surface

Figure 6.18 – **Swimmer F: surface of relative equilibria**. (a) Regime diagram. The different parameter regimes are separated by curves of bifurcations. There are no stable relative equilibria outside the cross-hatched region, which features one or two (in dark) stable relative equilibria. (b) Whole surface $\mathscr{S}$, (c) first half surface $\mathscr{S}_1$, and (d) second half surface $\mathscr{S}_2$ coloured by stability index. The mirror symmetry through the plane $\phi = \pi/2$ relating $\mathscr{S}_1$ on panel (c) and $\mathscr{S}_2$ on panel (d) reverses stability indices (cf. chapter 4).
To view these surfaces in rotation, click here (password: thesisPR) or scan the barcode.

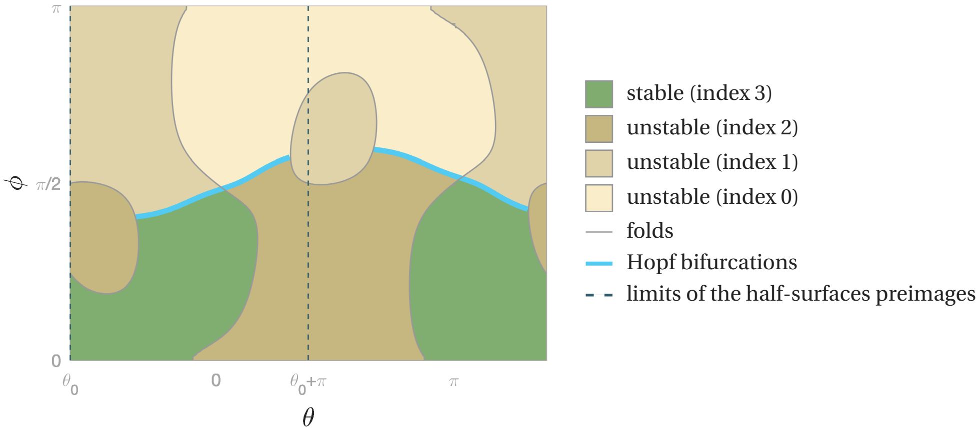

Figure 6.19 – **Swimmer F: pre-image of the relative equilibria mapping**. Each pair $(\theta,\phi) \in [\theta_0, \theta_0 + 2\pi) \times [0,\pi]$ uniquely parametrises a relative equilibrium. The plane is coloured by stability index, and regions with different stability indices are separated by curves of bifurcations.

have indeed that $c_{11} = -0.0051$, i.e. it is of a larger magnitude than for any of the helical swimmers, and $c_{11}/c_{12} = -0.0213$, so that the relative weight of c_{11} in the parametrisation (4.5) is also larger than for any of the helical swimmers. There are no curves of Hopf bifurcations in the wings, as for swimmers A (cf. fig. 4.6) and D (cf. fig. 6.13). The maximal Mason number for which there are relative equilibria is $a = 0.8092$, which is slightly smaller than for swimmers B and B' but larger than all other swimmers. The conical angles in the surface satisfy $\cos\psi \in [-0.2714, 0.2162]$, which is quite narrow, as for swimmers A and D.

6.2 Parameter Regimes and Phase Portraits

In chapter 4, phase portraits representing the rotational dynamics of swimmer A by means of quaternions for parameter regimes 1/4 (fig. 4.11), 2/4 (fig. 4.13) and 2/8 (fig. 4.12) were shown. To supplement these, phase portraits representing the dynamics of swimmers B (fig. 6.20-6.22), C (fig. 6.24-6.25), D (fig. 6.26-6.27), E (fig. 6.29-6.30) and F (fig. 6.31-6.32) are displayed in this section.

As a reminder, in these phase portraits, unit quaternions representing the orientation of a swimmer are represented by their vector part in the three-dimensional unit ball (cf. section 4.3.1). Since q and $-q$ parametrise the same rotation, representing the set of unit quaternions with a positive scalar part (i.e. $q_0 \geq 0$) is sufficient. Recall that antipodal points on the outer unit sphere represent the same rotation. Accordingly, in this representation, continuous trajectories may jump to the other side of the sphere. Note that the quaternions displayed were all multiplied on the left by the same unit quaternion that was chosen so as to reduce the number of such antipodal jumps – this operation corresponds to a change of basis of the body frame. These three-dimensional phase portraits are difficult to visualise on a two dimensional sheet of paper. In addition to the figures in this section, a video linked in the caption shows them

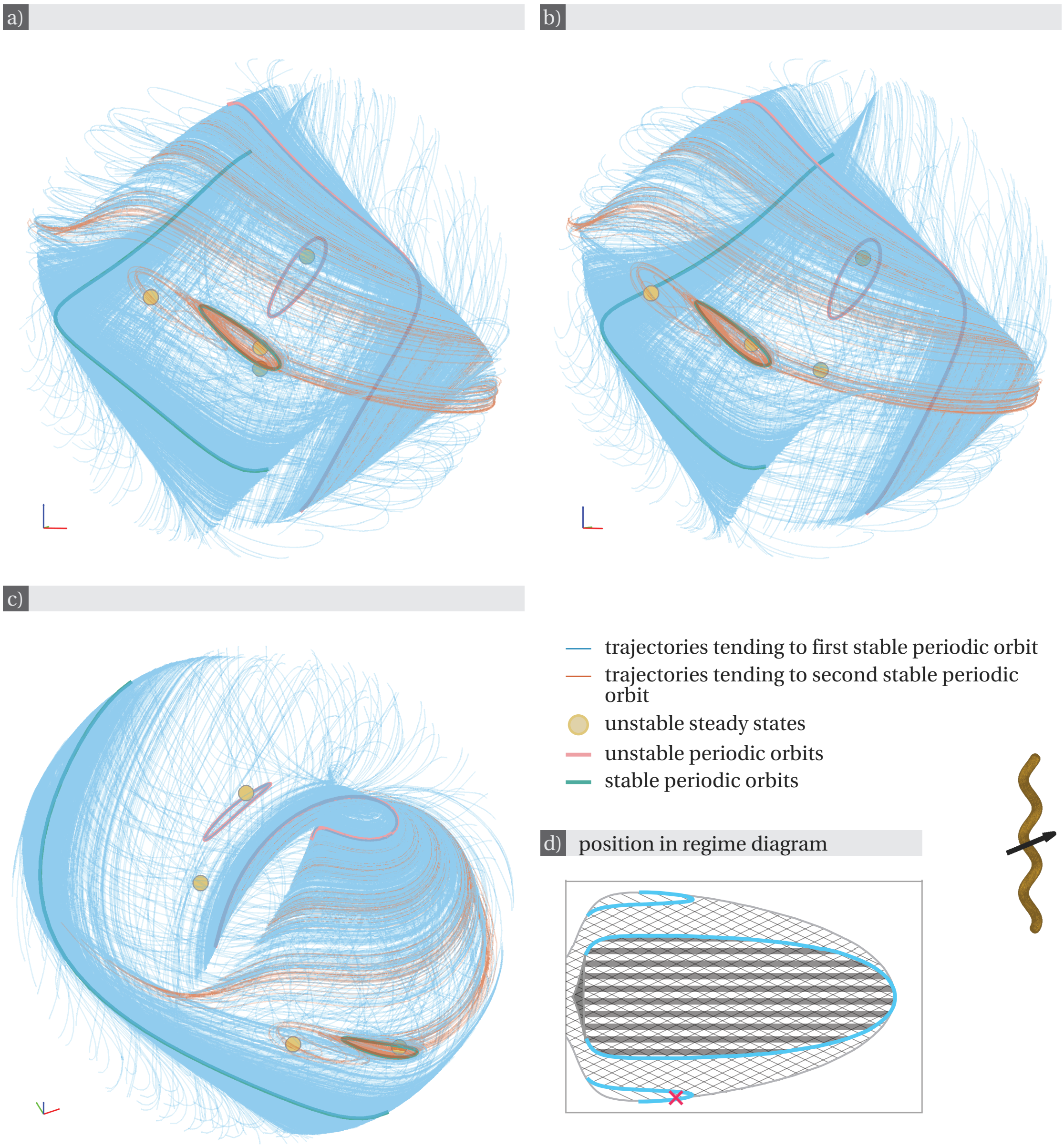

Figure 6.20 – **Swimmer B: phase portrait of the rotational dynamics in parameter regime 0/4**. Phase portrait of the dynamical system (3.14), which describes the rotational dynamics by means of quaternions (cf. section 4.3.2), for parameter values $a = 0.316$ and $\cos\psi = -0.8544$ (cf. the cross on panel (d)). Note the presence of two stable periodic orbits. The small one is on a foil of periodic orbits obtained by continuation starting from Hopf bifurcations (cf. fig. 4.10), and the large one is on a foil obtained by continuation starting from periodic orbits found by direct numerical integration.
Panels (a-c) show the same object under different angles. To view it in rotation, click here (password: thesisPR) or scan the barcode.

being rotated.

The phase portraits were obtained by direct numerical integration of (3.14) with a sampling of the possible initial conditions, using the standard integrator ode45 in MATLAB with absolute tolerance set to 10^{-8} and relative tolerance to 10^{-6} [87]. The sampling of initial conditions is done by first generating random unit quaternions with a positive scalar part, and then iteratively correcting their position to make their distribution within the half hypersphere more uniform. Starting from these initial conditions, the numerical integration is terminated either if it reaches a maximal time, or if $|\dot{q}| < 10^{-10}$, or if $\left|1-|q|^2\right| > 10^{-2}$. The observed solutions all converge either towards stable steady states or towards stable periodic solutions depending on the parameters a,ψ, and initial conditions. To ensure that this is the case, the maximal step size (MaxStep) and maximal integration time (MaxTime) were chosen on a case-by-case basis: for figures 4.11-4.13 MaxStep = $1/a$ and MaxTime = $10^3/a$; for figure 6.20 MaxStep = $10/a$ and MaxTime = $10^4/a$; for figure 6.21 MaxStep = $10^2/a$ and MaxTime = $10^5/a$; for figure 6.22 MaxStep = $10/a$ and MaxTime = $10^4/a$; for figure 6.23 MaxStep = $1/a$ and MaxTime = $10^4/a$; for figures 6.24-6.28 MaxStep = $1/a$ and MaxTime = $10^3/a$; for figure 6.29 MaxStep = $10^{-3}/a$ and MaxTime = $5 \cdot 10^4/a$; for figure 6.30 MaxStep = $10^{-3}/a$ and MaxTime = $10^2/a$; and for figures 6.31 and 6.32 MaxStep = $10^{-2}/a$ and MaxTime = $10^3/a$.

The steady states are completely classified in chapter 4. Numerical continuation starting from Hopf bifurcations on the set of steady states results in foils[1] of periodic orbits (cf. section 4.3.1). Only curves of Hopf bifurcations staying away from parameter values with $\psi = \pi/2$ (Hopf curves in the “wings” of the surface) were observed to give rise to foils comprising stable periodic orbits; such curves exist for swimmers B (cf. fig. 6.3), B’ (cf. fig. 6.7), C (cf. fig. 6.9), and E (cf. fig. 6.15).

Periodic solutions for parameters a and ψ for which there are no stable relative equilibria were explored by numerical continuation (MatCont [83]) starting from periodic solutions (that were obtained by direct numerical integration). More specifically: for each swimmer, a periodic orbit was found using the standard MATLAB integrator ode45 [87] with default parameters for arbitrary parameters outside the region featuring relative equilibria – for swimmer A: $a = 0.1$ and $\cos\psi = 0.1$; for swimmer B: $a = 1.5608$ and $\cos\psi = 0.8$; for swimmer B’: $a = 5$ and $\cos\psi = 0.5$; for swimmer C: $a = 0.5$ and $\cos\psi = 0.5$; for swimmer D: $a = 0.5$ and $\cos\psi = -0.8$; for swimmer E: $a = 0.6$ and $\cos\psi = 0.8$; for swimmer F: $a = 1$ and $\cos\psi = 0.5$. Then MatCont was used to obtain a branch of periodic orbit with fixed value of a and $\cos\psi \in [-1,1]$. To obtain this branch, the minimal step size was set to $10^{-6} \cdot \max\{\text{eigenvalue of } \mathsf{M}_{22}\}$ and the initial amplitude to 10^{-2}. Default values were kept for all the other MatCont parameters [84].

From this branch of periodic orbits obtained for a fixed value of a and $\cos\psi \in [-1,1]$, MatCont was used again to obtain branches of periodic orbits at fixed values of ψ letting a vary. Seventy points distributed uniformly along the first branch were used as the starting point, and

---

[1] Remember that each point in a curve of Hopf bifurcation gives rise to a branch of periodic orbit. We chose the term foil to name the two-dimensional set of periodic orbits formed by the union of branches arising from all Hopf bifurcations on the same curve.

numerical continuation was performed letting a both increase and decrease while ψ was kept fixed. The default MatCont options [84] were modified as follows: MinStepsize = 10^{-7}, FunTolerance = 10^{-12}, VarTolerance = 10^{-12}, and TestTolerance = 10^{-11}. Foils of periodic orbits are recovered by interpolation of these seventy branches. This procedure allowed to find connected foils of periodic orbits seemingly covering the entire parameter plane except for part of the region where stable steady states exist.

For the examples considered, two distinct foils of periodic orbits were actually found, both spanning most of the parameter plane; they are related to each other through the symmetry of system (3.7) under transformation $Q(t) \mapsto Q(-t)\,R_2(\pi)$ (cf. section 3.3). These sets intersect along a line seemingly close to $\psi = \pi/2$ corresponding to a stability exchange. One of them contains stable periodic solutions only on one side of the intersection line, and the other one only on the other side. Several other bifurcations corresponding to stability exchanges occur on these sets, notably fold bifurcations of periodic orbits resulting in regions where two distinct stable periodic solutions coexist. As already mentioned, loss of stability also occurs along some branches of periodic solutions as they approach a region with stable steady states, although the type of bifurcation was not identified. It is noteworthy that not all branches lose stability as they enter this region. In particular, stable periodic orbit may coexist with stable steady states, as shown in figures 6.21 and 6.29.

Regime 1/4, with four equilibria, one of which is stable, is represented in figures 6.21, and 6.26. This is the only observed regime for which there is a unique steady state. In figure 6.21, there is also a stable periodic orbit, and its basin of attraction looks larger than the basin of attraction of the steady state. In figure 6.26, all solutions computed by numerical integration reach the stable steady state after some time, suggesting that it is globally attractive.

Regime 2/4 is exemplified in figures 6.22, 6.23, 6.27, and 6.29. In figures 6.23 and 6.27, the basins of attraction of the two stable steady states appear to have similar sizes. In figure 6.22, one of the stable steady states attracts a majority of the trajectories. In figure 6.29, there is a stable periodic orbit in addition to the stable steady states and most solutions tend towards it. Unstable periodic orbits obtained by numerical parameter continuation from Hopf bifurcations are present in all figures. In figure 6.23, we can also observe unstable periodic orbits obtained by numerical continuation of stable periodic orbits obtained by direct numerical integration of equation (3.14) for parameter values in regime 0/0. Such unstable periodic orbits might also exist for the dynamics shown in 6.22 and 6.27: their absence in the figures could be due to the fact that numerical continuation did not reach the corresponding parameter values.

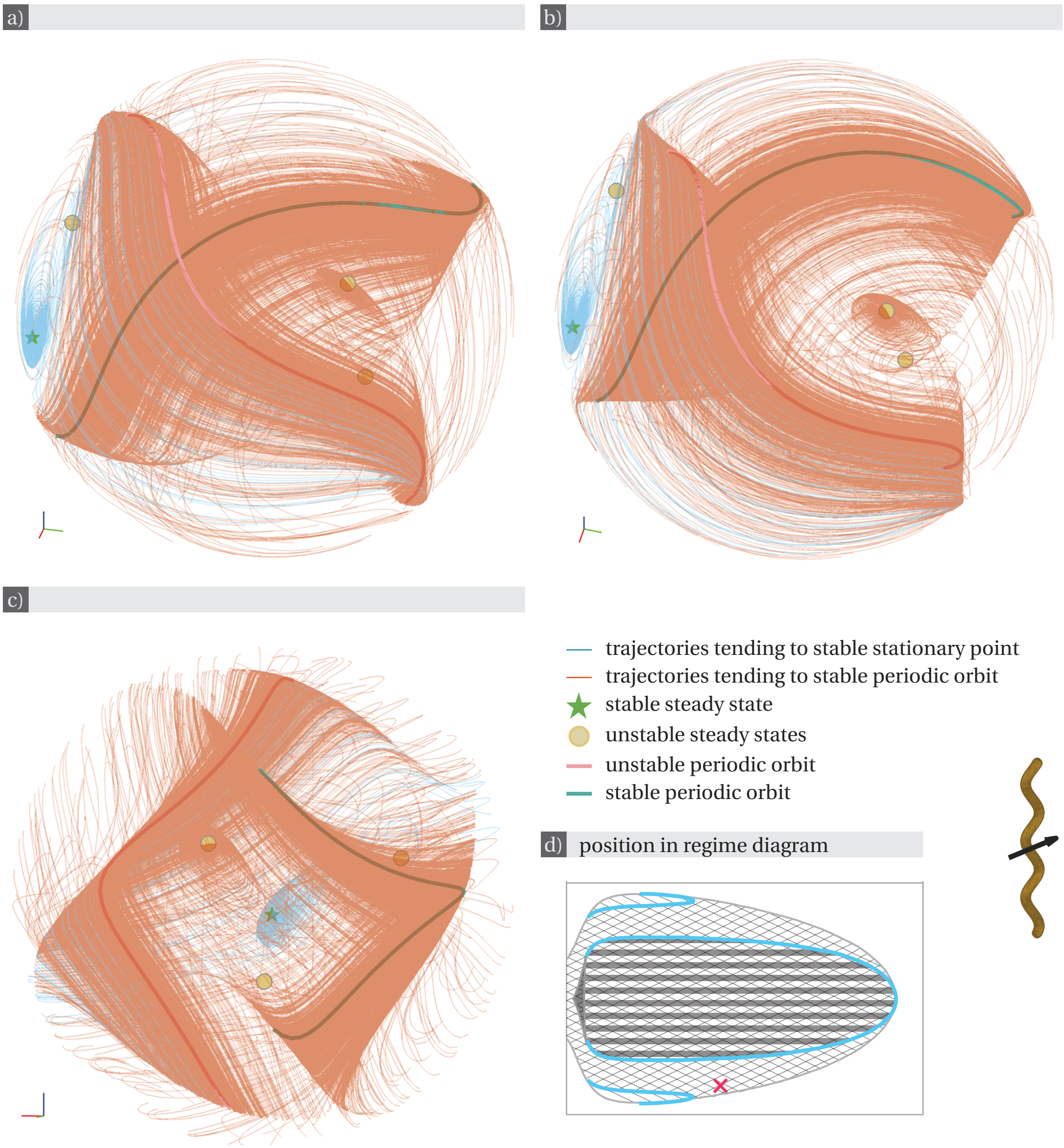

Figure 6.21 – **Swimmer B: phase portrait of the rotational dynamics in parameter regime 1/4**. Phase portrait of the dynamical system (3.14), which describes the rotational dynamics by means of quaternions (cf. section 4.3.2), for parameter values $a = 0.4362$ and $\cos\psi = -0.7577$ (cf. the cross on panel (d)). Note the presence of a stable periodic orbit that appears to attract most trajectories. It belongs to a foil of periodic orbits obtained by continuation starting from periodic orbits found by direct numerical integration.

Panels (a-c) show the same object under different angles. To view it in rotation, click here (password: thesisPR) or scan the barcode.

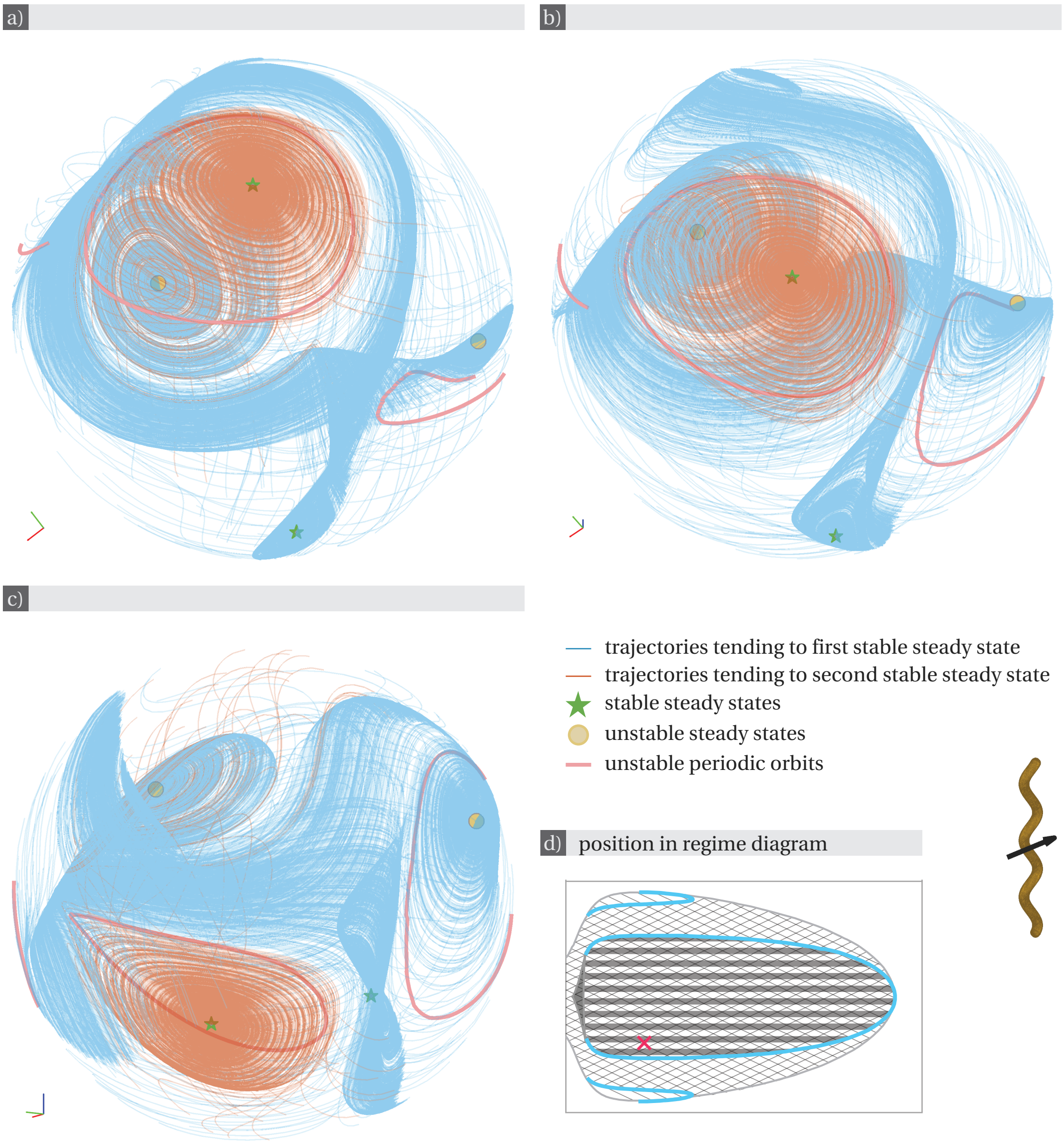

Figure 6.22 – **Swimmer B: phase portrait of the rotational dynamics in parameter regime 2/4**. Phase portrait of the dynamical system (3.14), which describes the rotational dynamics by means of quaternions (cf. section 4.3.2), for parameter values $a = 0.2198$ and $\cos\psi = -0.3989$ (cf. the cross on panel (d)).
The two unstable periodic orbits are on a foil of periodic orbits obtained by continuation starting from Hopf bifurcations (cf. fig. 4.10).
Panels (a-c) show the same object under different angles. To view it in rotation, click here (password: thesisPR) or scan the barcode.

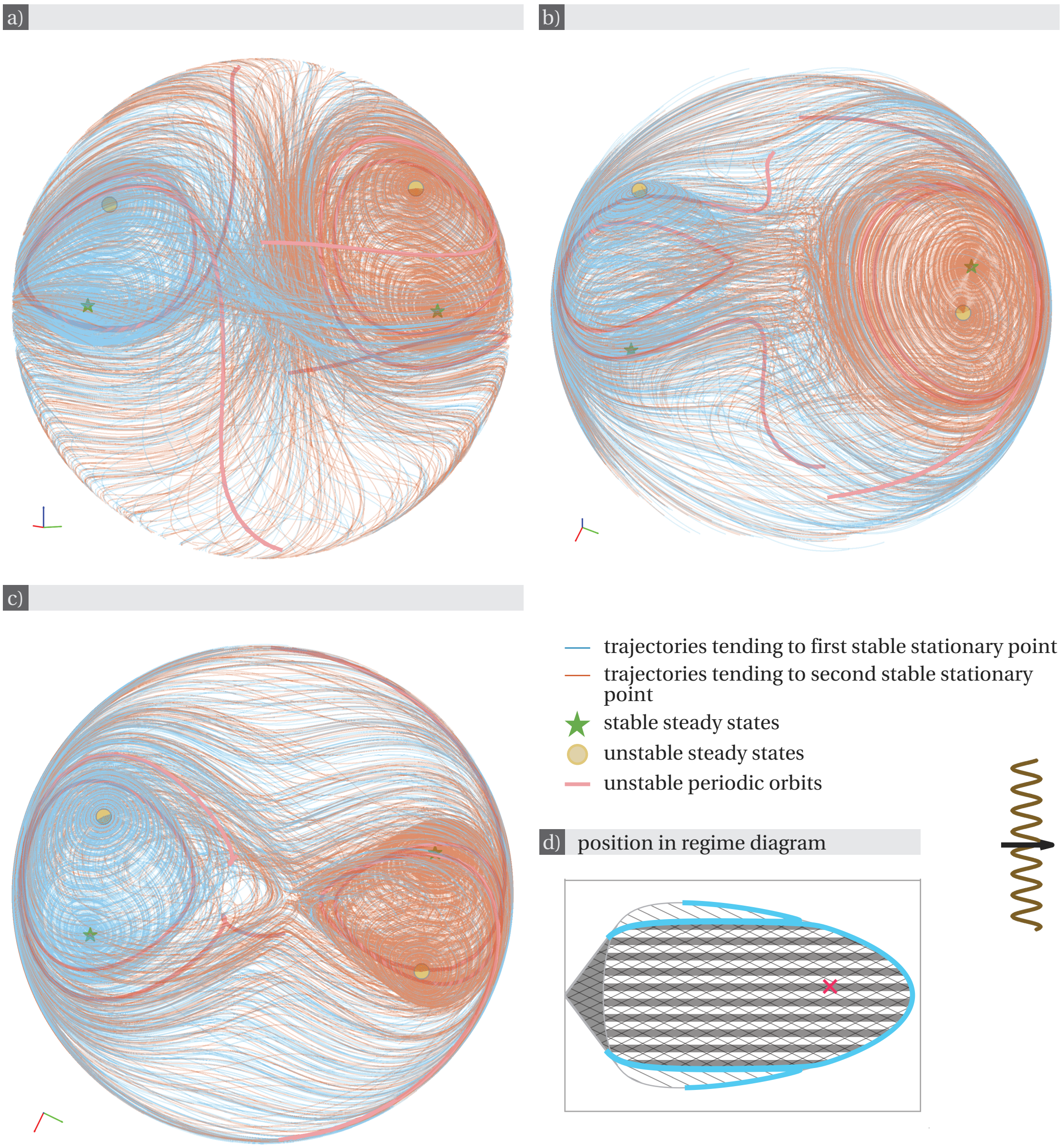

Figure 6.23 – **Swimmer C: phase portrait of the rotational dynamics in parameter regime 2/4**. Phase portrait of the dynamical system (3.14), which describes the rotational dynamics by means of quaternions (cf. section 4.3.2), for parameter values $a = 0.3$ and $\cos\psi = 0.1$ (cf. the cross on panel (d)). Note the presence of four unstable periodic orbits. The two smaller ones belong to foils of periodic orbits obtained by continuation starting from Hopf bifurcations, whereas the two larger ones are on foils obtained by continuation starting from periodic orbits found by direct numerical integration.
Panels (a-c) show the same object under different angles. To view it in rotation, click here (password: thesisPR) or scan the barcode.

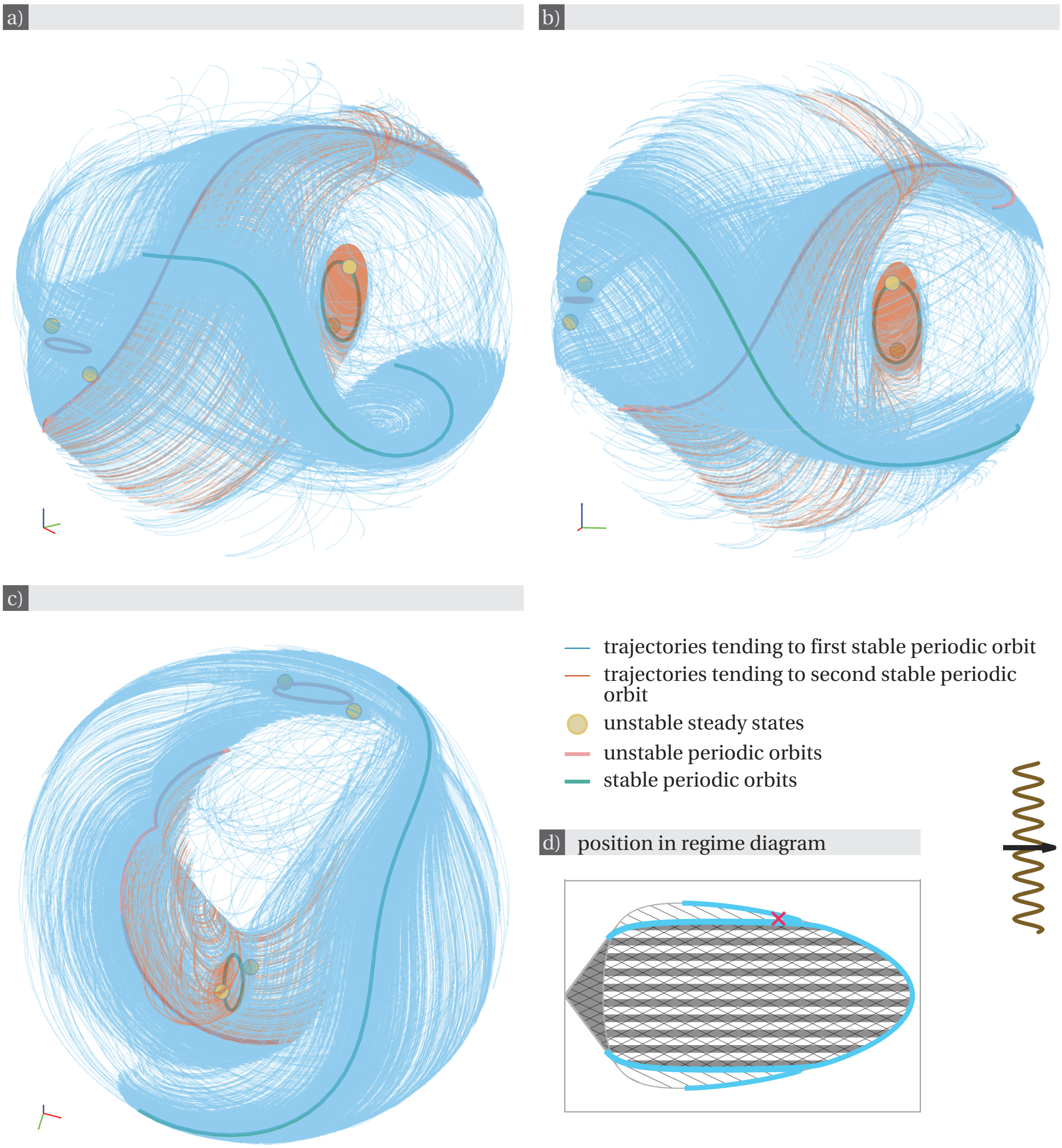

Figure 6.24 – **Swimmer C: phase portrait of the rotational dynamics in parameter regime 0/4**. Phase portrait of the dynamical system (3.14), which describes the rotational dynamics by means of quaternions (cf. section 4.3.2), for parameter values $a = 0.2399$ and $\cos\psi = 0.6709$ (cf. the cross on panel (d)). Note the presence of two stable periodic orbits. The small one belongs to a foil of periodic orbits obtained by continuation starting from Hopf bifurcations, and the large one is on a foil obtained by continuation starting from periodic orbits found by direct numerical integration.
Panels (a-c) show the same object under different angles. To view it in rotation, click here (password: thesisPR) or scan the barcode.

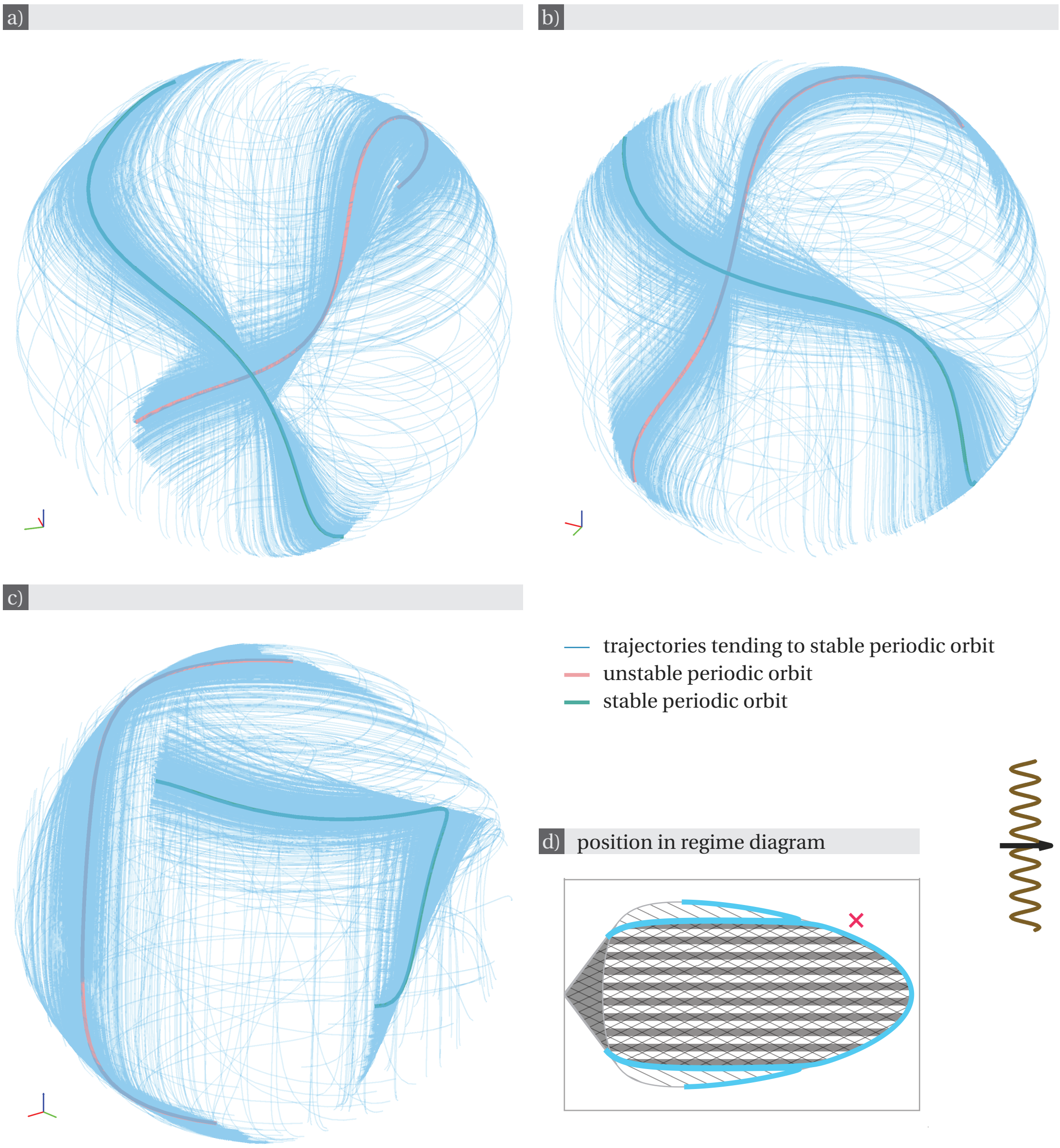

Figure 6.25 – **Swimmer C: phase portrait of the rotational dynamics in parameter regime 0/0**. Phase portrait of the dynamical system (3.14), which describes the rotational dynamics by means of quaternions (cf. section 4.3.2), for parameter values $a = 0.3299$ and $\cos\psi = 0.6515$ (cf. the cross on panel (d)). All trajectories exhibit the same asymptotic behaviour: they tend to a stable periodic orbit, which belongs to a foil of periodic orbit obtained by continuation starting from periodic orbits found by direct numerical integration.
Panels (a-c) show the same object under different angles. To view it in rotation, click here (password: thesisPR) or scan the barcode.

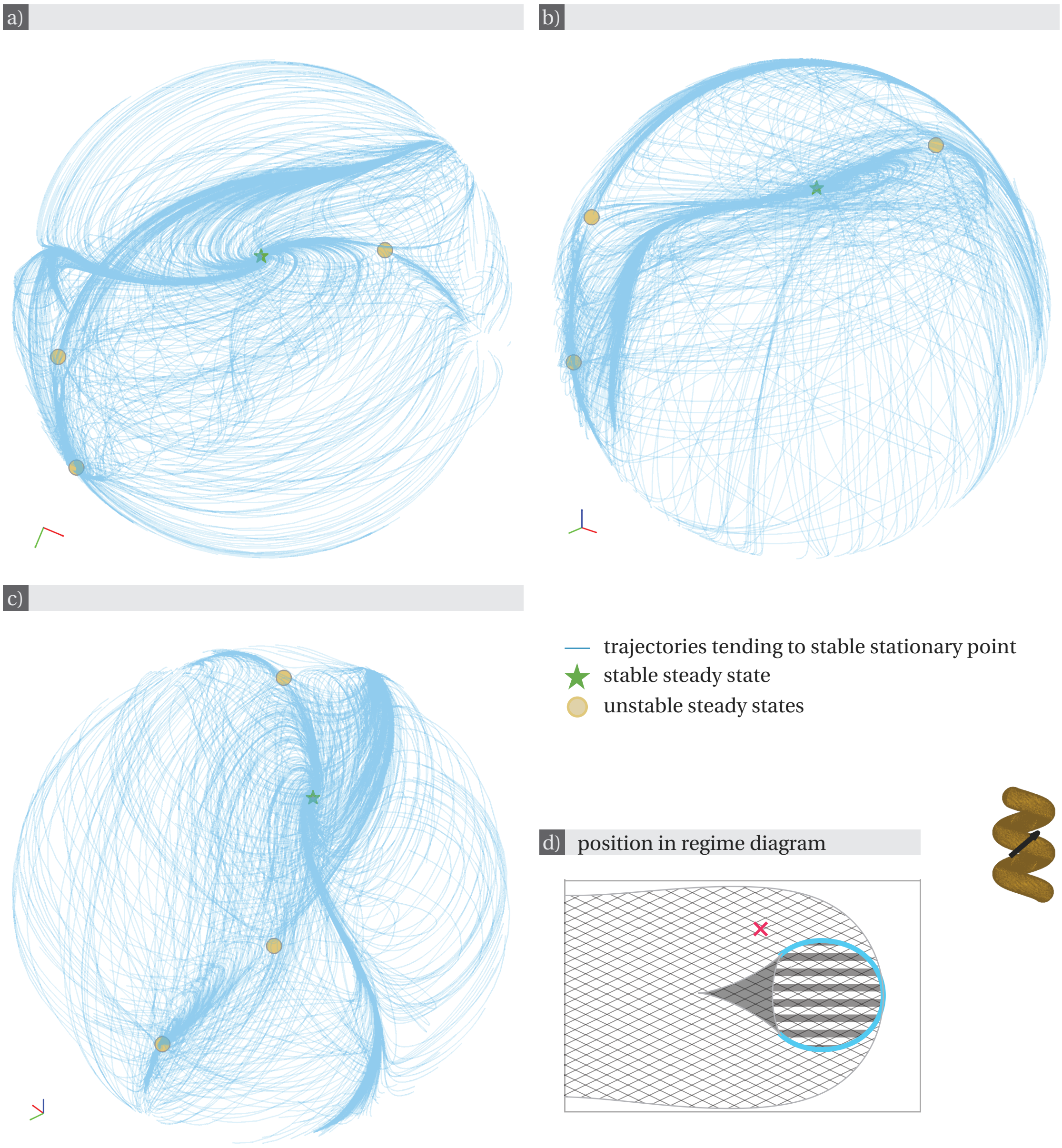

Figure 6.26 – **Swimmer D: phase portrait of the rotational dynamics in parameter regime 1/4**. Phase portrait of the dynamical system (3.14), which describes the rotational dynamics by means of quaternions (cf. section 4.3.2), for parameter values $a = 0.0220$ and $\cos\psi = 0.1730$ (cf. the cross on panel (d)). All trajectories tend to the unique stable steady state.
Panels (a-c) show the same object under different angles. To view it in rotation, click here (password: thesisPR) or scan the barcode.

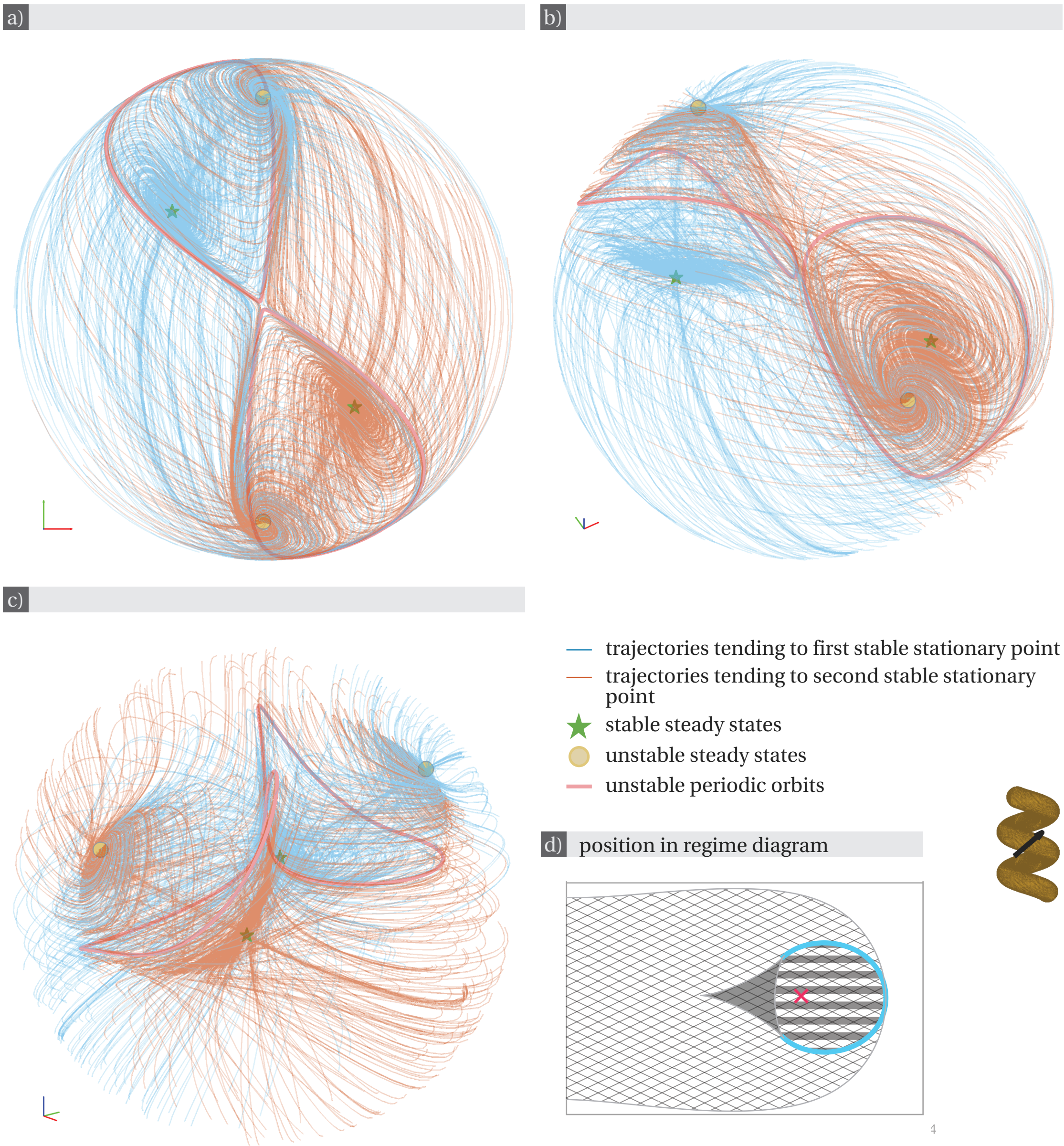

Figure 6.27 – **Swimmer D: phase portrait of the rotational dynamics in parameter regime 2/4**. Phase portrait of the dynamical system (3.14), which describes the rotational dynamics by means of quaternions (cf. section 4.3.2), for parameter values $a = 0.0263$ and $\cos\psi = 0.0076$ (cf. the cross on panel (d)). The basins of attraction of both stable steady states appear to have similar sizes. Note the presence of two unstable periodic orbits, which seem to belong to the boundary between the two basins of attraction. They lie on foils of periodic orbits obtained by continuation starting from Hopf bifurcations.
Panels (a-c) show the same object under different angles. To view it in rotation, click here (password: thesisPR) or scan the barcode.

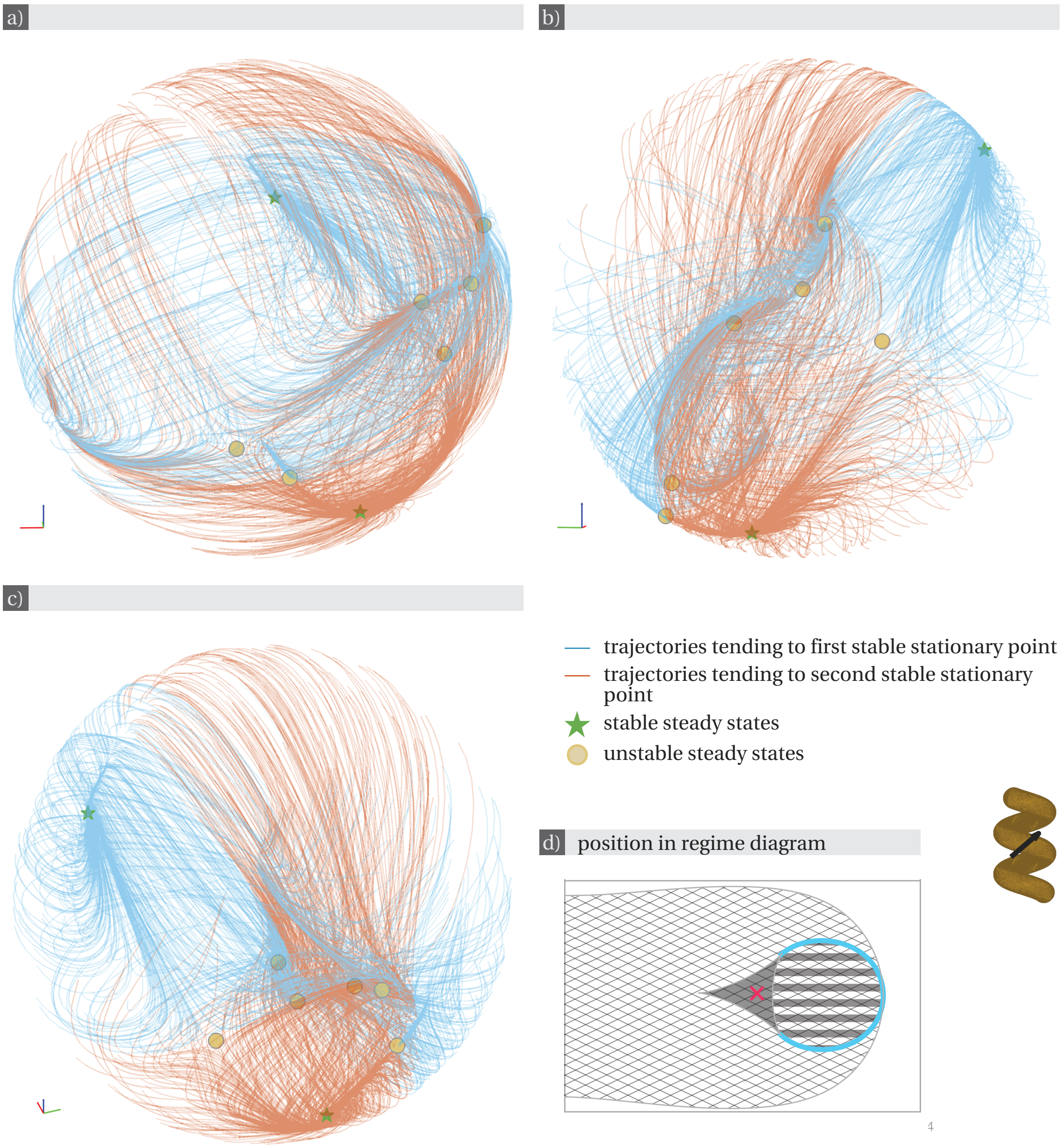

Figure 6.28 – **Swimmer D: phase portrait of the rotational dynamics in parameter regime 2/8**. Phase portrait of the dynamical system (3.14), which describes the rotational dynamics by means of quaternions (cf. section 4.3.2), for parameter values $a = 0.0217$ and $\cos\psi = 0.0090$ (cf. the cross on panel (d)). The basins of attractions of both stable steady states appear to be of similar size.
Panels (a-c) show the same object under different angles. To view it in rotation, click here (password: thesisPR) or scan the barcode.

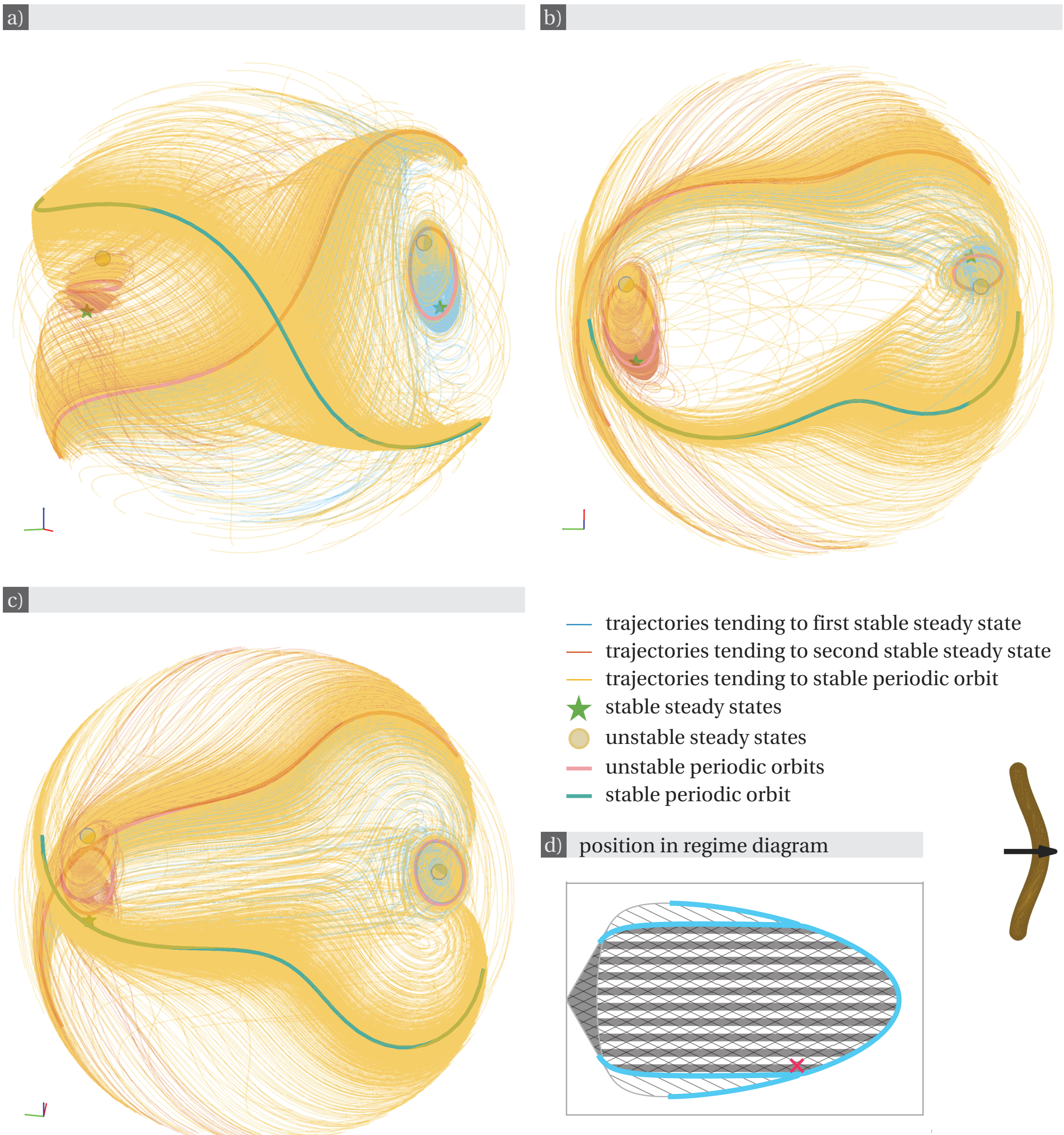

Figure 6.29 – **Swimmer E: phase portrait of the rotational dynamics in parameter regime 2/4**. Phase portrait of the dynamical system (3.14), which describes the rotational dynamics by means of quaternions (cf. section 4.3.2), for parameter values $a = 0.3292$ and $\cos\psi = -0.5957$ (cf. the cross on panel (d)). Note the presence of a stable periodic orbit in addition to the two stable steady states; it lies on a foil of periodic orbits obtained by continuation starting from periodic orbits found by direct numerical integration. The two smaller unstable periodic orbits, which appear to belong to the boundary between the basins of attraction of the three stable asymptotic solutions, are on foils obtained by continuation starting from Hopf bifurcations.
Panels (a-c) show the same object under different angles. To view it in rotation, click here (password: thesisPR) or scan the barcode.

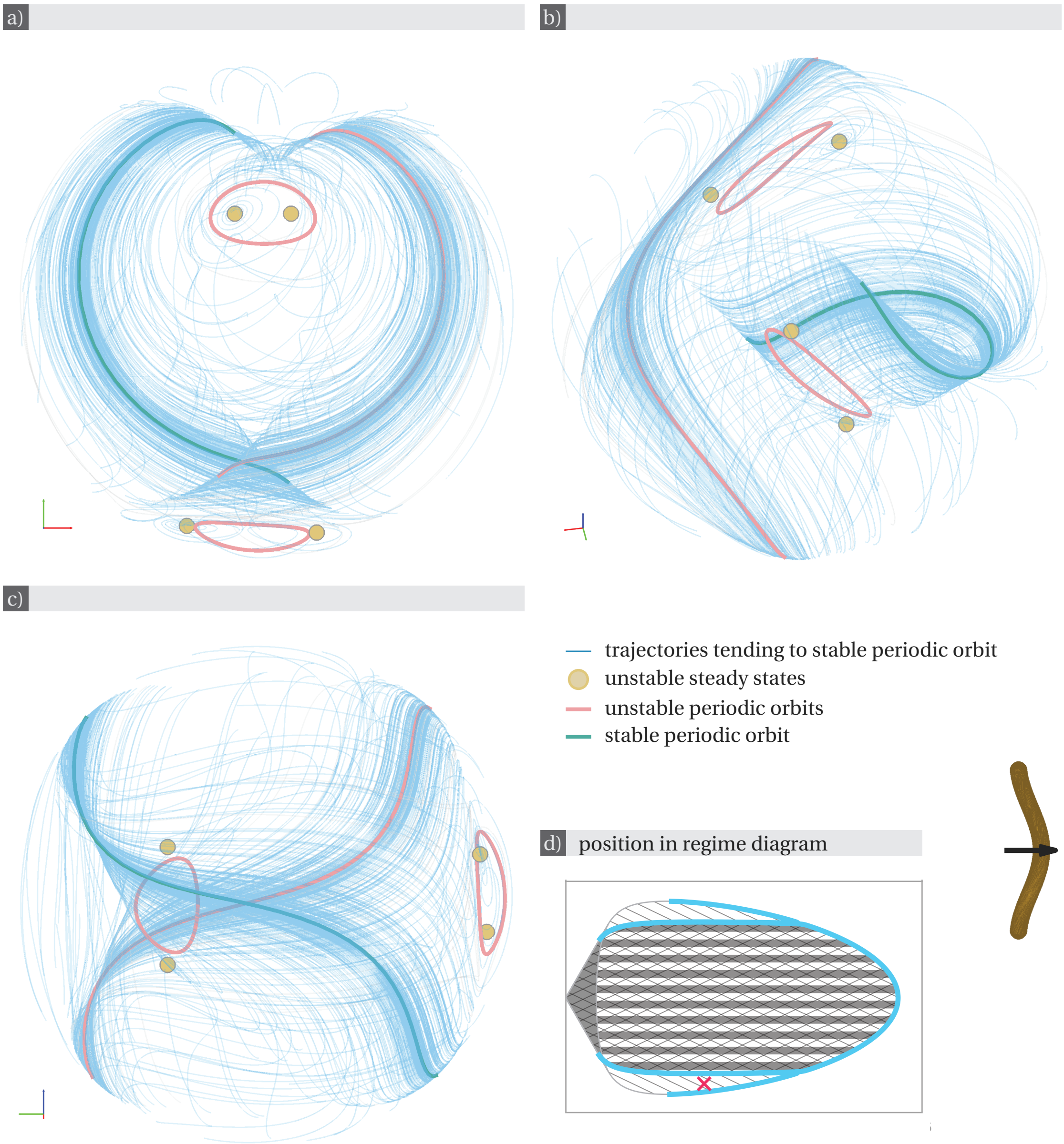

Figure 6.30 – **Swimmer E: phase portrait of the rotational dynamics in parameter regime 0/4**. Phase portrait of the dynamical system (3.14), which describes the rotational dynamics by means of quaternions (cf. section 4.3.2), for parameter values $a = 0.1948$ and $\cos\psi = -0.7484$ (cf. the cross on panel (d)). All trajectories tend to the unique stable periodic orbit, which belongs to a foil of periodic orbits obtained by continuation starting from periodic orbits found by direct numerical integration. Note the presence of two smaller unstable periodic orbits; they lie on a foil obtained by continuation starting from Hopf bifurcations.

Panels (a-c) show the same object under different angles. To view it in rotation, click here (password: thesisPR) or scan the barcode.

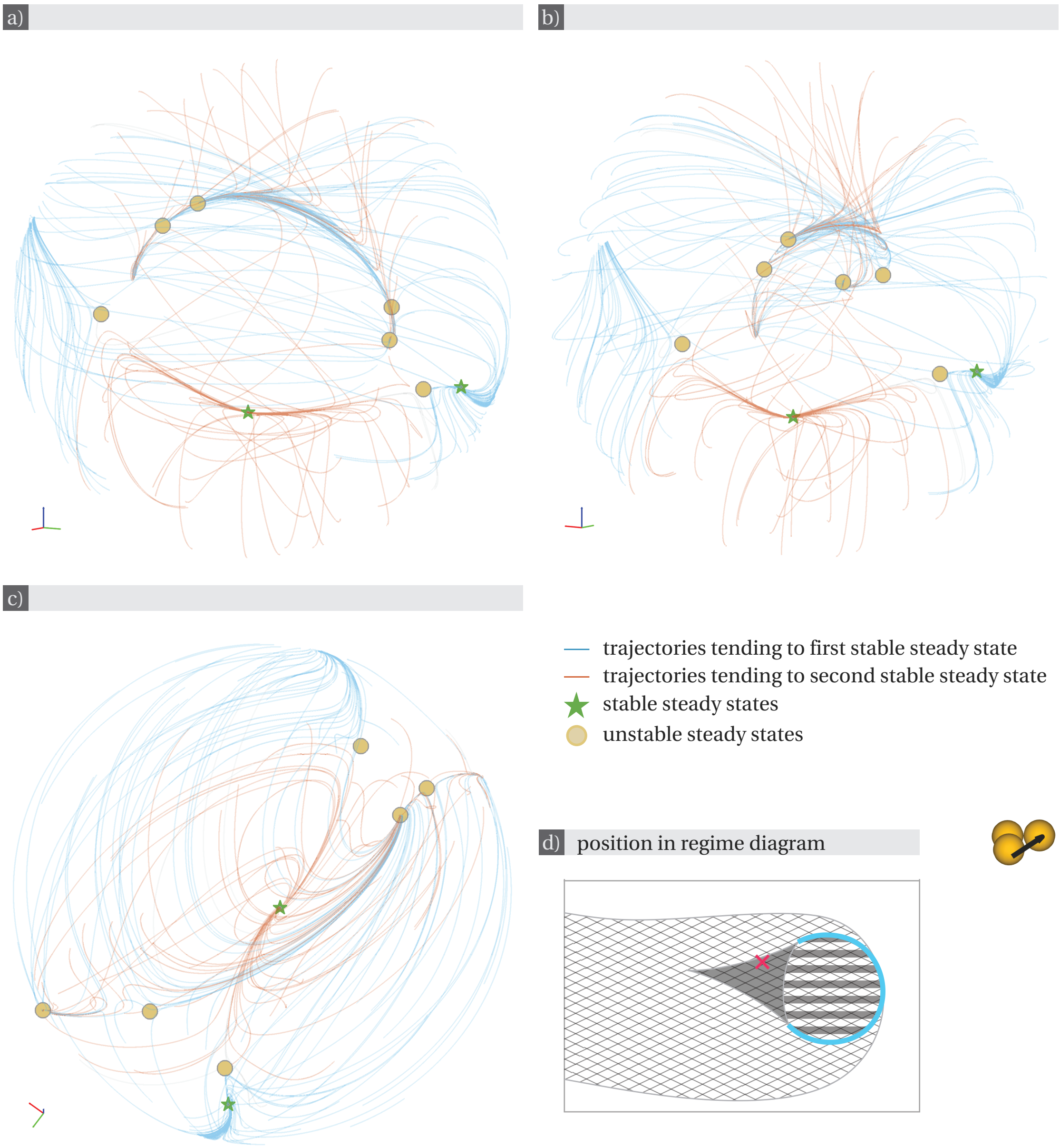

Figure 6.31 – **Swimmer F: phase portrait of the rotational dynamics in parameter regime 2/8**. Phase portrait of the dynamical system (3.14), which describes the rotational dynamics by means of quaternions (cf. section 4.3.2), for parameter values $a = 0.5$ and $\cos\psi = 0.0872$ (cf. the cross on panel (d)). In panels (a) and (b), note the accumulation of trajectories along lines linking the steady states: these might indicate the existence of heteroclinic orbits. The unstable steady state appear to lie on the boundary between the basins of attraction of the two stable steady states.
Panels (a-c) show the same object under different angles. To view it in rotation, click here (password: thesisPR) or scan the barcode.

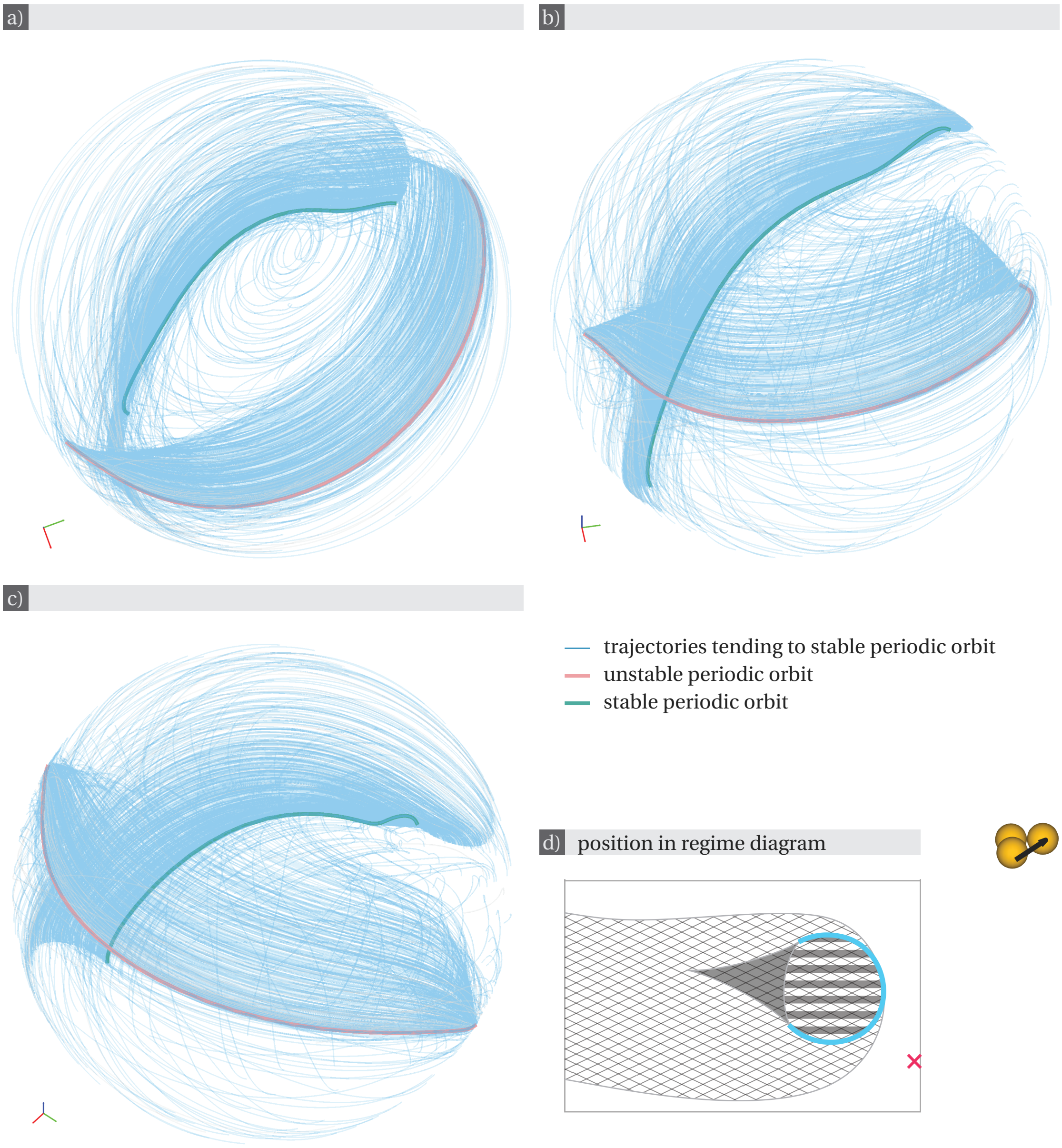

Figure 6.32 – **Swimmer F: phase portrait of the rotational dynamics in parameter regime 0/0**. Phase portrait of the dynamical system (3.14), which describes the rotational dynamics by means of quaternions (cf. section 4.3.2), for parameter values $a = 0.8841$ and $\cos\psi = -0.1692$ (cf. the cross on panel (d)). All trajectories tend to the unique stable periodic orbit. It belongs to a foil of periodic orbits obtained by continuation starting from periodic orbits founds by direct numerical integration.
Panels (a-c) show the same object under different angles. To view it in rotation, click here (password: thesisPR) or scan the barcode.

Phase portraits corresponding to regime 2/8 are shown in figures 6.28 and 6.31. In both cases, the trajectories converging to each stable steady state are neatly split into two groups (accounting for the periodic boundary of the outer sphere). In fig. 6.31, the small density of trajectories allows to locate regions where they accumulate: regions of higher density seem to form curves, that we expect to be homoclinic orbits. Stable periodic orbits were never observed in regime 2/8.

Regime 0/4 is displayed in figures 6.20, 6.24, and 6.30. In figure 6.30, a unique stable periodic orbit attracts all computed solutions. This periodic orbit belongs to a foil of periodic orbits that extends to small and large values of a beyond the parameter values for which there are relative equilibria. By comparison, in figures 6.20 and 6.24, there are two stable periodic orbits: one of them analogue to the stable periodic orbit present in figure 6.30 and the other one obtained by numerical continuation from Hopf bifurcations.

Parameter values for which there are no relative equilibria give rise to the dynamics represented in figures 6.25 and 6.32. In both figures, all trajectories tend asymptotically to a unique stable periodic orbit. Other types of dynamics with two or more stable periodic orbit might also arise.

6.3 Comparison between numerical and asymptotic solutions

In this section, the analytical predictions of chapter 5 are compared with solutions obtained by direct numerical integration with integrator ode45 in MATLAB [87].

Numerical solutions to (3.14) at large a and at small $\sin\psi$ were found to be periodic. We showed in sections 5.2 and 5.3 that the corresponding analytical solutions are not necessarily periodic but that they are nevertheless consistent with it. Numerical periodic solutions corresponding to the small a and large a regimes of section 5.1 and 5.2 are connected numerically by branches of periodic orbits that for small $\sin\psi$ correspond to the regimes found analytically in section 5.3.

6.3.1 Small Mason Number

For small Mason number a, limit cycles are obtained both numerically and analytically for $\psi \in [0, \pi/2 - \iota) \cup (\pi/2 + \iota, \pi]$ (cf. section 5.1). Figures 6.33-6.38 display the periods of limit cycles as predicted by equation (5.1) and as obtained numerically for several fixed values of a and varying $\psi \in [0, \pi/2 - \iota) \cup (\pi/2 + \iota, \pi]$ for swimmers A-F presented in section 6.1.

In each figure, the numerical solutions were obtained by direct integration of (3.14) for different values of ψ, with the exception of figure 6.34b, where the solutions were obtained by numerical continuation with MatCont [83] letting ψ vary. Note that to numerically characterise the periods, we must take into account that the quaternion parametrisation of SO(3) is a two to one covering: $-q$ and q parametrise the same rotation. Thus there can be symmetric limit

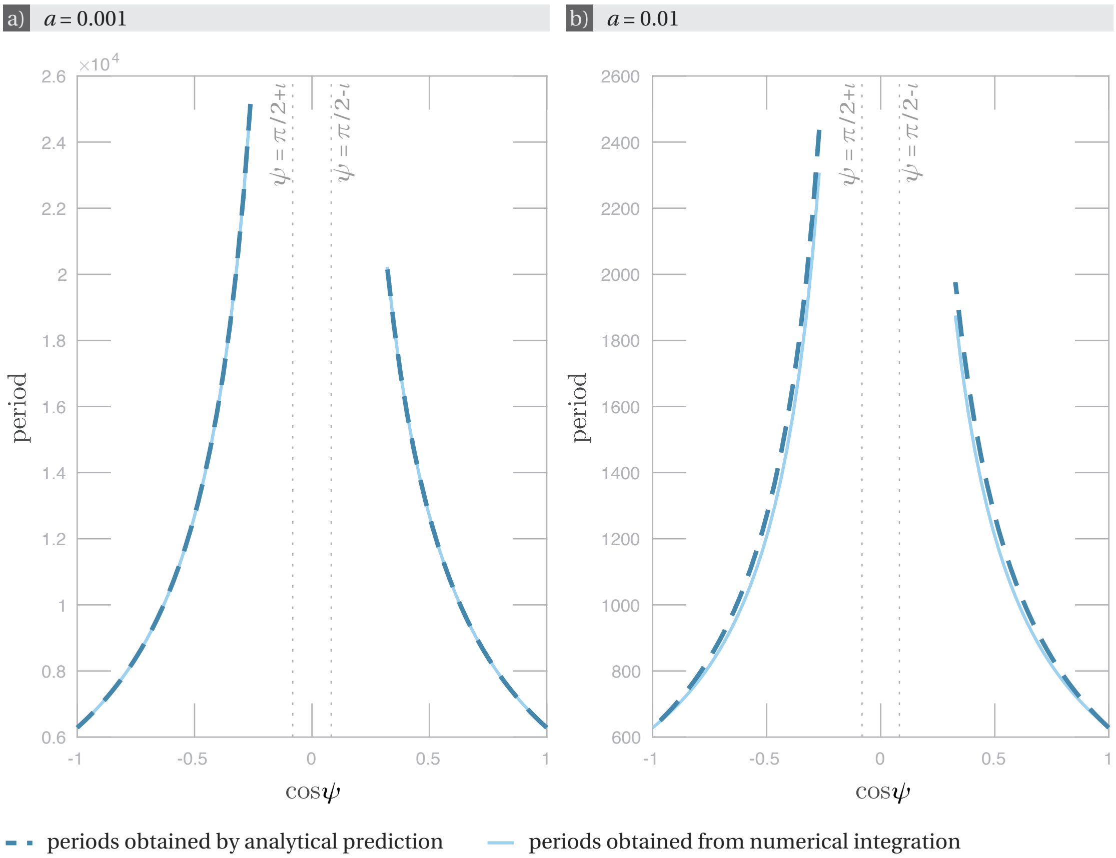

Figure 6.33 – **Swimmer A: comparison between numerics and analysis in the regime of small Mason number**. Comparison between periods obtained from numerical integrations of system (3.14) with corresponding parameters, and periods predicted analytically by (5.1) for (a) $a = 0.001$ and (b) $a = 0.01$. Note that $a = 0.01$ is too large to be in the scope of the analysis carried out in chapter 5, and yet the matching between the predicted and computed periods is still very good.

cycles [80, p. 282] in the quaternion coordinates that actually correspond to limit cycles in SO(3) of half the period. All the limit cycles found numerically for small a fall into this category. Therefore the period obtained analytically in (5.1) is compared with half the period obtained numerically.

For swimmer A with $a = 10^{-3}$ (cf. fig. 6.33a), the relative error between the period obtained numerically and the prediction (5.1) reaches a local maximum for $\psi < \pi/2 - \iota$ and seems to admit a vertical asymptote as ψ approaches $\pi/2 + \iota$ from the right. Note that prediction (5.1) has vertical asymptotes for $\psi = \pi/2 \pm \iota$, and that its accuracy is expected to decrease as ψ approaches these asymptotes. The local maximum is $4.3940 \cdot 10^{-4}$, and the relative error remains below this value for $\psi \leq \pi/2 - \iota - 0.2439$ and $\psi > \pi/2 + \iota + 0.5475$. The maximal relative error computed is $1.0029 \cdot 10^{-3}$.

For $a = 10^{-2}$ (cf. fig. 6.33b), the maximal relative error is $5.7178 \cdot 10^{-2}$. Periods could be computed numerically for $\psi \leq \pi/2 - \iota - 0.2514$ and $\psi \geq \pi/2 + \iota + 0.1911$. Note that $a = 10^{-2}$ is not considered asymptotically small: indeed, the singular values σ_1 and σ_2 (cf. section 3.2) provide characteristic scales, and for a to be considered asymptotically small, it must satisfy $a \ll \min\{\sigma_1, \sigma_2\}$. For swimmer A, this bound is $\sigma_2 = 2.4111 \cdot 10^{-2}$. That the numerical computation and analytical prediction fit so well for values of a just below this bound illustrates the robustness of the analysis of chapter 5.

For swimmer B with $a = 10^{-3}$ (cf. fig. 6.34a), the relative error between the predicted and computed periods has a locally maximal value of $7.6922 \cdot 10^{-5}$, and explodes as it approaches

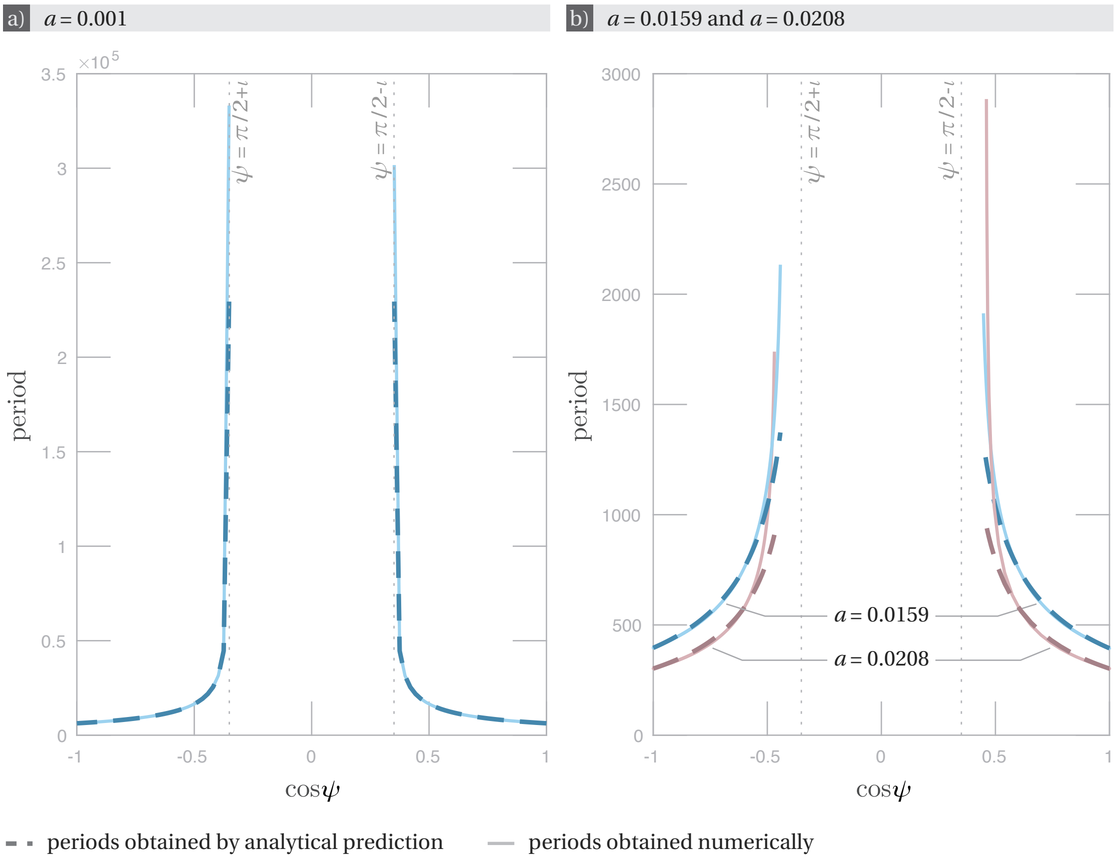

Figure 6.34 – **Swimmer B: comparison between numerics and analysis in the regime of small Mason number**. Comparison between periods obtained numerically, and periods predicted analytically by (5.1) for (a) $a = 0.001$, (b) $a = 0.0159$ and $a = 0.0208$. For $a = 0.001$ on panel (a), the numerical results are obtained from integration of system (3.14) with corresponding parameters. For $a = 0.0159$ and $a = 0.0208$ on panel (b), the periods obtained numerically are found by numerical continuation keeping a constant. Note that $a = 0.0159$ and $a = 0.0208$ lie beyond the scope of the analysis carried out in chapter 5, and yet the prediction still fits very well the computations.

$\pi/2-\iota$ from the left or $\pi/2+\iota$ from the right (the maximal computed value is 0.3688). Thus, the relative error is smaller than $7.6922 \cdot 10^{-5}$ for $\psi < \pi/2-\iota-0.1988$ and $\psi > \pi/2+\iota+0.2235$.

Note that $a = 0.0159$ and $a = 0.0208$ (cf. fig. 6.34b) don't fall into the category of asymptotically small a for this problem, since for swimmer B, asymptotically small a must verify $a \ll \min\{\sigma_1, \sigma_2\} = 0.0497$. For $a = 0.0159$ the relative error is smaller than 0.0198 for $\psi \in [0, \pi/2-\iota-0.2267) \cup (\pi/2+\iota+0.1002, \pi]$. For $a = 0.0208$, the relative error is smaller than 0.0291 for $\psi \in [0, \pi/2-\iota-0.2126) \cup (\pi/2+\iota+0.1297, \pi]$. Swimmer B' having symmetric solutions to swimmer B, the errors are similar.

For swimmer C, asymptotically small a must verify $a \ll \min\{\sigma_1, \sigma_2\} = 0.0433$. For $a = 10^{-3}$ (cf. fig. 6.35a), the relative error reaches a locally maximal value of $1.0213 \cdot 10^{-4}$ and seems

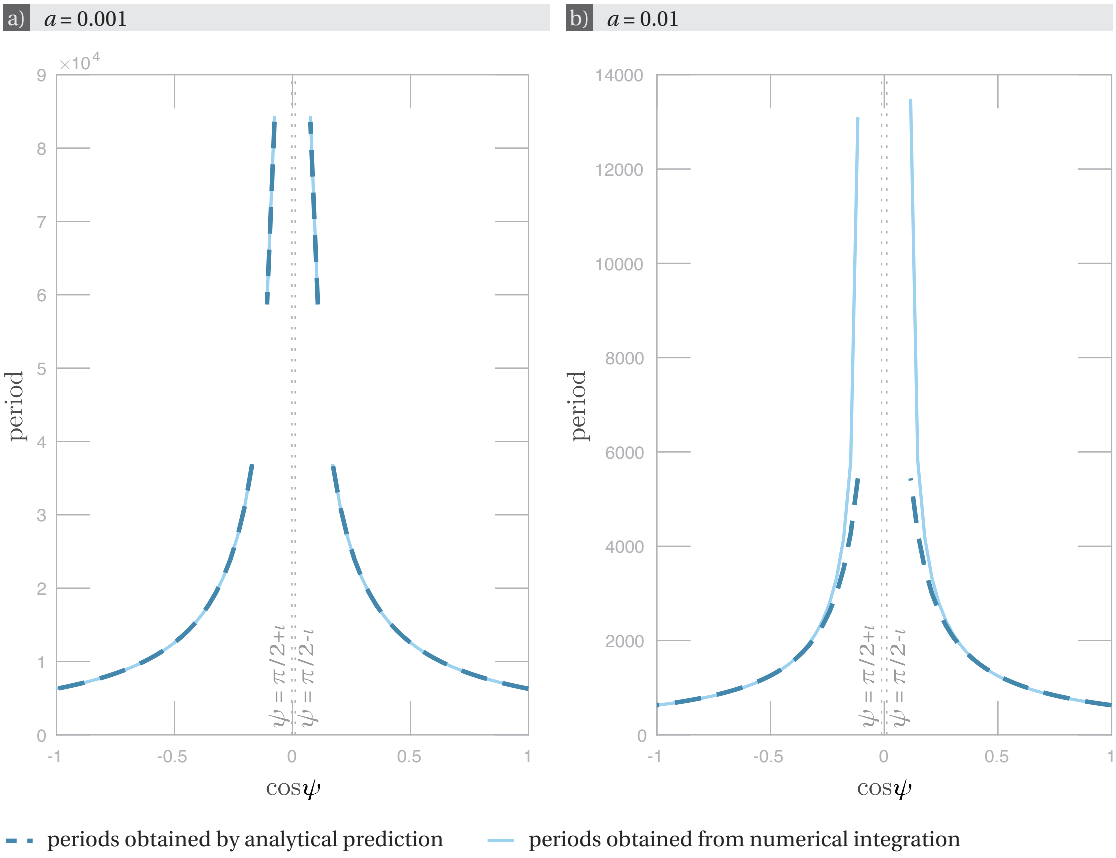

Figure 6.35 – **Swimmer C: comparison between numerics and analysis in the regime of small Mason number**. Comparison between periods obtained from numerical integrations of system (3.14) with corresponding parameters, and periods predicted analytically by (5.1) for (a) $a = 0.001$ and (b) $a = 0.01$. Note that $a = 0.01$ doesn't belong to the scope of the analysis presented in chapter 5, and yet the agreement between the prediction and the computations is still very good.
The gaps on panel (a) correspond to values of ψ for which the numerics didn't converge.

to admit a vertical asymptote as $\psi \to \pi/2 \pm \iota$: the relative error stays below $1.0213 \cdot 10^{-4}$ for $\psi \in [0, \pi/2 - \iota - 0.3508) \cup (\pi/2 + \iota + 0.3508, \pi/2]$. The maximal computed relative error is $9.5572 \cdot 10^{-3}$. For $a = 10^{-2}$ (cf. fig. 6.35b), the relative error is smaller than $9.8189 \cdot 10^{-3}$ for $\psi \in [0, \pi/2 - \iota - 0.3578) \cup (\pi/2 + \iota + 0.3578, \pi/2]$. The maximal computed relative error is 0.8504.

For swimmer D, asymptotically small a must verify $a \ll \min\{\sigma_1, \sigma_2\} = 0.0234$. For $a = 10^{-3}$ (cf. fig. 6.36a), the relative error reaches a locally maximal value of $4.3637 \cdot 10^{-4}$ and seems to admit a vertical asymptote as $\psi \to \pi/2 \pm \iota$: the relative error stays below $4.3637 \cdot 10^{-4}$ for $\psi \in [0, \pi/2 - \iota - 0.4797) \cup (\pi/2 + \iota + 0.1074, \pi/2]$. The maximal computed relative error is 0.1224. For $a = 10^{-2}$ (cf. fig. 6.36b), the maximal computed relative error is $7.1087 \cdot 10^{-2}$.

For swimmer E, asymptotically small a must verify $a \ll \min\{\sigma_1, \sigma_2\} = 4.2721 \cdot 10^{-2}$. For $a = 10^{-3}$ (cf. fig. 6.37a), the relative error reaches a locally maximal value of $1.0316 \cdot 10^{-4}$ and

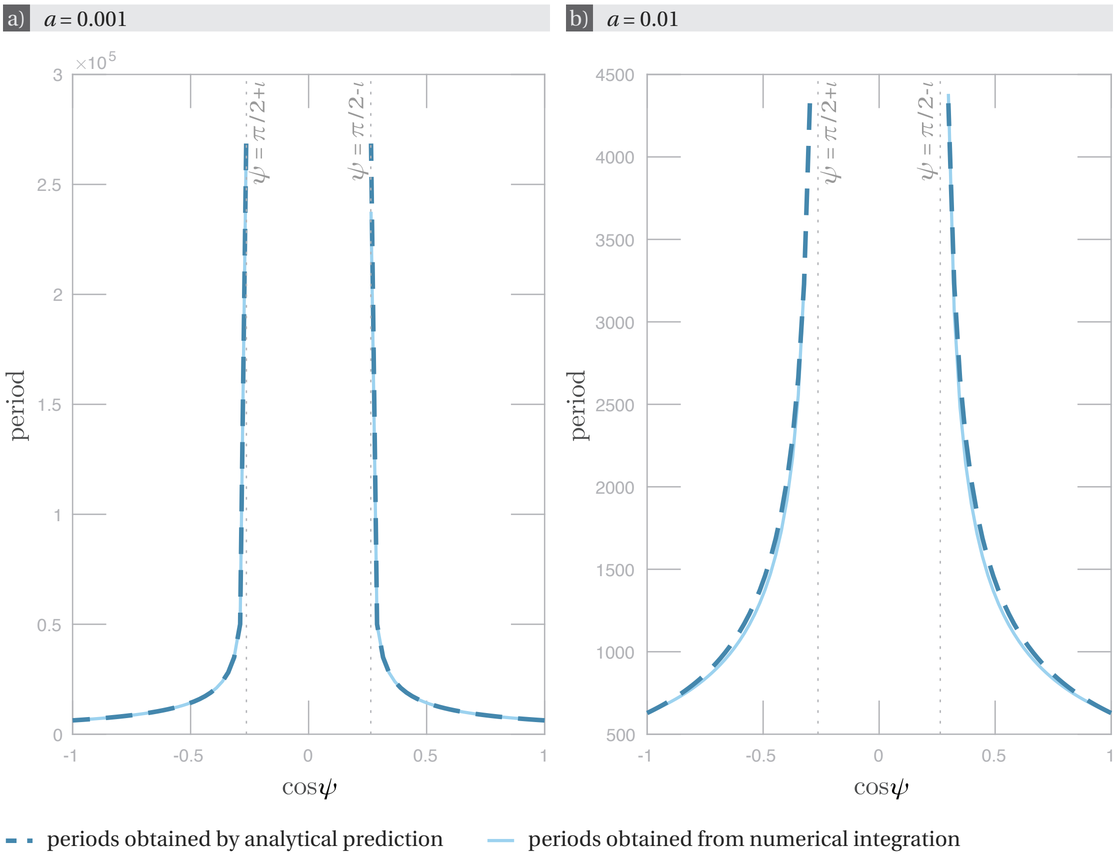

Figure 6.36 – **Swimmer D: comparison between numerics and analysis in the regime of small Mason number**. Comparison between periods obtained from numerical integrations of system (3.14) with corresponding parameters, and periods predicted analytically by (5.1) for $a = 0.001$ (panel (a)) and $a = 0.01$ (panel (b)). Note that $a = 0.01$ is too large to enter the scope of the analysis carried out in chapter 5, and yet the predicted period is still very close to the numerical computations.

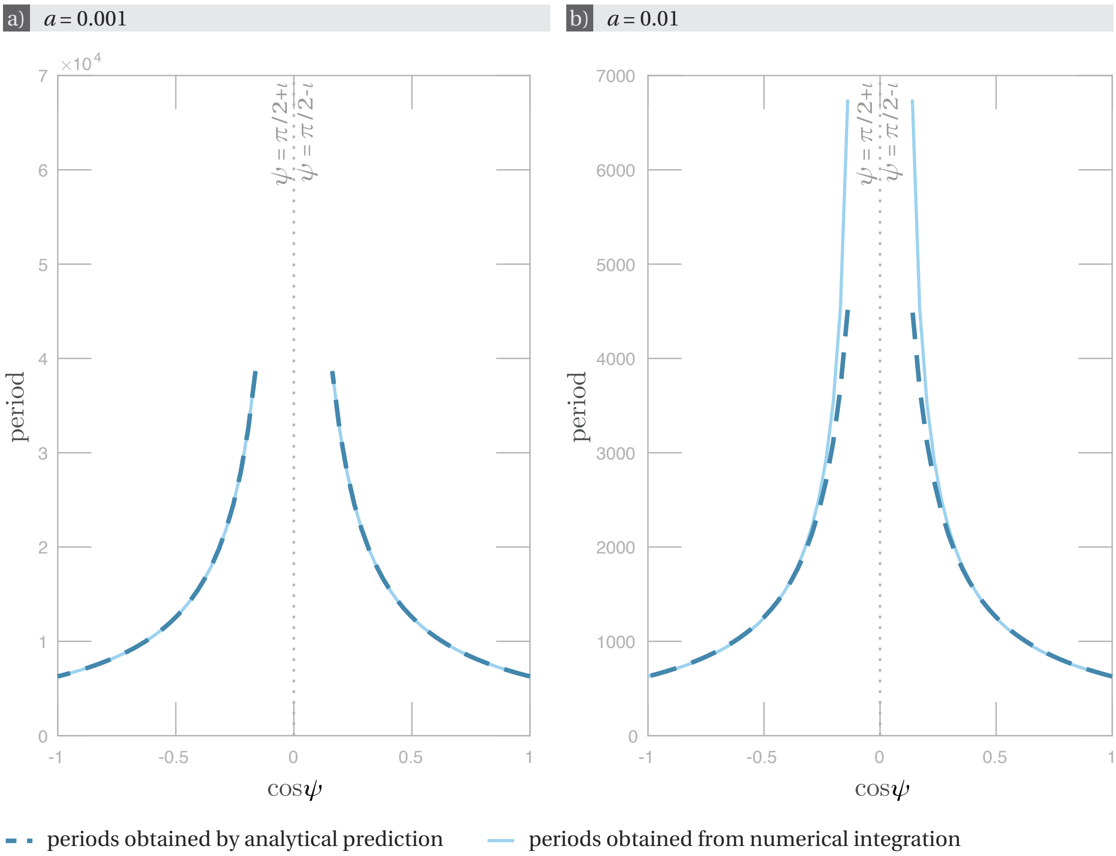

Figure 6.37 – **Swimmer E: comparison between numerics and analysis in the regime of small Mason number**. Comparison between periods obtained from numerical integrations of system (3.14) with corresponding parameters, and periods predicted analytically by (5.1) for (a) $a = 0.001$ and (b) $a = 0.01$. Note that $a = 0.01$ does not enter the scope of the analysis presented in chapter 5, and yet the prediction and the numerics still match very well.

seems to admit a vertical asymptote as $\psi \to \pi/2 \pm \iota$: the relative error stays below $1.0316 \cdot 10^{-4}$ for $\psi \in [0, \pi/2 - \iota - 0.3529) \cup (\pi/2 + \iota + 0.3529, \pi/2]$. The maximal computed relative error is $5.4259 \cdot 10^{-3}$. For $a = 10^{-2}$ (cf. fig. 6.37b), the relative error is smaller than $1.0168 \cdot 10^{-2}$ for $\psi \in [0, \pi/2 - \iota - 0.3598) \cup (\pi/2 + \iota + 0.3598, \pi/2]$. The maximal computed relative error is 0.3962.

For swimmer F, asymptotically small a must verify $a \ll \min\{\sigma_1, \sigma_2\} = 2.3450 \cdot 10^{-2}$. For $a = 10^{-3}$ (cf. fig. 6.38a), the relative error reaches a locally maximal value of $4.3637 \cdot 10^{-4}$ and seems to admit a vertical asymptote as $\psi \to \pi/2 \pm \iota$: the relative error stays below $4.3637 \cdot 10^{-4}$ for $\psi \in [0, \pi/2 - \iota - 0.4797) \cup (\pi/2 + \iota + 0.1074, \pi/2]$. The maximal computed relative error is 0.1224. For $a = 10^{-2}$ (cf. fig. 6.38b), the maximal computed relative error is $7.1087 \cdot 10^{-2}$.

To summarise, in all examples, we find good agreement between numerics and analytical predictions. As a reminder, the predicted period has a vertical asymptote at $\psi = \pi/2 \pm \iota$ and we expect the relative error to become larger and larger as ψ approaches these two values. The relative error was nevertheless found to be small for most values of ψ, including examples with values of a that are not so small in the asymptotic sense.

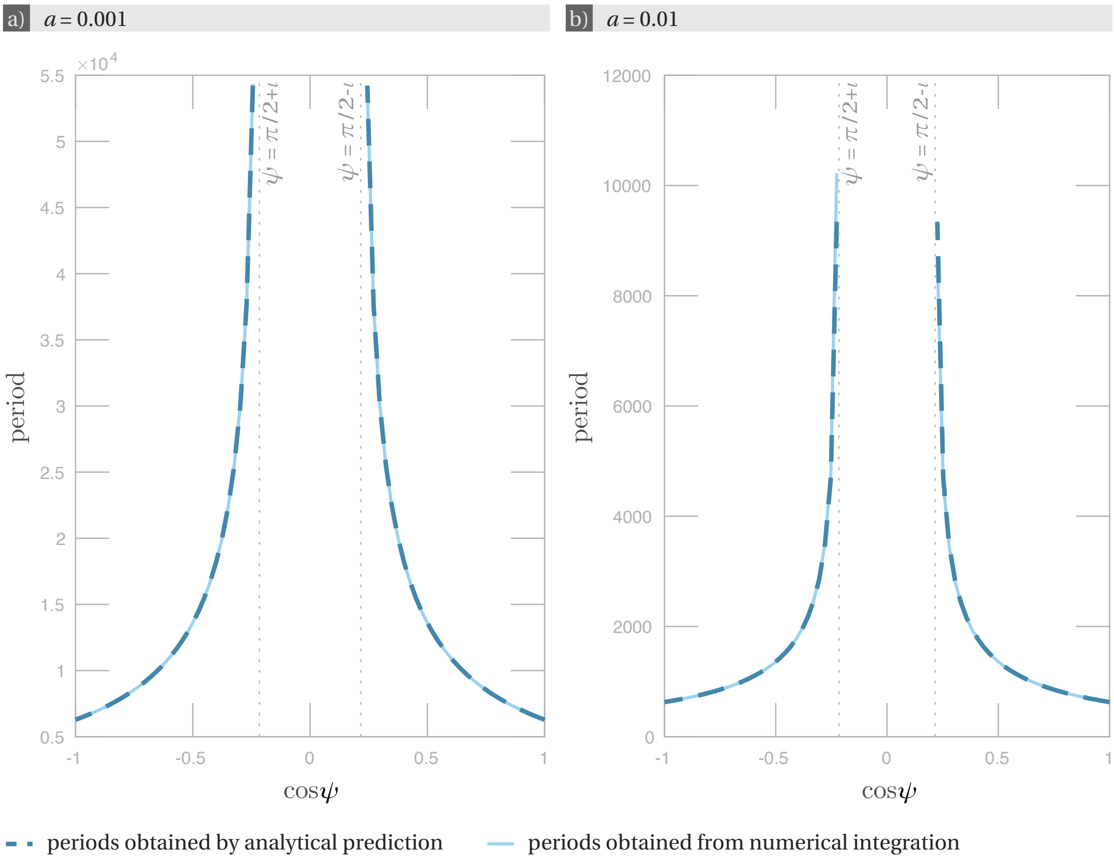

Figure 6.38 – **Swimmer F: comparison between numerics and analysis in the regime of small Mason number**. Comparison between periods obtained from numerical integrations of system (3.14) with corresponding parameters, and periods predicted analytically by (5.1) for (a) $a = 0.001$ and (b) $a = 0.01$. Note that $a = 0.01$ lies beyond the scope of the analysis carried out in chapter 5, and yet the prediction is still in very good agreement with the numerics.

6.3.2 Large Mason Number

In order to visualise the agreement between numerical and analytical solutions in both the large a and small $\sin\psi$ regimes, we find that it is useful to view the curve described by the magnetic moment **m** in the magnetic frame, that is in the frame locked to the rotating magnetic field **B**. In the large a regime, figures 6.39, 6.42a, 6.43, 6.46, 6.49, 6.52 and 6.55 exhibit a remarkable agreement between the curves obtained as a first order expansion as in section 5.2 and by direct numerical integration for $a = 100$ and different values of ψ for swimmers A-F.

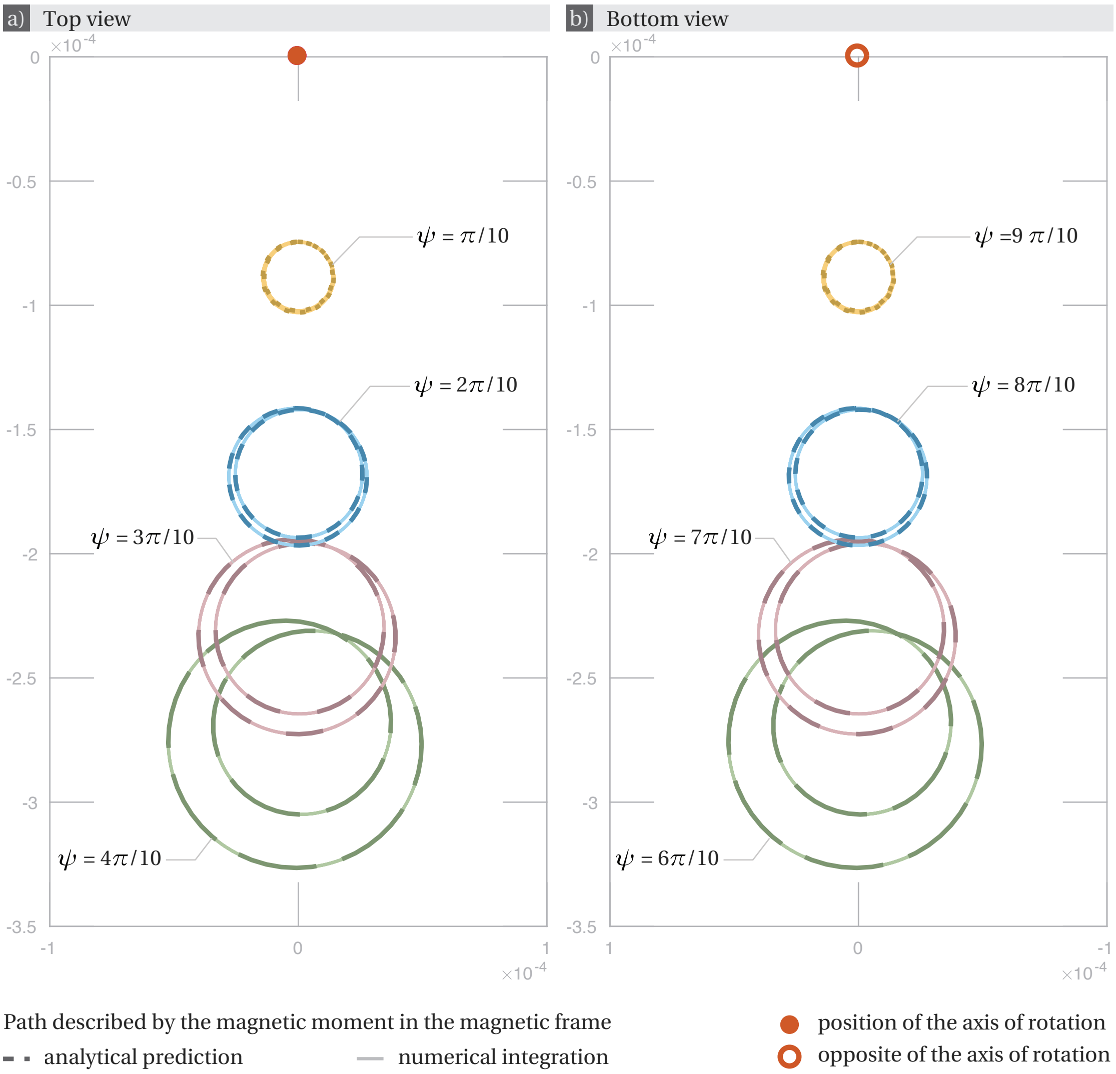

Figure 6.39 – **Swimmer A: comparison between numerics and analysis in the regime of large Mason number**. Trajectories described by the magnetic moment in the magnetic frame for $a = 100$ and several values of ψ. The analytical predictions are computed up to the first order. The views correspond to projections on the planes tangent to the unit sphere at (a) $\mathbf{e}_3$ and (b) $-\mathbf{e}_3$.

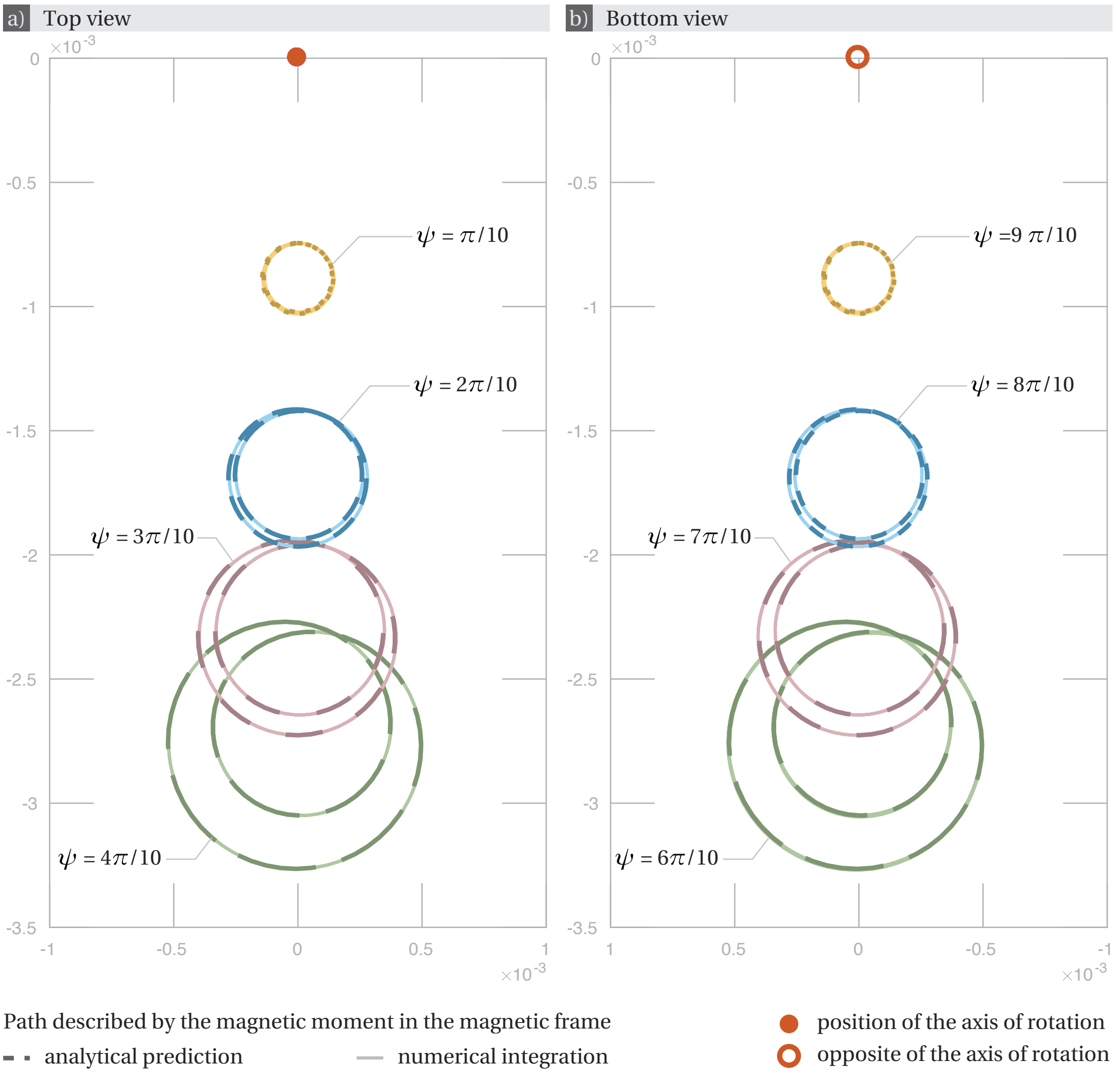

Figure 6.40 – **Swimmer A: comparison between numerics and analysis in the regime of large Mason number**. Trajectories described by the magnetic moment in the magnetic frame for $a = 10$ and several values of ψ. The analytical predictions are computed using first order expansion. The views correspond to projections on the planes tangent to the unit sphere at (a) $\mathbf{e}_3$ and (b) $-\mathbf{e}_3$.

For $a = 10$, in figures 6.40 for swimmer A and 6.50 for swimmer D, the agreement is still so good that the curves are undistinguishable from one another. While it is very good it is not quite as perfect for all the other swimmers (cf. fig. 6.42b, 6.44, 6.47, 6.53, 6.56). Note that characteristic scales for a are given by 1, and by the singular values σ_1 and σ_2 (cf. section 3.2). The differences in the agreements between numerics and analysis at $a = 10$ seems to be linked to the size of the singular values. Indeed for swimmers A and D, $\max\{\sigma_1, \sigma_2\} < 10^{-2}$, while for the other swimmers, $10^{-2} < \max\{\sigma_1, \sigma_2\} < 10^{-3}$. Namely, for swimmer A $\max\{\sigma_1, \sigma_2\} = 0.0333$ and for swimmer D $\max\{\sigma_1, \sigma_2\} = 0.0359$, while for swimmers B and B' $\max\{\sigma_1, \sigma_2\} = 0.9244$, for swimmer C $\max\{\sigma_1, \sigma_2\} = 0.3913$, for swimmer E $\max\{\sigma_1, \sigma_2\} = 0.4663$, and for swimmer F $\max\{\sigma_1, \sigma_2\} = 0.8093$.

Numerical and analytical solutions are also compared for values of a that are not large enough to be in the large a regime. Figure 6.41 shows that for swimmer A, the agreement between prediction and numerical solution is still very good for $a = 2$, and a similar conclusion is valid for swimmers D (cf. fig. 6.51) and E (cf. fig. 6.54), and for swimmer C with $a = 5$ and $a = 2$ (cf.

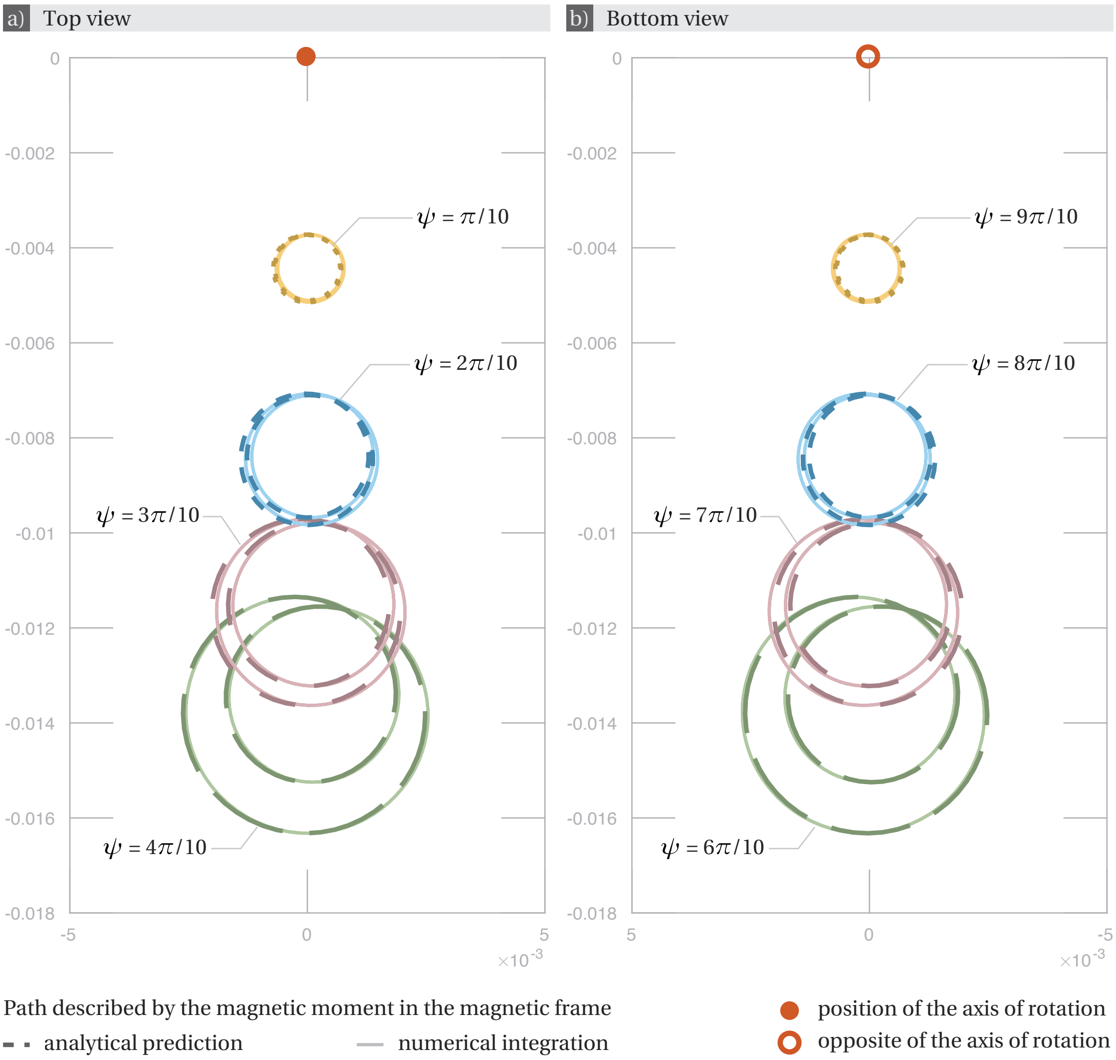

Figure 6.41 – **Swimmer A: comparison between numerics at $a = 2$ and analytical prediction for large Mason numbers**. Trajectories described by the magnetic moment in the magnetic frame for $a = 2$ and several values of ψ. The analytical predictions are computed using first order expansion. The views correspond to projections on the planes tangent to the unit sphere at (a) $\mathbf{e}_3$ and (b) $-\mathbf{e}_3$. Note that $a = 2$ is too small to fit in the scope of the analysis carried out in chapter 5, and yet the prediction is still remarkably accurate.

fig. 6.48). For swimmer B', $a = 2$ gives good agreement for small values of $\sin\psi$, but less so for ψ close to $\pi/2$ (cf. fig. 6.45).

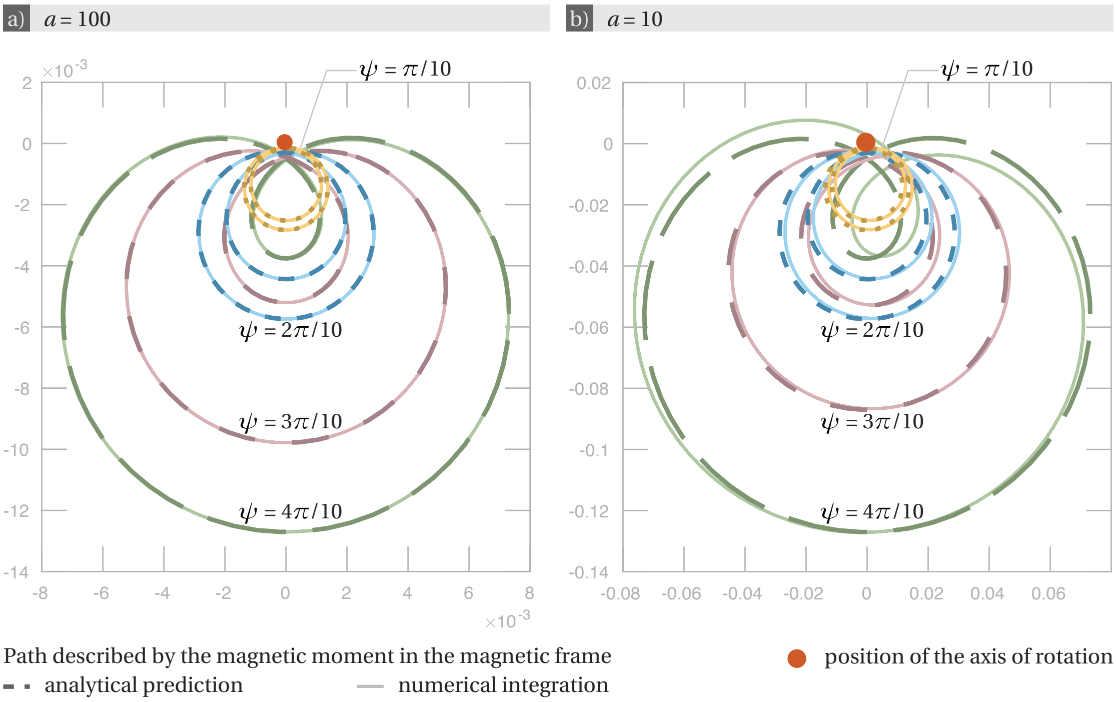

Figure 6.42 – **Swimmer B: comparison between numerics and analysis in the regime of large Mason number**. Trajectories described by the magnetic moment in the magnetic frame for (a) $a = 100$ and (b) $a = 10$, and several values of ψ. The analytical predictions are computed using first order expansion. The views correspond to projections on the plane tangent to the unit sphere at $\mathbf{e}_3$.

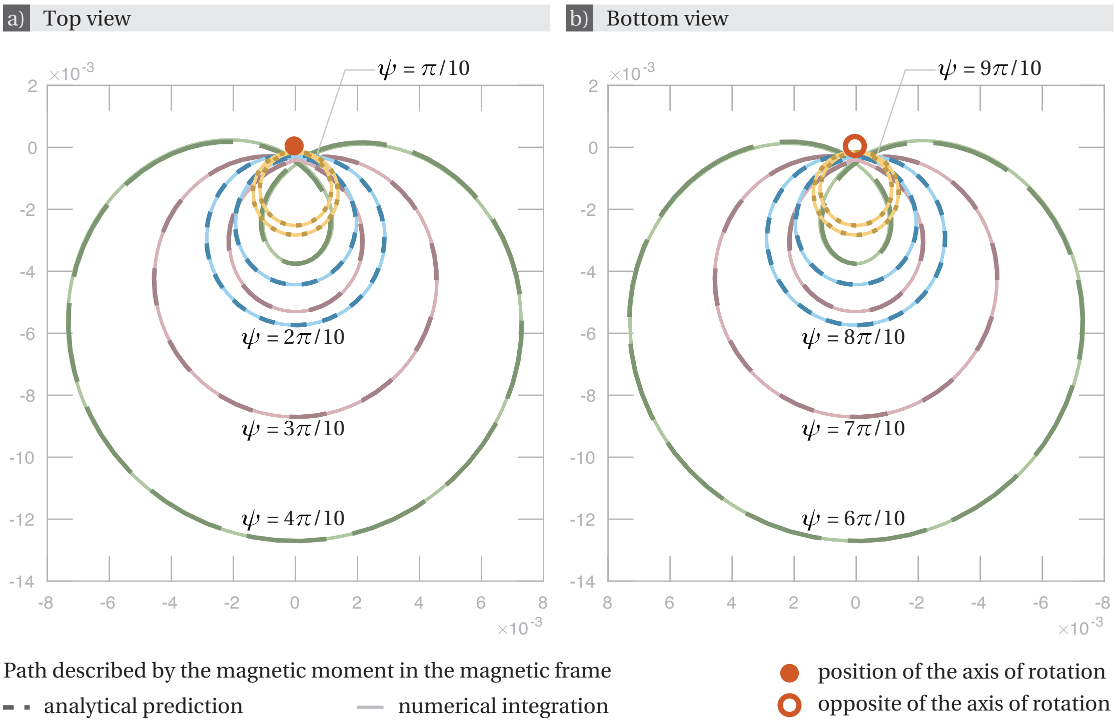

Figure 6.43 – **Swimmer B': comparison between numerics and analysis in the regime of large Mason number**. Trajectories described by the magnetic moment in the magnetic frame for $a = 100$ and several values of ψ. The analytical predictions are computed using first order expansion. The views correspond to projections on the planes tangent to the unit sphere at (a) $\mathbf{e}_3$ and (b) $-\mathbf{e}_3$.

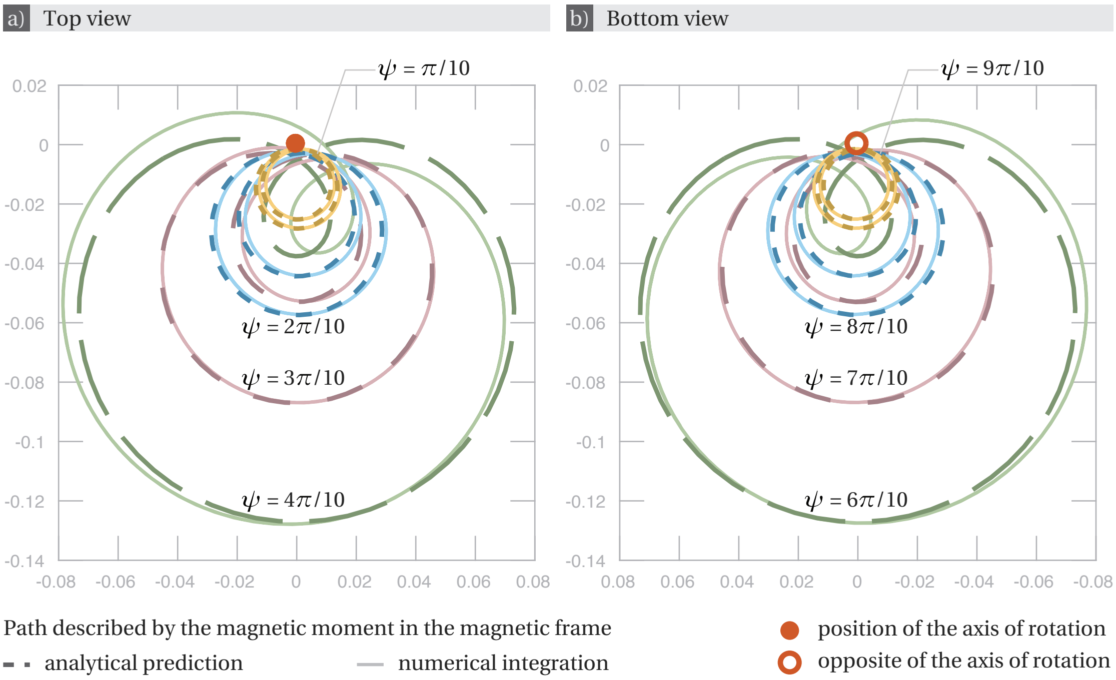

Figure 6.44 – **Swimmer B': comparison between numerics and analysis in the regime of large Mason number**. Trajectories described by the magnetic moment in the magnetic frame for $a = 10$ and several values of ψ. The analytical predictions are computed using first order expansion. The views correspond to projections on the planes tangent to the unit sphere at (a) $\mathbf{e}_3$ and (b) $-\mathbf{e}_3$.

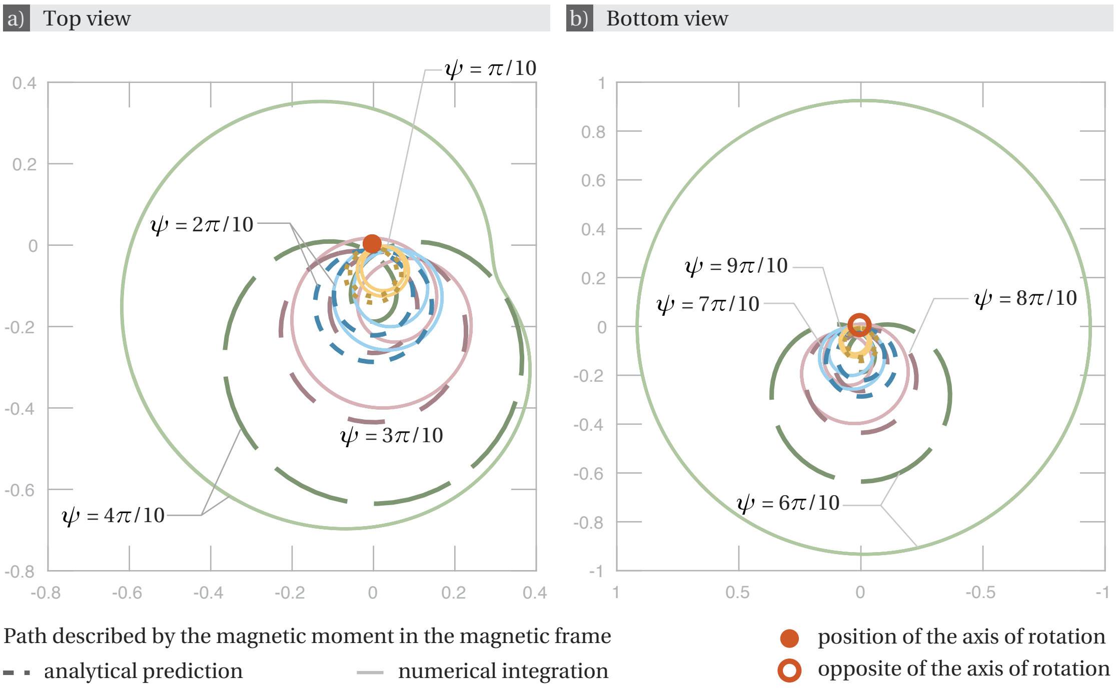

Figure 6.45 – **Swimmer B’: comparison between numerics at $a = 2$ and analytical prediction for large Mason numbers**. Trajectories described by the magnetic moment in the magnetic frame for $a = 2$ and several values of ψ. The analytical predictions are computed using first order expansion. The views correspond to projections on the planes tangent to the unit sphere at (a) $\mathbf{e}_3$ and (b) $-\mathbf{e}_3$. Note that $a = 2$ is below the scope of the analysis carried out in chapter 5, and yet the agreement between the prediction and the numerics is still quite good for values of ψ away from $\pi/2$, while it breaks out at $\psi = 4\pi/10$ and $\psi = 6\pi/10$.

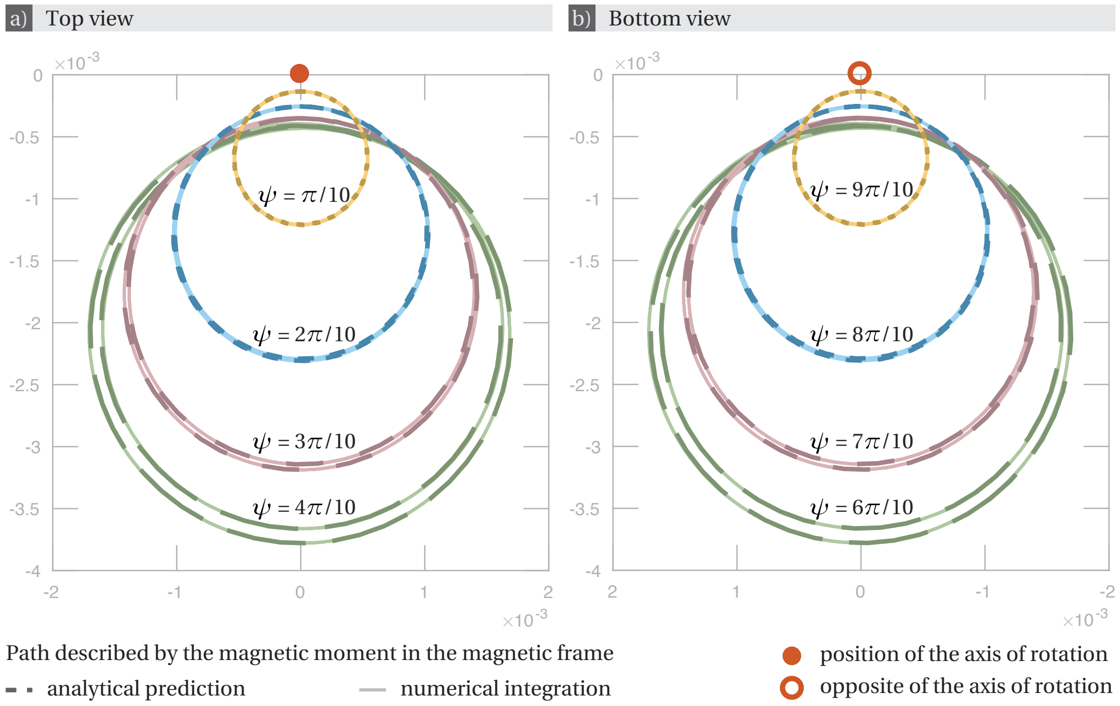

Figure 6.46 – **Swimmer C: comparison between numerics and analysis in the regime of large Mason number**. Trajectories described by the magnetic moment in the magnetic frame for $a = 100$ and several values of ψ. The analytical predictions are computed using first order expansion. The views correspond to projections on the planes tangent to the unit sphere at (a) $\mathbf{e}_3$ and (b) $-\mathbf{e}_3$.

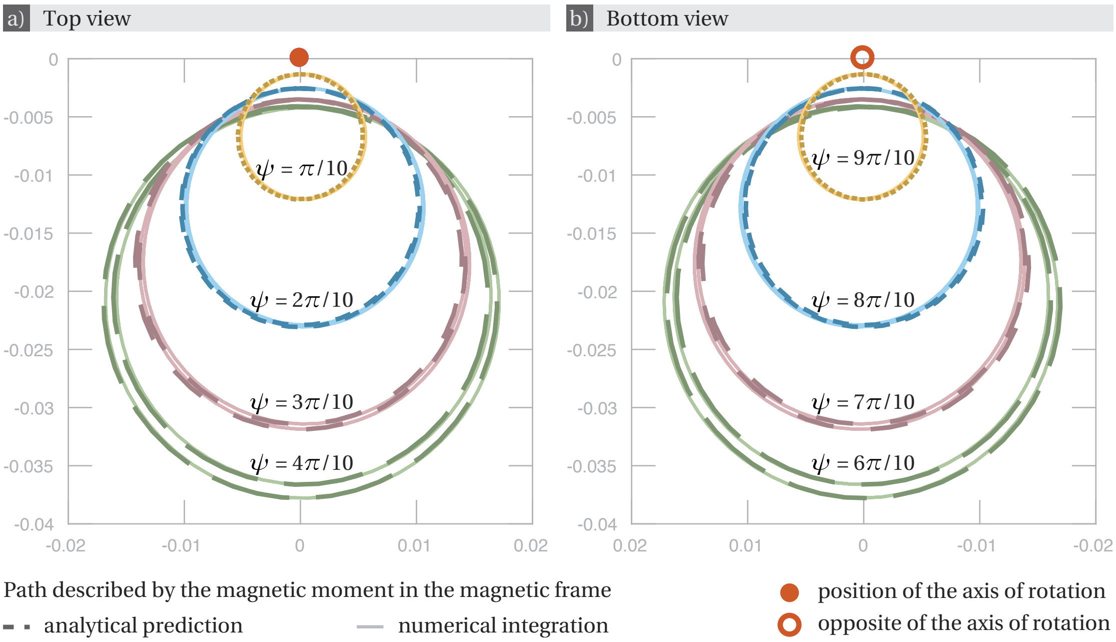

Figure 6.47 – **Swimmer C: comparison between numerics and analysis in the regime of large Mason number**. Trajectories described by the magnetic moment in the magnetic frame for $a = 10$ and several values of ψ. The analytical predictions are computed using first order expansion. The views correspond to projections on the planes tangent to the unit sphere at (a) $\mathbf{e}_3$ and (b) $-\mathbf{e}_3$.

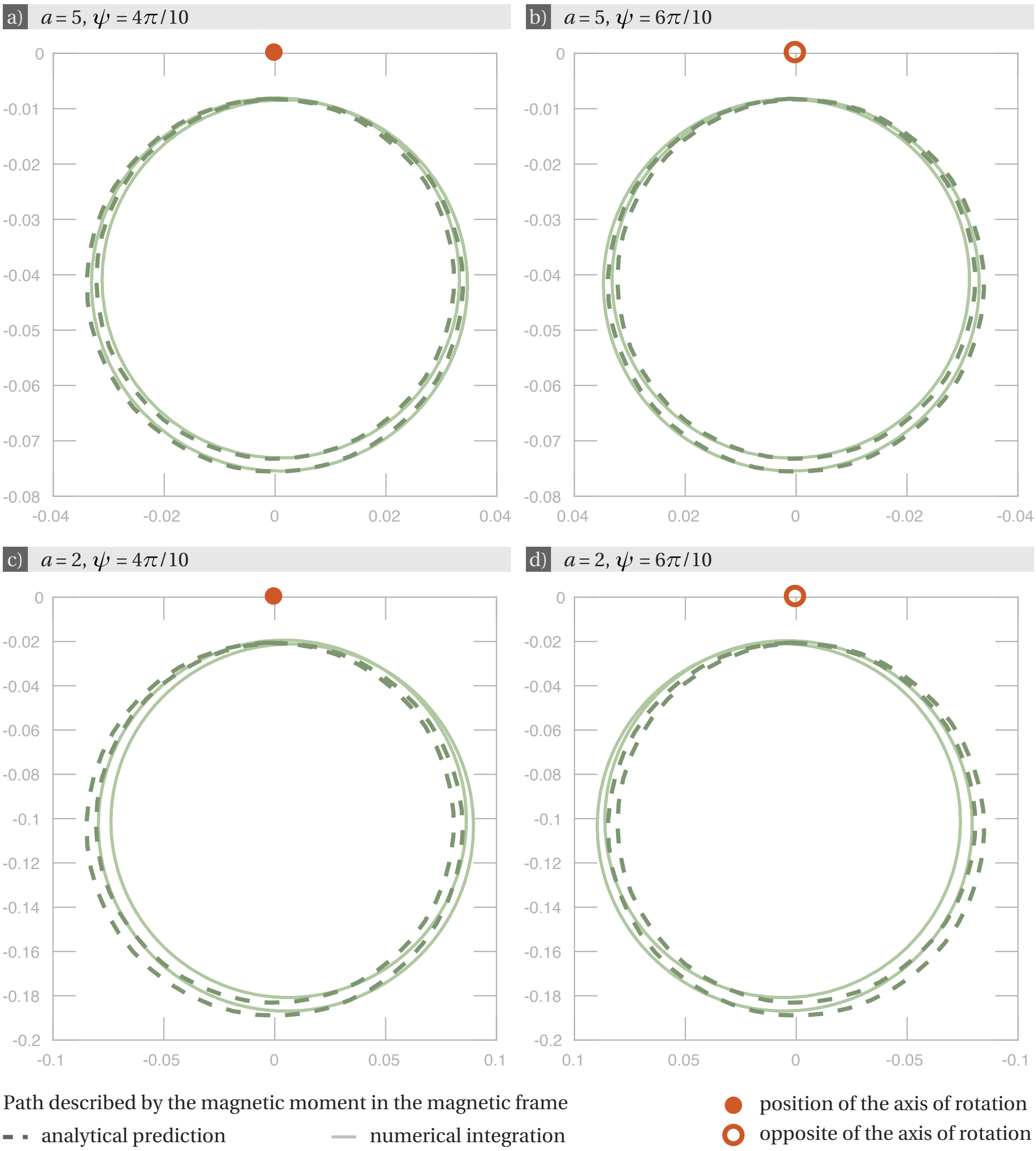

Figure 6.48 – **Swimmer C: comparison between numerics at $a = 5$ and $a = 2$ and analytical prediction for large Mason numbers**. Trajectories described by the magnetic moment in the magnetic frame for (a-b) $a = 5$ and (c-d) $a = 2$ and several values of ψ. The analytical predictions are computed using first order expansion. The views correspond to projections on the planes tangent to the unit sphere at (a) $\mathbf{e}_3$ and (b) $-\mathbf{e}_3$. Note that these values of a are too small to be in the scope of the analysis carried out in chapter 5, and yet the prediction and the numerics still match very well.

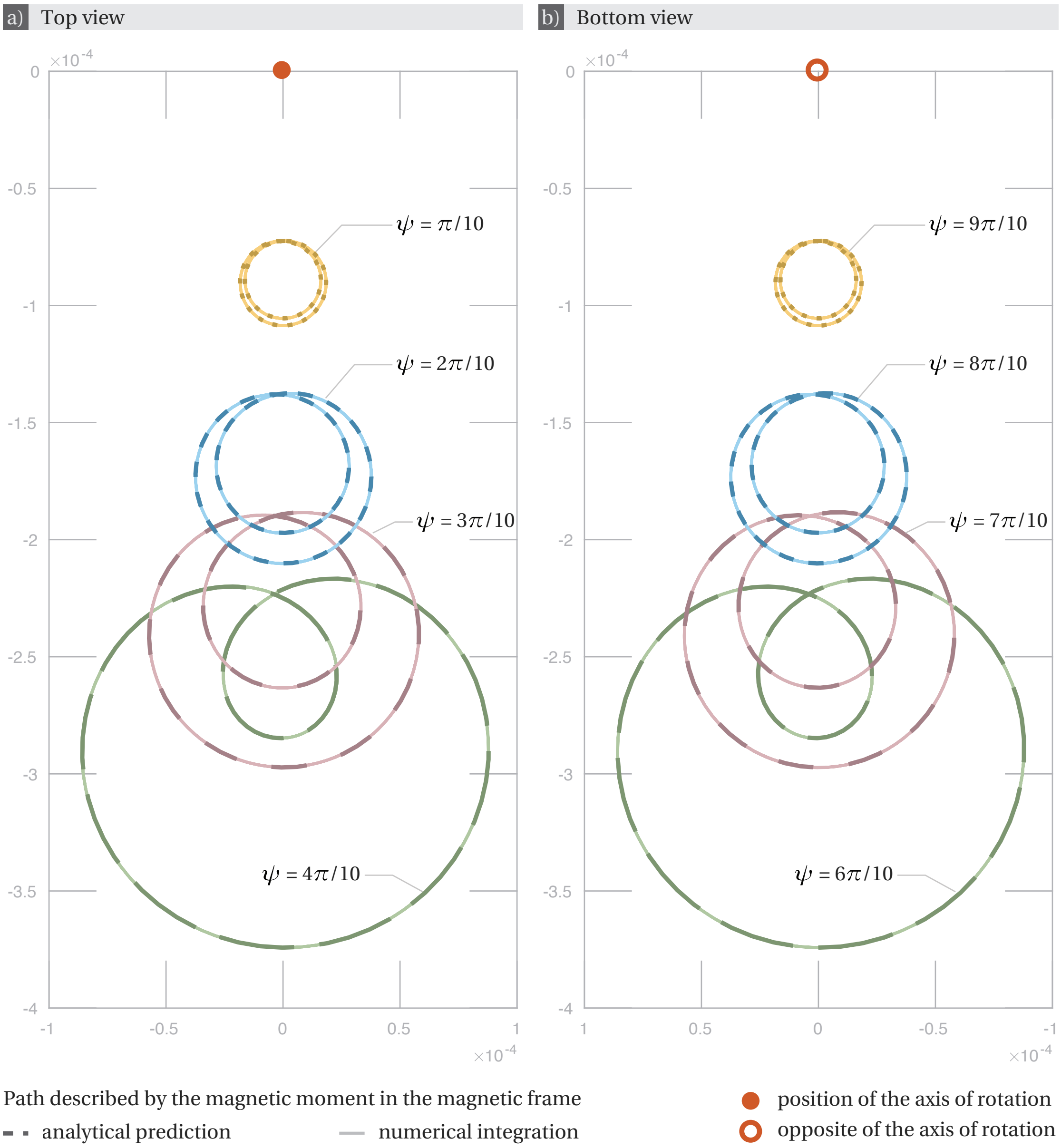

Figure 6.49 – **Swimmer D: comparison between numerics and analysis in the regime of large Mason number**. Trajectories described by the magnetic moment in the magnetic frame for $a = 100$ and several values of ψ. The analytical predictions are computed using first order expansion. The views correspond to projections on the planes tangent to the unit sphere at (a) $\mathbf{e}_3$ and (b) $-\mathbf{e}_3$.

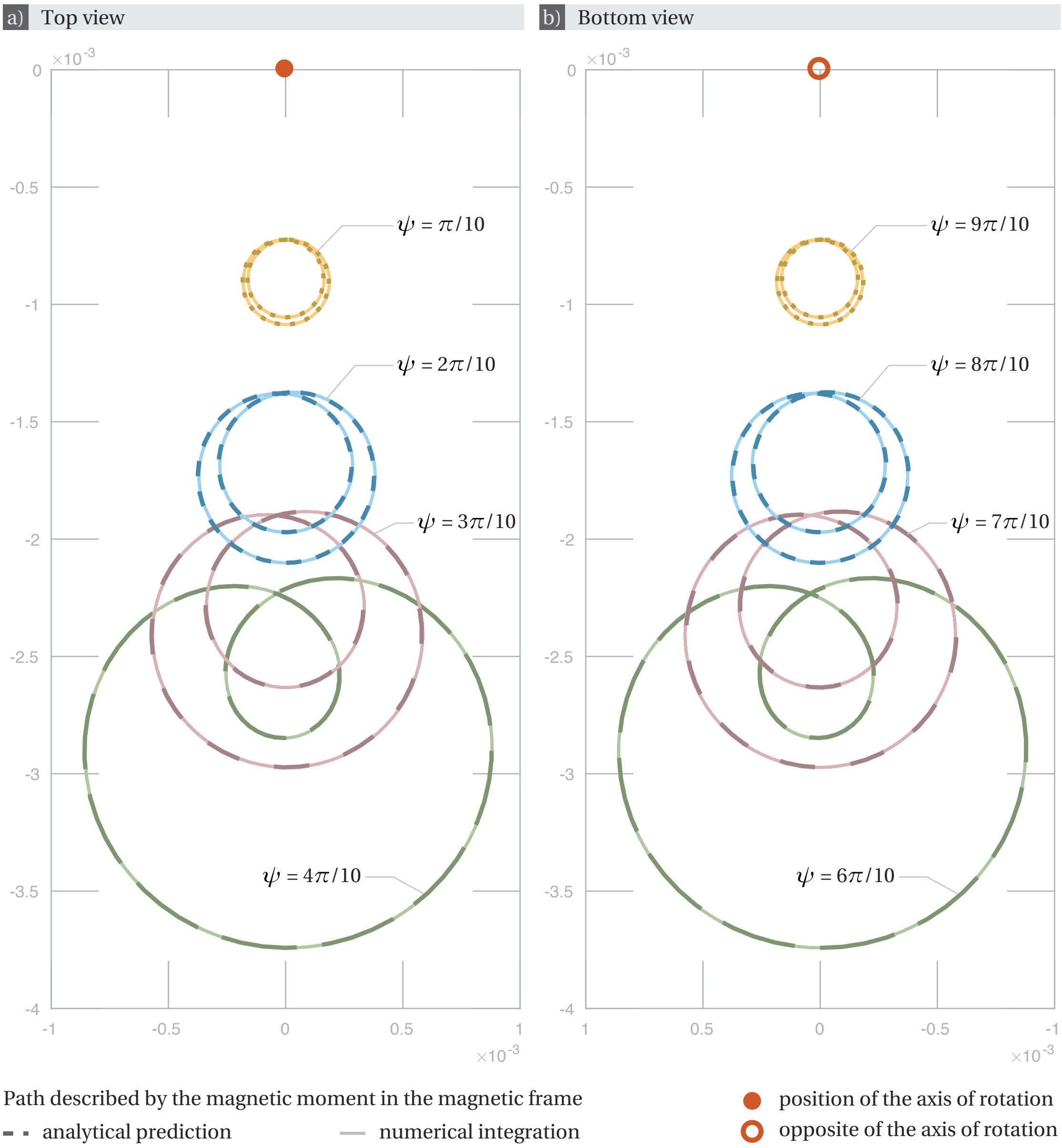

Figure 6.50 – **Swimmer D: comparison between numerics and analysis in the regime of large Mason number**. Trajectories described by the magnetic moment in the magnetic frame for $a = 10$ and several values of ψ. The analytical predictions are computed using first order expansion. The views correspond to projections on the planes tangent to the unit sphere at (a) $\mathbf{e}_3$ and (b) $-\mathbf{e}_3$.

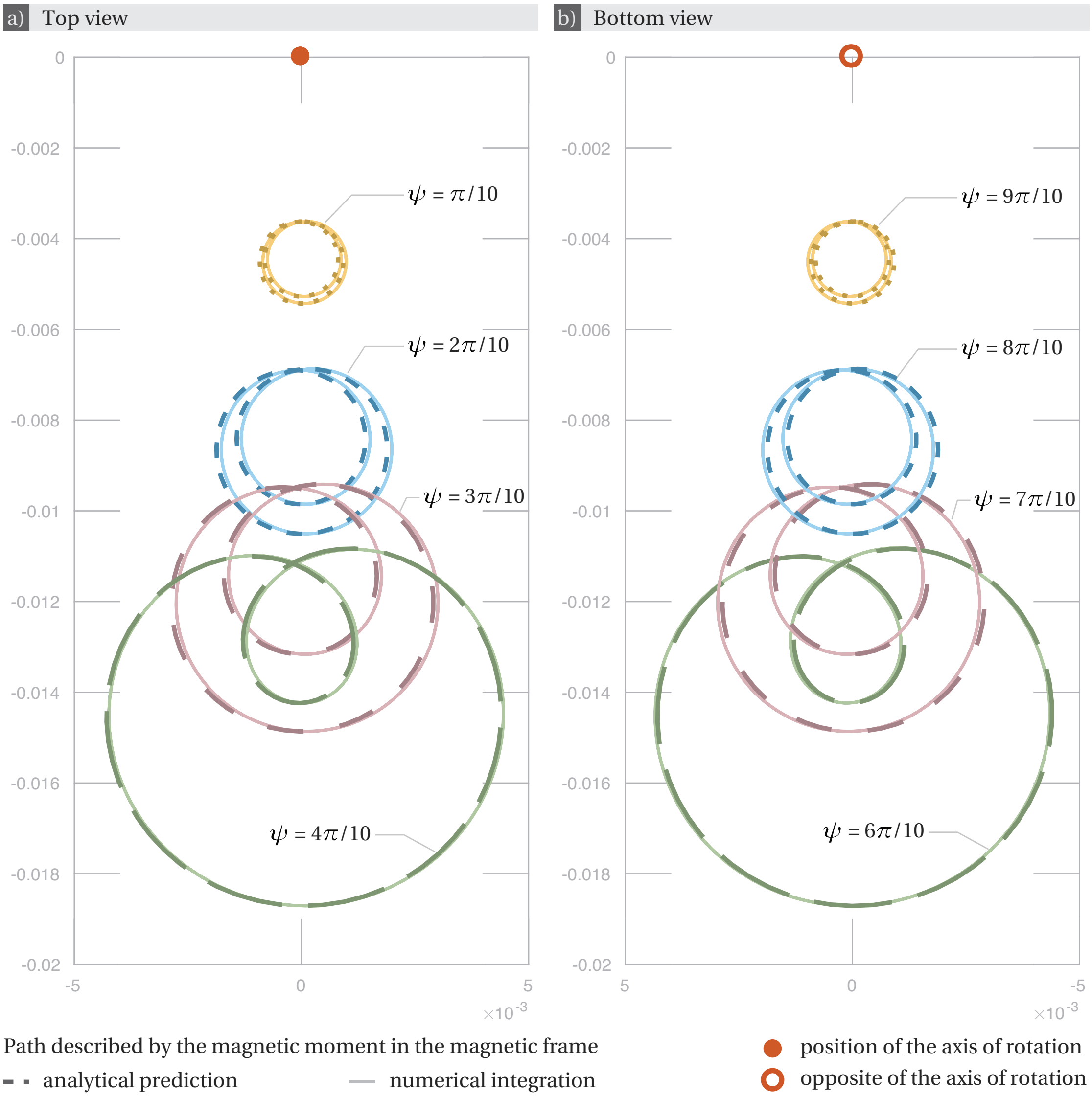

Figure 6.51 – **Swimmer D: comparison between numerics at $a = 2$ and analytical prediction for large Mason numbers**. Trajectories described by the magnetic moment in the magnetic frame for $a = 2$ and several values of ψ. The analytical predictions are computed using first order expansion. The views correspond to projections on the planes tangent to the unit sphere at (a) $\mathbf{e}_3$ and (b) $-\mathbf{e}_3$. Note that the prediction is still remarkably accurate, even though $a = 2$ is too small to fit in the scope of the analysis carried out in chapter 5.

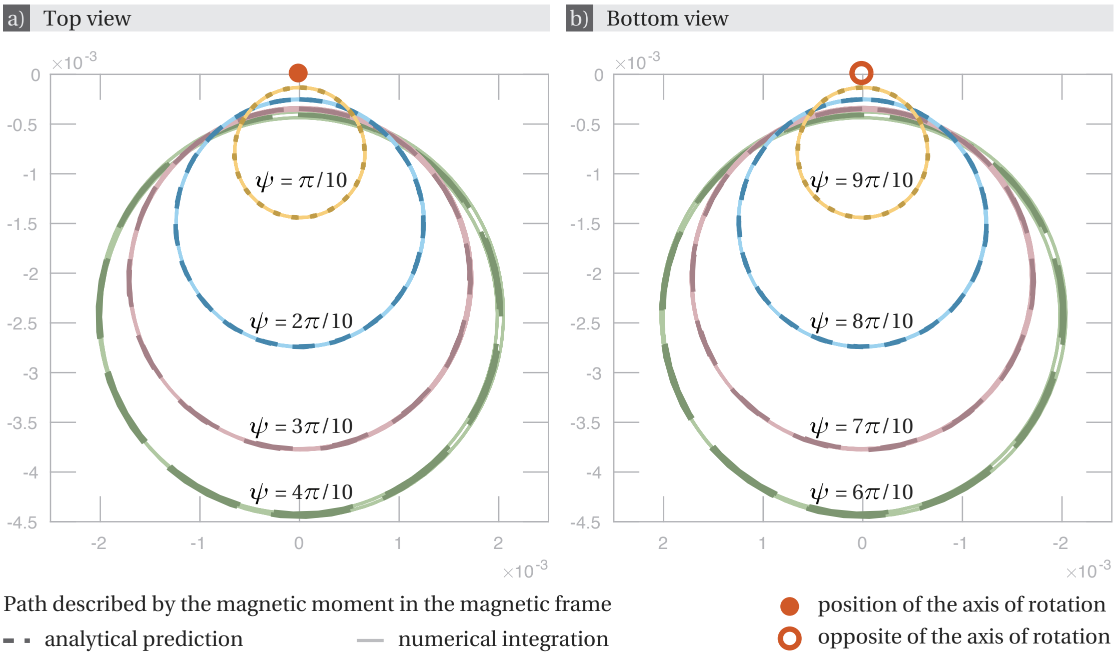

Figure 6.52 – **Swimmer E: comparison between numerics and analysis in the regime of large Mason number**. Trajectories described by the magnetic moment in the magnetic frame for $a = 100$ and several values of ψ. The analytical predictions are computed using first order expansion. The views correspond to projections on the planes tangent to the unit sphere at (a) $\mathbf{e}_3$ and (b) $-\mathbf{e}_3$.

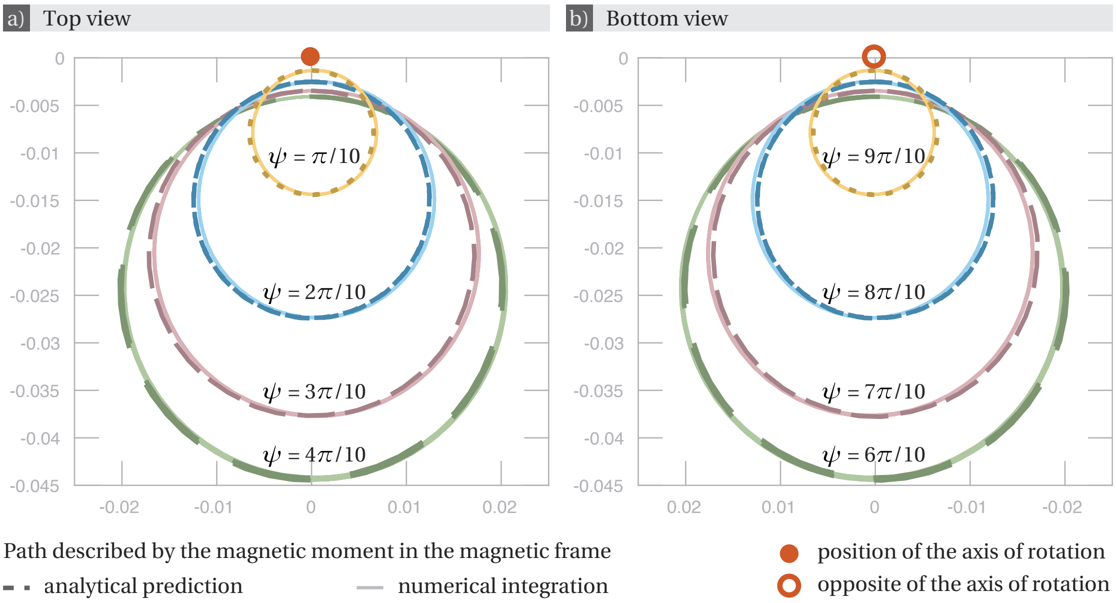

a) Top view

b) Bottom view

Figure 6.53 – **Swimmer E: comparison between numerics and analysis in the regime of large Mason number**. Trajectories described by the magnetic moment in the magnetic frame for $a = 10$ and several values of ψ. The analytical predictions are computed using first order expansion. The views correspond to projections on the planes tangent to the unit sphere at (a) $\mathbf{e}_3$ and (b) $-\mathbf{e}_3$.

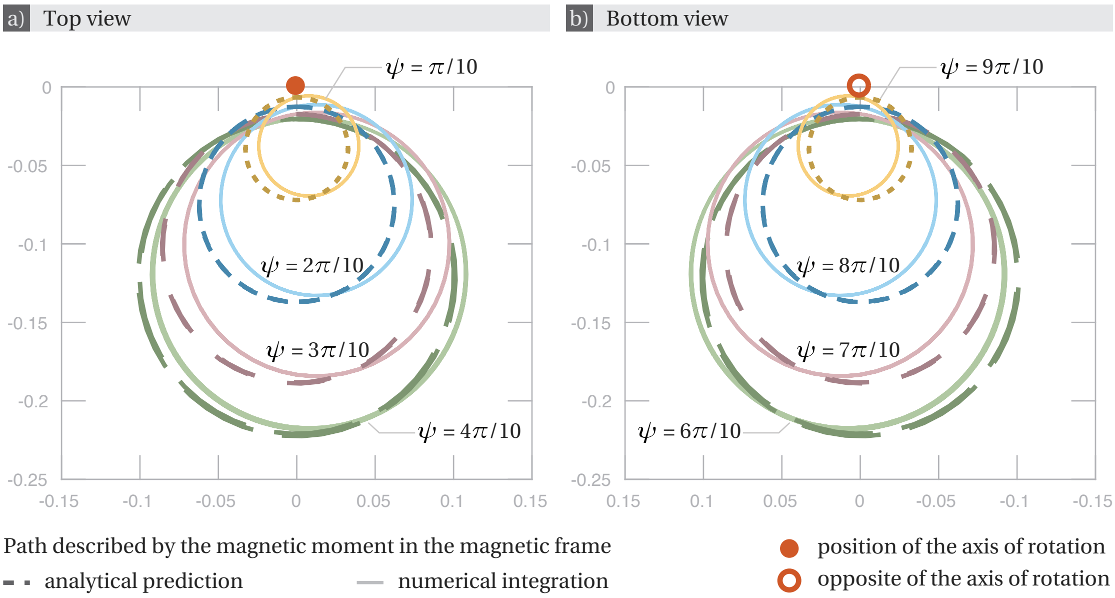

Figure 6.54 – **Swimmer E: comparison between numerics at $a = 2$ and analytical prediction for large Mason numbers**. Trajectories described by the magnetic moment in the magnetic frame for $a = 2$ and several values of ψ. The analytical predictions are computed using first order expansion. The views correspond to projections on the planes tangent to the unit sphere at (a) $\mathbf{e}_3$ and (b) $-\mathbf{e}_3$. Note that $a = 2$ is below the scope of the analysis presented in chapter 5. However, the prediction is still in good agreement with the numerics.

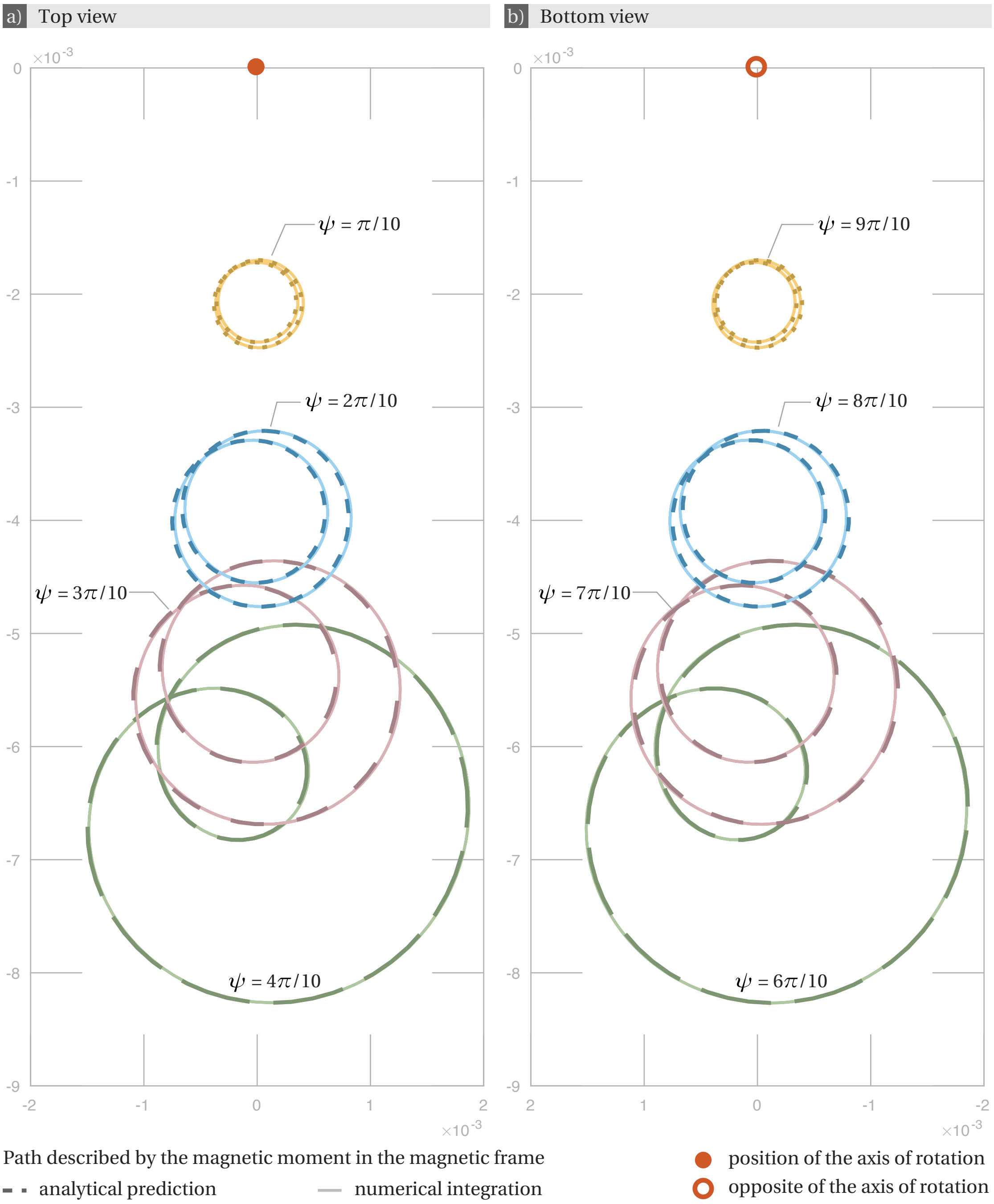

Figure 6.55 – **Swimmer F: comparison between numerics and analysis in the regime of large Mason number**. Trajectories described by the magnetic moment in the magnetic frame for $a = 100$ and several values of ψ. The analytical predictions are computed using first order expansion. The views correspond to projections on the planes tangent to the unit sphere at (a) $\mathbf{e}_3$ and (b) $-\mathbf{e}_3$.

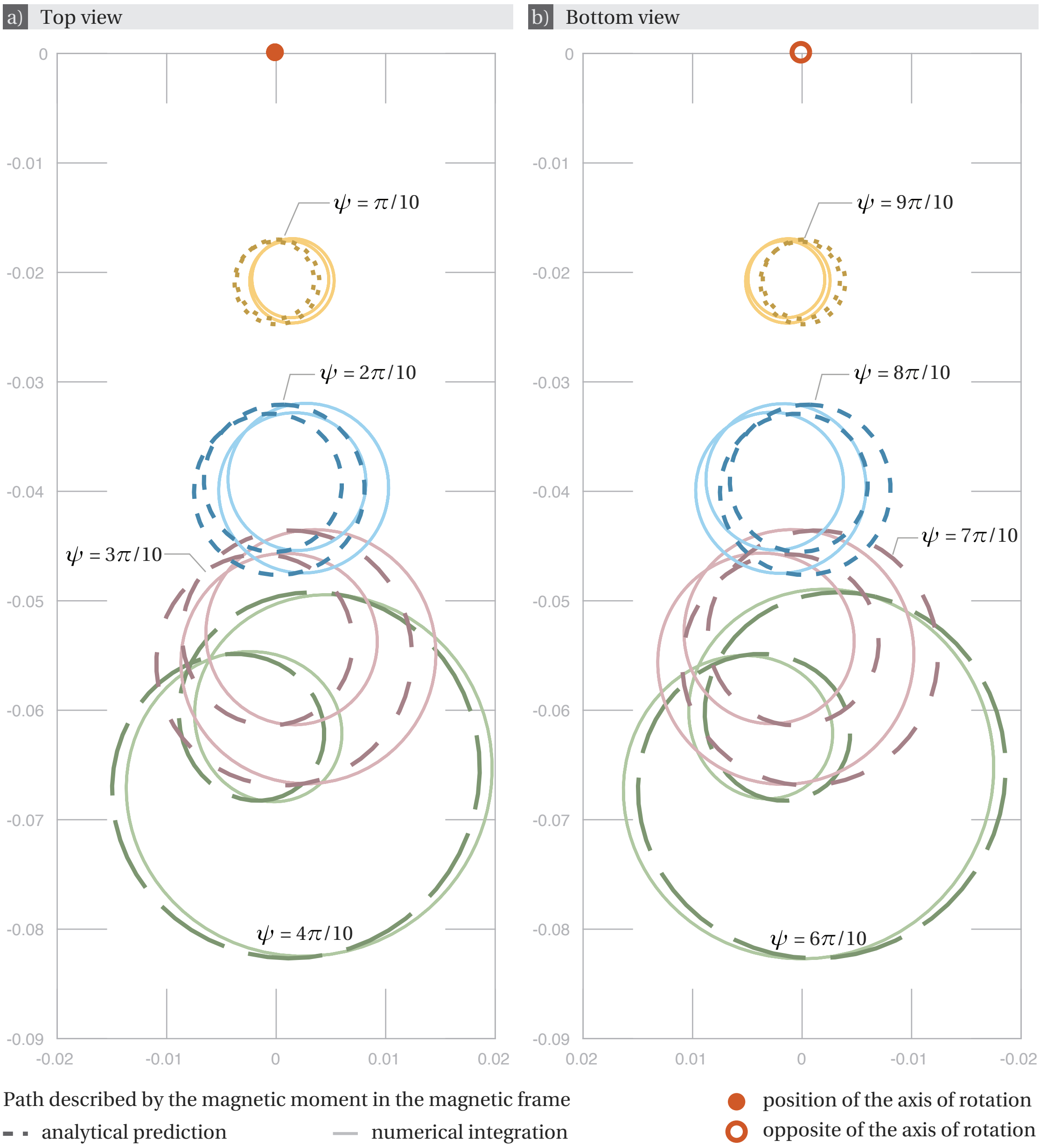

Figure 6.56 – **Swimmer F: comparison between numerics and analysis in the regime of large Mason number**. Trajectories described by the magnetic moment in the magnetic frame for $a = 10$ and several values of ψ. The analytical predictions are computed using first order expansion. The views correspond to projections on the planes tangent to the unit sphere at (a) $\mathbf{e}_3$ and (b) $-\mathbf{e}_3$.

6.3.3 Small Conical Angle

The small $\sin\psi$ regime is displayed in figure 6.57 for swimmer A, figure 6.58 for swimmer B, figure 6.60 for swimmer B', figure 6.62 for swimmer C, figure 6.64 for swimmer D, figure 6.65 for swimmer E, and figure 6.67 for swimmer F.

As for the limit of asymptotically large Mason number in the previous section, the comparisons are illustrated by displaying trajectories described by the magnetic moment $\mathbf{m}$ in the magnetic frame in which $\mathbf{B}$ is constant, as obtained analytically (cf. section 5.3.2) and by direct numerical integration of equation (3.14) with the integrator ode45 in MATLAB [87] with absolute tolerance set to 10^{-8}, relative tolerance to 10^{-6} and default values for all other integration parameters.

Figures 6.58 and 6.60 show a comparison between first and second order approximations for swimmers B and B', and $\psi = 0.1$. The circles predicted as a first order approximation (cf. section 5.3.2) give a good estimate of the trajectories, and the second order prediction (5.48) virtually overlaps the numerical solutions.

For each swimmer, values of ψ lying outside the scope of the asymptotic expansion of section 5.3 are also explored in figures 6.57c, 6.59, 6.61, 6.63, 6.64b, 6.66, and 6.67b. The curves described by $\mathbf{m}$ in the magnetic frame have a qualitatively similar behaviour, with a mean position moving from $\mathbf{B}$ to $\mathbf{e}_3$ as a increases, and a decreasing amplitude in both the low and large a limits. This is consistent with the asymptotic expansions in low and large a presented in sections 5.1 and 5.2.

a) $\psi = 0.01$ (first order approximation)

b) $\psi = 0.1$ (first order approximation)

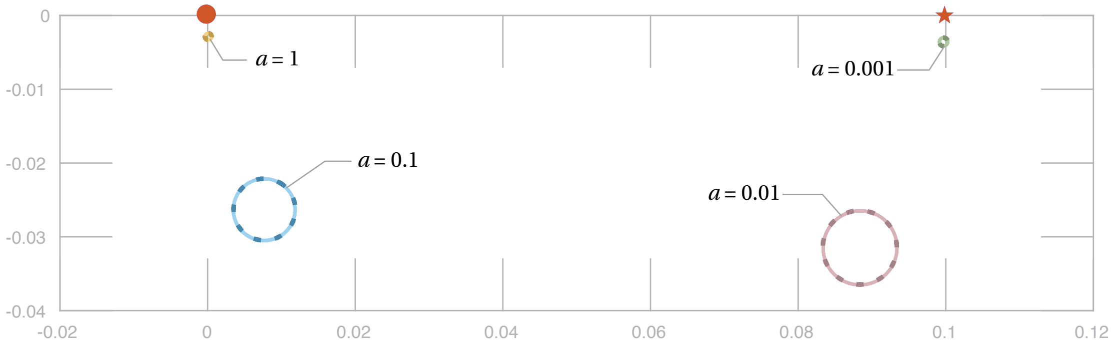

c) $\psi = \pi/6$ (second order approximation)

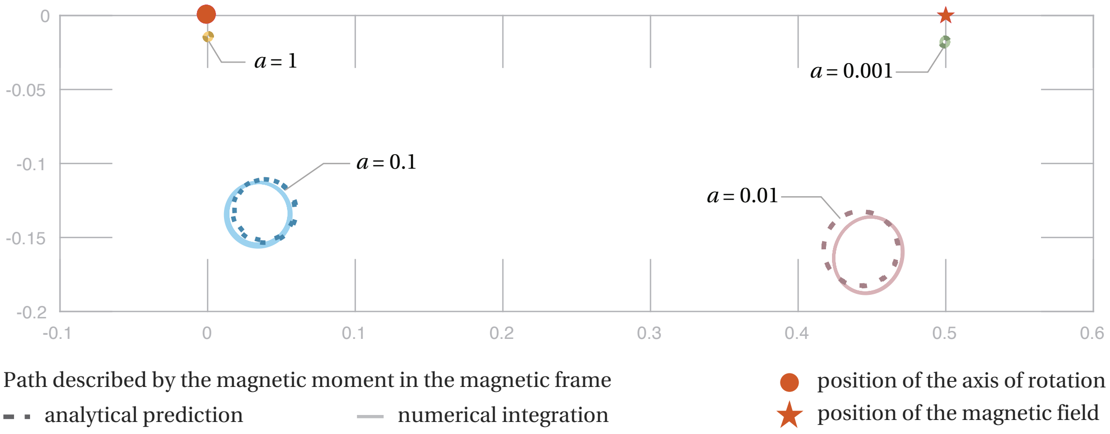

Figure 6.57 – **Swimmer A: comparison between numerics and analysis in the regime of small conical angle**. Trajectories described by the magnetic moment in the magnetic frame for (a) $\psi = 0.01$, (b) $\psi = 0.1$, (c) $\psi = \pi/6$ and several values of a. The views correspond to projections on the planes tangent to the unit sphere at $\mathbf{e}_3$. Note that $\pi/6$ is beyond the scope of the analysis carried out in chapter 5, and yet the prediction is still in good agreement with the numerics.

a) First order approximation

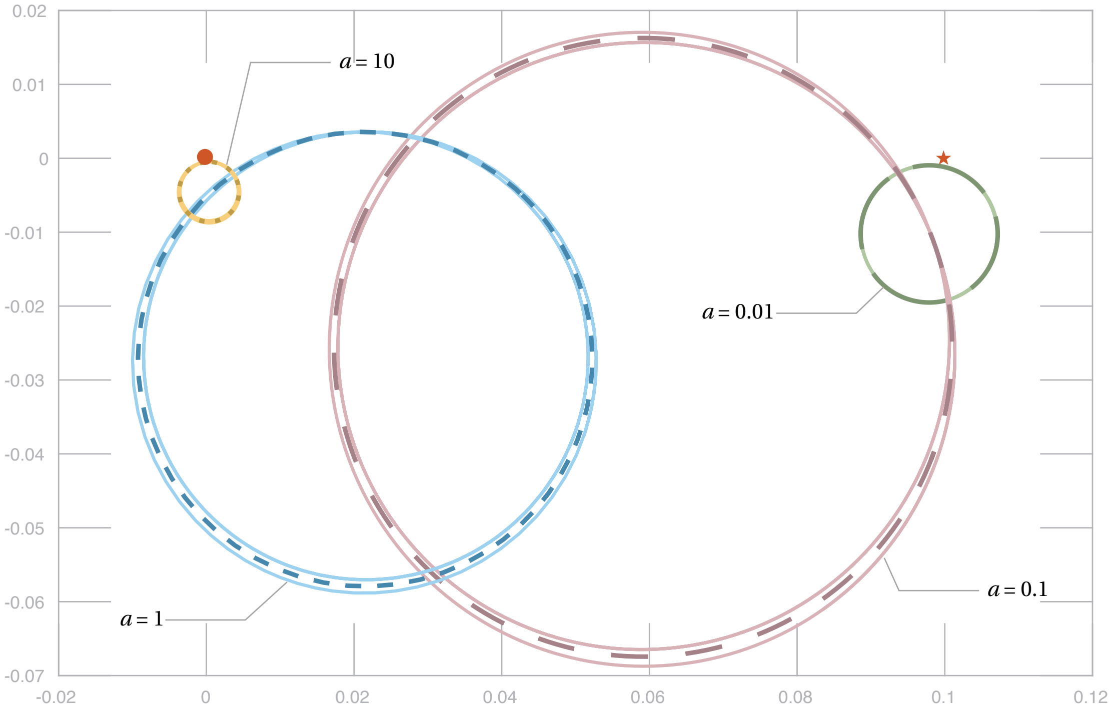

b) Second order approximation

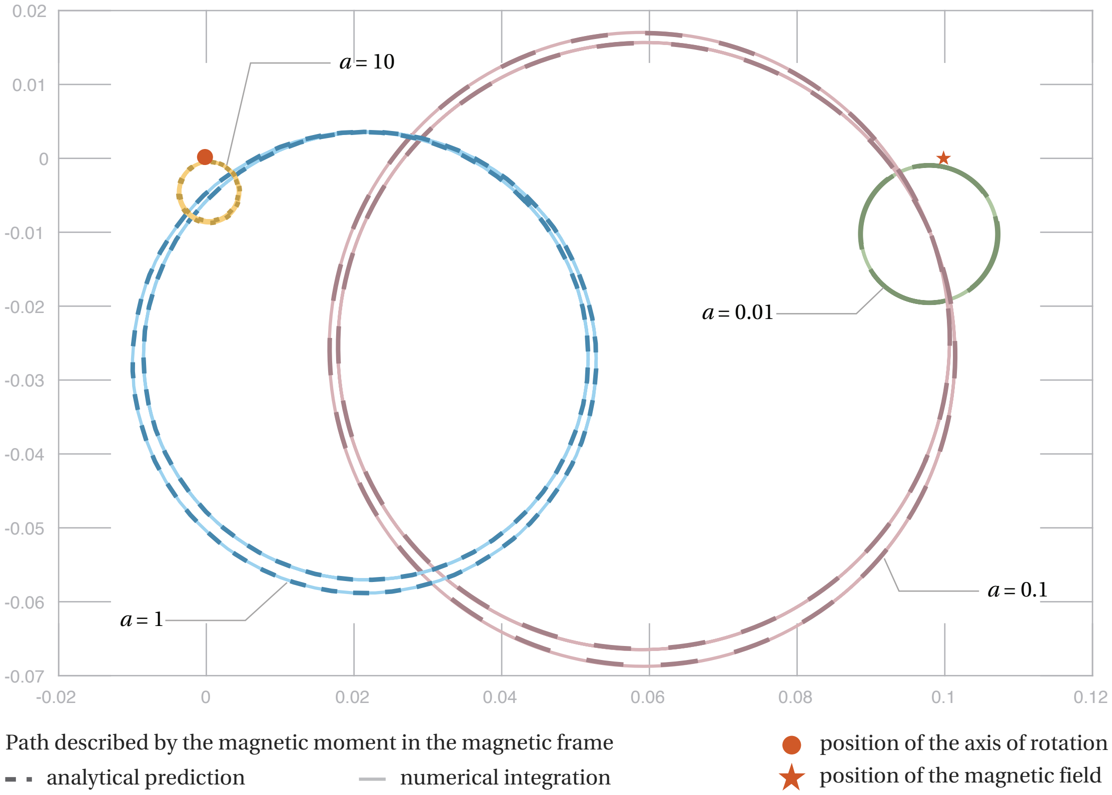

Figure 6.58 (previous page) – **Swimmer B: comparison between numerics and analysis in the regime of small conical angle**. Trajectories described by the magnetic moment in the magnetic frame for $\psi = 0.1$ and several values of a in the (a) first and (b) second order approximations. The views correspond to projections on the planes tangent to the unit sphere at $\mathbf{e}_3$.

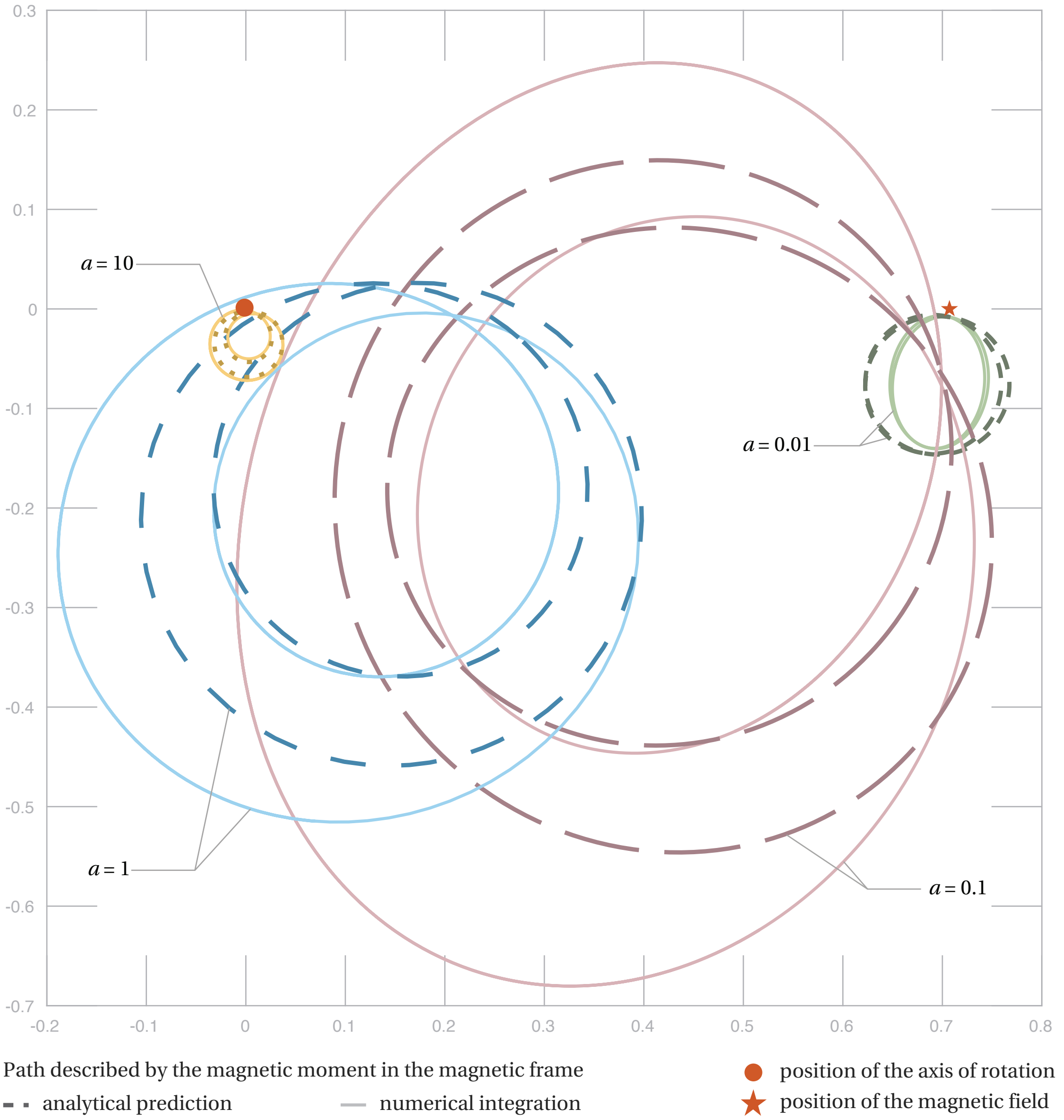

Figure 6.59 – **Swimmer B: comparison between numerics at $\psi = \pi/4$ and analytical prediction for small conical angles**. Trajectories described by the magnetic moment in the magnetic frame for $\psi = \pi/4$ and several values of a. The views correspond to projections on the planes tangent to the unit sphere at $\mathbf{e}_3$. Note that $\psi = \pi/4$ is beyond the scope of the analysis presented in chapter 5. However, the prediction is still in good qualitative agreement with the numerics.

a) First order approximation

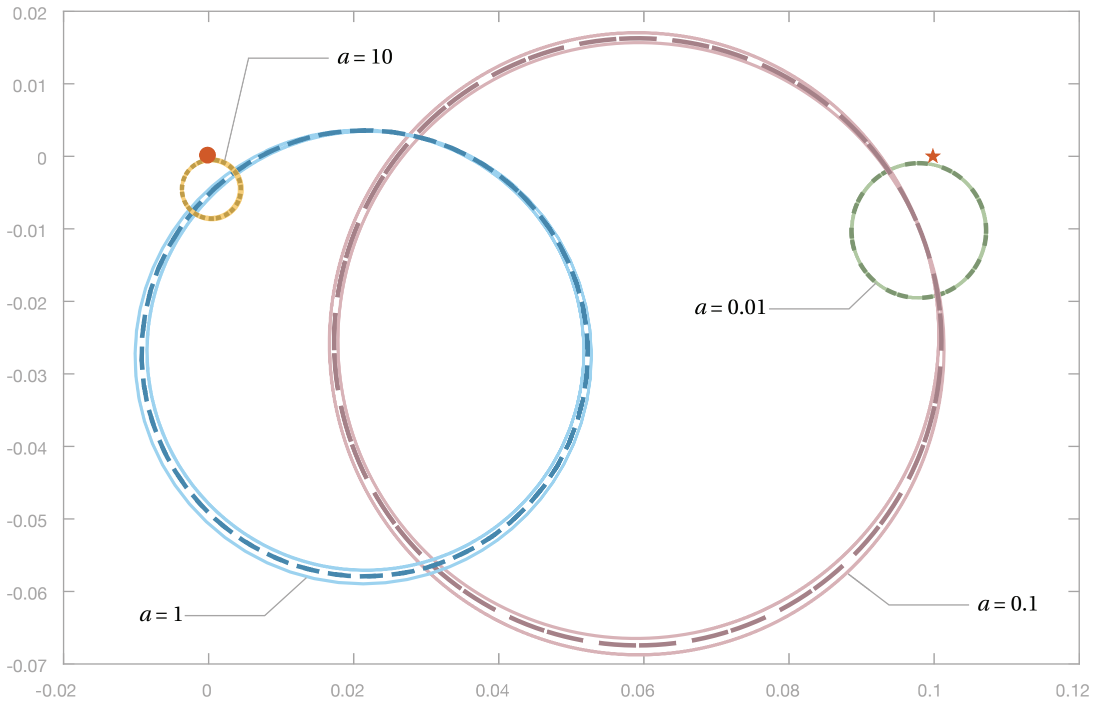

b) Second order approximation

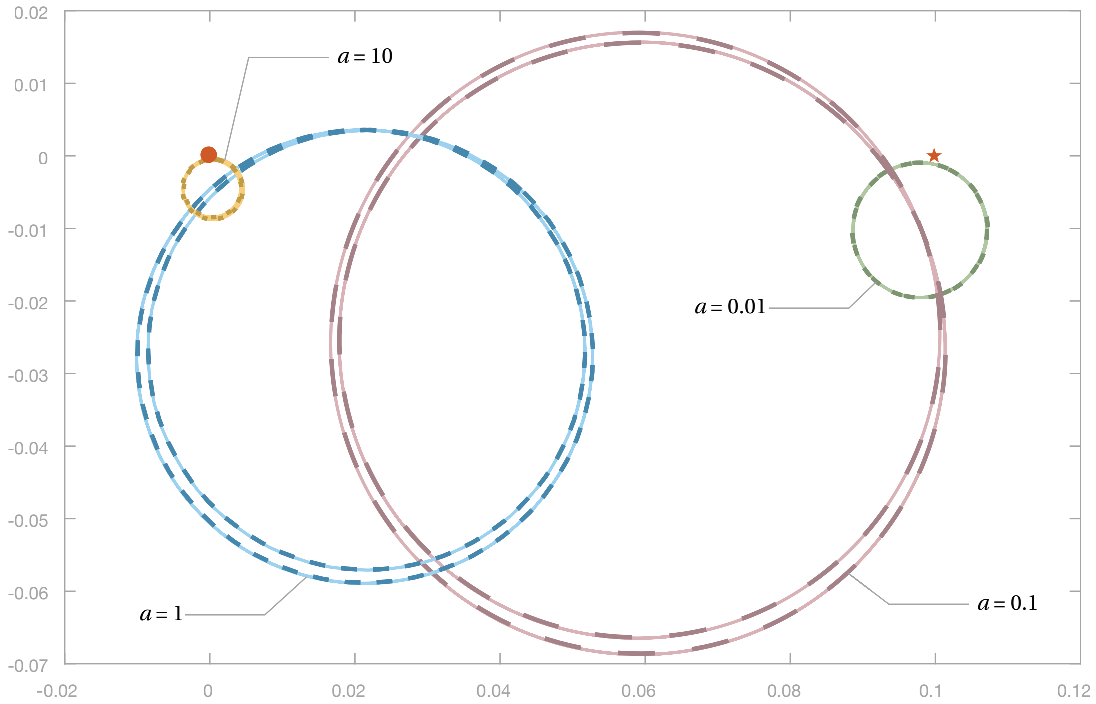

Path described by the magnetic moment in the magnetic frame

- - analytical prediction — numerical integration

● position of the axis of rotation

★ position of the magnetic field

Figure 6.60 (previous page) – **Swimmer B': comparison between numerics and analysis in the regime of small conical angle**. Trajectories described by the magnetic moment in the magnetic frame for $\psi = 0.1$ and several values of a in the (a) first and (b) second order approximations. The views correspond to projections on the planes tangent to the unit sphere at $\mathbf{e}_3$.

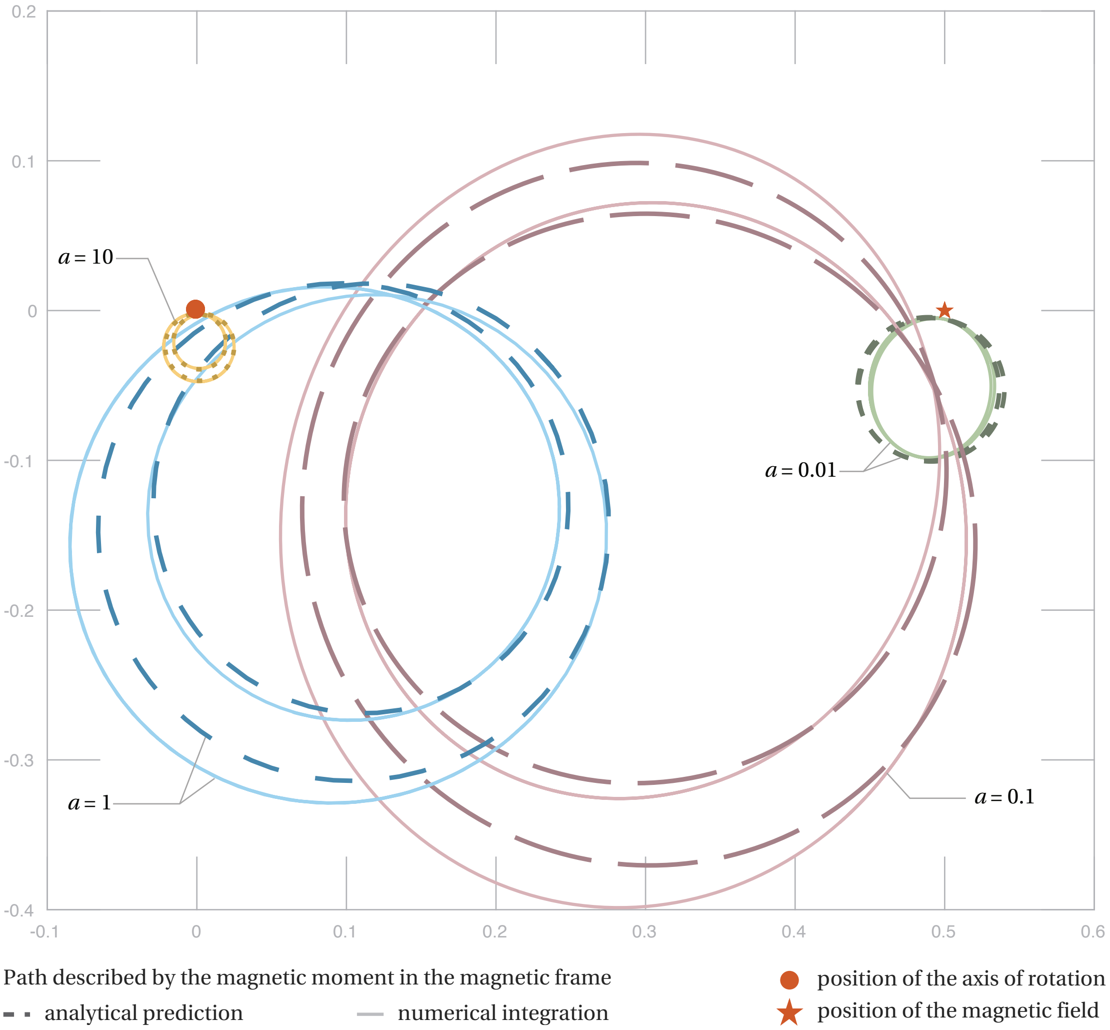

Figure 6.61 – **Swimmer B': comparison between numerics at $\psi = \pi/6$ and analytical prediction for small conical angles**. Trajectories described by the magnetic moment in the magnetic frame for $\psi = \pi/6$ and several values of a. The views correspond to projections on the planes tangent to the unit sphere at $\mathbf{e}_3$. Note that $\psi = \pi/6$ does not fit in the scope of the analysis presented in chapter 5, and yet the prediction is still quite accurate.

a) $\psi = 0.01$ (first order approximation)

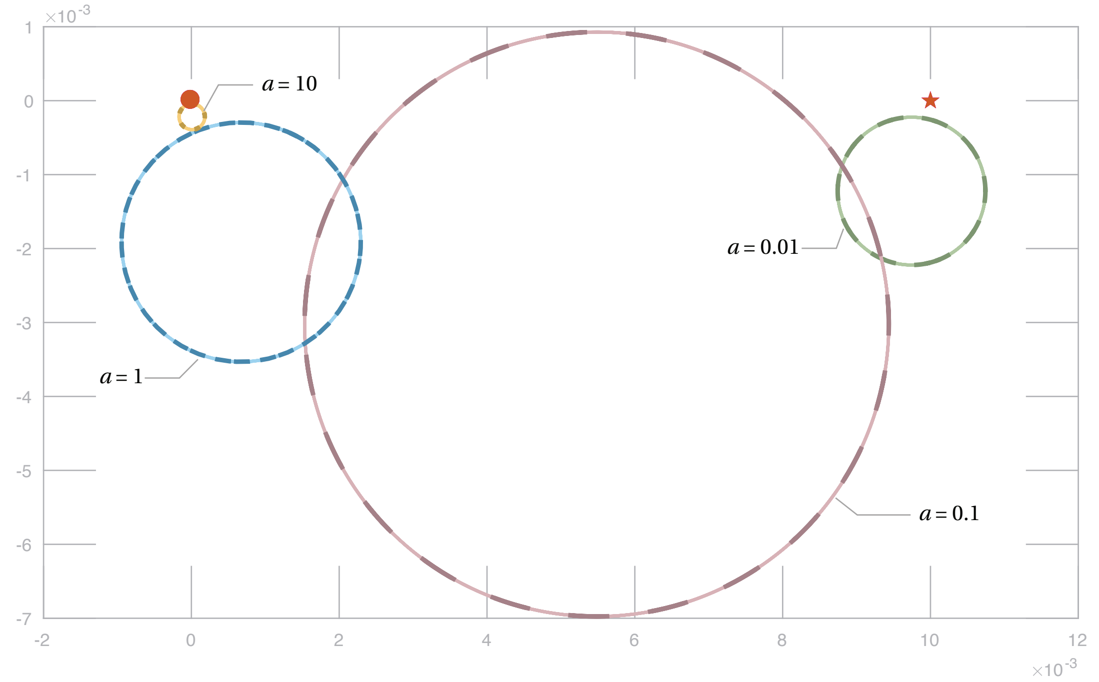

b) $\psi = 0.1$ (first order approximation)

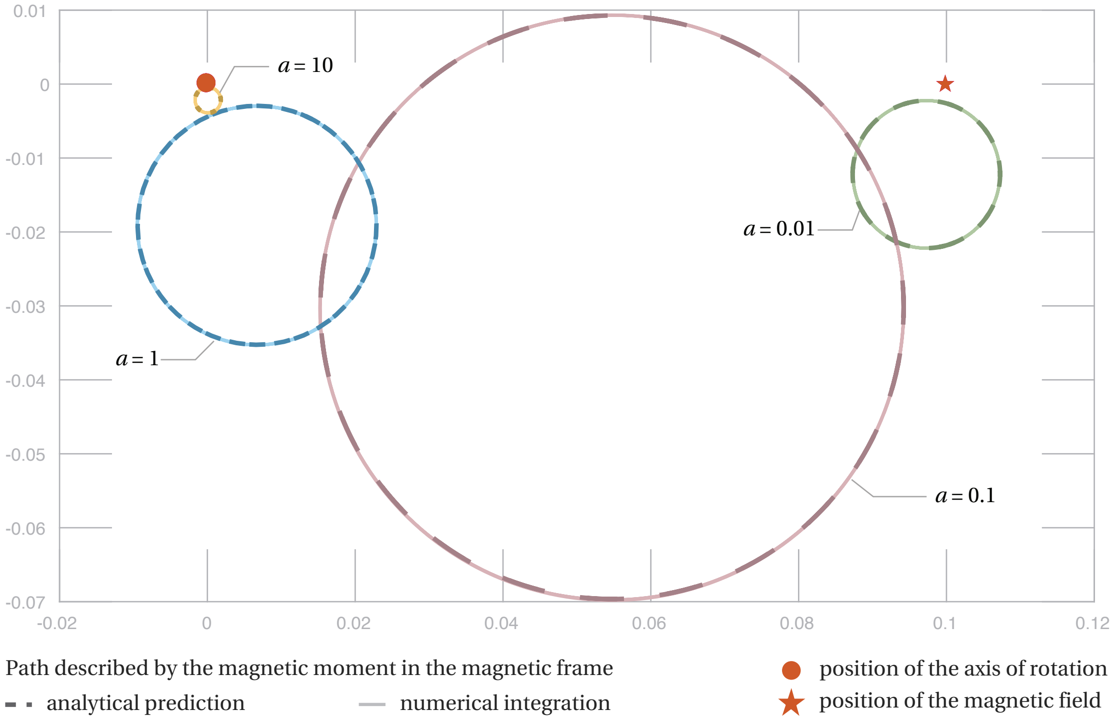

Figure 6.62 – **Swimmer C: comparison between numerics and analysis in the regime of small conical angle**. Trajectories described by the magnetic moment in the magnetic frame for (a) $\psi = 0.01$ and (b) $\psi = 0.1$, and several values of a. The views correspond to projections on the planes tangent to the unit sphere at $\mathbf{e}_3$.

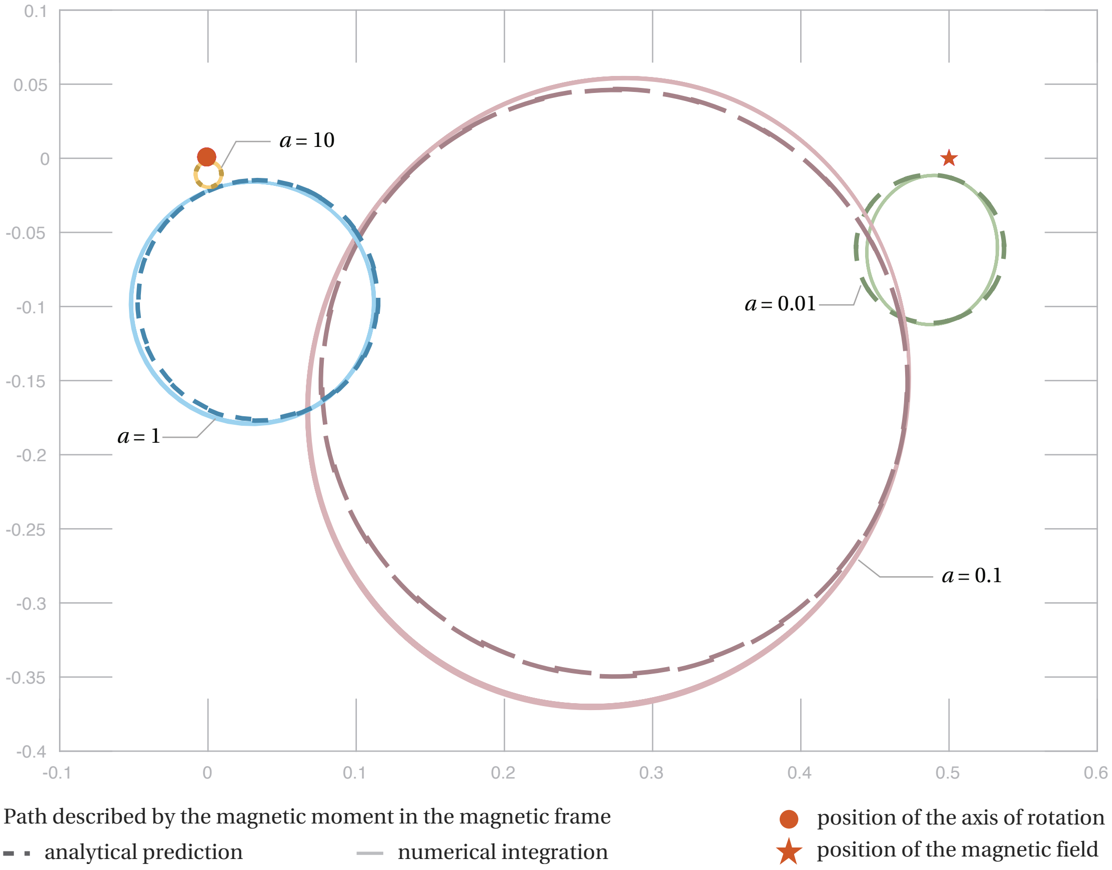

Figure 6.63 – **Swimmer C: comparison between numerics at $\psi = \pi/6$ and analytical prediction for small conical angles**. Trajectories described by the magnetic moment in the magnetic frame for $\psi = \pi/6$ and several values of a. The views correspond to projections on the planes tangent to the unit sphere at $\mathbf{e}_3$. Note that $\psi = \pi/6$ does not fit in the scope of the analysis presented in chapter 5, and yet the prediction is still quite accurate.

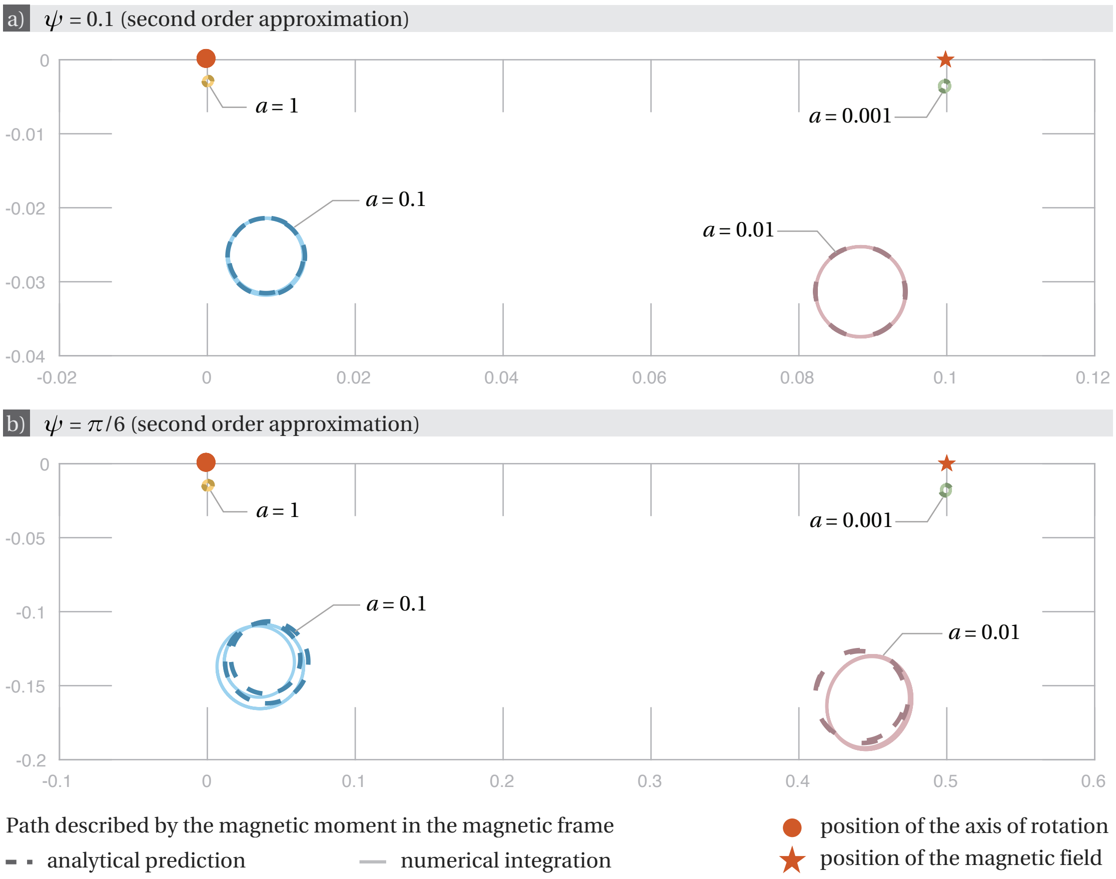

Figure 6.64 – **Swimmer D: comparison between numerics and analysis in the regime of small conical angle**. Trajectories described by the magnetic moment in the magnetic frame for (a) $\psi = 0.1$ and (b) $\psi = \pi/6$, and several values of a. The views correspond to projections on the planes tangent to the unit sphere at $\mathbf{e}_3$. Note that $\psi = \pi/6$ is beyond the scope of the analysis carried out in chapter 5 and yet the prediction is still in good qualitative agreement with the numerical computation.

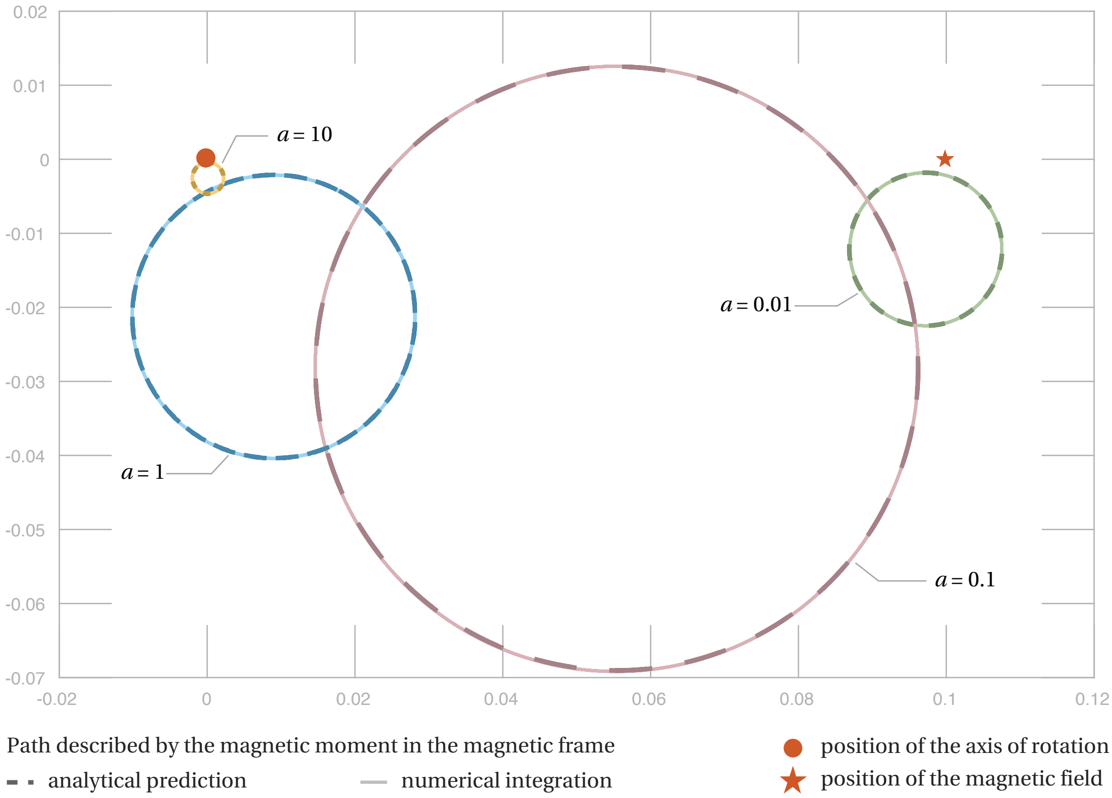

Figure 6.65 – **Swimmer E: comparison between numerics and analysis in the regime of small conical angle**. Trajectories described by the magnetic moment in the magnetic frame for $\psi = 0.1$ and several values of a. The views correspond to projections on the planes tangent to the unit sphere at $\mathbf{e}_3$.

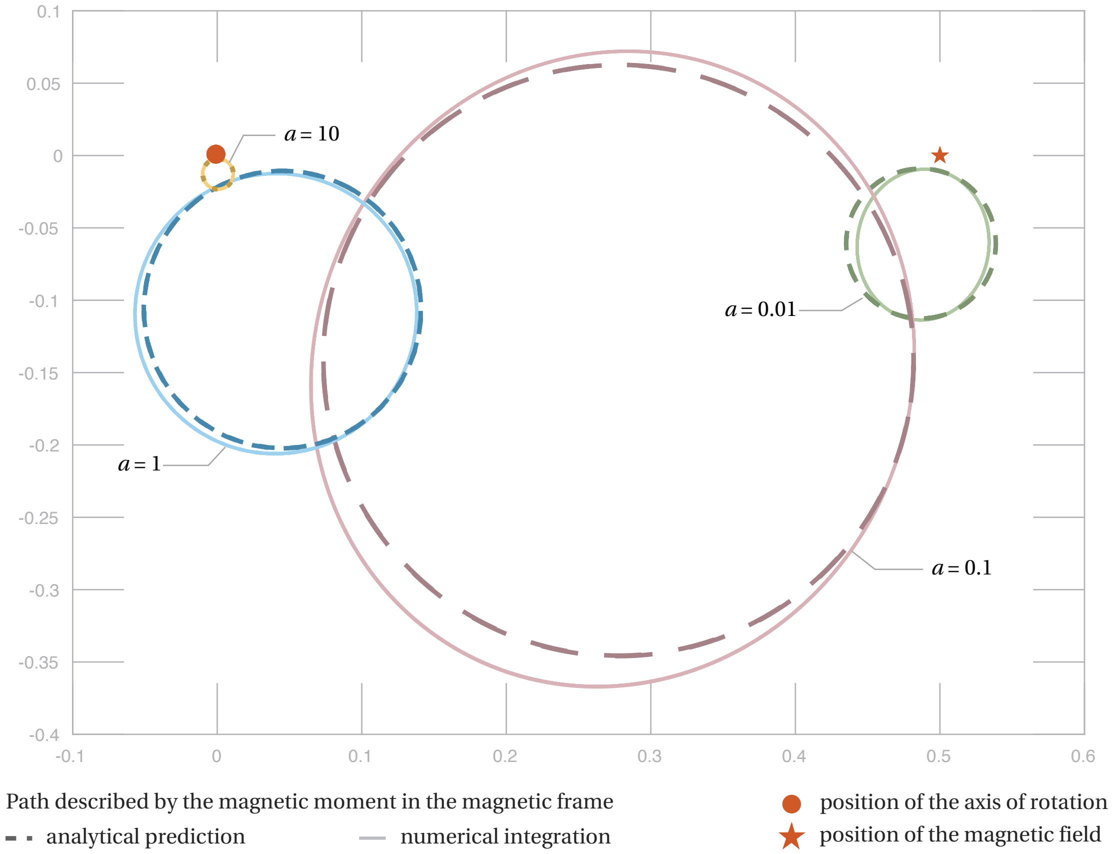

Figure 6.66 – **Swimmer E: comparison between numerics at $\psi = \pi/6$ and analytical prediction for small conical angles**. Trajectories described by the magnetic moment in the magnetic frame for $\psi = \pi/6$ and several values of a. The views correspond to projections on the planes tangent to the unit sphere at $\mathbf{e}_3$. Note that $\psi = \pi/6$ does not fit in the scope of the analysis presented in chapter 5, and yet the prediction is still quite accurate.

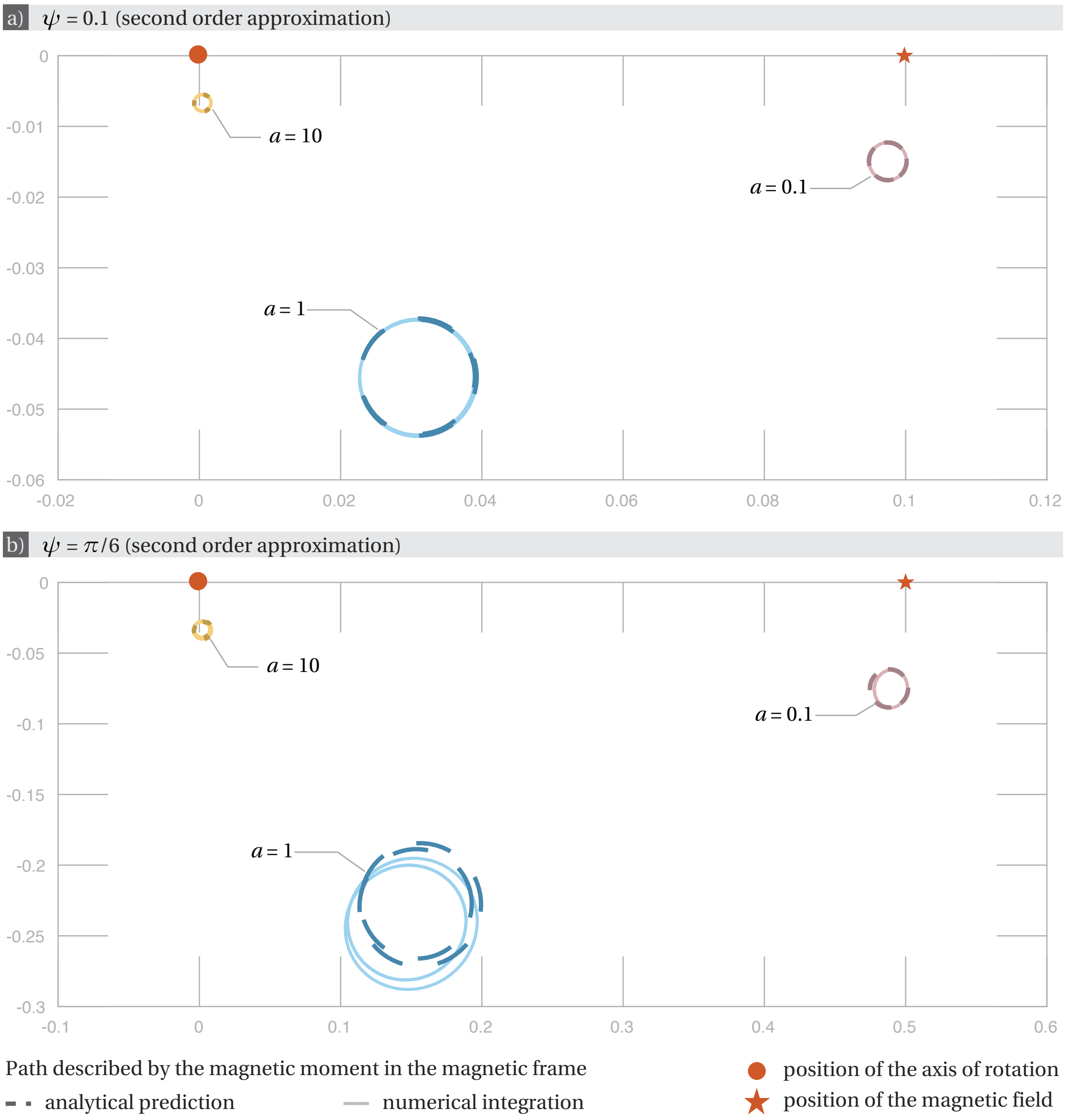

Figure 6.67 – **Swimmer F: comparison between numerics and analysis in the regime of small conical angle**. Trajectories described by the magnetic moment in the magnetic frame for (a) $\psi = 0.1$ and (b) $\psi = \pi/6$, and several values of a. The views correspond to projections on the planes tangent to the unit sphere at $\mathbf{e}_3$. Note that $\psi = \pi/6$ is beyond the scope of the analysis carried out in chapter 5 and yet the prediction is still in good qualitative agreement with the numerical computation.

7 Reconstructing the Translational Motion

Recall that the outer-layer dynamics of the swimmer considered are entirely prescribed by its trajectory $\boldsymbol{x}$, and its orientation R satisfying the system of equations

$$\dot{\boldsymbol{x}} = R^T \mathbf{v}\,, \tag{3.1a}$$

$$\mathbf{v} = \mathsf{M}_{12}\,[\mathbf{m}\times]\,\mathbf{B}\,, \tag{3.1b}$$

$$R = R_3(a\,t)\,Q^T\,, \tag{7.1}$$

$$\dot{Q} = [(a\mathbf{e}_3 - \boldsymbol{\omega})\times]\,Q\,, \tag{3.6a}$$

$$\boldsymbol{\omega} = \mathsf{M}_{22}\,[\mathbf{m}\times]\,\mathbf{B}\,, \tag{3.1d}$$

$$\mathbf{e}_3 = Q\begin{bmatrix} 0 \\ 0 \\ 1 \end{bmatrix}, \tag{3.6d}$$

$$\mathbf{B} = Q\begin{bmatrix} \sin\psi \\ 0 \\ \cos\psi \end{bmatrix}, \tag{3.6c}$$

where $\mathbf{v}$ and $\boldsymbol{\omega}$ are respectively the linear and angular velocities of the swimmer as expressed in the body frame, and $\mathbf{e}_3$ is the axis of rotation of the magnetic field $\mathbf{B}$, both expressed in the body frame.

In chapters 4-6, we have studied the rotational motion given by equations (3.6a, 3.1d, 3.6d, 3.6c). The translational motion can be deduced from it. Indeed, once $\boldsymbol{\omega}$ is specified, the trajectory $\boldsymbol{x}(t)$ is defined by the equation

$$\dot{\boldsymbol{x}}(t) \overset{(3.1a,\,3.1b)}{=} R^T\,\mathsf{M}_{12}\,[\mathbf{m}\times]\,\mathbf{B} \overset{(3.1d,\,3.4)}{=} R_3(a\,t)\,Q^T(t)\,\mathsf{M}_{12}\,\mathsf{M}_{22}^{-1}\,\boldsymbol{\omega}(t)\,.$$

This chapter characterises the trajectories followed by swimmers, first in relative equilibrium (sec. 7.1) and then for periodic solutions of the rotational dynamics (sec. 7.2). Finally, we present a few examples of trajectories obtained by numerical integration in section 7.3.

7.1 Helical Trajectories Corresponding to Relative Equilibria

Relative equilibrium trajectories are helical [88] (cf. fig. 7.1). This includes circles and straight lines as degenerate helices. Here, we show that the ability of a particular swimmer to exhibit circular, straight, or stationary trajectories, as well as the handedness of non-degenerate helical trajectories depends on the matrix $\mathsf{M}_{12}\,\mathsf{M}_{22}^{-1}$. Its symmetric part

$$\mathsf{C} = \frac{1}{2}\left(\mathsf{M}_{12}\,\mathsf{M}_{22}^{-1} + \mathsf{M}_{22}^{-1}\,\mathsf{M}_{12}^{T}\right) \tag{7.2}$$

will play a particular role,[1] as well as the orientation of the magnetic moment $\mathbf{m}$ in the rigid body of the swimmer with respect to the eigenvectors of $\mathsf{M}_{12}\,\mathsf{M}_{22}^{-1}$ and C. We will then discuss maximisation of the swimmer's velocity along the helical trajectory axis, which corresponds to the axis of rotation $\boldsymbol{e}_3$ of the magnetic field. This problem has been previously tackled by others [70]. It is presented here within the framework of this study. Note that a discussion on the relation between the magnetic moment direction and the axial velocity can also be found in [45].

By definition, trajectories corresponding to a relative equilibria have constant velocities $\mathbf{v}$ and $\boldsymbol{\omega}$ in the body frame and are therefore helical. Indeed, computing the curvature and torsion of the trajectory (3.1a) using the corresponding Frenet-Serret shows that they are constant, so that the trajectory is helical. The helix axis is along $\boldsymbol{\omega}$, and its pitch and radius can be computed in the following standard way.

The Frenet-Serret frame associated to trajectory $\boldsymbol{x}$ is $[\boldsymbol{n}, \boldsymbol{b}, \boldsymbol{t}]$, where $\boldsymbol{t}$ is the unit tangent to $\boldsymbol{x}$, i.e. $\boldsymbol{t} = \boldsymbol{v}/|\boldsymbol{v}|$, $\boldsymbol{n}$ is the principal normal to the curve, and $\boldsymbol{b}$ is the binormal, satisfying $\boldsymbol{b} = \boldsymbol{t} \times \boldsymbol{n}$. At relative equilibria, note that $|\boldsymbol{v}| = |\mathbf{v}|$ is constant, and that rescaling time as $T = |\mathbf{v}|\,t$ gives an arc-length parametrisation of the trajectory, allowing to compute the binormal as

$$\kappa\,\boldsymbol{n} = \frac{d}{dT}\boldsymbol{t} = \frac{1}{|\mathbf{v}|^2}\,\dot{\boldsymbol{v}} = \frac{1}{|\mathbf{v}|^2}\,\frac{d}{dt}(R\,\mathbf{v}) = \frac{1}{|\mathbf{v}|^2}\,R\,(\boldsymbol{\omega} \times \mathbf{v}),$$

where the dot denotes the derivative with respect to t, $\boldsymbol{n}$ is a unit vector, and κ is the curvature

---

[1] The matrix C is called the chirality matrix by Morozov et al. [70].

Figure 7.1 (next page) – **Swimmer A: equilibrium trajectory with parameters** $a = 0.02$ **and** $\cos\psi = 0.1$. (a-c) Helical trajectory in the lab frame. The corresponding non-dimensional pitch is $p = 0.1554$, and the corresponding radius $r = 5.4378 \cdot 10^{-3}$. The resulting non-dimensional axial velocity is $v_{\mathrm{ax}} = 4.9474 \cdot 10^{-4}$. The swimmer has been scaled so that the details of the trajectory remain visible: in actual proportions, the swimmer would be 368 times bigger. The proportions of the trajectory itself are respected. The width and depth of the plot box in panel (a) correspond to the axes dimensions of panel (c). (d) Orientation of the magnetic moment in the body frame. (e) Orientation of the swimmer in the magnetic frame. (f) Quaternion components of the corresponding rotational dynamics as functions of time: since the trajectory is a relative equilibrium, the components are constant.
This relative equilibrium is the only stable one that swimmer A admits for these parameter values (regime 1/4). The phase portrait of the corresponding rotational dynamics is shown in fig. 4.11.
To see the swimmer in motion, click here (password: thesisPR) or scan the barcode.

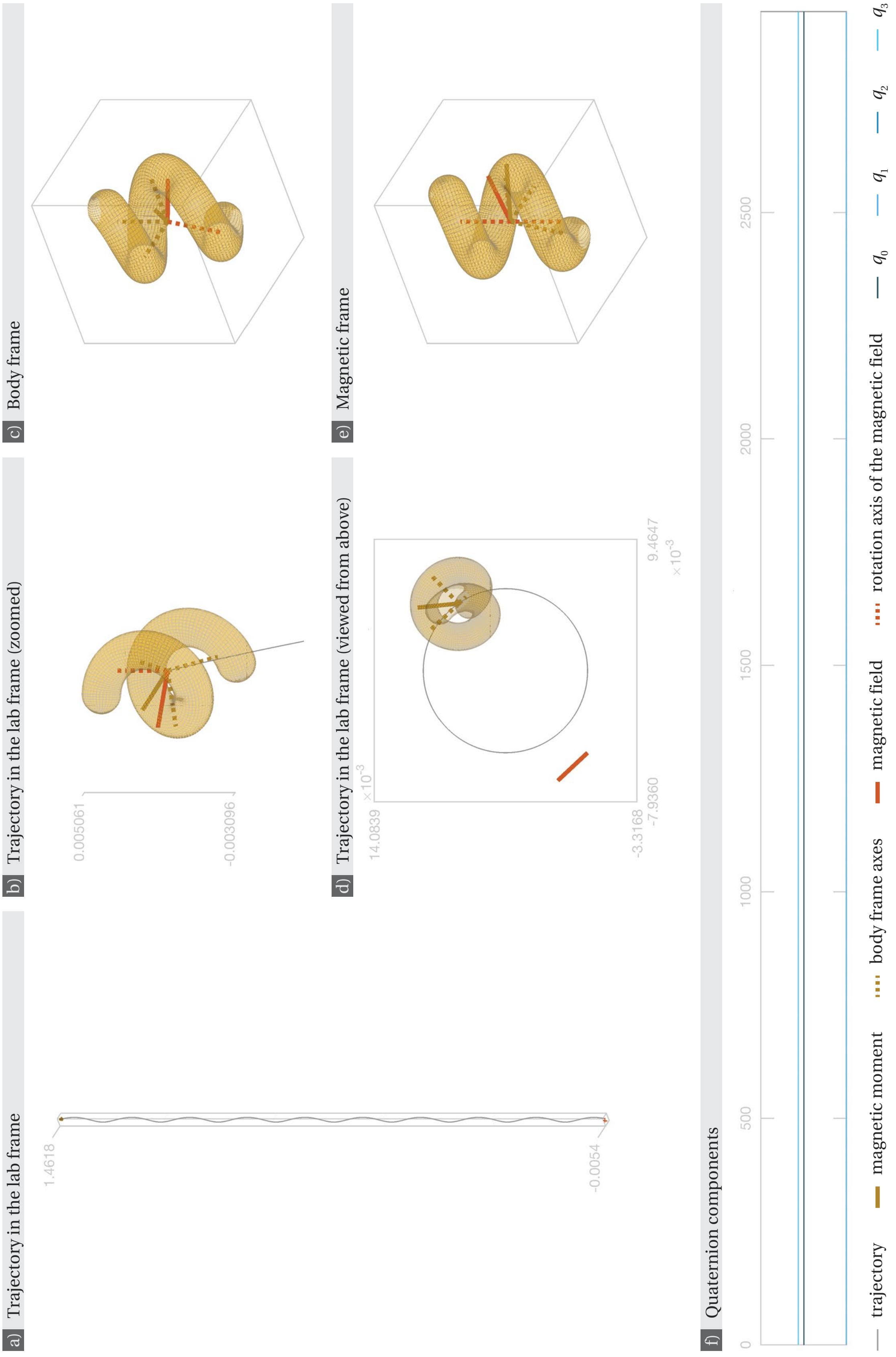
a) Trajectory in the lab frame

b) Trajectory in the lab frame (zoomed)

c) Body frame

d) Trajectory in the lab frame (viewed from above)

e) Magnetic frame

f) Quaternion components

of the trajectory, implying

$$\kappa = \frac{|\boldsymbol{\omega} \times \mathbf{v}|}{|\mathbf{v}|^2}\,, \qquad\qquad \boldsymbol{n} = \frac{R\,(\boldsymbol{\omega} \times \mathbf{v})}{|\boldsymbol{\omega} \times \mathbf{v}|}\,.$$

Using $\boldsymbol{b} = \boldsymbol{t} \times \boldsymbol{n}$ allows to compute

$$\boldsymbol{b} = \frac{1}{|\mathbf{v}|\,|\boldsymbol{\omega} \times \mathbf{v}|}\, R\big(\mathbf{v} \times (\boldsymbol{\omega} \times \mathbf{v})\big)\,,$$

so that the Frenet-Serret equation $-\tau\,\boldsymbol{n} = d\boldsymbol{b}/dT$, where τ is the torsion of the trajectory, becomes

$$-\tau\,\boldsymbol{n} = \frac{1}{|\mathbf{v}|^2\,|\boldsymbol{\omega} \times \mathbf{v}|}\,\frac{d}{dt}\Big(R\big(\mathbf{v} \times (\boldsymbol{\omega} \times \mathbf{v})\big)\Big) = -\frac{1}{|\mathbf{v}|^2\,|\boldsymbol{\omega} \times \mathbf{v}|}\,R\big(\boldsymbol{\omega} \times \mathbf{v}\,(\mathbf{v} \cdot \boldsymbol{\omega})\big) = -\frac{\mathbf{v} \cdot \boldsymbol{\omega}}{|\mathbf{v}|^2}\,\boldsymbol{n}\,.$$

Thus the curvature and torsion of the trajectory are

$$\kappa = \frac{|\boldsymbol{\omega} \times \mathbf{v}|}{|\mathbf{v}|^2}\,, \qquad\qquad \tau = \frac{\mathbf{v} \cdot \boldsymbol{\omega}}{|\mathbf{v}|^2}\,,$$

which are constant, so that the trajectory is helical. The pitch and radius are given in terms of curvature and torsion as (see for instance [89])

$$p = 2\pi\,\frac{\tau}{\kappa^2 + \tau^2}\,, \qquad\qquad r = \frac{\kappa}{\kappa^2 + \tau^2}\,,$$

which allows to find relations

$$p = \frac{2\pi}{|\boldsymbol{\omega}|^2}\,\boldsymbol{\omega} \cdot \mathbf{v} \qquad \text{and} \qquad r = \frac{1}{|\boldsymbol{\omega}|^2}\,|\boldsymbol{\omega} \times \mathbf{v}|\,. \tag{7.3}$$

Substituting the equilibrium condition

$$a\mathbf{e}_3 = \mathsf{P}\,\mathbf{B}\,, \tag{4.2}$$

where

$$\mathsf{P} = \mathsf{M}_{22}\,[\mathbf{m}\times]\,, \tag{3.8}$$

in the equations (3.1b, 3.1d) for $\mathbf{v}$ and $\boldsymbol{\omega}$ yields

$$\mathbf{v} = a\,\mathsf{M}_{12}\,\mathsf{M}_{22}^{-1}\,\mathbf{e}_3 \qquad\qquad \boldsymbol{\omega} = a\,\mathbf{e}_3\,. \tag{7.4}$$

Therefore a relative equilibrium trajectory is a helix of axis $\boldsymbol{e}_3$, and its pitch and radius are found by substituting (7.4) in (7.3) as

$$p = 2\pi\,\mathbf{e}_3 \cdot \mathsf{M}_{12}\,\mathsf{M}_{22}^{-1}\,\mathbf{e}_3 \qquad \text{and} \qquad r = \big|\mathbf{e}_3 \times \mathsf{M}_{12}\,\mathsf{M}_{22}^{-1}\,\mathbf{e}_3\big|\,. \tag{7.5}$$

From the analysis of relative equilibria proposed in chapter 4, at a relative equilibrium, the rotation axis $\mathbf{e}_3$ expressed in the body frame is constant, and is in the plane $\boldsymbol{\eta}_0^\perp = \left(\mathsf{M}_{22}^{-1}\,\mathbf{m}\right)^\perp$. From the parametrisation of relative equilibria (4.3), there exists and angle $\theta \in [0, 2\pi)$ such that

$$\mathbf{e}_3 = \cos\theta\,\boldsymbol{\eta}_1 + \sin\theta\,\boldsymbol{\eta}_2\,, \tag{4.3}$$

where $\boldsymbol{\eta}_1$ and $\boldsymbol{\eta}_2$ are right-singular vectors of the matrix P (cf. section 3.2). As a result, the pitch and radius (7.5) can be parametrised by θ, and do not depend on ϕ, the second parameter used to parametrise the set of relative equilibria (cf. chapter 4).

	p_{min}	p_{max}	r_{min}	r_{max}
swimmer A	−0.1042	0.1836	0.0054	0.0394
swimmer B	−0.0923	0.1916	0.0075	0.0474
swimmer B’	−0.1917	0.0923	0.0075	0.0475
swimmer C	−0.0382	0.1010	0.0046	0.0046
swimmer D	−0.2128	0.0512	0.0051	0.0480
swimmer E	−0.2622	0.0512	0.0278	0.1382
swimmer F	−0.0128	0.0307	0.1117	0.1903

Table 7.1 – **Ranges of pitches and radii of the helical trajectories** corresponding to the example swimmers presented in chapter 6. The pitch p and radius r of a helical trajectory corresponding to a relative equilibrium satisfy $p \in [p_{\text{min}}, p_{\text{max}}]$ and $r \in [r_{\text{min}}, r_{\text{max}}]$. All quantities are given in non-dimensional units. To obtain the dimensional equivalent, these numbers need to be multiplied by the gyration radius ℓ of the corresponding swimmer.

Table 7.1 gives the pitches and radii reached for relative equilibria corresponding to the the example swimmers presented in the previous chapter. Note that for swimmers A-D, the maximal radius is small compared to the pitch of maximal amplitude. We can therefore expect most helical trajectories to have small horizontal variation. For swimmers E, the radius of an equilibrium trajectory can reach values of the same magnitude as the extremal pitch, while for swimmer F, the radius can reach a larger magnitude than the pitch, suggesting trajectories with a large horizontal variation. The extremal values of pitches and radii are reached for stable relative equilibria in all these cases, except for swimmer C for which all stable relative equilibria have a positive pitch.

Positive pitches p correspond to right-handed helices, while negative pitches correspond to left-handed helices. Note that the pitch (7.5) can be rewritten as

$$p = 2\pi\,\mathbf{e}_3 \cdot \mathsf{C}\,\mathbf{e}_3\,, \tag{7.6}$$

where C is the symmetric part of $\mathsf{M}_{12}\,\mathsf{M}_{22}^{-1}$ (cf. (7.2)). The use of C rather than $\mathsf{M}_{12}\,\mathsf{M}_{22}^{-1}$ ensures that all the eigenvalues are real. If the swimmer is able to follow both right- and left-handed helical equilibrium trajectories, then the matrix C has both positive and negative eigenvalues, and $\mathbf{m}$ is such that the restriction of $\mathbf{z} \mapsto \mathbf{z} \cdot \mathsf{C}\,\mathbf{z}$ to $\left(\mathsf{M}_{22}^{-1}\,\mathbf{m}\right)^\perp$ reaches values of both signs.

Alternatively, with $\boldsymbol{\eta}_0 = \mathsf{M}_{22}^{-1}\,\mathbf{m}/|\mathsf{M}_{22}^{-1}\,\mathbf{m}|$, introducing the projection matrix

$$-\left[\boldsymbol{\eta}_0\times\right]^2$$

onto the plane $\boldsymbol{\eta}_0^{\perp} = \left(\mathsf{M}_{22}^{-1}\,\mathbf{m}\right)^{\perp}$, the two nonzero eigenvalues $\lambda_1 \leq \lambda_2$ of

$$\left[\boldsymbol{\eta}_0\times\right]^2 \mathsf{C} \left[\boldsymbol{\eta}_0\times\right]^2$$

are such that $p \in [2\pi\lambda_1, 2\pi\lambda_2]$.

Note that if C is either positive or negative semi-definite, helical equilibrium trajectories are either all right-handed or all left-handed, independent of the magnetic moment.

These helical trajectories degenerate to circles if $p = 0$, straight lines if $r = 0$, or points (the swimmer rotates about a fixed point) if $r = p = 0$. In the following, we examine the conditions for these cases to happen. Note that the expressions (7.5) are bounded, and therefore degenerate cases with $p \to \infty$ or $r \to \infty$ never occur.

Circular Trajectories

Circular trajectories are interesting as they provide a boundary between left- and right-handed helical trajectories. They will also be useful in chapter 8 where buoyancy terms are included to study the motion of heavy swimmers against gravity: indeed, circular trajectories then allow the swimmers to be maintained at a fixed altitude.

To obtain circular trajectories, the pitch p as given in equation (7.6) must vanish with $\mathbf{e}_3 \in \left(\mathsf{M}_{22}^{-1}\,\mathbf{m}\right)^{\perp}$. In particular, this requires that

$$\left\{\mathbf{z} \in \mathbb{S}^2 : \mathbf{z}\cdot\mathsf{C}\,\mathbf{z} = 0\right\} \cap \{\mathbf{z} \in \mathbb{S}^2 : \mathbf{z}\cdot\mathsf{M}_{22}^{-1}\,\mathbf{m} = 0\} \neq \emptyset\,. \tag{7.7}$$

Note that the first set of the intersection is empty if the matrix C is either positive or negative

Figure 7.2 (next page) – **Swimmer E: circular trajectory with parameters** $a = 0.0310$ **and** $\cos\psi = 0.1259$. (a-c) Helical trajectory in the lab frame. The corresponding pitch is $p = 3.8417\cdot 10^{-9}$, and the corresponding radius $r = 2.9632\cdot 10^{-2}$. The resulting axial velocity is $v_{\mathrm{ax}} = 1.8935\cdot 10^{-11}$. The swimmer has been scaled so that the details of the trajectory remain visible: in actual proportions, the swimmer would be 67 times bigger. The proportions of the trajectory itself are respected. The width and depth of the plot box in panel (a) correspond to the axes dimensions of panel (c). (d) Orientation of the magnetic moment in the body frame. (e) Orientation of the swimmer in the magnetic frame. (f) Quaternion components of the corresponding rotational dynamics as functions of time: since the trajectory is a relative equilibrium, the components are constant.
Swimmer E admits another stable relative equilibrium for these parameter values (regime 2/8), which does not yield a circular trajectory.
To see the swimmer in motion, click here (password: thesisPR) or scan the barcode.

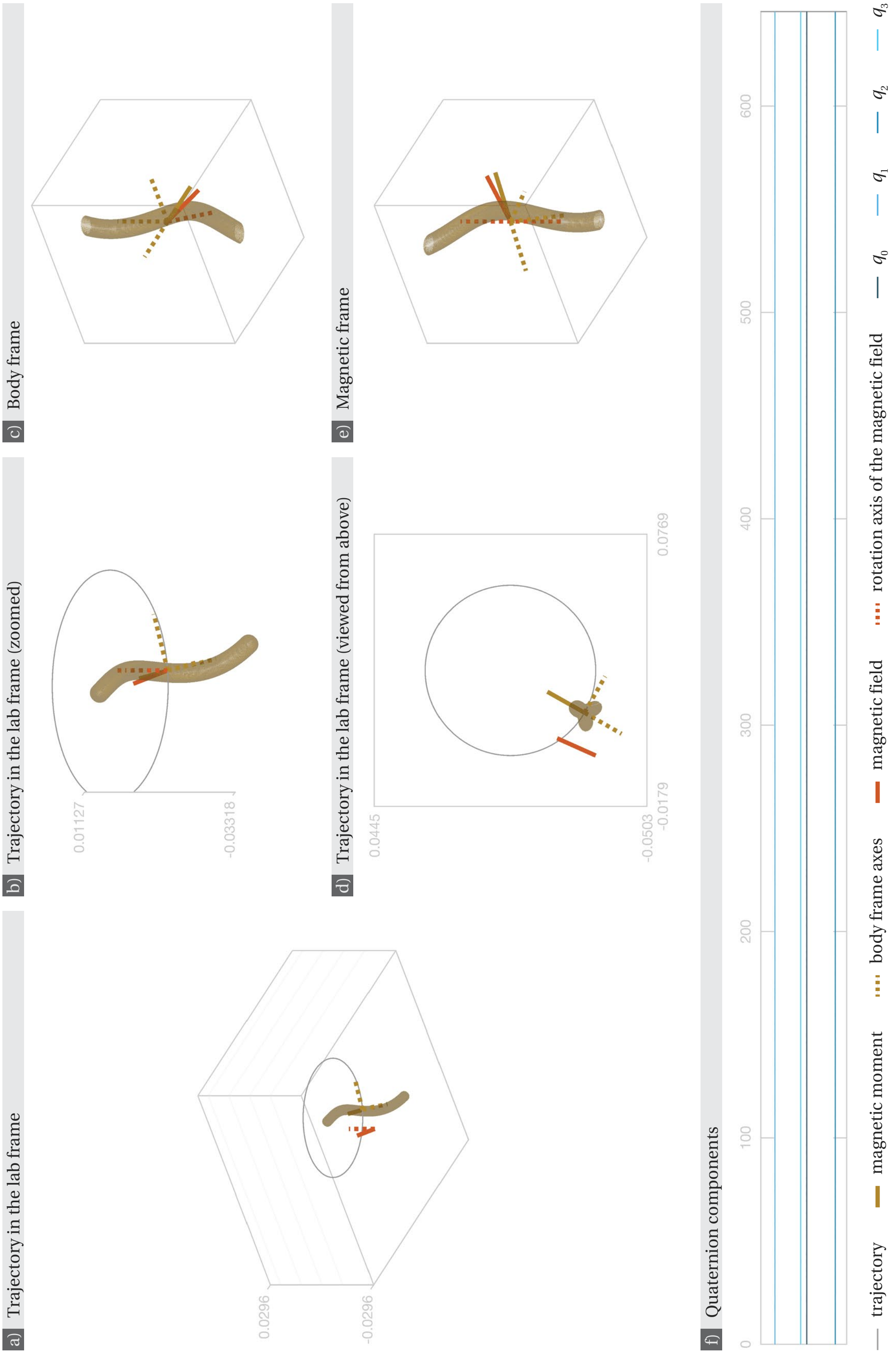
a) Trajectory in the lab frame
0.0296
-0.0296
b) Trajectory in the lab frame (zoomed)
0.01127
-0.03318
c) Body frame
d) Trajectory in the lab frame (viewed from above)
0.0445
-0.0503
-0.0179
0.0769
e) Magnetic frame
f) Quaternion components
0
100
200
300
400
500
600
trajectory
magnetic moment
body frame axes
magnetic field
rotation axis of the magnetic field
q_0
q_1
q_2
q_3

definite, which means that for some bodies it is not possible to obtain circular trajectories at all. In all other cases, the set

$$\left\{\mathbf{z} \in \mathbb{S}^2 : \mathbf{z} \cdot \mathsf{C}\mathbf{z} = 0\right\} = \mathbb{S}^2 \cap \left\{\mathbf{z} \in \mathbb{R}^3 : \mathbf{z} \cdot \mathsf{C}\mathbf{z} = 0\right\}$$

is non-empty, and different cases occur:

- if C has two eigenvalues of one sign and one of the opposite sign, the set is the intersection of the unit sphere and an elliptic cone
- if C is singular with one positive and one negative eigenvalue, the set is the intersection of the unit sphere and intersecting planes passing both through **0**
- if C has two zero eigenvalues, the set is the intersection of the unit sphere with a plane through **0**
- if C is singular with two eigenvalues of the same sign, the set is the intersection of the unit sphere with a straight line through **0**.

In all these cases, the first set of the intersection (7.7) is non empty. For a given body before magnetisation, the magnetic moment **m** could then be chosen so that the intersection (7.7) is not empty in order to be able to obtain circular trajectories.

To find the experimental parameters, i.e. the Mason number a and the conical angle ψ, for which the swimmer follows circular trajectories, one needs first to compute θ such that $\cos\theta = \mathbf{e}_3 \cdot \boldsymbol{\eta}_1$ and $\sin\theta = \mathbf{e}_3 \cdot \boldsymbol{\eta}_2$, where $\mathbf{e}_3$ is in the intersection (7.7) and $\boldsymbol{\eta}_1$ and $\boldsymbol{\eta}_2$ are computed as in section 3.2; and then one must compute a and ψ according to

$$\begin{aligned} a &= \sin\phi \left(\frac{\cos^2\theta}{\sigma_1^2} + \frac{\sin^2\theta}{\sigma_2^2} \right)^{-1/2} \\ \cos\psi &= \cos\phi \left(c_{01} \frac{\cos\theta}{\sigma_1} + c_{02} \frac{\sin\theta}{\sigma_2} \right) \\ &\quad + \sin\phi \left(\frac{\cos^2\theta}{\sigma_1^2} + \frac{\sin^2\theta}{\sigma_2^2} \right)^{-1/2} \left(c_{11} \left(\frac{\cos^2\theta}{\sigma_1^2} - \frac{\sin^2\theta}{\sigma_2^2} \right) + c_{12} \frac{\cos\theta \sin\theta}{\sigma_1 \sigma_2} \right), \end{aligned} \tag{4.5}$$

where the c_{ij} are given by (3.20) (cf. p. 38), and $\phi \in [0,\pi]$ is chosen arbitrarily. Note that in the examples shown in chapter 6, the values of ϕ corresponding to stable relative equilibria are all below $\pi/2$.

The matrices $\left[\boldsymbol{\eta}_0\times\right]^2 \mathsf{C} \left[\boldsymbol{\eta}_0\times\right]^2$ corresponding to the example swimmers introduced in chapter 6 all have both one positive and one negative eigenvalues, and accordingly all admit circular relative equilibria. However, for swimmer C, all of these circular trajectories are unstable. Consequently, the pitch of helical trajectories does not change sign within the set of stable relative equilibria. In the case of swimmer C, the set of stable relative equilibria is split into two disjoint sets, each of which is connected, and the pitch is strictly positive across each of these two regions – i.e. all the equilibrium trajectories of swimmer C are right-handed helices. In contrast, swimmers A, B, B', D, E, and F admit stable circular trajectories (cf. fig. 7.2), and stable helical trajectories of both handedness.

Straight and Stationary Trajectories

Trajectories are straight whenever the radius r as given in (7.5) vanishes: $\mathbf{e}_3$ is an eigenvector of $\mathsf{M}_{12}\,\mathsf{M}_{22}{}^{-1}$. Since the matrix $\mathsf{M}_{12}\,\mathsf{M}_{22}{}^{-1}$ is a real 3-by-3 matrix, it has at least one real eigenvector. As for circular trajectories, a given body before magnetisation can be made to be able to follow straight trajectories by designing $\mathbf{m}$ so that there is an eigenvector of $\mathsf{M}_{12}\,\mathsf{M}_{22}{}^{-1}$ in the plane $\left(\mathsf{M}_{22}^{-1}\mathbf{m}\right)^{\perp}$. The experimental parameters for which straight trajectories occur can then be found using the same procedure as for circular trajectories.

Figure 7.3 shows swimmer C' following a straight trajectory. Swimmer C' has the same geometry as swimmer C, but the direction of its magnetic moment has been modified so that the criterion for the existence of straight trajectories is met, namely there is an eigenvector of $\mathsf{M}_{12}\,\mathsf{M}_{22}{}^{-1}$ perpendicular to $\mathsf{M}_{22}^{-1}\mathbf{m}$. Accordingly, for swimmer C',

$$\mathbf{m}_{C'} = \begin{bmatrix} 0.0000 \\ 0.3202 \\ 0.9473 \end{bmatrix}$$

in the frame specified in chapter 6.

Stationary rotations can be obtained only if $\mathbf{e}_3$ is in the null space of $\mathsf{M}_{12}\mathsf{M}_{22}^{-1}$, that is this nullspace must be nonempty, and must intersect the plane $\left(\mathsf{M}_{22}^{-1}\mathbf{m}\right)^{\perp}$.

Axial Velocity

The velocity of a swimmer along the axis of rotation of the magnetic field is given by $\mathbf{v}\cdot\mathbf{e}_3$. For relative equilibria, using (7.4) and (4.2) this axial velocity is obtained as

$$v_{\mathrm{ax}} = a\mathbf{e}_3\cdot\mathsf{C}\,\mathbf{e}_3 = \mathsf{P}\,\mathbf{B}\cdot\mathsf{C}\,\frac{\mathsf{P}\,\mathbf{B}}{|\mathsf{P}\,\mathbf{B}|}, \tag{7.8}$$

where C is the symmetric part of $\mathsf{M}_{12}\,\mathsf{M}_{22}^{-1}$ as given in (7.2). Substituting the parametrisation (4.3, 4.5) to express a and $\mathbf{e}_3$ in terms of θ and ϕ allows to find the maximal axial velocity admissible for relative equilibrium trajectories as

$$v_{\mathrm{ax}}(\theta,\phi) = \frac{\sigma_1\,\sigma_2\,\sin\phi}{\sqrt{\sigma_2^2\cos^2\theta+\sigma_1^2\sin^2\theta}}\,\left(\cos\theta\,\boldsymbol{\eta}_1+\sin\theta\,\boldsymbol{\eta}_2\right)\cdot\mathsf{C}\,(\cos\theta\,\boldsymbol{\eta}_1+\sin\theta\,\boldsymbol{\eta}_2)\,.$$

This expression can be maximised in absolute value with respect to θ and ϕ to obtain the

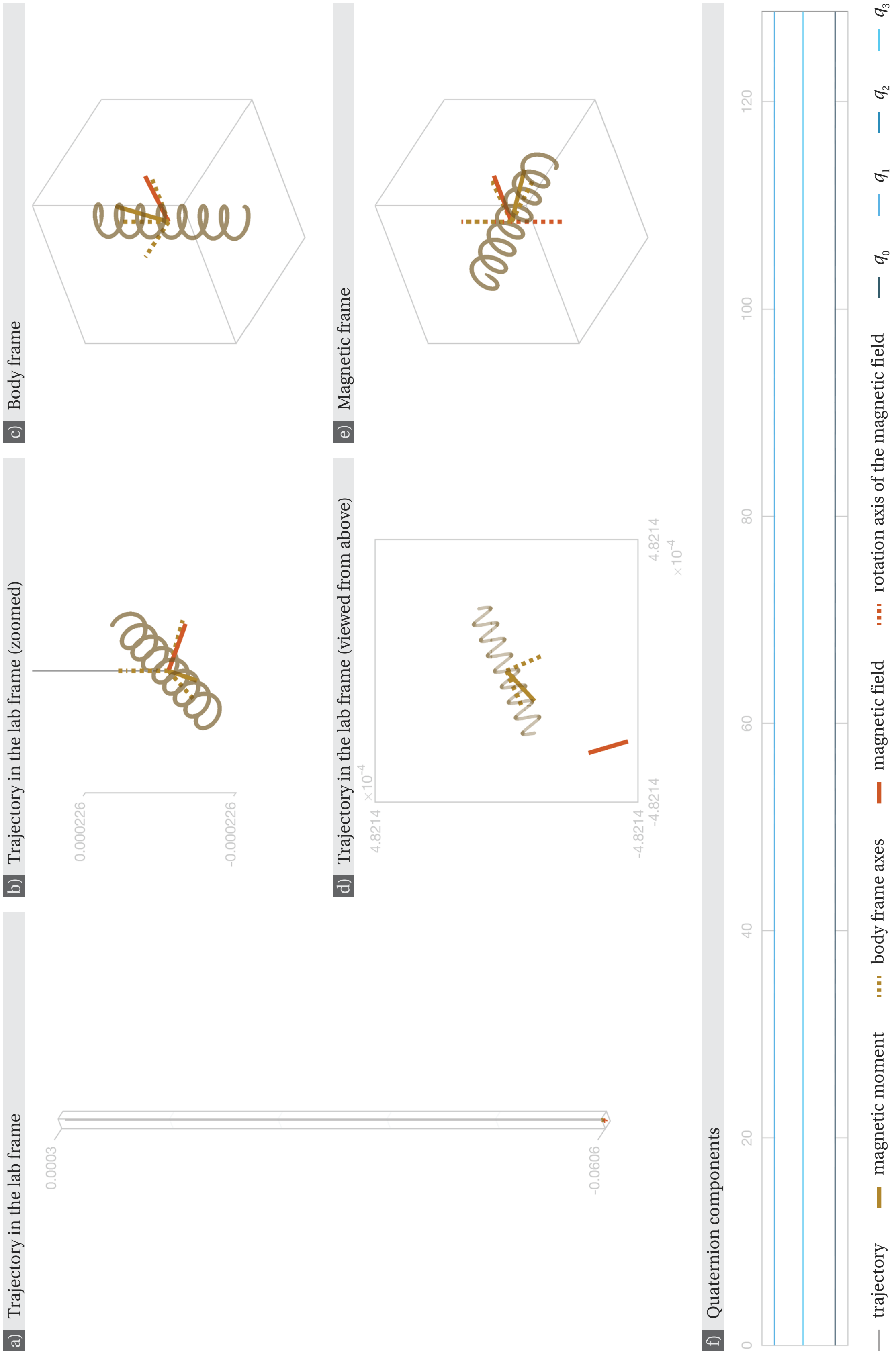
a) Trajectory in the lab frame
0.0003
-0.0606
b) Trajectory in the lab frame (zoomed)
0.000226
-0.000226
c) Body frame
d) Trajectory in the lab frame (viewed from above)
4.8214
$\times 10^{-4}$
-4.8214
-4.8214
4.8214
$\times 10^{-4}$
e) Magnetic frame
f) Quaternion components
0
20
40
60
80
100
120
trajectory
magnetic moment
body frame axes
magnetic field
rotation axis of the magnetic field
q_0
q_1
q_2
q_3

Figure 7.3 (previous page) – **Swimmer C': straight trajectory with parameters** $a = 0.0388$ **and** $\cos\psi = 2.1277 \cdot 10^{-14}$. (a-c) Helical trajectory in the lab frame. The corresponding pitch is $p = -7.5704 \cdot 10^{-2}$, and the corresponding radius $r = 3.8678 \cdot 10^{-15}$. The resulting axial velocity is $v_{\text{ax}} = -4.6806 \cdot 10^{-4}$. The swimmer has been scaled so that the details of the trajectory remain visible: in actual proportions, the swimmer would be 6637 times bigger. The proportions of the trajectory itself are respected. The width and depth of the plot box in panel (a) correspond to the axes dimensions of panel (c). (d) Orientation of the magnetic moment in the body frame. (e) Orientation of the swimmer in the magnetic frame. (f) Quaternion components of the corresponding rotational dynamics as functions of time: since the trajectory is a relative equilibrium, the components are constant.
This is the only relative equilibrium admitted by swimmer C' for these parameter values (regime 1/4).
To see the swimmer in motion, click here (password: thesisPR) or scan the barcode.

maximal axial velocity at relative equilibrium for a given swimmer. It is not guaranteed that the maximiser corresponds to a stable relative equilibrium however. Actually, since $v_{\text{ax}}(\theta, \phi)$ is maximised for $\phi = \pi/2$, and since the examples studied in chapter 6 exhibit stable relative equilibria only for $\phi < \pi/2$, the maximiser is unstable in all the examples that are considered (cf table 7.2).

	optimal axial velocity	corresponding relative equilibria	a	$\cos\psi$
swimmer A	$9.6398 \cdot 10^{-4}$	Hopf bifurcations	0.0331	−0.0465
swimmer B	$1.9976 \cdot 10^{-2}$	unstable	0.9210	0.0764
	$1.9970 \cdot 10^{-2}$	Hopf bifurcation	0.9207	0.0678
swimmer B'	$-1.9978 \cdot^{1} 0-2$	unstable	0.9210	−0.0764
	$-1.9972 \cdot 10^{-2}$	Hopf bifurcation	0.9207	−0.0678
swimmer C	0.0060	zero-Hopf bifurcations	0.3906	0.0525
swimmer D	$-1.2066 \cdot 10^{-3}$	unstable	0.0357	−0.0399
	$-1.2060 \cdot 10^{-3}$	Hopf bifurcation	0.0357	−0.0316
swimmer E	$1.1343 \cdot 10^{-2}$	Hopf bifurcations	0.4260	−0.3711
swimmer F	$3.3852 \cdot 10^{-3}$	unstable	0.7115	−0.1674
	$3.3091 \cdot 10^{-3}$	Hopf bifurcation	0.6995	−0.1177

Table 7.2 – **Optimal axial velocities** for the examples presented in chapter 6. All velocities are given in non-dimensional units. To obtain the corresponding dimensional velocities, they need to be multiplied by ℓ/t_c (cf. section 2.2). For swimmers A, C, and E, the maximisers are Hopf bifurcations, implying that there are stable relative equilibria in the neighbourhood of one of them. For swimmers B, B', D, and F, the optimisers are unstable relative equilibria, and the optimal axial velocity for stable relative equilibria is also given – actually, the velocity is optimised in all these four cases on the boundary of the region featuring stable relative equilibria, and accordingly the optimisers are bifurcations.

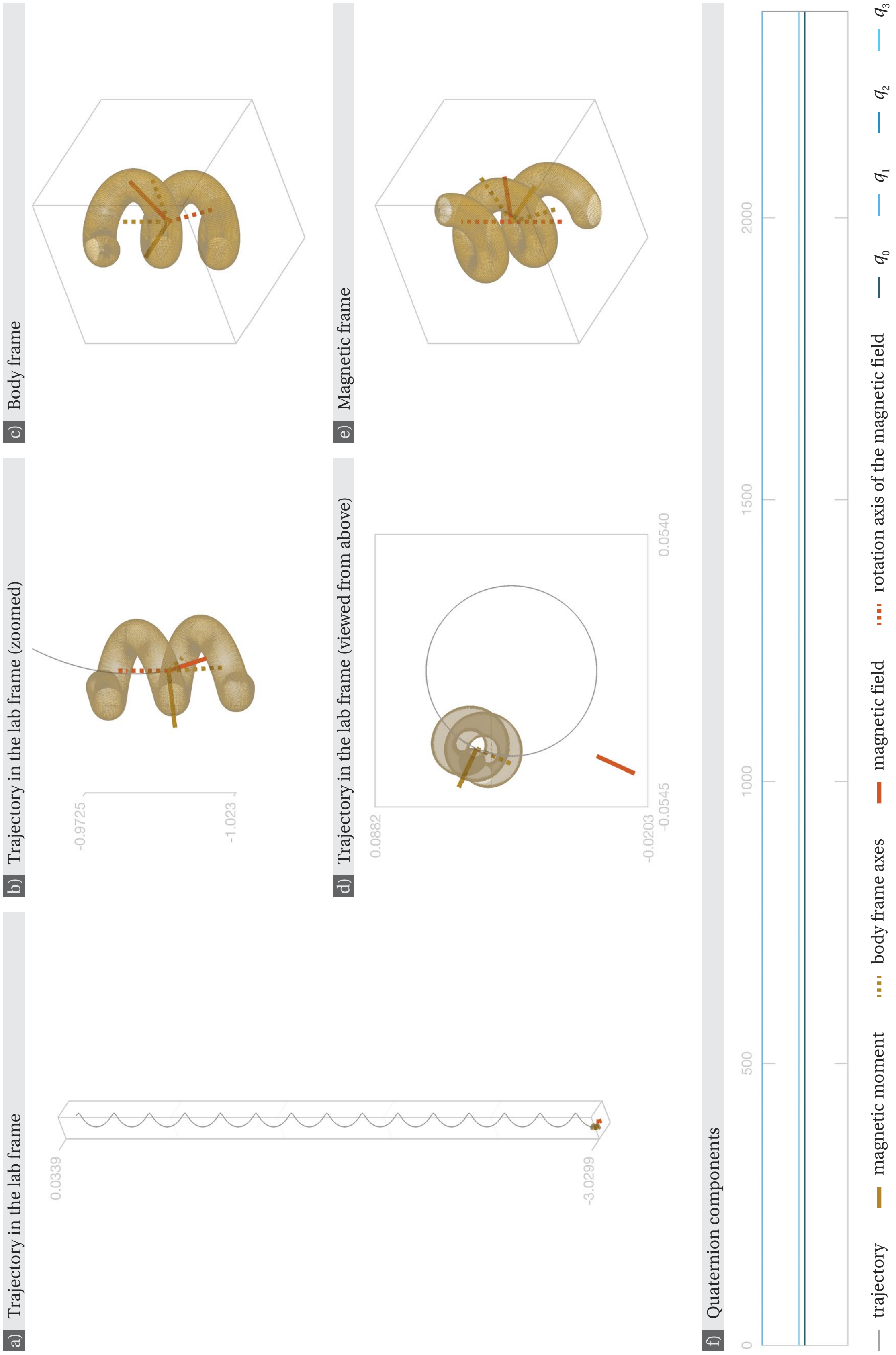
a) Trajectory in the lab frame
0.0339
-3.0299
b) Trajectory in the lab frame (zoomed)
-0.9725
-1.023
c) Body frame
d) Trajectory in the lab frame (viewed from above)
0.0882
-0.0203
-0.0545
0.0540
e) Magnetic frame
f) Quaternion components
0
500
1000
1500
2000
trajectory
magnetic moment
body frame axes
magnetic field
rotation axis of the magnetic field
q_0
q_1
q_2
q_3

Figure 7.4 (previous page) – **Swimmer D': equilibrium trajectory that optimises axial velocity**. Optimal axial velocity is reached with $a = 0.0390$ and $\cos\psi = -0.2031$. (a-c) Helical trajectory in the lab frame. The corresponding pitch is $p = -0.2040$, and the corresponding radius $r = 3.3896 \cdot 10^{-2}$. The resulting axial velocity is $v_{\text{ax}} = -1.2658 \cdot 10^{-3}$: this is the maximal velocity reachable with the geometry of swimmer D at a relative equilibrium. The swimmer has been scaled so that the details of the trajectory remain visible: in actual proportions, the swimmer would be 59 times bigger. The proportions of the trajectory itself are respected. The width and depth of the plot box in panel (a) correspond to the axes dimensions of panel (c). (d) Orientation of the magnetic moment in the body frame. (e) Orientation of the swimmer in the magnetic frame. (f) Quaternion components of the corresponding rotational dynamics as functions of time: since the trajectory is a relative equilibrium, the components are constant.
This relative equilibrium is very close to a Hopf bifurcation situated on a curve that borders a region of parameter plane corresponding to regime 2/4.
To see the swimmer in motion, click here (password: thesisPR) or scan the barcode.

Optimal Design

A related issue is how to magnetise a swimmer of a given shape to obtain the maximal axial velocity, i.e. optimisation of axial velocity over $\mathbf{m}$. To have all dependences of the axial velocity in $\mathbf{m}$ explicit, use the second expression for v_{ax} in (7.8), and use the definition $\mathsf{P}\,\mathbf{B} = \mathsf{M}_{22}\,(\mathbf{m}\times\mathbf{B})$ to obtain

$$v_{\text{ax}} = \frac{\mathsf{M}_{22}\,(\mathbf{m}\times\mathbf{B})\cdot\mathsf{C}\,\mathsf{M}_{22}\,(\mathbf{m}\times\mathbf{B})}{|\mathsf{M}_{22}\,(\mathbf{m}\times\mathbf{B})|} = \frac{(\mathbf{m}\times\mathbf{B})\cdot\mathsf{M}_{22}\,\mathsf{M}_{12}\,(\mathbf{m}\times\mathbf{B})}{|\mathsf{M}_{22}\,(\mathbf{m}\times\mathbf{B})|}.$$

Relative equilibria exist for all $\mathbf{B}\in\mathbb{S}^2$, and $\mathbf{m}\times\mathbf{B} = \sin\phi\,\mathbf{n}$ for some unit vector $\mathbf{n}$, so that the axial velocity can be rewritten

$$v_{\text{ax}} = \sin\phi\,\frac{\mathbf{n}\cdot\mathsf{M}_{22}\,\mathsf{M}_{12}\,\mathbf{n}}{|\mathsf{M}_{22}\,\mathbf{n}|}, \tag{7.9}$$

and the factors depending on ϕ and $\mathbf{n}$ can be maximised separately. Therefore, to obtain the maximal velocity for a swimmer of a given shape, find first the maximiser $\mathbf{n}^*\in\mathbb{S}^2$ of

$$\frac{|\mathbf{n}\cdot\mathsf{M}_{22}\,\mathsf{M}_{12}\,\mathbf{n}|}{|\mathsf{M}_{22}\,\mathbf{n}|}, \tag{7.10}$$

and then magnetise the swimmer so that $\mathbf{m}\perp\mathbf{n}^*$. The relative equilibria corresponding to $\mathbf{B} = \pm\mathbf{n}^*\times\mathbf{m}$ then maximise the axial velocity, since expression (7.9) is maximised for $\phi = \pi/2$ for any $\mathbf{n}$. However, it is not guaranteed that this relative equilibrium is stable. In fact, in the examples studied, stable relative equilibria satisfy $\phi < \pi/2$, which means that the relative equilibrium corresponding to $\mathbf{B} = \pm\mathbf{n}\times\mathbf{m}$ is unstable.

The presence of a Hopf bifurcation at the relative equilibrium corresponding to $\mathbf{B} = \mathbf{n}^*\times\mathbf{m}$ would guarantee the existence of stable equilibria in the neighbourhood of either $\mathbf{B} = \mathbf{n}^*\times\mathbf{m}$ or $\mathbf{B} = -\mathbf{n}^*\times\mathbf{m}$. Indeed, recall that the stability matrices of relative equilibria corresponding to $\mathbf{B}$ and $-\mathbf{B}$ have opposite eigenvalues. Therefore, the third eigenvalue of the stability matrix for one of the symmetric Hopf bifurcations is non-positive, which implies that the bifurcation borders stable steady states. It is unclear however whether $\mathbf{m}$ can be chosen in the plane $(\mathbf{n}^*)^\perp$ such that the relative equilibria corresponding to $\mathbf{B} = \pm\mathbf{n}^* \times \mathbf{m}$ are Hopf bifurcations.

For the geometry of swimmer D (cf. fig. 6.11), choosing

$$\mathbf{m} = \begin{bmatrix} 0.6599 \\ 0.7514 \\ 0.0013 \end{bmatrix}$$

(as expressed in the basis used in chapter 6) meets the criteria: $\mathbf{m}$ is perpendicular to the maximiser $\mathbf{n}^*$ of expression (7.10), where M_{12} and M_{22} are blocks of $\mathbb{M}_D$ (cf. sec. 6.1); and $\mathbf{B} = \mathbf{n}^* \times \mathbf{m}$ corresponds to a steady state of the rotational dynamics (3.9) for which the stability matrix admits two purely imaginary eigenvalues, i.e. a Hopf bifurcation. The swimmer D' thus obtained admits a relative equilibrium that optimises axial velocity for $a = 0.0390$ and $\cos\psi = -0.2031$ (cf. fig. 7.4). The optimal axial velocity thus obtained is $v_{\text{ax}} = -1.2658 \cdot 10^{-3}$, which is 5% larger than the maximal axial velocity reached by swimmer D for stable relative equilibria (cf. table 7.2).

To summarise, this section presented the trajectories $\boldsymbol{x}(t)$ followed by swimmers when the rotational dynamics admits a steady state. The corresponding trajectories are helical, and their pitch and radius were characterised. In particular, it was discussed how to obtain circular trajectories, i.e. a vanishing pitch, and straight trajectories, i.e. a vanishing radius. Optimisation of the axial velocity was also considered.

7.2 Trajectories Corresponding to Periodic Solutions of the Dynamics

In the examples shown in chapter 6, the asymptotic behaviours occurring besides relative equilibria correspond to periodic solutions of the rotational dynamics. Accordingly, this

Figure 7.5 (next page) – **Swimmer B': first trajectory corresponding to a periodic orbit with $a = 0.316$ and $\cos\psi = 0.8544$.** (a-c) Trajectory in the lab frame. The average axial velocity is $\overline{v_{\text{ax}}} = -7.2161 \cdot 10^{-5}$. The swimmer has been scaled so that the details of the trajectory remain visible: in actual proportions, the swimmer would be 119 times bigger. The proportions of the trajectory itself are respected. The width and depth of the plot box in panel (a) correspond to the axes dimensions of panel (c). (d) Final orientation of the magnetic moment in the body frame. (e) Final orientation of the swimmer in the magnetic frame. (f) Quaternion components of the corresponding rotational dynamics as functions of time, which are periodic. There is another stable periodic solution to eq. (3.14) for these parameter values (regime 0/4); the corresponding trajectory is shown in fig. 7.6.
To see the swimmer in motion, click here (password: thesisPR) or scan the barcode.

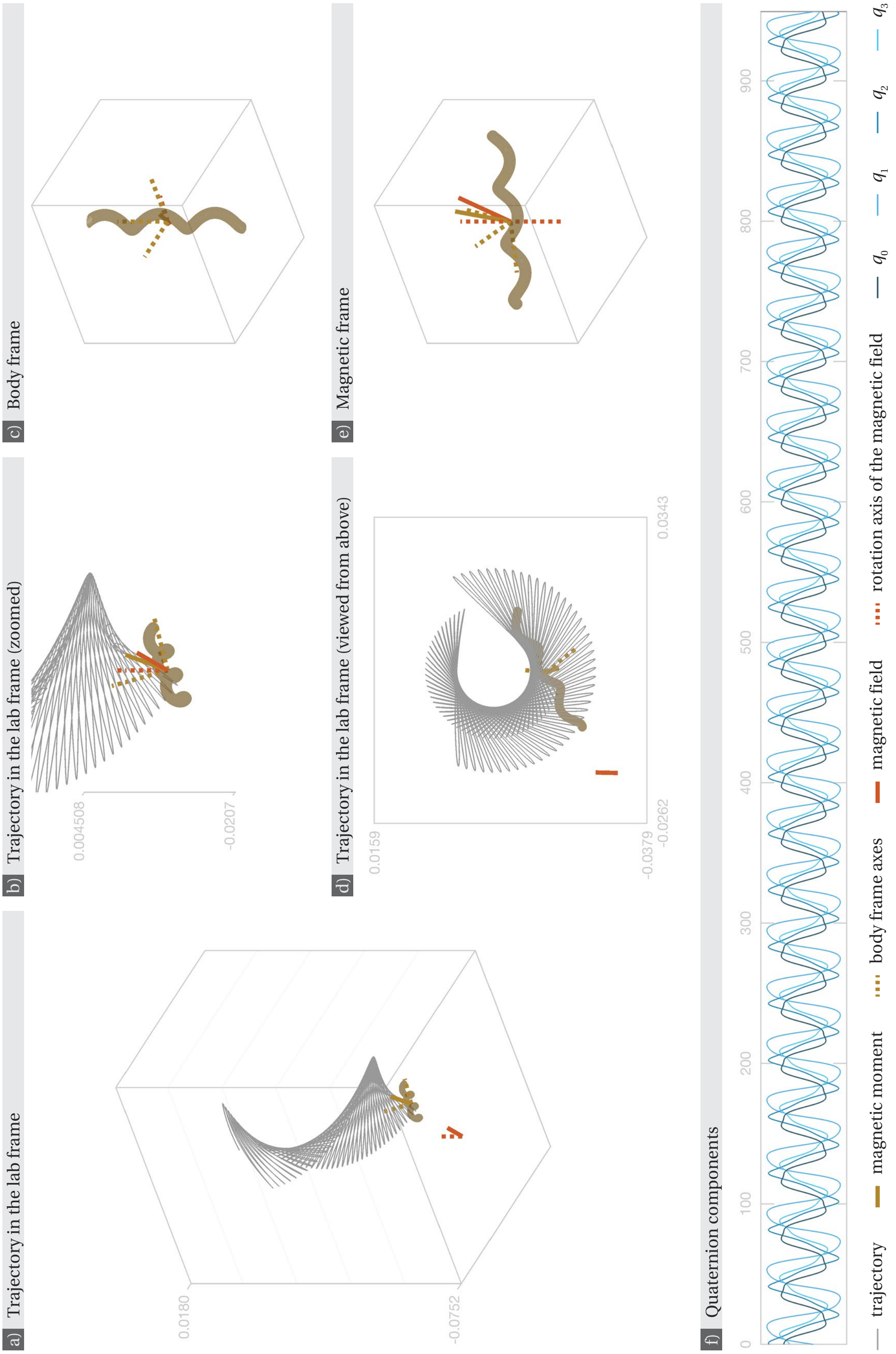
a) Trajectory in the lab frame
0.0180
-0.0752
b) Trajectory in the lab frame (zoomed)
0.004508
-0.0207
c) Body frame
d) Trajectory in the lab frame (viewed from above)
0.0159
-0.0379
-0.0262
0.0343
e) Magnetic frame
f) Quaternion components
0
100
200
300
400
500
600
700
800
900
trajectory
magnetic moment
body frame axes
magnetic field
rotation axis of the magnetic field
q_0
q_1
q_2
q_3

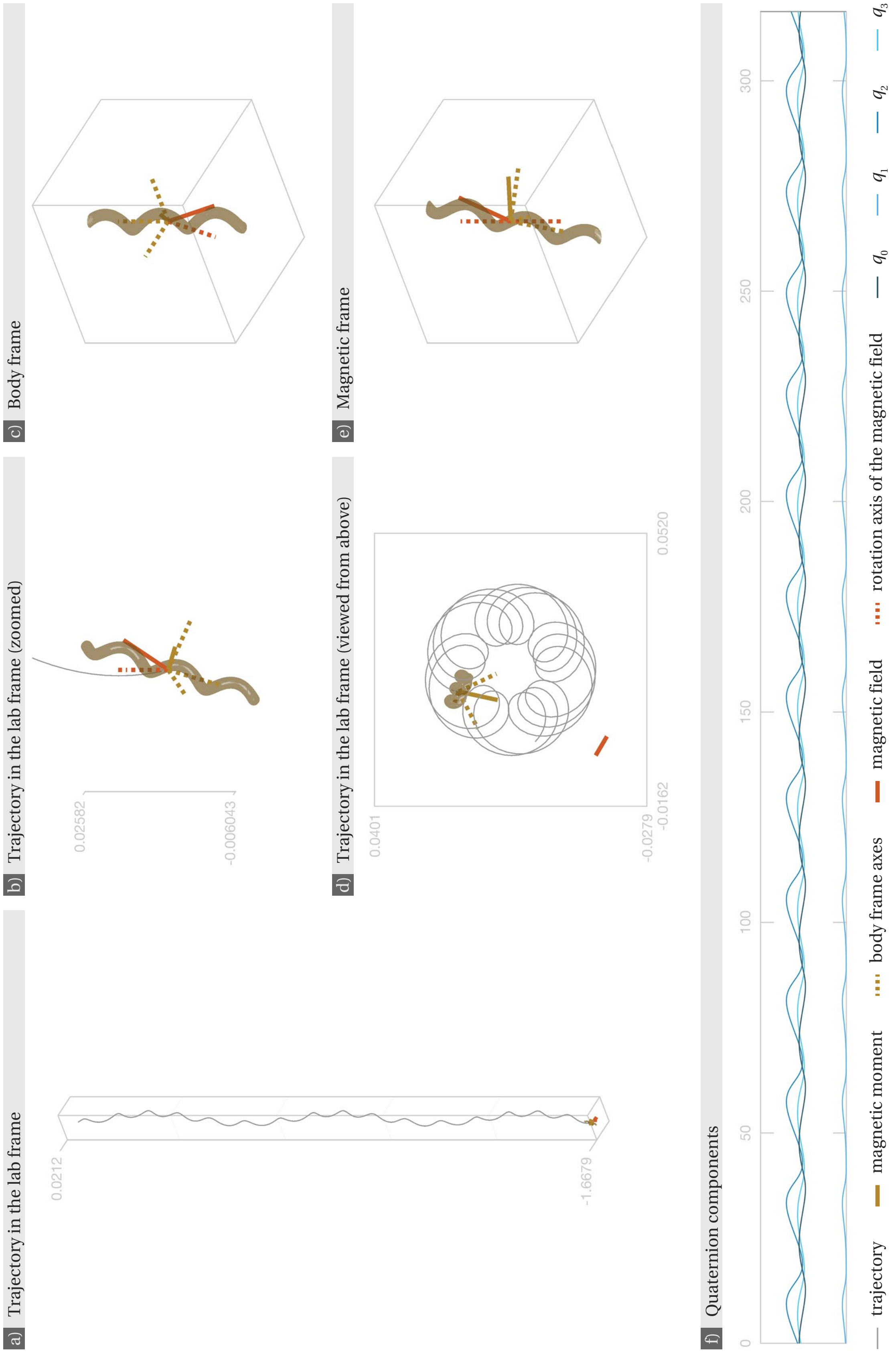
a) Trajectory in the lab frame
0.0212
-1.6679
b) Trajectory in the lab frame (zoomed)
0.02582
-0.006043
c) Body frame
d) Trajectory in the lab frame (viewed from above)
0.0401
-0.0279
-0.0162
0.0520
e) Magnetic frame
f) Quaternion components
0
50
100
150
200
250
300
trajectory
magnetic moment
body frame axes
magnetic field
rotation axis of the magnetic field
q_0
q_1
q_2
q_3

Figure 7.6 (previous page) – **Swimmer B': second trajectory corresponding to a periodic orbit with $a = 0.316$ and $\cos\psi = 0.8544$.** (a-c) Trajectory in the lab frame. The average axial velocity is $\overline{v_{\mathrm{ax}}} = -5.2281 \cdot 10^{-3}$. The swimmer has been scaled so that the details of the trajectory remain visible: in actual proportions, the swimmer would be 94 times bigger. The proportions of the trajectory itself are respected. The width and depth of the plot box in panel (a) correspond to the axes dimensions of panel (c). (d) Final orientation of the magnetic moment in the body frame. (e) Final orientation of the swimmer in the magnetic frame. (f) Quaternion components of the corresponding rotational dynamics as functions of time, which are periodic.
There is another stable periodic solution to eq. (3.14) for these parameter values (regime 0/4); the corresponding trajectory is shown in fig. 7.5.
To see the swimmer in motion, click here (password: thesisPR) or scan the barcode.

section focuses on the trajectories corresponding to these periodic solutions (cf. fig. 7.5-7.7).

Recall that the rotational dynamics are given by $Q \in \mathrm{SO}(3)$ satisfying

$$\dot{Q} = \left[\left(a\,Q\begin{bmatrix}0\\0\\1\end{bmatrix} - \mathsf{P}\,Q\begin{bmatrix}\sin\psi\\0\\\cos\psi\end{bmatrix}\right)\times\right] Q. \tag{3.7}$$

For periodic solutions of this equation, the swimmer's velocity

$$\boldsymbol{v} = R_3(a\,t)\,Q^T(t)\,\mathbf{v}(t) \tag{7.11}$$

is the product of the $2\pi/a$-periodic function $R_3(a\,t)$ and the periodic function

$$\boldsymbol{V}(t) := Q^T(t)\,\mathbf{v}(t) = Q^T(t)\,\mathsf{M}_{12}\,[\mathbf{m}\times]\,Q(t)\begin{bmatrix}\sin\psi\\0\\\cos\psi\end{bmatrix}. \tag{7.12}$$

The period of $\boldsymbol{V}(t)$ is denoted p. There is no general way to integrate the product of two periodic functions with different periods ,and this makes a general explicit formula for the trajectory $\boldsymbol{x}$ out of reach. In this section, we provide a way to obtain effective trajectories using Fourier analysis.

In particular, equation (7.11) guarantees that the third components of $\boldsymbol{v}$ is p-periodic: its average is given by $\hat{V}_3(0)$, the third component of the Fourier coefficient $\hat{\boldsymbol{V}}(n)$ for $n = 0$. The third component of the effective trajectory is accordingly linear in time.

We also find that the first and second components of the trajectory are bounded, except when the Mason number a and period p satisfy $a\,p/2\pi \in \mathbb{Z}$. In this case, the effective trajectory is given by the straight line

$$t\begin{bmatrix}\mathrm{Re}\left(\hat{V}_1\left(\frac{ap}{2\pi}\right)\right) + \mathrm{Im}\left(\hat{V}_2\left(\frac{ap}{2\pi}\right)\right)\\ \mathrm{Re}\left(\hat{V}_2\left(\frac{ap}{2\pi}\right)\right) - \mathrm{Im}\left(\hat{V}_1\left(\frac{ap}{2\pi}\right)\right)\\ \hat{V}_3(0)\end{bmatrix},$$

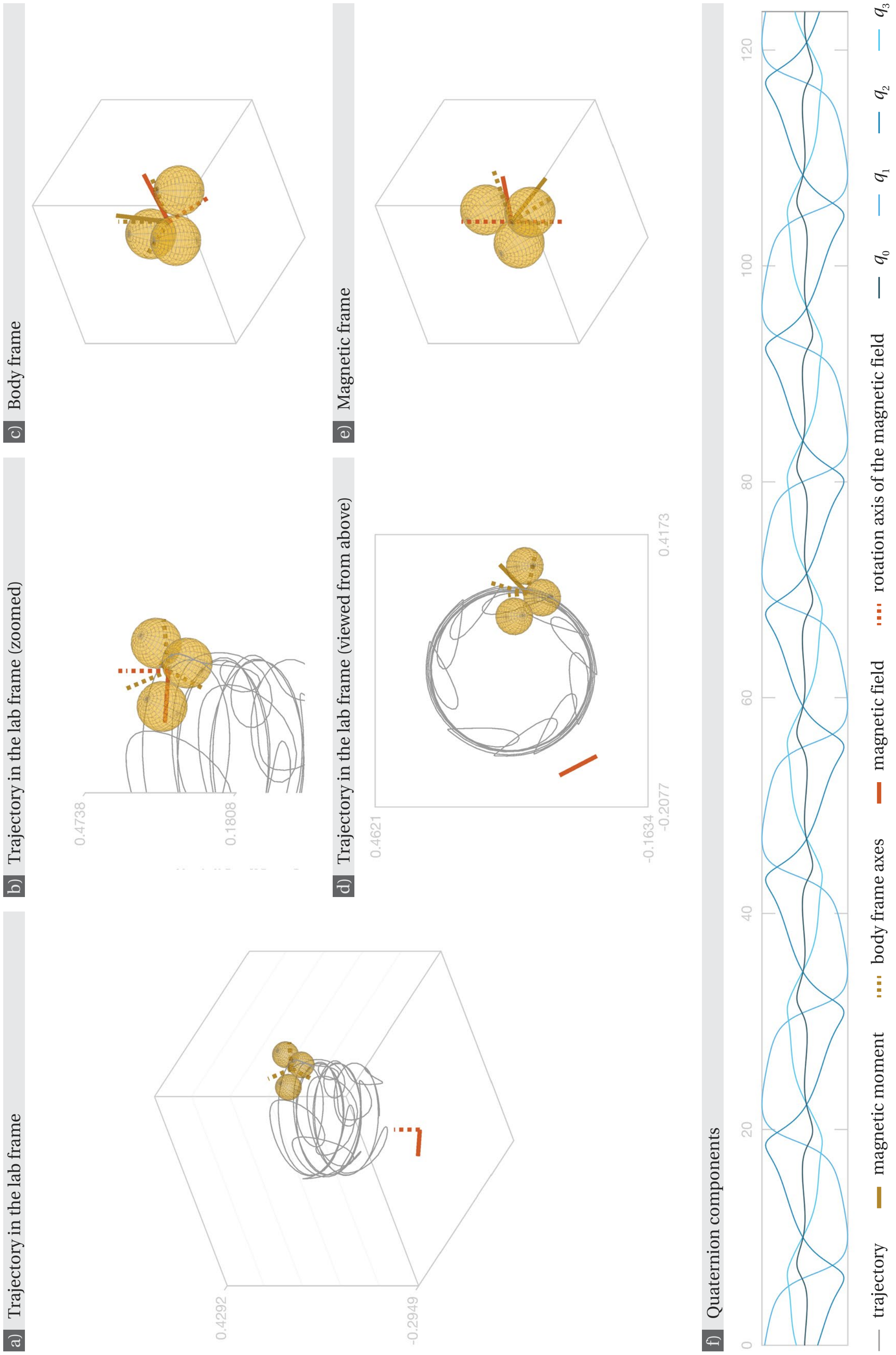
a) Trajectory in the lab frame
0.4292
-0.2949
b) Trajectory in the lab frame (zoomed)
0.4738
0.1808
c) Body frame
d) Trajectory in the lab frame (viewed from above)
0.4621
-0.1634
-0.2077
0.4173
e) Magnetic frame
f) Quaternion components
0
20
40
60
80
100
120
trajectory
magnetic moment
body frame axes
magnetic field
rotation axis of the magnetic field
q_0
q_1
q_2
q_3

Figure 7.7 (previous page) – **Swimmer F: trajectory corresponding to a periodic orbit with $a = 0.8810$ and $\cos\psi = -0.1692$.** (a-c) Trajectory in the lab frame. The average axial velocity is $\overline{v_{\mathrm{ax}}} = 1.4416 \cdot 10^{-3}$. The swimmer has been scaled so that the details of the trajectory remain visible: in actual proportions, the swimmer would be 10 times bigger. The proportions of the trajectory itself are respected. The width and depth of the plot box in panel (a) correspond to the axes dimensions of panel (c). (d) Final orientation of the magnetic moment in the body frame. (e) Final orientation of the swimmer in the magnetic frame. (f) Quaternion components of the corresponding rotational dynamics as functions of time, which are periodic.
This is the only stable solution admitted by swimmer F for these parameter values (regime 0/0). The phase portrait of the corresponding rotational dynamics is shown in fig. 6.32.
To see the swimmer in motion, click here (password: thesisPR) or scan the barcode.

where $\hat{V}_j(n)$ denotes the j^{th} component of the n^{th} Fourier coefficient of $\boldsymbol{V}$. The first two components in this expression depend on the value of $\boldsymbol{V}(0)$, and the direction of the average trajectory therefore depends on the initial orientation of the swimmer.

7.2.1 Fourier Analysis of Periodic Solutions

Since $\boldsymbol{V}$ is p-periodic, it can be written as a Fourier series, that is

$$\boldsymbol{V}(t) = \sum_{n=-\infty}^{\infty} \hat{\boldsymbol{V}}(n)\, e^{i\frac{2\pi n}{p}t},$$

where

$$\hat{\boldsymbol{V}}(n) = \frac{1}{p}\int_{-p/2}^{p/2} \boldsymbol{V}(t)\, e^{-i\frac{2\pi n}{p}t}\, dt. \tag{7.13}$$

Note that $\boldsymbol{V}$ is quadratic in Q, which is itself a solution to a dynamical system involving only smooth functions. Consequently, the Fourier series of $\boldsymbol{V}$ converges absolutely, i.e.

$$\sum_{n=-\infty}^{\infty} \left|\hat{\boldsymbol{V}}(n)\right| = C_V < +\infty,$$

which allows to do all computations coefficient by coefficient. The velocity $\boldsymbol{v}$ can therefore be rewritten using the Fourier coefficients as[2]

$$\begin{aligned}\boldsymbol{v}(t) = R_3(a\,t)\,\boldsymbol{V}(t) = &\begin{bmatrix} \frac{1}{2} & -\frac{1}{2i} & 0 \\ \frac{1}{2i} & \frac{1}{2} & 0 \\ 0 & 0 & 0 \end{bmatrix} \sum_{n=-\infty}^{\infty} \hat{\boldsymbol{V}}(n)\, e^{i\frac{2\pi n + a p}{p}t} + \begin{bmatrix} \frac{1}{2} & \frac{1}{2i} & 0 \\ -\frac{1}{2i} & \frac{1}{2} & 0 \\ 0 & 0 & 0 \end{bmatrix} \sum_{n=-\infty}^{\infty} \hat{\boldsymbol{V}}(n)\, e^{i\frac{2\pi n - a p}{p}t} \\ &+ \begin{bmatrix} 0 & 0 & 0 \\ 0 & 0 & 0 \\ 0 & 0 & 1 \end{bmatrix} \sum_{n=-\infty}^{\infty} \hat{\boldsymbol{V}}(n)\, e^{i\frac{2\pi n}{p}t},\end{aligned}$$

---

[2] We used $R_3(a\,t) = e^{i\,a\,t}\begin{bmatrix} \frac{1}{2} & -\frac{1}{2i} & 0 \\ \frac{1}{2i} & \frac{1}{2} & 0 \\ 0 & 0 & 0 \end{bmatrix} + e^{-i\,a\,t}\begin{bmatrix} \frac{1}{2} & \frac{1}{2i} & 0 \\ -\frac{1}{2i} & \frac{1}{2} & 0 \\ 0 & 0 & 0 \end{bmatrix} + \begin{bmatrix} 0 & 0 & 0 \\ 0 & 0 & 0 \\ 0 & 0 & 1 \end{bmatrix}$.

and the trajectory $\boldsymbol{x}$ can be obtained by integrating the series term by term:

$$\begin{aligned}\boldsymbol{x}(t)-\boldsymbol{x}(0) &= \int_0^t \boldsymbol{v}(\tau)\, d\tau \\ &= \begin{bmatrix} \frac{1}{2} & -\frac{1}{2i} & 0 \\ \frac{1}{2i} & \frac{1}{2} & 0 \\ 0 & 0 & 0 \end{bmatrix} \left(\sum_{\substack{n=-\infty \\ n\neq -ap/2\pi}}^{\infty} \hat{\boldsymbol{V}}(n)\, \frac{p\, e^{i \frac{2\pi n + ap}{p} t}}{i\left(2\pi n + ap\right)} + \chi_{\mathbb{Z}}\left(\frac{ap}{2\pi}\right) \hat{\boldsymbol{V}}\left(-\frac{ap}{2\pi}\right) t \right) \\ &\quad + \begin{bmatrix} \frac{1}{2} & \frac{1}{2i} & 0 \\ -\frac{1}{2i} & \frac{1}{2} & 0 \\ 0 & 0 & 0 \end{bmatrix} \left(\sum_{\substack{n=-\infty \\ n\neq ap/2\pi}}^{\infty} \hat{\boldsymbol{V}}(n)\, \frac{p\, e^{i \frac{2\pi n - ap}{p} t}}{i\left(2\pi n - ap\right)} + \chi_{\mathbb{Z}}\left(\frac{ap}{2\pi}\right) \hat{\boldsymbol{V}}\left(\frac{ap}{2\pi}\right) t \right) \\ &\quad + \begin{bmatrix} 0 & 0 & 0 \\ 0 & 0 & 0 \\ 0 & 0 & 1 \end{bmatrix} \left(\sum_{\substack{n=-\infty \\ n\neq 0}}^{\infty} \hat{\boldsymbol{V}}(n)\, \frac{p\, e^{i \frac{2\pi n}{p} t}}{i\, 2\pi n} + \hat{\boldsymbol{V}}(0)\, t \right),\end{aligned}$$

where $\chi_{\mathbb{Z}}$ is the indicator function of $\mathbb{Z}$.

Defining for $n \in \mathbb{Z}\backslash\{\pm ap/2\pi\}$

$$\boldsymbol{X}(n;t) := \frac{p}{i\left(2\pi n - ap\right)} \left(\begin{bmatrix} \frac{1}{2} & \frac{1}{2i} & 0 \\ -\frac{1}{2i} & \frac{1}{2} & 0 \\ 0 & 0 & 0 \end{bmatrix} \hat{\boldsymbol{V}}(n)\, e^{i \frac{2\pi n - ap}{p} t} - \begin{bmatrix} \frac{1}{2} & -\frac{1}{2i} & 0 \\ \frac{1}{2i} & \frac{1}{2} & 0 \\ 0 & 0 & 0 \end{bmatrix} \hat{\boldsymbol{V}}(-n)\, e^{-i \frac{2\pi n - ap}{p} t} \right),$$

the trajectory can be rewritten as

$$\begin{aligned}\boldsymbol{x}(t)-\boldsymbol{x}(0) &= \sum_{\substack{n=-\infty \\ n\neq ap/2\pi}}^{\infty} \boldsymbol{X}(n;t) + \chi_{\mathbb{Z}}\left(\frac{ap}{2\pi}\right) \left(\begin{bmatrix} \frac{1}{2} & -\frac{1}{2i} & 0 \\ \frac{1}{2i} & \frac{1}{2} & 0 \\ 0 & 0 & 0 \end{bmatrix} \hat{\boldsymbol{V}}\left(-\frac{ap}{2\pi}\right) + \begin{bmatrix} \frac{1}{2} & \frac{1}{2i} & 0 \\ -\frac{1}{2i} & \frac{1}{2} & 0 \\ 0 & 0 & 0 \end{bmatrix} \hat{\boldsymbol{V}}\left(\frac{ap}{2\pi}\right) \right) t \\ &\quad + \begin{bmatrix} 0 & 0 & 0 \\ 0 & 0 & 0 \\ 0 & 0 & 1 \end{bmatrix} \left(\sum_{\substack{n=-\infty \\ n\neq 0}}^{\infty} \hat{\boldsymbol{V}}(n)\, \frac{p\, e^{i \frac{2\pi n}{p} t}}{i\, 2\pi n} + \hat{\boldsymbol{V}}(0)\, t \right).\end{aligned} \tag{7.14}$$

Note that for all n and for all t, $\boldsymbol{X}(n;t) \cdot \begin{bmatrix} 0 \\ 0 \\ 1 \end{bmatrix} = 0$, and since the series $\sum_{n=-\infty}^{\infty} \left| \hat{\boldsymbol{V}}(n) \right|$ converges, the series of $\boldsymbol{X}(n;t)$ also converges absolutely [90], i.e.

$$\sup_t \left| \sum_{\substack{n=-\infty \\ n\neq ap/2\pi}}^{\infty} \boldsymbol{X}(n;t) \right| \leq \sup_t \sum_{\substack{n=-\infty \\ n\neq ap/2\pi}}^{\infty} \left| \boldsymbol{X}(n;t) \right| = C_{\boldsymbol{X}} < +\infty.$$

This is useful for computing the average trajectory that we will introduce in the next section.

7.2.2 Averaged Trajectories

We define $\boldsymbol{c}_0(t) = \boldsymbol{x}(t)$ and the sequence of averaged trajectories as

$$\boldsymbol{c}_k(t) = \frac{1}{p} \int_{t-\frac{p}{2}}^{t+\frac{p}{2}} \boldsymbol{c}_{k-1}(\tau)\, d\tau,$$

which is written in terms of $\boldsymbol{x}$ as

$$\boldsymbol{c}_k(t) = \int_{t-\frac{p}{2}}^{t+\frac{p}{2}} \int_{\tau_k-\frac{p}{2}}^{\tau_k+\frac{p}{2}} \dots \int_{\tau_2-\frac{p}{2}}^{\tau_2+\frac{p}{2}} \boldsymbol{x}(\tau_1)\, d\tau_1\, d\tau_2 \dots d\tau_k\,.$$

Since $\boldsymbol{x}$ satisfies (7.14), and the series of $\boldsymbol{X}(n;t)$ converges absolutely, the average trajectory $\boldsymbol{c}_k$ can be obtained by integrating it term by term:

$$\begin{aligned}\boldsymbol{c}_k\,(t) = &\sum_{\substack{n=-\infty\\ n\neq ap/2\pi}}^{\infty} \int_{t-\frac{p}{2}}^{t+\frac{p}{2}} \int_{\tau_k-\frac{p}{2}}^{\tau_k+\frac{p}{2}} \dots \int_{\tau_2-\frac{p}{2}}^{\tau_2+\frac{p}{2}} \boldsymbol{X}\,(n;\tau_1)\; d\tau_1\, d\tau_2 \dots d\tau_k\\ &+ \chi_{\mathbb{Z}}\left(\frac{ap}{2\pi}\right)\left(\begin{bmatrix} \frac{1}{2} & -\frac{1}{2i} & 0\\ \frac{1}{2i} & \frac{1}{2} & 0\\ 0 & 0 & 0\end{bmatrix}\hat{\boldsymbol{V}}\left(-\frac{ap}{2\pi}\right) + \begin{bmatrix} \frac{1}{2} & \frac{1}{2i} & 0\\ -\frac{1}{2i} & \frac{1}{2} & 0\\ 0 & 0 & 0\end{bmatrix}\hat{\boldsymbol{V}}\left(\frac{ap}{2\pi}\right)\right) t\\ &+ \begin{bmatrix} 0 & 0 & 0\\ 0 & 0 & 0\\ 0 & 0 & 1\end{bmatrix}\hat{\boldsymbol{V}}\,(0)\; t\,.\end{aligned}$$

Using the definition of $\boldsymbol{X}(n;t)$, the multiple integral can be computed as

$$\int_{t-\frac{p}{2}}^{t+\frac{p}{2}} \int_{\tau_k-\frac{p}{2}}^{\tau_k+\frac{p}{2}} \dots \int_{\tau_2-\frac{p}{2}}^{\tau_2+\frac{p}{2}} \boldsymbol{X}\,(n;\tau_1)\; d\tau_1\, d\tau_2 \dots d\tau_k = \left(\frac{\sin\left(\pi n - \frac{ap}{2}\right)}{\pi n - \frac{ap}{2}}\right)^k \boldsymbol{X}\,(n;t)\,.$$

- If $ap/2\pi \in \mathbb{Z}$ then $\sin(\pi n - ap/2)$ vanishes (remember that $n \neq ap/2\pi$ in the series) and the

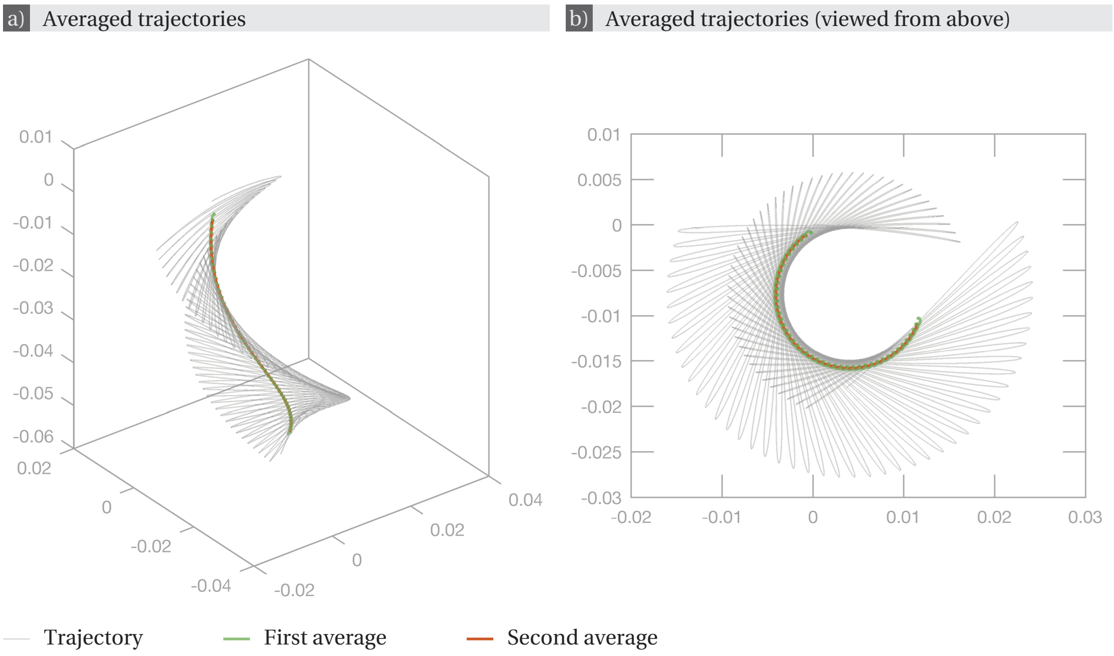

Figure 7.8 – **Swimmer B': averaged trajectories for** $a = 0.316$ **and** $\cos\psi = 0.8544$. The trajectory $\boldsymbol{x}(t)$ corresponds to the trajectory shown in fig. 7.5. The second averaged trajectory $\boldsymbol{c}_2(t)$ is helical.

integrals of the series of $\boldsymbol{X}(n;t)$ plays no role in the averaged trajectory $\boldsymbol{c}_k$ for $k \geq 1$, which becomes

$$\boldsymbol{c}_k(t) = \left(\begin{bmatrix} \frac{1}{2} & -\frac{1}{2i} & 0 \\ \frac{1}{2i} & \frac{1}{2} & 0 \\ 0 & 0 & 0 \end{bmatrix} \hat{\boldsymbol{V}}\left(-\frac{p}{2\pi}\right) + \begin{bmatrix} \frac{1}{2} & \frac{1}{2i} & 0 \\ -\frac{1}{2i} & \frac{1}{2} & 0 \\ 0 & 0 & 0 \end{bmatrix} \hat{\boldsymbol{V}}\left(\frac{p}{2\pi}\right) + \begin{bmatrix} 0 & 0 & 0 \\ 0 & 0 & 0 \\ 0 & 0 & 1 \end{bmatrix} \hat{\boldsymbol{V}}(0) \right) t \tag{7.15}$$

for all k. Consequently, $\boldsymbol{c}_k = \boldsymbol{c}_1$ for all $k \geq 1$ and is linear in t. It can be rewritten as

$$\boldsymbol{c}_k(t) = t \begin{bmatrix} \operatorname{Re}\left(\hat{V}_1\left(\frac{ap}{2\pi}\right)\right) + \operatorname{Im}\left(\hat{V}_2\left(\frac{ap}{2\pi}\right)\right) \\ \operatorname{Re}\left(\hat{V}_2\left(\frac{ap}{2\pi}\right)\right) - \operatorname{Im}\left(\hat{V}_1\left(\frac{ap}{2\pi}\right)\right) \\ \hat{V}_3(0) \end{bmatrix}.$$

Note that a periodic solution $Q(t)$ to (3.7) defines in fact an infinity of solutions $Q(t+\tau^*)$, where

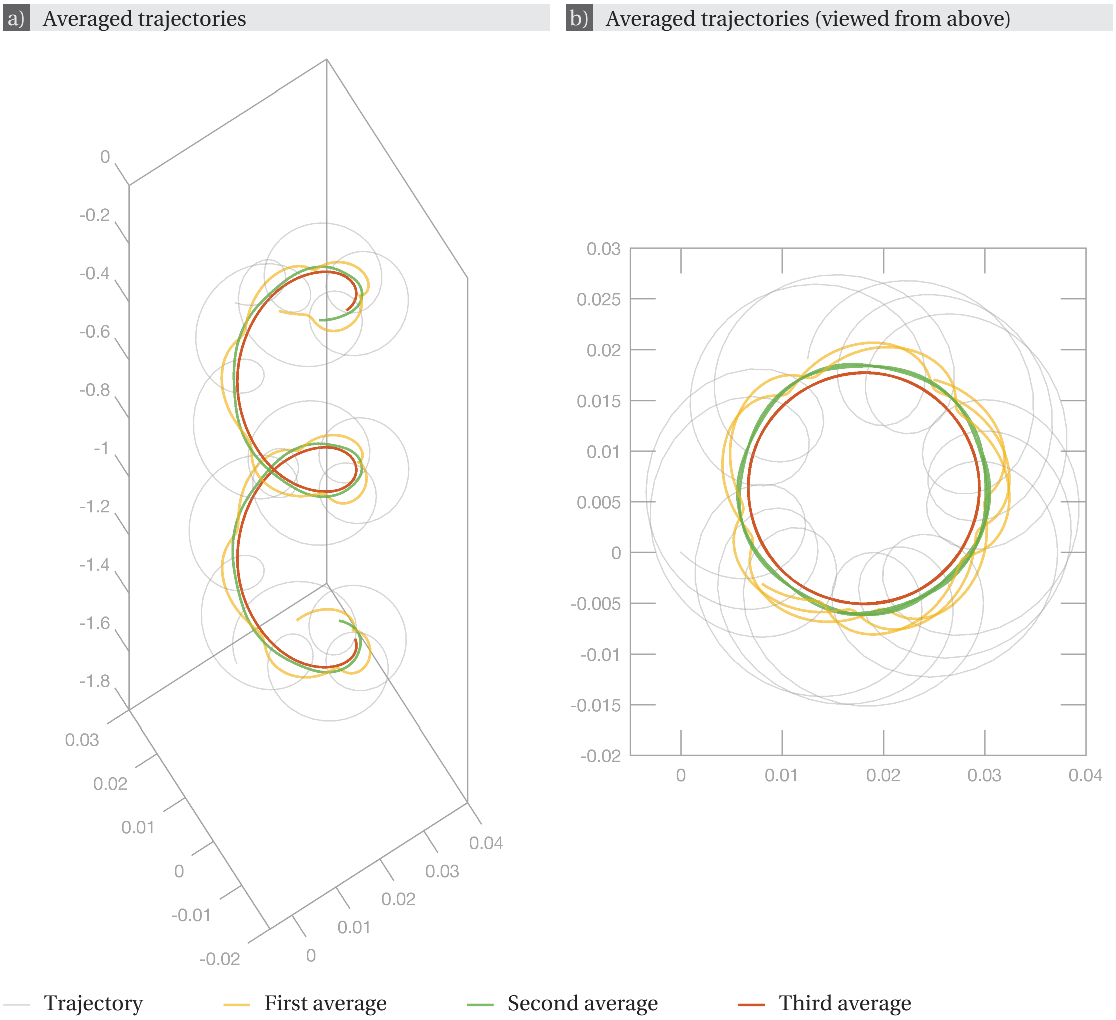

Figure 7.9 – **Swimmer B': averaged trajectories for** $a = 0.316$ **and** $\cos\psi = 0.8544$. The trajectory $\boldsymbol{x}(t)$ corresponds to the trajectory shown in fig. 7.6. The third averaged trajectory $\boldsymbol{c}_3(t)$ is helical.

$\tau^* \in [0, p)$. These solutions differ in the corresponding initial orientation of the swimmer given by $R = Q^T(\tau^*)$. The Fourier coefficient $\hat{\boldsymbol{V}}\left(\frac{ap}{2\pi}\right)$ computed as (7.13) depends on τ^* accordingly. Therefore, for different initial orientations of the swimmer, the average direction is different. The Fourier coefficient $\hat{\boldsymbol{V}}(0)$ is independent of the initial value of $\boldsymbol{V}(0)$ and therefore the third component of the average trajectory remains unchanged.

- If $ap/2\pi \notin \mathbb{Z}$ then

$$\boldsymbol{c}_k(t) = \sum_{n=-\infty}^{\infty} \left(\frac{\sin\left(\frac{\pi n - ap}{2}\right)}{\pi n - \frac{ap}{2}} \right)^k \boldsymbol{X}(n;t) + \begin{bmatrix} 0 & 0 & 0 \\ 0 & 0 & 0 \\ 0 & 0 & 1 \end{bmatrix} \hat{\boldsymbol{V}}(0)\; t\,. \tag{7.16}$$

The third component of $\boldsymbol{X}(n;t)$ vanishes for all n and t so the series exactly gives the first two components. Since

$$\left| \frac{\sin\left(\pi n - \frac{ap}{2}\right)}{\pi n - \frac{ap}{2}} \right| < 1$$

for all n, the averaging procedure has the effect of smoothening the trajectory by multiplying

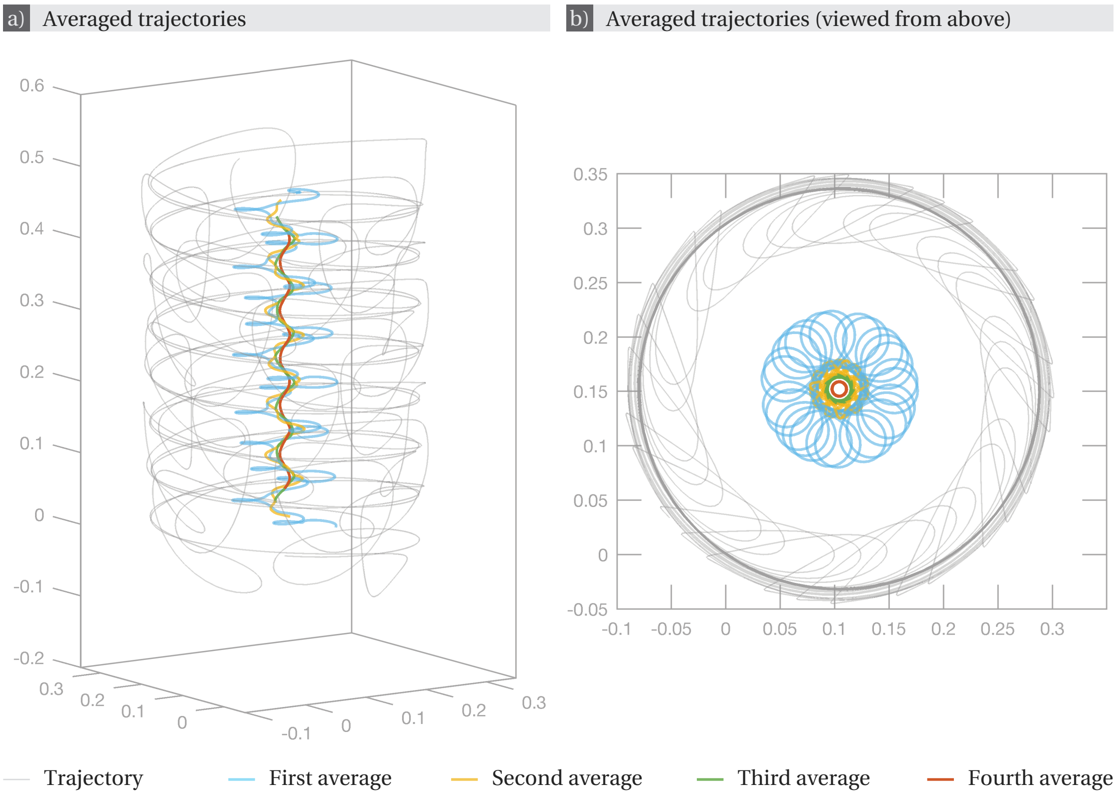
a) Averaged trajectories

b) Averaged trajectories (viewed from above)

Figure 7.10 – **Swimmer F: averaged trajectories for** $a = 0.8810$ **and** $\cos\psi = -0.1692$. The trajectory $\boldsymbol{x}(t)$ corresponds to the trajectory shown in fig. 7.7. The fourth averaged trajectory $\boldsymbol{c}_4(t)$ is helical.

the coefficients $\boldsymbol{X}(n;t)$ by factors that become smaller and smaller as k increases, and as the distance between n and $\frac{ap}{2\pi}$ increases.

The terms of the series contributing the most to the averaged trajectory $\boldsymbol{c}_k(t)$ are therefore terms for n within a close distance to $ap/2\pi$ and such that $\boldsymbol{X}(n;t)$ is large enough. Note that the $\boldsymbol{X}(n;t)$ are bounded by

$$\begin{aligned} |\boldsymbol{X}(0;t)| &\leq \frac{2\hat{\sigma}}{a} \\ |\boldsymbol{X}(n;t)| &\leq \frac{p^2\,(a+\sigma_1)\,\hat{\sigma}}{|\pi\,n|\,|\pi\,n-\frac{ap}{2}|} \quad \text{for } n \neq 0\,, \end{aligned}$$

where $\hat{\sigma}$ is the maximal singular value of the matrix $\mathsf{M}_{12}\,[\mathbf{m}\times]$, and σ_1 is the maximal singular value of P. Indeed, by definition,

$$|\boldsymbol{X}(n;t)| \leq \frac{p}{|2\pi\,n-a\,p|}\left(|\hat{\boldsymbol{V}}(n)|+|\hat{\boldsymbol{V}}(-n)|\right) \quad \text{for all } t\,.$$

The Fourier coefficients $\hat{\boldsymbol{V}}(n)$ are themselves bounded by

$$\begin{aligned} |\hat{\boldsymbol{V}}(0)| &\leq \frac{1}{p}\int_{-\frac{p}{2}}^{\frac{p}{2}} |\boldsymbol{V}(t)|\,dt \leq \hat{\sigma} \\ |\hat{\boldsymbol{V}}(n)| &\leq \frac{1}{|2\pi\,n|}\int_{-\frac{p}{2}}^{\frac{p}{2}} |\dot{\boldsymbol{V}}(t)|\,dt \leq \frac{1}{|2\pi\,n|}\int_{-\frac{p}{2}}^{\frac{p}{2}} 2|a\mathbf{e}_3-\mathsf{P}\,\mathbf{B}|\,|\boldsymbol{V}(t)|\,dt \\ &\leq \frac{p}{|\pi\,n|}\,(a+\sigma_1)\,\hat{\sigma} \quad \text{for } n \neq 0\,. \end{aligned}$$

If in the series for averaged trajectory $\boldsymbol{c}_k$, all terms have been smoothened out but one dominant term for $n = n^*$, i.e. there exists $\varepsilon \ll 1$ such that

$$\left|\sum_{\substack{n=-\infty \\ n\neq n^*}}^{\infty}\left(\frac{\sin\left(\frac{\pi n-ap}{2}\right)}{\pi n-\frac{ap}{2}}\right)^k \boldsymbol{X}(n;t)\right| < \varepsilon\,, \qquad \left|\left(\frac{\sin\left(\frac{\pi n^*-ap}{2}\right)}{\pi n^*-\frac{ap}{2}}\right)^k \boldsymbol{X}(n^*;t)\right| \gg \varepsilon\,,$$

then and approximation of order ε of $\boldsymbol{c}_k(t)$ is

$$\begin{aligned} &\frac{(-1)^{n^*k}\,2\,p\,\sin^k(a\,p/2)}{\left(\pi n^*-\frac{ap}{2}\right)^{k+1}}\left(\cos\left(\frac{2\pi\,n^*-a\,p}{p}\,t\right)\begin{bmatrix} \mathrm{Im}\left(\hat{V}_1(n^*)\right)-\mathrm{Re}\left(\hat{V}_2(n^*)\right) \\ \mathrm{Re}\left(\hat{V}_1(n^*)\right)+\mathrm{Im}\left(\hat{V}_2(n^*)\right) \\ 0 \end{bmatrix}\right. \\ &\qquad\qquad \left.+\sin\left(\frac{2\pi\,n^*-a\,p}{p}\,t\right)\begin{bmatrix} \mathrm{Re}\left(\hat{V}_1(n^*)\right)+\mathrm{Im}\left(\hat{V}_2(n^*)\right) \\ -\mathrm{Im}\left(\hat{V}_1(n^*)\right)+\mathrm{Re}\left(\hat{V}_2(n^*)\right) \\ 0 \end{bmatrix}\right)+\begin{bmatrix} 0 \\ 0 \\ \hat{V}_3(0) \end{bmatrix}, \end{aligned}$$

which is a vertical helix (cf. fig. 7.8-7.10).

Note that the average trajectory $\boldsymbol{c}_k(t)$ for $a\,p/2\pi \in \mathbb{Z}$ given by equation (7.15) is obtained as the limit of the generic expression (7.16) as $ap/2\pi \to n^* \in \mathbb{Z}$. Indeed the smoothing coefficients

$$\left(\frac{\sin\left(\pi n - \frac{ap}{2}\right)}{\pi n - \frac{ap}{2}}\right)^k$$

all tend to 0, except for $n = n^*$, where the limit is 1.

Axial Velocity

In both cases $ap/2\pi \in \mathbb{Z}$ and $ap/2\pi \notin \mathbb{Z}$, the averaged trajectories $\boldsymbol{c}_k(t)$ for $k \geq 1$ display constant velocity of the swimmer along the rotation axis of the magnetic field, and this average axial velocity is given by

$$\overline{v_{\text{ax}}} = \begin{bmatrix} 0 \\ 0 \\ 1 \end{bmatrix} \cdot \hat{\boldsymbol{V}}(0)\,,$$

where

$$\hat{\boldsymbol{V}}(0) = \frac{1}{p}\int_{-\frac{p}{2}}^{\frac{p}{2}} \boldsymbol{V}(t)\,dt = \frac{1}{p}\int_{-\frac{p}{2}}^{\frac{p}{2}} Q^T(t)\,\mathsf{M}_{12}\,[\mathbf{m}\times]\,Q(t)\begin{bmatrix} \sin\psi \\ 0 \\ \cos\psi \end{bmatrix} dt.$$

Using the notations $\mathbf{e}_3$ and $\mathbf{B}$, the axial velocity can be rewritten as

$$\overline{v_{\text{ax}}} = \frac{1}{p}\int_0^p \mathbf{e}_3(t)\cdot \mathsf{M}_{12}\,[\mathbf{m}\times]\,\mathbf{B}(t)\,dt.$$

This is indeed the average axial velocity obtained directly from (3.1b).

In this section, we studied the trajectories exhibited by swimmers when the rotational dynamics admit periodic solutions using Fourier analysis. In particular, an averaging procedure was introduced and allows to obtain an effective trajectory. The component along $\boldsymbol{e}_3$ of the effective trajectory is linear in time, while the components along the other lab frame vectors $\boldsymbol{e}_1$ and $\boldsymbol{e}_2$ are bounded in general, except when the period p and Mason number a satisfy $ap/2\pi \in \mathbb{Z}$.

7.3 Numerical Integration and Examples of Particular Swimmers

This section presents a few examples of trajectories obtained by numerical integration. Figures 7.11 and 7.12 each present one of the stable relative equilibria that swimmer B admits for $a = 0.2198$ and $\cos\psi = -0.3989$ (cf. the phase portrait of the rotational dynamics in fig. 6.22). The first one (fig. 7.11) has pitch $p = 0.1317$ and radius $r = 8.5473\cdot 10^{-3}$. The resulting axial velocity is $v_{\text{ax}} = 4.6088\cdot 10^{-3}$, which is slightly larger than the axial velocity corresponding to the second one (fig. 7.12): $v_{\text{ax}} = 3.2971\cdot 10^{-3}$. The pitch and radius for the second stable relative equilibrium are $p = 9.4251\cdot 10^{-2}$ and $r = 7.5316\cdot 10^{-3}$.

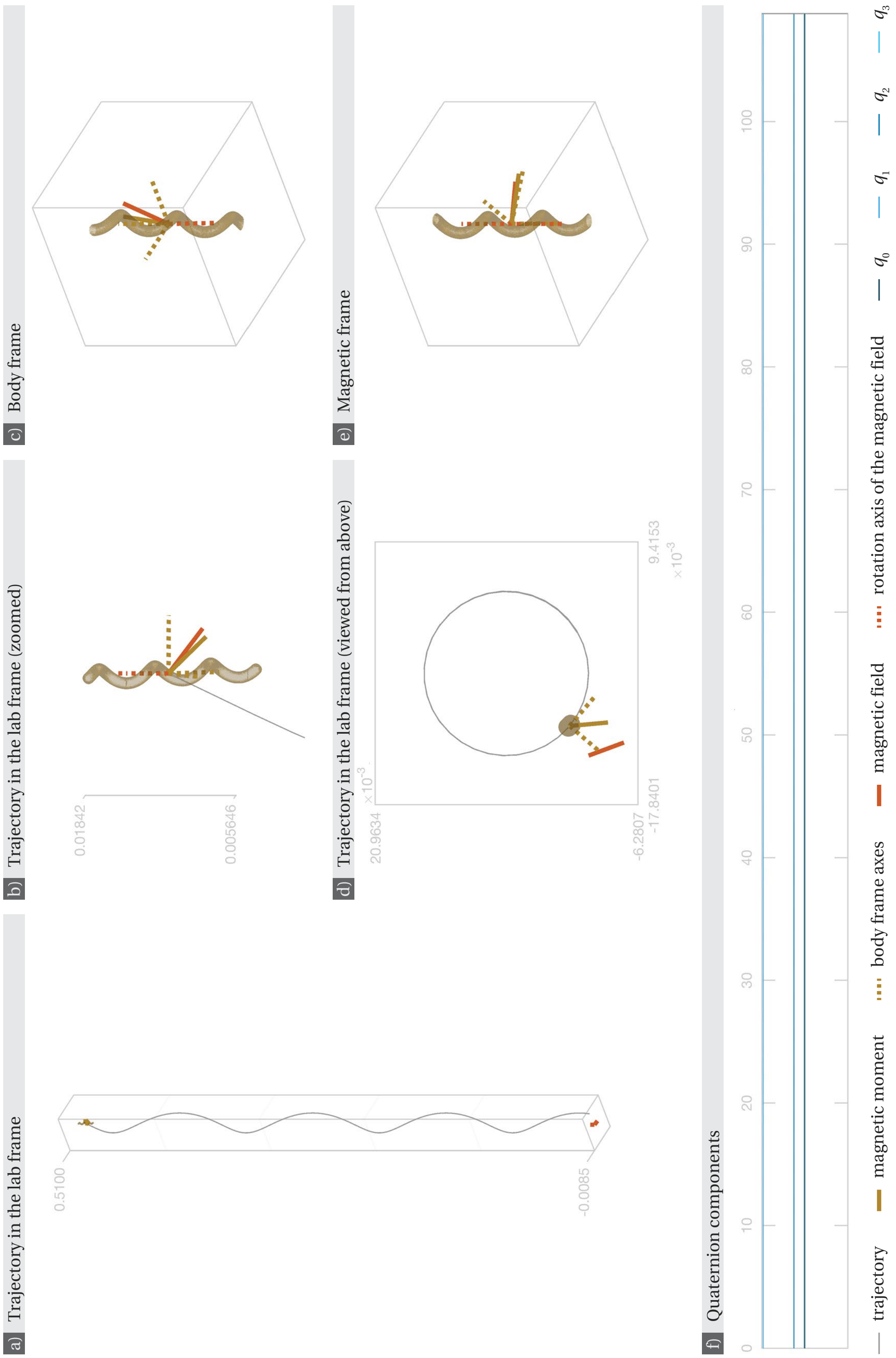
a) Trajectory in the lab frame
0.5100
-0.0085
b) Trajectory in the lab frame (zoomed)
0.01842
0.005646
c) Body frame
d) Trajectory in the lab frame (viewed from above)
20.9634
×10^-3
-6.2807
-17.8401
9.4153
×10^-3
e) Magnetic frame
f) Quaternion components
0
10
20
30
40
50
60
70
80
90
100
trajectory
magnetic moment
body frame axes
magnetic field
rotation axis of the magnetic field
q0
q1
q2
q3

Figure 7.11 (previous page) – **Swimmer B: first equilibrium trajectory with parameters** $a = 0.2198$ **and** $\cos\psi = -0.3989$. (a-c) Helical trajectory in the lab frame. The corresponding pitch is $p = 0.1317$, and the corresponding radius $r = 8.5473 \cdot 10^{-3}$. The resulting axial velocity is $v_{\text{ax}} = 4.6088 \cdot 10^{-3}$. The swimmer has been scaled so that the details of the trajectory remain visible: in actual proportions, the swimmer would be 245 times bigger. The proportions of the trajectory itself are respected. The width and depth of the plot box in panel (a) correspond to the axes dimensions of panel (c). (d) Orientation of the magnetic moment in the body frame. (e) Orientation of the swimmer in the magnetic frame. (f) Quaternion components of the corresponding rotational dynamics as functions of time: since the trajectory is a relative equilibrium, the components are constant.
There is another stable relative equilibrium for these parameter values (regime 2/4); the corresponding trajectory is shown in fig. 7.12. The phase portrait of the corresponding rotational dynamics is shown in fig. 6.22.
To see the swimmer in motion, click here (password: thesisPR) or scan the barcode.

Swimmer B' admits symmetric trajectories for the same value of a and $\cos\psi = 0.3989$ (cf. fig. 7.13-7.14): the radii are the same, but the pitches and axial velocities are the opposite to those of the corresponding relative equilibria for swimmer B.

Figures 7.15 and 7.16 show two different trajectories of swimmer C obtained by numerical integration of the rotational dynamics (3.14) for parameters $a = 0.2399$ and $\cos\psi = 0.6709$. Both solutions start in the neighbourhood of unstable relative equilibria and reach stable periodic orbits of the rotational dynamics (cf. the phase portrait in fig. 6.24). The relative equilibria have similar pitches, radii and axial velocities, but the periodic orbits yield very different asymptotic behaviours: in fig. 7.15 the swimmer drastically slows down when the periodic part of the rotational dynamics is reached, while in fig. 7.16, the swimmer keeps a similar pace. In fig. 7.15, the trajectory starts in the neighbourhood of a relative equilibrium of index 2. The corresponding pitch is $p = 0.1006$, the corresponding radius is $r = 7.1022 \cdot 10^{-3}$, and the resulting axial velocity is $v_{\text{ax}} = 3.8427 \cdot 10^{-3}$. When the trajectory reaches the periodic part of the quaternion dynamics, the average axial velocity decreases to $\overline{v_{\text{ax}}} = 6.7884 \cdot 10^{-5}$. In fig. 7.16, the trajectory starts in the neighbourhood of an unstable relative equilibrium of index 1. The corresponding pitch is $p = 0.1006$, the corresponding radius is $r = 7.1198 \cdot 10^{-3}$, and the resulting axial velocity is $v_{\text{ax}} = 3.8417 \cdot 10^{-3}$. The average axial velocity corresponding to the final periodic orbit is $\overline{v_{\text{ax}}} = 3.7327 \cdot 10^{-3}$, i.e. almost exactly the same.

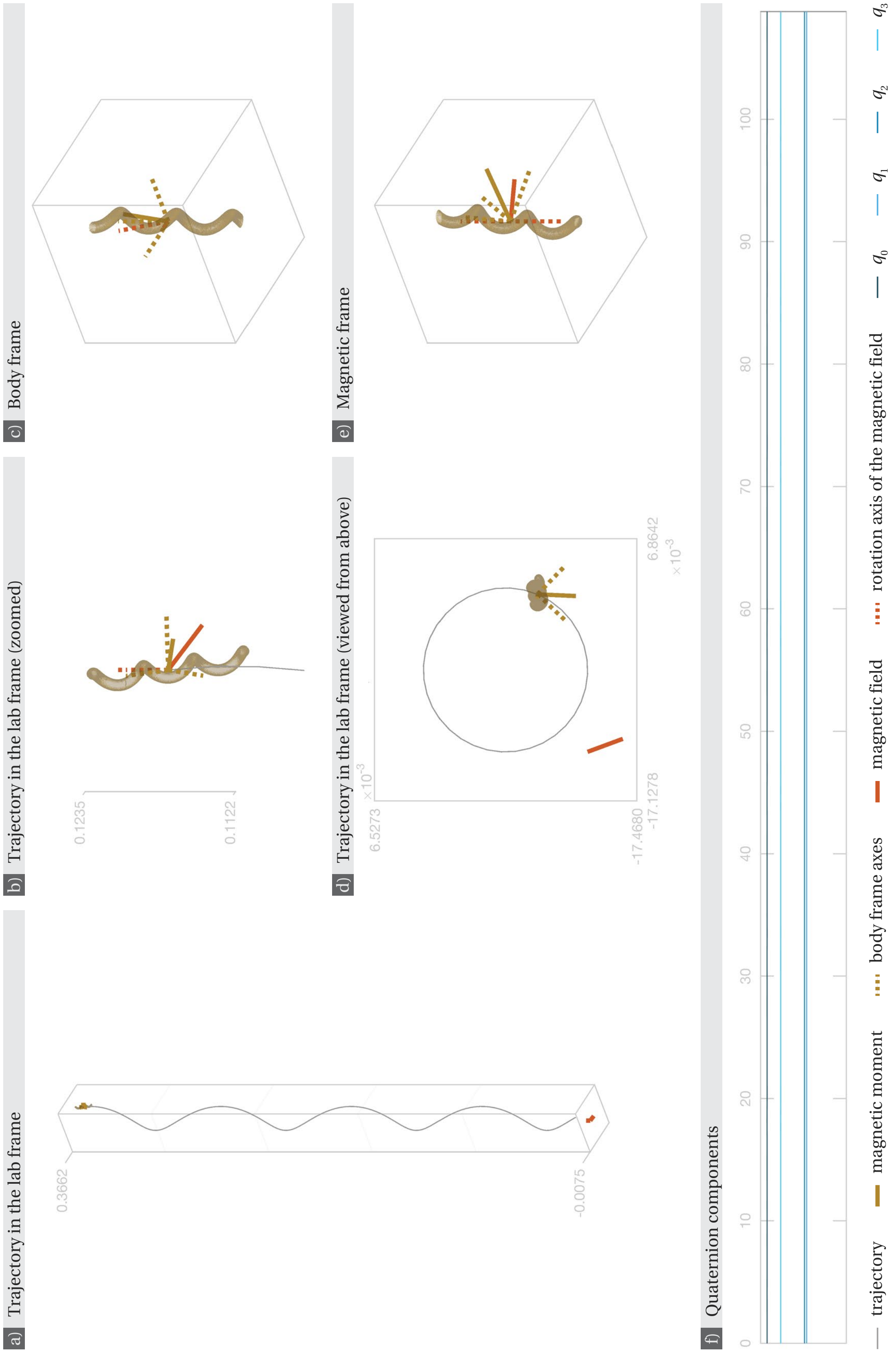
a) Trajectory in the lab frame
0.3662
-0.0075
b) Trajectory in the lab frame (zoomed)
0.1235
0.1122
c) Body frame
d) Trajectory in the lab frame (viewed from above)
6.5273
$\times 10^{-3}$
-17.4680
-17.1278
6.8642
$\times 10^{-3}$
e) Magnetic frame
f) Quaternion components
0
10
20
30
40
50
60
70
80
90
100
trajectory
magnetic moment
body frame axes
magnetic field
rotation axis of the magnetic field
q_0
q_1
q_2
q_3

Figure 7.12 (previous page) – **Swimmer B: second equilibrium trajectory with parameters** $a = 0.2198$ **and** $\cos\psi = -0.3989$. (a-c) Helical trajectory in the lab frame. The corresponding pitch is $p = 9.4251 \cdot 10^{-2}$, and the corresponding radius $r = 7.5316 \cdot 10^{-3}$. The resulting axial velocity is $v_{\mathrm{ax}} = 3.2971 \cdot 10^{-3}$. The swimmer has been scaled so that the details of the trajectory remain visible: in actual proportions, the swimmer would be 267 times bigger. The proportions of the trajectory itself are respected. The width and depth of the plot box in panel (a) correspond to the axes dimensions of panel (c). (d) Orientation of the magnetic moment in the body frame. (e) Orientation of the swimmer in the magnetic frame. (f) Quaternion components of the corresponding rotational dynamics as functions of time: since the trajectory is a relative equilibrium, the components are constant.

There is another stable relative equilibrium for these parameter values (regime 2/4); the corresponding trajectory is shown in fig. 7.11. The phase portrait of the corresponding rotational dynamics is shown in fig. 6.22.

To see the swimmer in motion, click here (password: thesisPR) or scan the barcode.

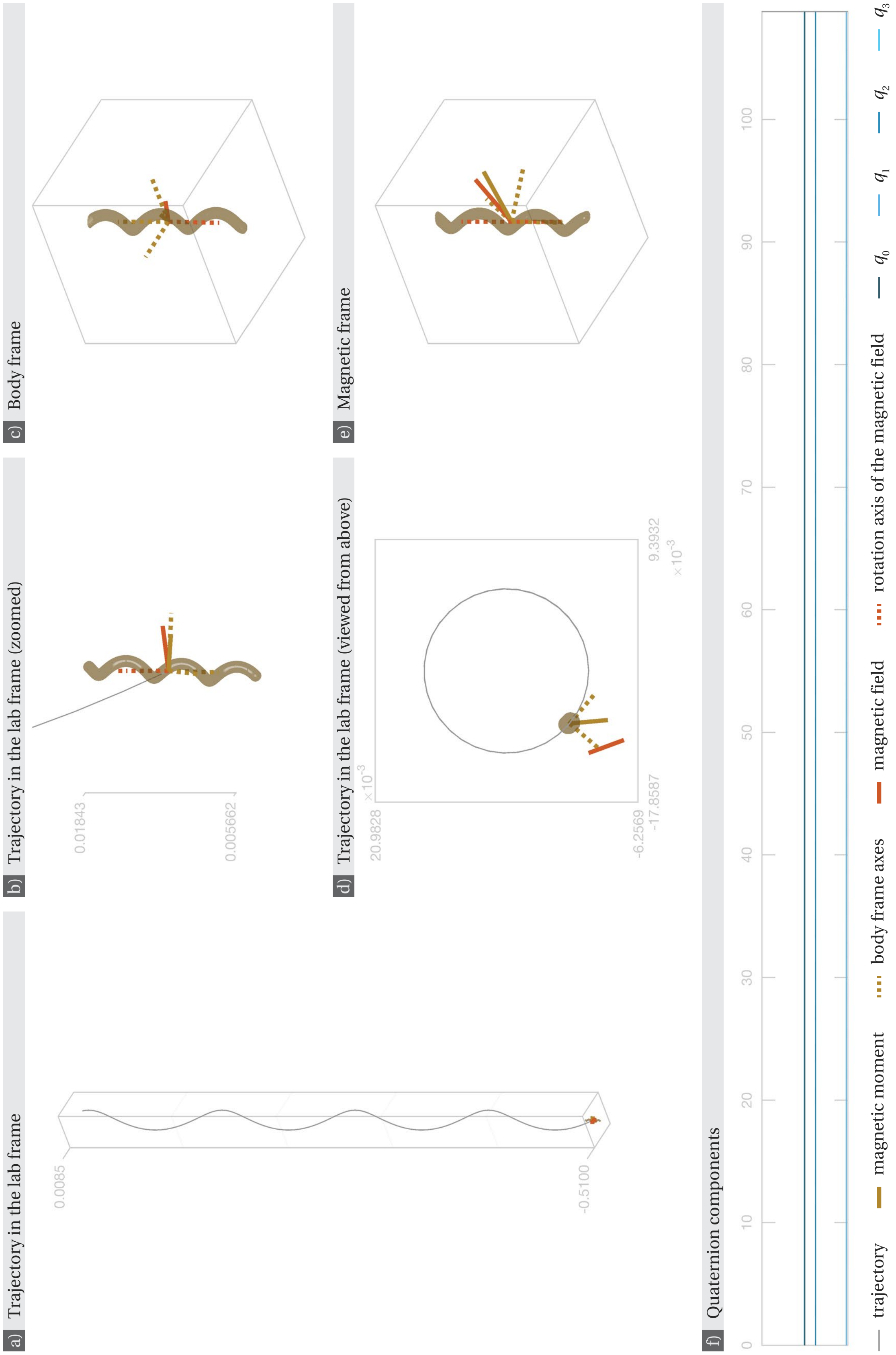
a) Trajectory in the lab frame
0.0085
-0.5100
b) Trajectory in the lab frame (zoomed)
0.01843
0.005662
c) Body frame
d) Trajectory in the lab frame (viewed from above)
20.9828
$\times 10^{-3}$
-6.2569
-17.8587
9.3932
$\times 10^{-3}$
e) Magnetic frame
f) Quaternion components
0
10
20
30
40
50
60
70
80
90
100
trajectory
magnetic moment
body frame axes
magnetic field
rotation axis of the magnetic field
q_0
q_1
q_2
q_3

Figure 7.13 (previous page) – **Swimmer B': first equilibrium trajectory with parameters $a = 0.2198$ and $\cos\psi = 0.3989$.** (a-c) Helical trajectory in the lab frame. The corresponding pitch is $p = -0.1317$, and the corresponding radius $r = 8.5430 \cdot 10^{-3}$. The resulting axial velocity is $v_{\text{ax}} = -5.8468 \cdot 10^{-3}$. The swimmer has been scaled so that the details of the trajectory remain visible: in actual proportions, the swimmer would be 235 times bigger. The proportions of the trajectory itself are respected. The width and depth of the plot box in panel (a) correspond to the axes dimensions of panel (c). (d) Orientation of the magnetic moment in the body frame. (e) Orientation of the swimmer in the magnetic frame. (f) Quaternion components of the corresponding rotational dynamics as functions of time: since the trajectory is a relative equilibrium, the components are constant.

This trajectory is symmetric (up to numerical imprecisions) to the trajectory of swimmer B shown in fig. 7.11. There is another relative equilibrium for these parameter values (regime 2/4); the corresponding trajectory is shown in fig. 7.14.

To see the swimmer in motion, click here (password: thesisPR) or scan the barcode.

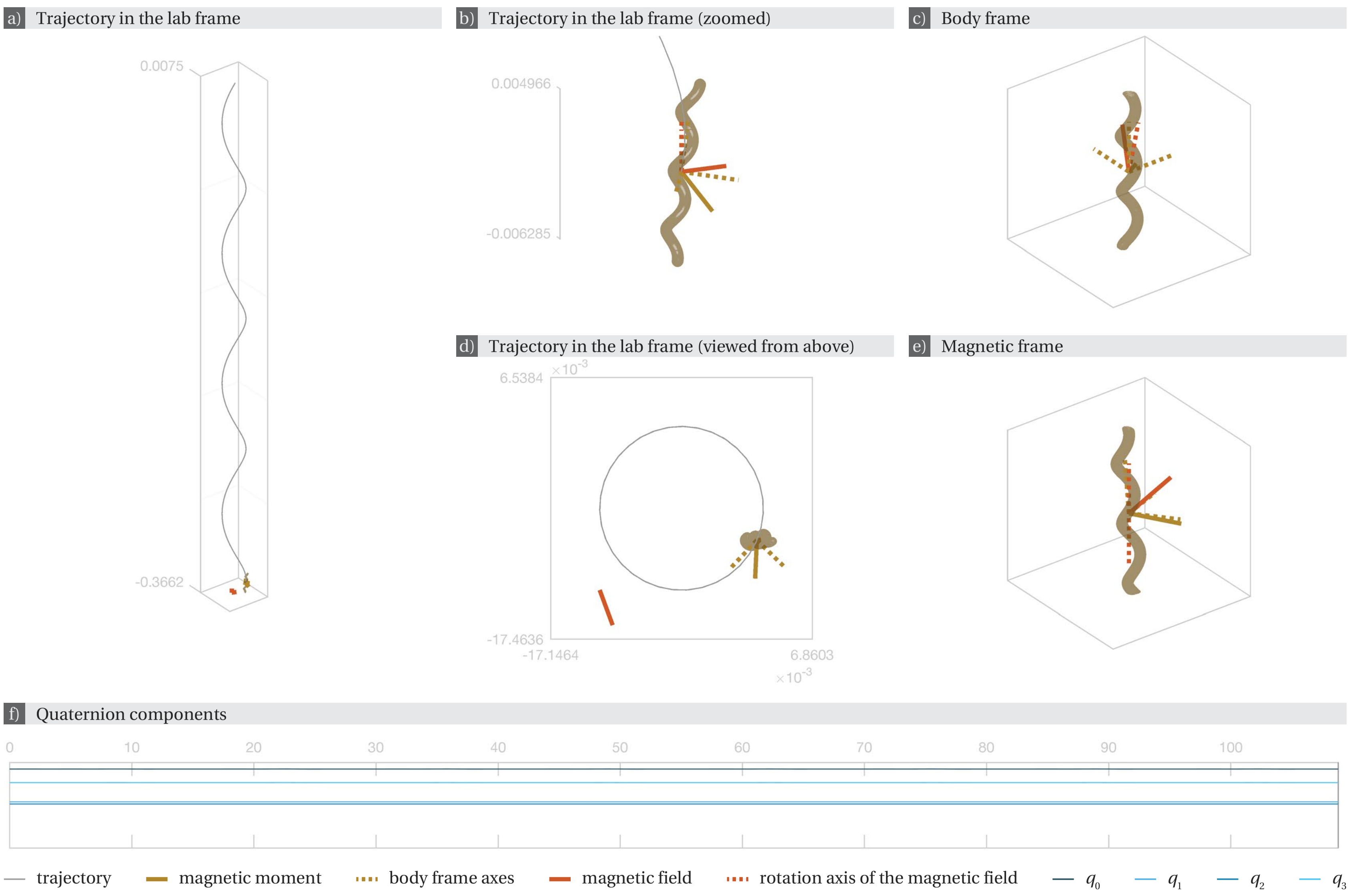
a) Trajectory in the lab frame
0.0075
-0.3662
b) Trajectory in the lab frame (zoomed)
0.004966
-0.006285
c) Body frame
d) Trajectory in the lab frame (viewed from above)
6.5384
$\times 10^{-3}$
-17.4636
-17.1464
6.8603
$\times 10^{-3}$
e) Magnetic frame
f) Quaternion components
0
10
20
30
40
50
60
70
80
90
100
trajectory
magnetic moment
body frame axes
magnetic field
rotation axis of the magnetic field
q_0
q_1
q_2
q_3

Figure 7.14 (previous page) – **Swimmer B': second equilibrium trajectory with parameters** $a = 0.2198$ **and** $\cos\psi = 0.3989$. (a-c) Helical trajectory in the lab frame. The corresponding pitch is $p = -9.4216 \cdot 10^{-2}$, and the corresponding radius $r = 7.5308 \cdot 10^{-3}$. The resulting axial velocity is $v_{\text{ax}} = -4.8498 \cdot 10^{-3}$. The swimmer has been scaled so that the details of the trajectory remain visible: in actual proportions, the swimmer would be 267 times bigger. The proportions of the trajectory itself are respected. The width and depth of the plot box in panel (a) correspond to the axes dimensions of panel (c). (d) Orientation of the magnetic moment in the body frame. (e) Orientation of the swimmer in the magnetic frame. (f) Quaternion components of the corresponding rotational dynamics as functions of time: since the trajectory is a relative equilibrium, the components are constant.
This trajectory is symmetric (up to numerical imprecisions) to the trajectory of swimmer B shown in fig. 7.12. There is another relative equilibrium for these parameter values (regime 2/4); the corresponding trajectory is shown in fig. 7.13.
To see the swimmer in motion, click here (password: thesisPR) or scan the barcode.

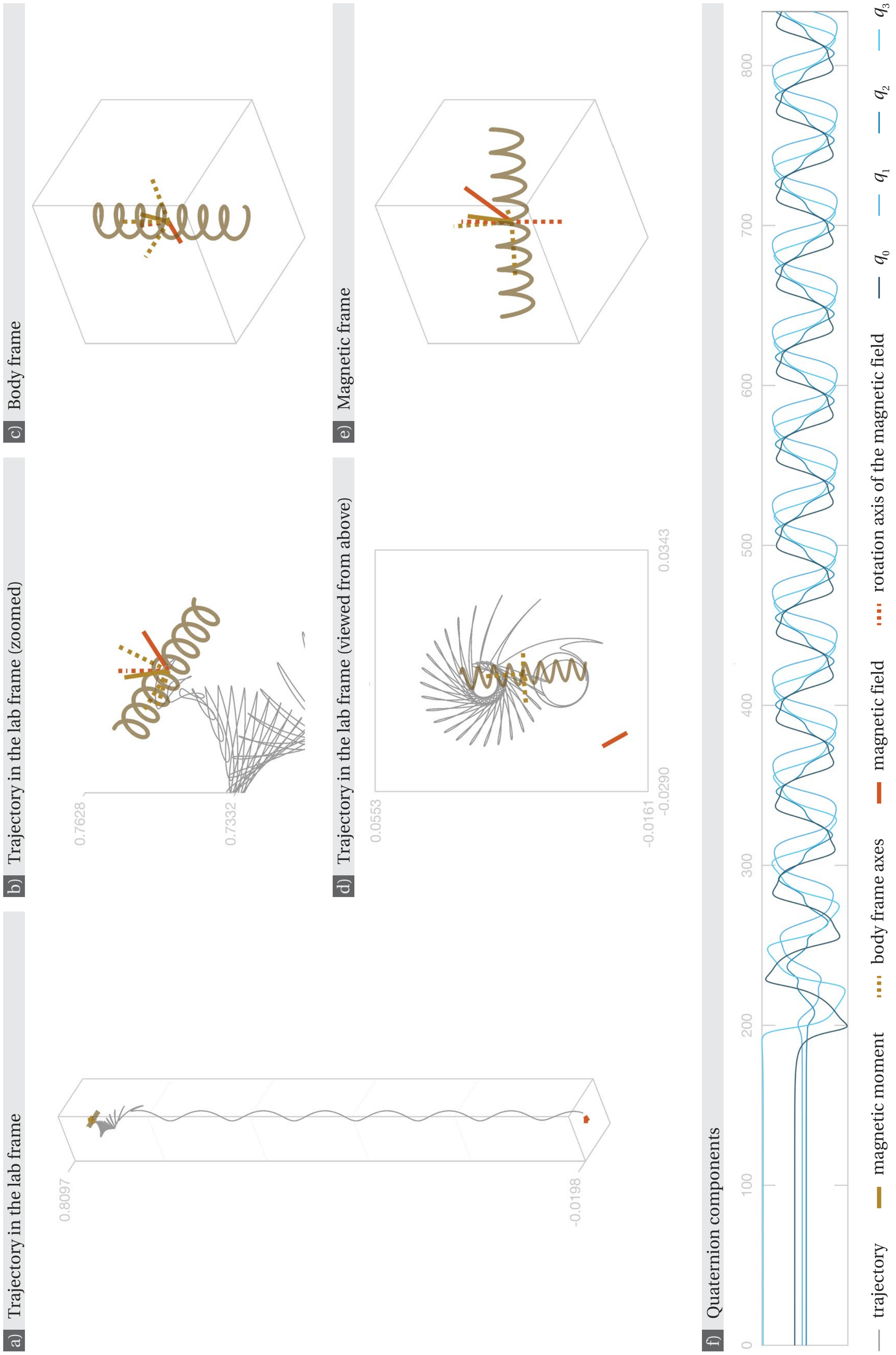
a) Trajectory in the lab frame
0.8097
-0.0198
b) Trajectory in the lab frame (zoomed)
0.7628
0.7332
c) Body frame
d) Trajectory in the lab frame (viewed from above)
0.0553
-0.0161
-0.0290
0.0343
e) Magnetic frame
f) Quaternion components
0
100
200
300
400
500
600
700
800
trajectory
magnetic moment
body frame axes
magnetic field
rotation axis of the magnetic field
q_0
q_1
q_2
q_3

Figure 7.15 (previous page) – **Swimmer C: first trajectory with parameters** $a = 0.2399$ **and** $\cos\psi = 0.6709$. (a-c) Trajectory in the lab frame. The rotational dynamics leave an unstable steady state and reach a stable periodic solution. The pitch corresponding to the unstable steady state is $p = 0.1006$, the radius is $r = 7.1022 \cdot 10^{-3}$, and the axial velocity is $v_{\mathrm{ax}} = 3.8427 \cdot 10^{-3}$. The average axial velocity corresponding to the periodic solution is $\overline{v_{\mathrm{ax}}} = 6.7884 \cdot 10^{-5}$. The swimmer has been scaled so that the details of the trajectory remain visible: in actual proportions, the swimmer would be 101 times bigger. The proportions of the trajectory itself are respected. The width and depth of the plot box in panel (a) correspond to the axes dimensions of panel (c). (d) Final orientation of the magnetic moment in the body frame. (e) Final orientation of the swimmer in the magnetic frame. (f) Quaternion components of the corresponding rotational dynamics as functions of time.

For these parameter values, the rotational dynamics of swimmer C admit another stable periodic orbit (regime 0/4); a trajectory tending to it is shown in fig. 7.16. The phase portrait of the corresponding rotational dynamics is shown in fig. 6.24.

To see the swimmer in motion, click here (password: thesisPR) or scan the barcode.

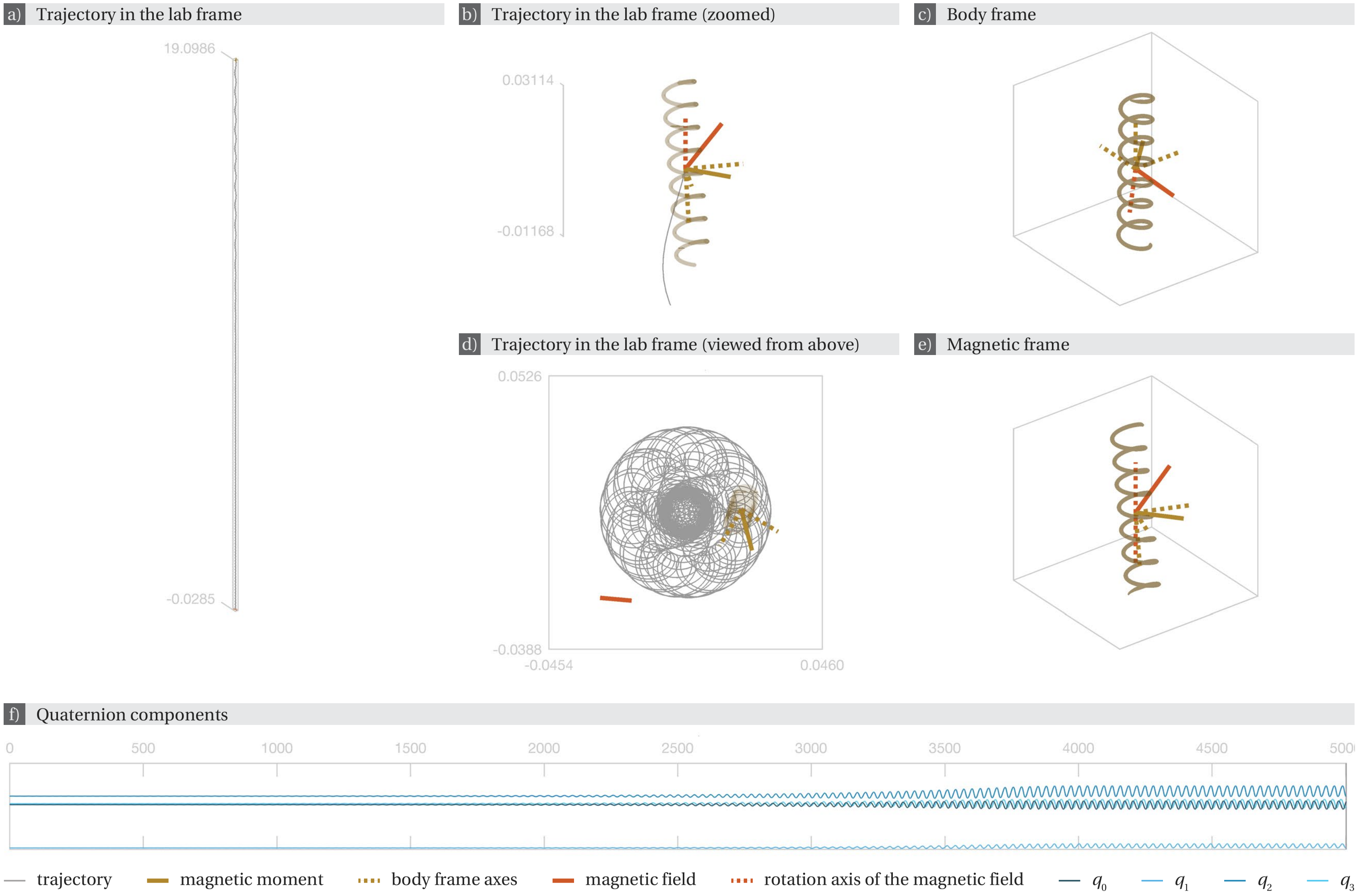
a) Trajectory in the lab frame
19.0986
-0.0285
b) Trajectory in the lab frame (zoomed)
0.03114
-0.01168
c) Body frame
d) Trajectory in the lab frame (viewed from above)
0.0526
-0.0388
-0.0454
0.0460
e) Magnetic frame
f) Quaternion components
0
500
1000
1500
2000
2500
3000
3500
4000
4500
500
trajectory
magnetic moment
body frame axes
magnetic field
rotation axis of the magnetic field
q_0
q_1
q_2
q_3

Figure 7.16 (previous page) – **Swimmer C: first trajectory with parameters** $a = 0.2399$ **and** $\cos\psi = 0.6709$. (a-c) Trajectory in the lab frame. The rotational dynamics leave an unstable steady state and reach a stable periodic solution. The pitch corresponding to the unstable steady state is $p = 0.1006$, the radius is $r = 7.1198 \cdot 10^{-3}$, and the axial velocity is $v_{\mathrm{ax}} = 3.8417 \cdot 10^{-3}$. The average axial velocity corresponding to the periodic solution is $\overline{v_{\mathrm{ax}}} = 3.7327 \cdot 10^{-3}$. The swimmer has been scaled so that the details of the trajectory remain visible: in actual proportions, the swimmer would be 21 times bigger. The proportions of the trajectory itself are respected. The width and depth of the plot box in panel (a) correspond to the axes dimensions of panel (c). (d) Final orientation of the magnetic moment in the body frame. (e) Final orientation of the swimmer in the magnetic frame. (f) Quaternion components of the corresponding rotational dynamics as functions of time.
For these parameter values, the rotational dynamics of swimmer C admit another stable periodic orbit (regime 0/4); a trajectory tending to it is shown in fig. 7.15. The phase portrait of the corresponding rotational dynamics is shown in fig. 6.24.
To see the swimmer in motion, click here (password: thesisPR) or scan the barcode.

Figure 7.17 shows a trajectory of swimmer D, obtained by numerical solution of the rotational dynamics (3.14) for parameters $a = 0.0217$ and $\cos\psi = 0.0090$ with an initial condition close to an unstable steady state of index 2. The rotational dynamics reach a stable steady state. The axial velocities of the initial and final relative equilibria have opposite signs, and as a result the swimmer reverses its direction. The pitch corresponding to the initial unstable steady state is $p = 4.7903 \cdot 10^{-2}$, the radius is $r = 1.8291 \cdot 10^{-2}$, and the axial velocity is $v_{\text{ax}} = 1.6544 \cdot 10^{-4}$. The rotational dynamics end up at a stable steady state, for which the pitch is $p = -7.3542 \cdot 10^{-2}$, the radius is $r = 2.6919 \cdot 10^{-2}$, and the axial velocity $v_{\text{ax}} = -2.5399 \cdot 10^{-4}$. The phase portrait of the corresponding rotational dynamics is shown in fig. 6.28. There is another stable relative equilibrium for the same parameter values: the corresponding pitch is $p = -7.3706 \cdot 10^{-2}$, the corresponding radius is $r = 2.6979 \cdot 10^{-2}$, and the resulting axial velocity is $v_{\text{ax}} = -2.5455 \cdot 10^{-4}$, which is very close to the axial velocity of the stable relative equilibrium shown in fig. 7.17.

Figures 7.18 and 7.19 show two trajectories of swimmer F for parameter values $a = 0.5$ and $\cos\psi = 0.0872$. Both were obtained by numerical integration of the rotational dynamics (3.14) starting in the neighbourhood of an unstable steady state, and each reaches a distinct stable relative equilibrium. Interestingly, the two relative equilibria yield two trajectories going in opposite direction with similar but opposite axial velocities. In figure 7.18, the initial unstable relative equilibrium (index 1) corresponds to a helical trajectory with pitch $p = -6.8503 \cdot 10^{-3}$, $r = 0.1126$, and axial velocity $v_{\text{ax}} = -5.4513 \cdot 10^{-4}$, and the final helical trajectory has pitch $p = 2.4830 \cdot 10^{-2}$, radius $r = 0.1898$, and axial velocity $v_{\text{ax}} = 1.9759 \cdot 10^{-3}$. In figure 7.19, the trajectory starts with a helix of pitch $p = 2.4831 \cdot 10^{-2}$, radius $r = 0.1898$, and axial velocity $v_{\text{ax}} = 1.9759 \cdot 10^{-3}$ and ends up as a helix of pitch $p = -1.2717 \cdot 10^{-2}$, radius $r = 0.1226$, and axial velocity $v_{\text{ax}} = -1.0120 \cdot 10^{-3}$. The phase portrait of the corresponding rotational dynamics is shown in fig. 6.31.

In the examples shown here, when two stable steady states coexist, the two resulting axial

Figure 7.17 (next page) – **Swimmer D: trajectory with parameters** $a = 0.0217$ **and** $\cos\psi = 0.0090$. (a-c) Trajectory in the lab frame. The rotational dynamics leave an unstable steady state and reach a stable steady state. The pitch corresponding to the unstable steady state is $p = 4.7903 \cdot 10^{-2}$, the radius is $r = 1.8291 \cdot 10^{-2}$, and the axial velocity is $v_{\text{ax}} = 1.6544 \cdot 10^{-4}$. The pitch corresponding to the stable steady state is $p = -7.3542 \cdot 10^{-2}$, the radius is $r = 2.6919 \cdot 10^{-2}$, and the axial velocity $v_{\text{ax}} = -2.5399 \cdot 10^{-4}$. The change of sign of the axial velocity implies that the swimmer reverses direction. The swimmer has been scaled so that the details of the trajectory remain visible: in actual proportions, the swimmer would be 73 times bigger. The proportions of the trajectory itself are respected. The width and depth of the plot box in panel (a) correspond to the axes dimensions of panel (c). (d) Final orientation of the magnetic moment in the body frame. (e) Final orientation of the swimmer in the magnetic frame. (f) Quaternion components of the corresponding rotational dynamics as functions of time.
Swimmer D admits another relative equilibrium for these parameter values (regime 2/8). The phase portrait of the corresponding rotational dynamics is shown in fig. 6.28.
To see the swimmer in motion, click here (password: thesisPR) or scan the barcode.

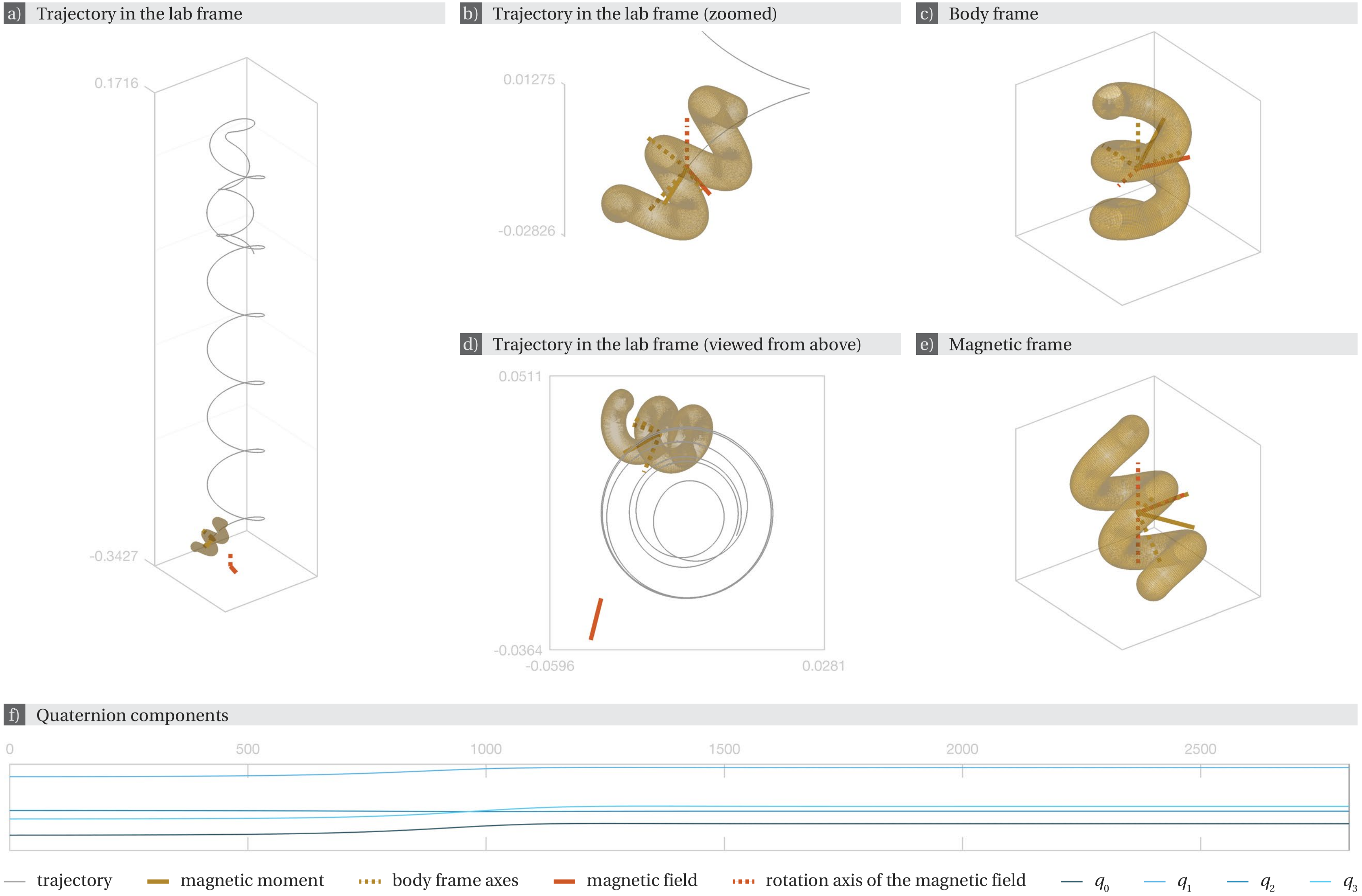
a) Trajectory in the lab frame
0.1716
-0.3427
b) Trajectory in the lab frame (zoomed)
0.01275
-0.02826
c) Body frame
d) Trajectory in the lab frame (viewed from above)
0.0511
-0.0364
-0.0596
0.0281
e) Magnetic frame
f) Quaternion components
0
500
1000
1500
2000
2500
trajectory
magnetic moment
body frame axes
magnetic field
rotation axis of the magnetic field
q_0
q_1
q_2
q_3

velocities have the same order of magnitude, but can be opposite, as pointed out in fig. 7.18-7.19. In all the other examples of rotational dynamics illustrated by the phase portraits of chapter 6 for which two stable steady states occur, the two resulting helical trajectories have similar axial velocities. As figures 7.15 and 7.16 emphasise, two coexisting stable periodic solutions might yield very different average axial velocities. The phase portraits of the rotational dynamics shown in figures 6.21 and 6.29 display both stable steady states and stable periodic orbits. For swimmer B with $a = 0.4362$ and $\cos\psi = -0.7577$ (phase portrait 6.21), the stable steady state results in a trajectory with axial velocity $v_{\text{ax}} = 8.2452 \cdot 10^{-3}$, while the stable periodic orbit results in a trajectory with an average axial velocity $\overline{v_{\text{ax}}} = 1.2005 \cdot 10{-}4$, which is remarkably slower. For swimmer E with $a = 0.3292$ and $\cos\psi = -0.5957$, the two stable steady states yield helical trajectories with respective axial velocities $v_{\text{ax}} = 1.0335 \cdot 10^{-2}$ and $v_{\text{ax}} = 1.0344 \cdot 10^{-2}$, while the stable periodic solution corresponds to a trajectory with average axial velocity $\overline{v_{\text{ax}}} = 9.9304 \cdot 10^{-3}$. These three axial velocities are similar in magnitude.

Figure 7.18 (next page) – **Swimmer F: first trajectory with parameters** $a = 0.5$ **and** $\cos\psi = 0.0872$. (a-c) Trajectory in the lab frame. The rotational dynamics leave an unstable steady state and reach a stable steady state. The pitch corresponding to the unstable steady state is $p = -6.8503 \cdot 10^{-3}$, the radius is $r = 0.1126$, and the axial velocity is $v_{\text{ax}} = -5.4513 \cdot 10^{-4}$. The pitch corresponding to the stable steady state is $p = 2.4830 \cdot 10^{-2}$, the radius is $r = 0.1898$, and the axial velocity $v_{\text{ax}} = 1.9759 \cdot 10^{-3}$. The swimmer has been scaled so that the details of the trajectory remain visible: in actual proportions, the swimmer would be 11 times bigger. The proportions of the trajectory itself are respected. The width and depth of the plot box in panel (a) correspond to the axes dimensions of panel (c). (d) Final orientation of the magnetic moment in the body frame. (e) Final orientation of the swimmer in the magnetic frame. (f) Quaternion components of the corresponding rotational dynamics as functions of time.
Swimmer F admits another stable relative equilibrium for these parameter values (regime 2/8); a trajectory tending to it is shown in fig. 7.19. Note that the other stable relative equilibrium results in a trajectory going in the opposite direction. The phase portrait of the corresponding rotational dynamics is shown in fig. 6.31.
To see the swimmer in motion, click here (password: thesisPR) or scan the barcode.

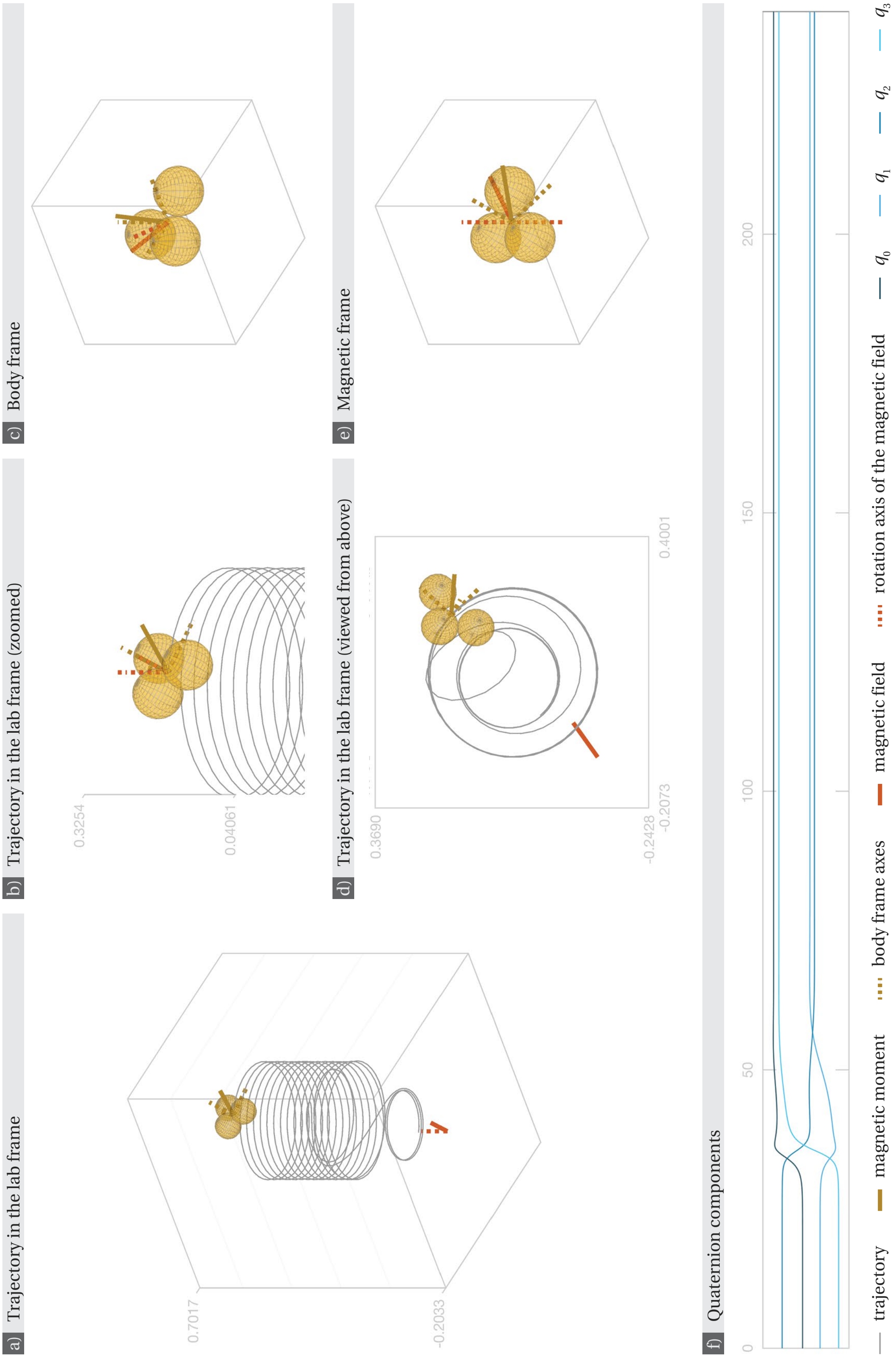

a) Trajectory in the lab frame

b) Trajectory in the lab frame (zoomed)

c) Body frame

d) Trajectory in the lab frame (viewed from above)

e) Magnetic frame

f) Quaternion components

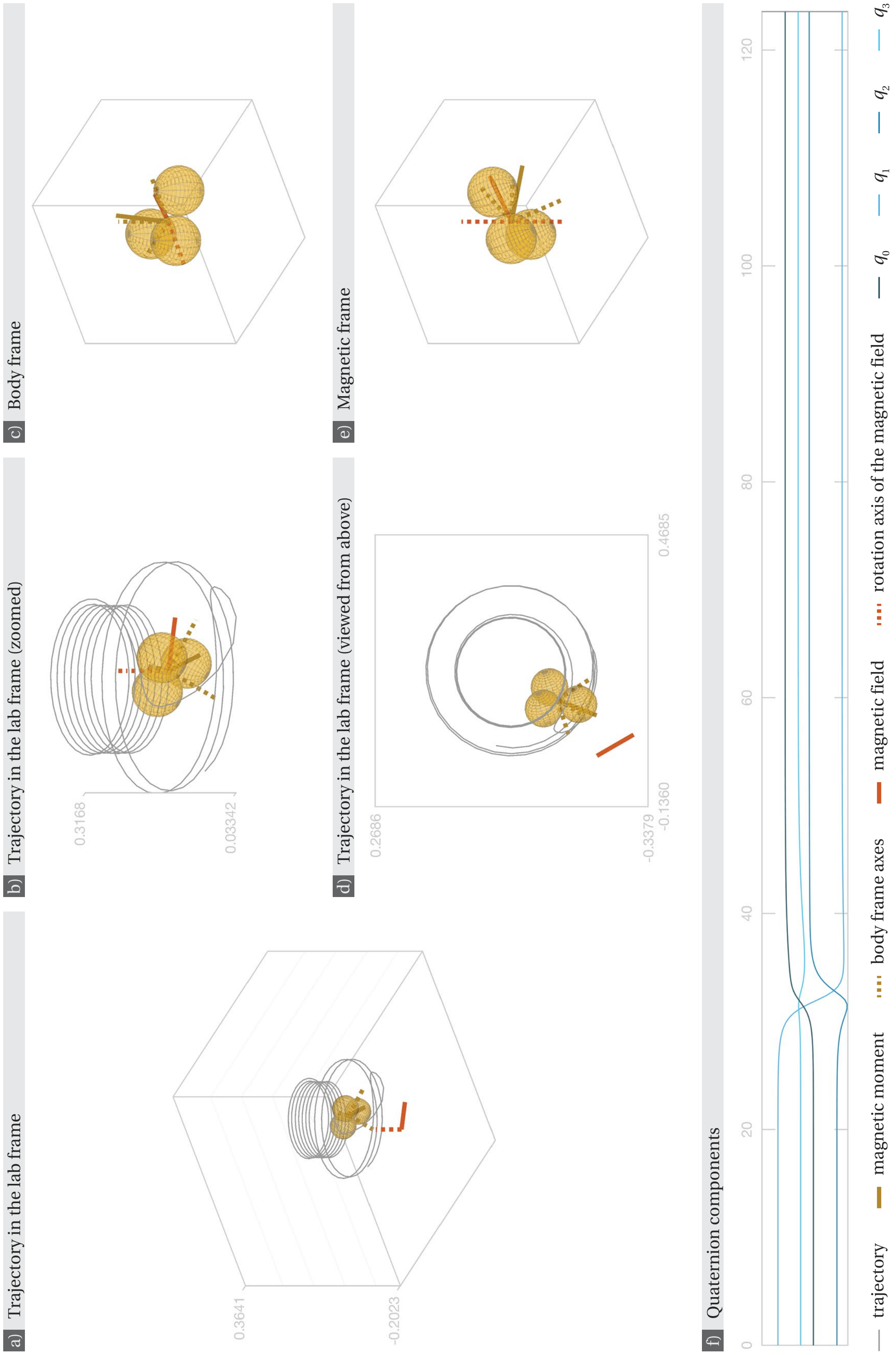
a) Trajectory in the lab frame
0.3641
-0.2023
b) Trajectory in the lab frame (zoomed)
0.3168
0.03342
c) Body frame
d) Trajectory in the lab frame (viewed from above)
0.2686
-0.3379
-0.1360
0.4685
e) Magnetic frame
f) Quaternion components
0
20
40
60
80
100
120
trajectory
magnetic moment
body frame axes
magnetic field
rotation axis of the magnetic field
q_0
q_1
q_2
q_3

Figure 7.19 (previous page) – **Swimmer F: second trajectory with parameters $a = 0.5$ and** $\cos\psi = 0.0872$. (a-c) Trajectory in the lab frame. The rotational dynamics leave an unstable steady state and reach a stable steady state. The pitch corresponding to the unstable steady state is $p = 2.4831 \cdot 10^{-2}$, the radius is $r = 0.1898$, and the axial velocity is $v_{\mathrm{ax}} = 1.9759 \cdot 10^{-3}$. The pitch corresponding to the stable steady state is $p = -1.2717 \cdot 10^{-2}$, the radius is $r = 0.1226$, and the axial velocity $v_{\mathrm{ax}} = -1.0120 \cdot 10^{-3}$. The swimmer has been scaled so that the details of the trajectory remain visible: in actual proportions, the swimmer would be 11 times bigger. The proportions of the trajectory itself are respected. The width and depth of the plot box in panel (a) correspond to the axes dimensions of panel (c). (d) Final orientation of the magnetic moment in the body frame. (e) Final orientation of the swimmer in the magnetic frame. (f) Quaternion components of the corresponding rotational dynamics as functions of time.
Swimmer F admits another stable relative equilibrium for these parameter values (regime 2/8); a trajectory tending to it is shown in fig. 7.18. Note that the other stable relative equilibrium results in a trajectory going in the opposite direction. The phase portrait of the corresponding rotational dynamics is shown in fig. 6.31.
To see the swimmer in motion, click here (password: thesisPR) or scan the barcode.

8 Swimming with Magnetic Rotation Axis Aligned with Gravity

Until now, only neutrally buoyant swimmers have been considered, i.e. swimmers with the centre of buoyancy coinciding with the centre of mass, and with a density equal to the density of the fluid. The subject of this chapter is the dynamics of swimmers that have a different density than the fluid. We treat explicitly the case of swimmers with a density higher than that of the fluid; they will be referred to as heavy swimmers.

The motion of a rigid body under the action of a rotating magnetic field $\mathbf{B}$ and of gravitation is specified by the equations (cf. section 2.4)

$$\begin{aligned}
\frac{\varepsilon}{1+\varepsilon_g}\left(\dot{\mathbf{v}}+\boldsymbol{\omega}\times\mathbf{v}\right) &= -\left(\mathsf{D}_{11}\mathbf{v}+\mathsf{D}_{12}\boldsymbol{\omega}\right) && +\gamma\frac{\varepsilon_g}{1+\varepsilon_g}\mathbf{g}\\
\frac{\varepsilon}{1+\varepsilon_g}\left(\dot{\mathbf{L}}+\boldsymbol{\omega}\times\mathbf{L}\right) &= -\left(\mathsf{D}_{12}^T\mathbf{v}+\mathsf{D}_{22}\boldsymbol{\omega}\right)+\mathbf{m}\times\mathbf{B} && +\gamma\boldsymbol{\Delta}\times\mathbf{g}.
\end{aligned} \tag{2.37}$$

After non-dimensionalisation, the magnetic moment $\mathbf{m}$, the magnetic field $\mathbf{B}$, and the opposite of gravitational acceleration $\mathbf{g}$ are unit vectors; $\boldsymbol{\Delta}$ is a vector going from the centre of mass of the swimmer to its centre of buoyancy, and the angular momentum $\mathbf{L}$ is related to the angular velocity $\boldsymbol{\omega}$ through $\mathbf{L}=\mathsf{I}_{\mathrm{cm}}\,\boldsymbol{\omega}$. The non-dimensional scalars ε and ε_g are given by $\varepsilon=\frac{V}{\ell^3}\,\mathrm{Re}$, where Re is the Reynolds number, and $\varepsilon_g=\rho_f/\rho_s-1$, where ρ_f and ρ_s are respectively the fluid and the swimmer density: if otherwise unloaded the swimmer floats if $\varepsilon_g>0$, is neutrally buoyant for $\varepsilon_g=0$, and sinks if $\varepsilon_g<0$. The number γ is the ratio between buoyancy and magnetic loads given by (cf. section 2.4)

$$\gamma=\frac{\rho_f\,V\,|\mathbf{g}|\,\ell}{m\,B}.$$

In the asymptotic limit of $\varepsilon/(1+\varepsilon_g)\ll 1$, the long term dynamics is entirely specified, as in the neutrally buoyant case, by

$$\dot{\boldsymbol{x}} = R^T \mathbf{v}, \tag{3.1a}$$

$$\dot{Q} = [(a\mathbf{e}_3 - \boldsymbol{\omega})\times]\, Q, \tag{3.6a}$$

$$R = R_3(a\,t)\, Q^T, \tag{7.1}$$

$$\mathbf{e}_3 = Q\begin{bmatrix}0\\0\\1\end{bmatrix}, \tag{3.6d}$$

where the linear and angular velocities are expressed as

$$\mathbf{v} = \mathsf{M}_{12}\,(\mathbf{m}\times\mathbf{B} + \gamma\,\boldsymbol{\Delta}\times\mathbf{g}) + \gamma\,\frac{\varepsilon_g}{1+\varepsilon_g}\,\mathsf{M}_{11}\,\mathbf{g}, \tag{2.39}$$

$$\boldsymbol{\omega} = \mathsf{M}_{22}\,(\mathbf{m}\times\mathbf{B} + \gamma\,\boldsymbol{\Delta}\times\mathbf{g}) + \gamma\,\frac{\varepsilon_g}{1+\varepsilon_g}\,\mathsf{M}_{12}^T\,\mathbf{g}, \tag{2.40}$$

with

$$\mathbf{B} = Q\begin{bmatrix}\sin\psi\\0\\\cos\psi\end{bmatrix}, \tag{3.6c}$$

$$\mathbf{g} = R^T\begin{bmatrix}\sin\chi\\0\\\cos\chi\end{bmatrix} = Q\,R_3^T(a\,t)\begin{bmatrix}\sin\chi\\0\\\cos\chi\end{bmatrix}, \tag{8.1}$$

where χ is the angle between $\mathbf{g}$ and $\mathbf{e}_3$. This choice for $\mathbf{g}$ implies that the magnetic field $\mathbf{B}$, its axis of rotation $\mathbf{e}_3$, and the lab vertical $\mathbf{g}$ are coplanar at time $t = 0$, which can be assumed without loss of generality. The translational dynamics decouples once again: that is, the rotational dynamics (2.40, 3.6c, 3.6a, 3.6d, 8.1) can be solved independently.

As in the previous cases, we further assume $\boldsymbol{\Delta} = 0$, i.e. the centres of mass and buoyancy coincide. Furthermore, in this chapter, we set

$$\tilde{\gamma} := -\gamma\,\frac{\varepsilon_g}{1+\varepsilon_g} > 0,$$

which implies that the swimmer sinks in the absence of magnetic loads. The linear and angular velocities (2.39, 2.40) are then

$$\mathbf{v} = \mathsf{M}_{12}\,(\mathbf{m}\times\mathbf{B}) - \tilde{\gamma}\,\mathsf{M}_{11}\,\mathbf{g}, \tag{8.2}$$

$$\boldsymbol{\omega} = \mathsf{M}_{22}\,(\mathbf{m}\times\mathbf{B}) - \tilde{\gamma}\,\mathsf{M}_{12}^T\,\mathbf{g}. \tag{8.3}$$

Substituting (3.6c, 8.1) in (8.3), and the result in (3.6a), the closed form equation for Q reads

$$\dot{Q} = \left[\left(a\,Q\begin{bmatrix}0\\0\\1\end{bmatrix} + \tilde{\gamma}\,\mathsf{M}_{12}^T\,Q\,R_3^T(a\,t)\begin{bmatrix}\sin\chi\\0\\\cos\chi\end{bmatrix} - \mathsf{P}\,Q\begin{bmatrix}\sin\psi\\0\\\cos\psi\end{bmatrix}\right)\times\right] Q, \tag{8.4}$$

where $\mathsf{P} = \mathsf{M}_{22}\,[\mathbf{m}\times]$. The swimmer dynamics is entirely determined by its solutions.

The non-dimensional number $\tilde{\gamma}$ is a new parameter. Note that it can be varied from one experiment to the next without altering the swimmer. Indeed, $\tilde{\gamma}$ is given by

$$\tilde{\gamma} = \frac{(\rho_s - \rho_f)\,V\,|\mathbf{g}|\,\ell}{m\,B}. \tag{8.5}$$

For a given swimmer, the density ρ_s, volume V, characteristic length ℓ, and magnetic moment magnitude m are fixed; the gravitational acceleration on earth $|\mathbf{g}|$ and fluid density ρ_f are fixed once and for all. But the magnitude of the magnetic field B can be varied from one experiment to the next. Therefore various values of $\tilde{\gamma}$ can be attained with the same swimmer. On the other hand, the Mason number satisfies

$$a = \frac{\alpha \eta \ell^3}{m B},$$

so that varying the magnetic field intensity affects the magnitude of both a and $\tilde{\gamma}$ in the same way, while varying the angular speed α of the magnetic field affects only a. To clarify the dependence of the non-dimensional parameters on the dimensional experimental parameters, we rewrite (8.4) as

$$\dot{Q} = \left[\left(\tilde{\gamma} \left(\overline{\alpha}\, Q \begin{bmatrix} 0 \\ 0 \\ 1 \end{bmatrix} + \mathsf{M}_{12}^T Q R_3^T(a t) \begin{bmatrix} \sin\chi \\ 0 \\ \cos\chi \end{bmatrix} \right) - \mathsf{P}\, Q \begin{bmatrix} \sin\psi \\ 0 \\ \cos\psi \end{bmatrix} \right) \times \right] Q, \tag{8.6}$$

where

$$\overline{\alpha} = \frac{a}{\tilde{\gamma}} = \frac{\alpha \eta \ell^2}{(\rho_s - \rho_f)\, V |\boldsymbol{g}|} \tag{8.7}$$

is varied from one experiment to the next only by changing the angular velocity of the magnetic field: $\overline{\alpha}$ depends neither on the magnitude of the magnetic field B nor on the conical angle ψ.

The symmetry of the neutrally buoyant equation discussed in section 3.3 is also verified for equation (8.6): let $Q(t)$ be a solution to (8.6) for the parameters $\tilde{\gamma}$, $\overline{\alpha}$, and ψ. Then the solution $\breve{Q}(t)$ defined by

$$\breve{Q}(t) := Q(-t) \begin{bmatrix} -1 & 0 & 0 \\ 0 & 1 & 0 \\ 0 & 0 & -1 \end{bmatrix} =: Q(-t)\, R_2(\pi) \tag{3.21}$$

also satisfies (8.6). Indeed, as in the neutrally buoyant case, we have $\breve{Q}(t) \begin{bmatrix} 0 \\ 0 \\ 1 \end{bmatrix} = -Q(-t) \begin{bmatrix} 0 \\ 0 \\ 1 \end{bmatrix}$, and $\breve{Q}(t) \begin{bmatrix} \sin\psi \\ 0 \\ \cos\psi \end{bmatrix} = -Q(-t) \begin{bmatrix} \sin\psi \\ 0 \\ \cos\psi \end{bmatrix}$. Furthermore,

$$\breve{Q}(t)\, R_3^T(a t) \begin{bmatrix} \sin\chi \\ 0 \\ \cos\chi \end{bmatrix} = -Q(-t) \begin{bmatrix} \sin\chi \cos(-a t) \\ -\sin\chi \sin(-a t) \\ \cos\chi \end{bmatrix} = -Q(-t)\, R_3^T(-a t) \begin{bmatrix} \sin\chi \\ 0 \\ \cos\chi \end{bmatrix},$$

where $a = \overline{\alpha}\tilde{\gamma}$, so that

$$\begin{aligned}
\dot{\breve{Q}}(t) &= \frac{d}{dt}\big(Q(-t)\, R_2(\pi)\big) = -\dot{Q}(-t)\, R_2(\pi) \\
&= -\left[\left(\tilde{\gamma} \left(\overline{\alpha}\, Q(-t) \begin{bmatrix} 0 \\ 0 \\ 1 \end{bmatrix} + \mathsf{M}_{12}^T Q(-t)\, R_3^T(-a t) \begin{bmatrix} \sin\chi \\ 0 \\ \cos\chi \end{bmatrix} \right) - \mathsf{P}\, Q(-t) \begin{bmatrix} \sin\psi \\ 0 \\ \cos\psi \end{bmatrix} \right) \times \right] Q(-t)\, R_2(\pi) \\
&= \left[\left(\tilde{\gamma} \left(\overline{\alpha}\, \breve{Q}(t) \begin{bmatrix} 0 \\ 0 \\ 1 \end{bmatrix} + \mathsf{M}_{12}^T \breve{Q}(t)\, R_3^T(a t) \begin{bmatrix} \sin\chi \\ 0 \\ \cos\chi \end{bmatrix} \right) - \mathsf{P}\, \breve{Q}(t) \begin{bmatrix} \sin\psi \\ 0 \\ \cos\psi \end{bmatrix} \right) \times \right] \breve{Q}(t).
\end{aligned}$$

As in the neutrally buoyant case, the angle $\phi(t)$ between the magnetic moment $\mathbf{m}$ and the magnetic field $\mathbf{B}(t)$ is in dipole symmetry with $\breve{\phi}(t) = \pi - \phi(-t)$. The linear and angular velocities in the body frame $\mathbf{v}(t)$ and $\boldsymbol{\omega}(t)$ are in correspondence with $\breve{\mathbf{v}}(t) = -\mathbf{v}(-t)$ and

$\boldsymbol{\omega}(t) = -\boldsymbol{\omega}(-t)$, and the trajectory given by position $\boldsymbol{x}(t)$ is the dipole symmetric twin of $\breve{\boldsymbol{x}}(t) = \boldsymbol{x}_0 + R_2(\pi)\big(\boldsymbol{x}(t) - \boldsymbol{x}_0\big)$. Finally, if $Q(t)$ represent an asymptotic behaviour of the system (8.6) as $t \to \infty$, then $\breve{Q}(-t)$ represents an asymptotic behaviour as $t \to -\infty$, as in the neutrally buoyant case (cf. section 3.3).

Contrarily to the neutrally buoyant equation (3.7), equation (8.6) is generally not autonomous: its dependence on $\mathbf{g}$, which is not constant in the magnetic frame, implies an explicit dependence on time. This prevents the existence of relative equilibria, and makes the methods of chapter 4 impossible to translate. Equation (8.6) is however autonomous in the specific case where $\sin\chi = 0$, i.e. the axis of rotation $\boldsymbol{e}_3$ is either parallel or antiparallel to the gravitational force. Accordingly, we focus on this specific setting; the foreseen application is the control of upward motion of heavy swimmers. In section 8.1, we apply similar techniques as those used in chapter 4 to study the set of relative equilibria for $\sin\chi = 0$. In section 8.2 we examine the resulting trajectories, and in particular we discuss how to optimise the axial velocity of a swimmer. In section 8.3, we study the perturbation arising when the axis of rotation is not exactly vertical.

8.1 Relative Equilibria

In this section, we study the relative equilibria of the differential equation (8.6) in the specific case where $\sin\chi = 0$, i.e. the axis of rotation $\boldsymbol{e}_3$ of the magnetic field is vertical in the lab frame, in the sense that it is aligned with gravity. In this case, the body frame expression $\mathbf{g}$ of the vertical can be rewritten as

$$\mathbf{g} = -\varsigma\,\mathbf{e}_3\,,$$

where $\varsigma := -\operatorname{sign}(\cos\chi)$. If $\varsigma = +1$, then the axis of rotation $\boldsymbol{e}_3$ points downwards in the lab frame, which means that the magnetic field rotates clockwise when viewed from above, and if $\varsigma = -1$, the axis of rotation $\boldsymbol{e}_3$ points upwards, so that the magnetic field rotates counterclockwise when viewed from above.

For $\sin\chi = 0$, equation (8.6) becomes autonomous and can be rewritten

$$\dot{Q} = \left[\left(\tilde{\gamma}\left(\overline{\alpha}\mathbf{I} - \varsigma\,\mathsf{M}_{12}^{T}\right) Q \begin{bmatrix}0\\0\\1\end{bmatrix} - \mathsf{P}\,Q\begin{bmatrix}\sin\psi\\0\\\cos\psi\end{bmatrix}\right)\times\right] Q\,. \tag{8.8}$$

As before, the notations

$$\mathbf{e}_3 = Q\begin{bmatrix}0\\0\\1\end{bmatrix}, \qquad\qquad \mathbf{B} = Q\begin{bmatrix}\sin\psi\\0\\\cos\psi\end{bmatrix}$$

will be used for short. For readability, $\tilde{\gamma}$ will be denoted γ from now on.

Equation (8.8) is in steady state if and only if

$$\gamma\left(\overline{\alpha}\mathbf{I}-\varsigma\,\mathsf{M}_{12}^{T}\right)\mathbf{e}_3=\mathsf{P}\,\mathbf{B}. \tag{8.9}$$

We provide a parametrisation of the set of steady states using the singular decomposition of a matrix $\tilde{\mathsf{P}}(\overline{\alpha})$ to be specified. This parametrisation allows to find that the number of steady states is generically 0, 4, or 8 for triples of parameters $(\gamma,\overline{\alpha},\psi)$.

The matrix $\tilde{\mathsf{P}}(\overline{\alpha})$

We define the matrix

$$\tilde{\mathsf{P}}(\overline{\alpha})=\left(\overline{\alpha}\mathbf{I}-\varsigma\,\mathsf{M}_{12}^{T}\right)^{\dagger}\mathsf{P},$$

where $\left(\overline{\alpha}\mathbf{I}-\varsigma\,\mathsf{M}_{12}^{T}\right)^{\dagger}$ is the Moore-Penrose pseudo inverse of $\left(\overline{\alpha}\mathbf{I}-\varsigma\,\mathsf{M}_{12}^{T}\right)$.

The Moore-Penrose pseudo-inverse of a real matrix C, denoted $C^{\dagger}$, is defined by [91]

- $C\,C^{\dagger}\,C=C$
- $C^{\dagger}\,C\,C^{\dagger}=C^{\dagger}$
- $(C\,C^{\dagger})^{T}=C\,C^{\dagger}$
- $(C^{\dagger}\,C)^{T}=C^{\dagger}\,C.$

Some properties of the Moore-Penrose pseudo-inverse are going to be used in the following:

- if C is invertible, then $C^{\dagger}=C^{-1}$
- $\mathbf{I}-C^{\dagger}\,C$ is the projector on Ker$C$
- the solutions of $C\boldsymbol{x}=\boldsymbol{y}$ are given by $\boldsymbol{x}=C^{\dagger}\,\boldsymbol{y}+(\mathbf{I}-C^{\dagger}\,C)\,\boldsymbol{z}$ for arbitrary vectors $\boldsymbol{z}$.

With this definition for $\tilde{\mathsf{P}}(\overline{\alpha})$, the equilibrium condition (8.9) is rewritten

$$\gamma\,\mathbf{e}_3=\tilde{\mathsf{P}}(\overline{\alpha})\,\mathbf{B}+\mathbf{z}, \tag{8.10}$$

where $\mathbf{z}$ is an arbitrary vector in $\mathrm{Ker}\left(\overline{\alpha}\mathbf{I}-\varsigma\,\mathsf{M}_{12}^{T}\right)$. In the following, the real eigenvalues of $\varsigma\,\mathsf{M}_{12}$ are assumed to have geometric multiplicity 1, so that $\mathrm{Ker}\left(\overline{\alpha}\mathbf{I}-\varsigma\,\mathsf{M}_{12}^{T}\right)$ is either zero or one-dimensional for all $\overline{\alpha}$. Note that there are at most three values of $\overline{\alpha}$ for which $\mathrm{Ker}\left(\overline{\alpha}\mathbf{I}-\varsigma\,\mathsf{M}_{12}^{T}\right)\neq\{\mathbf{0}\}$.

As in chapter 4, we will use the singular value decomposition of $\tilde{\mathsf{P}}(\overline{\alpha})$: its unit left-singular vectors are denoted $\tilde{\boldsymbol{\eta}}_j(\overline{\alpha})$, its singular values $\tilde{\sigma}_j(\overline{\alpha})$, and its unit right-singular vectors $\tilde{\boldsymbol{\beta}}_j(\overline{\alpha})$ for $j=0,1,2$. They satisfy

$$\tilde{\sigma}_j(\overline{\alpha})\,\tilde{\boldsymbol{\eta}}_j(\overline{\alpha})=\tilde{\mathsf{P}}(\overline{\alpha})\,\tilde{\boldsymbol{\beta}}_j(\overline{\alpha}),\qquad \tilde{\sigma}_j(\overline{\alpha})\,\tilde{\boldsymbol{\beta}}_j(\overline{\alpha})=\tilde{\mathsf{P}}^{T}(\overline{\alpha})\,\tilde{\boldsymbol{\eta}}_j(\overline{\alpha}).$$

For any value of $\overline{\alpha}$, $\tilde{\sigma}_1(\overline{\alpha})$ is assumed to be the largest singular value of $\tilde{\mathsf{P}}(\overline{\alpha})$. Note that the singular value decomposition of $\tilde{\mathsf{P}}(\overline{\alpha})$ is related to the singular value decomposition of P. Indeed

$$\tilde{\mathsf{P}}(\overline{\alpha})\,\boldsymbol{\beta}_0 = \left(\overline{\alpha}\mathbf{I} - \varsigma\,\mathsf{M}_{12}^T\right)^{\dagger}\mathsf{P}\,\boldsymbol{\beta}_0 = 0$$

for all values of $\overline{\alpha}$. This implies $\tilde{\sigma}_0(\overline{\alpha}) = \sigma_0 = 0$ is a singular value of $\tilde{\mathsf{P}}(\overline{\alpha})$, and $\boldsymbol{\beta}_0(\overline{\alpha}) = \tilde{\boldsymbol{\beta}}_0 = \mathbf{m}$ is a right-singular vector.

That $\tilde{\mathsf{P}}(\overline{\alpha})$ admits 0 as a singular value implies in particular that $\tilde{\mathsf{P}}(\overline{\alpha})\,\mathbf{B}$ is in the plane spanned by $\tilde{\boldsymbol{\eta}}_1(\overline{\alpha})$ and $\tilde{\boldsymbol{\eta}}_2(\overline{\alpha})$ for all $\mathbf{B}$, i.e. $\tilde{\mathsf{P}}(\overline{\alpha})\,\mathbf{B} \perp \tilde{\boldsymbol{\eta}}_0(\overline{\alpha})$.

Parametrisation of Relative Equilibria for $\overline{\alpha}$ not an eigenvalue of $\varsigma\,\mathsf{M}_{12}$

If $\overline{\alpha}$ is not an eigenvalue of $\varsigma\,\mathsf{M}_{12}$, then the matrix $\left(\overline{\alpha}\mathbf{I} - \varsigma\,\mathsf{M}_{12}^T\right)$ is invertible, and equation (8.10) can be rewritten

$$\gamma\,\mathbf{e}_3 = \tilde{\mathsf{P}}(\overline{\alpha})\,\mathbf{B}\,. \tag{8.11}$$

If $\mathbf{e}_3$ and $\mathbf{B}$ are unit vectors satisfying (8.11), there exist $\theta \in (-\pi, \pi]$ such that

$$\mathbf{e}_3 = \cos\theta\,\tilde{\boldsymbol{\eta}}_1(\overline{\alpha}) + \sin\theta\,\tilde{\boldsymbol{\eta}}_2(\overline{\alpha})\,, \tag{8.12}$$

and there exist $\xi \in (-\pi, \pi]$ and $\phi \in [0, \pi]$ such that

$$\mathbf{B} = \cos\phi\,\boldsymbol{\beta}_0 + \sin\phi\left(\cos\xi\,\tilde{\boldsymbol{\beta}}_1(\overline{\alpha}) + \sin\xi\,\boldsymbol{\beta}_2(\overline{\alpha})\right). \tag{8.13}$$

Projecting equation (8.11) on $\tilde{\boldsymbol{\eta}}_1(\overline{\alpha})$ and $\tilde{\boldsymbol{\eta}}_2(\overline{\alpha})$ yields that the angles θ and ξ are related through

$$\begin{aligned}
\gamma\,\cos\theta &= \sin\phi\,\cos\xi\,\tilde{\sigma}_1(\overline{\alpha})\,,\\
\gamma\,\sin\theta &= \sin\phi\,\sin\xi\,\tilde{\sigma}_2(\overline{\alpha})\,,
\end{aligned}$$

which allow to express γ in terms of θ and ϕ as

$$\gamma = \sin\phi\left(\frac{\cos^2\theta}{\tilde{\sigma}_1^2(\overline{\alpha})} + \frac{\sin^2\theta}{\tilde{\sigma}_2^2(\overline{\alpha})}\right)^{-1/2}, \tag{8.14}$$

and $\mathbf{B}$ as

$$\mathbf{B} = \cos\phi\,\tilde{\boldsymbol{\beta}}_0 + \frac{\sin\phi}{\sqrt{\tilde{\sigma}_2^2(\overline{\alpha})\,\cos^2\theta + \tilde{\sigma}_1^2(\overline{\alpha})\,\sin^2\theta}}\left(\tilde{\sigma}_2(\overline{\alpha})\,\cos\theta\,\tilde{\boldsymbol{\beta}}_1(\overline{\alpha}) + \tilde{\sigma}_2(\overline{\alpha})\,\sin\theta\,\tilde{\boldsymbol{\beta}}_2(\overline{\alpha})\right). \tag{8.15}$$

The equation

$$\cos\psi = \mathbf{e}_3(\overline{\alpha},\theta)\cdot\mathbf{B}(\overline{\alpha},\theta,\phi)\,,$$

where $\mathbf{e}_3(\overline{\alpha},\theta)$ is given by (8.12) and $\mathbf{B}(\overline{\alpha},\theta,\phi)$ by (8.15), gives an equilibrium condition for the angle ψ between $\mathbf{e}_3$ and $\mathbf{B}$. This condition can be developed as

$$\begin{aligned}\cos\psi = {} & \cos\phi\big(\tilde{c}_{01}(\overline{\alpha})\cos\theta + \tilde{c}_{02}(\overline{\alpha})\sin\theta\big) \\ & + \frac{\sin\phi}{\sqrt{\tilde{\sigma}_2^2(\overline{\alpha})\cos^2\theta + \tilde{\sigma}_1^2(\overline{\alpha})\sin^2\theta}}\big(\tilde{c}_{11}(\overline{\alpha})\cos^2\theta + \tilde{c}_{22}(\overline{\alpha})\sin^2\theta + \tilde{c}_{12}(\overline{\alpha})\cos\theta\sin\theta\big)\,,\end{aligned} \tag{8.16}$$

where $\tilde{c}_{01}(\overline{\alpha}) = \tilde{\boldsymbol{\beta}}_0\cdot\tilde{\boldsymbol{\eta}}_1(\overline{\alpha})$, $\tilde{c}_{02}(\overline{\alpha}) = \tilde{\boldsymbol{\beta}}_0\cdot\tilde{\boldsymbol{\eta}}_2(\overline{\alpha})$, $\tilde{c}_{11}(\overline{\alpha}) = \tilde{\sigma}_2(\overline{\alpha})\,\tilde{\boldsymbol{\beta}}_1(\overline{\alpha})\cdot\tilde{\boldsymbol{\eta}}_1(\overline{\alpha})$, $\tilde{c}_{22}(\overline{\alpha}) = \tilde{\sigma}_1(\overline{\alpha})\,\tilde{\boldsymbol{\beta}}_2(\overline{\alpha})\cdot\tilde{\boldsymbol{\eta}}_2(\overline{\alpha})$, and $\tilde{c}_{12}(\overline{\alpha}) = \tilde{\boldsymbol{\beta}}_1(\overline{\alpha})\cdot\big(\tilde{\mathsf{P}}(\overline{\alpha}) + \tilde{\mathsf{P}}^T(\overline{\alpha})\big)\,\tilde{\boldsymbol{\beta}}_2(\overline{\alpha})$.

Equations (8.12, 8.14, 8.15, 8.16) provide a complete parametrisation of the set of steady states to (8.8) in terms of $\overline{\alpha}\geq 0$, $\theta\in(-\pi,\pi]$, and $\psi\in[0,\pi]$ when $\overline{\alpha}$ is not an eigenvalue of $\varsigma\,\mathsf{M}_{12}$. The solution $Q\in\mathrm{SO}(3)$ to equation (8.8) can be computed from $\mathbf{B}$ and $\mathbf{e}_3$ as

$$Q = \left[\frac{1}{\sin\psi}(\mathbf{B} - \cos\psi\,\mathbf{e}_3)\,\middle|\,\frac{1}{\sin\psi}\mathbf{e}_3\times\mathbf{B}\,\middle|\,\mathbf{e}_3\right]. \tag{8.17}$$

The proposition of chapter 4 on the number of relative equilibria can be translated directly here.

Proposition For given experimental parameters γ, $\overline{\alpha}$, and ψ, the differential equation (8.8) admits almost always 0, 4, or 8 steady states. Namely, the parameter values for which the number of equilibria is different form a set of measure zero in the space of parameters.

Proof Let $\overline{\alpha}^*\geq 0$ be not equal to an eigenvalue of $\varsigma\,\mathsf{M}_{12}$. The steady states of (8.8) with $\overline{\alpha}=\overline{\alpha}^*$ are parametrised by θ and ϕ through equations (8.12, 8.15, 8.14, 8.16). This parametrisation has the same properties as the parametrisation (4.3, 4.4, 4.5) proposed for the neutrally buoyant case in chapter 4. In particular, the set

$$\tilde{\mathscr{S}}(\overline{\alpha}^*) = \big\{\big(\gamma(\overline{\alpha}^*,\theta,\phi),\cos\psi(\overline{\alpha}^*,\theta,\phi),\phi\big) : 0\leq\theta<2\pi\,,\,0\leq\phi\leq\pi\big\}\,,$$

where $\gamma(\overline{\alpha},\theta,\phi)$ is given by (8.14) and $\cos\psi(\overline{\alpha},\theta,\phi)$ by (8.16), is a particular instance of the surface $\mathscr{S}$ defined by equation (4.6). Consequently, for any given parameter values γ^* and ψ^*, the number of steady states to (8.8) with $\overline{\alpha}=\overline{\alpha}^*$, $\gamma=\gamma^*$, and $\psi=\psi^*$ is 0, 2, 4, 6, or 8; if it is either 2 or 6, there are pairs of parameters (γ,ψ) in any neighbourhood of (γ^*,ψ^*) for which (8.8) admits 0, 4, or 8 steady states.

The set of the eigenvalues of $\varsigma\,\mathsf{M}_{12}$ contains at most three elements, and consequently, any triple of parameters $(\overline{\alpha}^*,\gamma^*,\psi^*)$ is arbitrarily close to a triple of parameters $(\overline{\alpha},\gamma,\psi)$ for which the number of steady states to (8.8) is 0, 4, or 8. ■

Parametrisation of the set of relative equilibria for $\overline{\alpha}$ an eigenvalue of $\varsigma\,\mathsf{M}_{12}$

If $\overline{\alpha}$ is an eigenvalue of $\varsigma\,\mathsf{M}_{12}$, then every $\mathbf{z} \in \mathrm{Ker}\big(\overline{\alpha}\mathbf{I} - \varsigma\,\mathsf{M}_{12}^T\big)$ is a left-singular vector of $\tilde{\mathsf{P}}(\overline{\alpha})$ associated with 0. Indeed $\mathrm{Ker}\big(\overline{\alpha}\mathbf{I} - \varsigma\,\mathsf{M}_{12}^T\big) = \mathrm{Ker}\big(\overline{\alpha}\mathbf{I} - \varsigma\,\mathsf{M}_{12}^T\big)^{\dagger}$, and $\mathbf{z} \in \mathrm{Ker}\big(\overline{\alpha}\mathbf{I} - \varsigma\,\mathsf{M}_{12}\big)^{\dagger}$ satisfies

$$\tilde{\mathsf{P}}(\overline{\alpha})^T\,\mathbf{z} = \mathsf{P}^T\left(\overline{\alpha}\mathbf{I} - \varsigma\,\mathsf{M}_{12}\right)^{\dagger}\mathbf{z} = \mathbf{0}.$$

Accordingly, it can be specified that $\tilde{\boldsymbol{\eta}}_0(\overline{\alpha}) \in \mathrm{Ker}\big(\overline{\alpha}\mathbf{I} - \varsigma\,\mathsf{M}_{12}^T\big)$.

Assuming that $\mathrm{Ker}\big(\overline{\alpha}\mathbf{I} - \varsigma\,\mathsf{M}_{12}^T\big)$ has dimension one, the equilibrium condition (8.10) can then be rewritten as

$$\gamma\,\mathbf{e}_3 = \tilde{\mathsf{P}}(\overline{\alpha})\,\mathbf{B} + z\,\tilde{\boldsymbol{\eta}}_0(\overline{\alpha}), \tag{8.18}$$

for some scalar z. Writing $\mathbf{B}$ as (8.15) and projecting on $\tilde{\boldsymbol{\eta}}_j(\overline{\alpha})$ for $j = 0, 1, 2$ yields

$$\begin{aligned}
\gamma\,\mathbf{e}_3 \cdot \tilde{\boldsymbol{\eta}}_0(\overline{\alpha}) &= z \\
\gamma\,\mathbf{e}_3 \cdot \tilde{\boldsymbol{\eta}}_1(\overline{\alpha}) &= \sin\phi\,\cos\xi\,\tilde{\sigma}_1(\overline{\alpha}) \\
\gamma\,\mathbf{e}_3 \cdot \tilde{\boldsymbol{\eta}}_2(\overline{\alpha}) &= \sin\phi\,\sin\xi\,\tilde{\sigma}_2(\overline{\alpha}),
\end{aligned}$$

so that γ is given in terms of z, ϕ and ξ as

$$\gamma = \sqrt{z^2 + \sin^2\phi\big(\cos^2\xi\,\tilde{\sigma}_1^2(\overline{\alpha}) + \sin^2\xi\,\tilde{\sigma}_2^2(\overline{\alpha})\big)} \tag{8.19}$$

and $\mathbf{e}_3$ as

$$\begin{aligned}
\mathbf{e}_3 = \frac{1}{\sqrt{z^2 + \sin^2\phi\big(\cos^2\xi\,\tilde{\sigma}_1(\overline{\alpha}) + \sin^2\xi\,\tilde{\sigma}_2(\overline{\alpha})\big)}}&\Big(z\,\tilde{\boldsymbol{\eta}}_0(\overline{\alpha}) \\
&+ \sin\phi\big(\cos\xi\,\tilde{\sigma}_1(\overline{\alpha})\,\tilde{\boldsymbol{\eta}}_1(\overline{\alpha}) + \sin\xi\,\tilde{\sigma}_2(\overline{\alpha})\,\tilde{\boldsymbol{\eta}}_2(\overline{\alpha})\big)\Big).
\end{aligned} \tag{8.20}$$

In order for the equilibrium condition (8.18) to be satisfied, the conical angle ψ must verify

$$\cos\psi = \mathbf{e}_3(z, \phi, \xi) \cdot \mathbf{B}(\phi, \xi), \tag{8.21}$$

where $\mathbf{B}(\phi, \xi)$ is given by (8.15) and $\mathbf{e}_3(z, \phi, \xi)$ by (8.20).

Gathered together, equations (8.15, 8.19, 8.20, 8.21) provide a parametrisation of the set of relative equilibria in terms of z, ϕ and ξ when $\overline{\alpha}$ is a simple eigenvalue of $\varsigma\,\mathsf{M}_{12}$. The corresponding solution Q to equation (3.7) can be recovered using (8.17)

This procedure could be adapted if $\overline{\alpha}$ is a double eigenvalue of $\varsigma\,\mathsf{M}_{12}$: then a second singular value of $\tilde{\mathsf{P}}(\overline{\alpha})$ vanishes, i.e. $\tilde{\sigma}_2(\overline{\alpha}) = 0$, and the equivalent of (8.18) is

$$\gamma\,\mathbf{e}_3 = \tilde{\mathsf{P}}(\overline{\alpha})\,\mathbf{B} + z_0\,\tilde{\boldsymbol{\eta}}_0(\overline{\alpha}) + z_2\,\tilde{\boldsymbol{\eta}}_2(\overline{\alpha}),$$

for some scalars z_0 and z_2, with $\tilde{\mathsf{P}}(\overline{\alpha})\,\mathbf{B}$ parallel to $\tilde{\boldsymbol{\eta}}_1(\overline{\alpha})$ for all $\mathbf{B}$. Projecting on $\tilde{\boldsymbol{\eta}}_j(\overline{\alpha})$ for all $j = 0, 1, 2$ would yield equations allowing to find a parametrisation of the set of relative equilibria once again.

Linear Stability

The linear stability of the steady states to (8.8) is given by the eigenvalues of the stability matrix

$$A = -\gamma\left(\overline{\alpha}\mathbf{I} - \varsigma\,\mathsf{M}_{12}^T\right)[\mathbf{e}_3\times] + \mathsf{P}\,[\mathbf{B}\times]\,,$$

where $\mathbf{e}_3$ and $\mathbf{B}$ satisfy (8.9). The real part of the eigenvalues of A could be computed for each steady state computed on a mesh according to the parametrisation introduced above, and bifurcation diagrams similar to those obtained in chapter 4 could be constructed, but they would depend on the three experimental parameters $(\gamma, \overline{\alpha}, \psi)$ in contrast to the two parameters (a, ψ) appearing in the neutrally buoyant case.

Physical Bound on the Values of γ

Equation (8.8) relies on a scaling of the dimensional equations in which γ is at most of order 1, which implies that there exist $M > 0$ such that physically admissible values of γ satisfy $\gamma < M$. From a mathematical point of view, note that in order to satisfy equilibrium condition (8.9), γ has a superior bound depending on $\overline{\alpha}$: if $\overline{\alpha}$ is not an eigenvalue of $\varsigma\,\mathsf{M}_{12}$, then γ satisfies (8.14) for some $\theta \in (-\pi, \pi]$ and $\phi \in [0, \pi]$, which constrains it to be

$$0 < \gamma \le \tilde{\sigma}_1(\overline{\alpha})\,,$$

where $\tilde{\sigma}_1(\overline{\alpha})$ is the largest singular value of $\tilde{\mathsf{P}}(\overline{\alpha})$ and this superior bound is reached for some value of θ and ϕ. By contrast, if $\overline{\alpha}$ is an eigenvalue of $\varsigma\,\mathsf{M}_{12}$, then γ is parametrised by (8.19), and is unbounded.

Therefore the proposed parametrisation might yield values of γ that are admissible mathematically, but not physically. To clarify the dependence of γ on $\overline{\alpha}$ and study the implications of the physical condition $\gamma < M$, we are going to discuss the value of $\tilde{\sigma}_1(\overline{\alpha})$ when $\overline{\alpha}$ is not an eigenvalue of $\varsigma\,\mathsf{M}_{12}$.

Assume $\overline{\alpha}$ is not an eigenvalue of $\varsigma\,\mathsf{M}_{12}$. By definition, the square singular values $\tilde{\sigma}_1^2(\overline{\alpha})$ and $\tilde{\sigma}_2^2(\overline{\alpha})$ are the two non-zero eigenvalues of

$$\tilde{\mathsf{P}}^T(\overline{\alpha})\,\tilde{\mathsf{P}}(\overline{\alpha}) = \mathsf{P}^T\left(\overline{\alpha}\mathbf{I} - \varsigma\,\mathsf{M}_{12}^T\right)^{-T}\left(\overline{\alpha}\mathbf{I} - \varsigma\,\mathsf{M}_{12}^T\right)^{-1}\mathsf{P}\,,$$

implying

$$\tilde{\sigma}_1^2(\overline{\alpha}) + \tilde{\sigma}_2^2(\overline{\alpha}) = \mathrm{Tr}\left(\tilde{\mathsf{P}}^T(\overline{\alpha})\,\tilde{\mathsf{P}}(\overline{\alpha})\right).$$

Since $\tilde{\sigma}_1^2(\overline{\alpha})$ is the largest eigenvalue, it satisfies

$$\mathrm{Tr}\big(\tilde{\mathsf{P}}^T(\overline{\alpha})\,\tilde{\mathsf{P}}(\overline{\alpha})\big) \geq \tilde{\sigma}_1^2(\overline{\alpha}) \geq \frac{1}{2}\,\mathrm{Tr}\big(\tilde{\mathsf{P}}^T(\overline{\alpha})\,\tilde{\mathsf{P}}(\overline{\alpha})\big).$$

By Cayley-Hamilton theorem, the inverse of matrix $\overline{\alpha}\mathbf{I} - \varsigma\,\mathsf{M}_{12}^T$ is given by

$$\big(\overline{\alpha}\mathbf{I} - \varsigma\,\mathsf{M}_{12}^T\big)^{-1} = \frac{\mathbf{I}\,(\overline{\alpha}^2 - \overline{\alpha}\,\mathrm{Tr}\varsigma\,\mathsf{M}_{12}) + \overline{\alpha}\,\varsigma\,\mathsf{M}_{12}^T + |\varsigma\,\mathsf{M}_{12}|\,\varsigma\,\mathsf{M}_{12}^{-T}}{|\overline{\alpha}\mathbf{I} - \varsigma\,\mathsf{M}_{12}|},$$

so that $\tilde{\mathsf{P}}^T(\overline{\alpha})\,\tilde{\mathsf{P}}(\overline{\alpha})$ can be written as

$$\tilde{\mathsf{P}}^T(\overline{\alpha})\,\tilde{\mathsf{P}}(\overline{\alpha}) = \frac{1}{|\overline{\alpha}\mathbf{I} - \varsigma\,\mathsf{M}_{12}|^2}\left(\overline{\alpha}^4\,\mathsf{P}_4 + \overline{\alpha}^3\,\mathsf{P}_3 + \overline{\alpha}^2\,\mathsf{P}_2 + \overline{\alpha}\,\mathsf{P}_1 + \mathsf{P}_0\right),$$

where the P_js are matrices independent of $\overline{\alpha}$. This implies that $\mathrm{Tr}\big(\tilde{\mathsf{P}}^T(\overline{\alpha})\,\tilde{\mathsf{P}}(\overline{\alpha})\big)$ is the ratio of a polynomial of degree 4 and a polynomial of degree 6 in $\overline{\alpha}$. As such, it goes to 0 as $\overline{\alpha} \to \infty$, and it is unbounded when $\overline{\alpha}$ approaches eigenvalue of $\varsigma\,\mathsf{M}_{12}$.

Thus for $\overline{\alpha}$ large enough, all the steady states of (8.8) satisfy the condition $\gamma < M$. For values of $\overline{\alpha}$ not equal to the eigenvalues of $\varsigma\,\mathsf{M}_{12}$, the steady states are parametrised by $(\overline{\alpha},\theta,\phi)$ via equations (8.12, 8.14, 8.15, 8.16). In particular, there exist a triple $(\overline{\alpha},\theta,\phi)$ such that γ is given by (8.14), and the criterion $\gamma < M$ can be rewritten as

$$\sin\phi\left(\frac{\cos^2\theta}{\tilde{\sigma}_1^2(\overline{\alpha})} + \frac{\sin^2\theta}{\tilde{\sigma}_2^2(\overline{\alpha})}\right)^{-1/2} < M.$$

For a fixed value of $\overline{\alpha}$, this allows to compute the extent of the set of pairs (θ,ϕ) yielding values of γ of an admissible magnitude. For instance, as $\overline{\alpha}$ approaches eigenvalues of $\varsigma\,\mathsf{M}_{12}$ and $\tilde{\sigma}_1(\overline{\alpha})$ becomes larges and larger, values of θ close to 0 and π are admissible only for a restricted range of values of ϕ.

To summarise: in this section, we studied the steady states of the rotational dynamics of a heavy swimmer in the specific case where the axis of rotation $\boldsymbol{e}_3$ of the magnetic field is vertical in the lab frame, i.e. coincides with the direction of gravity. We built a complete parametrisation of the set of steady states of the dynamics given by (8.8) as the experimental parameters γ, $\overline{\alpha}$ and ψ vary. This parametrisation uses two different charts: one of them depends on parameters $(\overline{\alpha},\theta,\phi)$ when $\overline{\alpha}$ is not an eigenvalue of $\varsigma\,\mathsf{M}_{12}$, and the other one, used to parametrise the steady states arising when $\overline{\alpha}$ is an eigenvalue of $\varsigma\,\mathsf{M}_{12}$, depends on parameters (z,ϕ,ξ). Using these, we showed that the number of steady states to (8.8) for given values $(\gamma,\overline{\alpha},\psi)$ of the experimental parameters is generically 0, 4, or 8. We also gave explicitly the linear stability matrix. Finally, we discussed the value of the parameter γ with respect to the parametrisation of the set of steady states, referring to the initial scaling of the dynamics that requires that γ is at most of order one.

8.2 Optimising Axial Velocity

The previous section dealt with the rotational dynamics of a heavy swimmer when the axis of rotation of the magnetic field is vertical, given by (8.8). Here we examine the translational dynamics, that can be recovered from the solutions to (8.8). Trajectories corresponding to relative equilibria are helical; their axis is aligned with $\boldsymbol{\omega}$, and their pitch and radius are given by (cf. chapter 7)

$$p = \frac{2\pi}{|\boldsymbol{\omega}|^2}\,\boldsymbol{\omega}\cdot\mathbf{v} \qquad \text{and} \qquad r = \frac{1}{|\boldsymbol{\omega}|^2}\,|\boldsymbol{\omega}\times\mathbf{v}|\,. \tag{7.3}$$

In the following, expressions for the pitch and radius corresponding to the steady states of (8.8) studied in the previous section are derived. This allows to derive conditions that a specific swimmer must satisfy in order to achieve either circular or straight trajectories, which are degenerate helices corresponding respectively to $p = 0$ and $r = 0$. Then the axial velocity of the swimmer, i.e. its velocity along the helical trajectory's axis, is investigated; in particular, we discuss how to optimise it.

In the case considered, the linear and angular velocities are given by

$$\mathbf{v} = \mathsf{M}_{12}\,(\mathbf{m}\times\mathbf{B}) - \gamma\,\mathsf{M}_{11}\,\mathbf{g}\,, \tag{8.2}$$

$$\boldsymbol{\omega} = \mathsf{M}_{22}\,(\mathbf{m}\times\mathbf{B}) - \gamma\,\mathsf{M}_{12}^{T}\,\mathbf{g}\,, \tag{8.3}$$

with $\mathbf{g} = -\varsigma\,\mathbf{e}_3$. The equilibrium condition (8.9) gives $\mathbf{m}\times\mathbf{B}$ in terms of $\mathbf{e}_3$, γ and $\overline{\alpha}$ as

$$\mathbf{m}\times\mathbf{B} = \gamma\,\mathsf{M}_{22}^{-1}\left(\overline{\alpha}\,\mathbf{I} - \varsigma\,\mathsf{M}_{12}^{T}\right)\mathbf{e}_3\,. \tag{8.22}$$

Note that this can be satisfied for some $\mathbf{B}$ and $\mathbf{e}_3$ only if

$$\mathbf{m}\cdot\mathsf{M}_{22}^{-1}\left(\overline{\alpha}\,\mathbf{I} - \varsigma\,\mathsf{M}_{12}^{T}\right)\mathbf{e}_3 = 0\,,$$

or equivalently if $\mathbf{e}_3$ is in the plane $\left((\overline{\alpha}\,\mathbf{I} - \varsigma\,\mathsf{M}_{12})\,\mathsf{M}_{22}^{-1}\,\mathbf{m}\right)^{\perp}$. Furthermore, equation (8.22) also implies

$$\gamma = \frac{|\mathbf{m}\times\mathbf{B}|}{\left|\mathsf{M}_{22}^{-1}\left(\overline{\alpha}\,\mathbf{I} - \varsigma\,\mathsf{M}_{12}^{T}\right)\mathbf{e}_3\right|}\,.$$

The angle ϕ between $\mathbf{m}$ and $\mathbf{B}$ satisfies $\sin\phi = |\mathbf{m}\times\mathbf{B}|$. This allows to rewrite γ in terms of ϕ, $\overline{\alpha}$ and $\mathbf{e}_3$ as

$$\gamma = \frac{\sin\phi}{\left|\mathsf{M}_{22}^{-1}\left(\overline{\alpha}\,\mathbf{I} - \varsigma\,\mathsf{M}_{12}^{T}\right)\mathbf{e}_3\right|}\,.$$

Thus the linear and angular velocities for relative equilibria are expressed in terms of $\overline{\alpha}$ and $\mathbf{e}_3$

as

$$\begin{aligned}
\mathbf{v} &= \frac{\sin\phi}{\left|\mathsf{M}_{22}^{-1}\left(\overline{\alpha}\,\mathbf{I}-\varsigma\,\mathsf{M}_{12}^{T}\right)\mathbf{e}_3\right|}\left(\mathsf{M}_{12}\,\mathsf{M}_{22}^{-1}\left(\overline{\alpha}\,\mathbf{I}-\varsigma\,\mathsf{M}_{12}^{T}\right)\mathbf{e}_3-\varsigma\,\mathsf{M}_{11}\,\mathbf{e}_3\right),\\
\boldsymbol{\omega} &= \frac{\sin\phi}{\left|\mathsf{M}_{22}^{-1}\left(\overline{\alpha}\,\mathbf{I}-\varsigma\,\mathsf{M}_{12}^{T}\right)\mathbf{e}_3\right|}\,\overline{\alpha}\,\mathbf{e}_3\,,
\end{aligned}$$

and the pitch and radius of the helical trajectory as

$$\begin{aligned}
p &= 2\pi\,\mathsf{M}_{12}\,\mathsf{M}_{22}^{-1}\,\mathbf{e}_3\cdot\mathbf{e}_3-2\pi\,\frac{\varsigma}{\overline{\alpha}}\left(\mathsf{M}_{12}\,\mathsf{M}_{22}^{-1}\,\mathsf{M}_{12}^{T}+\mathsf{M}_{11}\right)\mathbf{e}_3\cdot\mathbf{e}_3\\
r &= \left|\mathsf{M}_{12}\,\mathsf{M}_{22}^{-1}\,\mathbf{e}_3\times\mathbf{e}_3-\frac{\varsigma}{\overline{\alpha}}\left(\mathsf{M}_{12}\,\mathsf{M}_{22}^{-1}\,\mathsf{M}_{12}^{T}+\mathsf{M}_{11}\right)\mathbf{e}_3\times\mathbf{e}_3\right|\,.
\end{aligned}$$

Note that these expressions are independent of the angle ϕ between the magnetic moment $\mathbf{m}$ and the magnetic field $\mathbf{B}$.

Defining the two symmetric matrices C_1 and C_2 that depend on the shape of the swimmer as

$$\mathsf{C}_1=\frac{1}{2}\left(\mathsf{M}_{12}\,\mathsf{M}_{22}^{-1}+\mathsf{M}_{22}^{-1}\,\mathsf{M}_{12}^{T}\right),\qquad\qquad \mathsf{C}_2=\mathsf{M}_{12}\,\mathsf{M}_{22}^{-1}\,\mathsf{M}_{12}^{T}+\mathsf{M}_{11}\,,$$

the pitch and radius can be simplified to

$$p=2\pi\,\mathbf{e}_3\cdot\left(\mathsf{C}_1-\frac{\varsigma}{\overline{\alpha}}\,\mathsf{C}_2\right)\mathbf{e}_3\,,\qquad\qquad r=\left|\left(\mathsf{M}_{12}\,\mathsf{M}_{22}^{-1}-\frac{\varsigma}{\overline{\alpha}}\,\mathsf{C}_2\right)\mathbf{e}_3\times\mathbf{e}_3\right|\,.$$

Thus, circular trajectories, i.e. trajectories with $p=0$, can be obtained only if there exists $\mathbf{e}_3$ such that $\mathbf{e}_3\cdot\left(\mathsf{C}_1-\frac{\varsigma}{\overline{\alpha}}\,\mathsf{C}_2\right)\mathbf{e}_3=0$, which requires in particular that the symmetric matrix $\mathsf{C}_1-\frac{\varsigma}{\overline{\alpha}}\,\mathsf{C}_2$ is neither positive definite, nor negative definite. This condition is fulfilled exactly when $\lambda_{\min}\le\frac{\varsigma}{\overline{\alpha}}\le\lambda_{\max}$, where $\lambda_{\min}$ and $\lambda_{\max}$ are respectively the minimum and maximum eigenvalues of $\mathsf{C}_1\,\mathsf{C}_2^{-1}$. In addition, since $\mathbf{e}_3$ is constrained to the plane $\left((\overline{\alpha}\,\mathbf{I}-\varsigma\,\mathsf{M}_{12})\,\mathsf{M}_{22}^{-1}\,\mathbf{m}\right)^{\perp}$, circular trajectories can be obtained only if

$$\left\{\mathbf{e}_3\in\mathbb{S}^2:\mathbf{e}_3\cdot\left(\mathsf{C}_1-\frac{\varsigma}{\overline{\alpha}}\,\mathsf{C}_2\right)\mathbf{e}_3=0\right\}\cap\left((\overline{\alpha}\,\mathbf{I}-\varsigma\,\mathsf{M}_{12})\,\mathsf{M}_{22}^{-1}\,\mathbf{m}\right)^{\perp}\neq\{\mathbf{0}\}$$

for some value of $\overline{\alpha}$. This gives a constraint on the directions of the magnetic moment so that a swimmer of a given shape admits circular trajectories as relative equilibrium motions.

Straight trajectories, i.e trajectories for which $r=0$, can be obtained only if $\mathbf{e}_3$ is an eigenvector of $\mathsf{M}_{12}\,\mathsf{M}_{22}^{-1}-\frac{\varsigma}{\overline{\alpha}}\,\mathsf{C}_2$. This requires in particular that $\mathsf{M}_{12}\,\mathsf{M}_{22}^{-1}-\frac{\varsigma}{\overline{\alpha}}\,\mathsf{C}_2$ admits an eigenvector in the plane $\left((\overline{\alpha}\,\mathbf{I}-\varsigma\,\mathsf{M}_{12})\,\mathsf{M}_{22}^{-1}\,\mathbf{m}\right)^{\perp}$ for some value of $\overline{\alpha}$. Again, a swimmer of a given shape can be magnetised in such a way that this condition is verified for a given $\overline{\alpha}$.

The axial velocity is given by

$$v_{\mathrm{ax}}=\frac{\boldsymbol{\omega}}{|\boldsymbol{\omega}|}\cdot\mathbf{v}\,.$$

At relative equilibria, it can be expressed in terms of $\mathbf{e}_3$, $\overline{\alpha}$ and ϕ as

$$v_{\mathrm{ax}} = \sin\phi \, \frac{\mathbf{e}_3 \cdot (\overline{\alpha}\,\mathsf{C}_1 - \varsigma\,\mathsf{C}_2)\,\mathbf{e}_3}{\left|\mathsf{M}_{22}^{-1}\left(\overline{\alpha}\,\mathbf{I} - \varsigma\,\mathsf{M}_{12}^{T}\right)\mathbf{e}_3\right|}\,.$$

For all values of $\mathbf{e}_3$ and $\overline{\alpha}$, this expression is maximised by $\phi = \pi/2$. Therefore finding the maximal axial velocity for a given swimmer is equivalent to maximising

$$v_{\mathrm{ax}}^{*}(\mathbf{e}_3, \overline{\alpha}) = \frac{\mathbf{e}_3 \cdot (\overline{\alpha}\,\mathsf{C}_1 - \varsigma\,\mathsf{C}_2)\,\mathbf{e}_3}{\left|\mathsf{M}_{22}^{-1}\left(\overline{\alpha}\,\mathbf{I} - \varsigma\,\mathsf{M}_{12}^{T}\right)\mathbf{e}_3\right|}\,.$$

in $\mathbf{e}_3$ and $\overline{\alpha}$ under the constraints

$$\mathbf{e}_3 \cdot \mathbf{e}_3 = 1\,, \qquad \mathbf{e}_3 \cdot \left(\overline{\alpha}\,\mathbf{I} - \varsigma\,\mathsf{M}_{12}\right)\mathsf{M}_{22}^{-1}\,\mathbf{m} = 0\,. \tag{8.23}$$

Note that the maximising pair $(\mathbf{e}_3, \overline{\alpha})$ is not guaranteed to represent a stable relative equilibrium.

This leads naturally to the question of how to magnetise a swimmer of a given shape so that it can attain axial velocities as large as possible. Note that the magnetic moment $\mathbf{m}$ appears only in the second constraint of (8.23), and that letting $\mathbf{m}$ vary allows the plane $\left((\overline{\alpha}\,\mathbf{I} - \varsigma\,\mathsf{M}_{12})\,\mathsf{M}_{22}^{-1}\,\mathbf{m}\right)^{\perp}$ to have any orientation. As a result, the maximisers $\mathbf{e}_3^{*}$ and $\overline{\alpha}^{*}$ of v_{ax}^{*} under the single constraint $\mathbf{e}_3 \cdot \mathbf{e}_3 = 1$ give the maximal possible axial velocity for a swimmer of a given shape as $v_{\mathrm{ax}}^{*}(\mathbf{e}_3^{*}, \overline{\alpha}^{*})$. Choosing then $\mathbf{m}$ in the plane $\left(\mathsf{M}_{22}^{-1}\,(\overline{\alpha}^{*}\,\mathbf{I} - \varsigma\,\mathsf{M}_{12}^{T})\,\mathbf{e}_3^{*}\right)^{\perp}$ ensures that this maximal axial velocity is reached at the relative equilibria that satisfy $\mathbf{B} = \pm\mathbf{B}^{*}$, where

$$\mathbf{B}^{*} = \mathbf{m} \times \frac{\mathsf{M}_{22}^{-1}\,(\overline{\alpha}^{*}\,\mathbf{I} - \varsigma\,\mathsf{M}_{12}^{T})\,\mathbf{e}_3^{*}}{\left|\mathsf{M}_{22}^{-1}\,(\overline{\alpha}^{*}\,\mathbf{I} - \varsigma\,\mathsf{M}_{12}^{T})\,\mathbf{e}_3^{*}\right|}\,.$$

It does not ensure its stability however. As in the neutrally buoyant case discussed in chapter 7, the corresponding relative equilibrium might be unstable.

In this section, the shape of the trajectories corresponding to relative equilibria was investigated. Since relative equilibria give rise to helical trajectories, an expression for the pitch and radius was derived. Circular and straight trajectories, obtained respectively when the pitch and radius vanish, can be obtained only if the swimmer's shape and the direction of its magnetic moment satisfy specific conditions for some values of the angular velocity $\overline{\alpha}$. These conditions were derived explicitly in the two cases. Then, we determined the axial velocity at relative equilibria, and discussed how to optimise it, both in terms of experimental parameters for a given swimmer, and with respect to the choice of the magnetic moment's direction for a swimmer of a given shape in order to enhance its performance.

8.3 First Order Perturbation when the Axis of Rotation is not Exactly Vertical

So far, this chapter focused on the specific case where the axis of rotation of the magnetic field is exactly vertical. In this section, we study the perturbation arising if there is a small misalignment, i.e if $0 < \sin\chi \ll 1$. In particular, we expand the dynamics in $\varepsilon := \sin\chi$ and give explicitly the first-order perturbation when the zeroth order solution is a stable steady state. We then use this to express the deviation of the trajectory.

The matrix $Q \in \mathrm{SO}(3)$ is expanded in ε as (cf. appendix A)

$$Q = Q^{[0]} + \varepsilon\,\left[\mathbf{u}^{[1]}\times\right] Q^{[0]} + \mathcal{O}(\varepsilon^2)\,.$$

Substituting this in

$$\dot{Q} = \left[\left(\gamma\left(\overline{\alpha}\,Q\begin{bmatrix}0\\0\\1\end{bmatrix} + \mathsf{M}_{12}^T\,Q\,R_3^T(a\,t)\begin{bmatrix}\sin\chi\\0\\\cos\chi\end{bmatrix}\right) - \mathsf{P}\,Q\begin{bmatrix}\sin\psi\\0\\\cos\psi\end{bmatrix}\right)\times\right] Q\,, \tag{8.6}$$

where

$$\begin{bmatrix}\sin\chi\\0\\\cos\chi\end{bmatrix} = -\begin{bmatrix}0\\0\\\varsigma\end{bmatrix} + \varepsilon\begin{bmatrix}1\\0\\0\end{bmatrix} + \mathcal{O}(\varepsilon^2)\,,$$

with $\varsigma = -\mathrm{sign}(\cos\chi)$ and matching at each order yields at zeroth order

$$\dot{Q}^{[0]} = \left[\left(\gamma\left(\overline{\alpha}\mathbf{I} - \varsigma\,\mathsf{M}_{12}^T\right)Q^{[0]}\begin{bmatrix}0\\0\\1\end{bmatrix} - \mathsf{P}\,Q^{[0]}\begin{bmatrix}\sin\psi\\0\\\cos\psi\end{bmatrix}\right)\times\right] Q^{[0]}\,. \tag{8.24}$$

which is the equation (8.8) governing the dynamics when there is perfect alignment between $\mathbf{g}$ and $\mathbf{e}_3$. At first order, we obtain (cf. appendix A)

$$\dot{\mathbf{u}}^{[1]} = \gamma\left(\overline{\alpha}\mathbf{I} - \varsigma\,\mathsf{M}_{12}^T\right)(\mathbf{u}^{[1]}\times\mathbf{e}_3^{[0]}) - \mathsf{P}\,(\mathbf{u}^{[1]}\times\mathbf{B}^{[0]}) + \gamma\,\mathsf{M}_{12}^T\,\mathbf{e}_1^{[0]}(t)\,,$$

where

$$\mathbf{B}^{[0]} = Q^{[0]}\begin{bmatrix}\sin\psi\\0\\\cos\psi\end{bmatrix}, \qquad \mathbf{e}_3^{[0]} = Q^{[0]}\begin{bmatrix}0\\0\\1\end{bmatrix}, \qquad \mathbf{e}_1^{[0]} = Q^{[0]}\,R^T(a\,t)\begin{bmatrix}1\\0\\0\end{bmatrix},$$

with $a = \gamma\,\overline{\alpha}$. This can be rewritten as

$$\dot{\mathbf{u}}^{[1]} - A(Q^{[0]})\,\mathbf{u}^{[1]} = \gamma\,\mathsf{M}_{12}^T\,\mathbf{e}_1^{[0]}(t)\,,$$

where we define A as

$$A(Q^{[0]}) = -\gamma\left(\overline{\alpha}\mathbf{I} - \varsigma\,\mathsf{M}_{12}^T\right)\left[\mathbf{e}_3^{[0]}\times\right] + \mathsf{P}\,\left[\mathbf{B}^{[0]}\times\right]. \tag{8.25}$$

If $Q^{[0]}$ is a steady state to (8.24), the matrix A is the associated stability matrix, and it is constant.

In that limit (after transients died out) $\mathbf{u}^{[1]}$ can be found explicitly by direct integration as

$$\mathbf{u}^{[1]} = e^{t\,A}\,\mathbf{u}_0^{[1]} + \gamma\left(A^2 + a^2\,\mathbf{I}\right)^{-1}\left(A\,\mathsf{M}_{12}^T\,Q^{[0]}\begin{bmatrix} -\cos(a\,t) \\ \sin(a\,t) \\ 0 \end{bmatrix} + a\,\mathsf{M}_{12}^T\,Q^{[0]}\begin{bmatrix} \sin(a\,t) \\ \cos(a\,t) \\ 0 \end{bmatrix}\right),$$

where $\mathbf{u}_0^{[1]}$ is an initial condition on $\mathbf{u}^{[1]}$. Thus, if $Q^{[0]}$ is a linearly stable equilibrium, i.e. the eigenvalues of A all have a negative real part, after a transient $\mathbf{u}^{[1]}$ is approximated by

$$\mathbf{u}^{[1]} = \gamma\left(A^2 + a^2\,\mathbf{I}\right)^{-1}\left(A\,\mathsf{M}_{12}^T\,Q^{[0]}\begin{bmatrix} -\cos(a\,t) \\ \sin(a\,t) \\ 0 \end{bmatrix} + a\,\mathsf{M}_{12}^T\,Q^{[0]}\begin{bmatrix} \sin(a\,t) \\ \cos(a\,t) \\ 0 \end{bmatrix}\right), \tag{8.26}$$

which is a $\frac{2\pi}{a}$-periodic function of t. The following lemma shows that the first order perturbation is bounded for a slowly rotating magnetic field of large magnitude.

Lemma Expression $\mathbf{u}^{[1]}$ is bounded for γ and $\overline{\alpha}$ small enough. In particular,

$$\left|\mathbf{u}^{[1]}\right| \leq \frac{7}{\hat{\sigma}}$$

for $0 \leq \gamma \leq \frac{1}{2}\,\frac{\sigma_1}{\hat{\sigma}}$ and $0 \leq \overline{\alpha} \leq \frac{1}{4}\,\hat{\sigma}$, where σ_1 is the largest singular value of P and $\hat{\sigma}$ is the largest eigenvalue of M_{12}.

Proof Note first that since $Q^{[0]}$ is a matrix of rotation,

$$\left|\mathbf{u}^{[1]}\right| \leq \gamma\,\frac{\left(\|A\| + a\right)\|\mathsf{M}_{12}\|}{\|A^2 + a^2\,\mathbf{I}\|} \leq \gamma\,\frac{\left(\|A\| + a\right)\|\mathsf{M}_{12}\|}{\left|\|A\|^2 - a^2\right|},$$

where $\|\cdot\|$ denotes a the Euclidian matrix norm. In particular, $\|\mathsf{M}_{12}\| = \hat{\sigma}$, where $\hat{\sigma}$ is the largest singular value of M_{12}.

Then, using the definition (8.25) of A, we obtain

$$\|A\| = \left\| -\gamma\left(\overline{\alpha}\,\mathbf{I} - \varsigma\,\mathsf{M}_{12}^T\right)\left[\mathbf{e}_3^{[0]}\times\right] + \mathsf{P}\left[\mathbf{B}^{[0]}\times\right] \right\| \geq \left| \|\mathsf{P}\| - \gamma\,\left\|\overline{\alpha}\,\mathbf{I} - \varsigma\,\mathsf{M}_{12}^T\right\| \right|.$$

If $\gamma\left(\overline{\alpha} + \|\mathsf{M}_{12}\|\right) \leq \|\mathsf{P}\| = \sigma_1$, this implies

$$\|A\| \geq \sigma_1 - \gamma\,\left(\|\mathsf{M}_{12}\| + \overline{\alpha}\right) = \sigma_1 - \gamma\,\hat{\sigma} - \gamma\,\overline{\alpha},$$

and since $a = \gamma\,a$, this yields

$$\left|\|A\|^2 - a^2\right| \geq \left|\sigma_1 - \gamma\,\hat{\sigma}\right|\,\left|\sigma_1 - \gamma\,\hat{\sigma} - 2a\right|$$

On the other hand, we have

$$\|A\| \leq \|\mathsf{P}\| + \gamma\,\|\mathsf{M}_{12}\| + \gamma\,\overline{\alpha} = \sigma_1 + \gamma\,\hat{\sigma} + a,$$

so that

$$\left|\mathbf{u}^{[1]}\right| \leq \frac{\gamma}{\left|\sigma_1 - \gamma\hat{\sigma}\right|}\,\frac{\sigma_1 + \gamma\hat{\sigma} + 2a}{\left|\sigma_1 - \gamma\hat{\sigma} - 2a\right|} = \frac{\gamma}{\left|\sigma_1 - \gamma\hat{\sigma}\right|}\,\frac{\sigma_1 + \gamma\,(\hat{\sigma} + 2\overline{\alpha})}{\left|\sigma_1 - \gamma\,(\hat{\sigma} + 2\overline{\alpha})\right|}\,.$$

The right-hand side is an increasing function in γ and a for $0 \leq \gamma < \sigma_1/\hat{\sigma}$ and $0 \leq \gamma\,(\hat{\sigma}+2\overline{\alpha}) < \sigma_1$. Consequently, for $0 \leq \gamma \leq \frac{1}{2}\,\frac{\sigma_1}{\hat{\sigma}}$ and $0 \leq \overline{\alpha} \leq \frac{1}{4}\hat{\sigma}$, we have

$$\left|\mathbf{u}^{[1]}\right| \leq \frac{7}{\hat{\sigma}}\,. \qquad \blacksquare$$

Drift

We now use expression (8.26) to study how the swimmer drifts when the axis of rotation is not exactly vertical, i.e. how its average direction deviates from the vertical. It will be shown that the angle between the swimmer's average direction and the vertical is bounded and of order ε when parameters γ and $\overline{\alpha}$ are small enough, which means that the magnetic field has a large magnitude and rotates slowly.

The average horizontal component of the lab frame velocity over one rotation of the magnetic field is

$$\overline{\boldsymbol{v}_{\text{hor}}} = \frac{a}{2\pi}\int_0^{\frac{2\pi}{a}} \underbrace{R_3(a\,t)\,Q^T}_{R^T}\,\underbrace{\left(\mathbf{I}-\mathbf{g}\,\mathbf{g}^T\right)\mathbf{v}}_{\substack{\text{projection}\\ \text{on the}\\ \text{horizontal}\\ \text{plane}}}\,dt = -\frac{a}{2\pi}\int_0^{\frac{2\pi}{a}} R_3(a\,t)\,Q^T\,\left[\mathbf{g}\times\right]^2\mathbf{v}\,dt, \tag{8.27}$$

where

$$\begin{aligned}
Q =& Q^{[0]} + \varepsilon\,\left[\mathbf{u}^{[1]}\times\right]\,Q^{[0]} + \mathcal{O}(\varepsilon^2)\\
\mathbf{g} =& \mathbf{g}^{[0]} + \varepsilon\,\mathbf{g}^{[1]} + \mathcal{O}(\varepsilon^2)\\
\overset{(8.1)}{=}& -\varsigma\,\mathbf{e}_3^{[0]} + \varepsilon\left(\mathbf{e}_1^{[0]} - \varsigma\,(\mathbf{u}^{[1]}\times\mathbf{e}_3^{[0]})\right) + \mathcal{O}(\varepsilon^2)\,,\\
\mathbf{v} =& \mathbf{v}^{[0]} + \varepsilon\,\mathbf{v}^{[1]} + \mathcal{O}\varepsilon^2)\\
\overset{(2.39)}{=}& \mathsf{M}_{12}\,(\mathbf{m}\times\mathbf{B}^{[0]}) - \gamma\,\mathsf{M}_{11}\,\mathbf{g}^{[0]} + \varepsilon\,\left(\mathsf{M}_{12}\left(\mathbf{m}\times(\mathbf{u}^{[1]}\times\mathbf{B}^{[0]})\right) - \gamma\,\mathsf{M}_{11}\,\mathbf{g}^{[1]}\right) + \mathcal{O}(\varepsilon^2)\,.
\end{aligned}$$

Note that $Q^{[0]}$, $\mathbf{g}^{[0]}$ and $\mathbf{v}^{[0]}$ are constant, whereas $\mathbf{u}^{[1]}$, $\mathbf{g}^{[1]}$ and $\mathbf{v}^{[1]}$ are $\frac{2\pi}{a}$-periodic, with time dependence arising only through factors $\cos(a\,t)$ and $\sin(a\,t)$. The horizontal component (8.27) is expanded as

$$
\begin{aligned}
\overline{\boldsymbol{v}_{\text{hor}}} &= \frac{a}{2\pi}\int_0^{\frac{2\pi}{a}} R_3(a\,t)\,Q^T\left(\mathbf{I}-\mathbf{g}\,\mathbf{g}^T\right)\mathbf{v}\,dt \\
&= -\frac{a}{2\pi}\int_0^{\frac{2\pi}{a}} R_3(a\,t)\,Q^{[0]\,T}\left[\mathbf{g}^{[0]}\times\right]^2\mathbf{v}^{[0]}\,dt \\
&\quad + \varepsilon\frac{a}{2\pi}\int_0^{\frac{2\pi}{a}} R_3(a\,t)\,Q^{[0]\,T}\Big(\left[\mathbf{u}^{[1]}\times\right]\left[\mathbf{g}^{[0]}\times\right]^2\mathbf{v}^{[0]} - \left[\mathbf{g}^{[1]}\times\right]\left[\mathbf{g}^{[0]}\times\right]\mathbf{v}^{[0]} \\
&\quad - \left[\mathbf{g}^{[0]}\times\right]\left[\mathbf{g}^{[1]}\times\right]\mathbf{v}^{[0]} - \left[\mathbf{g}^{[0]}\times\right]^2\mathbf{v}^{[1]}\Big)\,dt + \mathcal{O}(\varepsilon^2)
\end{aligned}
\tag{8.28}
$$

The zeroth order term of this integral vanishes: indeed

$$
\begin{aligned}
\frac{a}{2\pi}\int_0^{\frac{2\pi}{a}} R_3(a\,t)\,Q^{[0]\,T}\left[\mathbf{g}^{[0]}\times\right]^2\mathbf{v}^{[0]}\,dt &= \frac{a}{2\pi}\int_0^{\frac{2\pi}{a}} R_3(a\,t)\,dt\,Q^{[0]\,T}\left[\mathbf{g}^{[0]}\times\right]^2\mathbf{v}^{[0]} \\
&= \begin{bmatrix} 0&0&0\\0&0&0\\0&0&1 \end{bmatrix} Q^{[0]\,T}\left[\mathbf{g}^{[0]}\times\right]^2\mathbf{v}^{[0]} \\
&= \begin{bmatrix} 0\\ 0\\ \mathbf{e}_3^{[0]}\cdot\left[\mathbf{e}_3^{[0]}\times\right]^2\mathbf{v}^{[0]} \end{bmatrix} = \mathbf{0}.
\end{aligned}
$$

In the first order term, $\mathbf{u}^{[1]}$ defined in (8.26), $\mathbf{g}^{[1]}$ and $\mathbf{v}^{[1]}$ can be rewritten as as

$$
\begin{aligned}
\mathbf{u}^{[1]} &= \cos(a\,t)\,\mathbf{u}_c^{[1]} + \sin(a\,t)\,\mathbf{u}_s^{[1]} \\
\mathbf{g}^{[1]} &= \cos(a\,t)\,\mathbf{g}_c^{[1]} + \sin(a\,t)\,\mathbf{g}_s^{[1]} \\
\mathbf{v}^{[1]} &= \cos(a\,t)\,\mathbf{v}_c^{[1]} + \sin(a\,t)\,\mathbf{v}_s^{[1]},
\end{aligned}
\tag{8.29}
$$

where

$$
\begin{aligned}
\mathbf{u}_c^{[1]} &= \gamma\left(A^2+a^2\mathbf{I}\right)^{-1}\left(A\,\mathsf{M}_{12}^T\,Q^{[0]}\begin{bmatrix}-1\\0\\0\end{bmatrix} + a\,\mathsf{M}_{12}^T\,Q^{[0]}\begin{bmatrix}0\\1\\0\end{bmatrix}\right) \\
\mathbf{u}_s^{[1]} &= \gamma\left(A^2+a^2\mathbf{I}\right)^{-1}\left(A\,\mathsf{M}_{12}^T\,Q^{[0]}\begin{bmatrix}0\\1\\0\end{bmatrix} + a\,\mathsf{M}_{12}^T\,Q^{[0]}\begin{bmatrix}1\\0\\0\end{bmatrix}\right) \\
\mathbf{g}_c^{[1]} &= Q^{[0]}\begin{bmatrix}1\\0\\0\end{bmatrix} - \varsigma\,\mathbf{u}_c^{[1]}\times\mathbf{e}_3^{[0]} \\
\mathbf{g}_s^{[1]} &= Q^{[0]}\begin{bmatrix}0\\-1\\0\end{bmatrix} - \varsigma\,\mathbf{u}_s^{[1]}\times\mathbf{e}_3^{[0]} \\
\mathbf{v}_c^{[1]} &= \mathsf{M}_{12}\left(\mathbf{m}\times(\mathbf{u}_c^{[1]}\times\mathbf{B}^{[0]})\right) - \gamma\,\mathsf{M}_{11}\,\mathbf{g}_c^{[1]} \\
\mathbf{v}_s^{[1]} &= \mathsf{M}_{12}\left(\mathbf{m}\times(\mathbf{u}_s^{[1]}\times\mathbf{B}^{[0]})\right) - \gamma\,\mathsf{M}_{11}\,\mathbf{g}_s^{[1]}
\end{aligned}
$$

are constant.

Note that by the lemma on page 213, all these components are bounded for γ and $\overline{\alpha}$ small enough.

The first order term in (8.28) then becomes

$$\begin{aligned}
&\frac{a}{2\pi}\int_0^{\frac{2\pi}{a}} \cos(a\,t)\,R_3(a\,t)\,dt\,Q^{[0]\,T}\Big(\big[\mathbf{u}_c^{[1]}\times\big]\,\big[\mathbf{g}^{[0]}\times\big]^2\,\mathbf{v}^{[0]}-\big[\mathbf{g}_c^{[1]}\times\big]\,\big[\mathbf{g}^{[0]}\times\big]\,\mathbf{v}^{[0]}\\
&\qquad\qquad -\big[\mathbf{g}^{[0]}\times\big]\,\big[\mathbf{g}_c^{[1]}\times\big]\,\mathbf{v}^{[0]}-\big[\mathbf{g}^{[0]}\times\big]^2\,\mathbf{v}_c^{[1]}\Big)\\
&+\frac{a}{2\pi}\int_0^{\frac{2\pi}{a}} \sin(a\,t)\,R_3(a\,t)\,dt\,Q^{[0]\,T}\Big(\big[\mathbf{u}_s^{[1]}\times\big]\,\big[\mathbf{g}^{[0]}\times\big]^2\,\mathbf{v}^{[0]}-\big[\mathbf{g}_s^{[1]}\times\big]\,\big[\mathbf{g}^{[0]}\times\big]\,\mathbf{v}^{[0]}\\
&\qquad\qquad -\big[\mathbf{g}^{[0]}\times\big]\,\big[\mathbf{g}_s^{[1]}\times\big]\,\mathbf{v}^{[0]}-\big[\mathbf{g}^{[0]}\times\big]^2\,\mathbf{v}_s^{[1]}\Big)\\
&=\frac{1}{2}\begin{bmatrix}1&0&0\\0&1&0\\0&0&0\end{bmatrix}Q^{[0]\,T}\Big(\big[\mathbf{u}_c^{[1]}\times\big]\,\big[\mathbf{g}^{[0]}\times\big]^2\,\mathbf{v}^{[0]}-\big[\mathbf{g}_c^{[1]}\times\big]\,\big[\mathbf{g}^{[0]}\times\big]\,\mathbf{v}^{[0]}\\
&\qquad\qquad -\big[\mathbf{g}^{[0]}\times\big]\,\big[\mathbf{g}_c^{[1]}\times\big]\,\mathbf{v}^{[0]}-\big[\mathbf{g}^{[0]}\times\big]^2\,\mathbf{v}_c^{[1]}\Big)\\
&+\frac{1}{2}\begin{bmatrix}0&-1&0\\1&0&0\\0&0&0\end{bmatrix}Q^{[0]\,T}\Big(\big[\mathbf{u}_s^{[1]}\times\big]\,\big[\mathbf{g}^{[0]}\times\big]^2\,\mathbf{v}^{[0]}-\big[\mathbf{g}_s^{[1]}\times\big]\,\big[\mathbf{g}^{[0]}\times\big]\,\mathbf{v}^{[0]}\\
&\qquad\qquad -\big[\mathbf{g}^{[0]}\times\big]\,\big[\mathbf{g}_s^{[1]}\times\big]\,\mathbf{v}^{[0]}-\big[\mathbf{g}^{[0]}\times\big]^2\,\mathbf{v}_s^{[1]}\Big)\\
&=\begin{bmatrix}\mathbf{c}_1^{[0]}\cdot\big(\mathbf{u}_c^{[1]}\times\mathbf{v}^{[0]}-\mathbf{v}_c^{[1]}\big)-\mathbf{c}_2^{[0]}\cdot\big(\mathbf{u}_s^{[1]}\times\mathbf{v}^{[0]}-\mathbf{v}_s^{[1]}\big)-2\varsigma\,\mathbf{e}_3^{[0]}\cdot\mathbf{v}^{[0]}\\ \mathbf{c}_2^{[0]}\cdot\big(\mathbf{u}_c^{[1]}\times\mathbf{v}^{[0]}-\mathbf{v}_c^{[1]}\big)+\mathbf{c}_1^{[0]}\cdot\big(\mathbf{u}_s^{[1]}\times\mathbf{v}^{[0]}-\mathbf{v}_s^{[1]}\big)\\ 0\end{bmatrix},
\end{aligned}$$

where $\mathbf{c}_j^{[0]}$ stand for the j^{th} column of $Q^{[0]}$ for $j = 1, 2$, and

$$\begin{aligned}
\mathbf{u}_{c,s}^{[1]}\times\mathbf{v}^{[0]}-\mathbf{v}_{c,s}^{[1]}=&\Big(\big[\mathbf{u}_{c,s}^{[1]}\times\big]\,\mathsf{M}_{12}\,[\mathbf{m}\times]-\mathsf{M}_{12}\,[\mathbf{m}\times]\,\big[\mathbf{u}_{c,s}^{[1]}\times\big]\Big)\,\mathbf{B}^{[0]}\\
&+\varsigma\gamma\Big(\big[\mathbf{u}_{c,s}^{[1]}\times\big]\,\mathsf{M}_{11}-\mathsf{M}_{11}\,\big[\mathbf{u}_{c,s}^{[1]}\times\big]\Big)\,\mathbf{e}_3^{[0]}\,.
\end{aligned}$$

This gives the first order horizontal component of the average velocity over one rotation of the magnetic field expressed in the lab frame $\big[\boldsymbol{e}_1|\boldsymbol{e}_2|\boldsymbol{e}_3\big]$.

The horizontal component of the average velocity (8.27) is eventually written as

$$\overline{\boldsymbol{v}_{\text{hor}}}=\varepsilon\,\overline{\boldsymbol{v}_{\text{hor}}}^{[1]}\,, \tag{8.30}$$

where

$$\overline{\boldsymbol{v}_{\text{hor}}}^{[1]}=\begin{bmatrix}\mathbf{c}_1^{[0]}\cdot\big(\mathbf{u}_c^{[1]}\times\mathbf{v}^{[0]}-\mathbf{v}_c^{[1]}\big)-\mathbf{c}_2^{[0]}\cdot\big(\mathbf{u}_s^{[1]}\times\mathbf{v}^{[0]}-\mathbf{v}_s^{[1]}\big)-2\varsigma\,\mathbf{e}_3^{[0]}\cdot\mathbf{v}^{[0]}\\ \mathbf{c}_2^{[0]}\cdot\big(\mathbf{u}_c^{[1]}\times\mathbf{v}^{[0]}-\mathbf{v}_c^{[1]}\big)+\mathbf{c}_1^{[0]}\cdot\big(\mathbf{u}_s^{[1]}\times\mathbf{v}^{[0]}-\mathbf{v}_s^{[1]}\big)\\ 0\end{bmatrix}.$$

Note that $\overline{\boldsymbol{v}_{\text{hor}}}^{[1]}$ is bounded for γ and $\overline{\alpha}$ small enough. Indeed

$$\begin{aligned}
\left|\overline{\boldsymbol{v}_{\text{hor}}}^{[1]}\right| \le& \left|\mathbf{u}_c^{[1]} \times \mathbf{v}^{[0]} - \mathbf{v}_c^{[1]}\right| + \left|\mathbf{u}_s^{[1]} \times \mathbf{v}^{[0]} - \mathbf{v}_s^{[1]}\right| + 2\,|\mathbf{e}_3^{[0]} \cdot \mathbf{v}^{[0]}| \\
\le& \left|\left(\left[\mathbf{u}_c^{[1]}\times\right] \mathsf{M}_{12}\,[\mathbf{m}\times] - \mathsf{M}_{12}\,[\mathbf{m}\times]\,\left[\mathbf{u}_c^{[1]}\times\right]\right)\mathbf{B}^{[0]}\right| \\
&+\gamma\left|\left(\left[\mathbf{u}_c^{[1]}\times\right] \mathsf{M}_{11} - \mathsf{M}_{11}\,\left[\mathbf{u}_c^{[1]}\times\right]\right)\mathbf{e}_3^{[0]}\right| \\
&+\left|\left(\left[\mathbf{u}_s^{[1]}\times\right] \mathsf{M}_{12}\,[\mathbf{m}\times] - \mathsf{M}_{12}\,[\mathbf{m}\times]\,\left[\mathbf{u}_s^{[1]}\times\right]\right)\mathbf{B}^{[0]}\right| \\
&+\gamma\left|\left(\left[\mathbf{u}_s^{[1]}\times\right] \mathsf{M}_{11} - \mathsf{M}_{11}\,\left[\mathbf{u}_s^{[1]}\times\right]\right)\mathbf{e}_3^{[0]}\right| + 2\,|\mathbf{e}_3^{[0]} \cdot \mathbf{v}^{[0]}| \\
\le& 2\left|\mathbf{u}_c^{[1]}\right|\,\|\mathsf{M}_{12}\| + 2\gamma\left|\mathbf{u}_c^{[1]}\right|\,\|\mathsf{M}_{11}\| + 2\left|\mathbf{u}_s^{[1]}\right|\,\|\mathsf{M}_{12}\| + 2\gamma\left|\mathbf{u}_s^{[1]}\right|\,\|\mathsf{M}_{11}\| + 2\,|\mathbf{e}_3^{[0]} \cdot \mathbf{v}^{[0]}| \\
\le& 4\left|\mathbf{u}^{[1]}\right|\left(\|\mathsf{M}_{12}\| + \gamma\,\|\mathsf{M}_{11}\|\right) + 2\,|\mathbf{e}_3^{[0]} \cdot \mathbf{v}^{[0]}|,
\end{aligned}$$

and $\mathbf{u}^{[1]}$ is bounded by the lemma on page 213.

The average vertical component of the velocity over one rotation of the magnetic field is given by

$$\begin{aligned}
\overline{v_{\text{vert}}} &= \frac{a}{2\pi}\int_0^{\frac{2\pi}{a}} \mathbf{g}\cdot\mathbf{v}\,dt = \frac{a}{2\pi}\int_0^{\frac{2\pi}{a}} \left(\mathbf{g}^{[0]} + \varepsilon\,\mathbf{g}^{[1]}\right)\cdot\left(\mathbf{v}^{[0]} + \varepsilon\,\mathbf{v}^{[1]}\right) dt + \mathcal{O}(\varepsilon^2) \\
&= \frac{a}{2\pi}\int_0^{\frac{2\pi}{a}} \mathbf{g}^{[0]}\cdot\mathbf{v}^{[0]}\,dt + \varepsilon\,\frac{a}{2\pi}\int_0^{\frac{2\pi}{a}} \left(\mathbf{g}^{[0]}\cdot\mathbf{v}^{[1]} + \mathbf{g}^{[1]}\cdot\mathbf{v}^{[0]}\right) dt + \mathcal{O}(\varepsilon^2)
\end{aligned}$$

The first order component can be computed using (8.29) as

$$\begin{aligned}
\int_0^{\frac{2\pi}{a}} \left(\mathbf{g}^{[0]}\cdot\mathbf{v}^{[1]} + \mathbf{g}^{[1]}\cdot\mathbf{v}^{[0]}\right) dt = &\int_0^{\frac{2\pi}{a}} \cos(a\,t)\,dt\left(\mathbf{g}^{[0]}\cdot\mathbf{v}_c^{[1]} + \mathbf{g}_c^{[1]}\cdot\mathbf{v}^{[0]}\right) \\
&+ \int_0^{\frac{2\pi}{a}} \sin(a\,t)\,dt\left(\mathbf{g}^{[0]}\cdot\mathbf{v}_s^{[1]} + \mathbf{g}_s^{[1]}\cdot\mathbf{v}^{[0]}\right) = 0\,.
\end{aligned}$$

Thus, the average vertical component is

$$\overline{v_{\text{vert}}} = \mathbf{g}^{[0]}\cdot\mathbf{v}^{[0]} + \mathcal{O}(\varepsilon^2)\,. \tag{8.31}$$

Computations of the average horizontal component (8.30) and vertical component (8.31) allow to compute the angle of deviation from the vertical λ as

$$\tan\lambda = \varepsilon\,\frac{|\overline{\boldsymbol{v}_{\text{hor}}}^{[1]}|}{\mathbf{g}^{[0]}\cdot\mathbf{v}^{[0]}} + \mathcal{O}(\varepsilon^2)\,,$$

where $|\overline{\boldsymbol{v}_{\text{hor}}}^{[1]}|$ is bounded for γ and $\overline{\alpha}$ small enough.

In this section, we studied the first-order perturbation arising when the axis of rotation $\boldsymbol{e}_3$ is misaligned with the lab vertical $\boldsymbol{g}$, i.e. the angle χ between $\boldsymbol{e}_3$ and $\boldsymbol{g}$ satisfies $0 < \sin\chi \ll 1$. By expanding the dynamics (8.6) in $\varepsilon = \sin\chi$, we gave explicitly the first order perturbation (8.26) when the zeroth-order equation is in stable steady state. The corresponding deviation of the swimmer's trajectory, which at zeroth order corresponds to a helical path with a vertical axis, was expressed by computing the horizontal and vertical components of the average direction of the swimmer. The angle between the swimmer's average direction and the vertical was show to be of order ε for a slowly rotating magnetic field of large magnitude.

Altogether, this chapter gave an overview of the relative equilibrium dynamics of a heavy swimmer when the axis of rotation of the magnetic field is vertical in the lab frame. Exploiting the procedures established for studying the rotational dynamics of neutrally buoyant swimmers, we obtained a parametrisation of the set of relative equilibria that allowed to extend results of chapter 4. Following the lines of chapter 7, we then examined the corresponding helical trajectories; in particular, explicit expressions for the pitch and radius were derived, and optimisation of the axial velocity was discussed.

9 Conclusion and Discussion

This work provides an analysis of the dynamics of a hard magnetic, rigid body in Stokes flow under the action of an external rotating magnetic field. Such a body, referred to as a swimmer, is specified by its mobility matrix $\mathbb{M}$ and its magnetic moment $\mathbf{m}$, which is constant in the body frame. In an infinite fluid domain, $\mathbb{M}$ is also constant when expressed in the body frame, as described in chapter 2. In the absence of effects due to buoyancy, an experiment involving a particular swimmer is then determined by two parameters: the Mason number a and the conical angle ψ. The trajectory observed in an experiment is entirely prescribed by the rotational dynamics for which a decoupled, autonomous formulation was obtained. This formulation relies on the magnetic frame, a frame that is in steady rotation with respect to the lab frame (chapter 3).

The main contributions of this work are:

- A complete classification of all relative equilibria, or steady state motions, of a swimmer prescribed by $\mathbf{m}$ and $\mathbb{M}$ as a and ψ vary, and in particular a characterisation of the bounded region in the (a,ψ) parameter plane for which relative equilibria occur (chapter 4). The boundary of the region where stable relative equilibria occur corresponds to the phenomenon of step-out observed by experimentalists [64, 18, 51, 74].
- Asymptotic analyses that provide characterisations of the out-of-equilibrium dynamics of a swimmer at the boundaries in the (a,ψ) parameter plane $(0,\infty) \times [0,\pi]$ (chapter 5).
- A study of the dynamics of a rigid body when loadings arise both from a rotating magnetic field and from buoyancy, connecting the analysis presented in the first part of this work with the classification of relative equilibria of a rigid body under the effect of buoyancy only as presented in [14] (chapter 8).

Studying the steady states of the rotational dynamics (chapter 4) allowed us to obtain a one-to-one parametrisation of the set of all steady states. These correspond to solutions where the body frame is locked to the magnetic frame. Properties of this parametrisation produced the following result: for almost all given pairs of parameters (a,ψ), a specific swimmer admits either 0, 4 or 8 relative equilibria. This allowed the parameter plane to be divided into different regimes according to the number of stable and unstable relative equilibria occurring for a particular swimmer. For sufficiently large loadings, i.e. a small enough and ψ sufficiently close to $\pi/2$, there are either 4 or 8 relative equilibria. Moreover, the region of the (a, ψ) parameter plane where any steady state occurs is bounded. The relative equilibria arise in pairs related by the symmetry described in chapter 3, and this symmetry reverses stability: stable steady states of index 3 are paired with unstable steady states of index 0, and unstable steady states of index 2 are paired with unstable steady states of index 1. Stability exchanges within the set of relative equilibria occur either at folds or at Hopf bifurcations. Exploration of regime diagrams and phase portraits of the rotational dynamics (chapter 6) confirmed the persistence of observed features across several examples of swimmers.

Non-steady state solutions of the rotational dynamics were investigated in the three limits of asymptotically small a, asymptotically large a, and asymptotically small $\sin\psi$ (chapter 5). These three limits cover all four edges of the (a, ψ) parameter plane $(0, \infty) \times [0, \pi]$. In the small a limit, the magnetic moment of the swimmer tends to align with the magnetic field and, depending on the value of ψ, exhibits a periodic residual motion. Specifically, the rotational dynamics admit a stable steady state when $\psi \in [\pi/2 - \iota, \pi/2 + \iota]$ and a stable periodic orbits for ψ outside this range, with the angle ι defined as in chapter 3, equation (3.19). In the large a limit, the magnetic moment tends to align with the axis of rotation of the magnetic field, with a slow residual motion about it. The dynamics in the small $\sin\psi$ limit support a continuous change between the predicted regimes at small and large a. Comparisons between these predictions and numerical results yielded good agreement, even for parameter values that are far from the asymptotic limits (chapter 6). Moreover, numerical continuation for particular examples confirmed the continuous change between small a and large a solutions for ψ away from $\pi/2$, and suggested that the corresponding non-steady state solutions are periodic.

The full trajectories, including the translational dynamics, associated to steady states and periodic solutions of the rotational dynamics were recovered and characterised in chapter 7. In particular, a steady state is associated with a helical trajectory whose centreline is aligned with the axis of rotation of the magnetic field. Its pitch and radius are given by equation (7.5). Trajectories become circular as the pitch vanishes and straight as the radius vanishes. Whether or not each of these two degenerate cases actually occurs for a given swimmer depends explicitly on its mobility matrix $\mathbb{M}$ and magnetic moment $\mathbf{m}$. How to magnetise a swimmer of a given shape so that it reaches optimal velocity for some parameter values a and ψ was also discussed with the formalism used in the rest of the work. An averaging procedure was proposed to recover the effective trajectory associated with periodic solutions of the rotational dynamics. It was shown that when the Mason number a and period p satisfy $ap/2\pi \in \mathbb{Z}$, the effective trajectory is linear in time and its direction depends on the initial orientation of the swimmer (cf. eq. (7.15)).

Finally, in chapter 8, the assumption that the effects of buoyancy are negligible was released in order to study the dynamics of heavy swimmers in the case when the axis of rotation of the magnetic field is aligned with gravity. The number of parameters increased from two to three: instead of the Mason number a and conical angle ψ as in chapters 3-7, we used γ, $\overline{\alpha}$, and ψ as defined in equations (8.5, 8.7). Again, for almost all given triples of parameters $(\gamma, \overline{\alpha}, \psi)$, a specific swimmer admits 0, 4 or 8 relative equilibria corresponding to helical trajectories. The first order perturbation induced by a small misalignment of the axis of rotation with the vertical was shown to be bounded for γ and $\overline{\alpha}$ small enough, which means for a magnetic field of large enough magnitude that rotates slowly enough.

The study of heavy swimmers was motivated by comparison of our results with experiments planned by Prof. A. Petruska. Indeed, the assumptions made in chapters 3-7, namely

- that the fluid spans infinite space,
- that the swimmer is made of a permanent magnetic material,
- that the magnetic field is uniform,
- that the swimmer is not deformed by the applied loads,
- that buoyancy produces negligible effects,

are natural first approximations when initially tackling the problem mathematically. However, each of these hypotheses restricts the possible accuracy of comparison with experiment. We first planned to compare our results with micro-swimmers made by the group of Prof. B. Nelson which are soft magnetic. However, their small size made tracking of their orientation (as opposed to their location) problematic, especially when the micro-swimmers get away from the tank bottom [65]. In particular, both hard magnet and infinite space assumptions were likely quite inaccurate.

The currently proposed comparison with Petruska's experiments will involve larger swimmers (millimetre scale), which will be easier to track – the Reynolds number would be kept low by choosing a fluid more viscous than water. As Petruska's swimmers will be made of metal, the loads arising from buoyancy need to be taken into account as in chapter 8. Comparison between the results of chapter 8 and experiments realised by Petruska's group is an obvious next future step.

Future work could also include relaxing the other modelling assumptions, namely considering

- finite space – in particular half space,
- soft magnets,
- non-uniform fields
- flexible swimmers.

A half space analysis would allow the study of the dynamics of swimmers close to a tank wall or close to the tank bottom. However, this would require account to be taken of the position and orientation of the swimmer with respect to the wall when computing the mobility matrix $\mathbb{M}$, which would then change over time with both orientation and location. Nevertheless, the computation of such configuration dependent mobility matrices $\mathbb{M}$ could, at least in principle, be done using the method proposed in [24].

Soft magnetic materials are usually modelled by letting the magnetic moment $\mathbf{m}$ depend linearly on the magnetic field as

$$\mathbf{m} = \mathscr{X}\,\mathbf{B},$$

where $\mathscr{X}$ is the susceptibility tensor, which is assumed constant in the body frame [64]. The dynamics of a soft-magnetic swimmer would remain similar to the system studied in chapters 3-7, except that the rotational equation (3.7) would then be

$$\dot{Q} = [(a\mathbf{e}_3 - \mathsf{M}_{22}\,[(\mathscr{X}\,\mathbf{B})\times]\,\mathbf{B})\times]\,Q,$$

where $\mathbf{e}_3$ and $\mathbf{B}$ are defined from Q as before. The corresponding equilibrium condition is

$$a\mathbf{e}_3 = \mathsf{M}_{22}\left((\mathscr{X}\,\mathbf{B})\times\mathbf{B}\right).$$

Its solutions can be parametrised by writing $\mathbf{B}$ in spherical coordinates as

$$\mathbf{B}(\phi,\xi) = \cos\phi\,\boldsymbol{\beta}_0 + \sin\phi\left(\cos\xi\,\boldsymbol{\beta}_1 + \sin\xi\,\boldsymbol{\beta}_2\right)$$

for suitable vectors $\boldsymbol{\beta}_0$, $\boldsymbol{\beta}_1$, and $\boldsymbol{\beta}_2$. The corresponding Mason number is found as

$$a(\phi,\xi) = \left|\mathsf{M}_{22}\left((\mathscr{X}\,\mathbf{B}(\phi,\xi))\times\mathbf{B}(\phi,\xi)\right)\right|,$$

the axis of rotation as

$$\mathbf{e}_3(\phi,\xi) = \frac{\mathsf{M}_{22}\left((\mathscr{X}\,\mathbf{B}(\phi,\xi))\times\mathbf{B}(\phi,\xi)\right)}{a(\phi,\xi)},$$

and the conical angle as

$$\cos\psi(\phi,\xi) = \mathbf{e}_3(\phi,\xi)\cdot\mathbf{B}(\phi,\xi).$$

This parametrisation might yield similar results to those obtained in chapters 4 and 7 for hard-magnetic swimmers. Materials that are neither completely hard nor completely soft-magnetic could perhaps then also be considered by assuming a magnetic moment of the form $\mathbf{m} = \mathbf{m}_0 + \mathscr{X}\,\mathbf{B}$.

Taking into account a non-uniform magnetic field $\mathbf{B}$ would imply that the external loads exerted on the swimmer depend on its position. This would suppress the decoupling between rotational and translational dynamics that was used extensively in the analysis presented here, and therefore require another approach.

Modelling deformable swimmers with their fluid-structure interactions is likely to be challenging. For example, a complete classification of all helical equilibria of uniform rods under end loading has only been obtained relatively recently [88, 89], but that general analysis does not include the configuration dependent distributed loadings that would arise for a swimmer in Stokes flow. Some results for rodlike deformable swimmers have been achieved [92, 93, 94, 95, 96, 33, 97, 98, 34]. But we are unaware of any version of a general classification of possible motions for magnetically driven flexible bodies analogous to the one we have provided for the rigid body case. Nevertheless it seems likely that such a classification should exist, at least for slightly deformable bodies.

A Expansions in SO(3)

A.1 Asymptotic Expansions in SO(3)

Suppose $R \in \mathrm{SO}(3)$ depends continuously on a parameter ε in a neighbourhood of $\varepsilon = 0$. Then, R can be Taylor expanded as

$$R = R^{[0]} + \varepsilon\, R^{[1]} + \varepsilon^2\, R^{[2]} + O(\varepsilon^3)\,, \tag{A.1}$$

where

$$R^{[0]} = R|_{\varepsilon=0}\,, \qquad R^{[1]} = \frac{d}{d\varepsilon} R\bigg|_{\varepsilon=0} \qquad \text{and} \qquad R^{[2]} = \frac{1}{2}\,\frac{d^2}{d\varepsilon^2} R\bigg|_{\varepsilon=0}. \tag{A.2}$$

Since R is a rotation matrix, $R^{[0]}$ is also in SO(3) because of (A.2). Furthermore, differentiating the identity $R\,R^T = \mathbf{I}$ with respect to ε provides the existence of $\mathbf{u} \in \mathbb{R}^3$ such that

$$\frac{d}{d\varepsilon} R = [\mathbf{u}\times]\; R\,, \tag{A.3}$$

where (A.3) defines $\mathbf{u}$ in the same domain as R. Accordingly, $\mathbf{u}$ can itself be expanded as

$$\mathbf{u} = \mathbf{u}^{[1]} + 2\varepsilon\, \mathbf{u}^{[2]} + \mathcal{O}(\varepsilon^2)\,, \tag{A.4}$$

where

$$\mathbf{u}^{[2]} = \frac{1}{2}\,\frac{d}{d\varepsilon}\mathbf{u}\bigg|_{\varepsilon=0}.$$

Equations (A.3, A.4) allow to rewrite $R^{[1]}$ as

$$R^{[1]} = \left[\mathbf{u}^{[1]}\times\right]\, R^{[0]}. \tag{A.5}$$

Differentiating (A.3) with respect to ε again yields

$$\frac{d^2}{d\varepsilon^2}R = \left[\left(\frac{d}{d\varepsilon}\mathbf{u}\right)\times\right] R + [\mathbf{u}\times]^2\, R\,.$$

Substituting the expansion (A.4) and evaluating in $\varepsilon = 0$ yields

$$R^{[2]} = \left(\left[\mathbf{u}^{[2]}\times\right] + \frac{1}{2}\left[\mathbf{u}^{[1]}\times\right]^2\right) R^{[0]}\,. \tag{A.6}$$

As a consequence, the expansion (A.1) for $R \in \mathrm{SO}(3)$ can be rewritten in the form

$$R = R^{[0]} + \varepsilon\left[\mathbf{u}^{[1]}\times\right] R^{[0]} + \varepsilon^2\left(\left[\mathbf{u}^{[2]}\times\right] + \frac{1}{2}\left[\mathbf{u}^{[1]}\times\right]^2\right) R^{[0]} + \mathcal{O}(\varepsilon^3)\,. \tag{A.7}$$

A.2 First Order Ordinary Differential Equation in SO(3) Depending on a Small Parameter

A.2.1 Outer Solution

Expansions in SO(3) can be used to solve a first order ode in SO(3) of the form

$$\dot{R} = [\boldsymbol{\omega}\times]\, R\,, \tag{A.8}$$

where $\boldsymbol{\omega} = \boldsymbol{\omega}(R, t; \varepsilon)$ is continuous in ε in a neighbourhood of 0. Using standard singular perturbation methods [15], we search for solution $R = R(t, \varepsilon)$ valid for $t \gg \varepsilon$.

Expanding R in ε as (A.7), the total dependence of $\boldsymbol{\omega}$ in ε can be explicitly written as

$$\boldsymbol{\omega}\left(R^{[0]} + \varepsilon\left[\mathbf{u}^{[1]}\times\right] R^{[0]} + \varepsilon^2\left(\left[\mathbf{u}^{[2]}\times\right] + \frac{1}{2}\left[\mathbf{u}^{[1]}\times\right]^2\right) R^{[0]} + \mathcal{O}(\varepsilon^3), t; \varepsilon\right),$$

and this is used to expand $\boldsymbol{\omega}$ as

$$\boldsymbol{\omega} = \mathbf{w}^{[0]}(R^{[0]}, t) + \varepsilon\,\mathbf{w}^{[1]}(R^{[0]}, \mathbf{u}^{[1]}, t) + \varepsilon^2\,\mathbf{w}^{[2]}(R^{[0]}, \mathbf{u}^{[1]}, \mathbf{u}^{[2]}, t) + \mathcal{O}(\varepsilon^3)\,, \tag{A.9}$$

where the coefficients are obtained by computing

$$\begin{aligned}
\mathbf{w}^{[0]}(R^{[0]}, t) &= \left.\boldsymbol{\omega}\right|_{\varepsilon=0}\,,\\
\mathbf{w}^{[1]}(R^{[0]}, \mathbf{u}^{[1]}, t) &= \left.\left(\frac{\partial}{\partial R}\boldsymbol{\omega}\cdot\frac{\partial}{\partial\varepsilon}R + \frac{\partial}{\partial\varepsilon}\boldsymbol{\omega}\right)\right|_{\varepsilon=0}\\
\mathbf{w}^{[2]}(R^{[0]}, \mathbf{u}^{[1]}, \mathbf{u}^{[2]}, t) &= \left.\left(\frac{\partial^2}{\partial R^2}\boldsymbol{\omega}\cdot\frac{\partial}{\partial\varepsilon}R + \frac{\partial}{\partial R}\boldsymbol{\omega}\cdot\frac{\partial^2}{\partial\varepsilon^2}R + \frac{\partial^2}{\partial\varepsilon^2}\boldsymbol{\omega}\right)\right|_{\varepsilon=0}\,.
\end{aligned}$$

Substituting (A.7) and (A.9) in (A.8) yields

$$\begin{aligned}
&\dot{R}^{[0]} + \varepsilon \frac{d}{dt}\left(\left[\mathbf{u}^{[1]}\times\right] R^{[0]}\right) + \varepsilon^2 \frac{d}{dt}\left(\left(\left[\mathbf{u}^{[2]}\times\right] + \frac{1}{2}\left[\mathbf{u}^{[1]}\times\right]^2\right) R^{[0]}\right) + O(\varepsilon^3) \\
&= \left[\mathbf{w}^{[0]}\times\right] R^{[0]} \\
&\quad + \varepsilon\left(\left[\mathbf{w}^{[0]}\times\right]\left[\mathbf{u}^{[1]}\times\right] R^{[0]} + \left[\mathbf{w}^{[1]}\times\right] R^{[0]}\right) \\
&\quad + \varepsilon^2\left(\left[\mathbf{w}^{[0]}\times\right]\left(\left[\mathbf{u}^{[2]}\times\right] + \frac{1}{2}\left[\mathbf{u}^{[1]}\times\right]^2\right) R^{[0]} + \left[\mathbf{w}^{[1]}\times\right]\left[\mathbf{u}^{[1]}\times\right] R^{[0]} + \left[\mathbf{w}^{[2]}\times\right] R^{[0]}\right) \\
&\quad + \mathcal{O}(\varepsilon^3)\,,
\end{aligned} \tag{A.10}$$

and matching orders gives at zeroth order

$$\dot{R}^{[0]} = \left[\mathbf{w}^{[0]}\times\right] R^{[0]}\,, \tag{A.11}$$

at first order

$$\left[\dot{\mathbf{u}}^{[1]}\times\right] R^{[0]} + \left[\mathbf{u}^{[1]}\times\right] \dot{R}^{[0]} = \left[\mathbf{w}^{[1]}\times\right] R^{[0]} + \left[\mathbf{w}^{[0]}\times\right]\left[\mathbf{u}^{[1]}\times\right] R^{[0]}\,, \tag{A.12}$$

and at second order

$$\begin{aligned}
&\left(\left[\dot{\mathbf{u}}^{[2]}\times\right] + \frac{1}{2}\left[\mathbf{u}^{[1]}\times\right]\left[\dot{\mathbf{u}}^{[1]}\times\right] + \frac{1}{2}\left[\dot{\mathbf{u}}^{[1]}\times\right]\left[\mathbf{u}^{[1]}\times\right]\right) R^{[0]} + \left(\left[\mathbf{u}^{[2]}\times\right] + \frac{1}{2}\left[\mathbf{u}^{[1]}\times\right]^2\right)\dot{R}^{[0]} \\
&= \left[\mathbf{w}^{[2]}\times\right] R^{[0]} + \left[\mathbf{w}^{[1]}\times\right]\left[\mathbf{u}^{[1]}\times\right] R^{[0]} + \left[\mathbf{w}^{[0]}\times\right]\left(\left[\mathbf{u}^{[2]}\times\right] + \frac{1}{2}\left[\mathbf{u}^{[1]}\times\right]^2\right) R^{[0]}\,.
\end{aligned} \tag{A.13}$$

Substituting (A.11) in (A.12) and multiplying on the right by $R^{[0]\,T}$ yields

$$\left[\dot{\mathbf{u}}^{[1]}\times\right] + \left[\mathbf{u}^{[1]}\times\right]\left[\mathbf{w}^{[0]}\times\right] = \left[\mathbf{w}^{[1]}\times\right] + \left[\mathbf{w}^{[0]}\times\right]\left[\mathbf{u}^{[1]}\times\right]\,. \tag{A.14}$$

Using the identity

$$\left[\mathbf{y}\times\right][\mathbf{z}\times] - [\mathbf{z}\times]\left[\mathbf{y}\times\right] = \left[(\mathbf{y}\times\mathbf{z})\times\right]\,, \tag{A.15}$$

this can be simplified to

$$\dot{\mathbf{u}}^{[1]} + \mathbf{u}^{[1]}\times\mathbf{w}^{[0]} = \mathbf{w}^{[1]}\,. \tag{A.16}$$

Substituting (A.11) in (A.13) and multiplying on the right by $R^{[0]\,T}$ yields

$$\begin{aligned}
&\left[\dot{\mathbf{u}}^{[2]}\times\right] + \frac{1}{2}\left[\mathbf{u}^{[1]}\times\right]\left[\dot{\mathbf{u}}^{[1]}\times\right] + \frac{1}{2}\left[\dot{\mathbf{u}}^{[1]}\times\right]\left[\mathbf{u}^{[1]}\times\right] + \left(\left[\mathbf{u}^{[2]}\times\right] + \frac{1}{2}\left[\mathbf{u}^{[1]}\times\right]^2\right)\left[\mathbf{w}^{[0]}\times\right] \\
&= \left[\mathbf{w}^{[2]}\times\right] + \left[\mathbf{w}^{[1]}\times\right]\left[\mathbf{u}^{[1]}\times\right] + \left[\mathbf{w}^{[0]}\times\right]\left(\left[\mathbf{u}^{[2]}\times\right] + \frac{1}{2}\left[\mathbf{u}^{[1]}\times\right]^2\right).
\end{aligned}$$

Using again (A.15), this can be rearranged as

$$\begin{aligned}
&\left[\dot{\mathbf{u}}^{[2]}\times\right]+\left[(\mathbf{u}^{[2]}\times\mathbf{w}^{[0]})\times\right]+\frac{1}{2}\left[\mathbf{u}^{[1]}\times\right]\left(\left[\dot{\mathbf{u}}^{[1]}\times\right]+\left[\mathbf{u}^{[1]}\times\right]\left[\mathbf{w}^{[0]}\times\right]\right)\\
&=\left[\mathbf{w}^{[2]}\times\right]+\left(\left[\mathbf{w}^{[1]}\times\right]+\frac{1}{2}\left[\mathbf{w}^{[0]}\times\right]\left[\mathbf{u}^{[1]}\times\right]-\frac{1}{2}\left[\dot{\mathbf{u}}^{[1]}\times\right]\right)\left[\mathbf{u}^{[1]}\times\right].
\end{aligned}$$

Substituting (A.14), this becomes

$$\begin{aligned}
&\left[\dot{\mathbf{u}}^{[2]}\times\right]+\left[(\mathbf{u}^{[2]}\times\mathbf{w}^{[0]})\times\right]+\frac{1}{2}\left[\mathbf{u}^{[1]}\times\right]\left(\left[\mathbf{w}^{[1]}\times\right]+\left[\mathbf{w}^{[0]}\times\right]\left[\mathbf{u}^{[1]}\times\right]\right)\\
&=\left[\mathbf{w}^{[2]}\times\right]+\frac{1}{2}\left(\left[\mathbf{w}^{[1]}\times\right]+\left[\mathbf{u}^{[1]}\times\right]\left[\mathbf{w}^{[0]}\times\right]\right)\left[\mathbf{u}^{[1]}\times\right],
\end{aligned}$$

which, using again (A.15), can be simplified to

$$\left[\dot{\mathbf{u}}^{[2]}\times\right]+\left[(\mathbf{u}^{[2]}\times\mathbf{w}^{[0]})\times\right]=\left[\mathbf{w}^{[2]}\times\right]+\frac{1}{2}\left[(\mathbf{w}^{[1]}\times\mathbf{u}^{[1]})\times\right],$$

or equivalently

$$\dot{\mathbf{u}}^{[2]}+\mathbf{u}^{[2]}\times\mathbf{w}^{[0]}=\mathbf{w}^{[2]}+\frac{1}{2}\mathbf{w}^{[1]}\times\mathbf{u}^{[1]}. \tag{A.17}$$

Equations (A.11, A.16, A.17) are used to determine $R^{[0]}$, $\mathbf{u}^{[1]}$ and $\mathbf{u}^{[2]}$ approximating the solution R to (A.8) as an asymptotic expansion of the form (A.7).

A.2.2 Fast System

Expansions in SO(3) can also be used to solve a first order ode of the form

$$\varepsilon\dot{R}=[\boldsymbol{\omega}\times]\,R, \tag{A.18}$$

where $\boldsymbol{\omega}=\boldsymbol{\omega}(R,t;\varepsilon)$ is continuous in ε in a neighbourhood of 0. This is referred to as a fast system because the variable R varies with a rate of order $1/\varepsilon\gg 1$ if $\boldsymbol{\omega}$ is of order 1.

Note that a differential equation of this form is obtained for instance when looking for the inner layer solution valid for $t\sim\varepsilon$ to equation (A.8). Indeed, rescaling time as $t=\varepsilon\,T$, equation (A.8) becomes [15]

$$\varepsilon\frac{d}{dT}R=[\boldsymbol{\omega}\times]\,R.$$

Expanding R as (A.7) and $\boldsymbol{\omega}$ as (A.9) and substituting in (A.18), the analogue of equation (A.10) is

$$
\begin{aligned}
&\varepsilon\,\dot{R}^{[0]} + \varepsilon^2 \frac{d}{dt}\left(\left[\mathbf{u}^{[1]}\times\right] R^{[0]}\right) + O(\varepsilon^3)\\
&= \left[\mathbf{w}^{[0]}\times\right] R^{[0]}\\
&\quad + \varepsilon\Big(\left[\mathbf{w}^{[0]}\times\right]\left[\mathbf{u}^{[1]}\times\right] R^{[0]} + \left[\mathbf{w}^{[1]}\times\right] R^{[0]}\Big)\\
&\quad + \varepsilon^2\Big(\left[\mathbf{w}^{[0]}\times\right]\Big(\left[\mathbf{u}^{[2]}\times\right] + \frac{1}{2}\left[\mathbf{u}^{[1]}\times\right]^2\Big) R^{[0]} + \left[\mathbf{w}^{[1]}\times\right]\left[\mathbf{u}^{[1]}\times\right] R^{[0]} + \left[\mathbf{w}^{[2]}\times\right] R^{[0]}\Big)\\
&\quad + \mathcal{O}(\varepsilon^3)\,.
\end{aligned}
$$

Similar computations as in section A.2 yield the system

$$
\mathbf{w}^{[0]}(R^{[0]}, t) = 0 \tag{A.19}
$$

$$
\dot{R}^{[0]} = \left[\mathbf{w}^{[1]}(R^{[0]}, \mathbf{u}^{[1]}, t)\times\right] R^{[0]} \tag{A.20}
$$

$$
\dot{\mathbf{u}}^{[1]} + \mathbf{u}^{[1]} \times \mathbf{w}^{[1]}(R^{[0]}, \mathbf{u}^{[1]}, t) = \mathbf{w}^{[2]}(R^{[0]}, \mathbf{u}^{[1]}, \mathbf{u}^{[2]}, t)\,, \tag{A.21}
$$

that is used to determine $R^{[0]}$, $\mathbf{u}^{[1]}$, and $\mathbf{u}^{[2]}$. The solutions allow to write an approximation of the solution R to (A.18) up to order ε^2.

A.3 The Averaging Method in SO(3)

The averaging method [16], summarised in section 2.5 is used in chapter 5 to study a differential equation on SO(3) with periodic terms. In this section, the equations (2.47) giving the coefficients that determine the guiding system are adapted to SO(3).

Consider the system

$$
\dot{R} = \varepsilon\left[\mathbf{w}^{[1]}(R, t)\times\right] R + \varepsilon^2\left[\mathbf{w}^{[2]}(R, t)\times\right] R + \varepsilon^3 \Phi(R, t, \varepsilon)\,, \tag{A.22}
$$

where $\mathbf{w}^{[1]}$, $\mathbf{w}^{[2]}$, and Φ are T-periodic in t. The averaging method builds an approximation to a solution of (A.22) up to an order ε^2. It is given as the solution R_{av} to the guiding system

$$
\dot{R} = \varepsilon\left[\mathbf{g}^{[1]}\times\right] R + \varepsilon^2\left[\mathbf{g}^{[2]}\times\right] R\,, \tag{A.23}
$$

where the $\mathbf{g}^{[k]}$s are functions independent of t to be determined.

The main idea is to build a vector field $\mathbf{u}$ such that R is recovered from R_{av} by following $\mathbf{u}$ for a "time" ε. In practice, $\mathbf{u}$ is itself expanded up to order of ε:

$$
\mathbf{u} = \mathbf{u}^{[1]} + \varepsilon\,\mathbf{u}^{[2]}
$$

so that we can write

$$R = R_{\rm av} + \varepsilon\,\left[\mathbf{u}^{[1]}\times\right] R_{\rm av} + \varepsilon^2 \left(\left[\mathbf{u}^{[2]}\times\right] + \frac{1}{2}\left[\mathbf{u}^{[1]}\times\right]^2\right) R_{\rm av} + \mathcal{O}(\varepsilon^3)\,. \tag{A.24}$$

This is referred to as a *near identity transformation.* Substituting (A.24) in (A.22), we try to choose $\mathbf{u}^{[1]}$ and $\mathbf{u}^{[2]}$ T-periodic and such that the resulting equation for $R_{\rm av}$ is autonomous.

Note that (A.24) implies

$$\begin{aligned}\dot R =& \dot R_{\rm av} + \varepsilon\left(\left[\dot{\mathbf{u}}^{[1]}\times\right] R_{\rm av} + \left[\mathbf{u}^{[1]}\times\right] \dot R_{\rm av}\right)\\ &+ \varepsilon^2\left(\left(\left[\dot{\mathbf{u}}^{[2]}\times\right] + \frac{1}{2}\left[\dot{\mathbf{u}}^{[1]}\times\right]\left[\mathbf{u}^{[1]}\times\right] + \frac{1}{2}\left[\mathbf{u}^{[1]}\times\right]\left[\dot{\mathbf{u}}^{[1]}\times\right]\right) R_{\rm av} + \left(\left[\mathbf{u}^{[2]}\times\right] + \frac{1}{2}\left[\mathbf{u}^{[1]}\times\right]^2\right)\dot R_{\rm av}\right)\\ &+ \mathcal{O}(\varepsilon^3)\,,\end{aligned}$$

where the dot indicates the total derivative with respect to t. In particular,

$$\dot{\mathbf{u}}^{[k]}(R,t) = \partial_t \mathbf{u}^{[k]}(R,t) + \left(\partial_R \mathbf{u}^{[k]}(R,t)\right)\cdot \dot R\,,$$

where for any 3-by-3 matrix Z, $\partial_R \mathbf{u}^{[k]} \cdot Z$ denotes the vector $Z_{ij}\,\partial_{R_{ij}} \mathbf{u}^{[k]}$. Substituting (A.23) therein yields

$$\begin{aligned}\dot R =& \varepsilon\,\left[\left(\partial_t \mathbf{u}^{[1]} + \mathbf{g}^{[1]}\right)\times\right] R_{\rm av}\\ &+ \varepsilon^2\left(\left[\left(\left(\partial_R \mathbf{u}^{[1]}\right)\cdot\left(\left[\mathbf{u}^{[1]}\times\right] R_{\rm av}\right) + \partial_t \mathbf{u}^{[2]} + \mathbf{g}^{[2]}\right)\times\right]\right.\\ &\left.+ \frac{1}{2}\left[\partial_t \mathbf{u}^{[1]}\times\right]\left[\mathbf{u}^{[1]}\times\right] + \frac{1}{2}\left[\mathbf{u}^{[1]}\times\right]\left[\partial_t \mathbf{u}^{[1]}\times\right] + \left[\mathbf{u}^{[1]}\times\right]\left[\mathbf{g}^{[1]}\times\right]\right) R_{\rm av}\\ &+ \mathcal{O}(\varepsilon^3)\,.\end{aligned}$$

The vector fields $\mathbf{u}^{[k]}$ and $\mathbf{g}^{[k]}$ are determined by substituting (A.24) in (A.22) and matching orders. The equation at order ε is

$$\mathbf{w}^{[1]}(R_{\rm av}, t) = \partial_t \mathbf{u}^{[1]}(R_{\rm av}, t) + \mathbf{g}^{[1]}(R)\,. \tag{A.25}$$

For any T-periodic function $G(R,t)$,

$$\overline{G}(R) = \frac{1}{T}\int_0^T G(R,s)\,ds$$

denotes the average of G over one period, computed while keeping R constant (cf eq. (2.43)).

Averaging equation (A.25) and using the fact that $\mathbf{u}^{[1]}$ is T-periodic and $\mathbf{g}^{[1]}$ is independent of

t yields

$$
\begin{aligned}
\mathbf{g}^{[1]}(R_{\mathrm{av}}) &= \overline{\mathbf{w}^{[1]}}(R_{\mathrm{av}}) && \text{(A.26)}\\
\partial_t \mathbf{u}^{[1]}(R_{\mathrm{av}}, t) &= \mathbf{w}^{[1]}(R_{\mathrm{av}}, t) - \mathbf{g}^{[1]}(R_{\mathrm{av}})\,. && \text{(A.27)}
\end{aligned}
$$

Matching terms of order ε^2 gives

$$
\begin{aligned}
\left[\mathbf{w}^{[2]}\times\right] + \left[\mathbf{w}^{[1]}\times\right]\left[\mathbf{u}^{[1]}\times\right] &= \left[\left(\left(\partial_R \mathbf{u}^{[1]}\right)\cdot\left(\left[\mathbf{u}^{[1]}\times\right]R_{\mathrm{av}}\right) + \partial_t \mathbf{u}^{[2]} + \mathbf{g}^{[2]}\right)\times\right]\\
&\quad + \frac{1}{2}\left[\partial_t \mathbf{u}^{[1]}\times\right]\left[\mathbf{u}^{[1]}\times\right] + \frac{1}{2}\left[\mathbf{u}^{[1]}\times\right]\left[\partial_t \mathbf{u}^{[1]}\times\right] + \left[\mathbf{u}^{[1]}\times\right]\left[\mathbf{g}^{[1]}\times\right].
\end{aligned}
$$

Using (A.27), this can be rearranged as

$$
\begin{aligned}
\left[\mathbf{w}^{[2]}\times\right] &= \left[\left(\left(\partial_R \mathbf{u}^{[1]}\right)\cdot\left(\left[\mathbf{u}^{[1]}\times\right]R_{\mathrm{av}}\right) + \partial_t \mathbf{u}^{[2]} + \mathbf{g}^{[2]}\right)\times\right]\\
&\quad + \frac{1}{2}\left[\mathbf{u}^{[1]}\times\right]\left[\partial_t \mathbf{u}^{[1]}\times\right] - \frac{1}{2}\left[\partial_t \mathbf{u}^{[1]}\times\right]\left[\mathbf{u}^{[1]}\times\right] + \left[\mathbf{u}^{[1]}\times\right]\left[\mathbf{g}^{[1]}\times\right] - \left[\mathbf{g}^{[1]}\times\right]\left[\mathbf{u}^{[1]}\times\right]\\
&\overset{(A.15)}{=} \left[\left(\left(\partial_R \mathbf{u}^{[1]}\right)\cdot\left(\left[\mathbf{u}^{[1]}\times\right]R_{\mathrm{av}}\right) + \partial_t \mathbf{u}^{[2]} + \mathbf{g}^{[2]}\right)\times\right]\\
&\quad + \frac{1}{2}\left[\left(\mathbf{u}^{[1]}\times\partial_t \mathbf{u}^{[1]}\right)\times\right] + \left[\left(\mathbf{u}^{[1]}\times\mathbf{g}^{[1]}\right)\times\right],
\end{aligned}
$$

which simplifies to

$$
\mathbf{g}^{[2]} + \partial_t \mathbf{u}^{[2]} + \left(\partial_R \mathbf{u}^{[1]}\right)\cdot\left(\left[\mathbf{u}^{[1]}\times\right]R_{\mathrm{av}}\right) + \frac{1}{2}\mathbf{u}^{[1]}\times\partial_t \mathbf{u}^{[1]} + \mathbf{u}^{[1]}\times\mathbf{g}^{[1]} = \mathbf{w}^{[2]}\,. \tag{A.28}
$$

Taking the average, and using the assumption that the $\mathbf{u}^{[k]}$ are T-periodic and that $\mathbf{g}^{[2]}$ is independent of t, we find

$$
\mathbf{g}^{[2]} = \overline{\mathbf{w}^{[2]}} - \frac{1}{2}\overline{\mathbf{u}^{[1]}\times\partial_t \mathbf{u}^{[1]}}\,, \tag{A.29}
$$

where $\mathbf{u}^{[1]}$ is recovered as the integral of (A.27). In practice, this requires choosing an integration constant, which is chosen such that the average of $\mathbf{u}^{[1]}$ over one period vanishes.

Bibliography

[1] G. I. Taylor, "Analysis of the swimming of microscopic organisms," *Proc. R. Soc. Lond. A*, vol. 209, pp. 447–461, Nov. 1951.

[2] J. Lighthill, "Flagellar Hydrodynamics," *SIAM Review*, vol. 18, pp. 161–230, Apr. 1976.

[3] E. M. Purcell, "Life at low Reynolds number," *American Journal of Physics*, vol. 45, no. 1, 1977.

[4] E. Lauga and T. R. Powers, "The Hydrodynamics of Swimming Microorganisms," *Reports on Progress in Physics*, vol. 72, Sept. 2009.

[5] G. Cicconofri and A. DeSimone, "Modelling biological and bio-inspired swimming at microscopic scales: Recent results and perspectives," *Computers & Fluids*, Aug. 2018.

[6] B. J. Nelson, I. K. Kaliakatsos, and J. J. Abbott, "Microrobots for Minimally Invasive Medicine.," *Annual Review of Biomedical Engineering*, vol. 12, pp. 55–85, Aug. 2010.

[7] W. Gao and J. Wang, "The Environmental Impact of Micro/Nanomachines: A Review," *ACS Nano*, vol. 8, pp. 3170–3180, Apr. 2014.

[8] F. Mushtaq, M. Guerrero, M. S. Sakar, M. Hoop, A. M. Lindo, J. Sort, X. Chen, B. J. Nelson, E. Pellicer, and S. Pané, "Magnetically driven Bi 2 O 3 /BiOCl-based hybrid microrobots for photocatalytic water remediation," *Journal of Materials Chemistry A*, vol. 3, no. 47, pp. 23670–23676, 2015.

[9] H. C. Berg and R. A. Anderson, "Bacteria Swim by Rotating their Flagellar Filaments," *Nature*, vol. 245, pp. 380–382, Oct. 1973.

[10] D. J. Bell, S. Leutenegger, K. M. Hammar, L. X. Dong, and B. J. Nelson, "Flagella-like Propulsion for Microrobots Using a Nanocoil and a Rotating Electromagnetic Field," in *Proceedings 2007 IEEE International Conference on Robotics and Automation*, pp. 1128–1133, Apr. 2007.

[11] O. Gonzalez, "On stable, complete, and singularity-free boundary integral formulations of exterior Stokes flow," *SIAM Journal on Applied Mathematics*, vol. 69, no. 4, pp. 933–958, 2009.

[12] J. Li and O. Gonzalez, “Convergence and conditioning of a Nyström method for Stokes flow in exterior three-dimensional domains,” *Advances in Computational Mathematics*, vol. 39, no. 1, pp. 143–174, 2013.

[13] O. Gonzalez and J. Li, “A convergence theorem for a class of Nyström methods for weakly singular integral equations on surfaces in R3,” *Mathematics of Computation*, vol. 84, no. 292, pp. 675–714, 2015.

[14] O. Gonzalez, A. B. A. Graf, and J. H. Maddocks, “Dynamics of a Rigid Body in a Stokes Fluid,” *Journal of Fluid Mechanics*, vol. 519, pp. 133–160, 2004.

[15] E. J. Hinch, *Perturbation Methods.* Cambridge University Press, 1991.

[16] J. A. Sanders, F. Verhulst, and J. Murdock, *Averaging Methods in Nonlinear Dynamical Systems.* Applied Mathematical Sciences, New York: Springer-Verlag, 2 ed., 2007.

[17] K. E. Peyer, S. Tottori, F. Qiu, L. Zhang, and B. J. Nelson, “Magnetic helical micromachines.,” *Chemistry (Weinheim an der Bergstrasse, Germany)*, vol. 19, pp. 28–38, Jan. 2013.

[18] T.-Y. Huang, F. Qiu, H.-W. Tung, K. E. Peyer, N. Shamsudhin, J. Pokki, L. Zhang, X.-B. Chen, B. J. Nelson, and M. S. Sakar, “Cooperative manipulation and transport of microobjects using multiple helical microcarriers,” *RSC Advances*, vol. 4, no. 51, pp. 26771–26776, 2014.

[19] H. C. Fu, M. Jabbarzadeh, and F. Meshkati, “Magnetization directions and geometries of helical microswimmers for linear velocity-frequency response,” *Physical Review E*, vol. 91, no. 4, pp. 1–13, 2015.

[20] J. Happel and H. Brenner, *Low Reynolds Number Hydrodynamics: With Special Applications to Particulate Media.* Mechanics of Fluids and Transport Processes, Springer Netherlands, 1983.

[21] J. D. Jackson, *Classical Electrodynamics.* New York [etc.: Wiley, third ed. ed., 1999.

[22] G. K. Batchelor, “Geoffrey Ingram Taylor, 7 March 1886 - 27 June 1975,” *Biographical Memoirs of Fellows of the Royal Society*, vol. 22, pp. 565–633, Nov. 1976.

[23] E. Guazzelli, J. F. Morris, and S. Pic, *A Physical Introduction to Suspension Dynamics.* Cambridge: Cambridge University Press, 2011.

[24] Z. Gimbutas, L. Greengard, and S. Veerapaneni, “Simple and efficient representations for the fundamental solutions of Stokes flow in a half-space,” *Journal of Fluid Mechanics*, vol. 776, pp. R1–R1, 2015.

[25] G. Dal Maso, A. DeSimone, and M. Morandotti, “An Existence and Uniqueness Result for the Motion of Self-Propelled Microswimmers,” *SIAM Journal on Mathematical Analysis*, vol. 43, pp. 1345–1368, Jan. 2011.

[26] R. E. Johnson, "An improved slender-body theory for Stokes flow," *Journal of Fluid Mechanics*, vol. 99, pp. 411–431, July 1980.

[27] C. Pozrikidis, *Boundary Integral and Singularity Methods for Linearized Viscous Flow*. Cambridge: Cambridge University Press, 1992.

[28] R. Cortez, "The Method of Regularized Stokeslets," *SIAM Journal on Scientific Computing*, vol. 23, pp. 1204–1225, Jan. 2001.

[29] R. Cortez, L. Fauci, and A. Medovikov, "The method of regularized Stokeslets in three dimensions: Analysis, validation, and application to helical swimming," *Physics of Fluids*, vol. 17, p. 031504, Feb. 2005.

[30] B. Liu, K. S. Breuer, and T. R. Powers, "Helical Swimming in Stokes Flow Using a Novel Boundary-Element Method," *Physics of Fluids*, vol. 25, no. 6, 2013.

[31] K. Morozov and A. Leshansky, "The chiral magnetic nanomotors," *Nanoscale*, vol. 6, no. 3, pp. 1580–1588, 2014.

[32] J. Gray and G. J. Hancock, "The Propulsion of Sea-Urchin Spermatozoa," *Journal of Experimental Biology*, vol. 32, pp. 802–814, Dec. 1955.

[33] F. Alouges, A. DeSimone, L. Giraldi, and M. Zoppello, "Self-propulsion of slender microswimmers by curvature control: N-link swimmers," *International Journal of Non-Linear Mechanics*, vol. 56, pp. 132–141, Nov. 2013.

[34] N. Giuliani, L. Heltai, and A. DeSimone, "Predicting and Optimizing Microswimmer Performance from the Hydrodynamics of Its Components: The Relevance of Interactions," *Soft Robotics*, vol. 5, pp. 410–424, May 2018.

[35] Y. Man and E. Lauga, "The wobbling-to-swimming transition of rotated helices," *Physics of Fluids*, vol. 25, p. 071904, July 2013.

[36] K. E. Peyer, *Modeling and Optimization of Bio-Inspired Magnetically Actuated Swimming Microrobots*. PhD thesis, ETHZ, 2013.

[37] R. G. Cox, "The motion of long slender bodies in a viscous fluid Part 1. General theory," *Journal of Fluid Mechanics*, vol. 44, pp. 791–810, Dec. 1970.

[38] B. Rodenborn, C.-H. Chen, H. L. Swinney, B. Liu, and H. P. Zhang, "Propulsion of microorganisms by a helical flagellum," *PNAS*, vol. 110, no. 5, 2013.

[39] B. Liu, T. R. Powers, and K. S. Breuer, "Force-free swimming of a model helical flagellum in viscoelastic fluids," *Proceedings of the National Academy of Sciences*, vol. 108, pp. 19516–19520, Dec. 2011.

[40] S. Kim and S. J. Karrila, *Microhydrodynamics: Principles and Selected Applications*. Courier Corporation, 2013.

[41] K. B. Yesin, K. Vollmers, and B. J. Nelson, “Modeling and Control of Untethered Biomicrorobots in a Fluidic Environment Using Electromagnetic Fields,” *The International Journal of Robotics Research*, vol. 25, pp. 527–536, May 2006.

[42] M. P. Kummer, J. J. Abbott, B. E. Kratochvil, R. Borer, A. Sengul, and B. J. Nelson, “OctoMag: An Electromagnetic System for 5-DOF Wireless Micromanipulation,” *IEEE Transactions on Robotics*, vol. 26, pp. 1006–1017, Dec. 2010.

[43] H. Choi, J. Choi, G. Jang, J.-o. Park, and S. Park, “Two-dimensional actuation of a microrobot with a stationary two-pair coil system,” *Smart Materials and Structures*, vol. 18, p. 055007, Mar. 2009.

[44] Q. Cao, X. Han, B. Zhang, and L. Li, “Analysis and Optimal Design of Magnetic Navigation System Using Helmholtz and Maxwell Coils,” *IEEE Transactions on Applied Superconductivity*, vol. 22, pp. 4401504–4401504, June 2012.

[45] F. Meshkati and H. C. Fu, “Modeling rigid magnetically rotated microswimmers: Rotation axes, bistability, and controllability,” *Physical Review E*, vol. 90, no. 6, pp. 1–11, 2014.

[46] J. Gray, “Undulatory Propulsion,” *Journal of Cell Science*, vol. s3-94, pp. 551–578, Dec. 1953.

[47] J. Gray, “The Movement of Sea-Urchin Spermatozoa,” *Journal of Experimental Biology*, vol. 32, pp. 775–801, Dec. 1955.

[48] R. Dreyfus, J. Baudry, M. L. Roper, M. Fermigier, H. A. Stone, and J. Bibette, “Microscopic artificial swimmers,” *Nature*, vol. 437, pp. 862–865, Oct. 2005.

[49] T. Honda, K. I. Arai, and K. Ishiyama, “Micro Swimming Mechanisms Propelled by External Magnetic Fields,” *IEEE Transactions on Magnetics*, vol. 32, no. 5, pp. 5085–5087, 1996.

[50] M. A. Zeeshan, R. Grisch, E. Pellicer, K. M. Sivaraman, K. E. Peyer, J. Sort, B. Özkale, M. S. Sakar, B. J. Nelson, and S. Pané, “Hybrid Helical Magnetic Microrobots Obtained by 3D Template-Assisted Electrodeposition,” *Small*, vol. 10, no. 7, pp. 1284–1288, 2014.

[51] T.-Y. Huang, M. S. Sakar, A. Mao, A. J. Petruska, F. Qiu, X.-B. Chen, S. Kennedy, D. Mooney, and B. J. Nelson, “3D Printed Microtransporters: Compound Micromachines for Spatiotemporally Controlled Delivery of Therapeutic Agents,” *Advanced Materials*, vol. 27, no. 42, pp. 6644–6650, 2015.

[52] X.-Z. Chen, M. Hoop, F. Mushtaq, E. Siringil, C. Hu, B. J. Nelson, and S. Pané, “Recent developments in magnetically driven micro- and nanorobots,” *Applied Materials Today*, vol. 9, pp. 37–48, Dec. 2017.

[53] E. B. Steager, M. S. Sakar, C. Magee, M. Kennedy, A. Cowley, and V. Kumar, “Automated biomanipulation of single cells using magnetic microrobots,” *The International Journal of Robotics Research*, vol. 32, pp. 346–359, Mar. 2013.

[54] T.-Y. Huang, F. Qiu, H.-W. Tung, X.-B. Chen, B. J. Nelson, and M. S. Sakar, "Generating mobile fluidic traps for selective three-dimensional transport of microobjects," *Applied Physics Letters*, vol. 105, pp. 114102–114102, Sept. 2014.

[55] K. Bente, A. Codutti, F. Bachmann, and D. Faivre, "Biohybrid and Bioinspired Magnetic Microswimmers," *Small*, vol. 14, p. 1704374, July 2018.

[56] S. Palagi and P. Fischer, "Bioinspired microrobots," *Nature Reviews Materials*, vol. 3, pp. 113–124, June 2018.

[57] A. Servant, F. Qiu, M. Mazza, K. Kostarelos, and B. J. Nelson, "Controlled In Vivo Swimming of a Swarm of Bacteria-Like Microrobotic Flagella," *Advanced Materials*, vol. 27, pp. 2981–2988, May 2015.

[58] M. Medina-Sánchez, L. Schwarz, A. K. Meyer, F. Hebenstreit, and O. G. Schmidt, "Cellular Cargo Delivery: Toward Assisted Fertilization by Sperm-Carrying Micromotors," *Nano Letters*, vol. 16, pp. 555–561, Jan. 2016.

[59] X. Yan, Q. Zhou, M. Vincent, Y. Deng, J. Yu, J. Xu, T. Xu, T. Tang, L. Bian, Y.-X. J. Wang, K. Kostarelos, and L. Zhang, "Multifunctional biohybrid magnetite microrobots for imaging-guided therapy," *Science Robotics*, vol. 2, p. eaaq1155, Nov. 2017.

[60] A. Ghosh and P. Fischer, "Controlled Propulsion of Artificial Magnetic Nanostructured Propellers.," *Nano Letters*, vol. 9, pp. 2243–5, June 2009.

[61] L. Zhang, J. J. Abbott, L. Dong, B. E. Kratochvil, D. J. Bell, and B. J. Nelson, "Artificial Bacterial Flagella: Fabrication and Magnetic Control," *Applied Physics Letters*, vol. 94, no. 6, pp. 064107–064107, 2009.

[62] S. Tottori, L. Zhang, F. Qiu, K. K. Krawczyk, A. Franco-Obregón, and B. J. Nelson, "Magnetic helical micromachines: Fabrication, controlled swimming, and cargo transport.," *Advanced Materials*, vol. 24, pp. 811–816, Feb. 2012.

[63] J. Liu, T. Xu, Y. Guan, X. Yan, C. Ye, X. Wu, J. Liu, T. Xu, Y. Guan, X. Yan, C. Ye, and X. Wu, "Swimming Characteristics of Bioinspired Helical Microswimmers Based on Soft Lotus-Root Fibers," *Micromachines*, vol. 8, p. 349, Nov. 2017.

[64] A. W. Mahoney, N. D. Nelson, K. E. Peyer, B. J. Nelson, and J. J. Abbott, "Behavior of rotating magnetic microrobots above the step-out frequency with application to control of multi-microrobot systems," *Applied Physics Letters*, vol. 104, no. 14, pp. 1–5, 2014.

[65] S. Mohanty, A. Hong, C. Alcantara, A. J. Petruska, and B. J. Nelson, "Stereo Holographic Diffraction Based Tracking of Microrobots," *IEEE Robotics and Automation Letters*, vol. 3, pp. 567–572, Jan. 2018.

[66] J. Keller and S. Rubinow, "Swimming of Flagellated Microorganisms," *Biophysical Journal*, vol. 16, pp. 151–170, Feb. 1976.

[67] L. Alvarez, B. M. Friedrich, G. Gompper, and U. B. Kaupp, "The computational sperm cell," *Trends in Cell Biology*, vol. 24, pp. 198–207, Mar. 2014.

[68] M. A. Constantino, M. Jabbarzadeh, H. C. Fu, and R. Bansil, "Helical and rod-shaped bacteria swim in helical trajectories with little additional propulsion from helical shape," *Science Advances*, vol. 2, p. e1601661, Nov. 2016.

[69] A. Ghosh, P. Mandal, S. Karmakar, and A. Ghosh, "Analytical theory and stability analysis of an elongated nanoscale object under external torque," *Physical Chemistry Chemical Physics*, vol. 15, no. 26, pp. 10817–10823, 2013.

[70] K. I. Morozov, Y. Mirzae, O. Kenneth, and A. M. Leshansky, "Dynamics of arbitrary shaped propellers driven by a rotating magnetic field," *Physical Review Fluids*, vol. 2, p. 044202, Apr. 2017.

[71] J. J. Abbott, K. E. Peyer, M. C. Lagomarsino, L. Zhang, L. Dong, I. K. Kaliakatsos, and B. J. Nelson, "How Should Microrobots Swim?," *International Journal of Robotics Research*, vol. 28, pp. 1434–1447, July 2009.

[72] H. Gadêlha, "On the optimal shape of magnetic swimmers," *Regular and Chaotic Dynamics*, vol. 18, pp. 75–84, Apr. 2013.

[73] S. Walker and E. Keaveny, "Analysis of Shape Optimization for Magnetic Microswimmers," *SIAM Journal on Control and Optimization*, vol. 51, pp. 3093–3126, Jan. 2013.

[74] D. Walker, M. Kübler, K. I. Morozov, P. Fischer, and A. M. Leshansky, "Optimal Length of Low Reynolds Number Nanopropellers," *Nano Letters*, vol. 15, pp. 4412–4416, July 2015.

[75] U. K. Cheang, F. Meshkati, D. Kim, M. Kim, and H. C. Fu, "Minimal geometric requirements for nano- and micropropulsion via magnetic rotation," *Physical Review E*, vol. 033007, pp. 1–27, 2014.

[76] P. J. Vach, P. Fratzl, S. Klumpp, and D. Faivre, "Fast Magnetic Micropropellers with Random Shapes," *Nano Letters*, vol. 15, pp. 7064–7070, Oct. 2015.

[77] Y. Mirzae, O. Dubrovski, O. Kenneth, K. I. Morozov, and A. M. Leshansky, "Geometric constraints and optimization in externally driven propulsion," *Science Robotics*, vol. 3, p. eaas8713, Apr. 2018.

[78] S. L. Altmann, *Rotations, Quaternions, and Double Groups.* Courier Corporation, 2005.

[79] D. J. Dichmann, Y. Li, and J. H. Maddocks, "Hamiltonian Formulations and Symmetries in Rod Mechanics," *Mathematical Approaches to Biomolecular Structure and Dynamics, IMA Volumes in Mathematics and Its Applications*, vol. 82, pp. 71–113, 1996.

[80] Y. A. Kuznetsov, *Elements of Applied Bifurcation Theory.* No. 112 in Applied Mathematical Sciences, New York, NY: Springer, 3. ed ed., 2004. OCLC: 815949776.

[81] G. Strang, *Introduction to Linear Algebra.* Wellesley, Mass: Wellesley-Cambridge Press, 4th ed. ed., 2009.

[82] M. J. D. Powell, *Approximation Theory and Methods.* Cambridge University Press, 1981.

[83] A. Dhooge, W. Govaerts, Y. A. Kuznetsov, H. G. E. Meijer, and B. Sautois, "New features of the software MatCont for bifurcation analysis of dynamical systems," *Mathematical and Computer Modelling of Dynamical Systems*, vol. 14, pp. 147–175, Apr. 2008.

[84] W. Govaerts, Y. A. Kuznetsov, H. G. E. Meijer, B. Al-Hdaibat, V. D. Witte, A. Dhooge, N. Neirynck, A. M. Riet, and B. Sautois, "MATCONT: Continuation toolbox for ODEs in Matlab," tech. rep., 2018.

[85] N. Shamsudhin and A. J. Petruska, *Personnal Communication.* Mar. 2016.

[86] F. Meshkati and H. C. Fu, "Erratum: Modeling rigid magnetically rotated microswimmers: Rotation axes, bistability, and controllability [Phys. Rev. E **90** , 063006 (2014)]," *Physical Review E*, vol. 95, June 2017.

[87] L. F. Shampine and M. W. Reichelt, "The MATLAB ODE Suite," *SIAM Journal on Scientific Computing*, vol. 18, pp. 1–22, Jan. 1997.

[88] N. Chouaieb and J. H. Maddocks, "Kirchhoff's Problem of Helical Equilibria of Uniform Rods," *Journal of Elasticity*, vol. 77, pp. 221–247, June 2005.

[89] N. Chouaieb, A. Goriely, and J. H. Maddocks, "Helices," *Proceedings of the National Academy of Sciences*, vol. 103, no. 25, pp. 9398–9403, 2006.

[90] S. D. Chatterji, *Equations différentielles ordinaires et aux dérivées partielles*, vol. 3 of *Cours d'analyse.* Lausanne: Presses Polytechniques et Universitaires Romandes, 1998.

[91] A. Ben-Israel and Thomas N. E. Greville, *Generalized Inverses: Theory and Applications*, vol. 15 of *CMS Books in Mathematics.* New York: Springer, 2nd ed. ed., 2003.

[92] M. Roper, R. Dreyfus, J. Baudry, M. Fermigier, J. Bibette, and H. A. Stone, "On the dynamics of magnetically driven elastic filaments," *Journal of Fluid Mechanics*, vol. 554, pp. 167–190, Apr. 2006.

[93] E. E. Keaveny and M. R. Maxey, "Spiral swimming of an artificial micro-swimmer," *Journal of Fluid Mechanics*, vol. 598, pp. 293–319, Feb. 2008.

[94] T. R. Powers, "Dynamics of filaments and membranes in a viscous fluid," *Reviews of Modern Physics*, vol. 82, 2010.

[95] E. M. Strawbridge and C. W. Wolgemuth, "Surface traction and the dynamics of elastic rods at low Reynolds number," *Physical Review E*, vol. 86, Sept. 2012.

[96] R. Vogel and H. Stark, "Motor-Driven Bacterial Flagella and Buckling Instabilities.," *The European Physical Journal E*, vol. 35, Feb. 2012.

[97] G. Cicconofri and A. DeSimone, “Motion planning and motility maps for flagellar microswimmers,” *The European Physical Journal E*, vol. 39, p. 72, July 2016.

[98] L. Goyeau, R. Livanovičs, and A. Cēbers, “Dynamics of a flexible ferromagnetic filament in a rotating magnetic field,” *Physical Review E*, vol. 96, p. 062612, Dec. 2017.

Ce document a été imprimé au Centre d’impression EPFL,
imprimerie climatiquement neutre, certifiée myClimate.